2015

PREDICTION OF STRENGTH AND SHEAR MODULUS OF COMPACTED CLAYS WITHIN AN UNSATURATED CRITICAL STATE FRAMEWORK

Corrie Walton-Macaulay
University of Kentucky, cmacaulay@uky.edu

STUDENT AGREEMENT:

I represent that my thesis or dissertation and abstract are my original work. Proper attribution has been given to all outside sources. I understand that I am solely responsible for obtaining any needed copyright permissions. I have obtained needed written permission statement(s) from the owner(s) of each third-party copyrighted matter to be included in my work, allowing electronic distribution (if such use is not permitted by the fair use doctrine) which will be submitted to UKnowledge as Additional File.

I hereby grant to The University of Kentucky and its agents the irrevocable, non-exclusive, and royalty-free license to archive and make accessible my work in whole or in part in all forms of media, now or hereafter known. I agree that the document mentioned above may be made available immediately for worldwide access unless an embargo applies.

I retain all other ownership rights to the copyright of my work. I also retain the right to use in future works (such as articles or books) all or part of my work. I understand that I am free to register the copyright to my work.

REVIEW, APPROVAL AND ACCEPTANCE

The document mentioned above has been reviewed and accepted by the student's advisor, on behalf of the advisory committee, and by the Director of Graduate Studies (DGS), on behalf of the program; we verify that this is the final, approved version of the student's thesis including all changes required by the advisory committee. The undersigned agree to abide by the statements above.

Corrie Walton-Macaulay, Student

Dr. Sebastian Bryson, Major Professor

Dr. Yi-Tin Wang, Director of Graduate Studies

PREDICTION OF STRENGTH AND SHEAR MODULUS OF COMPACTED CLAYS WITHIN AN UNSATURATED CRITICAL STATE FRAMEWORK

DISSERTATION

A dissertation submitted in partial fulfillment of the
requirements for the degree of Doctor of Philosophy
in the College of Engineering
at the University of Kentucky

By:

Corrie Walton-Macaulay

Lexington, Kentucky

Director: Dr. L. Sebastian Bryson, Associate Professor of Civil Engineering

Lexington, Kentucky

2015

ABSTRACT OF DISSERTATION

PREDICTION OF STRENGTH AND SHEAR MODULUS OF COMPACTED CLAYS WITHIN AN UNSATURATED CRITICAL STATE FRAMEWORK

The objective of this research study is to determine whether the soil stiffness, from which the small-strain shear modulus is determined, can be used to predict the shearing resistance of compacted clay soil, which are invariably under conditions of partial saturation. The research program developed for this objective included three major soil testing programs of matric suction, shear modulus, and strength.

A method to estimate matric suction of field compacted clay soil was presented and it is based on the quantified effect of change in initial void ratio on the soil water characteristic behaviors. With the use of a non-nuclear soil stiffness gauge used in an incremental compaction laboratory scale model test (a field simulation), the nuclear footprint was eliminated when compared to the use of a nuclear density gauge typically used for soil compaction verification.

An enhanced void ratio function based on the effect of void ratio on shear modulus was developed using the resulting small-strain shear moduli determined from the use of the propagated shear waves in the laboratory scale model tests.

Simulating an as-compacted condition, which is generally during construction and for a limited time thereafter, within the soil strength program, plastic shear strains were shown to occur within the zone that is classically represented as a purely elastic zone. With the use of a flow rule to represent the occurrence of plastic shear strains within this zone a constitutive soil model was developed and presented that can use a field determined shear modulus parameter as input to predict the shearing resistance of the compacted clay soil.

KEYWORDS: Unsaturated Soil Mechanics, Compacted Clay, Soil-Water Characteristic Curve, Shear Modulus, Soil Stiffness, Shear Strength.

Corrie Walton-Macaulay
Student's Signature

May 6, 2015
Date

PREDICTION OF STRENGTH AND SHEAR MODULUS OF COMPACTED CLAYS WITHIN AN UNSATURATED CRITICAL STATE FRAMEWORK

By

Corrie Walton-Macaulay

Dr. L. Sebastian Bryson

Director of Thesis

Dr. Yi-Tin Wang

Director of Graduate Studies

To:

My father, the late Cyril Walton-Macaulay, I dedicate this work and the credential bestowned on me, Doctor of Philosophy, to you.

ACKNOWLEDGEMENTS

To Dr. Sebastian Lindsey Bryson. Wow, you are truly like a Dyson, a vacuum with cyclones that captures more 'dirt' than any other. Your ways have become my ways as if a brother. From a friend to an advisor like no other, a mentor and now a colleague and back to a friend, my druthers. We've come full circle in this short time, and the credentials I gained are for a lifetime. Now, I can thank you and blame you for talking me into this PhD thing. I appreciated your guidance through the processes of walking this tightrope string. Especially for allowing me to stick with unsaturated soils as we discussed options for redirection as time uncoils. We cut ties now, but whenever we see again, will be like coming home somehow.

I extend my gratitude to all my dissertation committee members, for your support has been like embers, still glowing hot even out of the fire. Dr. Kalinski, though not here at the end, your help was my dividend, and will keep paying as I transcend. They say patience is a virtue, Dr. Blandford. I'm glad there are six other heavenly virtues to award. Your keen awareness on my several completion date extensions, was cause for motivation. To you all, your patience these 5 years and 9 months is appreciated.

To all who helped me form and execute my research, thank you! To Jason Curd, thanks for your help with the laboratory scale model tests; To Manal Abdelsalam Salem, though we never spoke, your dissertation provided stoke; To Geocomp, Trautwein, and GDS, your customer support gets two thumbs up; To Dr. Laureano R. Hoyos, Dr. Y.P. Yao and Dr. Daichao Sheng, when I asked for help, your time was well spent, for you showed me what collaboration meant.

Dr. Reginald Souleyrette, even as an excellent researcher, you do care for students' success. Though you were not my advisor, I gained knowledge from you as it spews out like a geyser. You took time to edit my work, to assist with job prospects, and I can't forget your attempt to make me expresso.

Thanks to the Civil Engineering Department staff (current and past): Gene Yates for your technical, especially with electrical equipment, and assisting with much needed technical updates, and the daily morning newspaper; Shelia Williams for more so, your Christian faith and perspective on life, but also for routine tasks, that I didn't have to do, and much needed assistance with purchasing and return of equipment; Jim Norvell, I think there's one of you at every workplace, your incessant complaints of faculty put things in perspective for me, your technical assistance was much appreciated; Suzy Wampler, one word, overrides, you are a course registration queen, they tell me there's a course I can't take because of a prerequisite, ha, I say, I'll just talk to Suzy; and lastly, Miss Bettie, never had an issue with paycheck when receiving stipends through the CE department my first year, even though you wouldn't eat any of my far from healthy doughnuts, your warped and witty sense of humor made me laugh.

Thank you Dr. Joe Crabtree for the Friday doughnuts, just what a student needs.

To Dr. Isabel Gomez Gutierrez, no, no, no, that doesn't sound ok. I promise not to call you Dr., if you promise not to call that either. No handshakes, only big hugs for goodness sake. Five years working side by side, and now a friendship for a lifetime I abide. Thanks so much for your support and intellect discussions on soil mechanics over coffee, and your help with soil chemistry. Now that we both have our PhD's, a global collaboration is my decree.

Thanks to Mr. Sherron Jackson, Dr. Rana Johnson, and the Kentucky Council on Postsecondary Education for providing this education opportunity. Mr. Sherron Jackson, as you asked, I did not stop at being the first African American to be admitted to the Civil Engineering Program at the University of Kentucky to pursue a PhD, I completed the program and earned the PhD. I'm feeling pumped, as I 'trail blazed' in Kentucky. Thanks to the Council for the monetary support through the SREB fellowship. I extend my gratitude to the SREB, the University of Kentucky's Graduate school for their support, monetary and otherwise, and specifically to Ms. Anna Edwards, and Ms. Pat Bond.

Mmm mmm mmm, I would be remiss if I don't say that love transcends all. God knew to bless me with a wife that would sacrifice herself so that I can transcend. To my wife, Dana, it was a trying time, but somehow you stepped up with your support and loved me unconditionally. I love you more today, even though I said that yesterday. You ride, I ride! To my family, the kids, mom, sister, and in-laws, you were all in different ways motivation for completion.

TABLE OF CONTENTS

LIST OF TABLES

LIST OF FIGURES

1 INTRODUCTION

1.1 General Overview

The satisfactory performance of many engineering structures is dependent on the strength and stiffness of the soil beneath. Accurately predicting shear strength and stiffness of soils during or soon after construction is essential to its performance and to developing a better understanding of soil behavior.

Predictions of strength of soils are frequently made for the design of shallow foundation, drilled piers, individual or group piles, embankments, etc., when engineering calculations for bearing capacity, lateral earth pressures and slope stability, etc. are necessary.

Stiffness is a key material property used in geotechnical engineering to determine the resistance of soil to deformation by an applied external force. In geotechnical practices, the relationship of stress and strains are used more prominently than those of force and deformation. Stiffness is analogous to shear modulus, in that as stiffness is related to the applied force and resulting soil deformation, shear modulus is related to the applied shear stress and resulting shear strain, given a set of prescribed stress states. One such stress state is the stress condition associated with “working” strain (i.e. the range of stain levels generated under specific or intended service conditions). Another stress state is the stresses associated with the compaction condition of the soil matrix.

Compaction is the most common means in geotechnical engineering for increasing shear strength and shear modulus of fill material and subgrade soils. Typical fill and

construction specifications include requirements for compaction energy and moisture content. For a given energy, variations in moisture content produce different soil state conditions (i.e. void ratio) that in turn significantly affect the state of stresses, thereby the shear strength and shear modulus. By virtue of Proctor compaction theory, soil is placed at an optimum moisture content and a maximum dry density, which is invariably an unsaturated condition. Field data suggest that most compacted soils placed above the water-table never reach saturation and thus normally remain in an unsaturated state (Roberson, 2002). Therefore, understanding the behavior of such soil in an unsaturated state during and soon after construction is necessary for predicting performance.

This research included the use of unsaturated triaxial testing, which involved testing partially saturated soil under constant-water-content conditions to simulate the field as-compacted state. In addition, changes to the soil structure (via changes to the soil density) without variation of the water content were included in the testing regime to further simulate the field as-compacted state. Water content variations in subgrade soils are expected to change with time or over the life cycle of the structural system it supports. However, structural systems such as bridges, pavements, and culverts are often designed with drainage systems that considerably reduce the water content variation in subgrade soils. Thus, the variation of water content for an as-compacted soil state is minimal.

Quality assurance acceptance criteria for embankment fills and compacted subgrade soils support various mechanistic-empirical design procedures associated with structural systems, such as those for flexible pavements. These mechanistic-empirical procedures

require the input of mechanical properties for the soil and aggregates such as that of Young's modulus or shear modulus. The modulus of soil layers plays a key role in the overall quality and performance of a structural system. One approach to rapidly and directly assess soil modulus, is to do so under small-strain modulus tests. The relevance of using small-strain modulus tests is that they are a non-destructive way to assess soil condition in the field, and when used in the laboratory, they can reproduce similar results to those measured in the field (Gupta et al., 2007).

Some of the studies previously listed used seismic waves velocities of compression (P), or shear (S) wave to determine the small-strain Young or shear modulus respectively. This study furthers soil research into small-strain shear modulus by the use of seismic waves propagated by bender elements and by simulating cross-hole seismic tests. Quality assurance criteria for compaction conditions are currently based on a specified target dry density of soil in conjunction with a target optimum moisture content. This is typically assessed by use of a portable nuclear gauge. The licenses to allow the possession and use of these nuclear gauges are getting increasingly more expensive, and the current laws surrounding these gauges are cumbersome.

This study also considered the mechanical behavior of compacted clays within a critical state framework. The critical state framework is the use of triaxial tests to observe the behavior of soils where continued shear distortions occur without further changes in the mean effective stress, deviatoric stress, or specific volume. This study establishes a prediction model for estimating stiffness and strength under "working" strain (small strain), and physical conditions (compacted – unsaturated) within a critical

state framework. This model will help designers to better predict the strength and stiffness of compacted clays based on working or in-service conditions.

Figure 1.1 shows an example of the seasonal variation in the soil subgrade water content for a well-designed pavement structure for different soil types. The variation of moisture content is higher for sands, much less for silts and very minimal for clays. This may be an indication that clay type soils retain their initial conditions longer. This research thus presents an essential study of the experimental behavior and predictive performance of the behavior of clay type soils within an as-compacted state condition.

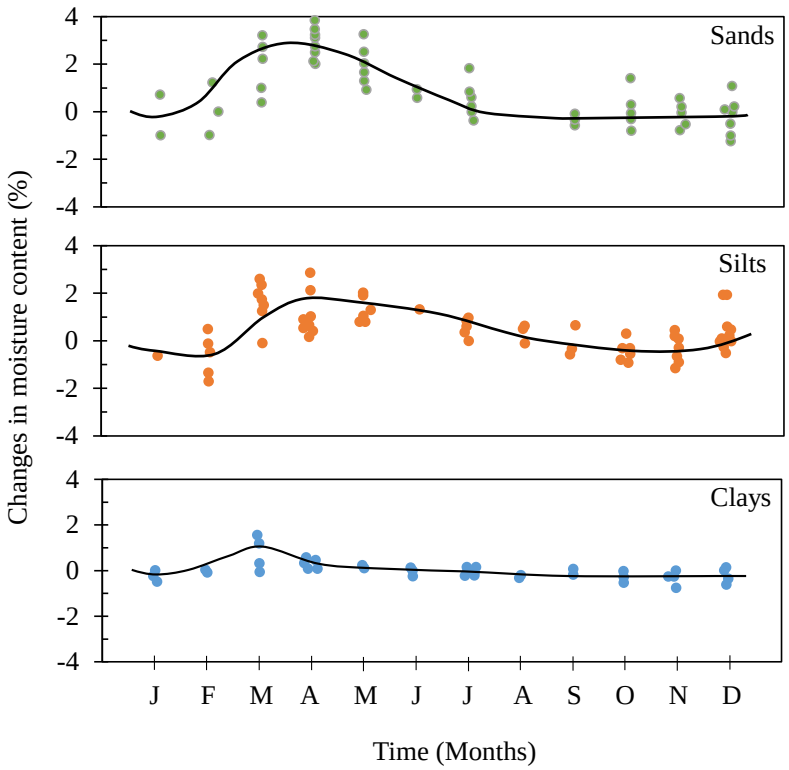

Figure 1.1 Seasonal subgrade water content changes in Pennsylvania (After Cumberledge et al., 1974).

1.2 Relevance of Research

1.2.1 Problem Statement

The licensing process of portable nuclear density gauges is becoming extremely difficult and bureaucratic. With this difficulty, the costs of licensing is also increasing. In the Commonwealth of Kentucky, the cost of licensing a portable moisture/density gauge is increasing from $390 per year to $1,300 per year starting this year, 2015. This is a 333% increase in cost of just the license to possess these gauges. Beyond licenses, the paper-trail requires companies to employ a person as a radiation safety officer to be abreast of all necessary documentations and trainings, such as posting employee notifications, employee monitoring, gauge leak testing, safety trainings and briefings, proper transportation, and the safe use of these gauges. In a New Mexico Technician Training and Certification Program in August, 2010, it was stated that the direct costs to the New Mexico Department of Transportation of having and using these nuclear gauges is about $1,031,024 for the past 5 years (2005 to 2009), which is over $200,000 per year.

In the year 2013, a nuclear gauge was lost in West Virginia, and believe to have fallen out of the back of a company pick-up truck. Similar events of lost or stolen nuclear gauges have occurred in many other States. It is believe that a few of these gauges can be used to make a ‘dirty’ bomb and therefore, raises national level security concerns with their uses.

1.2.2 Problem Solution

The need to reduce costs and bureaucracy associated with licensing, training and calibration of these nuclear gauges is critical. Portable non-nuclear gauges are becoming of more interest in the field determination of soil properties.

In the transportation industry, approximately 17 % of construction costs are allocated for subgrade preparation (Kishore and Abraham, 2009). It is essential that the final constructed product be as per the design. This study presents a method of using a simple, non-nuclear field test for soil stiffness, to predict the stress-strain response of compacted soils. To measure the soil stiffness, a Geogauge that measures the stiffness properties of soil layers by measuring the deflection resulting from surface small-stain vibrations at varying frequencies was employed.

There are two very critical states of compacted soil that are generally considered by civil engineers. These states are the as-compacted and post-compacted states. The as-compacted state represents the initial conditions during compaction and for a time thereafter where the moisture regime is considered unchanged or the change is still small enough that is does not affect the initial compaction state. The post-compaction state represents the in-service condition responding to climatic and environmental changes, which results in significant moisture and suction regime changes.

1.3 Objectives of Research

The main objective of this research is to characterize the shear and stiffness behavior of compacted clay soils within the framework of unsaturated soil mechanics and the critical state theory. The specific objectives designed to be studied are:

- Simulate a field test in the laboratory, the laboratory scale model, whereby the Geogauge can be used to determine stiffness/shear modulus at different degrees of compaction or density.
- Develop a shear wave velocity test within the laboratory scale model test to determine the small-strain shear modulus. Use the Hardin and Black (1968) equation for maximum shear modulus for comparison with the modulus obtained from the Geogauge tests, and determine if a new void ratio function is necessary under unsaturated conditions.
- Develop soil-water characteristic curves (SWCC) of the soils, in order to understand their behavior under different densities. Use the SWCC at different densities to develop a method based on the Zhou et al. (2012) model to predict the matric suction within the laboratory scale model test at different densities.
- Develop a triaxial test system to determine the volumetric, matric suction, and shear strength behavior of the soils with respect to an as-compacted state. Use embedded bender elements within the triaxial cell to measure the small-strain shear wave velocity of the soils within the triaxial system for saturated and unsaturated conditions. Compare the shear modulus values from the soil

stiffness Geogauge and the bender elements, and develop or modify a shear modulus equation to include the field determined shear modulus as an input parameter.

- Develop and verify a model for describing the stress strain response of an as-compacted soil using field obtained shear modulus as an input parameter.

1.4 Conceptual Overview

Figure 1.2 presents a conceptual overview of the research idea. Three overarching program processes were considered and used in this research. A soil suction program that resulted in the prediction of matric suction in the laboratory scale model tests and hence, the possibility of predicting matric suction in the field. A soil shear modulus program where three different methods of measuring shear modulus were employed. Two of the three methods (crosshole seismic and Geogauge) were used within the laboratory scale model program. The determined shear modulus from the crosshole seismic method was used to develop an enhanced void ratio function. The third method of measuring shear modulus was done with the use of bender elements within the unsaturated triaxial testing system. The overarching feature of the laboratory scale model tests is the comparison of the shear modulus from the Geogauge to that obtained from the bender element tests. This comparison led to the resulting modification of an existing shear modulus equation. The concept of the third program, the soil strength program, was to understand the volumetric and stress-strain behavior of clay soils tested under unsaturated triaxial conditions of constant-water content, which is a simulation of an as-compacted state. Finally, the concept included the possibility of presenting a model that

can incorporate a field test parameter (i.e., the determined shear modulus from the laboratory scale model test), to predict the volumetric, matric suction and stress-strain behavior of compacted clay soils.

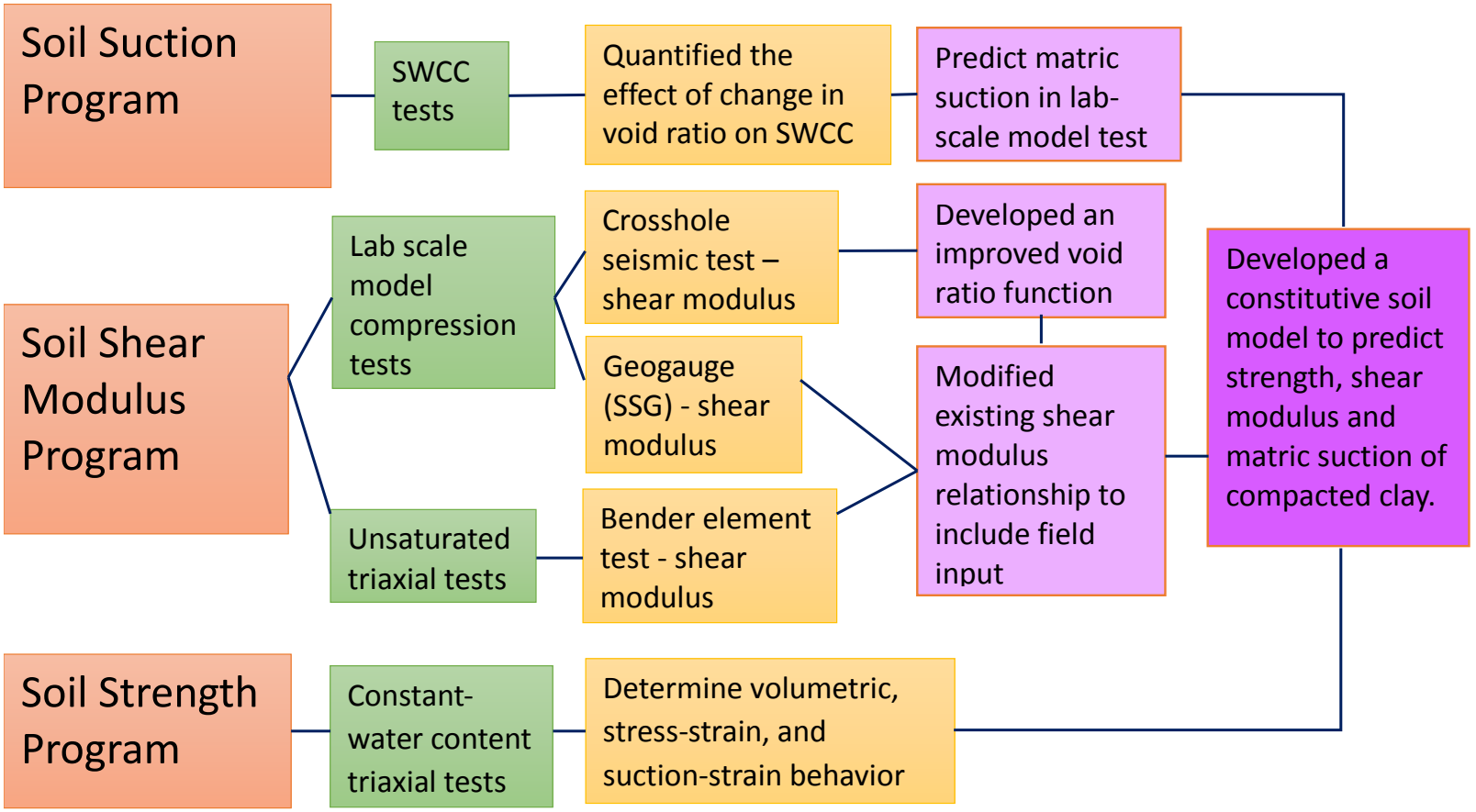

Figure 1.2 Conceptual overview of the research process.

1.5 Content of Dissertation

In the previous sections of Chapter 1, discussions for the reader to understand the necessity of this study were presented. Within the discussions, the behavior of unsaturated soil was paramount, and this specific study into unsaturated soils was therefore justified.

Chapter 2 delves into a technical background review of some of the factors that affect the behavior of unsaturated soil, and some controls that were used within this study to simulate those behaviors. Specifically, the factors reviewed that affect the behavior of unsaturated soils were: the state of stress, matric suction, and small-strain shear modulus. The controls that were used in this study to simulate soil behavior were the compaction conditions and the simulation of field loading. Different tests were performed using one or both of those controls. The technical background on controls centered on the SWCC and the triaxial testing, whereby the stress state variable(s) can be independently controlled.

In Chapter 3, the nature of the soils are presented, and the experimental program the soils were subjected to is discussed. The nature of the soils are characterized by index properties, and classified according to the Unified soil classification system. The experimental program is presented as three programs (suction, strength, and shear modulus) necessary to satisfactorily describe unsaturated soil properties.

Chapter 4 presents the results of the soil suction program. It exhibits the experimental SWCCs, a basic but necessary unsaturated soil property. An existing model

was used to extend the experimental data to the full range of matric suction. Using the full range of SWCCs for each soil, estimations of SWCC for changes in state conditions (void ratio) were validated using another existing model. The calibration of this model resulted in findings specific to a parameter of the model not yet presented in literature.

Chapter 5 presents the results and analyses of the shear modulus program from both the laboratory scale model tests, and the bender element tests. The effects of void ratio on the stiffness and shear modulus based on the use of the Geogauge are initially presented, following the effects of void ratio on shear wave velocities and shear modulus based on the simulation of field crosshole seismic tests. Analyses of shear wave velocities and shear modulus led to the development of a new void ratio function. Lastly, a method of estimation of matric suction at different compaction states due to increasing densities during a laboratory scale model test was developed using the developments from the SWCC analyses as discussed in Chapter 4. Chapter 5 also includes the experimental results and interpretation of the dynamic property behavior of the unsaturated soils, from bender element tests.

Chapter 6 presents the experimental results of the triaxial specimens subjected to constant-water content conditions of only isotropic compressions, and isotropic compressions and shear stages respectively. The triaxial specimens subjected only to isotropic compressions, presented in Section 6.1, were subjected to high compressive pressures to understand the true volumetric behavior and to try and obtain the volumetric stiffness parameters. Triaxial specimens subjected to the shear phase, as presented in

Sections 6.2 through 6.4, provided a means to understand the strength properties of unsaturated soils under different state conditions.

In Chapter 7, predictions of small-strain shear modulus were made based on the experimental results presented in Chapter 5, by modifying an existing shear modulus equation. Secondly, robust determination of two model parameters were presented. Finally, ideas from a few existing stress-strain constitutive models were used in conjunction with the observed behaviors of compacted soils in this study to develop a constitutive model that uses a field determine shear modulus to predict the stress-strain relationship.

Conclusions and recommendations are presented in Chapter 8, including the novel contribution based on this research study. Several Appendixes (A through J) are included as supplemental data to support the body of this dissertation.

2 TECHNICAL BACKGROUND OF UNSATURATED SOILS

2.1 Introduction

Chapter two delves into a technical background review of some of the factors that affect the behavior of unsaturated soil, and some controls that were used within this study to simulate those behaviors. Specifically, the factors reviewed that affect the behavior of unsaturated soils were: the state of stress, matric suction, and small-strain shear modulus. The controls that were used in this study to simulate soil behavior were the compaction conditions and the simulation of field loading. Different tests were performed using one or both of those controls. The technical background review on controls centered on the soil-water characteristic and the triaxial testing, whereby the stress state variable(s) can be independently controlled.

2.2 Soil Suction

The question, 'What is soil suction' has been extensively discussed in literature and can also be found in most available unsaturated soil textbooks. The basis of soil suction is therefore only presented in Appendix A.

2.2.1 Effects of compaction conditions on matric suction

The effects of compaction conditions on the matric suction $(u_a - u_w)$ of compacted soils have been investigated in several studies (Olson and Langfelder, 1965; Krahn and Fredlund, 1972; Fredlund and Rahardjo, 1993; Tsai and Petry, 1995; Wan et al., 1995; Bernier et al., 1997; Sivakumar and Wheeler, 2000; and Agus and Schanz, 2006). Data

reported in these studies regarding the effect of compaction conditions (e.g., compaction energy; moisture content; density, degree of saturation) on the matric suction appear to be contradicting, but were in agreement regarding the effect of water content on matric suction (i.e., matric suction increases/decreases as the water content decreases/increases, respectively).

The effect of water content on matric suction is known as the soil-water retention data, or the soil-water characteristic curve (SWCC) as it is generally known today. Quantifications (models) of the water retention property have also been presented by several authors (Ahuja and Swartzendruber, 1972; Endelman et al., 1974; Mualem, 1976; Haverkamp et al., 1977; van Genuchten, 1980; Fredlund and Xing, 1994). Detailed discussion of the water retention property and the van Genuchten, (1980) model is presented in Section 2.3.3, Estimation of matric suction.

Other researchers, (Croney and Coleman, 1954; Olson and Langfelder, 1965; Krahn and Fredlund, 1972; Fredlund and Rahardjo, 1993; Tsai and Petry, 1995; Wan et al., 1995; Bernier et al., 1997; Babour, 1998; Vanapalli et al., 1999; Sivakumar and Wheeler, 2000; and Agus and Schanz, 2006) all showed that the matric (or total) suction in compacted soils was highly dependent on the compaction water content and with very little to no dependency on the dry unit weight. The relationship shown in Figure 2.1 for Goose Lake clay taken from Olson and Langfelder (1965), is typical of the other relationships. Similarly, Croney and Coleman (1954) showed that a unique relationship may exist between the matric suction and the water content regardless of the state of soil

structure. Mou and Chu (1981) showed that at water contents dry of optimum, matric suction increased significantly, with only a slight decrease in the water content.

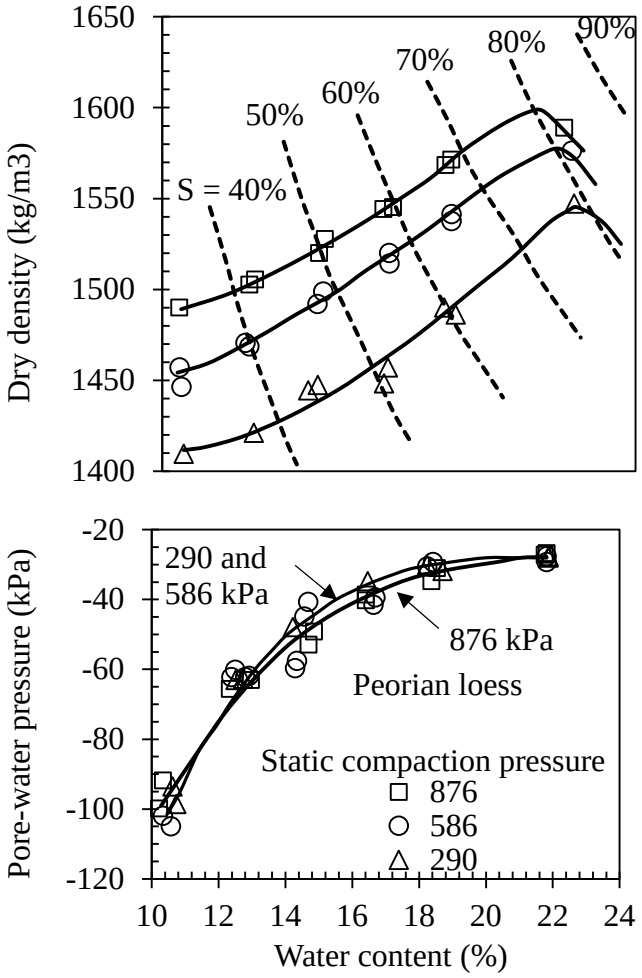

Figure 2.1 Effect of compaction water content and dry unit weight on matric suction for compacted Goose Lake clay (After Olson and Langfelder, 1965).

Gonzalez and Colmenares (2006) showed contours of constant suction on Proctor compaction curves and matric suction measurements as shown in Figure 2.2. The suction contours were nearly vertical at low dry unit weights, but at high dry unit weights, they generally showed some dependency with negative trends. At moisture contents around and above the standard Proctor optimum water content, the suction contours showed signs of asymptotic behavior to the 100% degree of saturation line. The authors therefore

concluded that the influence of the water content on matric suction is very clear, though some influence of the dry unit weight and even lesser influence of the compaction technique (static or dynamic) may exist.

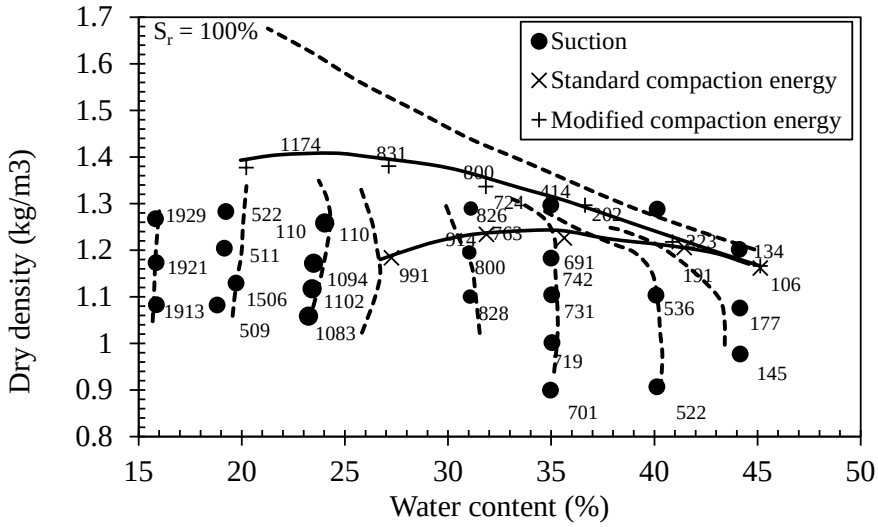

Figure 2.2 Proctor compaction curves, initial compaction water content and dry unit weight of tested specimens, and suction contours (After Gonzalez and Colmenares, 2006).

As the latter study by Gonzalez and Colmenares (2006) showed some influence on dry unit weight at high unit weights, Shackel (1973) also stated that the matric suction depended primarily on the degree of saturation but with a slight dependency on the dry unit weight.

Contradicting reports were found on past studies regarding the effect of the compaction dry unit weight on the matric suction at a constant water content. Yong (1980) observed that there was a single soil-water potential surface (total suction), that describes the relationship between the water content, dry unit weight, and soil-water potential for a given soil. Mou and Chu (1981) stated that matric suction increased, though slightly, for increasing unit weights when compacted at higher unit weights and at

the same water contents; but Sudhakar and Revanasiddappa (2003) stated that for a given water content, the matric suction decreased for increasing compaction dry unit weight. The effect of the compaction dry unit weight and degree of saturation on the matric suction was investigated by Sudhakar and Revanasiddappa (2000) and Gonzalez and Colmenares (2006). In both studies, the authors agreed that at a constant dry unit weight, the matric suction decreased with an increase in the compaction degree of saturation; and at a constant degree of saturation, the matric suction increased with an increase in the compaction dry unit weight as shown in Figure 2.3.

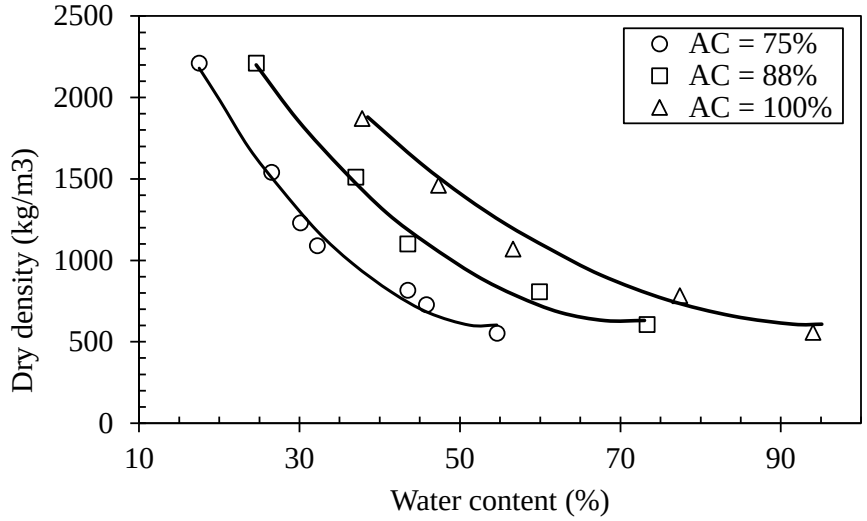

Figure 2.3 Effect of compaction degree of saturation and dry unit weight on the matric suction (After Gonzalez and Colmenares, 2006).

Figure 2.4, shows the influence of soil texture, consolidation and compaction on the SWCC of soil from Barbour (1998) and Vanapalli et al., (1999). The SWCC in Figure 2.4, are presented on a degree of saturation versus soil suction plots. Figure 2.4(a) shows that soil suction increases with increasing soil texture (smaller pores due to increasing plasticity: Sand < Botkin silt < Indian Head till < Regina clay), at a given degree of saturation. Similarly, the increasingly smaller pores resulting from increasing

consolidation stresses and soils compacted with increasing initial moisture contents from dry to wet of optimum Proctor, results in increasing soil suction at a given degree of saturation. These effects are shown in Figures 2.4(b) and 2.4(c) for consolidation and compaction respectively.

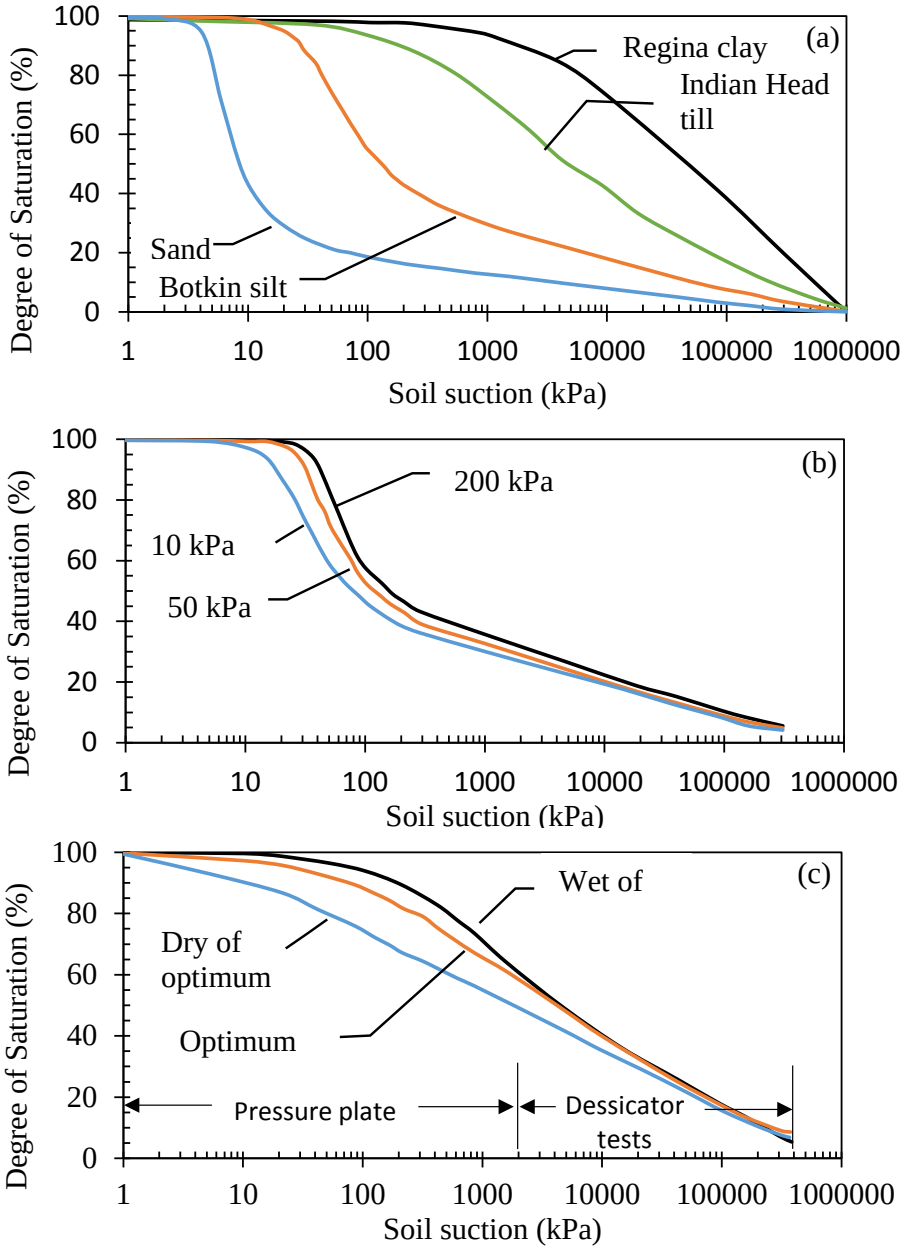

Figure 2.4 Influence of (a) soil texture; (b) consolidation; and (c) compaction on the water retention properties of soil (After Delage, 2002; Barbour, 1998; and Vanapalli et al., 1999).

Romero et al. (2011) considered the effects of porosity on the water retention properties, by applying matric suctions, following wetting paths, to soil specimens at different void ratio. Instead of using water content, the parameter water-ratio, $e_w = wG_s = Se$, was used, where, w, G_s, s, and e represents the gravimetric water content, specific gravity, degree of saturation, and void ratio, respectively. The water ratio e_w, describes the amount of water in compacted soils (Toll, 1995), because of its idealism in describing the adsorptive mechanisms. Figure 2.5 shows the water retention properties for three soils, which indicate that the effects of void ratio (hence porosity) on matric suction (or the water retention property) is negligible at higher matric suction, but is clearly distinguishable at lower matric suction. Romero et al. (2011), deduced that the effect of void ratio at low matric suction is due to the higher stored water being high enough to be able to saturate the micropores (pores inside the aggregate or intra-aggregate pores). In a wetting path, the intra-aggregate pores will become saturated first before water begins to be stored in the macropores.

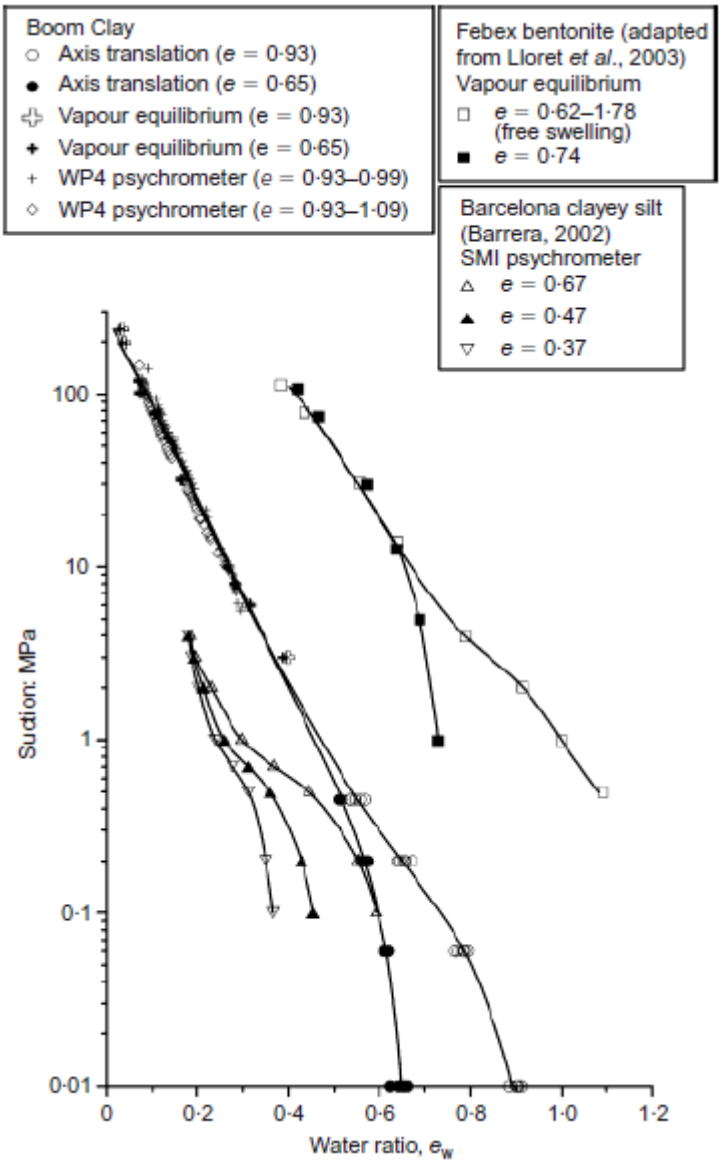

Figure 2.5 Wetting paths on three materials compacted on the dry side of optimum (Boom Clay, Febex bentonite and Barcelona clayey silt) at different void ratios (Romero et al., 2011)

Edil and Motan (1979), Edil et al. (1981), and Motan and Edil (1982) investigated the effects of compaction moisture content, degree of saturation, and suction on mechanical properties of subgrade soils. The authors proposed that the matric suction is a fundamental parameter in characterizing the moisture state. They further proposed that the matric suction may be a better determinant, (than compaction moisture content or

degree of saturation alone), of the effects of soil type and fabric, compaction, climatic variation, and fluctuation of groundwater table on the mechanical behavior of soils. Finally, they suggested that matric suction, in addition to the compaction moisture content should be used as a required basic soil moisture parameter for pavement subgrade quality control and performance evaluation. Therefore, this study provides a method for estimation of matric suction from field or laboratory test data of moisture content and density, whereby the degree of saturation and void ratio can be determined and used in the estimation process.

2.2.2 Estimation of matric suction

The SWCC usually refers to the hydraulic property of the soil, whereby only the changes in water content during desorption or adsorption are accounted for, i.e., the initial total volume is assumed to be constant. When the soil undergoes volume change during desorption/adsorption, the mechanical behavior becomes important. In lieu of using the water content in the SWCC relationship, the degree of saturation can be used which can represent the hydraulic and/or the mechanical behavior. The degree of saturation references the volume of water to the instantaneous volume of voids, and therefore requires a measurement of the instantaneous total volume of the soil, though it does not quantify overall volume change (Fredlund et al., 2012).

A number of closed-form, empirical relationships for SWCC to best fit laboratory data are present in literature (Brooks and Corey, 1964; Brutsaert, 1967; Laliberte, 1969; Campbell, 1974; van Genuchten, 1980; McKee and Bumb, 1984, 1987; Fredlund and

Xing, 1994; Pereira and Fredlund, 2000; Pham and Fredlund, 2005). The Brooks and Corey (1964), van Genuchten (1980), and the Fredlund and Xing (1994) models are commonly used, and they are listed in Table 2.1.

Table 2.1 Commonly Used Empirical Equations to Best Fit Soil Water Retention Data

Reference	Model	Description
Brooks and Corey (1964)	$w(\psi) = w_s$ or $\Theta_n = 1$ for $\psi \le \psi_{aev}$ $\Theta_n = \left[\frac{\psi}{\psi_{aev}}\right]^{-\lambda_{bc}}$ where $\Theta_n = \frac{w(\psi) - w_r}{w_s - w_r}$	ψ = matric suction; ψ_{aev} = air-entry value of soil; λ_{bc} = pore size distribution index; w_r = residual water content; w_s = saturated water content; $w(\psi)$ = water content at any given value of matric suction; and Θ_n = Normalized water content
Van Genuchten (1980)	$\Theta_n = \frac{1}{\left[1 + (a\psi)^n\right]^m}$ where $\Theta_n = \frac{w(\psi) - w_r}{w_s - w_r}$	Θ_n = Normalized water content; a = fitting parameter primarily related to inverse of air-entry value; n = fitting parameter primarily related to rate of water extraction from soil once air-entry value has been exceeded; m = fitting parameter primarily related to residual water content; ψ = matric suction; w_r = residual water content; w_s = saturated water content; and $w(\psi)$ = water content at any given value of matric suction
Fredlund and Xing (1994)	$\Theta_d = \frac{w(\psi)}{w_s} = C(\psi)\frac{1}{\left\{\ln\left[e + (\psi/a)^n\right]\right\}^m}$ where $C(\psi) = 1 - \frac{\ln(1 + \psi/\psi_r)}{\ln\left[1 + (10^6/\psi_r)\right]}$	Θ_d = Normalized water content; a = fitting parameter primarily related to the air-entry value; n = fitting parameter primarily related to rate of water extraction from soil once air-entry value has been exceeded; m = fitting parameter primarily related to residual water content; $C(\psi)$ = correction factor related to suction corresponding to residual water content; ψ = matric suction; ψ_r = residual matric suction.

Zhou et al., (2012) stated that the air-entry value is a very inaccurate measure of the experimental suction threshold where the soil becomes saturated. The van Genuchten (1980), and the Fredlund and Xing (1994) models do not use this air-entry threshold suction., However, it is very difficult to rearrange the Fredlund and Xing (1994) model to solve for matric suction, because it uses a correction factor that extends the range of suction beyond residual suction to completely dry condition.

Though the Fredlund and Xing (1994) model provides a better description of the soil-water characteristic curve over a wide range of suction (Leong and Rahardjo, 1997), the van Genuchten (1980) was selected for use in this study as it provides additional flexibility to the soil-water characteristic curve (Fredlund et al., 2012).

The van Genuchten (1980), and the Fredlund and Xing (1994), models are similar since the difference in the Fredlund and Xing (1994) is the modification of the pore-size distribution function, and that the SWCC is forced through the point $w(\psi) = w\left(10^6\right) = 0$. The fitting parameters have the same meaning. Van Genuchten (1991), stated that the stability of the SWCC curve is improved by using a fixed relationship for the m, and n parameters as suggested by the hydraulic conductivity relationship by Mualem (1976) as follows:

$$m = 1 - \frac{1}{n} \tag{2.1}$$

2.2.3 Suction-saturation-density relationship

In an attempt to show the effect of mechanical behavior on the SWCC of soils, Zhou et al. (2012) quantified the effect of initial density on the SWCC of unsaturated soils. A change in soil density is a common feature of compacted soils. A change in density can lead to significant changes in the SWCC (Assouline, 2006). Using changes in the void ratio, e, to represent changes in density, Zhou et al. (2012) used an incremental approach to simulate the relationship between degree of saturation, S, and void ratio, e, under an arbitrary suction s, such that:

$$\frac{dS}{de} = f(s,e) \tag{2.2}$$

In Equation (2.2), $f(s,e)$ is a general function of suction and void ratio. Assuming that only the macroscopic degree of saturation is effected by a change initial density, whereas the microscopic degree of saturation is assumed to equal the residual degree of saturation, S^{res}, and independent of the initial density, Zhou et al. (2012), derived the constrained, such that:

$$-\frac{S_e}{e} \le \frac{dS}{de} \le \frac{1-S_e}{e} \tag{2.3}$$

In Equation 2.3, S_e is the effective degree of saturation, which is a function of the residual degree of saturation, S^{res}, such that:

$$S_e = \frac{S - S^{res}}{1 - S^{res}} \tag{2.4}$$

The volume change in this case is due only to a change in stress, with the suction being constant. Under conditions of hydraulic behavior of the SWCC, the void ratio in the constraint of Equation 2.3, is the initial saturated void ratio at the start of a drying test. Based on the above reasons, Zhou et al., (2012) proposed the incremental relationship between the degree of saturation and the initial void ratio, e_i, to describe the effect of the initial density on the SWCC:

$$\frac{dS_e}{de_i} = -\frac{S_e}{e_i}(1-S_e)^{\zeta} \tag{2.5}$$

In Equation (2.5), ζ is a fitting parameter. A reference state, such as the reference degree of saturation, S^{ref}, at a reference initial void ratio, e_i^{ref}, is necessary to solve Equation (2.5) by integration. Any SWCC can be used as the reference state. Rearranging and integrating Equation (2.5) yield the following:

$$\int_{e_i^{ref}}^{e_i} -\frac{de_i}{e_i} = \int_{S_e^{ref}}^{S_e} \frac{dS_e}{S_e(1-S_e)^{\zeta}} \tag{2.6}$$

For simplicity, the Simpson's rule for numerical approximation of the definite integrals was employed to the right side of Equation (2.6) to obtain an approximate closed-form equation as follows:

$$\int_{e_i^{ref}}^{e_i} -\frac{de_i}{e_i} = \ln\frac{e_i^{ref}}{e_i} \approx \frac{\left(S_e - S_e^{ref}\right)}{6}\left[f\left(S_e^{ref}\right) + 4f\left(\frac{S_e^{ref}+S_e}{2}\right) + f\left(S_e\right)\right] \tag{2.7}$$

In Equation 2.7, the general function terms $f(\,)$, are expressed as:

$$f(x) = \frac{1}{x(1-x)^{\zeta}} \tag{2.8}$$

The Equation (2.6), adds only one new parameter, ζ, that can be taken as a soil-specific constant (Zhou et al., 2012) (i.e. it changes only with soil type). To determine the new parameter, the model must be calibrated using two soil-water characteristic curves. The first is the reference SWCC, and it is estimated from experimental data using one of the water retention models (such as van Genuchten, 1980). The second is the calibration SWCC, performed at a different initial void ratio (from the reference SWCC), and used to calibrate the new fitting parameter, ζ. With the new fitting parameter, the calibrated model is then used to determine the SWCC at any selected initial void ratio.

Using experimental results from other researchers, Zhou et al. (2012) determined the ζ parameters for each soil type as presented in Table 2.2. Reviewing the ζ parameters presented in Table 2.2 for different soil types, no definitive trend was noted with soil type.

This study shows that though the ζ parameter does not correlate well with soil type, it correlates with the n parameter of the van Genuchten (1980) SWCC model. Further analyses of the ζ-parameter indicate that this parameter may not be a material property, but may depend on the state of stress on the sample, the condition of the specimen, or the shape of the SWCC as discussed in Chapter 4 of this dissertation.

Table 2.2 Calibrated ζ parameters using the Zhou et al. (2012) model.

Study	Soil Type	Reference initial void ratio	Range of initial void ratio	ζ parameter
Huang et al. (1998)	Silty sand	0.525	0.525-0.426	0.2
Aubertin et al. (1998)	Tailings	0.802	0.802-0.695	0.5
Romero (1999)	Boom clay	0.93	0.93-0.33	0.37
Vanapalli et al. (1999)	Compacted till	0.517	0.517-0.444	0.03
Salager et al. (2010, 2011)	Clayey sand	1.01	1.01-0.44	0.1
Tarantino (2009)	Barcelona silt	0.62		0.05
		0.54		
		0.5		

The soil suction-saturation-density relationship review presented above gives insight into the state of stress response of soil, a mechanical behavior. The dynamic behavior of soil, specifically, the small strain shear modulus response is also a very important property of compacted soil and is discussed in the following section.

2.3 Small Strain Shear Modulus

The small-strain shear modulus parameter, $G_{\max}$, is essential in measuring or predicting the dynamic response of soils, for the design and the analysis of both the static and dynamic soil‐structure interactions, liquefaction assessments, and soil improvement control (Lee and Santamarina, 2005; Biglari et al., 2012). The shear modulus is a relationship between shear stress and shear strains and is synonymous with stiffness, which is the relationship between force and deformation, given a set of boundary conditions on the soil matrix.

2.3.1 Background of small strain shear modulus for saturated soils

Hardin and Black (1968) presented a functional relationship indicating various quantities that may have an effect on the elastic small-strain shear modulus:

$$G = f\left(\sigma_0', e, H, S, \tau_0, C, A, f, t, \theta, T\right) \tag{2.9}$$

In Equation (2.9), σ_o' is the effective mean principle stress (octahedral normal stress); e is the void ratio; H is the ambient stress and vibration history; S is the degree of saturation; τ_0 is the octahedral shear stress; C is the particle characteristics, particle shape, size, grading, and mineralogy; A is the strain amplitude; f is the vibration frequency; t is the secondary effects that are functions of time and magnitude of load increment; θ is the soil structure; T is the temperature including freezing.

The prevalent effects of some of these various quantities by Hardin and Black (1968) were further developed by Hardin and Black, (1968, 1969), and Hardin (1978), and the respective relationships for shear modulus presented as follows:

$$G = A(T)OCR^k\ f(e)\left(\sigma_0'\right)^n \tag{2.10}$$

$$\frac{G_{\max}}{p_a} = S\ f(e)OCR\left(\frac{p'}{p_a}\right)^n \tag{2.11}$$

In Equations (2.10) and (2.11), $A(T)$, and S are a dimensionless stiffness material constant coefficient, $f(e)$ is a void ratio function that describes increasing G or $G_{\max}$ with decreasing void ratio, k is a power exponent for the OCR, n is a power exponent

for the mean normal stress (approximately 0.5), p_a is atmospheric pressure, and p' is the mean effective stress. The Hardin (1978) presented the Equation (2.11) expression for soils under isotropic stress conditions. These equation indicates that increases in OCR and the effective stress, and decreases in e lead to increases in the shear modulus for the void ratio function presented by Hardin and Black (1968) as:

$$f(e) = \frac{(2.97 - e)^2}{1 + e} \tag{2.12}$$

The Hardin and Black (1968) void ratio function is based on a relationship determined by Hardin and Richart (1963), relating the shear wave velocities, V_s, with the void ratio, e, and hydrostatic confining pressure, $\bar{\sigma}_0$, for angular grained soils. Hardin (1965) presented the shear wave relationship as follows:

$$V_s = (159 - 53.5e)\bar{\sigma}_0^{1/4} \tag{2.13}$$

Using elastic theory, which is approximately valid at small strains, the shear modulus can be expressed in terms of total density, ρ, (which is a function of the total mass M_t to the total volume V_t), by the relationship as follows:

$$G = \rho V_s^2 = \left(\frac{M_t}{V_t}\right) V_s^2 = \frac{M_t}{1 + e} V_s^2 \tag{2.14}$$

Substituting Equation (2.13) into Equation (2.14), results as follows:

$$G = \frac{M_t (159 - 53.5e)^2 \bar{\sigma}^{1/2}}{1+e} \tag{2.15}$$

Knowing the total mass, Hardin (1965) presented the equation for the resulting dynamic shear modulus, G_d, as follows:

$$G_d = \frac{(30.09 - 10.12e)^2}{1+e} \bar{\sigma}_0^{1/2} \tag{2.16}$$

Factoring out the void ratio multiplier value of 10.12, the Hardin and Black (1968) void ratio function given by Equation (2.12), is then defined within the shear modulus equation as follows:

$$G_d = \frac{[10.12(2.973 - e)]^2}{1+e} \bar{\sigma}_0^{1/2} \tag{2.17}$$

The factored constant of $(10.12)^2$ is then attributed as part of the material constant coefficient, $A(T)$ in Equation (2.10). Empirical equations for estimating the small-strain shear modulus, G, are usually based on void ratio, e (Kawaguchi and Tanaka, 2008). Generally, with increases in the mean effective stress, p', the void ratio decreases, as is especially true in normally consolidated clay soils. Therefore, the void ratio function $f(e)$, is also a function of the mean effective stress.

Regarding the overconsolidation ratio, OCR, Jamiolkowski et al. (1994) suggested that its influence on the small-strain shear modulus is diminished, if the proper void ratio function is chosen. If the $f(e)$ is dependent on p' and OCR has minimal effect on G,

then, the shear modulus G, may be directly dependent only on the mean effective stress p'. It should be noted that with increases in p' for an overconsolidated soil, OCR decreases as it is a ratio of the current stress to a past maximum stress. Therefore, its effect on G diminishes as p' increases.

The determination of small-strain shear modulus has been extended into unsaturated soils states, empirically and theoretically, by considering the effects of matric suction as further discussed herein.

2.3.2 Background of small strain modulus for unsaturated soils

Several studies have used the Hardin and Black (1968) relationship for small-strain shear modulus, and extended it into conditions for unsaturated soils, by relating it to one stress state variable, matric suction, $(u_a - u_w)$ or both stress state variables of matric suction $(u_a - u_w)$ and net mean stress $(p - u_a)$.

A few examples of studies that considered only the matric suction stress state variable are Mendoza et al. (2005) and Oh and Vanapalli (2009). These researchers considered only the effect of suction on small-strain modulus, because the hydraulic behavior of sands were under investigation.

Other studies that considered the effects of both stress state variables (Mancuso et al., 2002; Vassalo et al., 2007; Ng and Yung, 2008; Khosravi and McCartney, 2009; Sawangsuriya et al., 2009). The soil types used in these studies varied widely. Mancuso et al. (2002) used silty sand with a plasticity index (PI) of 13.7; Vassalo et al. (2007) used

clayey silt with a PI of 17.9; Ng and Yung, (2008) used clayey silt with a PI of 14; Khosravi and McCartney, (2009) used literature data involving soil types of clayey sand, lean clay, silt, and a silt with high plasticity; and Sawangsuriya et al., (2009) used five types of fine-grained soils ranging from a clayey sand to a fat clay with PI ranging from 9 for a lean clay to 52 for the fat clay. The verification of their model indicate that in regards to stress state variables, the shear modulus is dependent on both the net mean stress and the matric suction stress state variables. The shear modulus is also dependent on the void ratio or a function of void ratio as suggested by Hardin and Black (1968).

Mancuso et al. (2002), in realizing that the soil fabric resulting from compaction and the molding water content, presented a set of equations to represent the small-strain shear modulus G_0, along different stages of suction. The resulting equations are shown in Table 2.3

Vassalo, et al. (2007), realized that suction significantly affected the shear modulus, whereby the shear modulus versus net mean stresses have similar slopes, but shifts upwards with different constant suctions. Vassalo et al. (2007) therefore incorporated a shifting parameter that quantifies how much the curves shifts for changes in suction. The resulting equation is shown in Table 2.3.

Table 2.3 Some small-strain shear modulus relationships in literature

Mancuso et al. $\frac{G_0}{p_{atm}} = A\left[\frac{(p-u_a)}{p_{atm}}\right]^n OCR \qquad s = 0$ $\frac{G_0}{p_{atm}} = A\left[\frac{(p-u_a)+s}{p_{atm}}\right]^n OCR^m \qquad s \le s_{ev}$ $G_0 = (G_0)_{s^*}\left\{[1-r]e^{-\beta(s-s^*)} + r\right\} \qquad s > s_{ev}$	p_{atm}, is the atmospheric pressure; s is the matric suction; s_{ev} is the suction at air-entry; s^* is the suction value that characterizes the transition between bulk-water regulated behavior and menisci-water regulated behavior; β, is the parameter that controls the rate of increase of soil stiffness with increasing suction; and r is the ratio between the shear stiffness at s^*, and the threshold value of G_0 for increasing suction.
Vassalo et al., (2007) $\frac{G_0}{f(e)\,p_{atm}} = S\left[\frac{(p-u_a)}{p_{atm}}\right]^n + F(u_a - u_w)$	The $F(u_a - u_w)$ function, quantifies the shift in the normalized shear modulus curve for different values in suction.
Ng and Yung, (2008) $G_{0(ij)} = S_{ij}F(e)\left[\frac{(\sigma_i - u_a)}{p_r}\times\frac{(\sigma_j - u_a)}{p_r}\right]^n\left[1+\frac{(u_a-u_w)}{p_r}\right]^{2bij}$ where $F(e) = \frac{[f(e)]^2(G_s + S_r e)}{1+e}; \qquad S_{ij} = C_{ij}^2\rho_w$	$F(e)$ may be considered as a function of void ratio relating shear modulus to void ratio; S_{ij} is a material constant reflecting soil fabric; and p_r is a reference pressure.
Sawangsuriya et al., (2009) – 2 Models $(G_{o,us})_{hh} = A\,f(e)(\sigma_o - u_a)^n + C\Theta^\kappa(u_a - u_w)$ $(G_{o,us})_{hh} = A\,f(e)\left[(\sigma_o - u_a) + \Theta^\kappa(u_a - u_w)\right]^n$	C and κ are fitting parameters; and Θ is the normalized volumetric water content

Ng and Yung (2008) considered the anisotropy of compacted soils. Since the test specimens were subjected to isotropic compression tests in a triaxial system, the anisotropy considered is a structural or initial anisotropy that exists by how the material was formed, (in this case, axial compaction), which is an inherent (fabric) anisotropy, and not a stress or evolving anisotropy that depends on subsequent anisotropic stress-strain

changes that some soils may be subjected to (e.g. as in a triaxial shear stage). This led to the concept that fabric anisotropy can cause changes in the ratio of shear wave velocities of which both are propagated in the same direction i, (say horizontally), but one is polarized in vertical plane j, and the other in the horizontal plane, i. The resulting equation is shown in Table 2.3.

Sawangsuriya et al. (2009) presented two models for shear modulus. The first model is based on two parts: the first of which is based on the Hardin and Black (1968) relationship where the net normal stress variable is expressed in terms of a power of the net confining pressure; and the second by a relationship by Oleo and Fredlund (1998) relating resilient modulus to matric suction. The second model utilized the Bishop (1959) relationship for a single-valued effective stress variable based on the effective stress principle for unsaturated soils. This single-valued effective stress is incorporated into the Hardin and Black, (1968) relationship, as the net normal stress variable, thereby extending the Hardin and Black (1968) relationship into unsaturation soil conditions. The relationships for small-strain shear modulus presented by Sawangsuriya et al. (2009) is shown in Table 2.3.

In this study, both stiffness and shear wave velocity measurements were used to determine the small-strain shear modulus. The stiffness was measured by use of a GeoGauge and the theory and background of the GeoGauge is presented in Section 2.3.6 of this dissertation. Shear wave velocity measurement were measured by means of simulating a field crosshole seismic testing in the laboratory and by use of piezoelectric transducers (Bender elements). The second shear modulus model presented by

Sawangsuriya et al. (2009), which uses the Bishop (1959) single-value effect stress, was used to predict shear modulus data for comparison with those obtained by the crosshole seismic testing. The crosshole seismic testing and Bender element testing are further discussed in Sections 2.3.3, and 2.3.4 respectively of this dissertation.

2.3.3 Seismic cross-hole shear wave test

There are various methods in literature to determine the shear modulus, and the common methods are listed in Table 2.2.

Table 2.4 Some existing methods to determine soil shear modulus.

Direct Field Methods	***Laboratory Methods***
Seismic Reflection Method	Cyclic Triaxial Compression Test
Seismic Refraction Method	Resonant Column Test
Seismic Cross-Hole Shear Wave Test	Bender Element Test
Seismic Downhole, Uphole Method	
Spectrum Analysis of Surface Wave Technique (SASW)	
Indirect Field Methods	
In Situ Measurement	
Hardin's Empirical Equation	

Hight and Higgins (1995), and Jardine (1995), presented the following factors that affect ground and structure movements:

- Site conditions
- Construction details
- Ground characteristics (mechanical properties)

- Stress-strain behavior
- Shear strength and yield criteria
- Permeability

The Crosshole Seismic Testing is a site specific measure of site conditions to determine the stiffness or shear modulus of ground profile. This is a field testing method, whereby two or three bore-holes are drilled, shear waves are generated at a selected elevation in one of the bore-holes and the transmitted wave through the soil is received by geophones placed at the same elevation in the other hole(s), as shown in the schematics of Figure 2.6.

The travel time t, of the shear waves, starting from the point at which the wave was generated to the point at which the signal was received (i.e., the travel distance, L) are measured and used to calculate the shear wave velocity as follows:

$$V_s = \frac{L}{T} \tag{2.18}$$

The shear modulus can then be determined from the shear wave velocity, V_s, with its relationship to the total density, ρ, as follows:

$$G = \rho V_s^2 \tag{2.19}$$

This method is typically used as a site-specific determination of compression and shear wave velocities for the determination of the dynamic elastic moduli for the various soil layers that can be encounter in field. This field seismic method of measurement of

shear wave velocity was simulated in the laboratory scale model tests performed for this research.

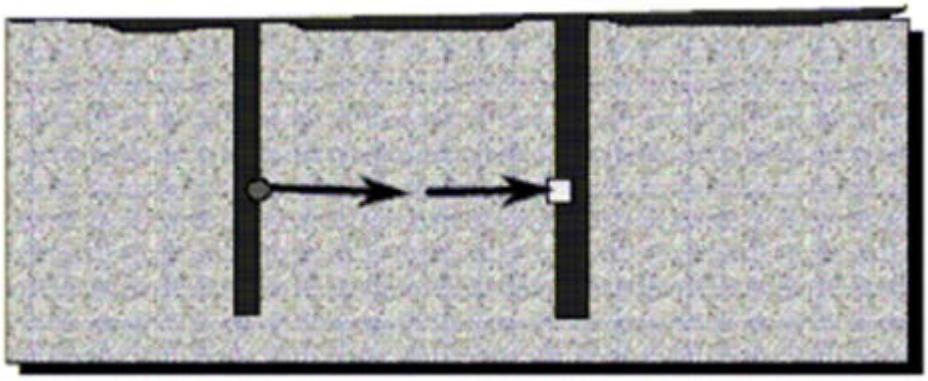

Figure 2.6 Seismic Cross-Hole Shear Wave Test (Kramer, 1996)

2.3.4 Measurements using piezoelectric transducers (Bender elements)

It is believed that Shirley and Hampton (1978) first introduced bender elements for shear wave generation in soil tests (Lee and Santamarina, 2005). It has since been used extensively in soils laboratory testing such as oedometers, torsional resonant columns, and triaxial cells (Dyvik and Madshus, 1985; Thomann and Hryciw, 1990; Agarwal and Ishibashi, 1991; Fam and Santamarina, 1995; Viggiani and Atkinson, 1995a, 1995b; Brignoli et al., 1996; Gajo et al., 1997; Rampello et al., 1997; Shibuya et al., 1997; Jovicic and Coop, 1997; Cabarkapa et al., 1999; Lohani et al., 1999; Blewett et al., 2000; Pennington et al., 2001; Callisto and Rampello, 2002; Mohsin and Airey, 2003; Theron et al., 2003; Leong et al., 2005, 2006; Valle, 2006; Ng and Yung, 2008; Yamashita et al., 2009; Alvarado and Coop, 2012; and Rees et al., 2013.)

Upon application of a voltage across the element, the two piezoelectric plates bend in the same direction by elongating and shortening respectively, thereby generating shear

waves at the free end (Strassburger, 1982). Additional instrumentation required for experimental testing with Bender elements are the function generator, the amplifier, the oscilloscope, and a computer, as shown in the schematics of Figure 2.7. The function generator produces the excitation signal; the amplifier then makes the signal stronger (amplifies) prior to transmission; the oscilloscope allows for the display of both the source and received signals, and also allows for noise reduction of the received signal by stacking (averaging method), if digital; and the computer can be used for storage and analysis of the received and recorded waves (Agarwal and Ishibashi, 1991; Brignoli et al., 1996). A similar setup was used in this research.

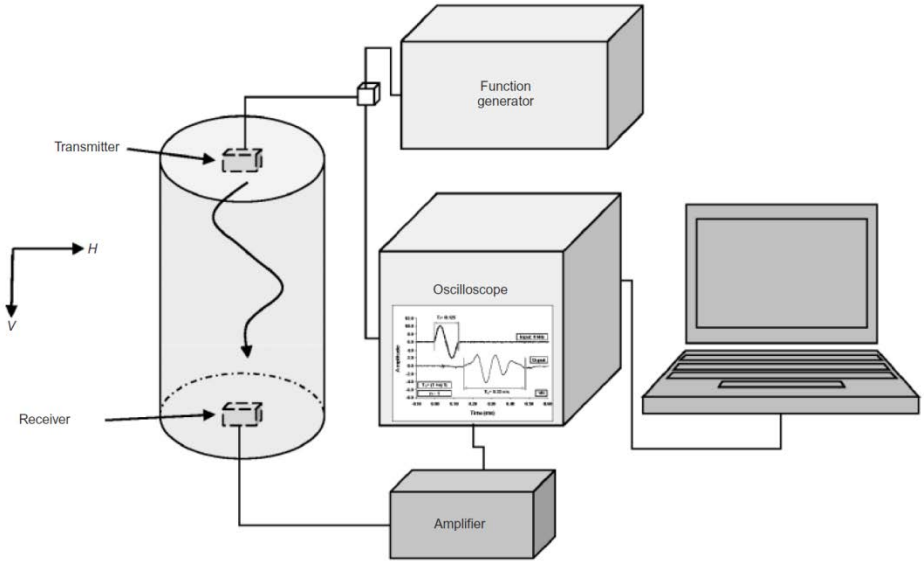

Figure 2.7 Bender element set-up for measurement of shear wave velocities in triaxial test (After Alvarado and Coop, 2012).

2.3.5 Travel time methods of estimation (Cross correlation, Characteristic Points)

Shear wave travel time estimation can be categorized into two methods; the time-domain and the frequency domain methods. There are generally two techniques applied in the time-domain method; observation of characteristic points of the source and

received Bender element signals, or the cross-correlation of the signals, whereas the frequency domain method involves a cross-power spectrum calculation of the signals (Yamashita et al., 2009).

Based on estimates of travel time from parallel tests in the frequency and time domains, there is more variability in the travel times using the frequency domain, therefore the use of time domain methods are recommended (Yamashita et al., 2007). Though the time-domain method is recommend, the techniques of observation, in the determination of the arrival times using the time domain is controversial. The controversial recommendations and criteria vary depending on the installation, the application and the input signal (Abbiss, 1981; Dyvik and Madshus, 1985; Mancuso et al., 1989; Fam and Santamarina, 1995; Viggiani and Atkinson, 1995a, 1995b; Jovicic et al., 1996; Santamarina and Fam, 1997; Blewett et al., 1999; Lohani et al., 1999; and Kawaguchi et al. 2001). Figure 2.8, shows the varying recommended points of time of arrival on a received signal.

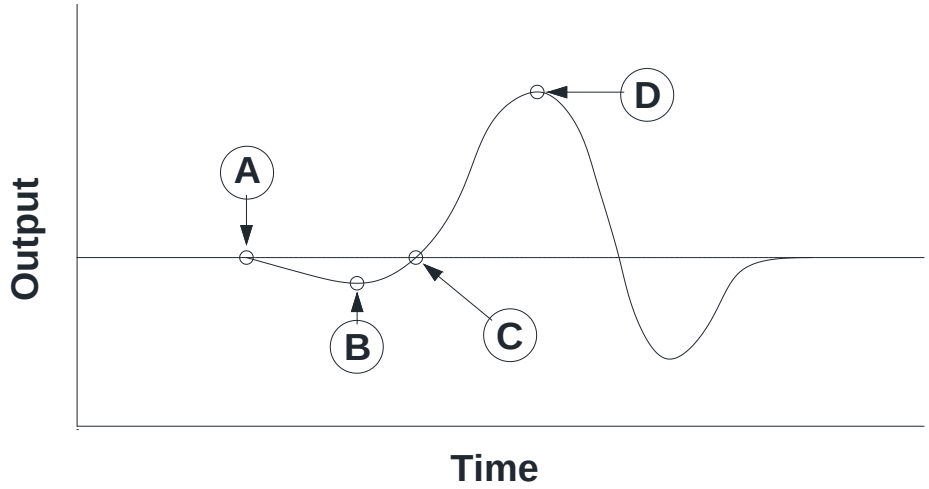

Figure 2.8 Idealized received shear wave signal showing the characteristic points (After Lee and Santamarina, 2005)

2.3.5.1 Characteristic point technique

The observations of characteristic points are usually done visually, but Rees et al., (2013), suggests that these techniques should be automated as is usually done for the cross-correlation technique, to reduce the subjectivity in analyzing the travel time.

The observation of characteristic points includes the (A) first arrival, (B) first trough, (C) zero crossing, and (D) first peak points, as was shown in Figure 2.8. The travel time determined using the first arrival of the received wave has been defined as the time between the start of the source signal and the first significant excursion in the received signal that has the proper polarity (Brignoli et al., 1996). However, the travel time for the other characteristic points does not include the start of the source signal, but is the distance between the start of a similar characteristic point in the source wave to its occurrence in the received wave, as shown in Figure 2.9. Therefore, travel time estimated from characteristic points other than first arrival, must have the same nature form of the source and received signal waves. Travel time estimates based on observation of characteristic points have been used extensively in literature (Manke and Gallaway, 1966; Sanchez-Salinero et al., 1986; Thomann and Hryciw, 1990; Marinho et al., 1995; Brignoli et al., 1996; Gajo et al., 1997; Jovicic and Coop, 1997; Shibuya et al., 1997; Cabarkapa et al., 1999; Lohani et al., 1999; Pennington et al., 2001; Callisto and Rampello, 2002; Theron et al., 2003; Jung, 2005; Leong et al., 2005; Puppala et al., 2006; and Valle, 2006).

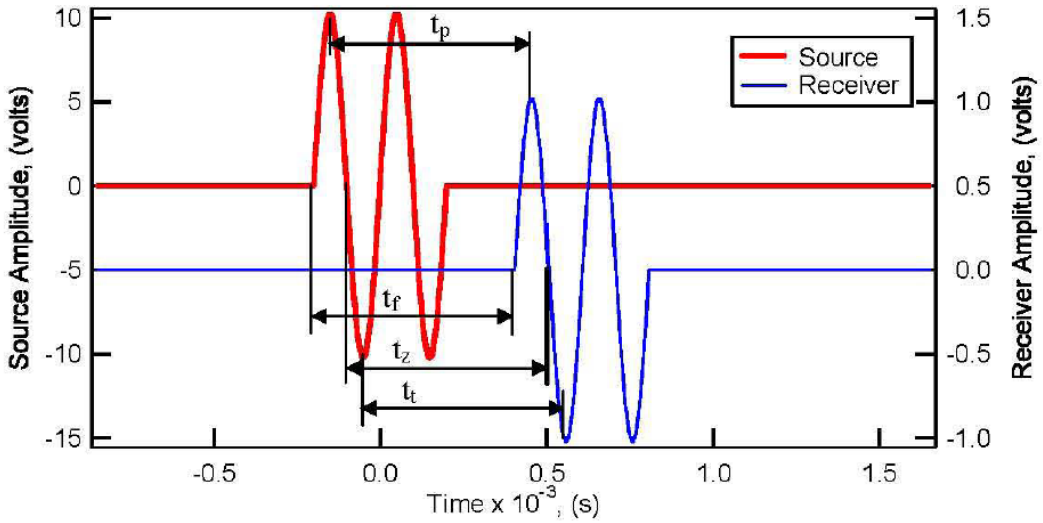

Figure 2.9 Travel times using first arrival (tf) and characteristic points: first peaks (tp), first troughs (tt), and zero crossings (tz) (Salem, 2006).

2.3.5.2 Cross-correlation technique

Cross-correlation has also been extensively used in literature to determine the travel time of transmitted and received signals (Woods, 1978; Sanchez-Salinero et al., 1986; Viggiani and Atkinson, 1995a; Gajo et al., 1997; Santamarina and Fam, 1997; Mohsin and Airey, 2003; Lee and Santamarina, 2005; and Leong et al., 2005.

Using the source and received signal recorded on the same time scale, each point on the two signals are multiplied and the results summed for the entire time record, t, to constitute one point in the cross-correlation sequence. The second point on the cross-correlation sequence is obtained by first shifting the received signal by an increment Δt on the time record, whereby the cross-correlation sequence will consists of $(2n-1)$ data points if n is the number of data points on each of the transmitted and received signal for the time record. After the shift, each point on the signals are again multiplied and summed to constitute the second point in the cross-correlation sequence. This process is

repeated for $(2n-1)$ shifts of the transmitted signal. The travel time is then the time between the maximum peak amplitude and the zero-lag (mid-point, at the n^{th} shift) time on the cross-correlation sequence, as shown in Figure 2.10.

Using the maximum peak amplitude in the cross correlation sequence corresponds well with the travel time if the transmitted and received signals were of the same nature form. In the event the signals are not of the same nature (e.g. sinusoidal), then any one of the peaks may correspond better to the travel time, than the maximum peak, therefore a visual observation of the peak that would correspond best to the correct travel time is necessary.

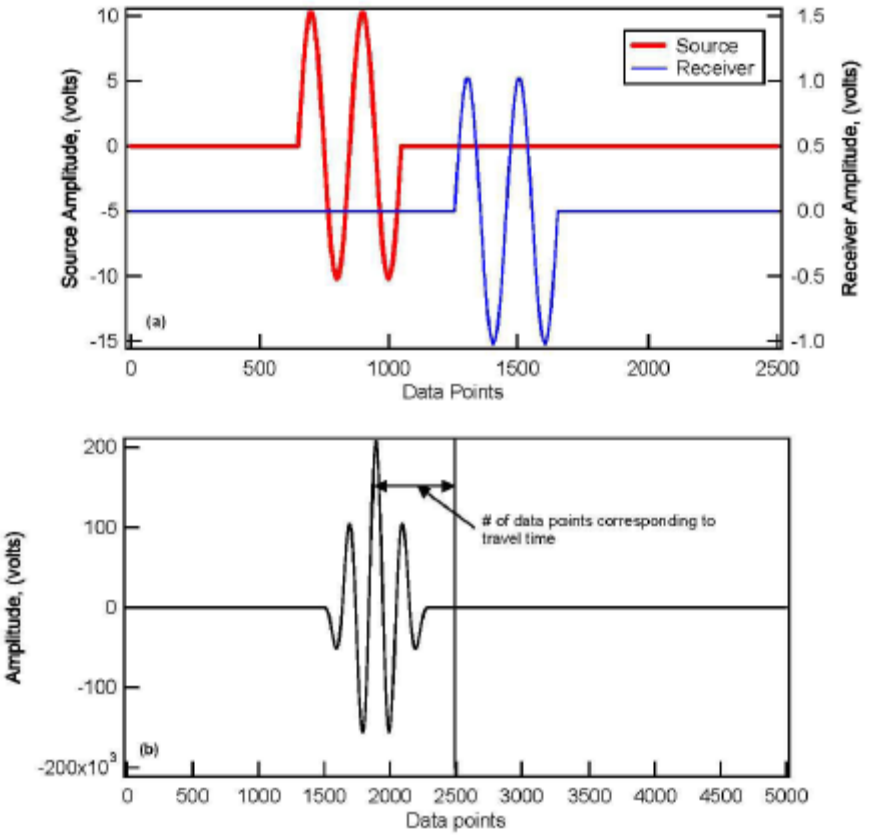

Figure 2.10 (a) Transmitted and received waveforms and (b) cross-correlation sequence (Salem, 2006).

2.3.6 Background, theory and field measurements using the GeoGauge.

The GeoGauge is manufactured by Humboldt Manufacturing Company, headquartered in Elgin, Illinois, USA. It is generally used as an in-situ, non-destructive field measure of soil stiffness and modulus of soil. At frequencies ranging from 100 to 196 Hz, and displacements less than 1.27 x 10^{-3} mm, the GeoGauge measures soil stiffness and modulus at the surface by imparting very small displacements to the soil on an annularly loaded ring through a harmonic oscillator, while operating over 25 steady state frequencies (Humboldt, 2007).

Many current methods of measuring material modulus or lift stiffness in the field require large forces to produce a measurable deflection. The GeoGauge imparts very small frequency controlled vibratory loads that produce small changes in force, and uses advanced technology to measure the very small deflections. The soil deflects an amount δ, which is proportional to the applied load P. The applied load P, is therefore equivalent to the deflection δ, multiplied by a stiffness factor K. The stiffness of the soil can therefore be determined based on the ratio of the force to displacement, as follows:

$$K = \frac{P}{\delta} \tag{2.20}$$

Based on the similarities of the GeoGauge tests with plate load tests, the Young's modulus and shear modulus can be similarly determined. When the Poisson's ratio v of the soil is known (or assumed), the Young's modulus E, and shear modulus G, can be determined from the stiffness relationship as follows:

$$K = \frac{P}{\delta} = \frac{1.77RE}{\left(1-\nu^2\right)} \approx \frac{3.54RG}{\left(1-\nu\right)} \tag{2.21}$$

In Equations (2.21), R is the outside radius of the ring foot. The assumptions associated with Equations (2.21), are that the underlying soil is (1) linear elastic, (2) homogeneous, (3) isotropic, and (4) in an infinite half-space. The assumptions of homogeneity, isotropy, and elasticity are considered to be valid for applications involving geomaterials under conditions of small operating strains. The GeoGauge produces soil stress levels common for many pavement and foundation applications, which are around 27.6 kPa (Humboldt, 2007).

2.3.7 Effects of soil properties on small-strain shear modulus

There are several studies in literature that have investigated the effects of compacted soil properties such as water content, dry unit weight, degree of saturation, compaction energy and technique on the small strain shear modulus, shear wave velocity or stiffness for unsaturated soils (Stephenson, 1978; Wu et al., 1984; and Qian et al., 1991; Lenke et al., 2001; Ooi and Pu, 2002, 2003; Inci et al., 2003; D'Onforio and Penna, 2003; Edil and Sawangsuriya, 2005; Sawangsuriya et al., 2006; Ng et al., 2009; Biglari et al., 2012; Clayton, 2011).

Regarding the effect of as-compacted water content on the shear modulus, literature gives contradicting data on the point of occurrence of a peak or maximum shear modulus, if any. Ooi and Pu (2002, 2003) showed that the maximum stiffness was achieved at an

as-compacted water content that is dry of the standard Proctor optimum moisture content, for tests subjected to the same compaction effort as shown in Figure 2.11(a).

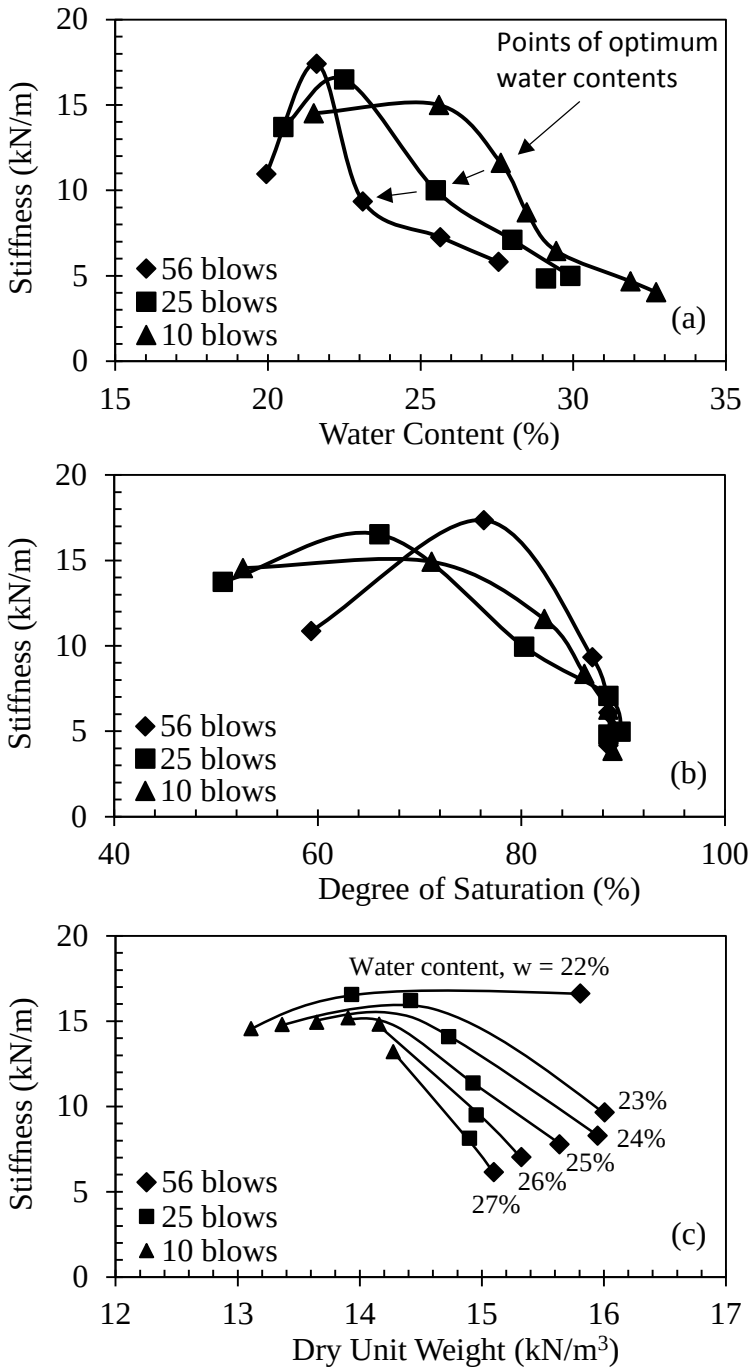

Figure 2.11 The effect of soil properties (a) water content, (b) degree of saturation, and (c) dry unit weight on soil stiffness of compacted silt. (After Ooi and Pu, 2003).

D'Onforio and Penna (2003) showed that for specimens compacted at the same compactive effort, the maximum shear wave velocity was achieved at an as-compacted water content that is on or close to the standard Proctor optimum moisture content. Similarly, Lenke et al. (2001) varied water content on specimens compacted at the same compactive effort and found a maximum or peak in the soil stiffness, but stated that the peak does not necessarily coincide with the optimum moisture contents, but was found to vary with soil type. However, Inci et al. (2003) and Sawangsuriya et al. (2006) showed that the shear modulus generally increased as the compaction water content decreased. Sawangsuriya et al. (2006) indicated this trend of increasing shear modulus with decreasing water content to be true for the range of water contents between $\pm 4\%$ of the standard Proctor optimum water content as shown in Figure 2.12.

It should be noted that though Lenke et al. (2001) only varied the water content, the dry unit weight would also change for the other specimens compacted with the same compaction effort, but at different moisture contents, as dry unit weights would change along a Proctor curve.

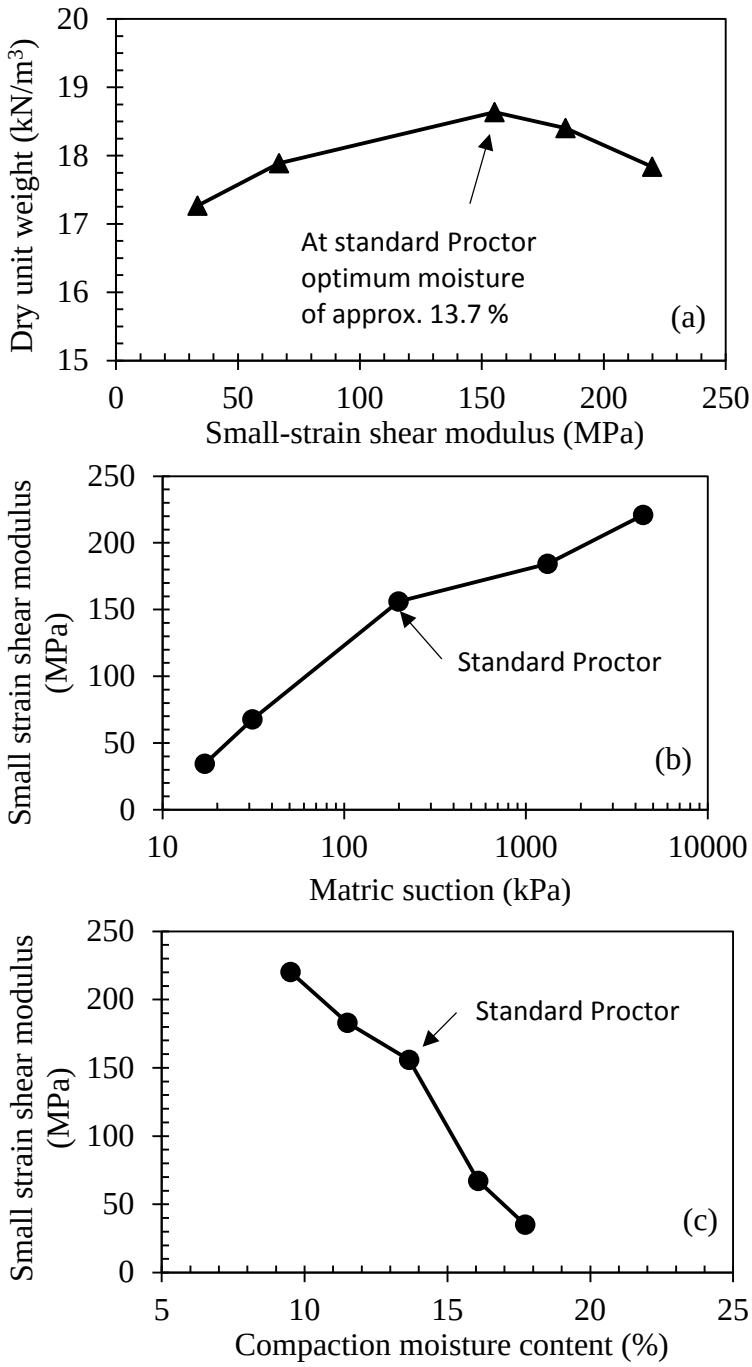

Figure 2.12 Results of stiffness testing on compacted clayey sand: (a) dry unit weight versus shear modulus; (b) effect of matric suction on shear modulus; and (c) effect of compaction water content on shear modulus. (After Sawangsuriya, 2006).

Regarding the effect of compaction dry unit weight on the shear modulus or stiffness, literature also gives contradicting data as to a definitive trend. Using void ratio

to show the changes in unit weight, Stephenson (1978) and Clayton (2011) showed that the test results of shear modulus increased with decreasing void ratio. Similarly, Edil and Sawangsuriya, (2005), show that shear modulus increased with increasing dry unit weight for several different soil types. Data from Clayton (2011) is shown in Figure 2.13. Data from Ooi and Pu (2002, 2003) as shown in Figure 2.11(c) show that for changes in dry unit weight at constant moisture content, the stiffness first increases slightly as dry unit weight increases to a peak state, then decreased at a very high rate for further increases in dry density. However, Sawangsuriya et al. (2006) determined that there is no conclusive trend or effect of dry density on the shear modulus, as can be seen in Figure 2.12(a).

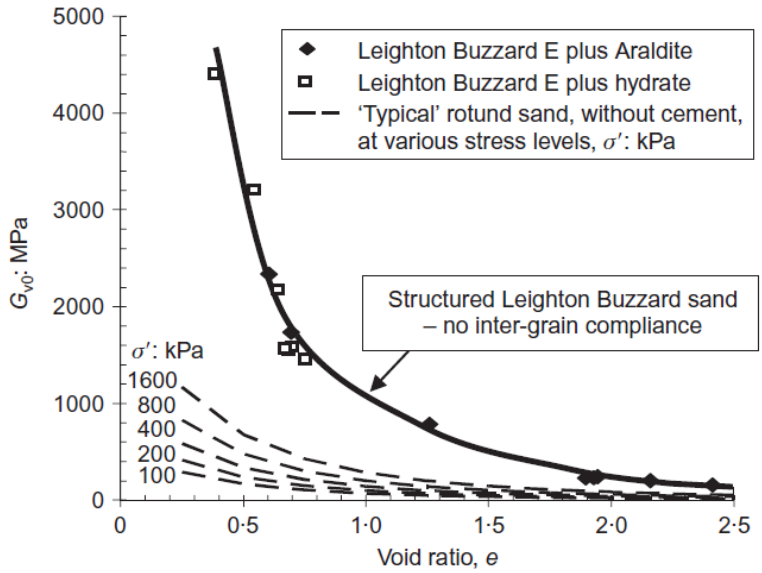

Figure 2.13 Effect of void ratio on cemented Leighton Buzzard fraction E sand (After Clayton, 2011)

Regarding the effect of the degree of saturation on the shear modulus, a review of literature shows an agreement in observed trends. In agreement, and at constant void ratio, data from Wu et al., (1984) and Qian et al., (1991), as shown in Figures 2.14 and 2.15, respectively, indicate that the shear modulus initially increased with increasing

degree of saturation, to maximum values at increasing degree of saturation between 5 and 20%, after which the shear modulus decreases. Also, in agreement, data from Ooi and Pu, (2002, 2003), as shown in Figure 2.11(b), indicate similar trends, but with the maximum shear modulus (or shear modulus ratio), at degrees of saturation between 65 and 80 %. The wide variation in the degree of saturation at which the maximum shear modulus occurs, can be attributed to the differences in soil type, but more so to the state of compaction.

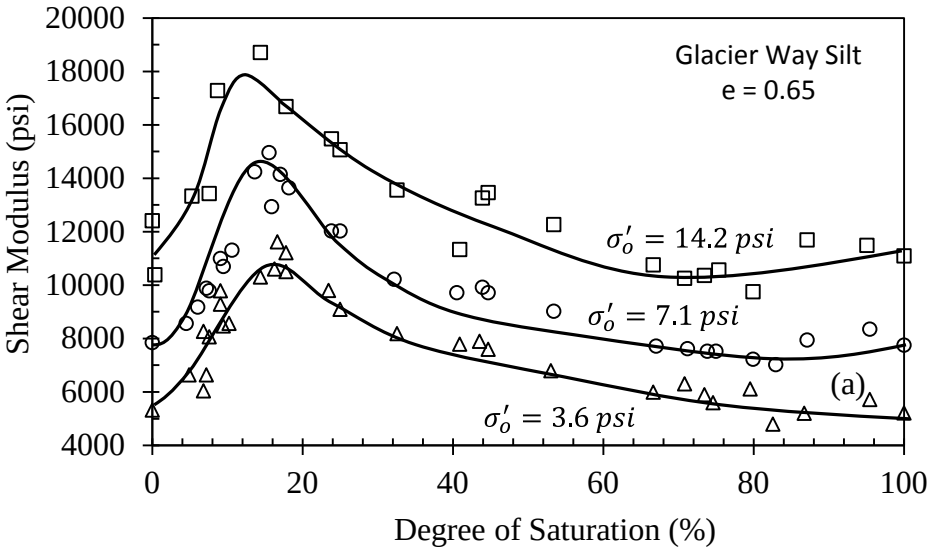

Figure 2.14 Effect of degree of saturation on shear modulus at small strains (After Wu et al., 1984).

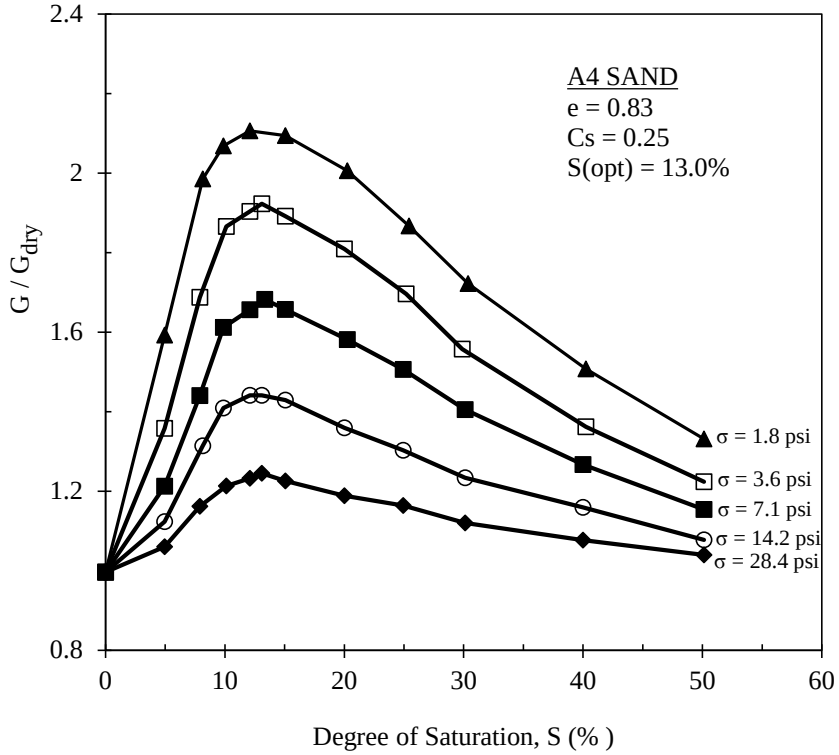

Figure 2.15 Effect of degree of saturation and confining pressure on shear modulus ratio, G_{max}/G_{dry}, (After Qian et al., 1991).

2.4 Testing Under Controlled State of Stress

2.4.1 Introduction

Some of the early researchers that are credited with modifications of triaxial cells for unsaturated soil testing are: Bishop et al. (1960), Bishop and Donald (1961), Matyas and Radhakrishna (1968), Josa et a1. (1987), Fredlund and Rahardjo (1993), Sivakumar (1993), Romero et al. (1997), Cabarkapa et al. (1999), and Rampino et al. (1999, 2000). These researchers modified the triaxial cell for independent application or measurement of the pore-air and pore-water pressures. The modifications include the use of a high air-entry porous disc/stone (HAEPD) for the pore-water pressure measurements and a course porous stone for the pore-air pressure measurements. Bishop et al. (1960), Bishop and

Donald (1961), Josa et al. (1987), Fredlund and Rahardjo (1993), Sivakumar (1993), Cabarkapa et al. (1999), Rampino et al. (1999, 2000), and including this research, had the HAEPD in the bottom platen and the coarse porous stone in the top platen of the triaxial cell, with independent application of the pore-water and pore-air pressures. Figure 2.16 shows a schematic diagram of a triaxial cell, modified for unsaturated soils.

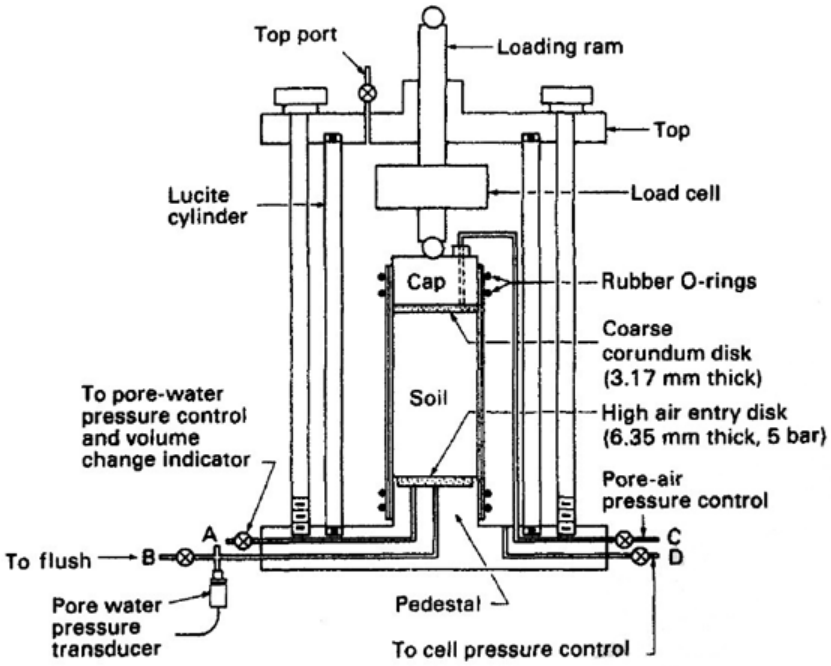

Figure 2.16 Modified triaxial cell for testing unsaturated soils (Fredlund and Rahardjo, 1993).

2.4.2 Types of test procedures

The independent control of the pore-air and pore-water phases determines how the specimen volume change can be determined, hence, it determines the type of triaxial test procedures subjected on the specimens. In general, there are four triaxial shearing test procedures: drained, constant-water-content, undrained, and unconfined compression.

All of these tests, with exception of the unconfined compression, can be subjected to a consolidation process prior to shearing.

The drained tests have both the pore-air and pore-water in a drained condition (i.e., flow is allowed in or out) for both consolidation and shearing phases. The constant-water-content shearing tests have the pore-air in a drained condition, while maintaining a constant pore-air pressure, but the pore-water is in an undrained condition (no-flow), with pore-water pressure monitored throughout the test. The shearing phase of undrained triaxial test has the pore-air and pore-water in undrained conditions, but in general, if a consolidation phase is performed prior to shearing, this phase is performed with pore-air and pore-water in a drained condition. The undrained procedure can be performed with or without pore pressure measurements, but noting that it may be difficult to maintain an undrained air phase condition due to air diffusion. (Fredlund et al., 2012). The unconfined compression test procedure has no control or measurement of the pore-air or pore-water, and in general, has no confining pressure on the soil specimen.

Undrained tests are not common in literature and among researchers, because it is generally hard to measure the pore-air pressure over a long period because of the ability of air to diffuse through rubber membranes, water, tubing, fittings, and other materials (Bishop et al., 1960; and Fredlund and Rahardjo, 1993). In the three types of tests where the state of stress is controlled (i.e., drained, constant-water-content, and undrained), the axis translation technique is used to avoid cavitation in the water phase below the HAEPD, for matric suctions higher than one atmosphere.

In the study, both saturated and unsaturated tests were performed. The unsaturated triaxial tests were performed under a series of constant-water-content tests to simulate the conditions anticipated during construction. This included the consolidation phase, which is termed the compression phase as it was done without allowing flow of water out of the specimens, but subjects the specimen to conditions of construction such as additional placement of soil lifts without immediate drainage.

As previously mentioned, the independent control of the pore-air and pore-water phases, determines how the specimen volume change can be determined, and it is briefly reviewed in the subsequent section.

2.4.3 Measurement of volume change

The total volume change of a saturated soil can be attributed to the change in water volume and is generally measured by a volume change gauge. The total volume change for an unsaturated soil specimen is not just the change in water volume, but also includes the change in the air volume. The total volume change is therefore, the sum of water-phase and air-phase volume changes as the soil solids are assume to be incompressible. Any two of the total, pore-water, and pore-air volumes can be used to describe the volumetric behavior of an unsaturated soil. The volume measurements can be obtained by measurements of the cell fluid, direct air and water volume measurements, and by local strain, i.e., the on-sample measurements of vertical and radial deformation (Geiser et al., 2000)

Some researchers that have used the measurements of the cell fluid to determine the total volume of the specimen are: Sivakumar (1993); Rampino et al. (1999); Sivakumar and Wheeler (2000); Toyota et al., (2001); Ng et al., (2002); Lauer and Engel, (2004, 2005); Chavez et al. (2005); Mun et al., (2006); Padilla et al., (2006); and Schwarz et al. (2006). When obtaining volume measurements by measurements of the cell fluid level, the measurements may be affected by expansion and contraction of the cell due to pressure increments, creep of the cell wall under constant pressure, temperature variations, air trapped inside the cell, absorption of water into the perspex cell wall, movement of the piston and leakage of water in the cell, (Head 1992). Bishop and Donald, (1961); Wheeler, (1986); Sivakumar, (1993); Maleki and Bayat, (2012) minimized the errors caused by some of the factors listed by Head (1992), by using a double-walled triaxial cell. The used of a double-walled cell minimized the effect of expansion and contraction, and creep of the inner cell as the fluid pressure is exerted on both sides of the inner cell.

This study made use of a double-walled cell, and the movement of the piston was accounted for by knowing the volume of the piston per unit length, and leakage was monitored for by monitoring for inconsistent pressure or volume changes and checking the water content of the specimen at the end of testing (since the constant-water-content test was used).

2.5 Constitutive Modeling of Soil Behavior

2.5.1 Introduction

A model is an appropriate simplification of reality. A constitutive model would then be the simplified relationship between the components (constitutive elements) of such reality. Therefore, constitutive modeling of soil behavior can be said in general to be a simplified physical process, whereby only the essential components (variables) are represented and related to predict behavior. Non-essential variables with little or no influence on the nature of the process are neglected (Muller, 1978). More specific to soils, a more robust definition of a constitutive soil model is given by Wood, (1990); the constitutive model for a material is a set of equations relating stress to strain and possibly strain history of the soil and the future stress changes that the soil is likely to experience.

Several authors have proposed constitutive models that relate the stress state behavior to represent soil behavior (Roscoe and Schofield, 1963; Roscoe and Burland, 1968; Fredlund and Morgenstern, 1977; Lloret et al., 1987; Lade and Nelson, 1987; Alonso et al., 1990; Toll 1990; Gens and Alonso 1992; Alonso et al., 1994; Wheeler and Sivakumar, 1995; Shuai and Fredlund, 1998; Alonso et al., 1999; Vaunat et al. 2000; Matsuoka et al., 2002; Matsuoka and Hajime, 2006; Sun et al., 2006; Sheng et al., 2008, and Yao et al., 2014)

In general, these authors have modeled both the volume change behavior and the mechanical behavior of an unsaturated soil. When used as the essential stress state variables, the stress state variables of net mean stress (total stress σ, over pore-air

pressure u_a), and the matric suction (pore-air pressure u_a, over the pore-water pressure u_w), have led to the modeling of volume change behavior when related to the volumetric strain ε_v or void ratio e, and several aspects of the mechanical behavior when related to the deviatoric stress (Fredlund and Rahardjo, 1993).

2.5.2 Critical State Theory

The first Critical State models, which are the Cam Clay (CC) model by Roscoe et al. (1958), and the Modified Cam Clay (MCC) model by Roscoe and Burland (1968), were formulated to describe the behavior of remolded clay soils. In a similar manner, the unsaturated soil behavior has been successfully described using critical state framework (Alonso et al., 1990; Kohgo et al., 1993; Wheeler and Sivakumar, 1995; Maâtouk et al., 1995; Cui and Delage, 1996; Geiser et al., 2000; Jommi, (2000); Vaunat et al., 2000; Sun et al., 2000; Tang and Graham, 2002). Similar to saturated soils constitutive relationships, the constitutive relations of unsaturated soils based on critical state theory, require some assumptions to be made. Kurtay and Reece (1970), presented the following assumptions:

- Soil material is homogeneous and isotropic.
- Soil is not viscous material.
- Soil behavior can be described using the appropriate stress state variables.
- Soil behavior representation is not subjected to interaction between individual particles and can be described using macroscopic continuum mechanics theory.
- Soil behavior is not time dependent.

In terms of critical state framework, the variables used to present critical state expressions in axisymmetric conditions are as follows:

$$p - u_a = \frac{\sigma_a + 2\sigma_r}{3} - u_a \qquad \text{net mean stress} \qquad (2.22)$$

$$q = \sigma_a - \sigma_r \qquad \text{deviator stress} \qquad (2.23)$$

$$s = u_a - u_w \qquad \text{matric suction} \qquad (2.24)$$

$$\dot{\varepsilon}_v = \dot{\varepsilon}_a + 2\dot{\varepsilon}_r \qquad \text{total volumetric strain increment} \qquad (2.25)$$

$$\dot{\varepsilon}_q = \frac{2\left(\dot{\varepsilon}_a - \dot{\varepsilon}_r\right)}{3} \qquad \text{total deviatoric strain increment} \qquad (2.26)$$

The variables σ_a and σ_r are the total axial and radial normal stresses, $\dot{\varepsilon}_a$ and $\dot{\varepsilon}_r$ are the increments in the axial and radial strain respectively, p is the mean total stress, q is the deviatoric stress, u_a is the pore-air pressure, u_w is the pore-water pressure, and $\dot{\varepsilon}_v$ and $\dot{\varepsilon}_q$ are the increments of total volumetric and deviatoric strains. The total strain increment are the summation of the elastic and plastic strain increments:

$$\dot{\varepsilon}_v = \dot{\varepsilon}_v^e + \dot{\varepsilon}_v^p \qquad (2.27)$$

$$\dot{\varepsilon}_q = \dot{\varepsilon}_q^e + \dot{\varepsilon}_q^p \qquad (2.28)$$

The variables presented prior for critical state were developed for elasto-plastic critical state models, which is an improvement on elastic models as they consider the occurrence of elastic strains as well as plastic strains. The main disadvantage of an elastic model is that it does not differentiate between reversible and irreversible strains (Wheeler and Karube, 1996). Irreversible strains are plastic strains that are permanent, after the subsequent removal of loading (i.e. the strains do not all go back to zero).

An elasto-plastic constitutive model was presented in this study to model soil behavior subjected to a constant-water-content condition. It is based on the considerations of several models as follows: Barcelona Basic model; Sheng, Fredlund and Gens model; and the Unified Hardening model. These models are discussed in the ensuing sections.

2.5.3 Barcelona basic model

The critical state based Barcelona Basic Model (BBM) proposed by Alonso et al. (1990) is an extension of the Modified Cam-Clay (MCC) model proposed by Roscoe and Burland (1968). The BBM is defined in terms of four state variables. As with the MCC model, three of the four state variables of the BBM are defined by a net mean stress, a deviatoric stress and the specific volume, represented by the terms p, q, and v respectively. The fourth state variable is the matric suction, represented by the term s. These four state variables are defined as follows:

$$p = \frac{1}{3}\left(\sigma_1 + \sigma_2 + \sigma_3\right) - u_a \tag{2.29}$$

$$q = (\sigma_1 - \sigma_3) \tag{2.30}$$

$$s = u_a - u_w \tag{2.31}$$

$$v = 1 + e \tag{2.32}$$

The BBM was proposed to represent the behavior of slight to moderately expansive unsaturated soils. In particular; sands, silts, clayey sands, sandy clays and low plasticity clays. The BBM can also represent, to a degree, some behaviors of expansive clays. The BBM features a state boundary hypersurface wherein only elastic strains occur when the soil state lies inside this surface, i.e., the stress state of the soil at any time is between the state boundary hypersurface and a zero stress state. The formation of plastic strains occur when the soil state reaches the state boundary hypersurface and beyond. As the soil state traverses beyond the state boundary hypersurface, plastic behavior then, corresponds to an expansion of a yield surface in $(p:q:s)$ space (Alonso et al., 1990).

2.5.3.1 Isotropic Stress States

Considering both loading-collapse (LC) behavior and a swelling-collapse behavior, Figure 2.17(a) & (b) represents these behavior in the $(s:p)$ and $(v:p)$ space respectively. Increasing the isotropic loading under constant suction, the effect of the net mean total stress p on the specific volume, is defined as follows:

$$v = N(s) - \lambda(s) \ln \frac{p}{p^c} \tag{2.33}$$

In Equation (2.33), $N(s)$ is the specific volume at $p = p^c$ which varies with matric suction s; $\lambda(s)$ is the soil stiffness parameter which depend on matric suction s; p^c is the reference stress state for which $v = N(s)$; is the soil stiffness parameter which is defined as:

$$\lambda(s) = \lambda(0)\left[(1-r)\exp(-\beta s) + r\right] \tag{2.34}$$

In Equation (2.34) r is the constant related to the maximum stiffness of the soil such that $r = \lambda(s \to \infty)/\lambda(0)$, and β is the parameter controlling the rate of increase of $\lambda(s)$ with matric suction, s.

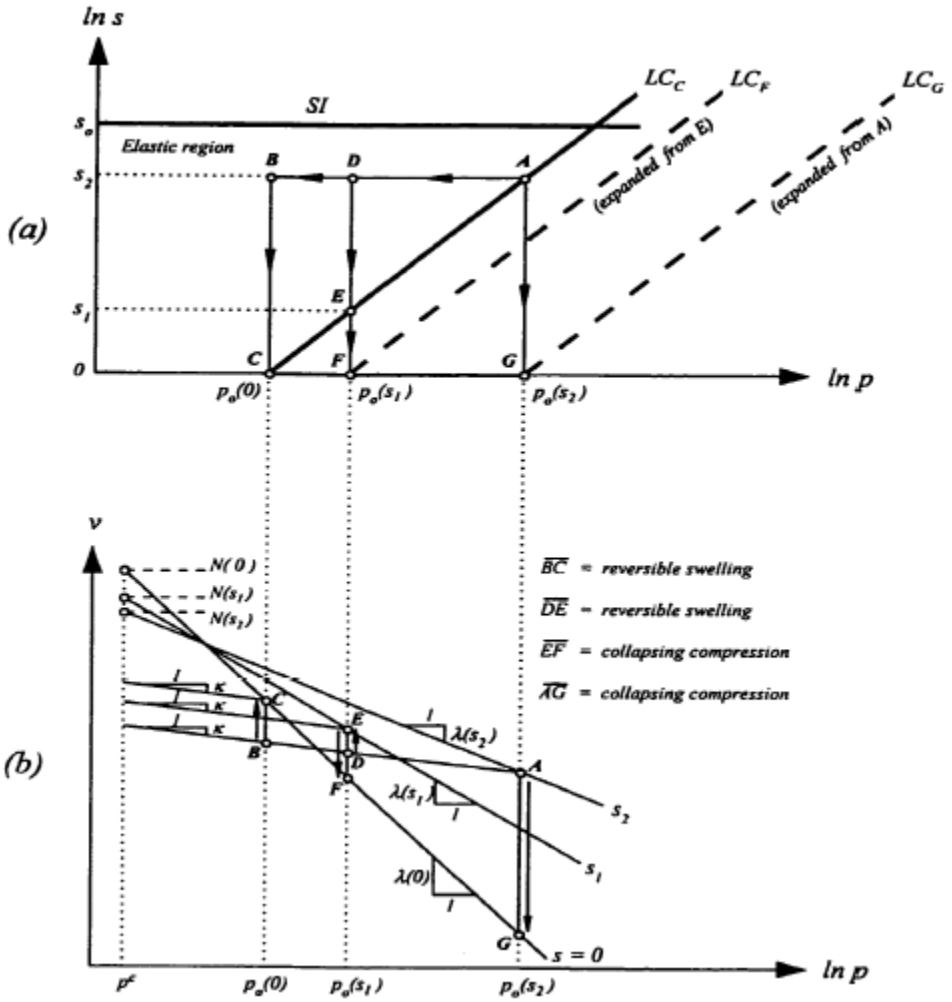

Figure 2.17 Model's framework for isotropic stress states: (a) loading-collapse (LC) yield curve; (b) swelling-collapse behavior $v - p$ plane (from Laikram, 2007)

Alonso et al. (1990) assumed elastic behavior on the unloading-reloading line (URL), depicted in Figure 2.17(b) with slopes, κ, the elastic swelling index. The change in specific volume within the elastic region is defined by:

$$dv = -\kappa \frac{dp}{p} \tag{2.35}$$

Figure 2.17 (b) presents the response of isotropic loading of three soil samples that were subjected to different constant suctions; a fully saturated case at $s = 0$ and increased

suctions of s_1 and s_2 with $s = 0 < s_1 < s_2$. The third sample under constant suction, s_2 yields at Point A, with the largest isotropic stress $p_o(s_2)$. Point A in Figure 2.17 represents an unsaturated soil sample under volumetric and stress state condition. At Point C, $s = (u_a - u_w) = 0$, a condition considered as fully saturated, the net mean stress, $p_0(0)$ is the isotropic preconsolidation stress of the soil sample under fully saturated conditions. If Points A and C are on the same yield curve on the $(p:s)$ plane as shown in Figure 2.17(a). Alonso et al. (1990) postulated that a relationship can be determined between the yield stress $p_o(s_2)$ or any generic yield stress, $p_o(s)$ and the saturated value $p_o(0)$. This relationship considers the specific volumes at a point on the yield curve such as A and that at C, which follows a virtual path such as ABC in Figure 2.17(a). This isotropic preconsolidation stress $p_o(0)$ of the soil under fully saturated $(s = 0)$ conditions, induces an initial loading-collapse (LC) yield curve in the $(p:s)$ plane. The equation relating $p_o(0)$, and the corresponding isotropic preconsolidation stress, $p_o(s)$ (yield net mean stress) at any particular value, s, of matric suction, is given as follows:

$$\frac{p_o(s)}{p^c} = \left(\frac{p_o(0)}{p^c} \right)^{\frac{\lambda(0)-\kappa}{\lambda(s)-\kappa}} \tag{2.36}$$

Equation (2.34) and (2.36) can be used to describe the spatial location of the loading-collapse, LC, yield curve in the $(p:s)$ plane (Alonso et al., 1990). The loading-collapse (LC) yield curve as presented by Equation (2.36) for an unsaturated soil under isotropic

loading condition in the $(p:s)$ plane explains not only the apparent increase in the preconsolidation stress associated with increasing matric suction, but also the collapse phenomena observed during decreasing matric suction caused by inundation (wetting).

2.5.3.2 Anisotropic Stress States

The BBM as presented by Alonso et al. (1990) is an elasto-plastic constitutive model, based on the critical state framework. The elasto-plastic model suggest that only elastic behavior occurs when the soil state lies inside the yield locus, and plastic strains will start to occur when the soil state reaches the initial yield locus and will continue when traversing this initial yield locus. As the soil state traverses the yield locus, the theory suggests that the plastic behavior induces an expansion of the yield loci in the $(p:q:s)$ stress space. The critical state framework is synonymous to triaxial compression tests, whereby when soils are continuously distorted (sheared), they eventually reach a well-defined critical state. This critical state is defined at its onset whereby, no further changes occur in the state variables p, q, or v for continued changes in shear strains. Figure 2.18(b) shows the corresponding elastic region enclosed by the loading-collapse (LC) and suction-increase (SI) yield loci in the $(p:s)$ plane.

Extending the model formulation for isotropic stress states in the $(p:s)$ plane, a third stress state parameter, the deviatoric stress, $q=(\sigma_1-\sigma_3)$, is incorporated to include the effect of shear stresses. For consistency and simplicity, the BBM also predicts soil behaviors for fully saturated condition, i.e. when $s=0$. The yield surface adopted as the limit condition in the BBM for fully saturated soils, is the elliptical yield surface of the

Modified Cam-Clay (MCC) model (Roscoe and Burland, 1968; Wood, 1990; Gens and Alonso, 1992). At a constant suction, the elliptical yield curve exhibits an isotropic preconsolidation stress (i.e., the yield net mean stress), $p_o(s)$, that relates to the isotropic preconsolidation stress, $p_o(0)$ under a fully saturated condition as defined by Equation (2.36).

The critical failure states in the BBM are represented by the critical state line (CSL). For any non-zero suction, the CSL is graphically defined in Figure 2.18(a) by maintaining the critical failure slope, M (i.e., parallel to the CSL for zero suction), and intersecting with the p-axis on the right intercept of the yield curve and the p-axis. The effect of matric suction, s is therefore represented by an increase in apparent cohesion of the soil, graphically shown as the intercept of the critical state line (CSL) with the q-axis, as shown in Figure 2.18. Alonso et al. (1990), represents the increase in apparent cohesion of the soil as a linear relationship with suction, thereby presenting the point of intercept of the elliptical curve and the p-axis as follow:

$$p = -p_s = -ks \tag{2.37}$$

In Equation (2.37), k is a constant. In the $(p:q)$ plane, the yield curve is represented by the ellipse, with major axis extending on the p-axis from $-p_s$ to $p_o(s)$ and defined as follows:

$$f(p,q,s) = q^2 - M^2(p + p_s)\left[p_0(s) - p\right] = 0 \tag{2.38}$$

The SI yield locus, which is defined by the maximum previously attained value of suction s_o is defined by $s = 0 = \text{constant}$. The SI yield locus extends in the positive q space as a plane parallel to the q-axis as depicted in the schematics of Figure 2.19.

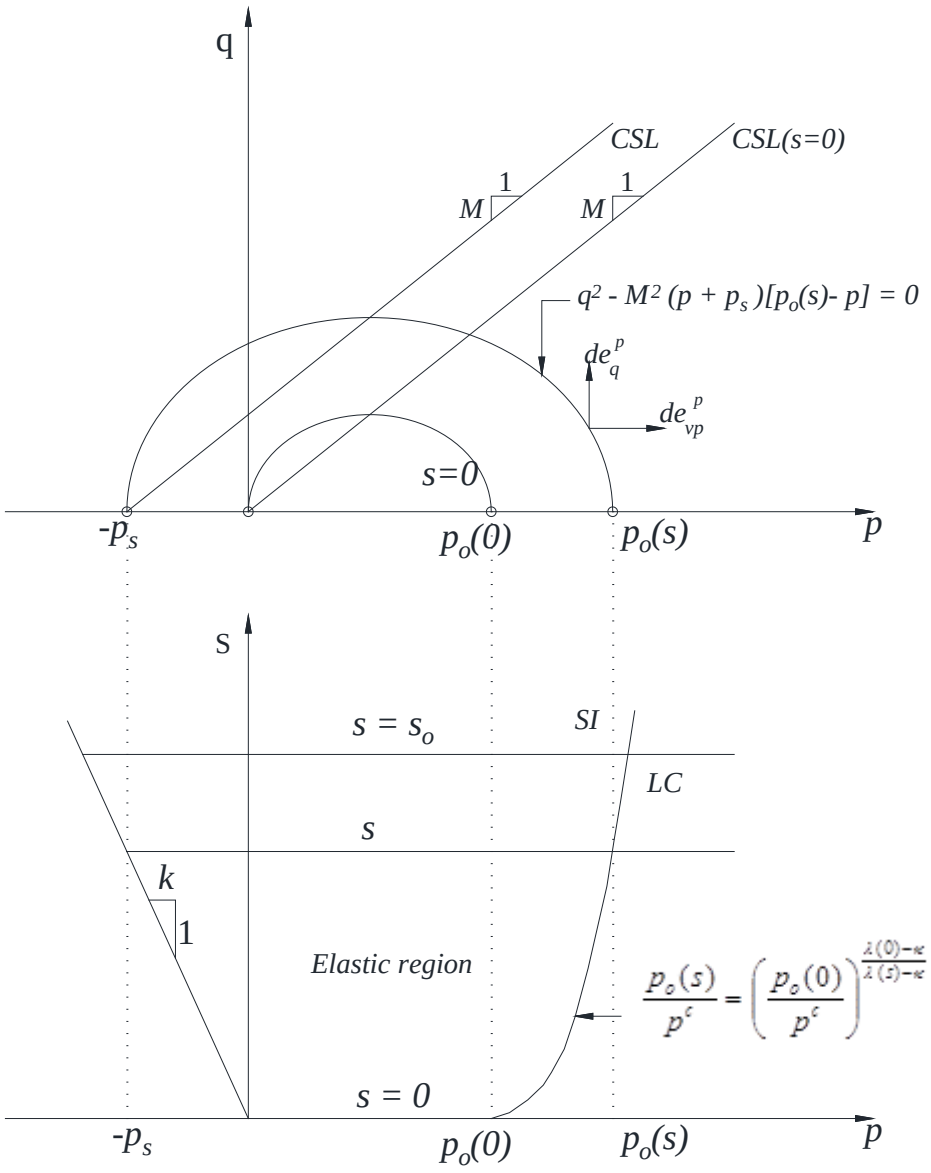

Figure 2.18 Barcelona model formulation in (a) $p-q$ plane, (b) $s-p$ plane (After Macari et al. 2003)

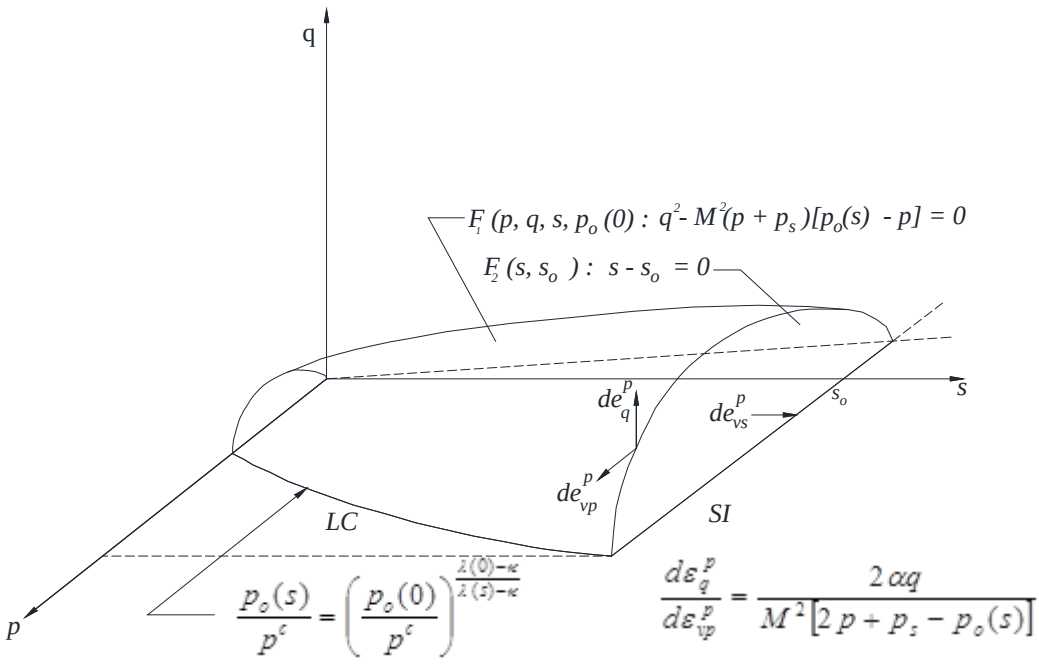

Figure 2.19 Three-dimensional view of the yield loci in $(p:q:s)$ stress space (After Laikram, 2007)

Strain-hardening Rule

The BBM assumes that strain hardening laws govern the evolution of the parameters, $p_o(0)$ and s_o and how their evolution effects the yield surface and yield locus. Therefore, increases in net mean stress or matric suction will have an effect on the elastic and plastic volumetric strains in the modelling of unsaturated soils. The elastic, plastic and total volumetric strain increments, $d\varepsilon_v^e$, $d\varepsilon_v^p$, and $d\varepsilon_v$, are respectively determined as follows:

$$d\varepsilon_v^e = d\varepsilon_{vp}^e + d\varepsilon_{vs}^e \tag{2.39}$$

$$d\varepsilon_v^p = d\varepsilon_{vp}^p + d\varepsilon_{vs}^p \tag{2.40}$$

$$d\varepsilon_v = d\varepsilon_v^e + d\varepsilon_v^p \tag{2.41}$$

In the latter three equations, $d\varepsilon_{vp}^e$ and $d\varepsilon_{vs}^e$ are the elastic volumetric strain increments due to changes in the net mean stress and matric suction respectively. $d\varepsilon_{vp}^p$ and $d\varepsilon_{vs}^p$ are the plastic volumetric strain increments due to changes in the net mean stress and matric suction respectively.

As such, the total volumetric strain increments due solely to changes in net mean stress, $d\varepsilon_{vp}$ or solely to changes in matric suction, $d\varepsilon_{vs}$ are respectively given as follows:

$$d\varepsilon_{vp} = d\varepsilon_{vp}^e + d\varepsilon_{vp}^p \tag{2.42}$$

$$d\varepsilon_{vs} = d\varepsilon_{vs}^e + d\varepsilon_{vs}^p \tag{2.43}$$

Based on elastic volumetric changes induced by changes in the net mean stress p, which was previously defined by Equation (2.35), the elastic volumetric strain can be defined as:

$$d\varepsilon_{vp}^e = -\frac{dv}{v} = \frac{\kappa}{v}\frac{dp}{p} \tag{2.44}$$

As the net mean stress, p reaches and traverses the LC yield value $p_0(s)$ the total volumetric strain under a constant matric suction, s, is defined as:

$$d\varepsilon_{vp} = \frac{\lambda(s)}{v}\frac{dp_o(s)}{p_o(s)} \tag{2.45}$$

From the total volumetric strain, the volumetric plastic component is obtained by subtracting the volumetric elastic component, Equation (2.44) from the total volumetric strain, Equation (2.45). The resulting equation for the plastic volumetric strain is given in terms of $p_o(s)$, or based on the LC yield loci, in terms of $p_o(0)$ as follows:

$$d\varepsilon_{vp}^{p} = \frac{\lambda(s)-\kappa}{v}\frac{dp_0(s)}{p_0(s)} = \frac{\lambda(0)-\kappa}{v}\frac{dp_0(0)}{p_0(0)} \tag{2.46}$$

Similar to the determination of volumetric strain increments due to changes in net mean stress, p, changes in suction, s, will also result in volumetric strain increments. The elastic volumetric strain due to changes in suction is defined as:

$$d\varepsilon_{vs}^{e} = \frac{\kappa_s}{v}\frac{ds}{(s+p_{atm})} \tag{2.47}$$

As the suction reaches and traverses the SI yield locus, the total volumetric strain due to changes in suction is defined as:

$$d\varepsilon_{vs} = \frac{\lambda_s}{v}\frac{ds_o}{(s_o+p_{atm})} \tag{2.48}$$

The plastic volumetric strain due to changes in matric suction is obtained by subtracting the volumetric elastic component, Equation (2.47) from the total volumetric

strain, Equation (2.48). The resulting equation for the plastic volumetric strain due to changes in matric suction is given as:

$$d\varepsilon_{vs}^{p} = \frac{\lambda_s - \kappa_s}{v} \frac{ds_o}{(s_o + p_{atm})} \tag{2.49}$$

Alonso et al. (1990) stated that the plastic strains control the position of the LC and SI yield loci, which implies that the hardening laws affect the yield curves independently. In an effort to present hardening laws that suggest a dependency of both curves on the hardening laws, Alonso et al. (1990) cites experimental research evidence by Josa et al. (1987) that suggests a definite coupling between the curves. Alonso et al. (1990) then presents proposed hardening laws that couple the curves based on the idea that the plastic volumetric strains may have similar effects on both curves. Alonso et al (1990) stated that this idea of plastic strains having similar effect on both curves is an initial attempt for estimation, leaving open the possible suggestion of further research on this issue.

Flow Rule

Alonso et al. (1990) suggested the use of a non-associative flow rule for the BBM. The parameter α is used to modify the associative flow rule to the non-associative flow rule in regards to the direction of the plastic shear strain increments $d\varepsilon_q^p$ associated with the yield surface in $(p:q:s)$ space, as depicted in the schematics of Figure 2.19. The non-associative flow rule is defined as follows:

$$\frac{d\varepsilon_q^p}{d\varepsilon_{vp}^p} = \frac{2q\alpha}{M^2\left[2p + p_s - p_o(s)\right]} \tag{2.50}$$

In Equation 2.50, $d\varepsilon_{vp}^{p}$ is the plastic volumetric strain increments, and M is the suction-independent slope of the critical state line (CSL). The parameter constant α is defined by the following equation:

$$\alpha = \frac{M(M-9)(M-3)}{9(6-M)}\left[\frac{1}{1-\frac{\kappa}{\lambda(0)}}\right] \tag{2.51}$$

The elastic strain increments induced by changes in the deviatoric stress, q are determined as a function of the shear modulus G, as follows:

$$d\varepsilon_{d}^{e} = \frac{\sqrt{2}}{3}\sqrt{\left(d\varepsilon_{1}^{e}-d\varepsilon_{2}^{e}\right)^{2}+\left(d\varepsilon_{2}^{e}-d\varepsilon_{3}^{e}\right)^{2}+\left(d\varepsilon_{3}^{e}-d\varepsilon_{1}^{e}\right)^{2}} = \frac{1}{3G}dq \tag{2.52}$$

The parameters required for the implementation of the model fall into four categories, which are the parameters for: compressibility, shear strength, initial state, and reference state. These parameters are listed in Table 2.4

Table 2.5 Information required for full implementation of Barcelona model

Compressibility parameter for changes in net mean stress, p $\lambda(0)$ volumetric stiffness for changes in p and virgin conditions $s = 0$ κ elastic volumetric stiffness for changes in p β parameter controlling the rate of increase of $\lambda(s)$ with matric suction, s r parameter defining the maximum soil stiffness, i.e., $r = \lambda(s \to \infty)/\lambda(0)$ p^c reference stress state parameter
Compressibility parameter for changes in matric suction, s $\lambda(s)$ volumetric stiffness for changes in p under virgin conditions $(s > s_o)$ κ_s elastic volumetric stiffness for changes in s
Shear strength parameters G elastic shear modulus M slope of the critical state line (CSL) k parameter indicating the rate of increase in apparent cohesion with s
Initial volumetric state and stress state conditions p_{ini} initial net mean stress q_{ini} initial deviatoric stress s_{ini} initial matric suction v_{ini} initial specific volume
Reference stress parameters $p_o(0)$ initial isotropic preconsolidation pressure ($s = 0$) s_o initial yield suction

Macari and Arduino (1995) showed that the MCC model does not properly support the response of heavily overconsolidated soils. Therefore, as the MCC is the basis of the BBM, the BBM critical state framework also does not support the response of heavily overconsolidated soil conditions. However, the BBM framework does support the lightly overconsolidated and normally consolidated soil conditions.

An explicit step-by-step integration procedure of the BBM constitutive relations for an initially lightly overconsolidated soil, responding to a drained (constant–s) conventional triaxial compression (CTC) test is provided in Appendix B.

2.5.4 SFG Model (Sheng et al., 2008)

Sheng et al. (2008), proposed a model that attempts to explain the true nature of experimental data of unsaturated soils. Specifically, Sheng et al. (2008) addressed three ideas: The change in yield stress with soil suction; occurrence of changes in plastic volume during desorption (drying); and the nature of the experimental smooth curvature of the nominal compression lines that is obtained at constant suctions, and visualized on a void ratio versus logarithmic mean stress plot. The Sheng et al. (2008) model, therefore, only considers the effect of changes in net mean stress on the volume (void ratio) of soil, and the effect of changes in matric suction on the net mean stress (and yielding stress). As such, the model exists in the space, $(v:s:p)$ and does not consider the critical state deviatoric stress, q. The model, however considers the effect of the yield stress on cohesion, which in turn can be used in shear stress estimations. Nonetheless, the consideration of the SFG model for this study, is its volumetric behavior, and it can be easily coupled with shear strength in a critical state framework.

2.5.4.1 Volumetric behavior

The SFG model presents the relationship of volumetric behavior between the variables of specific volume, v net mean stress, p, and suction, s. Considering the change in total volumetric strain, $d\varepsilon_v$, the relationship is presented as follows:

$$d\varepsilon_v = -\frac{dv}{v} = \lambda_{vp}\frac{dp}{p+s} + \lambda_{vs}\frac{ds}{p+s} \tag{2.53}$$

In Equation (2.53), λ_{vp} is the slope of the normally consolidated line (NCL) for normally consolidated soils, and λ_{vs} is given as a function of suction, by the following relationships:

$$\lambda_{vs} = \begin{cases} \lambda_{vp} & s < s_{sa} \\ \lambda_{vp}\dfrac{s_{sa}+1}{s+1} & s \geq s_{sa} \end{cases} \tag{2.54}$$

The slope λ_{vs} is the slope λ_{vp} of the NCL, when the soil is fully saturated, and s_{sa} is the saturation suction. In an unsaturated state, and as the soil suction becomes increasingly higher, the slope λ_{vs} gradually decreases to zero. Under desorption condition, the s_{sa} is the air-entry value. s_{sa} is generally smaller than the air-entry value, under adsorption conditions. Figure 2.20 presents a typical trend of the slopes λ_{vp} and λ_{vs}, and their analogy (visual trend) to a typical shrinkage test result.

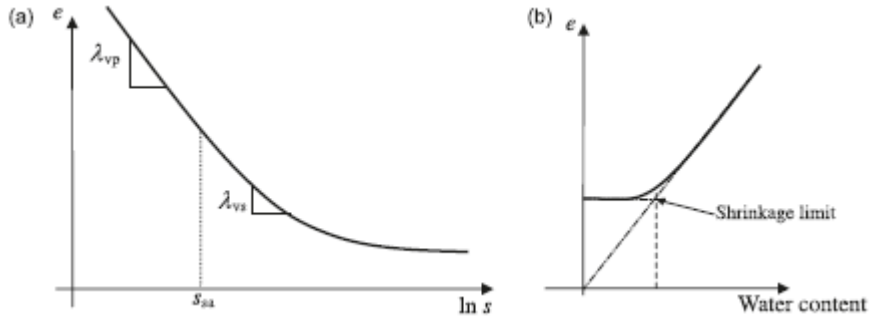

Figure 2.20 Typical plot of void ratio versus suction under constant net mean stress. (a) Specific volume versus suction. (b) Shrinkage test result (from Sheng et al., 2008).

Similarly, for elastic volumetric change, $d\varepsilon_v^e$, the relationship is given as follows:

$$d\varepsilon_v^e = \kappa_{vp}\frac{dp}{p+s} + \kappa_{vs}\frac{ds}{p+s} \tag{2.55}$$

In Equation (2.55), κ_{vp} is the slope of the unload-reload line (URL) for over-consolidated soils, and κ_{vs} is given as a function of suction, by the following relationships:

$$\kappa_{vs} = \begin{cases} \kappa_{vp} & s < s_{sa} \\ \kappa_{vp}\dfrac{s_{sa}+1}{s+1} & s \geq s_{sa} \end{cases} \tag{2.56}$$

Plastic volumetric strains can therefore be deduced from the representation of change in total strain as the sum of the change in both elastic and plastic strains, such that:

$$d\varepsilon_v = d\varepsilon_v^e + d\varepsilon_v^p \tag{2.57}$$

$$d\varepsilon_v^p = \left(\lambda_{vp} - \kappa_{vp}\right)\frac{dp}{p+s} + \left(\lambda_{vs} - \kappa_{vs}\right)\frac{ds}{p+s} \tag{2.58}$$

2.5.4.2 Yield stress and hardening law

In the BBM, Alonso et al. (1990) presented the loading collapse yield surface as a function, projected on the $p-s$ plane as follows:

$$\frac{p_o(s)}{p^c} = \left(\frac{p_o(0)}{p^c}\right)^{\frac{\lambda(0)-\kappa}{\lambda(s)-\kappa}} \tag{2.36}$$

The SFG model presents a unique yield surface, by first considering that there should be no change in the plastic strain at the yield surface, therefore, setting the change in plastic strain at yield equal to zero, Equation (2.58) becomes:

$$d\varepsilon_v^p = \left(\lambda_{vp} - \kappa_{vp}\right)\frac{dp_y}{p_y + s} + \left(\lambda_{vs} - \kappa_{vs}\right)\frac{ds}{p_y + s} = 0 \tag{2.59}$$

Rearranging, the relationship for the trajectory of the initial yield stress at an arbitrary suction emerges, and by intergrating within the limits as shown in Equation (2.60), the relationship for p_y results as shown in Equation (2.61).

$$\int_{p_{y0}}^{p_y} dp_y = \int_0^s \frac{\lambda_{vs} - \kappa_{vs}}{\lambda_{vp} - \kappa_{vp}} ds \tag{2.60}$$

$$p_y = \begin{cases} p_{y0} - s & s < s_{sa} \\ p_{y0} - s_{sa} - (s_{sa} + 1)\ln\dfrac{s+1}{s_{sa}+1} & s \geq s_{sa} \end{cases} \tag{2.61}$$

The relationship for the tensile strength due to changes in suction is determined by integrating Equation (2.60), between limits of net mean stress from 0 to p_o, and matric suction from 0 to s, resulting in the relationship as follows:

$$p_0 = \begin{cases} -s & s < s_{sa} \\ -s_{sa} - (s_{sa} + 1)\ln\dfrac{s+1}{s_{sa}+1} & s \geq s_{sa} \end{cases} \tag{2.62}$$

The yield surface p_y, which is shown in Figure 2.21, is only valid for a soil that was initially consolidated to p_{y0} at zero suction. When a consolidated soil is further compressed, and the initial yield curve is loaded from an initial yield stress p_y to a new yield stress p_{yn} at constant suction, Sheng et al. (2008) concluded that experimental data show that the higher initial void ratio (lower initial density) will initially lead to higher initial yield stress under constant suction, then the lower initial void ratio (higher initial density) will lead to higher yield stress, p_{yn} after compression. Equation (2.63), which is the hardening law, governs the evolution of the yield surface p_y to the new yield surface p_{yn}. When the soil is loaded without undergoing a drying-wetting cycle, and under constant suction, Sheng et al. (2008) presented a relationship for the new yield curve as follows:

$$p_{yn} = \begin{cases} p_{yn0} - s & s < s_{sa} \\ \dfrac{p_{yn0}}{p_{y0}} \left[p_{y0} + s - s_{sa} - (s_{sa} + 1) \ln \dfrac{s+1}{s_{sa}+1} \right] & s \geq s_{sa} \end{cases} \tag{2.63}$$

In Equation (2.63), p_{yn0} is the new yield stress at zero suction. Figure 2.21 shows the evolution of the yield surface to a new yield surface under constant suction conditions. New yield surfaces can result when the soil is loaded under different stress path, as shown in Figure 2.22, for loading under constant net mean stress. From Figure 2.21, the new yield surface show that the new yield stress initial decreases with increased matric suction, to a minimum yield point, after which it increases with increased matric suction. The matric suction at which the new yield stress is minimum, is the minimum

collapsible suction, s_c whereby soil collapse will occur if the soil is wetted from suction higher than s_c.

Similarly to obtaining the evolution of the yield surface to the new yield surface in terms of the net mean stress, Sheng et al. (2008) presented a relationship for the evolution of the yield surface to the new yield surface in terms of the suction value. If every suction point on the current yield surface, s_y is dried to a new yield surface, s_{yn} under a constant net mean stress, the new yield surface can be analytically described as follows:

$$s_{yn} = \left\{ \begin{array}{ll} \dfrac{Ap-1}{1-A} & p \le p_{y0} - s_{sa} \\ \dfrac{Bp-1}{1-B} & p_{yn0} - s_{sa} \ge p > p_{y0} - s_{sa} \\ p_{yn0} - p & p > p_{yn0} - s_{sa} \end{array} \right|_{p \neq 1} \tag{2.64}$$

where

$$A = \left(\frac{p_{yn0}}{p_{y0}} \right)^{\frac{p-1}{s_{sa}+1}} \frac{s_y + 1}{s_y + p} \tag{2.65}$$

$$B = \left(\frac{p_{yn0}}{p + s_{sa}} \right)^{\frac{p-1}{s_{sa}+1}} \frac{s_{sa} + 1}{s_{sa} + p} \tag{2.66}$$

The Equation (2.98) for the new yield surface is not defined at $p = 1$, therefore the following function can be used:

$$s_{yn} = \begin{cases} \dfrac{1}{\dfrac{1}{s_y+1} - \dfrac{1}{s_{sa}+1}\ln\dfrac{p_{yn0}}{p_{y0}}} - 1 & p \le p_{y0} - s_{sa} \\ \dfrac{s_{sa}+1}{1-\ln\dfrac{p_{yn0}}{p+s_{sa}}} - 1 & p_{yn0} - s_{sa} \ge p > p_{y0} - s_{sa} \\ p_{yn0} - p & p > p_{yn0} - s_{sa} \end{cases}\Bigg|_{p=1} \qquad (2.67)$$

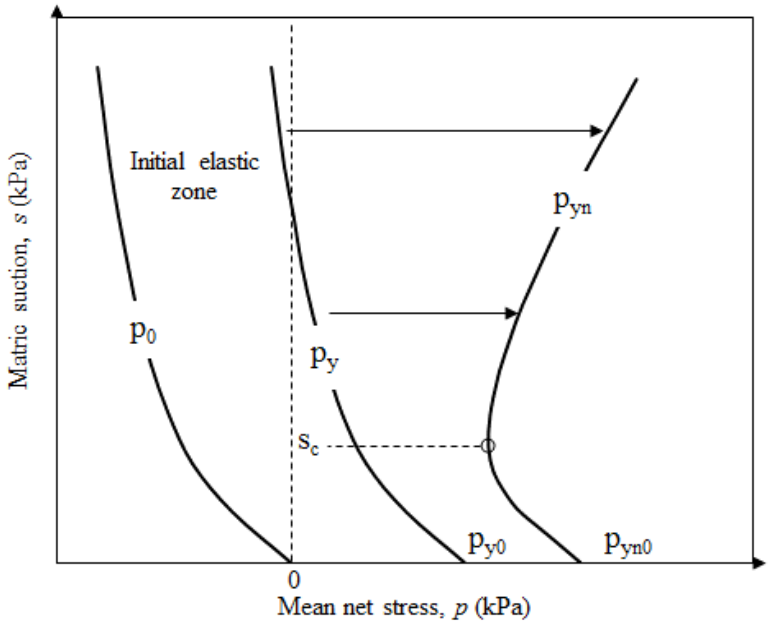

Figure 2.21 The Evolution of the initial yield surface to a new yield surface under constant suction (reproduced from Sheng et al. 2008).

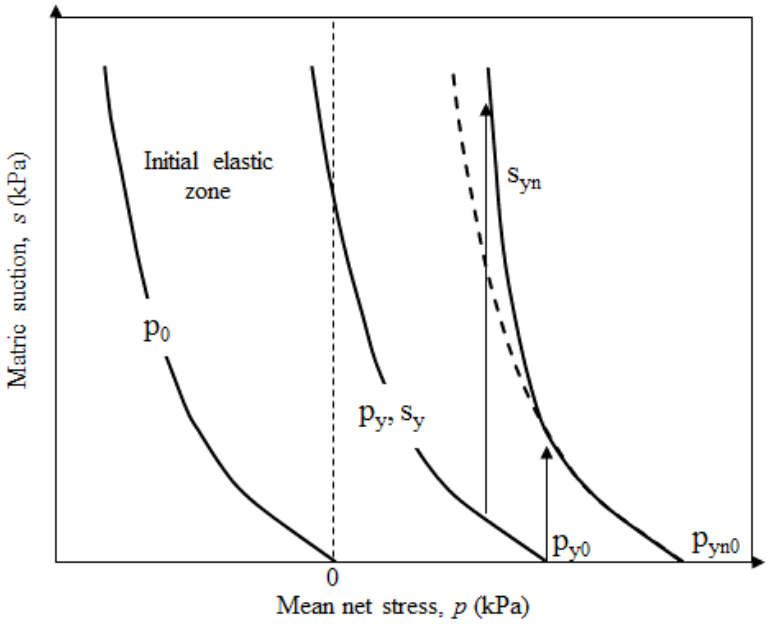

Figure 2.22 The Evolution of the initial yield surface to a new yield surface under constant net mean stress (reproduced from Sheng et al., 2008).

2.5.1 Unified Hardening Model

Yao et al. (2014) proposed a practical model to simulate the behavior of highly overconsolidated unsaturated soils by combining theories of modelling overconsolidated soils with those of unsaturated soils. The Unified Hardening (UH) Model proposed by Yao et al. (2014) for overconsolidated unsaturated soils, is based on the Yao et al. (2009) UH Model for overconsolidated saturated clays. The framework of the proposed model is based on the critical state Barcelona Basic Model (BBM) by Alonso et al. (1990) and Gens and Alonso (1992). Yao et al. (2014) relates the current yield surface, which is similar to the BBM yield surface to a reference yield surface. The BBM defines the yield surface at constant suction as follows:

$$q^2 - M^2(p + p_s)[p_o(s) - p] = 0 \tag{2.38}$$

Using a similar formulation to that of the BBM yield surface, Yao et al. (2014) presented the current yield surface as follows:

$$\ln(p+p_s)+\ln\left[1+\frac{q^2}{M^2(p+p_s)^2}\right]-\ln\left[p_o(s)+p_s\right]=0 \tag{2.68}$$

In Equation (2.68), $p_o(s)$ is the net mean stress at the right intersection of current yield surface and the p-axis at a known suction s, M is the slope of the critical state line, and p_s is the value of the left intersection of current yield surface and the p-axis at a known suction s. The current yield surface in the $q-p$ plane is shown in Figure 2.23. The formulation of the current yield surface in $p-s$ plane, as shown in Figure 2.24 (i.e. the current LC yield surface), is defined, as in the BBM, by the equations:

$$\frac{p_o(s)}{p^c}=\left(\frac{p_o(0)}{p^c}\right)^{\frac{\lambda(0)-\kappa}{\lambda(s)-\kappa}} \tag{2.36}$$

$$\lambda(s)=\lambda(0)\left[(1-r)\exp(-\beta s)+r\right] \tag{2.34}$$

A unified hardening parameter H is adopted in place of the volumetric strain ε_v^p, and the proposed relationship for the hardening law is as follows:

$$\frac{\lambda(0)-\kappa}{1+e_o}d\left[\ln p_o(s)\right]=dH \tag{2.69}$$

In Equation (2.69), e_o is the initial void ratio.

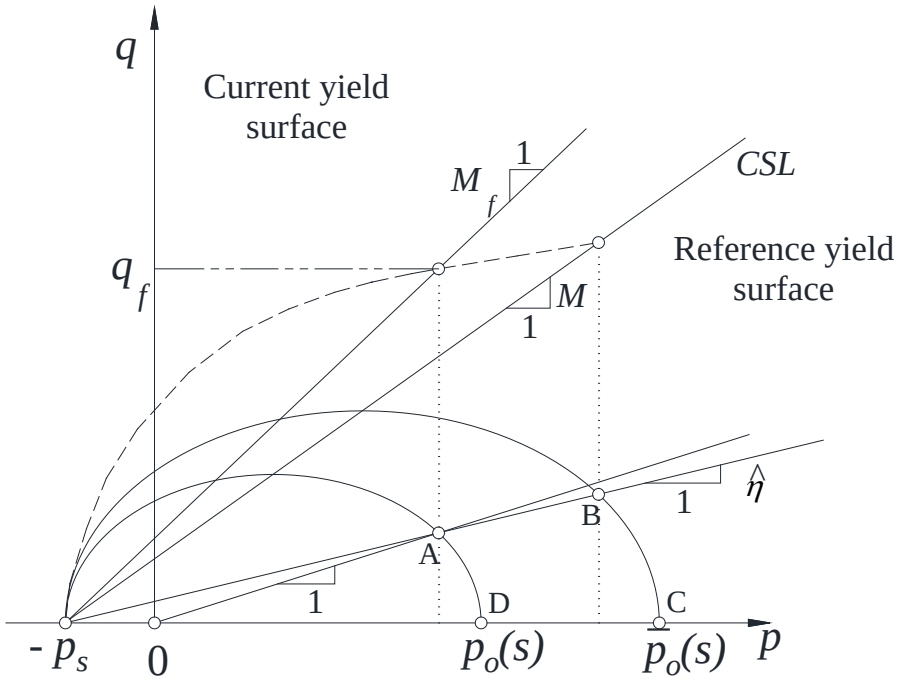

Figure 2.23 Current yield surface and reference yield surface in p-q plane (reproduced from Yao et al., 2013).

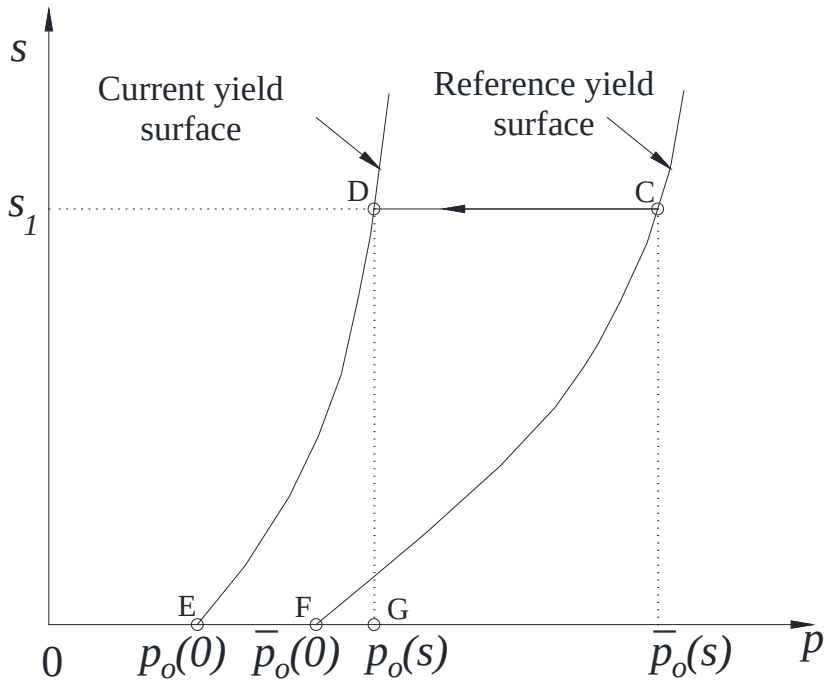

Figure 2.24 Current yield surface and reference LC yield surface in *p-s* plane (reproduced from Yao et al., 2014).

Yao et al. (2014) presented a relationship between a current and a reference yield surface, whereby the reference yield locus is similar to the "inner" plastic response included in the modified BBM by Alonso et al. (1999). The model can reasonably model the behavior of softening and shear dilatancy for overconsolidated unsaturated clays (Yao et al. 2014).

The current yield function in the $q-p$ plane describes the relationship between the current effective stress (p,q) and the current preconsolidation stress $p_o(s)$, at a constant suction s, as shown by points A and D in Figure 2.25. The current LC yield function describes the relationship between the current preconsolidation stress, $p_o(s)$, under unsaturated conditions with the current preconsolidation stress, $p_o(0)$, under fully saturated conditions as shown by the curve DE in Figure 2.25.

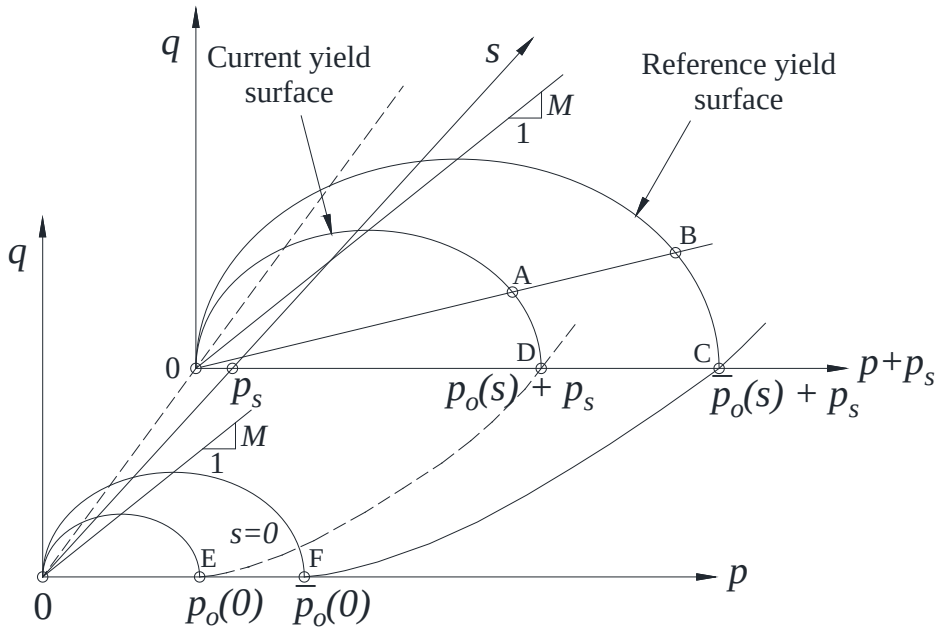

Figure 2.25 Current yield surface and reference yield surface in *p*-*q*-*s* space (reproduced from Yao et al., 2013).

Yao et al. (2014) developed the reference yield surface so that its relationship with the current yield surface can describe the stress history and the effect of variation in OCR. The formulation of the reference yield surface is defined by the equation of the BBM yield surface. The reference stress point $(\bar{p},\bar{q},\bar{s})$ is located on the reference yield surface, where $\bar{p}$ and $\bar{q}$ are the reference net mean stress and reference deviatoric stress respectively. The defined identity relationship between the reference stress point and the current stress point is the same stress ratio, and it is given as follows:

$$\eta = \frac{q}{(p + p_s)} = \frac{\bar{q}}{(\bar{p} + p_s)} \tag{2.70}$$

Similarly as the current yield surface is defined, the reference yield surface in $p-q$ plane and $p-s$ plane as shown in Figure 2.23 and Figure 2.24 can be expressed respectively as

$$\ln(\bar{p} + p_s) + \ln\left[1 + \frac{\bar{q}^2}{M^2(\bar{p} + p_s)^2}\right] - \ln[\bar{p}_o(s) + p_s] = 0 \tag{2.71}$$

$$\frac{\bar{p}_o(s)}{p^c} = \left(\frac{\bar{p}_o(0)}{p^c}\right)^{\frac{\lambda(0)-\kappa}{\lambda(s)-\kappa}} \tag{2.72}$$

In Equations (2.71) and (2.72), $\bar{p}_o(s)$ and $\bar{p}_o(0)$ are the net mean stress at the right intersection of reference yield surface and p-axis under unsaturated condition with a known suction s and under fully saturated condition respectively. Assuming the

reference yield surface represents a normally consolidated soil, ε_v^p is adopted as the hardening parameter and the relationship between ε_v^p and $p_o(0)$ can be given as:

$$\frac{\lambda(0)-\kappa}{1+e_o} d\left[\ln p_o(0)\right] = d\varepsilon_v^p \tag{2.73}$$

Similar to the current yield function, the reference yield function provides the relationship between the reference stress and reference preconsolidation stress. Therefore, the relationship between the current yield surface and the reference yield surface allows for the determination of the changes in the plastic volumetric strain.

In summary, when loading at constant suction, the current yield surface expands outwards. Since $dH > 0$, $d\varepsilon_{vp}^p > 0$, hardening of reference yield surface occurs. When unloading at constant suction, as the current stress point moves inwards, the current yield surface also moves inwards, and the plastic volumetric strain, $d\varepsilon_{vp}^p = 0$. Since only elastic volumetric strain contributes to the total volumetric strain, the reference yield surface remains unchanged.

2.5.1.1 Evolution law of overconsolidation parameter R

Yao et al. (2014), defines the unsaturated overconsolidation parameter, R to describe the degree of overconsolidation as the ratio of the current total net mean stress to the reference total net mean stress taking the effect of suction into account as follows:

$$R = \frac{p+p_s}{\overline{p}+p_s} = \frac{p_o(s)+p_s}{\overline{p}_o(s)+p_s} \qquad 0 < R < 1 \tag{2.74}$$

Substituting equations (2.69), (2.72) and (2.73) into equation (2.74), and then solving the differential equation gives

$$R = \frac{p + p_s\left(1 + \dfrac{\eta^2}{M^2}\right)}{\bar{p}_o \exp\left[\dfrac{\lambda(0) - \kappa}{\lambda(s) - \kappa}\left(\dfrac{\varepsilon_v^p}{c_p}\right)\right] + p_s} \tag{2.75}$$

In Equation (2.75), $\bar{p}_o$ is the initial reference preconsolidation pressures under unsaturated condition [the initial value of $\bar{p}_o(s)$] and the parameter c_p is given as follows:

$$c_p = \frac{\lambda(0) - \kappa}{1 + e_o} \tag{2.76}$$

Equation (2.75) shows that R is related to (p, q, s) and ε_v^p, which indicates that R also depends on the stress path and the stress history.

2.5.1.2 Evolution law of potential failure stress ratio M_f

Yao et al. (2014) presented a potential failure stress ratio M_f to represent the potential capacity of overconsolidated unsaturated clays in resisting shear failure under the current stress condition, density and suction. M_f is related to the peak strength of the clays and is given as:

$$M_f = 6\left[\sqrt{\frac{\chi}{R}\left(1+\frac{\chi}{R}\right)}-\frac{\chi}{R}\right] \tag{2.77}$$

The parameter χ in Equation (2.77), is given as follows:

$$\chi = \frac{M^2}{12(3-M)} \tag{2.78}$$

In accordance with Equation (2.77), M_f will decrease as R increases. When $R=1$, $M_f = M$, which means a complete loss of overconsolidation.

2.5.1.3 Unified hardening parameter H

Yao et al. (2014) presents the unified hardening parameter H for unsaturated overconsolidated clays, to describe the mechanical behaviors, such as strain-hardening/softening, shear dilatancy, stress-path-dependent behavior, and suction effect. In order to do so, the potential failure stress ratio M_f, stress ratio η, and characteristic state stress ratio M are incorporated in H.

$$H = \int dH = \int \frac{M_f^4 - \eta}{M^4 - \eta} d\varepsilon_{vp}^p = \int \frac{1}{\Omega} d\varepsilon_{vp}^p \tag{2.79}$$

$$\Omega = \frac{M_f^4 - \eta}{M^4 - \eta} \tag{2.80}$$

In Equation 2.79, when the value of OCR equals to 1 (i.e. $\Omega = 1$), H reduces to ε_v^p. In the hardening region, dH is always non-negative:

(1) when $0 < \eta < M$, $d\varepsilon_{vp}^{p} > 0$, which describes negative dilatancy.

(2) when $\eta = M$, $d\varepsilon_{vp}^{p} = 0$, which corresponds to the point of the characteristic state.

(3) when $M < \eta < M_f$, $d\varepsilon_{vp}^{p} < 0$, which means negative dilatancy.

In the softening region, since $dH < 0$, $\eta > M$, and η is slightly higher than M_f , then $d\varepsilon_{vp}^{p} < 0$, which indicates negative dilatancy.

Equations (2.75), (2.77) and (2.79), show that the overconsolidated parameter R, the potential failure stress ratio M_f , and H can reflect the decay of overconsolidation, the damage caused by shearing, and the variation in volumetric strain increment.

2.5.2 Summary

The BBM presented by Alonso et al. (1990), has been used by many researchers as the basis for extending an unsaturated soil model. Sheng et al. (2008), presented a new model, the SFG model, for soil volume behavior using concepts presented in the BBM for the occurrence of elastic and plastic volumetric strains. The SFG model presents analytics to describe the changes in the slopes the URL and NCL. The URL and NCL slopes, due to changes in suction, are the same as that for the slopes due to changes in net mean stress for suctions less than the saturation suction, after which, they decrease gradually to a zero state. The volumetric behavior as presented by the SFG model, shows different forms of the tensile strength than the BBM and the RBBM; different forms for the loading collapse yield curve and its evolution in the $s - p$ plane to a new yield

surface. The SFG model does not describe anisotropy, and therefore, for stress-strain modelling, it can easily be coupled with most models that describe shearing such as that of the BBM.

The Unified Model for unsaturated soils presented by Yao et al. (2014), incorporates the behavior of heavily over-consolidated soils, which was not considered by the BBM. By incorporating the evolution of the overconsolidation ratio, the behavior of over-consolidation can be described, when the current stress is related to a reference stress. The basis of the developed model based on this research is from the BBM, but the current stress is governed by a different hardening parameter, which includes the current yield pre-consolidation stress, and the reference stress evolves as does the BBM using the change in plastic volumetric strain as the hardening parameter.

In the ensuing chapters, the experimental program and procedures used are discussed for each type of testing performed, and they will form a basis for the calibration of the parameters necessary for input into the As-compacted state model. The types of soil material used in this study, and their physical properties are presented in the following chapter.

3 MATERIAL PROPERTIES AND EXPERIMENTAL PROCEDURES

3.1 Introduction

Four clay type soils were selected for this research program. The selected soils were all native to the Commonwealth of Kentucky. The soils were obtained from two Kentucky Transportation Cabinet active construction sites and two possible borrow sites. The soils are from Daviess County, Fayette County, Henderson County and Lee County, all labelled accordingly with the Kentucky County from which they were obtained. The County locations from which the soils were sampled are depicted in Figure 3.1. These soils represent a very wide range of clay soils throughout the Commonwealth of Kentucky ranging from fat to lean clays.

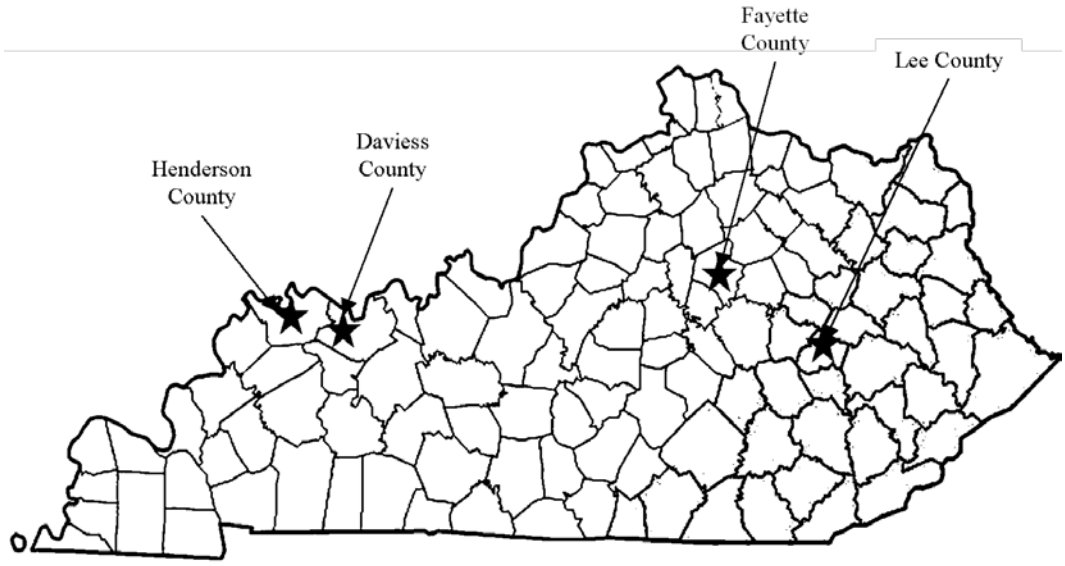

Figure 3.1 Kentucky County locations from which the test soils were obtained

3.2 Physical Properties

The geotechnical index properties of the four Commonwealth of Kentucky soils selected for this research program are tabulated in Table 3.1. Two specific gravity tests were performed for each soil in accordance with ASTM D854 and the average value reported. The Atterberg limits of the soils were determined in according with ASTM D4318. Grain size distribution of the each test soils was determined in accordance with ASTM C117 and D422. The optimum moisture content and maximum dry unit weight were determined by performing the Standard Proctor compaction test in accordance with ASTM D698 to determine the compaction moisture-density relationships for the soils.

Table 3.1 Geotechnical index properties of the Kentucky soils used in this study.

Soil Location	**Daviess County**	**Fayette County**	**Henderson County**	**Lee County**
Specific Gravity Gs	2.72	2.86	2.69	2.65
Liquid Limit (%)	23.3	64.3	28.2	55
Plasticity Index (%)	3.9	29.3	8.5	23
Percent Fines (%)	95.6	86.8	99.4	66.5
Clay Fraction (%)	21	74	20	88
Max. Dry Unit Wt. (kN/m^3)	17.4	13.9	16.5	15.9
Optimum Moisture Content (%)	16.4	31	14.6	22.8
USCS	CL-ML Silty clay	MH Elastic silt	CL Lean clay	MH Elastic silt
Sample Name	**DCsclay**	**FCesilt**	**HCclay**	**LCesilt**

USCS - Unified Soil Classification System

The Fayette and Lee County clays are classified as silts using the Unified Soil Classification System (USCS). In the USCS plasticity chart, the A-line generally separates the more claylike materials from silty materials. Figure 3.2 shows the plasticity relationship of the Fayette and Lee County clays to plot very close to the A-line, which suggests that claylike properties may exist in the soils, therefore they are considered clay

type soils for this research program. Visual classification determined the Fayette and Lee County soils to be fat clays.

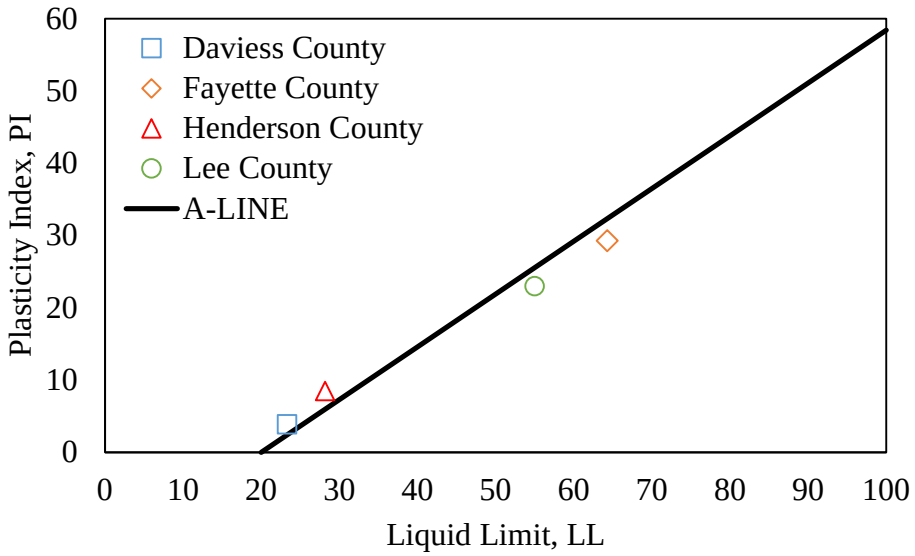

Figure 3.2 Plasticity properties of the Kentucky clay type soils with the USCS A-line.

3.3 Experimental Program

A brief overview of the experimental programs is discussed in this section. Detailed experimental procedures are included in Appendix C. Several test specimens were fabricated and subjected to different test procedures for this study. The experimental procedure consisted of three parts in general: a soil suction program; a soil strength program; and a soil shear modulus program. The experimental test data results obtained from these programs are presented in Chapter 4 through 7, with discussions of their typical mechanical and dynamic behaviors.

The experimental program for this study was designed to observe the effect of density on strength, suction, and shear modulus behaviors in unsaturated and saturated soils, and to use the observed properties to develop robust and useful relationships that

can be easily used in the civil engineering industry. Four clays were selected within the Commonwealth of Kentucky, representing typical clays used in the construction of roadways and embankments.

3.3.1 Soil Suction Program

The soil suction program consisted on performing soil-water retention tests for each of the four Kentucky clays at four different densities for a total of 16 tests. The Standard Proctor maximum dry density (MDD) of each soil type was used as the reference density, and the four selected target densities were based on 80, 90, 100, and 110 percent of the MDD. The soil-water retention tests were performed without any external loading (i.e., at zero net normal stress) and on a drying path, using the pressure plate and the pressure cell apparatus. The drying path extended from a fully saturated state to a maximum matric suction of 1,500 kPa. Each soil-water retention test data was then fitted to the Van Genuchten (1980) equation. The Zhou et al., (2012) model was then used to quantify the effect of initial soil density on the soil-water retention property or the soil-water characteristic curve (SWCC).

The experimental SWCC testing performed provided a means for the estimation of matric suction based on a determined SWCC at an initial density and the possible changes in initial soil density. This process of matric suction estimation was applied to the laboratory scale model tests, where matric suction was not physically measured. Details of the experimental SWCC testing procedures are provided in Appendix C.1.

3.3.2 Soil Strength Program

The soil strength program consisted of performing several strength testing regimes under both saturated and unsaturated conditions. Experimental strength testing involved performing consolidated-isotropic-undrained triaxial tests; constant-water content triaxial tests; constant-water content isotropic compression tests; and laboratory scale model tests.

The consolidated-isotropic-undrained triaxial testing also included all four of the Kentucky soils, each statically compacted at the Standard Proctor MDD and the optimum moisture contents for a total of four test specimens. Soil specimens for the consolidated-isotropic-undrained triaxial testing were first isotropically compressed to an effective pressure of about 70 kPa, to simulate stresses that soils may encounter in a shallow embankment. The soil specimens were then loaded to failure in the shearing phase to determine strength properties under the critical state framework. The selected rate of loading during the isotropic consolidation phase was 3.54 kPa/min (0.5 psi/min), and the selected axial strain rate of loading during the shearing phase was 3 %/hr (0.05%/min). Typical strain rates in literature for consolidated undrained tests generally range from 0.05 to 1 %/min (Maleki and Bayat, 2012).

The constant-water content triaxial testing program included only three of the four Kentucky clay type soils, and each of the three soils having three specimens statically compacted to different density at the Standard Proctor optimum moisture contents. The compacted specimens were loosely wrapped in plastic wrap first, then securely wrapped in bubble wrap and stored for one to two days to allow excess pore pressure buildup from

the compaction process to dissipate. In addition, the storing time also allows for specimen curing, which is the equalization of matric suction, as not only the pore-water pressures would buildup, but pore-air pressures would also buildup during compaction. Most unsaturated soil triaxial test studies do not allow or indicate a storing time for compacted specimens. Inherently, in most studies, the water content of the specimens are changed to establish a pre-defined matric suction, whereby equilibrium is then achieved. Salem, (2006), did allow at least one day, with compacted specimen wrapped in plastic wrap and sealed in a container, prior to being tested.

The constant-water content test specimens were subjected to three phases in triaxial testing; equalization, isotropic compression; and shearing. The equalization phase included the application of a selected air-pressure and allowing the specimen to 'equalize', reaching a state of constant pore-water pressure for the determination of an equivalent, equilibrium matric suction. Isotropic compressions were performed to 70 kPa, as with the CIU tests to simulate stresses that soils may encounter in a shallow embankment. The isotropic compressions were performed under constant-water content conditions to continue to simulate construction phase conditions. The selected rate of loading during the isotropic consolidation phase was 7 kPa/hr. The specimens were then loaded triaxially to failure, with a constant radial stress, and a constant strain rate of 0.5 kPa/hr for the axial loading. Selected axial strains were assumed to be suitable for the critical state condition to be reached, based on tests on similar soil types by Chiu and Ng, (2003); Toll and Ong, (2003); Ma et al., (2013); Rahardjo et al., (2004); and Thu et al., (2006). As was anticipated, the testing shearing phase of this testing program gave

insight into the behavior of shear strength and matric suction under constant water content conditions.

The constant-water content isotropic compression testing was also only performed on three of the four Kentucky clay type soils. Separate specimens from those of the specimens to undergo shearing were made for this test because the magnitude of the isotropic compression of the triaxial test samples were determined to be too small and would not provide details of volumetric behavior under constant-water content conditions. Specimens from each of the three Kentucky soil types used were compacted to the target Standard Proctor MDD and optimum moisture content. Similar storing times for dissipation of pore pressures were used as was done for the constant water content triaxial shearing test specimens. The samples were then subjected to a two-phase approach, namely, the equilibrium phase, and then the isotropic compression phase. The equilibrium phase is the same as that for the constant-water content triaxial shearing specimens, but these specimens were subjected to an increased loading in the isotropic compression phase. The specimens were loaded, unloaded and reloaded to determine the volumetric behavior of unsaturated soils under constant-water content condition and to determine volumetric stiffness parameters with changes in net mean stress. Loading was applied to the specimens to achieve high saturation and to observe the behavior of the resulting changes in matric suction.

As previously stated, the experimental program for this study was designed to observe the effect of density on strength, suction, and shear modulus behaviors in unsaturated and saturated soils, and to use the observed properties to develop robust and

useful relationships that can be easily used in the civil engineering industry. Pertaining to the development of relationships, a specific objective of this research was to determine the effect of shear modulus on shear strength, and if significant, provide a coupling whereby, the prediction of shear strength can be based on changes in shear modulus. For this objective, a laboratory test to simulation field conditions for the determination of shear modulus was fabricated. This simulated test of field conditions was termed the laboratory scale model test, as the amount of soil necessary for testing was much greater than that of a triaxial test and also necessary for the placement of a field stiffness gauge for the determination of shear modulus. Details of the experimental strength testing procedures are provided in Appendix C.2.

3.3.3 Soil Shear Modulus Program

The laboratory scale model testing included all four of the Kentucky soils, each placed loosely in bulk, at four different moisture contents for a total of eight tests. Each bulk sample was statically compacted to incremented densities with the final density at or around the Standard Proctor MDD. At each density increment, shear modulus was determined by the use of a field soil stiffness gauge, and also by use of accelerometers placed in such a way as to receive shear waves transmitted through the bulk soil. Shear modulus obtained by the transmitted shear waves was used in determining the relationship based on the effect of void ratio on shear modulus, to provide a modified void ratio function to that first suggested by Hardin and Black (1968). The shear modulus determined by use of the field soil stiffness gauge provided the means of coupling shear modulus from a field setting to shear strength in triaxial condition.

Bender Element (BE) tests were also performed during the soil strength program to study the behavior of shear modulus with respect to shear strength and net mean stress. The BE tests performed during the shearing phase of the consolidated-isotropic-undrained tests, and the constant-water content tests were used to verify the shear modulus relationship with states of net mean stress and matric suction presented by Sawangsuriya et al., (2009). Details of the experimental shear modulus testing procedures are provided in Appendix C.3.

4 RESULTS OF SOIL SUCTION PROGRAM

The test data results from the soil-water characteristic tests, for the four Kentucky clay type soils at their standard Proctor maximum dry densities are presented in Section 4.1 of this chapter. Section 4.1 also includes test data results at different densities for the clay soil from Henderson County (HCclay). In Section 4.2 of this chapter, estimations of the soil-water characteristic curve (SWCC) for the entire range of matric suction (0 to 1000 MPa) are graphically presented for the HCclay, based on the van Genuchten (1980) model. The model parameters for all four soils are also presented in table form. Estimations of the SWCC for the HCclay, based on the effect of density changes is presented in Section 4.2.2, and 4.2.3, using the Zhou et al. (2012) model. Experimental test data and estimations of the SWCC for all four soils are presented in Appendix E. Details of the calibration and estimation process for the SWCC due to density changes are presented in Appendix F. Section 4.3, comprises of a method of estimation of matric suction at different compaction states due to increasing densities during a laboratory scaled model test. This method presents a soil matric suction and degree of saturation (suction-saturation) characteristic of an unsaturated soil. Therefore, with changes in soil density, a soil suction-saturation characteristic (SSSC), (i.e., the soil-water retention path due to changes in void ratio), can be determined. The discussion and presentation of the method of estimation matric suction includes only the data from the HCclay soil. Estimations of matric suction by the presented method, for all four clays (including the HCclay soil presented in this Chapter) are presented in Appendix G

4.1 Mechanical Behavior of Soil-Water Characteristic Curve Tests

The experimental SWCC test data for the four compacted Kentucky soils are presented in Figure 4.1. The SWCC data were determined from the SWCC methods described in Chapter 3, and are shown in Figure 4.1(a) with respect to water content, and (b) with respect to the degree of saturation. These specimens were compacted at or close to the Standard Proctor maximum dry density and optimum moisture content. The initial saturated gravimetric water contents vary from 0.207 for the Daviess County soil to 0.394 for the Fayette County soil. The matric suction range from 0.01 kPa (for fully saturated specimens) to close to 1500 kPa, which is the maximum permissible with use of the 15 bar HAEPD. For all soils, the water content and the degree of saturation decreases with increase in matric suction. This trend is consistent with other research studies that show that there is a matric suction dependency on the compaction water content. (Olson and Langfelder, 1965; Krahn and Fredlund, 1972; Fredlund and Rahardjo, 1993; Tsai and Petry, 1995; Wan et al., 1995; Bernier et al., 1997; Sivakumar and Wheeler, 2000; and Agus and Schanz, 2006).

The SWCC show the air entry values for the silty clay (DCsclay) and clay (HCclay) soils are lower than those of the elastic silt soils (LCesilt and FCesilt), and they also exhibit lower degrees of saturation within the transition zone for selected matric suctions. In other words, the very high plastic soils exhibit higher matric suctions than soils of lower and medium plasticity. In interpreting the behavior of the lower plasticity soil (DCsclay and HCclay), the clay (HCclay) soil exhibits lower matric suctions than that of the silty clay (DCsclay) soil. Though the soils were both similar types, the clay soil is slightly more plastic, therefore, this behavior was unexpected as higher plastic soils

generally will exhibit higher matric suctions. This may be due to the clay soil having slightly less percent fines and therefore a more open structure when compacted to its maximum dry density.

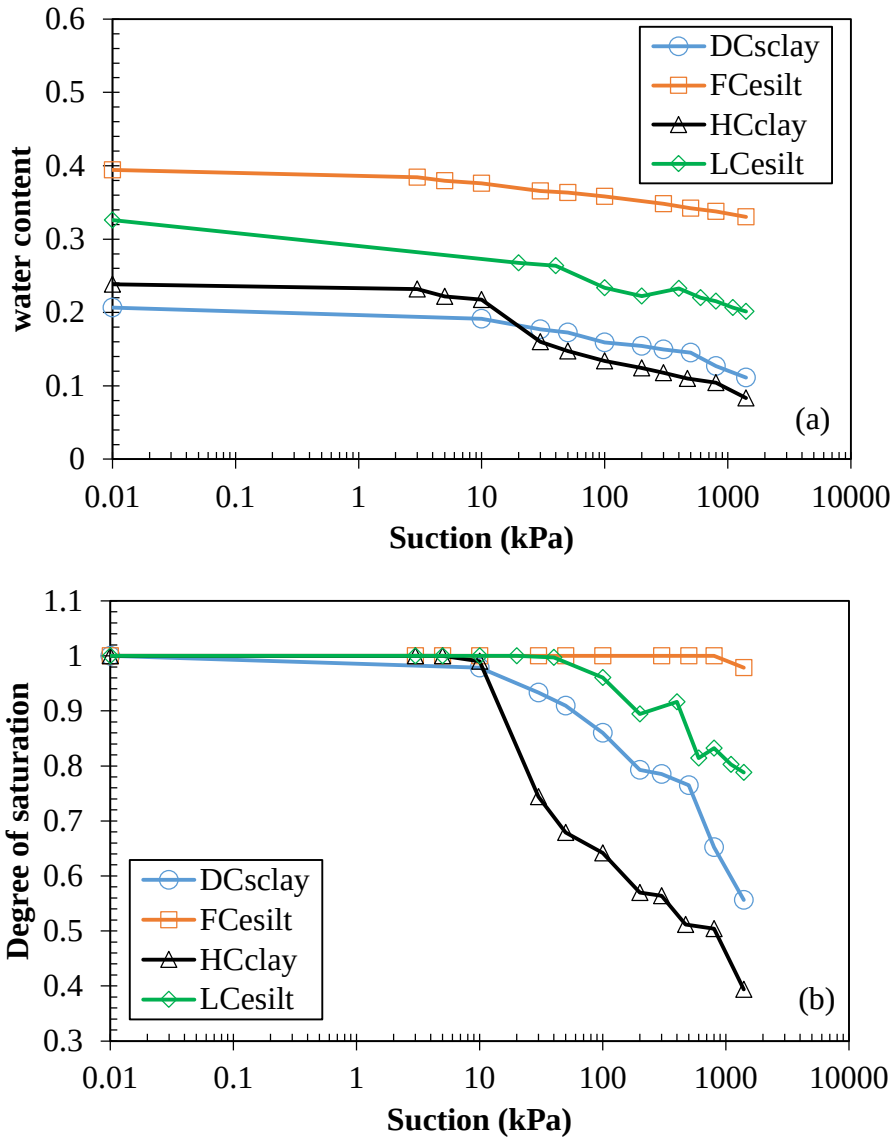

Figure 4.1 Experimental soil-water retention test data for the Kentucky clay type soils at their respective standard Proctor maximum dry density, and optimum moisture contents; (a) with respect to water content; (b) with respect to degree of saturation.

The Kentucky soils were not only subjected to SWCC tests when compacted at or close to their Standard Proctor maximum dry density (100%), but also subjected to

SWCC tests at about 80, 90 and 110% maximum dry density. The effect of change in initial density (or initial void ratio) on SWCC is shown in Figure 4.2, with respect to both water content and degree of saturation for the HCclay soil. The effect of change in initial density is typical in all four Kentucky soils and therefore only the effect in the HCclay soil is discussed here. The plots of the experimental soil-water retention data for all 4 soils are presented in Appendix E.

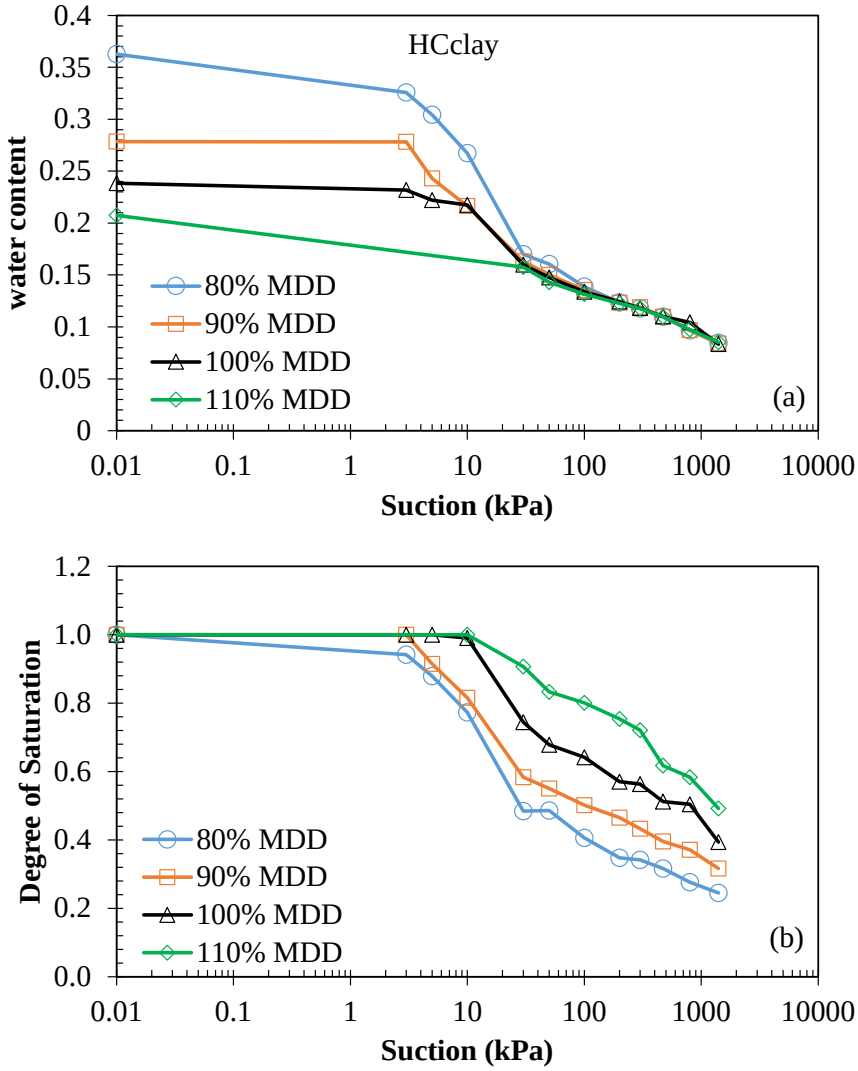

Figure 4.2 Experimental soil-water retention test data for the HCclay soil at different compacted states (a) with respect to water content; (b) with respect to degree of saturation.

The effect of change in initial density in the HCclay soil, as shown in Figure 4.2(a), shows the saturated water content to range from about 0.207 to 0.363 for the most dense to the least dense specimen respectively. The experimental SWCC data, when plotted with respect to water content, as shown in Figure 4.2(a) indicate the matric suction increased as the water content decreased, but more importantly, the figure shows that there exists a water content of about 0.136 (weight of water per unit weight of dry soil), where the matric suctions are equivalent regardless of the initial density (or initial void ratio). Below this critical water content, the rate of decrease in matric suction with water content is also equivalent, therefore there is no effect of change in initial density on the SWCC below this critical water content. This deduction of a non–dependent effect of the initial density on the SWCC, at least for the given matric suction range discussed, is also consistent with the researchers that also indicate that the dependency of SWCC on water content is little to none (Olson and Langfelder, 1965; Krahn and Fredlund, 1972; Fredlund and Rahardjo, 1993; Tsai and Petry, 1995; Wan et al., 1995; Bernier et al., 1997; Sivakumar and Wheeler, 2000; and Agus and Schanz, 2006).

For this reason, the effect of change in initial density on the SWCC of soils is best interpreted using a matric suction and degree of saturation (or $s - S$) plot instead of a suction-moisture plot. A clear dependency of the SWCC on the initial density within the transition zone is noted in the SWCC plot as shown in Figure 4.2(b). The figure shows that there is little change in the degree of saturation for matric suctions below 3 kPa. Matric suction or degree of saturation increases with increase in initial density of the soil.

Noting that both the air-entry values, ψ_{ae} (point of change from saturation to transition zone), and the suction at the inflection points within the transition zones ψ_i, changes with initial void ratio, Figure 4.3 show the effect of the changes in initial void ratio on these two parameters. With both ψ_{ae}, and ψ_i, in logarithmic scale, similar trends (though of different magnitudes) are noted for the effect of changes in initial void ratio on , ψ_{ae} and ψ_i.

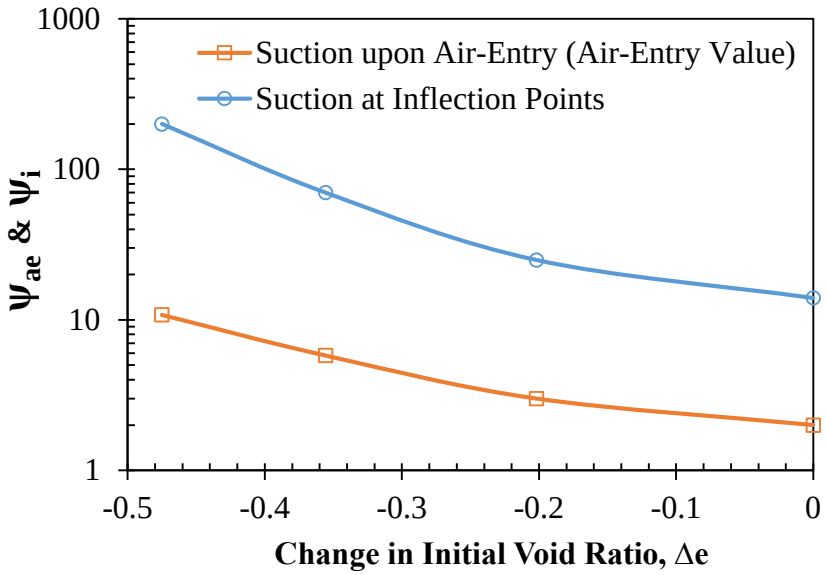

Figure 4.3 The effect of change in initial void ratio with suction at air-entry value ψ_{ae}, and suction at the transition zone inflection points ψ_i for the HCclay soil.

The experimental SWCC data plot in Figure 4.2 defines the saturation and transition zones of the SWCC, but does not define the residual zones. Assumptions can be made to define the residual zone or can be determined using predictive estimations such as that of van Genuchten (1980).

4.2 Predictions of Soil-Water (Degree of Saturation) Characteristic Curves

4.2.1 Estimations of Soil-Water Characteristic Curves

Since data at low water contents (low degree of saturation) were difficult to obtain due to the limiting HAEPD air-entry pressure capacity of 1500 kPa, one assumption made in order to define the residual zones, was that the residual degree of saturation is zero (i.e., $S_r = 0$) for all soils at all tested initial void ratios. This assumption was made for simplicity and for consistency within soils in this research program. Under such circumstances of $S_r = 0$, more reliable fits can be estimated (van Genuchten et al., 1991).

The model used for estimating the SWCC fit to the experimental data is a form of the Van Genuchten (1980) equation.

$$\Theta_n = \frac{w(\psi) - w_r}{w_s - w_r} = \left[1 + \left(\frac{\psi}{a}\right)^n\right]^{-m} \tag{4.1}$$

In the van Genuchten model presented in Equation (4.1), the parameter Θ_n is a dimensionless, normalized water content; $w(\psi)$ is the water content at any given suction; the subscripts r and s indicate residual and saturated values of the soil water content w, respectively; and a, n, and m are fitting parameters where the a parameter is related to the air-entry value; the n parameter is related to the rate of water extraction from soil after the air-entry value has been exceeded; and the m parameter is related to the residual

water content. The normalized water content Θ_n can be describe in terms of degree of saturation S, similarly as it relates to the water content, as follows:

$$\Theta_n = \frac{w(\psi) - w_r}{w_s - w_r} = \frac{S(\psi) - S_r}{S_s - S_r} \tag{4.2}$$

With the assumption previously mentioned of a zero residual degree of saturation, ($S_r = 0$), and that at zero suction ($\psi = 0$), the degree of saturation is one, (i.e., $S(0) = 1$), the van Genuchten (1980) model presented in Equation (4.1), can be simplified such that:

$$S(\psi) = \left[1 + \left(\frac{\psi}{a}\right)^n\right]^{-m} \tag{4.3}$$

Furthermore, as suggested by van Genuchten (1980), the Mualem (1976) relationship between the two parameters n, and m, was used, in order to reduce the number of the independent fitting parameters of the model from three to two. The Mualem (1976) relationship between the two parameters n, and m is given as:

$$m = 1 - \frac{1}{n} \tag{4.4}$$

Optimization between the experimental and predicted data by the van Genuchten-Mualem model was performed to obtain the fitting parameters that provides a best fit estimation to the data. The fitting parameters a, and n were optimized such that an

objective function of the least sum squares difference is minimized. The objective function is given as:

$$O(a,n) = SSD = \sum_{i=1}^{M} \left(S_{mi} - S_{pi}\right)^2 \tag{4.5}$$

In Equation (4.5), S_{mi} represents a degree of saturation measured data point from a set of M applied suction points, and S_{pi} represents a predicted degree of saturation data point from the set of M applied suction points. The Microsoft Office Excel, data Solver function, utilizing the Generalized Reduced Gradient (GRG) non-linear algorithm was used to aid in solving for the minimized objective function. Details of the optimization process is presented in Appendix D.

The a, n, and m parameters for the predicted drying SWCC, based on the optimized least squares difference best fit to the experimental drying SWCC data are tabulated in Table 4.1. The coefficient of determination (i.e., the R^2 value) for each fit, and the soil property of the initial void ratio and average dry density are also presented.

Table 4.1 Van Genuchten equation parameters for the Kentucky soils.

Sample Identification	Initial Void Ratio	Average Dry Density	Van Genuchten Parameters			Squared Difference	Coefficient of Determination
		(kg/m3)	*a*	*n*	*m*		R^2
DCsclay	0.851	1469.3	1.36	1.15	0.13	0.0081	0.986
	0.654	1644.7	4.32	1.13	0.11	0.0189	0.957
	0.519	1797.7	67.26	1.17	0.14	0.0056	0.974
	0.455	1868.5	750.79	1.20	0.17	0.0005	0.988
LCesilt	1.087	1270.4	2.85	1.12	0.11	0.0157	0.964
	0.887	1405.0	3.47	1.08	0.08	0.0186	0.932
	0.680	1577.2	158.55	1.11	0.10	0.0039	0.957
	0.552	1707.8	4000	1.08	0.08	0.0009	0.475
HCclay	0.930	1393.9	4.19	1.27	0.21	0.0190	0.982
	0.728	1556.7	4.61	1.21	0.17	0.0195	0.977
	0.574	1708.7	10.77	1.18	0.15	0.0210	0.967
	0.455	1849.0	38.77	1.18	0.15	0.0064	0.983
FCesilt	1.375	1204.1	2.16	1.05	0.04	0.0043	0.953
	1.105	1358.6	28.63	1.03	0.03	0.0002	0.994
	0.965	1455.1	3000	1.04	0.04	0.0002	0.599
	0.897	1507.5	7000	1.02	0.02	0.0000	

The estimated/predicted SWCC for the HCclay soil at four different initial void ratios are shown in Figure 4.4, along with the experimental data. The predicted SWCC compare well with SWCC for similar type soils reported in literature. The figure shows that the air entry value and the slope of the SWCC changes with increasing initial void ratios, which is consistent with other literatures (Huang 1994; Vanapalli et al., 1999; Lee et al., 2005; Zhou et al., 2012). The approximate air entry values for the HCclay specimens are 2, 3, 5.8, and 10.8 kPa, for increasing initial void ratios of 0.455, 0.574, 0.728 and 0.930 respectively. Similarly, the slopes of the SWCC decreases with increasing initial void ratio. The slopes can be relatively compared at the inflection point of the SWCC, which is the point on a curve where the curvature changes, and it is within the transition zone. The slopes at the inflection points will be the ratio of the degree of

saturation and corresponding matric suction at inflection. The matric suction at inflection for increasing initial void ratios are 14, 25, 70, and 160 kPa, with the corresponding calculated slopes of 0.050, 0.027, 0.010, and 0.005 kPa^{-1} respectively.

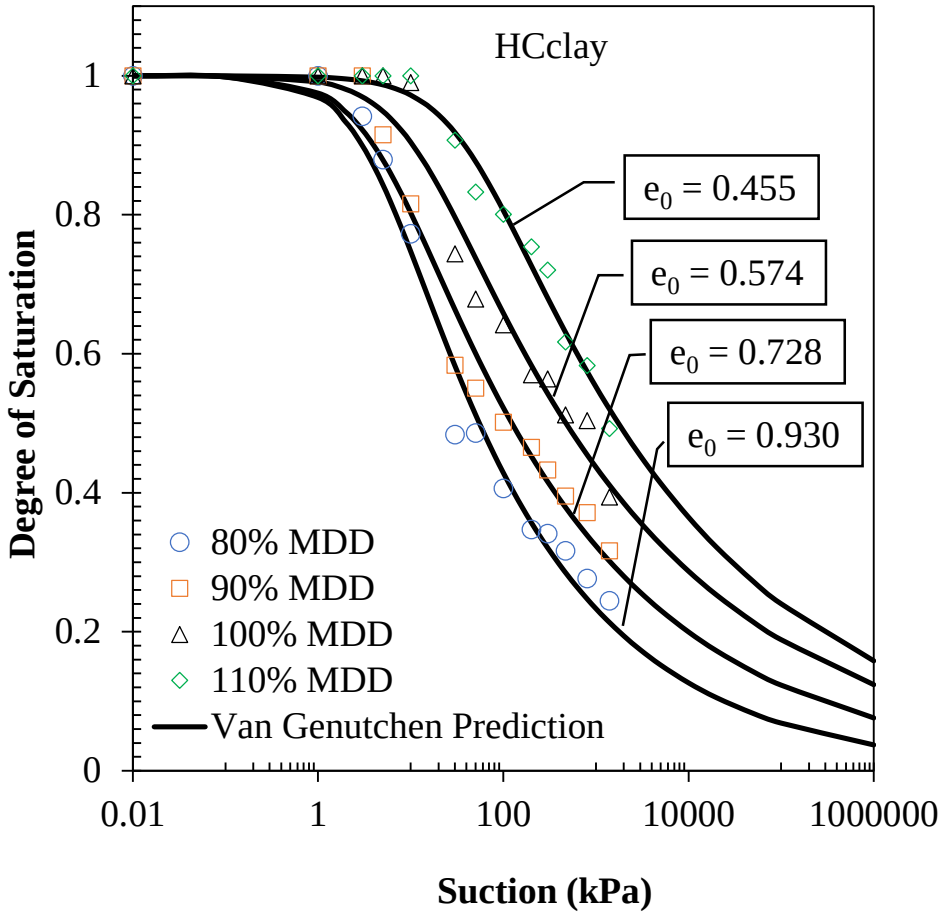

Figure 4.4 Soil-water characteristic curves at different initial void ratio for Kentucky HCclay soil with optimized van Genuchten (1980) – Mualem (1976) model predictions.

The Van Genuchten a parameter is related to the air entry values, therefore, the a parameter increases similarly to the increase of air entry values for the HCclay soils relative to the SWCC plots with increasing initial void ratios.

The n parameter, controls the slope of the transition zone of the SWCC (Fredlund et al., 2012). In general, the slope of the transition zone decreases (becomes flatter) with decrease in the n parameter with respect to a decrease in initial void ratio. Figure 4.4 shows that as the initial void ratio decrease, the Henderson County clay soils desaturated at a decreasing rate in the transition zone, with very minimal change in the rate for the two lowest initial void ratio specimens. This may be due to the assumption of a constant residual degree of saturation, regardless of changes in density. Zhou et al. (2012) presented a model to predict the shifts in SWCC due to changes in the initial void ratio, in other words, estimations of a new SWCC can be made for changes in density or compaction state.

4.2.2 Estimation of SWCC due to density changes - model parameter calibration

The previous sections, Sections 4.1 and 4.2.1, presented the experimental data from the SWCC tests. This and the following section, discusses the quantification of the effect of change in void ratio on the SWCC. Figure 4.5 gives an overview of this section within the overall research program.

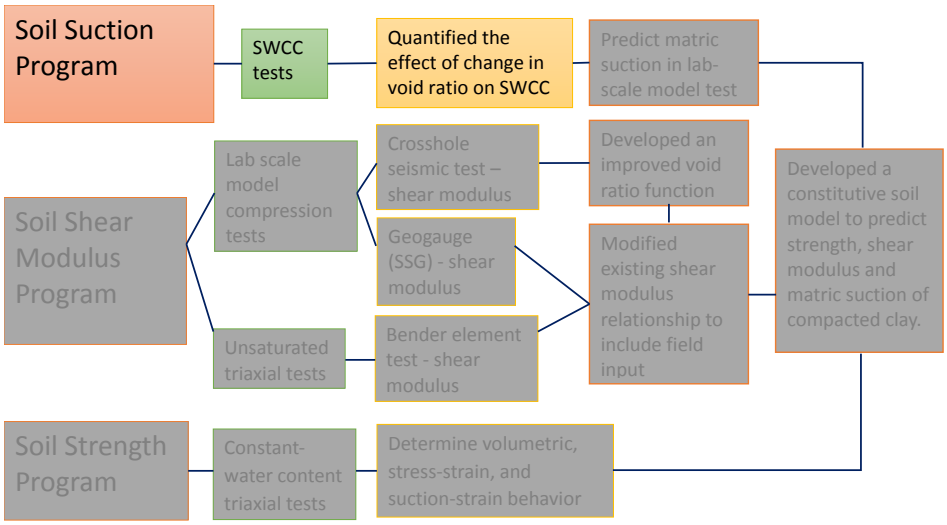

Figure 4.5 A visual of the point of discuss (effect of density no SWCC) within the overall research program.

The Zhou et al. (2012) model was used for estimating the degree of saturation due to initial void ratio changes. The model is given as follows:

$$\int_{e_i^{ref}}^{e_i} -\frac{de_i}{e_i} = \ln\frac{e_i^{ref}}{e_i} \approx \frac{\left(S_e - S_e^{ref}\right)}{6}\left[f\left(S_e^{ref}\right) + 4f\left(\frac{S_e^{ref} + S_e}{2}\right) + f\left(S_e\right)\right] \tag{4.6}$$

In Equation (4.6), the general function terms $f(\,)$, are expressed as:

$$f(x) = \frac{1}{x(1-x)^{\zeta}} \tag{4.7}$$

A closed form solution of the model to determination of the effective degree of saturation is readily available for only two values of the ζ-parameter, 0.50 and 1.00. Due to the complex nature of the approximation form of Equation (4.6), iterations must be performed for the determination of the ζ-parameter, and for the estimation of an effective degree of saturation.

In the experimental validation of the Zhou et al. (2012) model with the Kentucky soils, Visual Basic for Applications (VBA) coding were developed to first calibrate a selected reference SWCC, and secondly to predict the SWCC shift based on a change in void ratio. The VBA coding Zhou2012zetacalibration and Zhou2012SWCCshift are presented in Appendix F.

In calibrating the ζ-parameter, two sets of SWCC experimental data should be available, and both used to determine fitted SWCC data by optimizing the model parameters for each. In this study, the van Genuchten (1980) – Mualem (1976) SWCC model was used. One of the SWCC is selected as a reference SWCC and the other as the calibration SWCC. The experimental data and model parameter for both are input parameters for the VBA code for calibrating the ζ-parameter. The VBA code develops SWCC shifts from the reference SWCC based on changing the ζ-parameter, and then compares the SWCC shifts with that of the calibration SWCC and selects the ζ-parameter that results in a best fit. As previously stated, a detailed presentation of the calibration coding is included in Appendix F.

In the experimental calibration of the ζ-parameter in the Zhou et al. (2012) model using the Kentucky soils, the 90 and 100% MDD SWCC where selected as the reference and calibration SWCC respectively. The HCclay calibration results are discussed here. See Appendix F for results of the other Kentucky soils. For the HCclay, the test data with initial void ratio of 0.728 was selected as the reference SWCC. The van Genuchten's fitting parameters for the reference SWCC are as follows: $a = 4.61$, $n = 1.21$, $m = 0.17$, $S_{res} = 0$. The test data with initial void ratio of 0.574 were

employed to calibrate the ζ-parameter, resulting in the value of 0.13. The selection of the reference SWCC and calibrated SWCC, resulted in a condition where the void ratio is greater for the reference than that of the calibrated SWCC.

Further analyses of the ζ-parameter indicate that this parameter may not be a material property, but may depend on the state of stress on the sample, the condition of the specimen, or the shape of the SWCC. The ζ-parameter changes for the reference SWCC void ratio being higher or lower than the SWCC used for calibration. For the four Kentucky soils, when the SWCC used for calibrating the ζ-parameter, was used as the reference SWCC and the reference SWCC used as the calibrating SWCC (reference and calibrating SWCC were switched), a different ζ-parameter resulted. The ζ-parameter was consistently lower for a reference SWCC with void ratio greater than that of the calibrating SWCC. The calibrated ζ-parameter for the soil suction-saturation shifts are shown in Table 4.2.

Table 4.2 Calibrated ζ-parameter based on the Zhou et al. (2012) model.

WM14HCclay		
Reference Parameters	Parameters for $e_i^{ref} > e_i$	Parameters for $e_i^{ref} < e_i$
ζ	0.13	0.32
a	4.61	10.77
n	1.21	1.18
m	0.17	0.15

4.2.3 Estimation of SWCC due to density changes - model validation

If the reference SWCC is chosen as such that estimation of SWCC shifts with void ratios lower and higher are necessary, then both ζ-parameters for $e_i^{ref} > e_i$ and for $e_i^{ref} < e_i$ should be used for predictions. For example, if the SWCC for the HCclay soil compacted with an initial void ratio of 0.728 (approximately 90% MDD) is used as the reference, predictions of SWCC at a higher void ratio of 0.930 (80% MDD) will make use of the ζ-parameter of 0.32 for $e_i^{ref} < e_i$. Then, predictions of SWCC for an initial void ratio of 0.574 (approximately 100% MDD) will require the use of the other ζ-parameter of 0.13 for $e_i^{ref} > e_i$. Assuming that the ζ-parameter for $e_i^{ref} > e_i$ is valid for prediction of SWCC at any void ratio as long as the criteria $e_i^{ref} > e_i$ is met, then one ζ-parameter can be used for prediction if the reference SWCC is chosen as the SWCC with the highest void ratio. Experimental validations of SWCC shifts were made using the experimental data with the largest void ratio as the reference SWCC and predicting the SWCC for the remaining three experimental SWCC data at lower void ratios for each soil. Figure 4.6 shows the reference SWCC and the measured and predicted SWCC at different void ratios for the HCclay soil. Experimental validations of SWCC shifts for the other soils are included in Appendix F of this report.

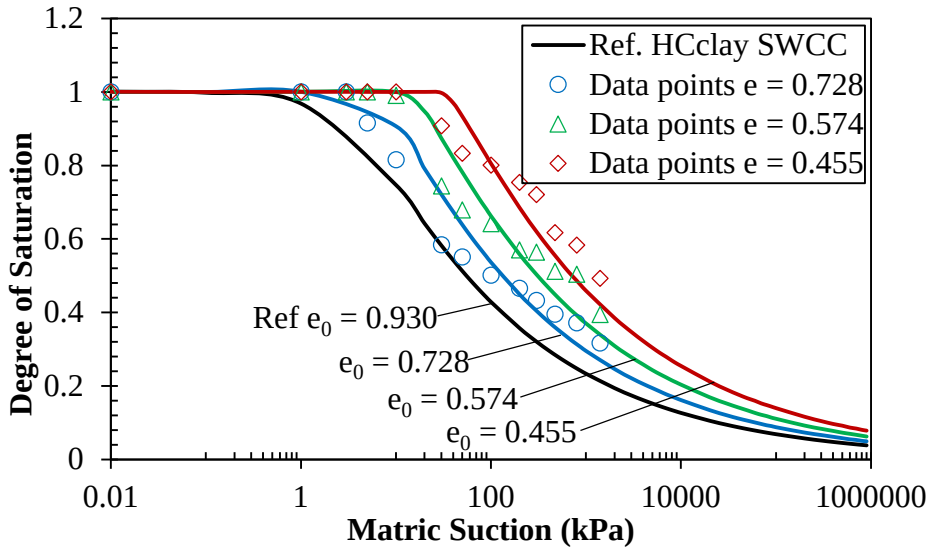

Figure 4.6 Selected reference SWCC, and the measured and predicted SWCC for different initial density of the HCclay soil, based on a form of the van Genuchten (1980) and the Zhou et al. (2012) model; $a = 4.61$, $n = 1.21$, $m = 0.17$, and $\zeta = 0.13$.

The SWCC shifts are consistent with trends of SWCC shifts presented by Zhou et al. (2012). As indicated by Zhou et al. (2012), predicted SWCC shifts in conjunction with the use of the Brooks and Corey (1964) SWCC model, show similar variations to SWCC shifts in this study. Figure 4.6, shows that within reason, the Zhou et al. (2012) SWCC shift model can represent the experimental shift due to changes in initial density. At the top section of the transition zone, prediction of SWCC shift is generally slightly higher, whilst at the bottom section it is closer to or lower than the experimental data. Zhou et al. (2012) further showed that the predicted SWCC shifts in conjunction with the three-parameter van Genuchten (1980), and the Fredlund and Xing (1994) models, predicts experimental data well. Variations, in part, experienced in the predictions are therefore attributed to the use the simplified van Genuchten (1980) – Mualem (1976) model, which uses only two-parameters.

4.3 Estimation of Matric Suction

The state of stress on soil is an important condition necessary to be known for geotechnical designs and analyses, because changes in the state of stress can lead to significant changes in the geotechnical soil properties such as strength and stiffness. Bishop and Blight (1963) and Matyas and Radhakrishna (1968) proposed the use the net mean stress, $(\sigma - u_a)$, and matric suction $(u_a - u_w)$ as independent stress state variables, which are the most widely used two combination of the stress state variables today. In consideration for a field compacted soil, the pore-air pressure is considered to be atmospheric (i.e., zero gauge pressure), thereby reducing the stress state variables to the total stress σ, and negative pore-water pressures, $-u_w$. The net mean stress (or total stress can therefore be determined if the external stress (if any) is known. The matric suction (or negative pore-water pressure) is not as easily determined, and therefore an estimation process for determining the matric suction was developed. Figure 4.7 gives an overview of this section within the overall research program

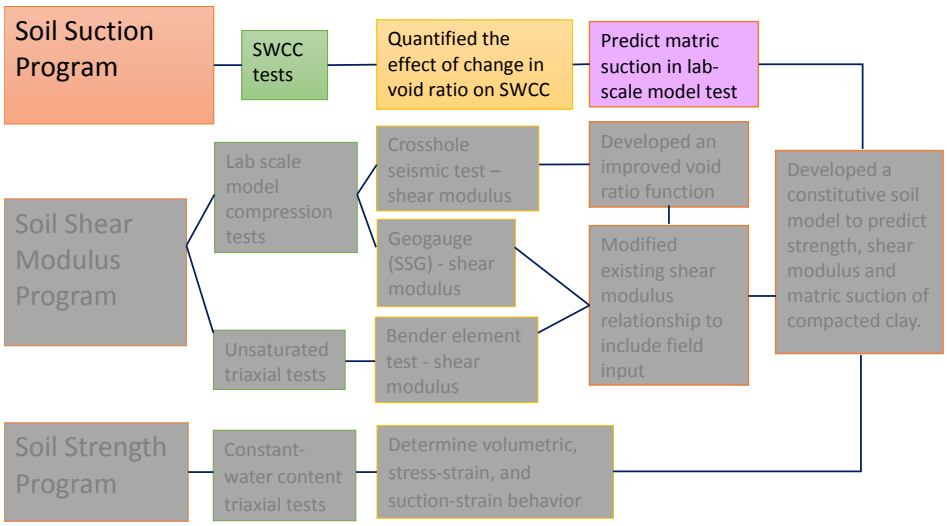

Figure 4.7 A visual of the point of discuss (matric suction prediction) within the overall research program.

In Section 4.2.1, estimation of the SWCC was presented using the van Genuchten (1980) model, whereby for a known density (or void ratio), and a known matric suction, the degree of saturation can be determined. Also in Sections 4.2.2 and 4.2.3, estimation of the SWCC was presented using the Zhou et al. (2012) model in conjunction with the van Genuchten (1980) model, whereby for a change in density (or void ratio), at a known matric suction, the degree of saturation of saturation can be determined. Using these principles, a method for estimation of matric suctions along a path of changing density (void ratio) and degree of saturation is developed, and matric suction is estimated at different void ratios within the laboratory scale model tests.

The VBA codes previously discussed for calibration of the ζ-parameter, and predicting the shift in SWCC due to change in initial void ratio, estimates the degree of saturation for a given matric suction. Another VBA code was developed, and named Zhou2012SWCCshiftforsuction, to estimate the matric suction, for a known degree of saturation given the reference SWCC.

The VBA coding, Zhou2012SWCCshiftforsuction, is presented in Appendix G. The VBA code performs the estimation in two processes. In the first process, the VBA model uses the input parameters of the current void ratio e_i, a known degree of saturation S_r, at the current void ratio; the calibrated ζ-parameter of the Zhou et al. (2012) model; and the known void ratio e_i^{ref} of a reference SWCC, to determine the degree of saturation S_r^{ref}, on the reference SWCC. In the second process, the VBA model uses the determine degree of saturation S_r^{ref} from the first process, with additional input fitting parameter a, n, and m, of the reference SWCC, and the van Genuchten (1980) model to determine the

matric suction, which represents the matric suction on the reference SWCC and at the current void ratio point. The van Genuchten (1980) model was rearranged to solve for matric suction. The use of the Fredlund and Xing (1994) model would have been very difficult to rearrange to solve for matric suction, because of the form and function of the correction factor.

The matric suction was estimated at each point of incremental compaction within the laboratory scale model tests, for the resulting density (void ratio) and degree of saturation at each point of compaction, for the four Kentucky soils. The points of estimated matric suction and the corresponding degree of saturation form a suction-saturation path when plotted on an SWCC plot. In this study, this path was called the soil suction-saturation characteristic (SSSC), as shown in Figure 4.8.

Figure 4.6 also shows the predicted SWCC curves for the initial ($e_{initial} = 2.394$) and final ($e_{final} = 0.627$) void ratios at the start and end of the laboratory scale model test respectively for the HCclay, using the Zhou et al. (2012) procedures discussed in Chapter 4. With estimates of matric suction at compression intervals during the test, the suction-saturation characteristics is shown as the SSSC path for the HCclay at close to optimum moisture content.

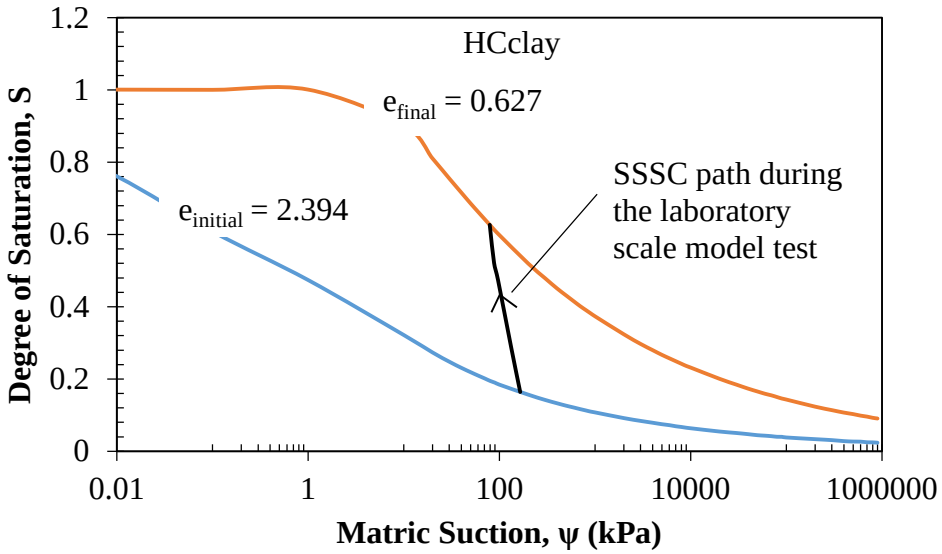

Figure 4.8 Predicted SSSC for changes in void ratio during the laboratory scaled model test, and SWCC at the initial and final void ratios of the test for the HCclay soil under condition of the standard Proctor optimum moisture content.

The calibrated ζ-parameters for the HCclay soil was presented and discussed in Section 4.22. Two ζ-parameters of 0.13 and 0.32 were determined for the void ratio relationships, $e_i^{ref} > e_i$, and for $e_i^{ref} < e_i$ respectively. Using the calibrated ζ-parameters, the reference SWCC parameters, a, n, and m (presented in Table 4.2), estimations of matric suctions were obtained as previously discussed using the two-process VBA coding.

The experimental test data for Henderson County soil at four different moisture contents and the corresponding estimations of degree of saturation for the reference SWCC, and matric suction are shown in Table 4.3. The four moisture contents includes one test below optimum, one at the optimum, and two tests above the optimum moisture content. The reference SWCC used has a reference void ratio of 0.728. Tabulated results of estimations of matric suction for all four Kentucky soils are presented in Appendix G.

Table 4.3 Estimated matric suctions and reference SWCC data for corresponding measured test data, and the ζ-parameters used for estimating the matric suction for the HCclay soil within the laboratory scaled model tests.

Measured Experimental Data					Estimated data		
Moisture Content (%)	Void Ratio	Degree of Saturation	Effective Degree of Saturation	zeta	Reference Effective Degree of Saturation	Reference Degree of Saturation	Matric Suction
(%)	e	S_r	S_e	ζ	S_e^{ref}	S_r^{ref}	ψ (kPa)
11.4	2.086	0.147	0.147	0.32	0.382	0.382	452.7
	1.458	0.210	0.210	0.32	0.391	0.391	403.3
	1.189	0.258	0.258	0.32	0.398	0.398	371.7
	0.850	0.361	0.361	0.32	0.412	0.412	315.6
	0.701	0.438	0.438	0.13	0.422	0.422	281.6
14.6	2.393	0.164	0.164	0.32	0.471	0.471	165.3
	1.371	0.287	0.287	0.32	0.493	0.493	133.2
	0.829	0.474	0.474	0.32	0.526	0.526	96.9
	0.754	0.521	0.521	0.32	0.536	0.536	88.1
	0.627	0.627	0.627	0.13	0.548	0.548	79.4
16	2.016	0.213	0.213	0.32	0.516	0.516	105.8
	1.206	0.357	0.357	0.32	0.542	0.542	83.7
	0.724	0.595	0.595	0.13	0.591	0.591	54.5
	0.654	0.658	0.658	0.13	0.598	0.598	51.3
	0.577	0.746	0.746	0.13	0.609	0.609	46.6
19.7	1.899	0.279	0.279	0.32	0.618	0.618	43.4
	1.168	0.454	0.454	0.32	0.655	0.655	32.3
	0.696	0.762	0.762	0.13	0.733	0.733	17.5
	0.647	0.820	0.820	0.13	0.743	0.743	16.2
	0.579	0.915	0.915	0.13	0.764	0.764	13.7

Each HCclay soil SSSC path in the laboratory scaled model test for the four different moisture contents are shown in Figure 4.9. The SSSC paths for soils wetter than the standard Proctor optimum moisture content will shift to the left and for soil dryer than the optimum moisture content will shift to the right of the SSSC path for the optimum moisture content, as shown in Figure 4.9. The SSSC paths for laboratory scaled model

tests at close to optimum moisture content for all the Kentucky soils are shown in Appendix G.

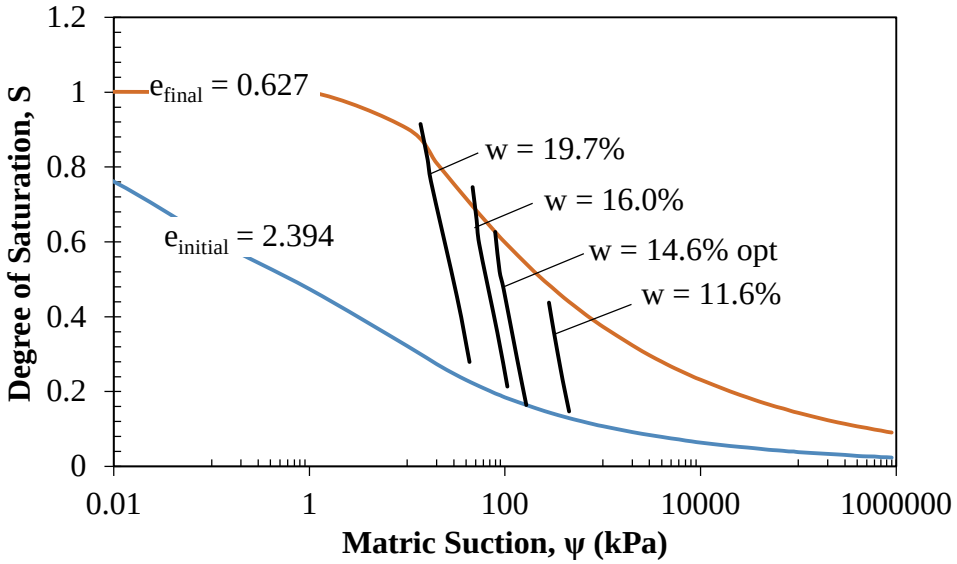

Figure 4.9 Predicted SSSC for changes in void ratio during the laboratory scaled model test, at different moisture content, shown with the predicted SWCC at the initial and final void ratios of the test under condition of the standard Proctor optimum moisture content for the HCclay soil

5 RESULTS OF THE SOIL SHEAR MODULUS PROGRAM

Dynamic test data results from the laboratory scaled model tests for the four Kentucky clay type soils under conditions of the varying moisture contents and increasing densities are presented in this Chapter. The mechanical behaviors, though pertinent, are not discussed in this dissertation. The effects of void ratio on the stiffness and shear modulus based on the use of the Geogauge are presented in Section 5.1. In Section 5.2, shear wave velocities and shear modulus obtained from the simulation of field crosshole seismic tests are presented and discussed. Analyses of shear wave velocities and shear modulus leads to the development of a new void ratio function that is used for predictions of small-strain shear modulus in Chapter 8.

Lastly, the bender element test data obtained during the shearing phase of the unsaturated triaxial tests and the subsequent determination of shear modulus from the data are presented in Section 5.3. The experimental test data results for the HCclay soil was used to discuss the trends and responses of test data in Sections 5.1 and 5.2. The discussion and interpretation of the bender element tests was based on the typical response of the DCsclay soil.

The experimental test data results of the laboratory scale model tests and the bender element tests are presented in Appendix H.1.

5.1 Geogauge Shear Stiffness and Shear Modulus

Figure 5.1 gives an overview of this section within the overall research program.

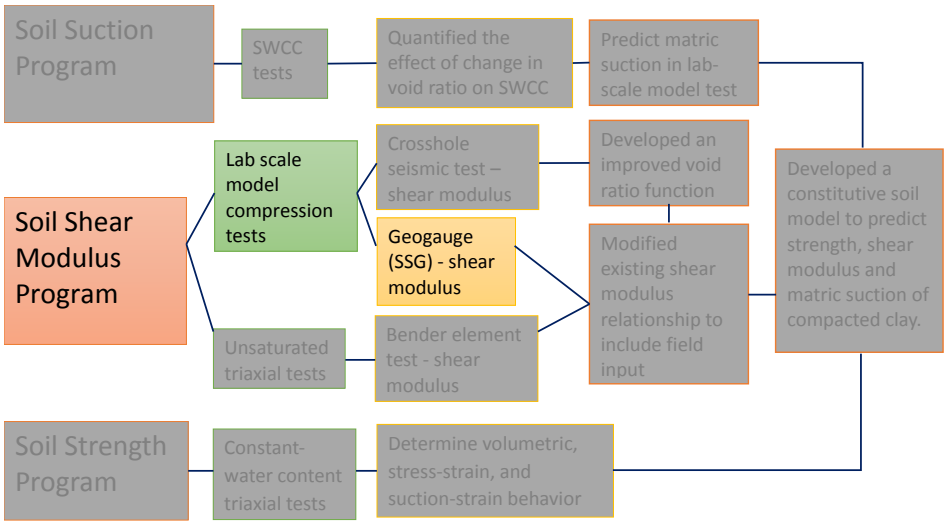

Figure 5.1 A visual of the point of discuss (Geogauge tests) within the overall research program.

The Geogauge was used to determine the soil stiffness at different void ratios within the laboratory scale model test. Figure 5.2 shows the effect of change in void ratio on the stiffness of the Kentucky soils at or close to their Standard Proctor optimum moisture contents. In general, stiffness of the soils increases with decreasing void ratio, and since the void ratio is directly related to the dry density based on the method of testing, the soil stiffness can also be said to increase with increases in dry density. The stiffness trends with dry density or void ratio as shown in Figure 5.2, are consistent with the case study data presented by Humboldt, (2007). But, in literature in general, there are contradicting conclusions with respect to the effect of compaction dry unit weight on stiffness or shear modulus as will be discussed later in this section.

More importantly, the figure shows that soil plasticity may have an effect on soil stiffness. At any given void ratio, the soil stiffness for Daviess, Henderson, Lee and Fayette County soils increases respectively as does their plastic index.

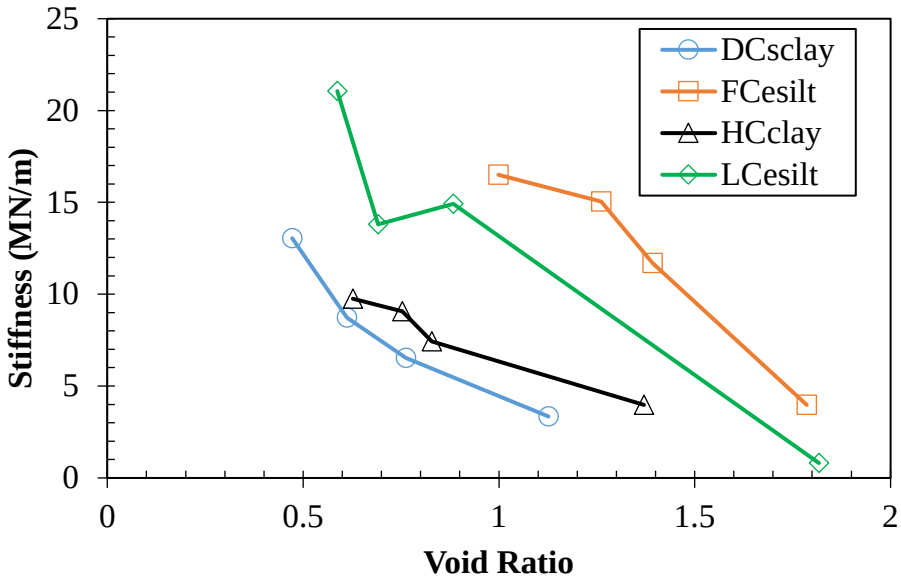

Figure 5.2 Experimental results of Geogauge soil stiffness test data with respect to void ratio for the four Kentucky clay type soils under the conditions of targeted standard Proctor optimum moisture contents.

To determine the effect of change in initial density on stiffness due to changes in moisture content, the data for each soil tested at different moisture contents were used. The effect of change in initial density for the HCclay soil is shown in Figure 5.3. The plots of all four Kentucky soils are included in Appendix H.1. The figure shows that in general, for Henderson clay at the optimum moisture content, stiffness or shear modulus increases as void ratio decreases. But, for moisture contents drier and wetter than the optimum content, the stiffness or shear modulus initially increases with decreasing void ratio and then decreases. This decrease in stiffness may be due to an increase in pore-water pressures within the soil matrix. No measurements of in-situ pore-water pressures were determined for the laboratory scale model tests. In general, where the soil stiffness increases with decreasing void ratios, the soil stiffness also increases with decreasing water content, for a given void ratio. At higher densities (lower void ratios), the soil

stiffness initially increases as moisture content decreases until the point of optimum moisture, after which the soil stiffness decreases.

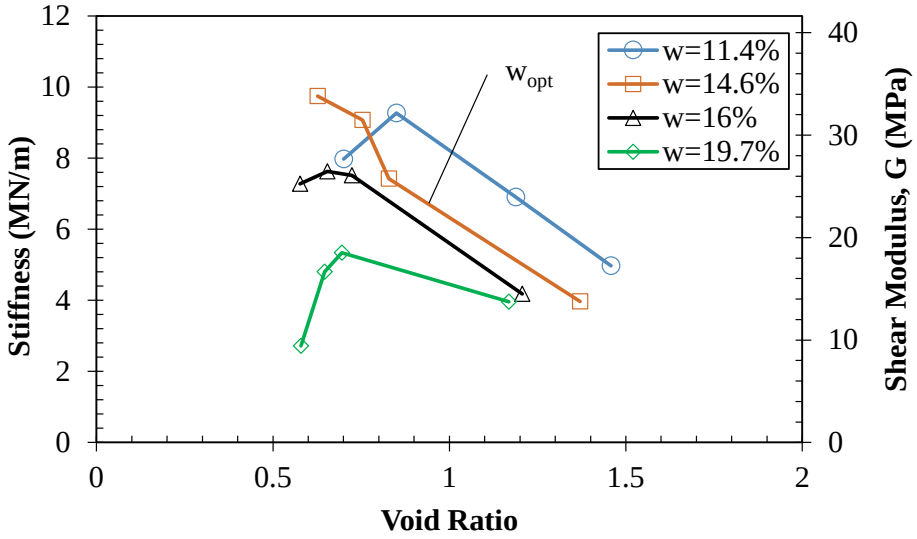

Figure 5.3 Experimental results of Geogauge soil stiffness test data with respect to void ratio for the HCclay soil under conditions of different moisture contents.

The trends shown in Figure 5.3 for water contents wet of optimim are consistent with data from other research studies such as Ooi and Pu (2002, 2003). The trends of soil stiffness or shear modulus for optimum moisture contents are also consistent with Stephenson (1978) and Edil and Sawangsuriya (2005).

As previously discussed in Chapter 2, Section 2.3.7, literature data show some contradictions regarding the effect of compaction dry unit weight on the shear modulus or stiffness. Though Stephenson (1978), Edil and Sawangsuriya (2005), and Clayton (2011) gave similar conclusions of increasing shear modulus with decreasing void ratio, they differ from that given by Ooi and Pu (2002, 2003) of increasing stiffness to a peak state and then decreasing with increases in dry density, and all still differ from the conclusion given by Sawangsuriya et al. (2006) of no effect of dry density on shear modulus.

Though literature data show some contradictions, the results of the Geogauge stiffness tests gives insight into the possible reasons for inconsistencies of the effect of dry density on stiffness. It appears that there are thresholds of both compaction efforts and water contents that effect the trends in soil stiffness of clay type soils. This threshold point is not noted in Figure 5.2, as the stiffness appear to continue to increase with increasing density (decreasing void ratio). It should be noted that soil data presented in Figure 5.1 are in a state for optimum compaction, i.e., they are at moisture contents that are suitable for optimum compaction (at least under conditions of standard Proctor). Therefore, there may be an increased range of increasing densities whereby stiffness continues to increase for soils in a state of optimum compaction.

When the optimum data (HCclay in Figure 5.2), is compared with stiffness test data at different moisture contents as shown in Figure 5.3, changes in the stiffness trends occur at threshold points of void ratio. Further, the threshold points of void ratios in Figure 5.3 appear to initially decrease slightly with decreasing moisture content up to the point of optimum moisture, after which they increase (assuming the threshold for the point of optimum moisture is eminent). In terms of dry density, as the water content decreases, the threshold dry density increases to a point (the optimum), after which the threshold density decreases. This is analogous with dry density – water content (Proctor) curves for different compaction efforts.

Furthermore, a change in dependency of compaction on void ratio to soil stiffness is noted in Figure 5.4. In Figure 5.3, each of the four plots at different moisture contents have four points. Each point on the plots corresponds to a compaction effort based on

unit displacement in the laboratory scale model containment apparatus. Comparing the points at each similar unit displacement, the trends are developed as shown in Figure 5.4. For the range of moisture content test conditions (11.4 to 19.7 %), it appears that at high void ratios (low densities), there is little to no dependency of soil stiffness on the void ratio (or density). In other words, changes in water content of soil at low densities has no effect on the stiffness, but has a significant effect on the volume changes (significant changes in void ratios), which is a collapse or settlement phenomenon. As void ratios decrease (increasing densities), soil stiffness becomes increasingly more dependent on the compaction efforts, and at low void ratios (high densities), changes in water content of soil has significant effects on the soil stiffness with a much diminished effect on volume changes.

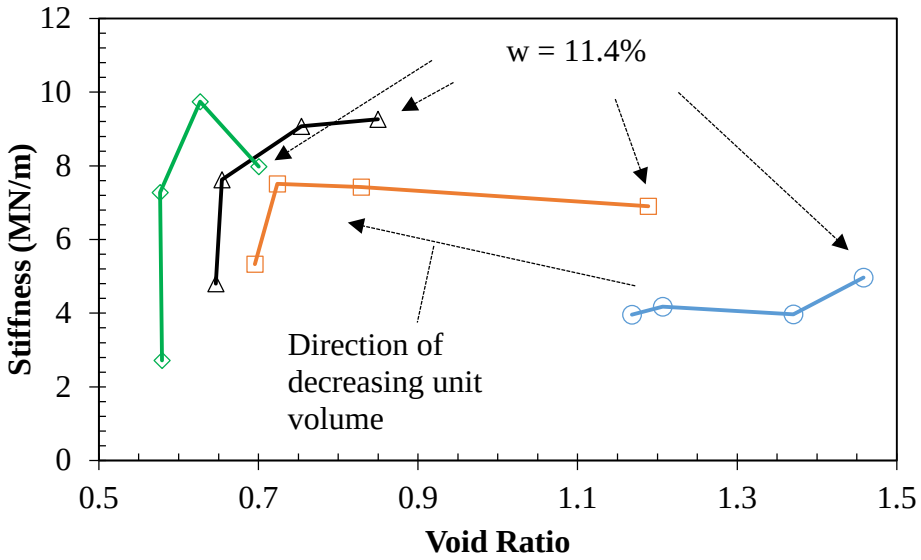

Figure 5.4 Experimental results of Geogauge soil stiffness test data with respect to void ratio for the HCclay soil under conditions of different unit displacements within the laboratory scale model test.

5.2 Picoscope Shear Wave Velocities and Shear Modulus

The Picoscope was used to determine shear wave velocity by simulation of crosshole seismic method within the laboratory scale model tests. Figure 5.5 gives an overview of this section within the overall research program.

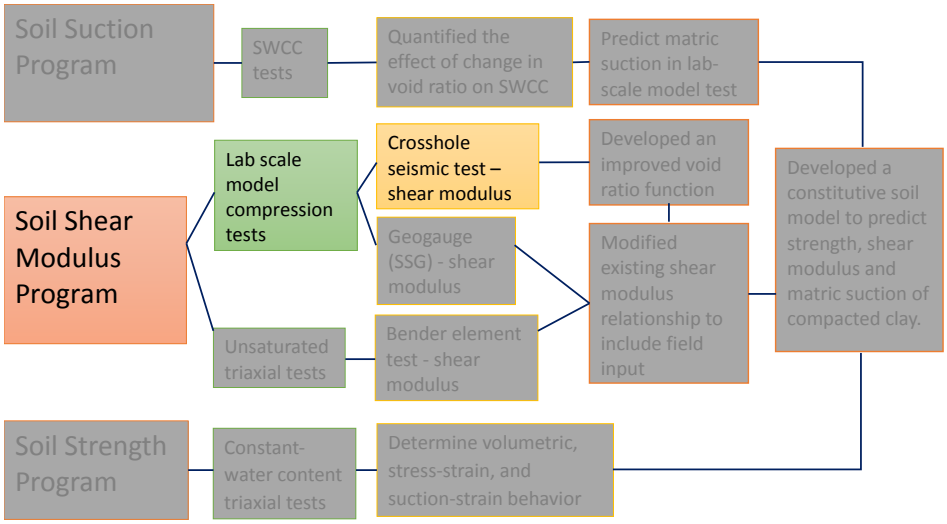

Figure 5.5 A visual of the point of discuss (crosshole seismic tests) within the overall research program.

The experimental shear wave velocity data for the HCclay soil is presented in Figure 5.6, plotted with respect to the void ratio, in order to determine the effect of void ratio on the shear wave velocity with changes in moisture content. The experimental data plots for all four Kentucky clay type soil tests are included in Appendix H.1

For the HCclay bulk soil specimen, and as shown in Figure 5.6, the shear wave velocity generally increases with decreasing void ratio, with exception. The latter trend was true for bulk soils under conditions that are at or dry of the optimum moisture content. The exception to this trend is noted for the bulk soil, wet of the standard Proctor optimum moisture content, whereby the shear wave velocity was essentially constant under initial compaction conditions until a threshold void ratio, after which stiffness

increases with decreasing void ratio. These trends agree with data in literature: Hardin and Richart (1963) and Skora (1987) show shear wave velocity increases with decreasing void ratio; as did Salem (2006), but in addition, Salem (2006) showed that for compacted soils that were compacted wet of the optimum moisture content, the initial increase in shear modulus with dry unit weight is negligible at low dry unit weights, and significantly increases as dry unit weights continue to increase.

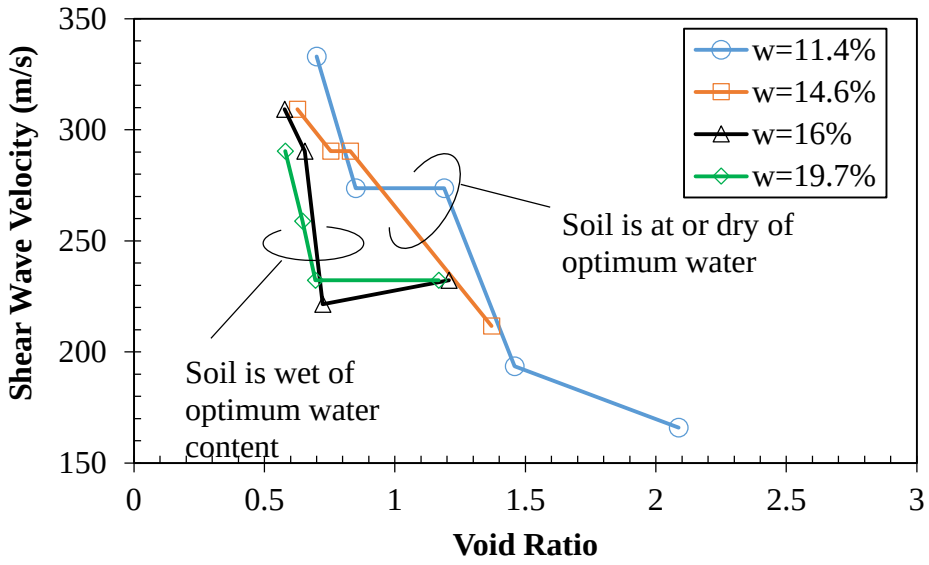

Figure 5.6 Experimental shear wave velocity test data from the crosshole seismic simulation tests plotted with respect to void ratio for the HCclay soil under conditions of different moisture contents.

Dynamic shear modulus was determined from both the stiffness measurements and the shear wave velocities measurements. As discussed previously in Section 5.1, the dynamic shear modulus determined from the Geogauge stiffness measurements generally increases until a peak stiffness, then decreases for further increase in void ratio. For the dynamic shear modulus determined from shear wave velocities measurement, the effect of changes in void ratio is shown in Figure 5.7. In general, the shear modulus increases as the void ratio decreases. From the figure, it appears that the plots can be grouped into

two categories; at and dry of optimum water content; and wet of optimum water content. With this grouping, the shear modulus is generally lower for samples wet of optimum water content than those at or dry of optimum water content, for a given void ratio. Shear modulus determined from shear wave velocities does not show a peak as was noted with the shear modulus determined from the stiffness measurements.

The trends of shear modulus determined from shear wave velocities, with void ratio agree with data from literature (Hardin and Richart, 1963; Hardin and Black, 1968, 1969; and Stephenson, 1978)

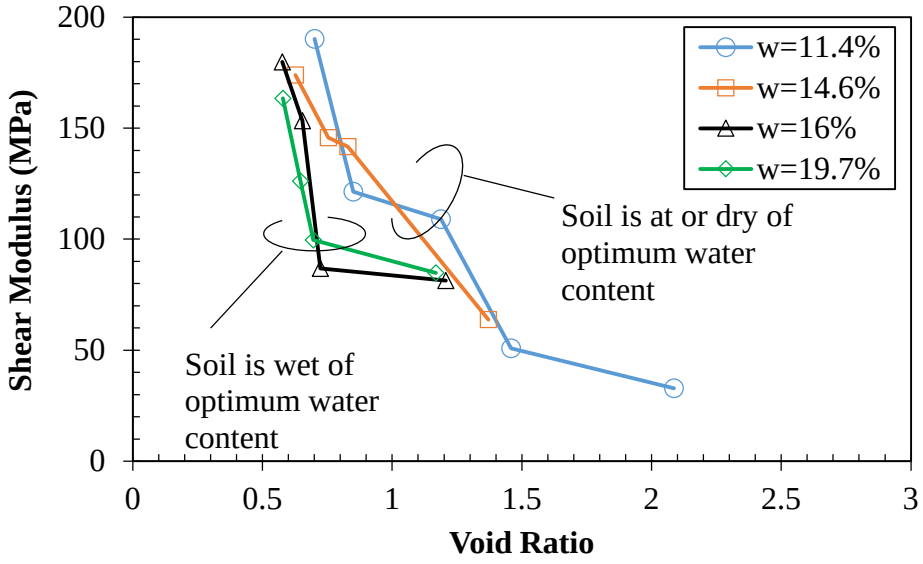

Figure 5.7 Experimental shear modulus test data from the crosshole seismic simulation tests plotted with respect to void ratio for the HCclay soil under conditions of different moisture contents.

To determine the effect of void ratio on the shear modulus across the four Kentucky clay type soil, the shear modulus from the readily compactable soils, i.e., the soils at or very close to the standard Proctor optimum moisture contents, were used. The shear modulus were normalized to the initial shear modulus at the first compaction state, for

consistency in interpretation. The normalized shear moduli for these soils were plotted with respect to the void ratio as shown in Figure 5.8. In general consistency with previously noted shear modulus behavior, the normalized shear modulus or modulus ratio increases as the void ratio decreases for all four soils. Though this behavior is generally consistent between the clay type soils, there was no conclusive behavior of the shear modulus ratio with soil types for all the soils. Of note is that there is a defined trend for three of the four soils types; DCsclay, HCclay, and FCesilt, whereby for a given shear modulus ratio, the void ratio of the soils increases as their plasticity increases. As such, at a given void ratio (or density), the shear modulus ratio increases for each soil type as the soil plasticity increases. The plasticity index of the DCsclay, HCclay, and FCesilt soils are 3.9, 8.5, and 29.3 % respectively.

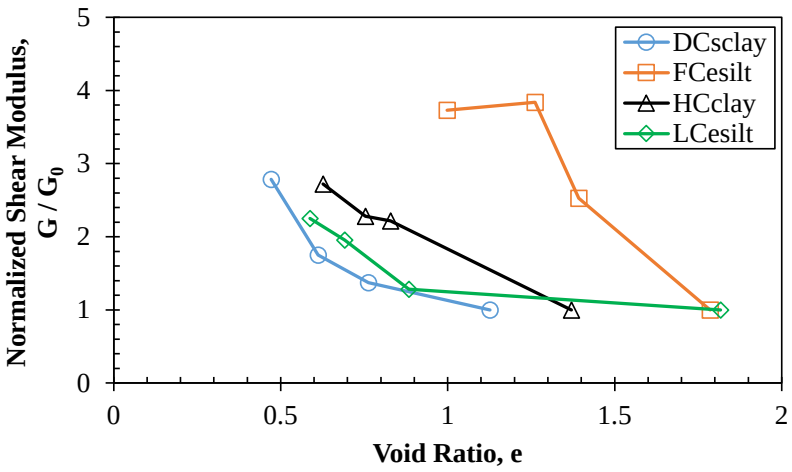

Figure 5.8 Experimental test data results of shear modulus ratio with void ratio for the Kentucky soils under conditions of targeted standard Proctor optimum moisture contents.

The LCesilt is an elastic silt soil of high plasticity ($PI = 23$), though not as high as that of the FCesilt soil. It was expected that the shear modulus or the shear modulus ratio would trend higher than the DCsclay and HCclay (sandy-clay and clay) soils. The lower

modulus ratio of the LCesilt soil can most likely be attributed to its heavily overconsolidated soil structure.

5.2.1 The Determination of a Void Ratio Function

From the shear modulus determined by the crosshole seismic tests within the laboratory scale model tests, an enhanced void ratio function was determined. Figure 5.9 gives an overview of this section within the overall research program.

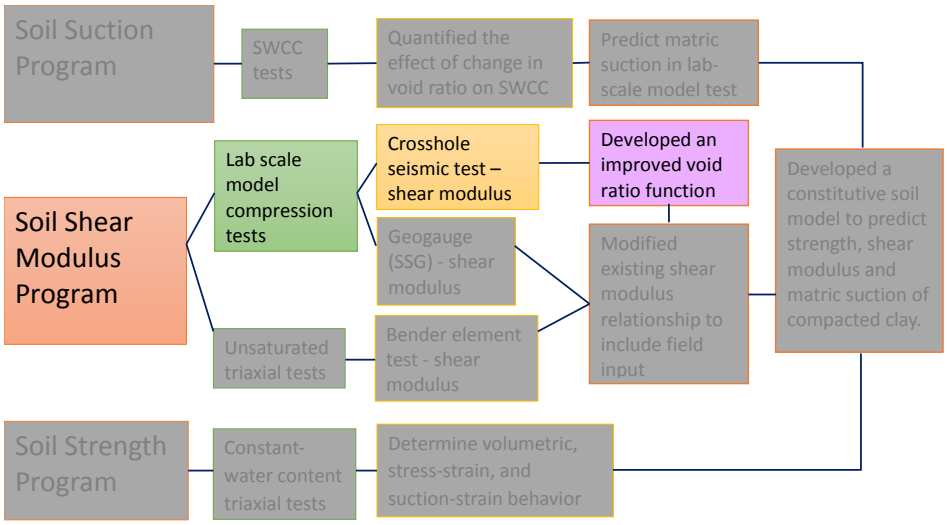

Figure 5.9 A visual of the point of discuss (an enhanced void ratio function) within the overall research program.

The effect of change in void ratio on shear modulus determined from the shear wave velocities agrees with those presented by Hardin and Black (1969). The Hardin and Black (1968) void ratio function equation was presented and discussed in Chapter 2, Section 2.3, within the background reviews section of this dissertation. The Hardin and Black (1968) void ratio function $F(e)$, is based on a relationship determined by Hardin and Richart (1963) of shear wave velocities, and it is given as follows:

$$F(e) = \frac{(2.97 - e)^2}{1 + e} \tag{5.1}$$

Hardin and Richart (1963) show that the relationship of shear wave velocities V_s, void ratios, e, and hydrostatic confining pressure, $\bar{\sigma}_0$, for angular grained soils presented in Equation (2.13) indicate a linear relationship of V_s with e, and a power function relationship of V_s with $\bar{\sigma}_0$, both in two dimensional space. In the laboratory scaled model tests, the shear wave velocities were determined at densities (void ratios) during the unloaded phases, after the soil was allowed to rebound. External stress was used to produce changes in void ratio, and hence changes in soil structure in the laboratory scaled model tests. But since the external stresses were unloaded and the bulk soil was allowed to rebound, the dependency of void ratio on external stress is minimized and the dependency of void ratio on soil structure is enhanced.

In an effort to compare the Hardin and Black (1968) void ratio function to a void ratio function derived from the Kentucky soils data, the linear relationship was initially adopted for the relationship between shear wave velocities and void ratios of the Kentucky soils. Figure 5.10(a) shows the data for shear wave velocities with void ratio and their linear relationship. The dashed lines were drawn to indicate the limiting trend of the data, and as such, they show that the data points flare to the left and upwards, indicating an increasing variation of shear wave velocities and an increasing rate of change as void ratio decreases. The best fit linear predictive relationship does not capture or portray this effect of an increasing rate of change in shear wave velocity as void ratio decreases.

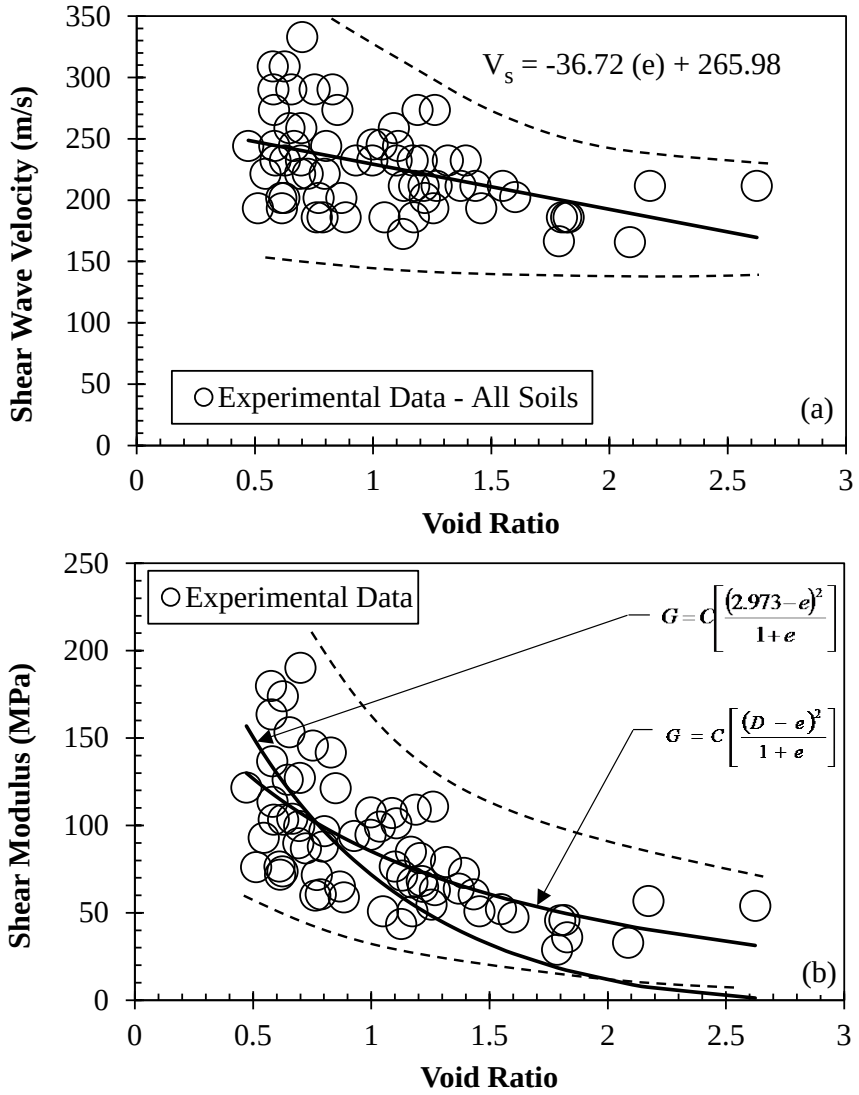

Figure 5.10 Experimental data and predictive trends of the Kentucky soils for: (a) Shear wave velocity with void ratio data and a linear predictive trend; (b) Shear modulus with void ratio data and predictive trends using Hardin and Black void ratio function, and an optimized function.

The dynamic shear modulus data were determined from the shear wave velocity data. The data for shear modulus and void ratio for the Kentucky soils are plotted in Figure 5.10(b), and the general form of a shear modulus relationship as presented in Equation (5.5), is used to show the effect of void ratio on shear modulus:

$$G = C\,F(e) \tag{5.2}$$

In the Equation (5.5), the parameter C is a constant. The predictive effect of void ratio on shear modulus using Equation (5.5) with the Hardin and Black (1968) void ratio function, with a unitless constant of 2.973, is plotted in the Figure 5.10(b). The Hardin and Black void ratio function does not appear to portray well the effect of void ratio on shear modulus. The Hardin and Black void ratio function estimates much lower values of shear modulus for higher void ratios. Using the form of the Hardin and Black void ratio function, that was determined from a linear trend, optimization was performed to determine the best fit relationship by changing the value of the unitless constant, D, as shown in Figure 5.10(b) (see Appendix D for the optimization procedure). The optimized value of D is 9.839 for the linear form of the void ratio function, which portrays well, the effect of void ratio on shear modulus. This is a significant difference between the optimized unitless constant of 9.839 to the Hardin and Black constant of 2.973.

A better fit of a function to the shear wave velocity data in Figure 5.10(a) would be a power function to capture the increasing rate of shear wave velocity within the limits of void ratio of 2.62 to 0.47. This function is shown in Figure 5.11(a). The power function appears to be a better fit to the data as it portrays well the effect of changes in void ratio on shear wave velocities. The power function captures the trend of increasing rate of shear modulus with decreasing void ratio. The best fit power function relationship is given as follows:

$$V_s = 223.17\, e^{-0.18} \tag{5.3}$$

Substituting Equation (5.3) into the elastic theory shear modulus equation $G = \rho V_s^2$, the resulting void ratio function $F(e)$, bounded by limits of void ratio between 2.7 to 0.4 is given as :

$$F(e) = \left[\frac{1}{e^{0.36}(1+e)} \right] \tag{5.4}$$

Figure 5.11(b) shows the shear modulus data with void ratio for the Kentucky soils. In addition, the general form of the equation $G = C\,F(e)$ is used to show the effect of changes in void ratio on shear modulus. Using the latter $F(e)$ form based on a power function relationship, the solid curve shown in Figure 5.11(b) portrays well the effect of void ratio on shear modulus. When this form of the general equation is optimized by changing the constant C, and D, the power of e, and plotted as the dashed curve in Figure 5.11(b), there is statistically no difference between the plots. The optimized value of D is 0.207. The similarities in the curves indicate the effect of void ratio on shear modulus can be well portrayed by the void ratio function based on a power function.

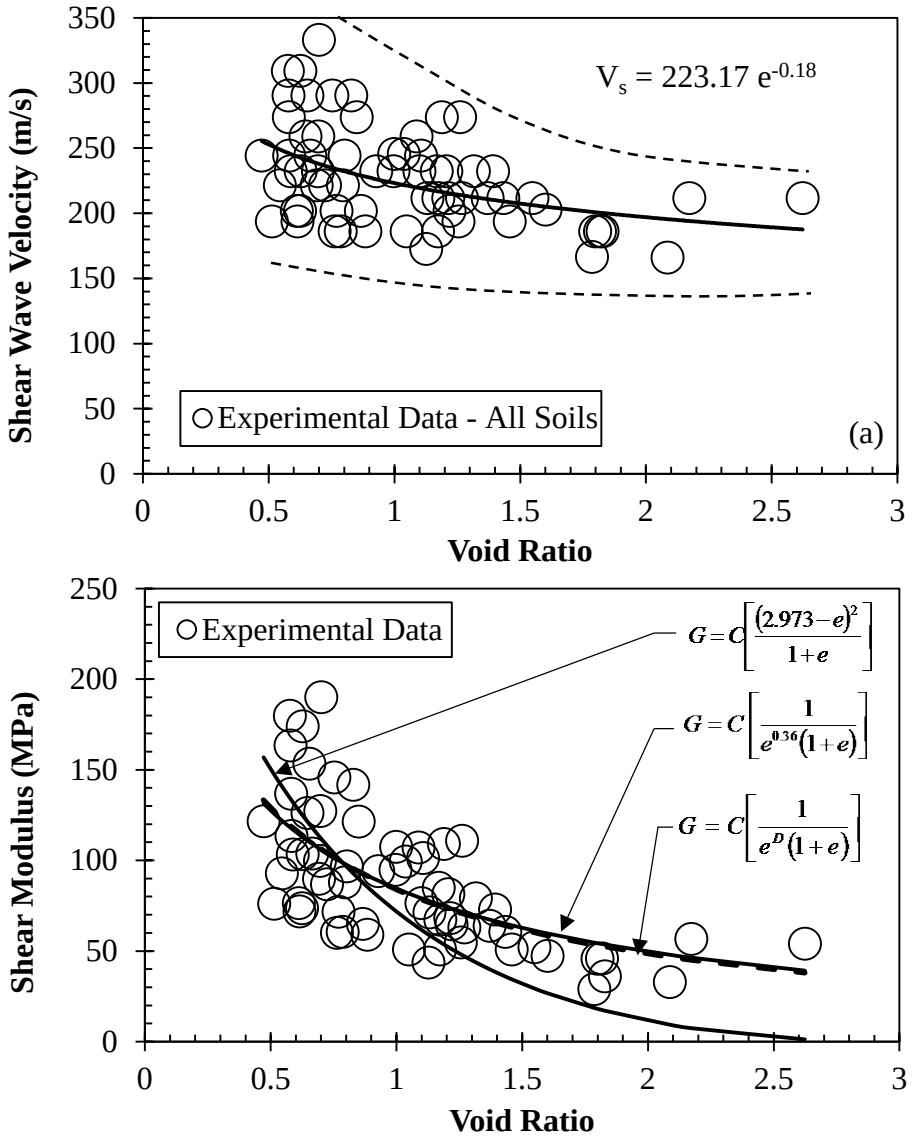

Figure 5.11 Experimental data and predictive trends of the Kentucky soils for: (a) Shear wave velocity with void ratio data and a power function predictive trend; (b) Shear modulus with void ratio data and predictive trends using Hardin and Black void ratio function; a void ratio function based on a power function, and an optimized function

The general form of the equation $G = C\,F(e)$, using the Hardin and Black (1969) void ratio function is also plotted in Figure 5.11(b) for comparison. It is clear that the power form of the void ratio function is a much better predictor of dynamic shear modulus for the Kentucky soils. The void ratio function used in this research program is given as:

$$F(e) = \left[\frac{1}{e^{0.207}(1+e)} \right] \tag{5.5}$$

Three considerations that may result in slightly reduced soil shear wave magnitudes in this study are given under the acronym NTS for near field effects, test setup, and surface waves.

Consideration of near field effects is given to the determination of the time of arrival of the shear waves. The first point of movement of the received wave was considered to be that of a near field effect from P- (compression) waves; therefore the characteristic point of first trough was used in determining the actual arrival of the S (Shear) waves. This selection of first trough resulted in an increase in the time of arrival, therefore a decrease in shear wave velocity.

The test setup configuration may also result in a slightly decreased magnitude of shear wave velocity. Shear waves were propagated within the soil from copper tubes placed in diagonal corners of the laboratory scale model containment apparatus. A steel rod was then placed into one of the copper tube and wedged to make contact with the tube at a desired depth. The point of generation of the shear wave was at the top of a steel rod protruding out of the copper tube. Consideration was not given for the time of travel of the wave vertically through the rod to the wedged portion. It was assumed to be too small to be of significance, but nevertheless a source of reduced accuracy.

Lastly, surface waves are theoretically what is propagated through the soil. Compressed and Shear waves would only exist in an infinite, homogeneous, isotropic

medium (Richart et al., 1970; Telford et al., 1990), but in practice, the ground and more so, bulk soil in the laboratory does not extend to infinity in all directions. The soils in the field and the laboratory are bounded by a finite space, therefore, soils are in a half space, and surface waves are generated in half space. The total input energy distribution amongst compression, shear, and surface waves was 7 %, 26 % and 67 % respectively for a vertically oscillating, uniformly distributed, circular energy source of a homogenous, isotropic, half-space (Miller and Purse, 1995). Therefore, reduced wave velocities are associated with surface waves.

5.3 Bender Element Shear Wave Velocities and Shear Modulus

As with the shear modulus determined by both crosshole seismic and the soil stiffness gauge methods within the laboratory scale model tests, shear modulus was also determined during the constant-water content triaxial tests using bender elements. Figure 5.12 gives an overview of this section within the overall research program.

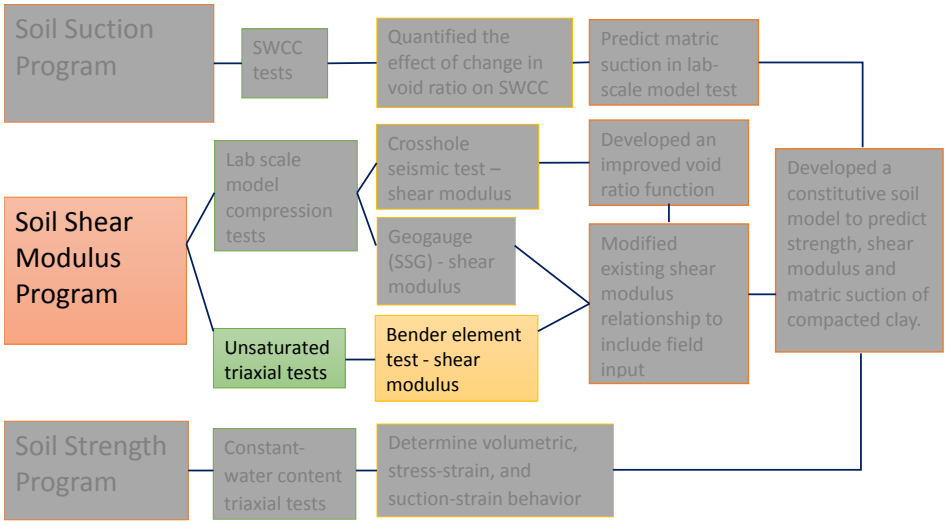

Figure 5.12 A visual of the point of discuss (shear modulus by bender elements) within the overall research program.

5.3.1 Wave travel time

In interpreting the wave signal, a typical S-wave signal is shown in Figure 5.13. The initial point of deflection of the S-wave (Point A) indicates the presence of a near field component. Since the near-field component of shear wave propagates with the compression wave velocity, a P-wave signal obtained immediately after the S-wave (specimen condition unchanged) is shown in Figure 5.13 just below the S-wave with corresponding periods. The defined arrival of the P-wave at Point D, corresponds well with the initial deflection of the S-wave, thereby confirming that the start of the near field component is due to the presence of a P-wave.

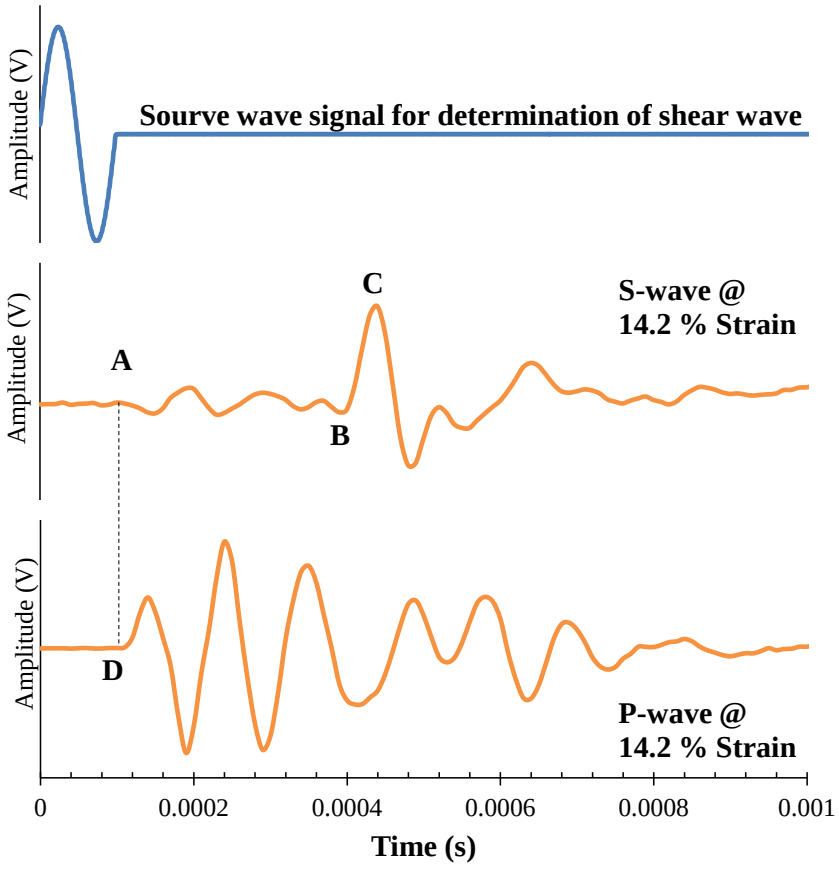

Figure 5.13 Shear (S) and compression (P) wave received for the DCsclay soil specimen under the same stress state conditions, showing the near field effect.

To determine the wave signal travel time, three techniques were considered. A manual visual technique was used to select the first bump characteristic point. The first bump was selected because, 1) it reduces the errors of the near field effect, and 2) it is the point at which the polarization of the wave signal goes from negative to positive, matching the initial polarity of the source wave. The other two techniques are automated techniques for first bump and cross-correlation determination, by use of the Bender Element Analysis Tool (BEAT) software

Point C was determined to be the first peak signal of the received S-wave. Point B is then the first point prior to the first S-wave signal peak that has the same polarity (positive) as that of the initial source wave. For this reason, Point B was selected as the visual first bump characteristic point. This visual selection technique was used on all bender element tests to manually determine the first bump characteristic points. Figure 5.14 shows the source and received shear wave signals determined by Bender element tests on the DCsclay soil specimen, S-CW-DC-16.4-1682, during shearing. The characteristic points of first bump are shown on the chart and are connected by dashed lines that extends through all the received signals. The travel time was determined to be the change in time from the start of the source signal to the point of first bump. These manually determined travel times were compared to those obtained using the Bender Element Analysis Tool (BEAT) automated software.

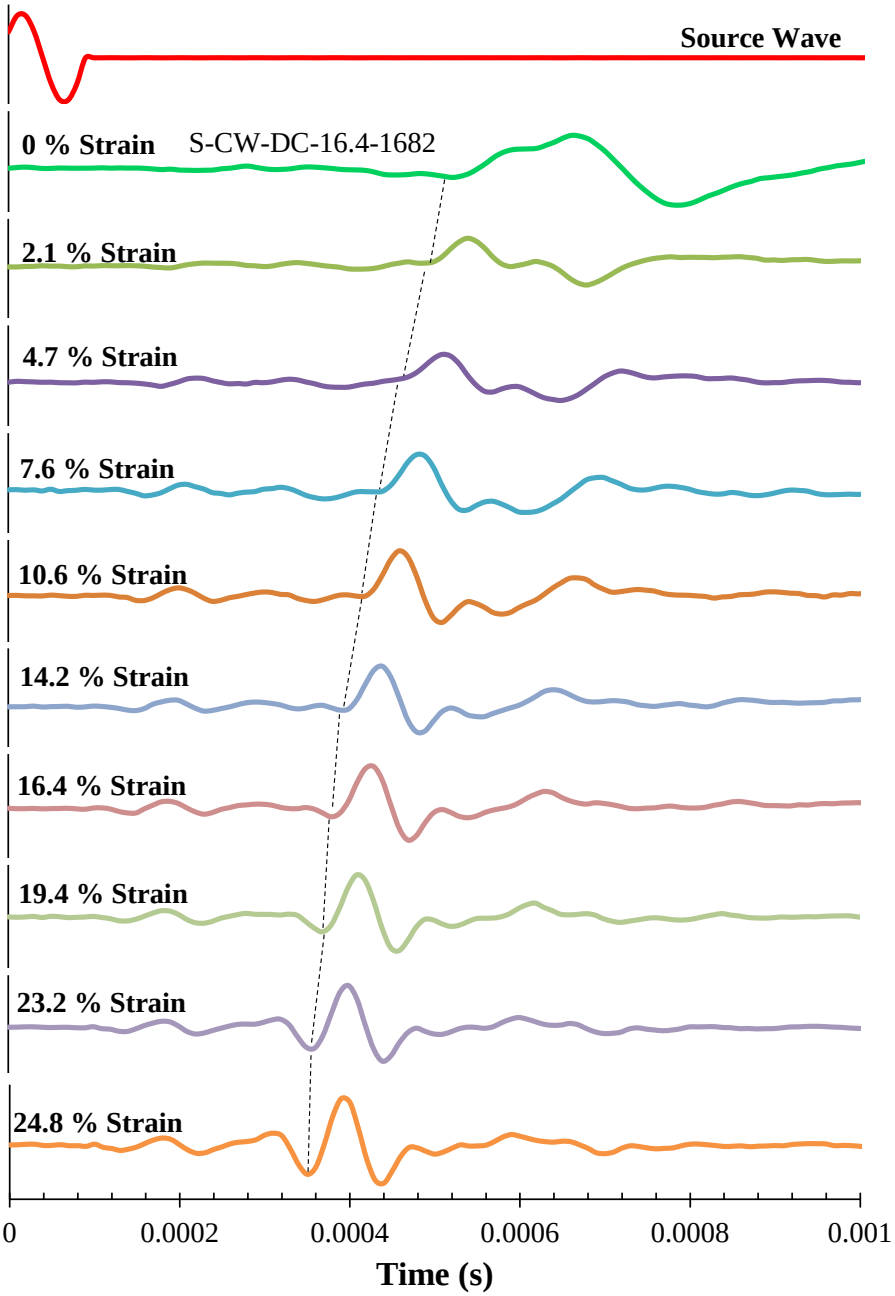

Figure 5.14 Shear (S) waves received for the DCsclay soil specimen S-CW-DC-16.4-1682, at different points of axial strain, showing the trend of characteristic point of first trough.

BEAT automated software was also used to determine travel times by automated techniques for the first bump characteristic points and the cross-correlation method. The results of travel times obtained by the BEAT software where compared with that obtained

from the visual technique previously presented. The comparison shown in Figure 5.15, indicates that though there are travel time differences between the three techniques, all three techniques show similar general trends of decreasing time with axial strain. The differences include a higher initial time determined by the cross-correlation by BEAT, and that in general the times become increasingly higher with the respective methods: first bump by BEAT, first bump by the visual method, and the cross-correlation by BEAT. The trends of the travel times for the cross-correlation by the BEAT software appear to be much closer to the travel times for the first bump by the visual method, after the initial time at zero strain, than that of the first bump by the BEAT software.

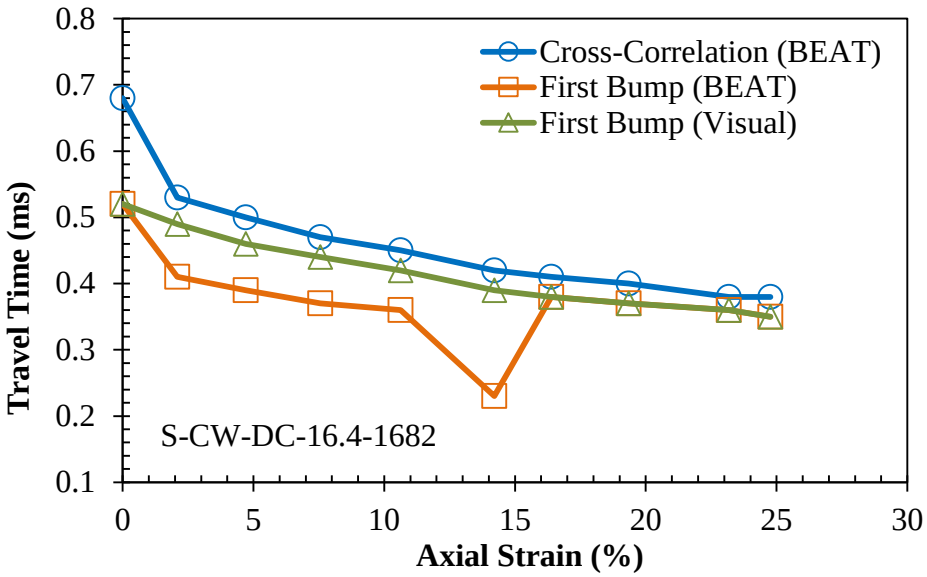

Figure 5.15 Comparison of estimates of shear wave travel times with axial strain for the DCsclay soil specimen S-CW-DC-16.4-1682, obtained by the software BEAT for characteristic points of cross-correlation and first bump and the characteristic point of first bump determination by graphical visual method.

The maximum travel time difference between the cross-correlation by BEAT and the visually determined first bump characteristic points is about 0.069 Ms. To understand why the BEAT software results in minor magnitude differences in travel times, the

algorithms of the software should be understood. The algorithm in the BEAT software implements the procedure for travel time determination of characteristic points as shown in Figure 5.16, in the following order (Rees et al., (2013):

1. Point D is first determined by scanning and finding the maximum positive amplitude for the output signal. Point D is then defined as the point of maximum positive amplitude and the corresponding time signature.
2. Point B is determined next by scanning and finding the minimum amplitude between time zero (0), and the determined Point D. Point B is then defined as the point of minimum (most negative) amplitude between time zero and Point D and its corresponding time signature.
3. Point C is then determined by scanning and finding the output of the signal between Point B and Point D that is closest to zero. Point C is defined as the point between B and D that is closest to zero and its corresponding time signature.
4. Point A is lastly determined using an iteration process, whereby the mean and standard deviations of 10 consecutive outputs, $(n_1 - n_{10})$, starting at the first output, are assessed with the successive five outputs, $(n_{11} - n_{15})$, to determine if all of the successive five outputs are at least three standard deviations more negative than the mean. If the condition is false, the iteration process continues to determine the mean and standard deviation of the next set of 10 consecutive outputs, $(n_2 - n_{11})$, and assess with the successive five outputs, $(n_{12} - n_{16})$, until the condition is true. When the condition is true, the

corresponding time for the first of the successive five outputs is then used to define Point A.

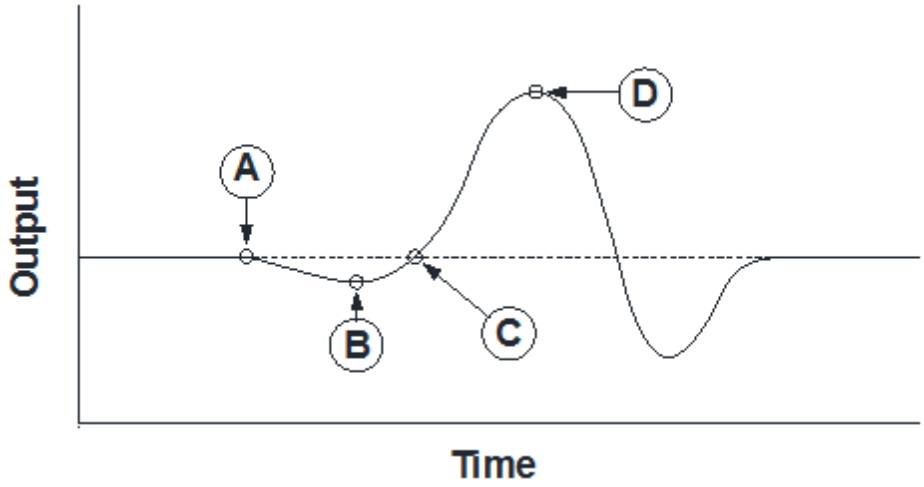

Figure 5.16 Idealized received shear wave signal showing the characteristic points (reproduced from Lee and Santamarina, 2005)

For the determination of the first bump characteristic points, the first and second procedures in the BEAT algorithm for the determination of Points D and B, are of significance. Consider the received shear wave signal at 8 % strain for the Lee County soil specimen, S-CW-LC-22.8-1618, as shown in Figure 5.17. The determined characteristic Points D, and B, determined visually (Point D, and B not enclosed) do not correspond with those determined by the BEAT (Point D, and B with square enclosure). The BEAT determines Point D first and is the peak point with maximum amplitude, then determines Point B, as the point on the time scale between zero and D with the most negative amplitude. Visually, the Point D is the first significant peak that is a clear indication of the shear wave arrival, though not the maximum peak. Consequently, the Point B is the trough point prior to the selected peak point. This resulting discrepancy in the different techniques is believed to be a reason for differences in travel times between

the cross-correlation by BEAT and the visually determined first bump characteristic points. In many cases, the BEAT results were very similar to those of visual determination. BEAT was used for travel time determination of characteristic points for this research, for consistency and to reduce subjectivity in the interpretation..

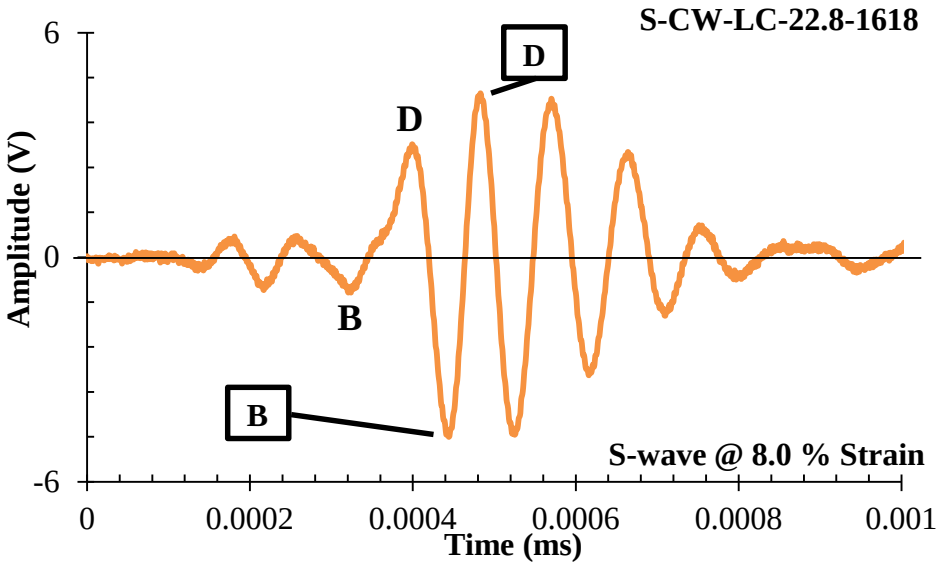

Figure 5.17 Received shear wave signal for the LCesilt soil specimen S-CW-LC-22.8-1618, showing the comparison of characteristic points from the BEAT software (points enclosed) and from a graphical visual determination method (points not enclosed).

The BEAT software also analyzes the Bender element data by a frequency domain method of Cross-power spectrum for determination of travel times. The results of the BEAT analyses are compared in Figure 5.18, with the travel times determined by the BEAT cross-correlation results and by the visual technique for the first bump characteristic point. The comparisons show that the frequency domain cross-power spectrum determination of travel times does not correlates as well with the cross-correlation by BEAT and the first bump by the visual method. The frequency domain method resulted in an increase between the first two travel times, which is inconsistent with the other travel time trends. After the initial increase, the rate of change in travel

time decreases with increasing axial strain, similar to the other methods, but at a slightly higher rate.

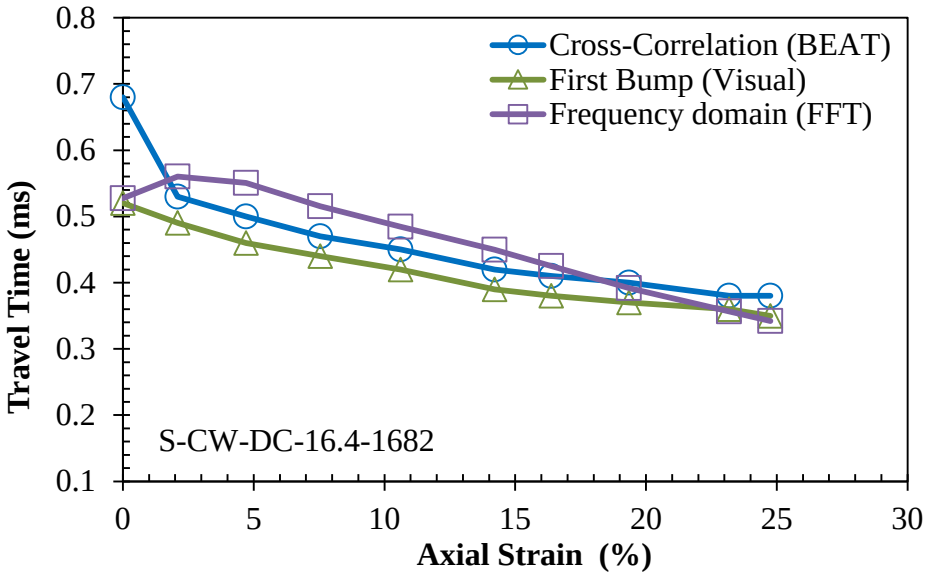

Figure 5.18 Estimates of shear wave travel times with axial strain for the LCesilt soil specimen S-CW-LC-22.8-1618, obtained by the software BEAT for a frequency domain method and characteristic points of cross-correlation method, and by a graphical visual method of the characteristic point of first bump determination.

5.3.2 Shear Modulus

Literature on variation of shear wave velocities and shear modulus during triaxial shearing phase is scarce. Most researchers have presented the variation of shear wave velocities and shear modulus during the compression or desaturation stage of an unsaturated triaxial or resonant column tests (Cabarkapa et al., 1999; Vinale et al., 1999; Mancuso et al., 2002; Vassalo et al., 2007; Ng and Yung, 2008; Khosravi et al., 2009; Khosravi and McCartney, 2013).

Other researchers generally assume the shear modulus to be constant during shearing as has been introduced in constitutive models (Roscoe and Burland, 1968; Alonso et al.,

1999; Wheeler and Sivakumar, 1993; and Vaunat et al., 2000). Typically, constitutive models use an initial shear modulus to predict elastic strains during a triaxial shearing test. The initial shear modulus is determined at the start of shearing and assumed to be constant during testing.

Shear wave velocity was determined intermittently during shearing on triaxial specimens by use of Bender elements attached to the top and bottom platens in the triaxial apparatus. The results of determination of the shear wave velocity are shown in Figure 5.19 for the HCclay soil. In general, the shear wave velocity increases with increase in net mean stress. As previously discussed, other researchers have shown variation of shear wave velocity, and it is well documented that with increases in external confining stress (a simulation of overburden pressure), shear wave velocity increases at different rates depending on the range of confining stresses. Figure 5.19 shows there is no defined relationship on the effect of the intrinsic stress state (density) on shear wave velocity for specimens sheared under the same confining stress. This interpretation compares well with interpretations by Edil and Sawangsuriya (2005), that the variation of dry unit weight exerts relatively small effect on the shear modulus.

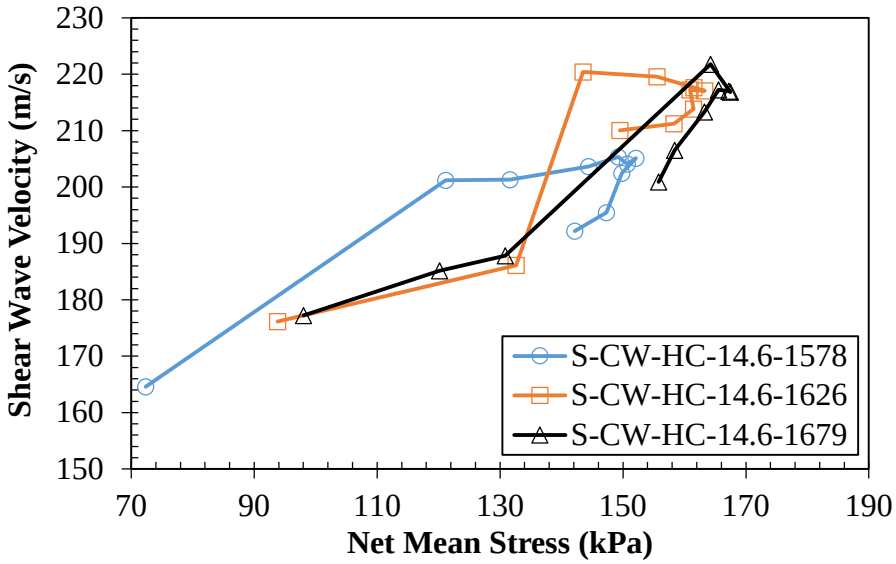

Figure 5.19 Experimental test data results of the shear wave velocity with net mean stress for the HCclay soils at different density for the bender element tests during the triaxial shearing stage.

Estimations of shear modulus, G, were determined using the elastic theory relationship, $G = \rho V_s^2$. With changes in the total density between specimens, there are only slight variations between trends in Figure 5.19 of shear wave velocity and those in Figure 5.20 of shear modulus with respect to the net mean stress. Similar to the trends of shear wave velocities, shear modulus increases with increase in the net mean stress. The rate of increase in generally high initially then becomes much lower or decreases as the net mean stress nears its maximum value and then decreases.

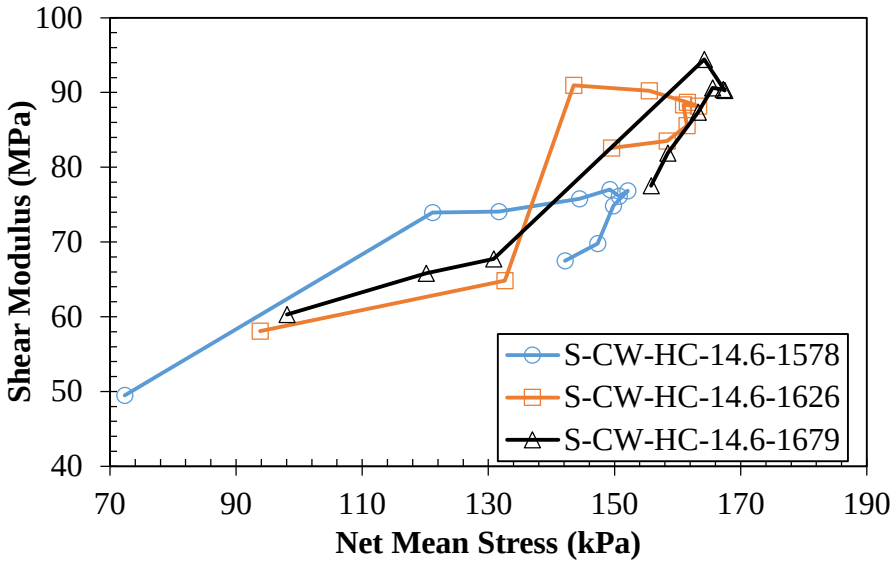

Figure 5.20 Shear modulus obtained from experiment tests with net mean stress for the HCclay soils at different density for the bender element tests during the triaxial shearing stage

The initial increases of shear moduli for the specimens with initial density of 1578, 1626, and 1679 kg/m^3 are about 24.4, 32.9, and 34.1 MPa respectively. These initial increases in shear modulus correspond to the initial high rates of increase in deviatoric stresses (see the stress-strain plot of Figure 6.19 in Chapter 6). The high rate of increase in deviatoric stresses is the zone in the stress-strain curve that is widely considered to be the elastic zone. The increase in shear modulus within this zone is contrary to the assumptions of constitutive models such as the Barcelona Basic and the Oxford models. These models are the basis of many other unsaturated soil models, which assume that a single constant shear modulus exists for the shearing phase, and also that this single constant shear modulus, G, relates the incremental change of shear elastic strains, $d\varepsilon_q^e$, to the incremental deviatoric stress, dq, by the equation:

$$d\varepsilon_q^e = \frac{1}{3G} dq \tag{5.6}$$

6 RESULTS OF THE SOIL SHEAR STRENGTH PROGRAM

Chapter 6 presents the mechanical behavior of the unsaturated triaxial tests, i.e., the soil shear strength program. Figure 6.1 gives an overview of this section within the overall research program.

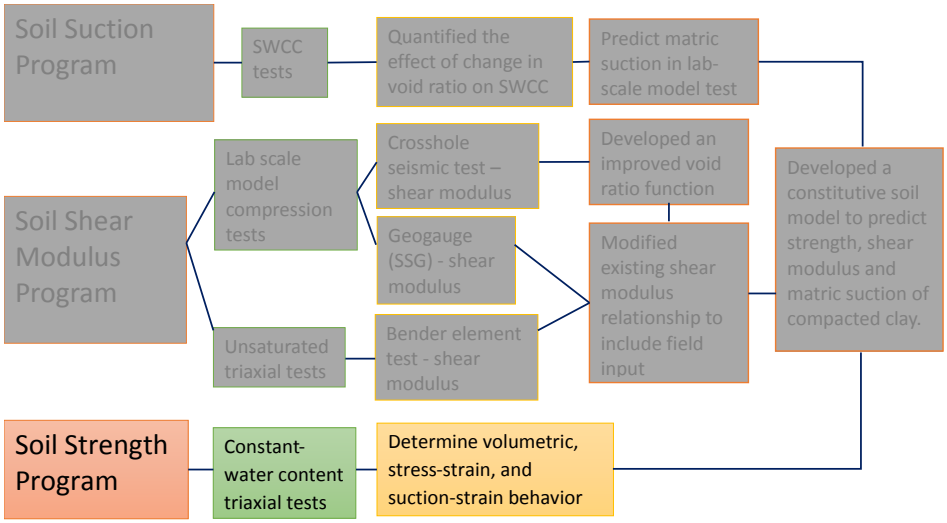

Figure 6.1 A visual of the point of discuss (mechanical behavior of unsaturated triaxial tests) within the overall research program.

Triaxial isotropic compression tests under constant-water content conditions were performed on specimens fabricated specifically to be subjected isotropic loading, unloading and reloading. The three Kentucky clay type soils; DCsclay, HCclay, and LCesilt, used for this test, were compacted to initial conditions of their standard Proctor maximum dry density and optimum moisture content. The test data results from the triaxial isotropic compressions are presented in Section 6.1.

The typical trends and responses of the experimental test data for the unsaturated triaxial specimens under conditions of constant-water content, subjected to equalization, isotropic, and shearing stages, are presented in Sections 6.2, 6.3, and 6.4 respectively.

The equalization stage is presented in Section 6.2, and includes equilibrium trends of pore-air pressures and matric suction with time. The isotropic compression stage is presented in Section 6.3, which includes the volume change and matric suction responses during compression. The experimental triaxial test data for the shearing phase is presented in Section 6.4, under two general headings of volume change response and state of stress response.

The experimental test data results for the HCclay soil was used to discuss the trends and responses of test data in Sections 6.2 through 6.4. The experimental test data results and measurements, including data trends and responses for the three Kentucky clay soils used (DCsclay, HCclay, and LCesilt) are included in Appendix H.3

6.1 Isotropic loading to high stresses

The fabricated specimens subjected to only isotropic compression tests (not sheared) under constant-water content conditions are discussed in this section. These specimens were subjected to isotropic loading, unloading and reloading to a high stress. The plot of specific volume v, where $v = 1 + e$, with the natural logarithm of the net mean stress, p, is presented in Figure 6.1. The net mean stress, p, is the net of the total stress, σ, i.e., the isotropic confining stress or the cell pressure), over the pore-air pressure u_a, such that $p = (\sigma - u_a)$. In general, for all three soils, the specific volume decreases with increase in the net mean stress, and the rate of change of loss in specific volume increases as the net mean stress increases. These trends are similar to trends that have been reported in literature, though they were reported under conditions of constant suction, (Wheeler et al., 2003; Lloret et al., 2003; and Futai and de Almeida, 2005; Sheng, 2011; Sheng and

Zhou, 2011; Liu, 2012). The unload-reload portions of the curves are well defined but appear to be non-conforming to literature data. Wheeler et al. (2003) show that the rate of change of specific volume with net mean stress (the slope) of the unload-reload portion, is of similar magnitude to that at the initial loading portion of the curve. The rate of change in specific volume loss of the unload-reload portion of the compression curves in Figure 6.2 are generally higher than at the initial loading portions of the curves. The final loading in normal compression of the LCesilt soil resulted in a very high rate of loss in specific volume.

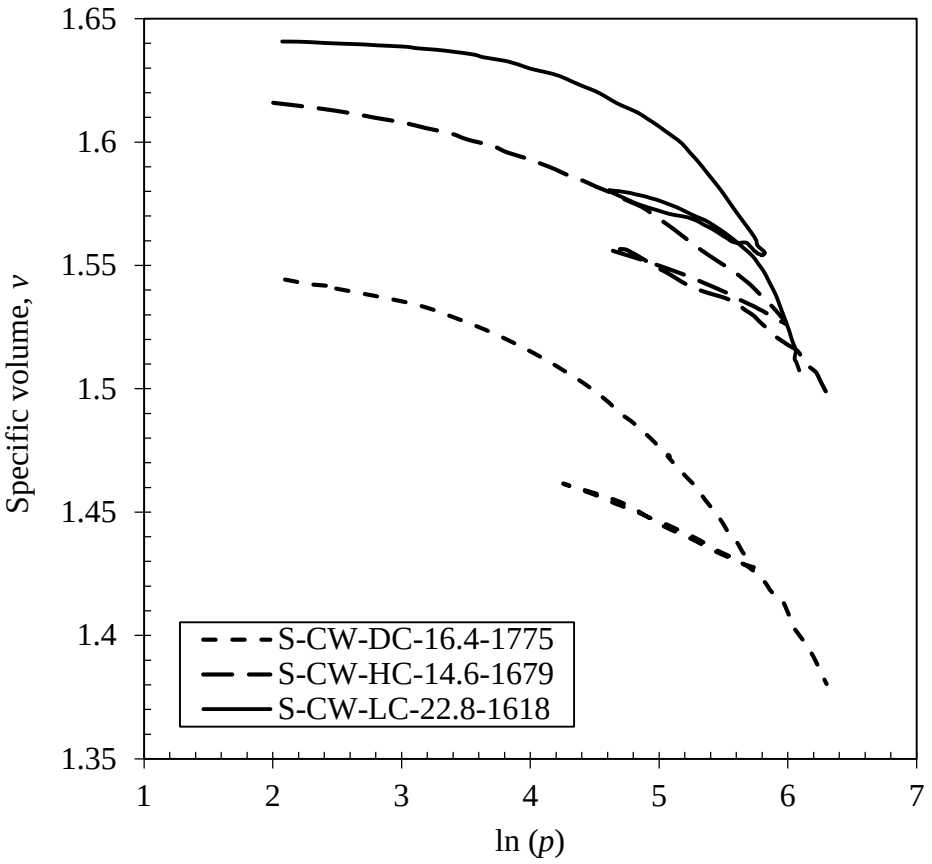

Figure 6.2 Experimental test data results of specific volume with the natural log of net mean stress for the Kentucky soil specimens, initially compacted to their and standard Proctor maximum dry density and optimum moisture contents, and isotropically compressed under conditions of constant water contents.

In saturated soil, isotropic compression curves when plotted with the mean effective stress on a logarithmic scale (natural or base 10), show two distinct linear rates of change for the initial and final portions, whereby the intersection of these two distinct trends is generally taken as the preconsolidation stress. The isotropic compression curves in Figure 6.2 are not distinctively linear, in fact they initially show smooth trends of a continuously increasing rate of loss of specific volume, until a point at which they appear to become linear. In literature, isotropic compression curves are usually reported under conditions of constant suction, and at different suctions, the slopes of the compression curves become increasingly flatter as the constant suction level increases (Wheeler and Sivakumar, 2000; Sheng, 2011). Therefore, the smooth trends of continuous rate of loss of specific volume can be attributed in part, to changes in matric suction. Wetting or drying is not performed in constant-water content test, therefore, under conditions of constant-water content, changes in matric suction is only caused by the increasing pore-water pressures due to the loading (net mean stress) increases.

The resulting matric suctions of the DCsclay soil is presented in Figure 6.3(a), with a plot of specific volume versus matric suction. The general trend indicates that as the specific volume decreases, matric suction also decreases. The plot shows that the matric suction reduces to zero under loading, then increased during the unloading phase, and reduced back to zero under the reloading phase. The matric suction stayed at or near zero and did not continue to decrease to higher negative values due to the axis-translation method. As the pore-water pressure increased to magnitudes of the pore-air pressure, the pore-air pressures automatically increased to maintain the matric suction near zero. In Figure 6.3(b) the specific volume versus the natural logarithm of matric suction is

presented. This trend indicates a decreasing rate of loss of specific volume with decreasing matric suction, consistent with literature data (Amaral et al., 2013) for a constant-water content compression, but is the opposite of the trends for constant suction compression tests in literature.

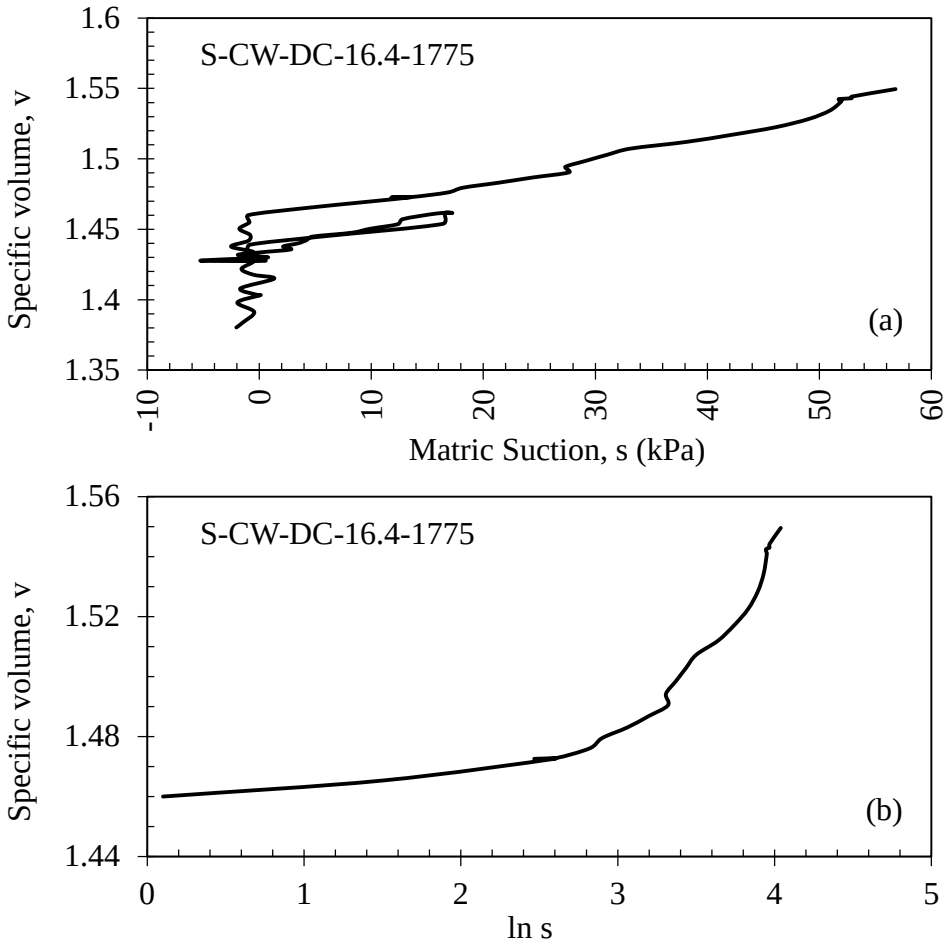

Figure 6.3 Experimental test data trends of specific volume for the DCsclay soil initial compacted to the standard Proctor maximum dry density and optimum moisture content, isotropically compress under conditions of constant water content: (a) with respect to matric suction; (b) with respect to the natural logarithm of matric suction.

The decrease in matric suction is attributed to the increase in pore-water pressures during the isotropic compression test, but the true trend of the pore-water pressure is not apparent from the matric suction plot in Figure 6.3, due to the implementation of the axis

translation technique. The trends of excess pore-water pressure with time for the three Kentucky soil are presented in Figure 6.4(a). The trends show significant increase and decrease in the excess pore-water pressures during isotropic loading and unloading of the DCsclay and the LCesilt soils, but only a minimal changes in the pore-water pressures for the HCclay soil.

In order to understand the different trends depicted in Figure 6.4(a), the trends of the degree of saturation S, with time is considered, and are presented in Figure 6.4(b). The trends show that for the DCsclay and LCesilt soils, the degree of saturation at initial compaction were above 0.9, and therefore, close to being fully saturated. These soils, being close to complete saturation at the start, became fully saturated ($S = 1$) during the initial isotropic compression loading phase, and remained in a fully saturated state for the duration of the test, even under the unloading phase. However, for the HCclay soil, the degree of saturation at the initial compaction condition was about 0.63, and increased and decreased respectively during the loading and unloading phases of isotropic compression. At the end of the test (maximum loading), the final degree of saturation for the HCclay soil was about 0.78.

The significant increase in the excess pore-water pressure for the DCsclay and LCesilt soils can therefore be attributed to full saturation conditions of the soil specimen. Increases in excess pore-water pressures are typical of saturated soils, when loaded under undrained condition. Since the pore-air phase is diminished with fully saturated conditions, and the air-pressure increases with increases in excess pore-water pressure

(axis-translation to maintain zero suction), the air pressure may possibly increase the total stress on the sample since it now acts as an external applied pressure.

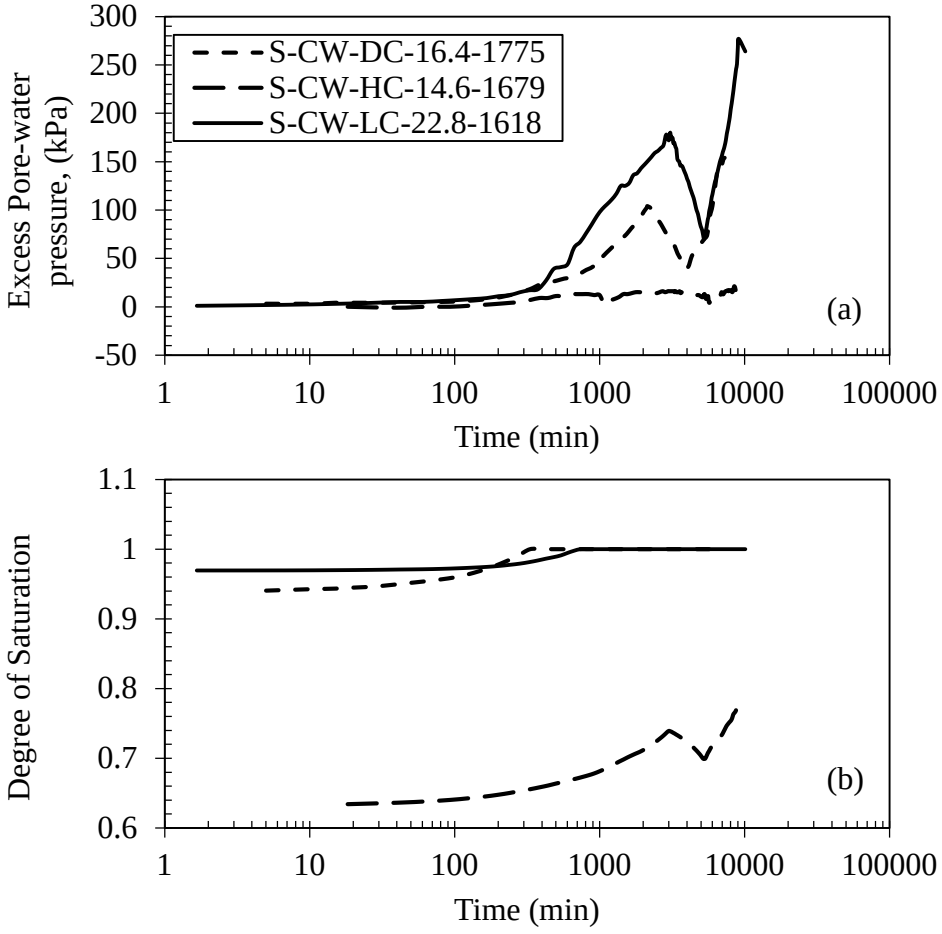

Figure 6.4 Experimental test data trends of (a) pore-water pressure with time; (b) degree of saturation with time; for the Kentucky soils initially compacted to their standard Proctor maximum dry density and optimum moisture content and isotropically compressed under conditions of constant water content.

6.2 Equalization Stage

At each stage of constant-water content triaxial testing in this study, the pore-water pressure remained undrained. The undrained pore-water pressure was necessary for equalization, as equalization under the as-compacted conditions was the objective. With the pore-water pressure undrained, the water content will remain unchanged, but the

pressure transducers start to register negative pore-water pressures as the sample tries to take in water. Since water under pressures less than -1 atm cavitates, axis-translation technique was used, by increasing the pore-air pressure in order to register positive pore-water pressures. The axis-translation technique allows for increasing the pore-air pressure, which would result in the same magnitude of increase in the pore-water pressure, thereby, the difference in the pore-air and –water pressures, hence the matric suction, remains unchanged.

6.2.1 Effect of time on pore-air pressure

A typical pore-water pressure over time curve during the equalization stage is shown in Figure 6.5. The typical trend shown is from the experimental data for the HCclay soil specimen, compacted to initial conditions of standard Proctor maximum dry density and optimum moisture content. The legend shown in the Figure, S-CW-HC-14.6-1679, represents the triaxial specimen identification, where S means that the specimen was subjected to a test to determine the 'Shear modulus'; CW means that the specimen was tested under 'constant-water content' conditions; HC represents the sampled location of the soil, which is Henderson County, and can be ascribed to a soil type, as all HC soils are classified as clay soils (HCclay); 14.6 represents the standard Proctor optimum moisture content; and lastly, 1679 represents the dry density in kg/m^3 of the specimen.

Generally, the cell and pore-air pressures were increased in sync to a predetermined pore-air pressure, with the cell pressure higher than the pore-air pressure, for a difference or net mean stress of about 5 to 10 kPa. Though the assumed pressure of the as-

compacted specimen is zero (or atmospheric), the net mean stress of 10 kPa is considered small enough to represent the as-compacted state. The application of a small net mean stress was necessary to keep the membrane on the specimen.

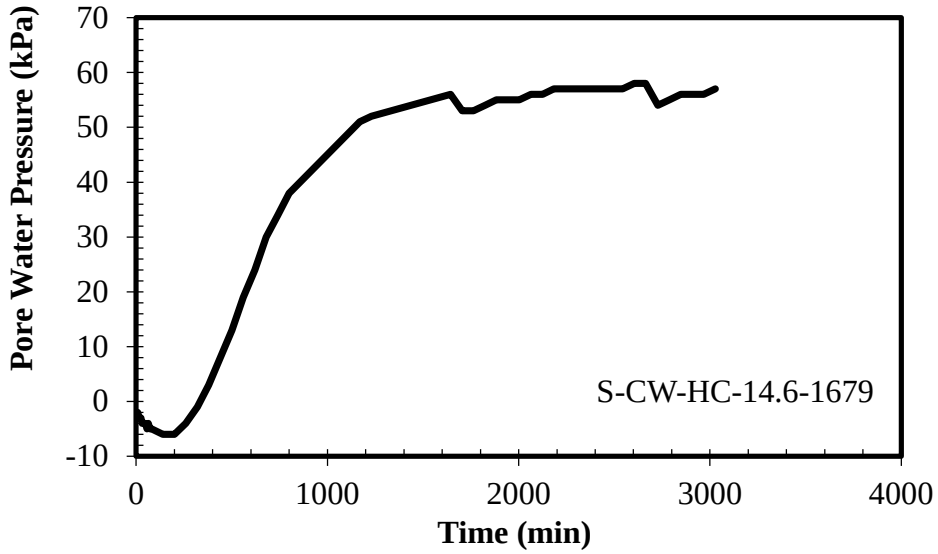

Figure 6.5 A typical experimental test data trend of pore-water pressure with time during the equalization stage of the constant-water content triaxial test. Test data of the HCclay soil, under initial conditions of standard Proctor maximum dry density and optimum moisture content.

The resulting changes in pore-water pressure show an initial increase in negative pore water pressure during the first few hours, after which it changes into a positive increase with time, going from negative to positive pressures. In the positive pressure range, the pore-water pressure generally increased with time at a decreasing rate until it becomes almost asymptotic, which indicates equilibrium was achieved. Though the equilibrium pore-water pressure is based on the current state of pressures on the sample, the resulting difference in pore-air and pore-water pressures (matric suction) is believed to be at equalization whereby any change in pore-air pressure will result in the same change in pore-water pressure.

6.2.2 Effect of time on matric suction

The resulting matric suction $(u_a - u_w)$ during the equalization stage is shown in Figure 6.6. With an in-sync and continuous rate of application of increasing the confining cell and pore-air pressures by 7 kPa/hr, the resulting matric suction initially goes higher then decreases back to its equilibrium value. This indicates a time lag between the increasing pore-air with increasing pore-water pressures. That is, at the peak matric suction, the pore-air pressure reaches its targeted constant value while the pore-water pressure is still increasing to its asymptotic value. This behavior was also reported by Salem (2006) who used incremental increases of cell and pore-air pressures and noted that this behavior was due to short time intervals between increasing the pressure. This behavior was also previously observed by Bocking and Fredlund (1980), and showed that this behavior is effected by the soil structure compressibility (an equivalent to the volume compressibility of soils). A higher structure compressibility exhibits the typical behavior show in Figure 6.6.

Equilibrium was achieved at the section of the curve where changes in matric suction are minimal to none. The irregularities noted at this section of the curve are due to air diffusion through the HAEPD, and purging of the diffused air. All matric suction-time response curves for the equalization stage for the four Kentucky soils at each density are presented in Appendix H.3

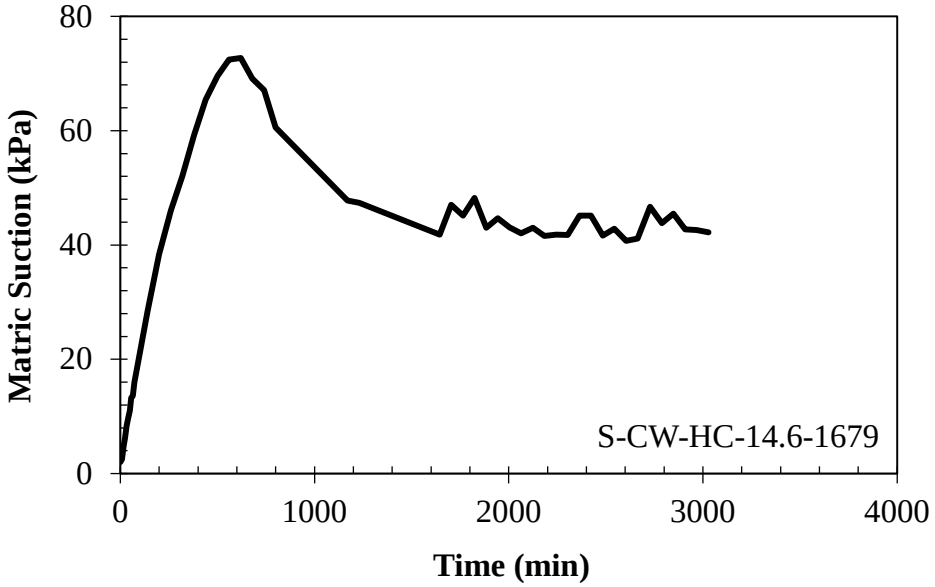

Figure 6.6 A typical experimental test data trend of matric suction with time during the equalization stage of the constant-water content triaxial test. Test data of the HCclay soil, under initial conditions of standard Proctor maximum dry density and optimum moisture content.

The sample volume was expected to remain constant during this phase, therefore, no measurements of sample volume change were performed. The triaxial apparatus and setup measures volume change by the change in water volume of the inner cell. But during this phase, the cell pressure increased (but net mean stress remained constant). Therefore, the apparent volume change is only due to the increase in cell pressure and not of the sample. An on-sample strain gauge would be necessary for accurate sample volume change if any, during this stage. Since no data are available, the assumption of constant volume was made because the states of stresses on the specimens before and after the equalization stage were similar.

6.3 Isotropic Compression Stage

Isotropic compressions were started soon after equalization was achieved. The specimens were isotropically compressed by only increasing the confining cell pressure.

The pore-air pressure was not changed but was maintained at its constant target value achieved during the equalization stage. The confining cell pressures were increased to the targeted confining pressures of 70 kPa for all specimens to achieve a baseline reference. The rate of increase to the targeted pressure was 7 kPa/hr. Typical volumetric strain and matric suction time response curves; the effect of confining pressures on void ratio and matric suction are discussed in the succeeding section.

6.3.1 Volume change response

The volumetric strain versus time response curve for the Henderson County soil specimen with a density of 1578 kg/m^3 is presented in Figure 6.7. This curve is typical of the volumetric strain-time response curves of all the other specimens where the net confining stress was increased to 70 kPa at a constant rate of 7 kPa/hr. In general, the response of volumetric strain-response curve can be divided into two phases. The first phase shows an almost constant high rate of decrease in volumetric strain. The second phase is defined by a lower and decreasing rate of volumetric strain to a point at which minimal to no change in strain occurs. Equilibrium in the compression stage is achieved at the point of minimal to no change in volumetric strain. The negative volumetric strains indicate a loss in volume. This loss in volume constitutes a loss only in the air volume phase of the soil. The water and solids volume remain unchanged in compression tests under constant-water content.

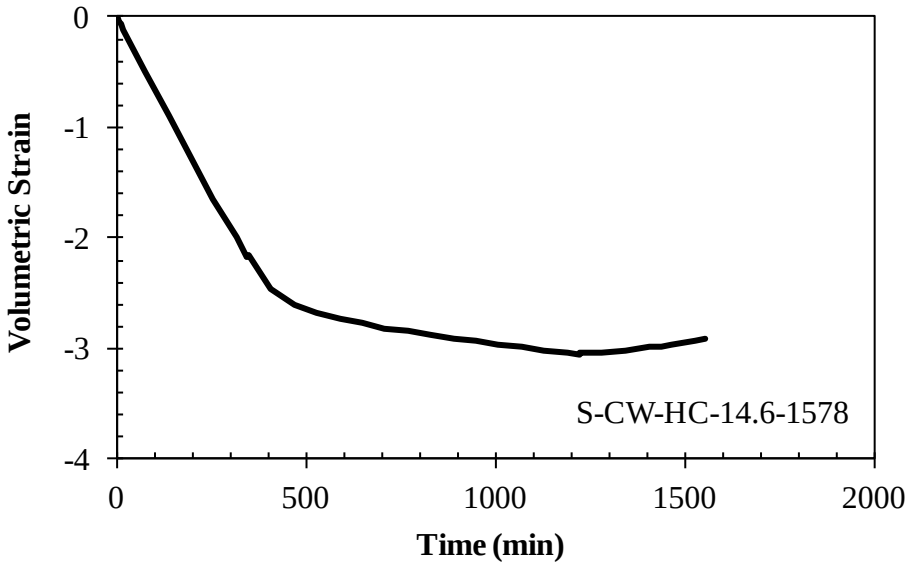

Figure 6.7 A typical experimental test data trend of volumetric strain with time during the isotropic compression stage under constant-water content condition. Test data of an HCclay soil triaxial specimen.

The effect of the net confining stress on void ratio is shown in Figure 6.8. This trend is similar to the initial portion of the compression curves under constant-water content conditions to high isotropic loads as previously discussed in Section 6.1. The loading for this isotropically compressed sample was to 70 kPa. It may appear that the plot is typical of compression curves for saturated specimens, where an initial stage is defined by the linear low rate of change in void ratio typical of an overconsolidation state and then an increased linear rate of change in void ratio defined by the steeper curve which is typical of a virgin compression state. Since the final compression load was only to 70 kPa, the curve is not well defined, and only shows the initial loading portion prior to the preconsolidation yield stress (preconsolidation stresses are discussed in Section 6.4.2). Therefore, even for the initial portion of the compression curve, an increasing rate of void ratio with loading is noted.

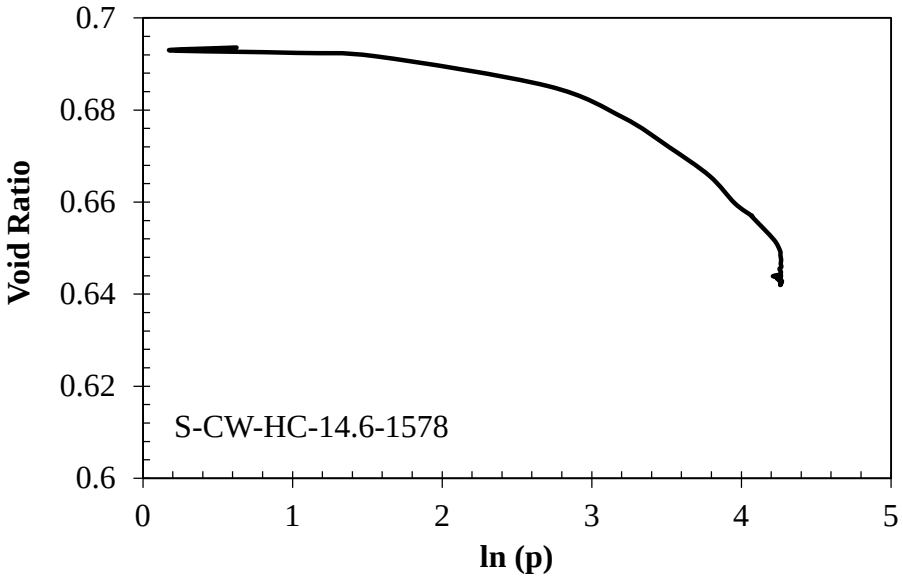

Figure 6.8 A typical experimental compression curve of void ratio with the natural logarithm of the net mean stress during the isotropic compression stage under constant-water content condition. Test data of an HCclay soil triaxial specimen.

6.3.2 Matric suction response

The typical variation of matric suction-time response curve for specimens subjected to 70 kPa at a rate of 7 kPa/hr is shown in Figure 6.9. In general, the matric suction decreases at a decreasing rate during compression. The decrease in matric suction is due to the undrained water phase causing an increase in pore-water pressure.

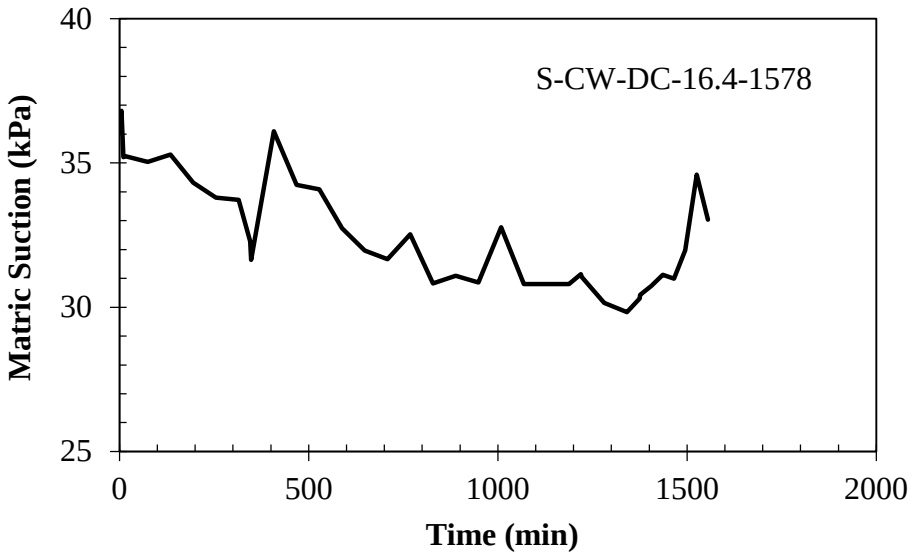

Figure 6.9 A typical experimental test data trend of matric suction with time during the isotropic compression stage under constant-water content condition. Test data of an HCclay soil triaxial specimen.

Figure 6.9 also shows a high variation in matric suction while it is decreasing. The variation in matric suction was due to two factors, which are variations from the air pressure pump equipment and diffusion of air through the HAEPD. Air pressures sometimes varied by as much as ±2 kPa from the target pressure. Figure 6.10 shows the comparison of typical matric suction variations with and without variations in air-pressures. The number of significant variations in the matric suction-time response is reduced to two when there are no air pressure variations from the air pump. These two noted variations are most likely due to the effect of air diffusion through the HAEPD and periodic water flushing of the diffused air. Significant variation typically occurs under low confining stresses and diminishes as the confining stress increases (Salem, 2006). Increases in matric suction are noted when air has diffused and decreases in matric suction occur after periodic flushing.

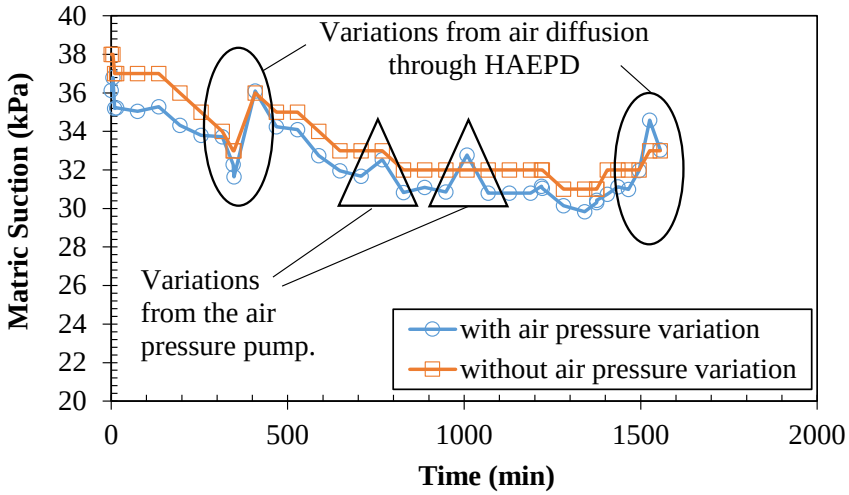

Figure 6.10 Comparison of matric suction variations with and without variations in air-pressures.

The effect of the net confining stress on matric suction for the Henderson County soil specimen with initial density of 1626 kg/m^3 is shown in Figure 6.11. In general, the matric suction decreased with increasing confining stress fairly linearly. This response of matric suction is typical of all specimens compressed to the low stress confining of 70 kPa at a rate of 7 kPa/hr.

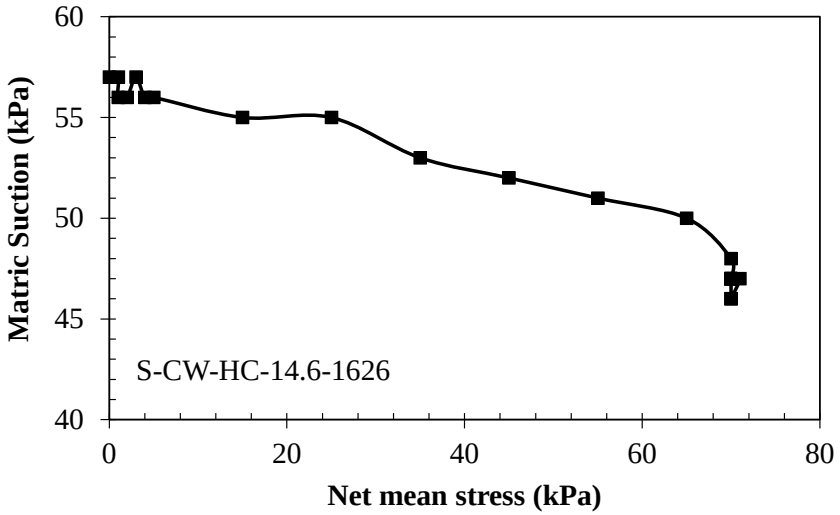

Figure 6.11 A typical experimental test data trend of matric suction with the net mean stress during the isotropic compression stage under constant-water content condition. Test data of an HCclay soil triaxial specimen

6.4 Shearing Stage

6.4.1 Volume change response during shearing

Figure 6.12 shows the measured volumetric strain of the three Henderson County clay specimens at initial compacted densities of 1578, 1626, and 1679 kg/m^3. Plots of volumetric strain with axial strain for all the Kentucky soils at each initial compacted density are presented in Appendix H.3. The specimens were isotropically compressed to a low net confining stress of 70 kPa before shearing. The specimens experienced volumetric contraction (negative strain indicating loss of volume) and volumetric expansion (positive strain indicating dilation). Volumetric contraction occurs for the loosest compacted specimen with initial density of 1578 kg/m^3. For the other two specimens with increased initial density, volumetric contraction initially occurred, then followed by volumetric expansion with increased axial strain. The third specimen (1626 kg/m^3) which is compacted at or close to the Standard Proctor maximum dry density, initially experienced the least amount of volumetric contraction, and then experienced the most dilation. The volumetric contraction and expansion indicate that reduced volume contraction occurs with increased density or compaction effort. This is due to more closely packed particles with increased density, which results in reduced interconnections between pore-air spaces (Maleki and Bayat, 2012). In other words, higher density results in stiffer specimens, therfore, smaller soil compressibility, and higher dilatancy.

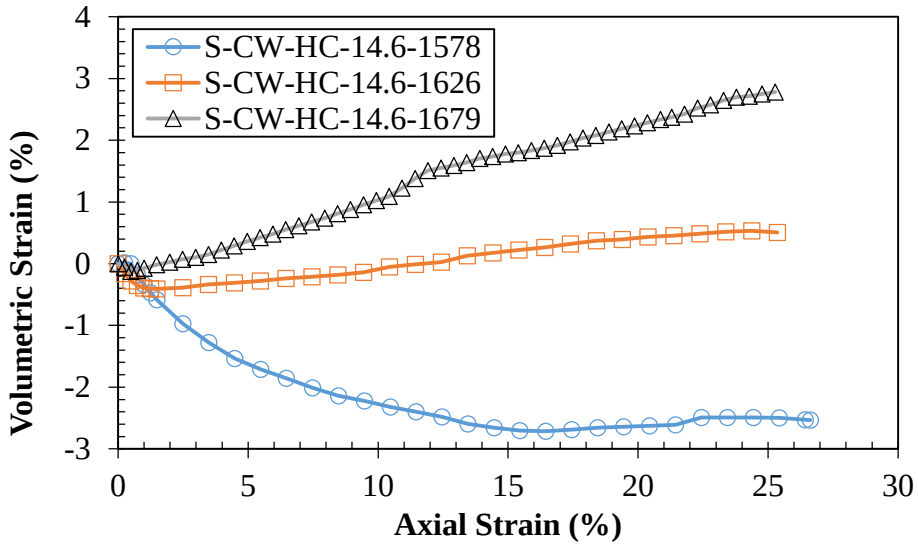

Figure 6.12 Experimental test data results of volumetric with axial strains at different initial densities of the HCclay soil during the triaxial shearing stage under constant-water content test condition.

The figure shows that initial density affects the point at which constant volume condition is achieved. Constant volume condition is achieved at about 16, 23, and 25 (or greater) percent axial strain for specimen with initial densities of 1578, 1626, and 1679 kg/m^3 respectively.

Figure 6.13 shows the changes in specific volume with axial strain during shearing under constant water content condition for the HCclay specimens. The specific volumes either decreased or increased with axial strain dependent on specimen compression or dilation respectively. The final specific volume for all three specimens reached an approximate single value at the end of shearing. This single value specific volume was observed prior to the end of shearing for the specimens with initial densities of 1578 and 1626 kg/m^3. The specimen with initial density of 1679 kg/m^3 reached this value just at the end of shearing. The resulting single value specific volume can be attributed to a critical state specific volume where increase axial strain causes no additional changes in

specific volume. Since there is no change in water content, this critical state specific volume is attributed to the air volume phase of the specimens and therefore may be dependent on the state of the drained pore-air pressure.

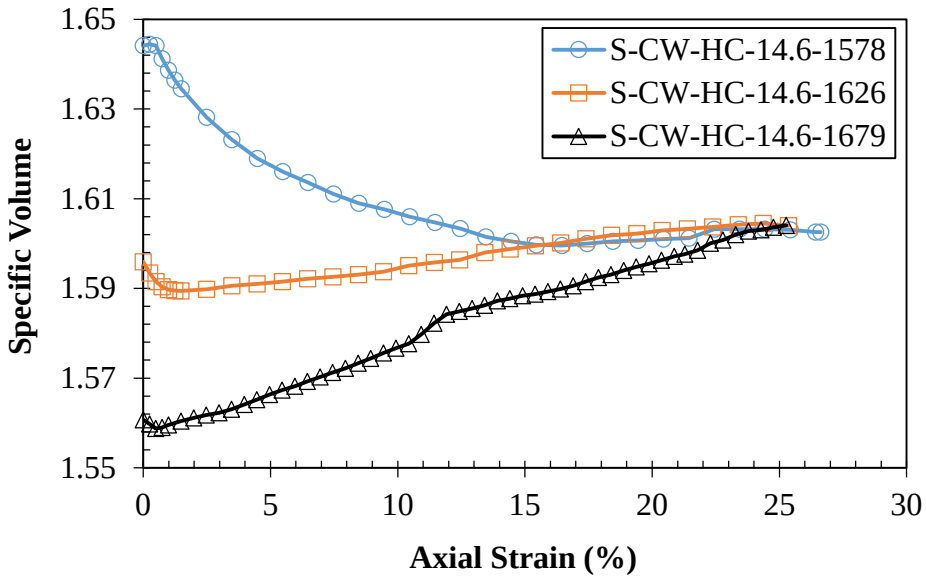

Figure 6.13 Experimental test data results of specific volume with axial strains at different initial densities of the HCclay soil during the triaxial shearing stage under constant-water content test condition.

Figure 6.14 shows the experimental compression curves (i.e., changes in void ratio with loading). Loading is represented by the net mean stress on the specimen during shearing. The trend of the change in void ratio for the least dense specimen with a density of 1578 kg/m^3 is typical to that during compression. The change in void ratio for this specimen includes a virgin compression stage. With increased density, the other two specimens show the typical overconsolidation state with initial rate of change of void ratio similar to the specimen with least density. But, they do not show a virgin compression state. As previously noted, these specimens showed signs of dilation with continued loading.

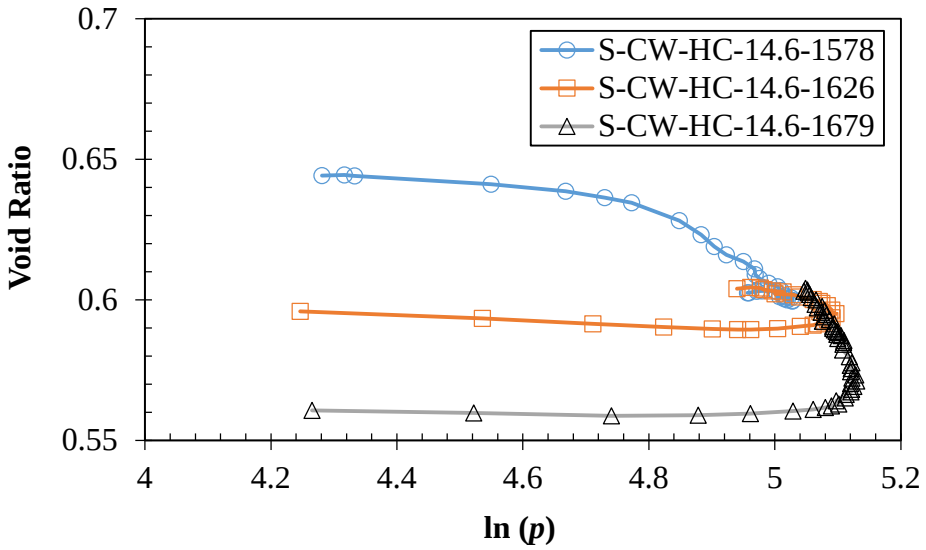

Figure 6.14 Experimental test data results of void ratio with axial strains at different initial densities of the HCclay soil during the triaxial shearing stage under constant-water content test condition

6.4.2 State of stress response during shearing

Changes in matric suction for the three specimens compacted to different initial densities for the Henderson County clay soil are shown in Figure 6.15. In general, there appears to be a stable state of minimal increase in matric suction below about 2 percent axial strain, after which matric suction increases at a decreasing rate to a final state of minimal to no change.

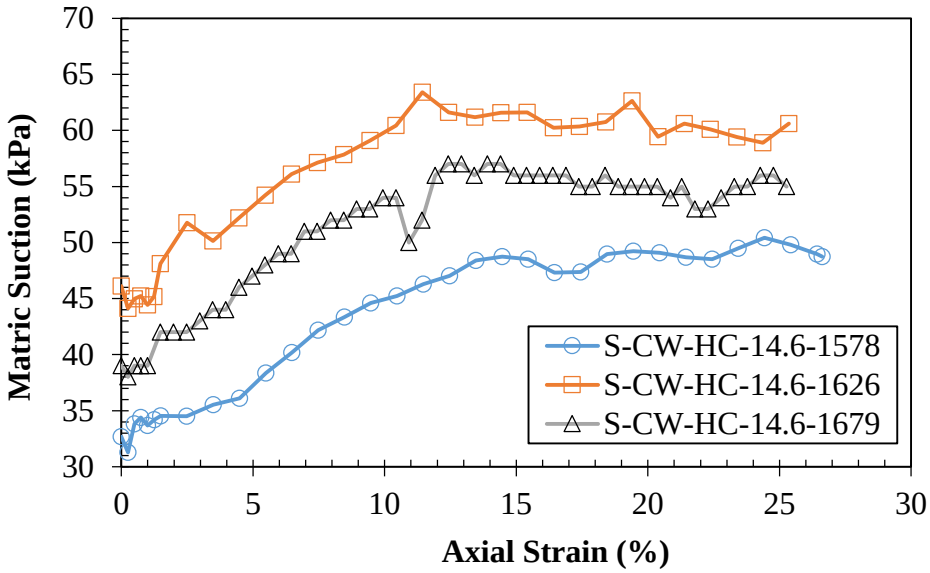

Figure 6.15 Experimental test data results of matric suction with axial strains at different initial densities of the HCclay soil during the triaxial shearing stage under constant-water content test condition.

The decreasing rate of matric suction increase is in accordance with data presented by Maleki and Bayat (2012). Several authors have shown that matric suction does not increase but decreases with shear strain (Chiu and Ng, 2003; Rahardjo et al., 2004; Ma et al., 2013). It is also inferred from other authors (Toll and Ong, 2003; and Thu et al., 2006) that matric suction decreases during shearing based on their data showing increasing pore-water pressures during shearing.

Maleki and Bayat (2012) show that matric suction increases during shearing at lower confining pressures and may decrease at higher confining pressures. For example, Maleki and Bayat (2012) show that for a silty sand soil, matric suction increases during shearing for specimens subjected to 25, 50, 100, and 162 kPa confining pressures, when compacted to a lower initial dry unit weight of 16.26 KN/m^3. For the specimens compacted to a higher initial dry unit weight of 17.94 KN/m^3, only the specimen with the higher confining pressure of 162 kPa, shows a decrease in matric suction during shearing.

One possible reason for matric suction to increase during shearing in this study, is that the degree of saturation of the specimen is still below a fully saturated state, having a pore-air space for the pore-water pressure to dissipate into, thereby resulting in increasing matric suction. This appears to be consistent with the findings presented in Section 6.1, whereby pore-water pressures increased significantly for isotropically compressed specimen that became fully saturated, therefore for soils still in a partially saturated state, pore-water pressure will dissipate. Also, based on the results presented in Section 6.1 (isotropic compressions) and Section 6.4 (shearing), it appears that isotropic compression loading has a much more significant effect on the pore-water pressure, hence, matric-suction, than does loading by shearing.

The air phase during shearing is drained (constant), therefore, the plots in the plane of deviatoric stress and net mean stress with respect to the air phase $q-(p-u_a)$ are expected to show constant positive rates of increase as is typical of drained tests and as shown in Figure 6.16. On the other hand, the initial expectation for plots in the plane of $q-(p-u_w)$, also shows a drained condition even though the pore-water pressure valves were closed to simulate an undrained condition. Pore-water pressure dissipated during shearing because the rate of shearing was low enough to allow any possible water pressure build up to dissipate through the interconnected void spaces into the air phase of the soil; and also because the specimens were at moderate to low degrees of saturation. With dissipation of pore-water pressures u_w, matric suction (u_a-u_w), increases during shearing.

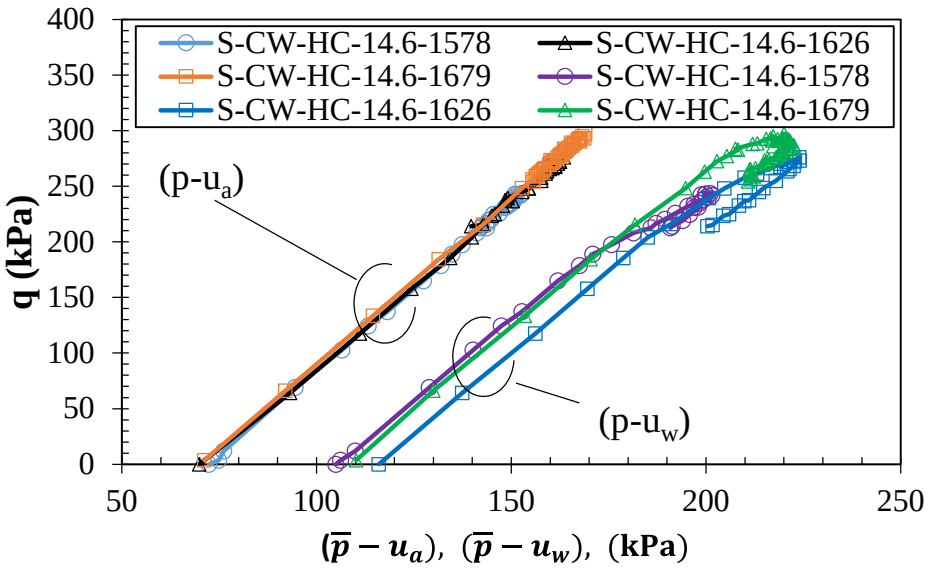

Figure 6.16 Experimental test data trends of deviatoric stress with net mean stress; $(\bar{p}-u_a)$ - with respect to pore-water pressure, and $(\bar{p}-u_w)$ - with respect to pore-air pressure, at different initial densities of the HCclay soil during the triaxial shearing stage under constant-water content test condition.

Variations of matric suction are noted within each matric suction curve in Figure 6.17, but appears significant for the specimen compacted to 1626 kg/m^3. Reasons for variations in matric suction during testing are discussed in Section 6.3.2. The matric suction is lowest for the specimen with the lowest initial density of 1578 kg/m^3. The matric suction for specimen compacted to an initial density of 1626 kg/m^3 is higher than that of the specimen compacted to an initial density of 1679 kg/m^3. Therefore, there is no defined relationship between matric suction and changes in density. But, Maleki and Bayat (2012), concluded that the variation of matric suction under constant-water content is more sensitive to the initial density of specimens than to the net confining pressure and the initial matric suction.

There appears to be a relationship between the initial and final matric suctions of the specimens. That is, the magnitudes of change appear consistent between specimens. The

determined ratios (final to initial) of matric suction change during shearing are 1.49, 1.31, and 1.51 for the three HCclay specimens with increasing initial density respectively. This consistency is contrary to huge disparities found by Rahardjo et al. (2004), with specimens sheared with the same confining pressures but at different initial matric suction. The consistency of change in matric suction for this research program may be attributed to the similar initial degrees of saturation of the specimens.

The effect of net mean stress on changes in matric suction is shown in Figure 6.17. In general, there is minimal to no change in matric suction until a point at which the change in matric suction starts to increase. There is an increase in net mean stress with increasing density at the point in which changes in matric suction starts to occur.

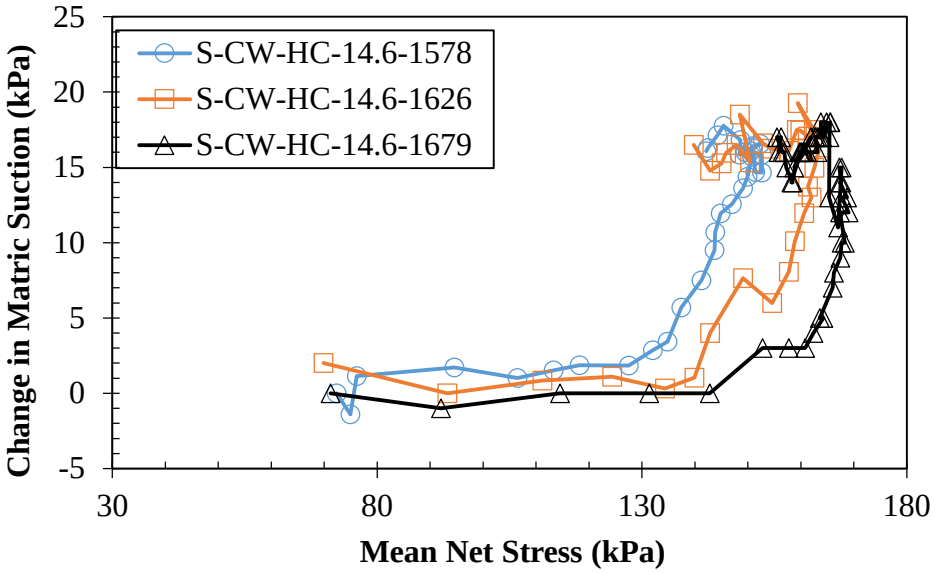

Figure 6.17 Experimental test data results of matric suction with net mean stress at different initial densities of the HCclay soil during the triaxial shearing stage under constant-water content test condition.

Matric suction or suction in general within this study consists of two components; a capillary and an adsorptive component. The capillary component of pore space geometry

in soils and other media is typically represented as the "bundle of cylindrical capillaries" representation. It is the basis of many conceptual models for liquid flow, transport and distribution in unsaturated porous media (Millington and Quirk, 1969; Mualem, 1976). In unsaturated soils, the bundle of cylindrical capillaries models interconnected cylindrical pores, of which a portion is completely liquid filled, but the larger pores are completely empty. Capillary potential will be dominant at relatively high degrees of saturation. When pore-water exists as adsorbed water films, the adsorptive potential becomes more dominant in matric suction. The practical interpretation of liquid retention in soil pore space and the determination of media pore size distribution from measurements of soil water characteristics rely solely on cylindrical capillarity, ignoring the role of surface area and adsorbed liquid films. Because of the relatively large surface area in most porous media, interfacial forces are likely to play a larger role in solute transport and biological activity than predicted by the conventional BCC model (Tuller et al., 1999). Adsorptive potential will be more sensitive to normally consolidated soils as the pore spaces, hence soil structure changes more significantly as is typical of the $e - \ln p$ curves. Therefore, the point at which the matric suction starts to show significant change represents a change from overconsolidation to a normally consolidated soil. This point of net mean stress is then considered to be the initial yield stress and it lies on the initial yield curve in the $(q - p)$ plane.

Experimental yield stresses are typically obtained from the $v - \ln p$ plots of specific volume with net mean stress. The CW test results in Figure 6.18 show the variation of the specific volume, v, with the net mean stress, p, and the corresponding variation of

the matric suction, with the net mean stress on the $s - p$ plots. The yield stress values are identified on the plots and are tabulated in Table 6.1.

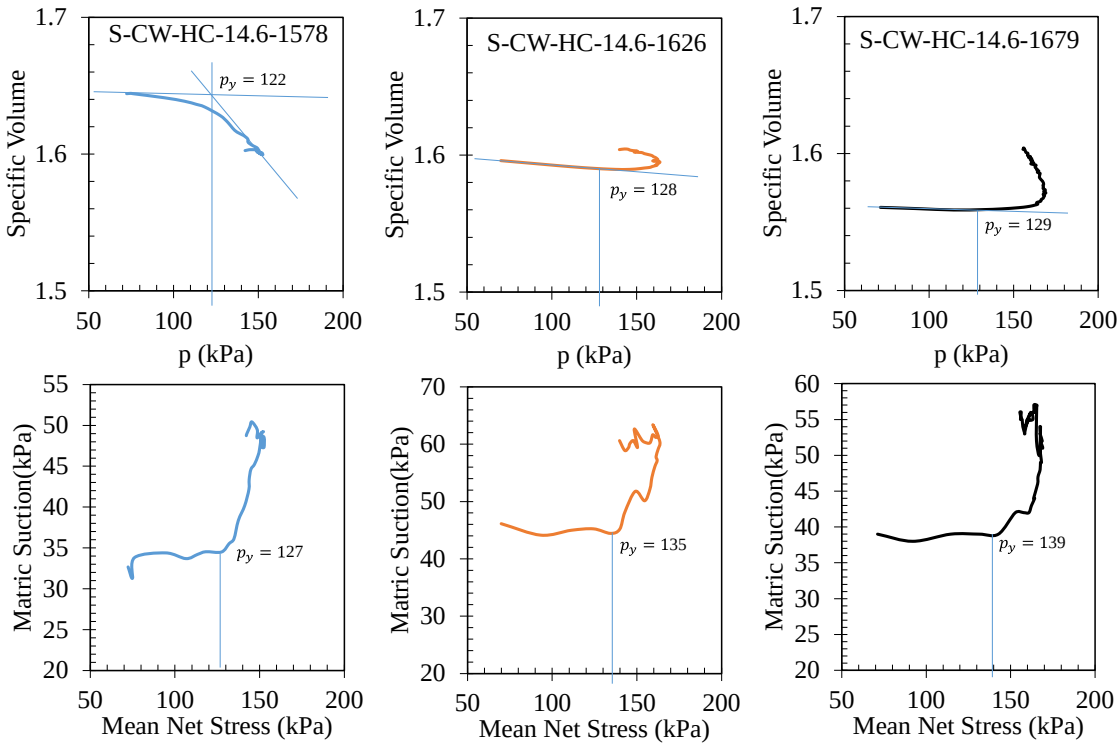

Figure 6.18 Experimental determination of the yield stress using plots of specific volume with net mean stress, and matric suction with net mean stress. Data from HCclay soil at tested at three different densities.

Table 6.1 Preconsolidation (yield) stress for the three Kentucky soil determined experimentally from $v - \ln p$ and $s - p$ plots.

Soil	Experimental yield stress p_y (kPa)	
	$v - \ln p$ plots	$s - p$ plots
DCsclay	115	116
	126	122
	129	128
HCclay	121	127
	130	134
	141	142
LCesilt	133	134
	128	130
	156	158

Comparison of the yield stresses obtained from the $v - \ln p$ and $s - p$ plots are similar and therefore, the use of the $s - p$ plots to select the preconsolidation yield stress is justified.

The deviator stress at the constant rate of axial strain is shown in Figure 6.19. The ductility of the specimens increased with the increasing initial density for all specimens at the same confining pressure. The peak deviator stress occurs at lower strains for increasing initial density.

The figure shows that the stress–strain curves exhibited evidence of post-peak strain softening. The exhibition of post peak-softening behavior for the compacted soils can be explained by the dominant behavior of the soil "packets" formed by the aggregation of clayey particles (Croney et al., 1958; Burland, 1965; Barden and Sides, 1970; Collins and McGown, 1974). The post-peak strain softening commonly observed in overconsolidated soils suggests that the compaction conditions were not affected by compressing all the specimens to an initial low confining stress of 70 kPa prior to shearing. That is, the

confining stress did not bring the specimens into a normally consolidated state, and therefore the state of compaction is still represented in the specimen behaviors.

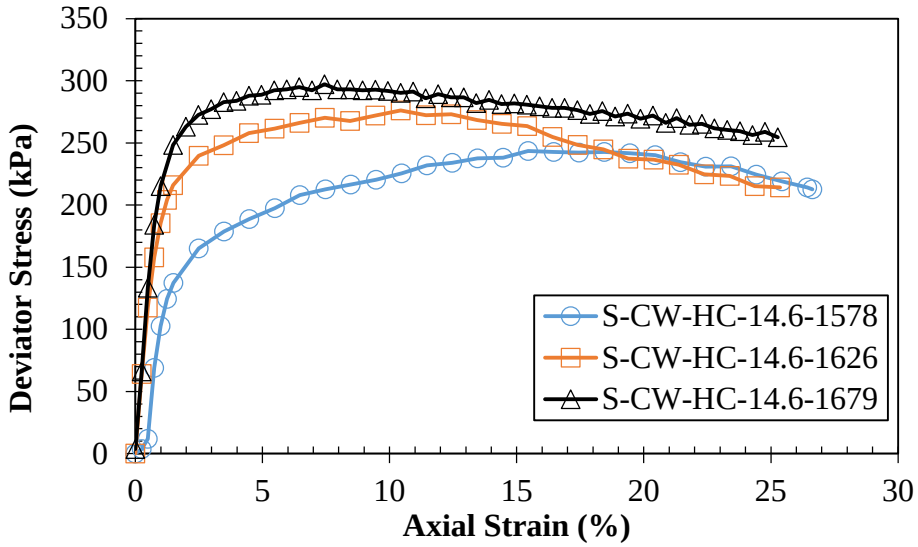

Figure 6.19 Experimental test data results of deviatoric stress with axial strain of the HCclay soil at different initial densities during the triaxial shearing stage under constant-water content test condition.

The suggested critical state variables for unsaturated soils (Wheeler and Sivakumar, 1995; Maatouk et al., 1995; Rampino et al., 1998; and Adams and Wulfsohn, 1997) are the net mean stress, deviatoric stress and specific volume. Defining a true critical-state condition is difficult for dense materials as they often fail through the development of distinct shear surfaces, where non-homogeneous deformations (and the possibility for clay particle alignment) affects the results (Toll and Ong, 2003). In this case, Figure 6.13 shows that a volumetric condition presents a more easily defined condition of critical state, than does a loading condition.

In summary, a three-dimensional plot in $p-q-s$ space is show in Figure 6.20. The projections of the three-dimensional plot unto the two-dimensional planes gives insight

into the typical behavior of a constant water content test under triaxial shearing conditions. In the p-q space, the test simulates a drained test, which is the direct result of a drained air-phase (or constant pore-air pressure). The projection of the plot unto the $q-s$, and $p-s$, shows that matric suction remains fairly constant up to a shear stress or net mean stress after which matric suction increases with continued increases in shear and net mean stresses. The projected increase in matric suction in the $p-s$ plane is defined by the yielding stresses p_y and q_y on the yield curve in the $p-q$ plane.

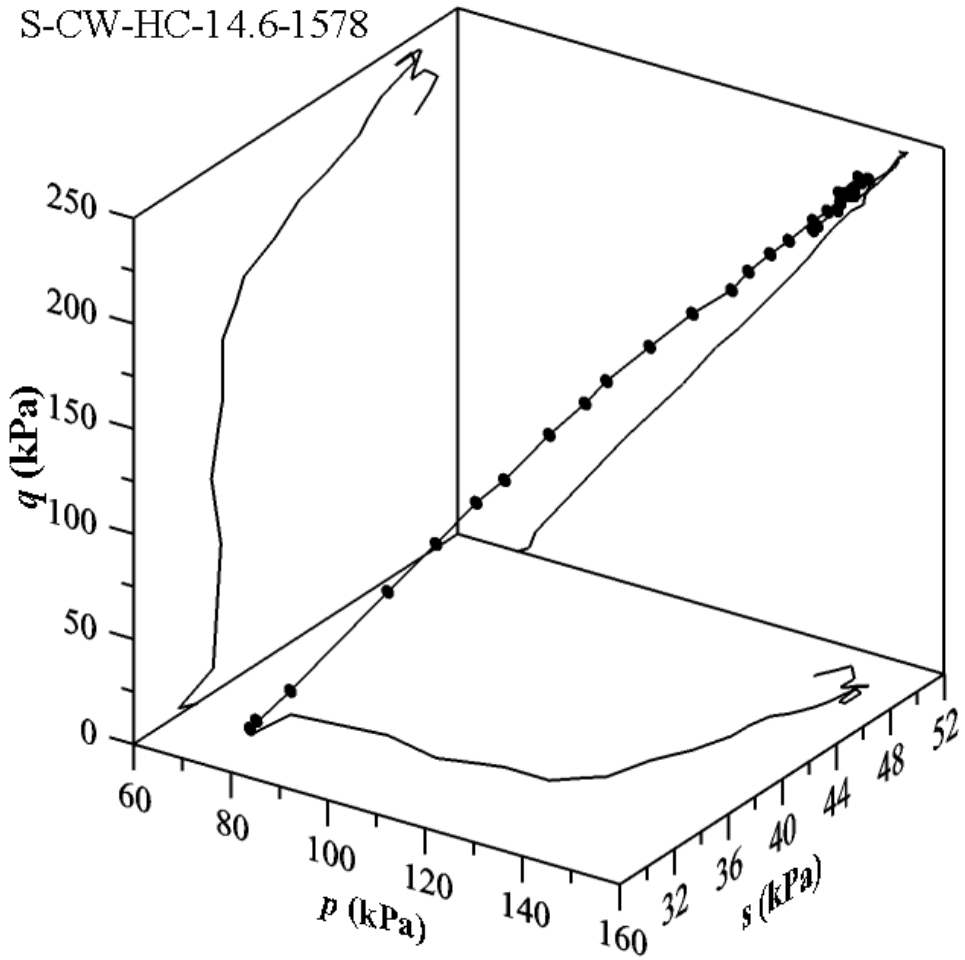

Figure 6.20 Three-dimensional $p-q-s$ plot of experimental test data results of the triaxial shearing stage for an HCclay under conditions of constant-water content.

The three-dimensional plot in $v-p-s$ space is shown in Figure 6.21. The projections of the plot on to the two-dimensional planes gives insight into previous discussions and the typical behavior of a constant-water content test under triaxial shearing conditions. In the $v-p$ plane, a typical compression curve of decreasing specific volume with increasing net mean stress is an indication of a lightly overconsolidated or normally consolidated soil. In the $v-s$ plane, the specific volume decreases with increasing matric suction, with a significant change in rate of loss of specific volume at a threshold matric suction, corresponding to the preconsolidation yield stress. Lastly in the $p-s$ plane, matric suction is fairly constant until the yield stress is exceeded at which point the matric suction increases with increases in the net mean stress. As previously discussed, this increase in matric suction may be due to lower confining stress on the specimen. At higher confining stress, the matric suction is expected to decrease with increasing net mean stress as indicated by literature data (see earlier discussion).

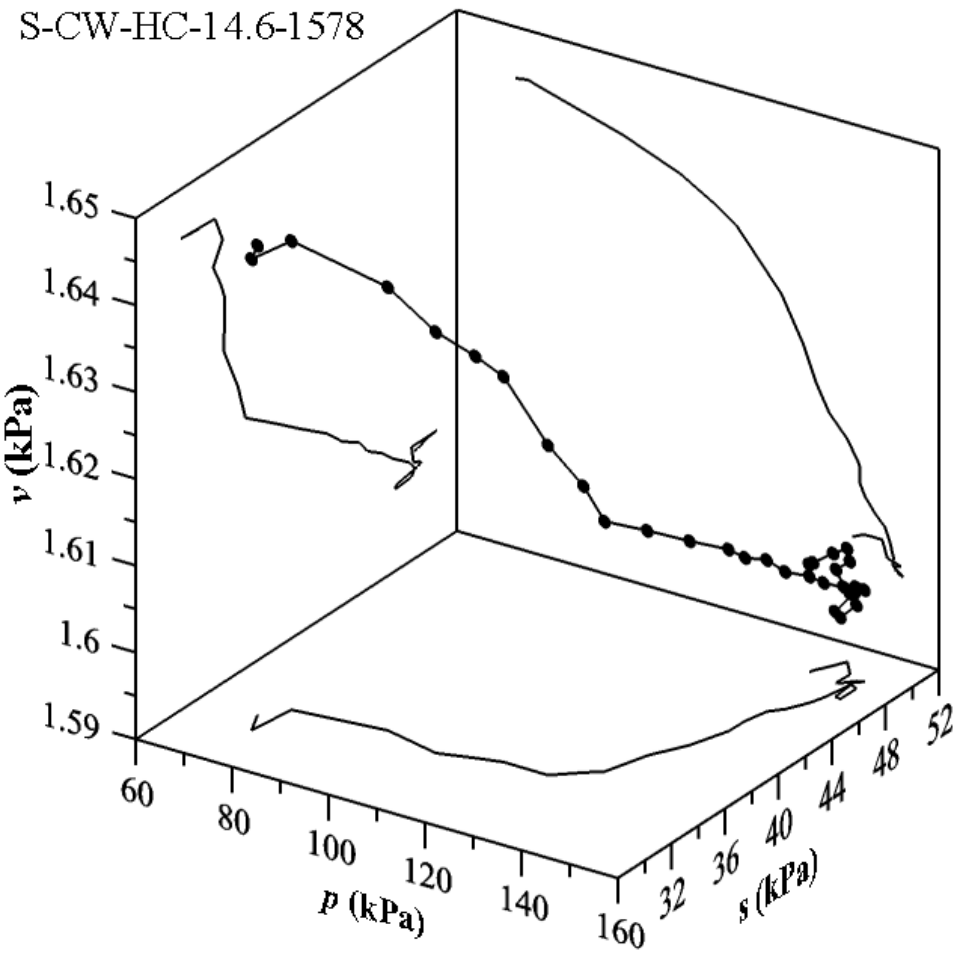

Figure 6.21 Three-dimensional v-p-s plot of experimental test data results of the triaxial shearing stage for an HCclay under conditions of constant-water content.

7 PREDICTIONS OF DYNAMIC PROPERTIES AND MECHANICAL BEHAVIORS.

In this Chapter, theoretical and empirical relationships are used to predict experimental data from this and other studies. Predictions of the dynamic property of shear modulus of soil is presented in Section 7.1. The form of the Hardin and Black (1969) relationship, further developed by Sawangsuriya et al (2009) was used for shear modulus predictions and performance. The parameter of the empirical model is robustly analyzed for a relationship with soil material properties. In addition, the parameter of the Zhou et al. (2012) equation for estimation of the shifts in SWCC curves with changes in initial density is also robustly analyzed for its relationship with a parameter of an SWCC model such as that of the van Genuchten (1980) model. Presented in Section 7.2 is a constitutive model based on the mechanical behaviors of soils used in this study. The constitutive model combines aspects of several existing unsaturated soil models to suitable predict the behavior of the Kentucky clay type soils under the conditions tested.

7.1 Predictions of Small Strain Shear Modulus

Edil and Sawangsuriya (2005) show that the effect of changes in dry unit weight on shear modulus is relatively small. Several other researchers (Mancuso et al., 2002; Mendoza et al., 2005; Vassallo et al., 2007a; Sawangsuriya et al., 2009; Ng et al., 2009) have investigated the effects of net mean stress $(p-u_a)$, and the matric suction (u_a-u_w) on initial shear modulus. In general, these researchers have shown that positive or negative changes in initial shear stiffness tends to correspond in a nonlinear

fashion, to the associated positive and negative changes in net mean stress and matric suction. Some of these researchers have proposed empirical relationships describing the maximum shear modulus $G_{\max}$, of unsaturated soils as a function of void ratio and both matric suction and net stress

Sawangsuriya et al. (2009) presented a form of the Hardin and Black (1969) equation for normally consolidated soil, modified for unsaturated conditions as follows:

$$G_{\max} = A\, f(e)\left[(\sigma_o - u_a) + S^{\kappa}(u_a - u_w)\right]^n \tag{7.1}$$

In Equation (7.1) A is the material parameter that is associated with the soil type and microstructure; $f(e)$ is the void ratio function which depends on the void ratio; S is the degree of saturation; κ is the saturation exponent; $(u_a - u_w)$ is the matric suction; and n is the stress exponent based on contact between particles and strain amplitude.

The term $(\sigma_0 - u_a)$ is the net confining pressure, which is an isotropic pressure subjected on the specimen. For this research, the effect of stress states on the shear modulus is considered during shearing, therefore the term $(\sigma_0 - u_a)$ becomes the net mean stress on the specimen, $p = (\bar{\sigma} - u_a)$ which is an anisotropic pressure. $\bar{\sigma}$ in this case is the total mean stress $(\sigma_1 + \sigma_2 + \sigma_3)/3$. Sawangsuriya et al. (2009) dropped the overconsolidation ratio term, OCR^k, from the Hardin and Black (1969) equation because of the use of reconstituted soil. OCR is the overconsolidation ratio, and k is the overconsolidation ratio exponent based on plasticity index. The OCR term is

reintroduced into the equation because this research made use of compacted soils. The resulting equation is as follows:

$$G_{\max} = A\, f(e) OCR^{k} \left(p + S^{\kappa} s\right)^{n} \tag{7.2}$$

Note that the term s, is used for matric suction, [i.e. $s = (u_a - u_w)$]. The parameters, A, k, κ and n can be determined by optimizing the least square difference between the measured and predicted values of the small-strain shear modulus, or through secondary empirical relationships. The parameters A and κ were determined by optimization. Garven and Vanapalli (2006) correlated the saturation exponent parameter, κ with plasticity index (PI) and suggested that the parameter was constrained between 1 and 3, where $\kappa = 1$ for $PI = 0$ and $\kappa \approx 3$ for $PI = 47$. However, the correlations were for a limited number of data sets and appeared to be influenced by the method of sample preparation procedures (i.e., slurry consolidated, dynamically or statically compacted, natural) (Vanapalli and Fredlund, 2000). Thus for this study, κ was found by optimizing the least square difference between the measured and predicted values, with constrained limits between 1 and 3 inclusive.

The parameters k and n, were determined through empirical relationships. The overconsolidation ratio exponent, k, was determined using a best fit curve of the data for calculated k values with corresponding plasticity indices, PI, presented by Hardin and Black (1969). The equation for the best fit curve is as follows:

$$k = -0.00005\, PI^{2} + 0.0096\, PI - 0.0044 \tag{7.3}$$

The stress exponent, n, was taken to be 0.5 for this study. Hardin and Black (1969) show that n, depends on the plasticity index of the soil, but also show that small-strain shear modulus can be represented in normally and overconsolidated soils with the use of a single value of the stress exponent, $n = 1/2$. Hardin and Black (1969) reasonably limits the overconsolidation to soils other that those with high overconsolidation ratios of very plastic soils.

The data presented in the Sawangsuriya et al. (2009) study had a constant net confining pressure representing typical pavement subgrade confinement, and presented this as a possible limitation on this equation. It is important to note that this study also uses a low confining pressure and therefore considered this equation to be suitable for estimations of shear modulus.

It is noted that Sawangsuriya et al. (2009) used the void ratio function suggested by Hardin (1978) in their efforts. For this research, the void ratio function presented in Section 5.2.1 of this report and presented as Equation (5.5) was used. The empirical equation presented as Equation (7.2) is used to describe changes in the small-strain shear modulus with changes in stress states for this study.

7.1.1 Performance of small strain shear modulus relationship

The efficacy of the modified Sawangsuriya et al., (2009) equation for anisotropic stress, Equation (8.2), was assessed by optimizing the relationship between the calculated shear modulus from measured shear wave velocities and the predicted shear modulus using the equation. Equation (8.2) is suited for unsaturated soils, but can be used for

saturated soils as it reduces to the form of the Hardin and Black equation with saturated soil parameters of zero matric suction and degree of saturation of one. The difference in the reduced form to that of Hardin and Black (1969) is that the anisotropic net mean stress parameter, p, is replaced by the anisotropic effective stress parameter, $(\bar{\sigma} - u_w) = p'$, when used to estimate shear modulus for shearing during a consolidated isotropic undrained (CIU) triaxial tests as follows:

$$G = A\, f(e) OCR^k (\bar{\sigma} - u_w)^n \tag{7.4}$$

Figure 7.1 shows the comparisons between the measured and predicted data of the CIU tests for all four of the Kentucky soils, each compacted to a density that is at or close to its Standard Proctor maximum density value, and optimum moisture content (all subjected to a net confining pressure of 70 kPa). In general the figure shows excellent agreements between the measured and predicted data for the saturated soils. The measured data for the HCclay, LCesilt, and DCsclay soils show a slight variation from the predicted data at very low effective stresses. This may be due to the overconsolidation effect at low stress states.

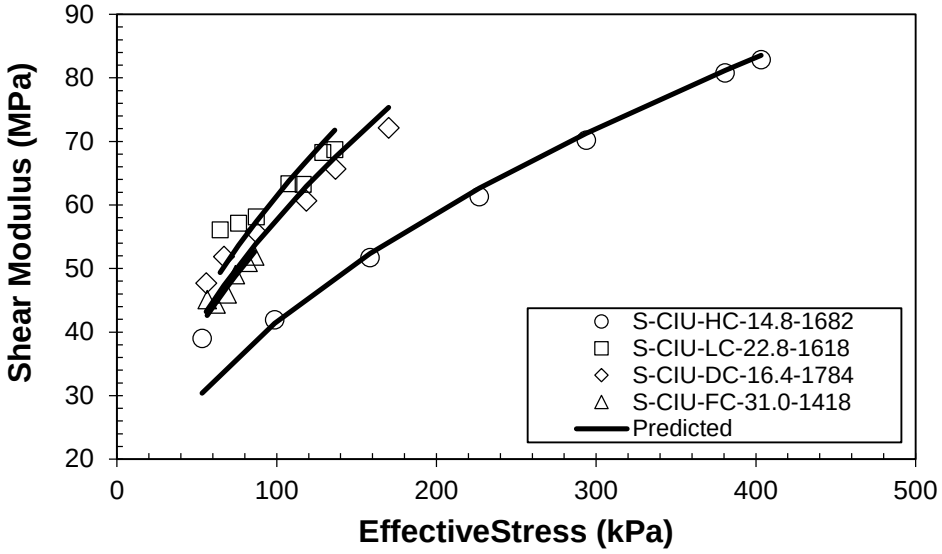

Figure 7.1 Experimental data and prediction performance of small-strain shear modulus plotted with effective stress during the saturated undrained triaxial shearing stage of CIU tests of the Kentucky soils under conditions of standard Proctor maximum dry density and optimum moisture content.

The agreement between the measured and predicted data is shown in the line of unity plot of Figure 7.2. An exceedingly good correlation is shown for the measured and predicted shear modulus above 60 MPa, as these data points are all essentially on the line of unity. A slight increase in variation is noted for values below the shear modulus of 60 MP, with predicted values of about the same magnitude or just slightly lower than the measured data. The empirical constitutive shear modulus equation predicted measured shear modulus data with coefficients of determination of 0.959, 0.511, 0.846, and 0.841 respectively, for the HC, LC, DC, and FC soils subjected to CIU triaxial shearing tests.

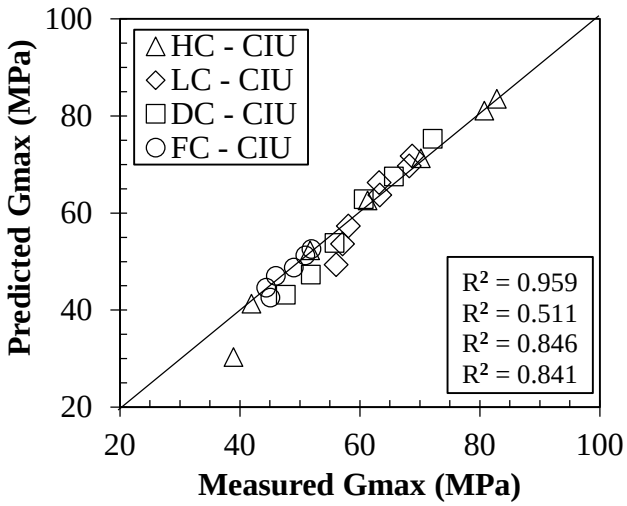

Figure 7.2 Line of unity plot of agreement between predicted and measured small-strain shear modulus for the triaxial shearing stage of the consolidated isotropic undrained (CIU) tests.

Predictions were made with Equation (7.4) for the latter CIU tests and also for unsaturated specimens subjected to the constant water content (CW) method using Equation (7.2). Three specimens for each soil type of HCclay, LCesilt, and DCsclay soils were subjected to the CW tests. The CW test specimens were compacted with different compaction energies and compacted near the Standard Proctor optimum moisture contents. The resulting initial void ratios, optimized and empirically determined parameters, and the coefficients of determination in comparing measured to predicted data using Equation (7.2), are tabulated in Table 7.1.

Table 7.1 Determined parameters for the empirical shear modulus models with corresponding initial void ratios and coefficient of determination (R^2) of best fit predicted to experimental data.

		Initial e	A	n	κ	OCR	k	R^2
HC	CW	0.641	8027	0.5	3	2.45	0.07	0.830
		0.597	8645	0.5	3	2.73	0.07	0.764
		0.561	8271	0.5	3	3.17	0.07	0.759
	CIU	0.607	5998	0.5	1	1.07	0.07	0.959
LC	CW	0.687	10186	0.5	3	2.56	0.19	0.815
		0.646	9338	0.5	1	3.61	0.19	0.683
		0.610	7953	0.5	1	3.70	0.19	0.193
	CIU	0.600	7587	0.5	1	2.24	0.19	0.511
DC	CW	0.560	9166	0.5	3	2.22	0.03	0.882
		0.526	9321	0.5	3	2.43	0.03	0.895
		0.481	9001	0.5	3	2.83	0.03	0.895
	CIU	0.501	7444	0.5	1	1.37	0.03	0.846
FC	CIU	0.959	8823	0.5	1	2.61	0.23	0.841

In general, the coefficient of determination indicates good correlations between measured and predicted shear modulus for the HCclay, DCsclay, and FCesilt soils with coefficient of determinations above 0.758. The coefficients of determination for the constant water content tests range between 0.759 and 0.830 for the HCclay soils, and between 0.882 and 0.895 for the DCsclay soils. The LCesilt soil generally yielded lower coefficients of determination between measured and predicted shear modulus than the other soils when using Equations (7.2) and (7.4). The coefficient of determination of 0.815 for the CW specimen with highest void ratio (least compaction effort), indicate a very good correlation, but correlation is lost with decreasing void ratio or increasing compaction effort.

The saturation exponent parameter, κ optimized to the maximum constraint value of 3 for all the HCclay and DCsclay constant water content specimens, and also for the specimen LCesilt constant-water content specimen with the highest void ratio. The optimized value changed to 1 for the other two LCesilt constant-water content specimens with lower void ratios.

7.1.2 The A parameter

The optimized A parameters range only minimally for the constant-water content test specimens of the HCclay and DCsclay soils. The HCclay specimens' A parameter range between 8,027 and 8,645 and the DCsclay specimens range between 9,001 and 9,321. These minimal ranges of the A parameters results in changes that are less than 10 percent. The constant-water content LCesilt specimens show a slightly higher variation with a range of 7,953 to 10,186. Variations between the A parameters for the constant-water content tests and that of the CIU tests are also noted. Average values of the constant-water content tests for the HCclay, LCesilt, and DCsclay soil specimens are 8315, 9,160, and 9,163 respectively, and 5,998, 7,587, 7,444 respectively for the CIU tests.

A plot of the variation of the A parameter with void ratio is shown in Figure 7.3. The figure indicates that void ratio has minimal effect on the HC and DC constant-water specimens. Though this in an indication of the A parameter being associated with soil type, it is not consistent for the LCesilt soil specimens. There is a clear indication of dependency of void ratio (soil structure) with the LCesilt specimens.

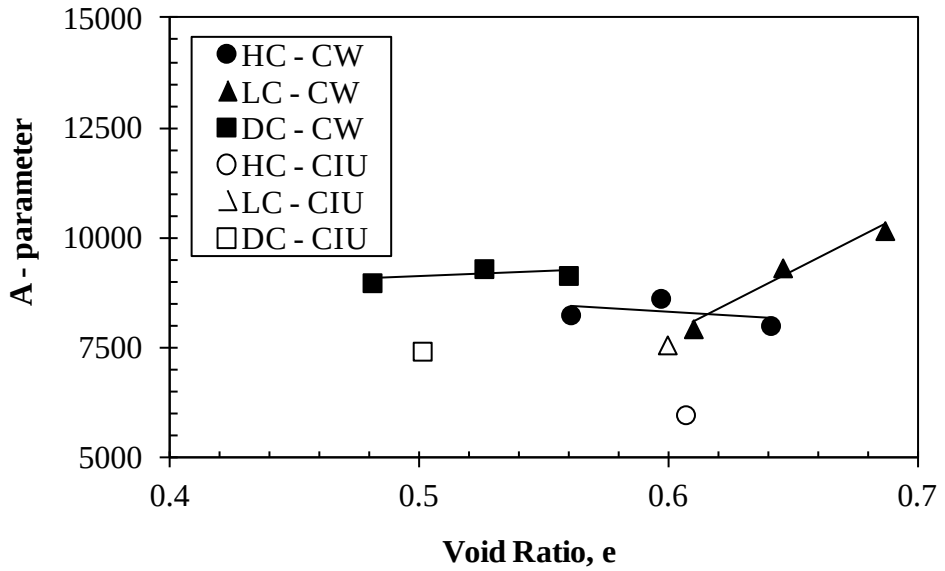

Figure 7.3 Variation of the A - parameter with void ratio for constant-water content (CW) tests and consolidated isotropic undrained (CIU) tests.

The A parameter is a parameter that is generally associated with the soil type and microstructure. Based on the changes in the optimized A parameters within the LCesilt soil type and the changes between unsaturated and saturated tests, the A parameter may not be a true material property under anisotropic conditions.

Analyses were performed to determine the relationship of the A parameter with functions of material properties. Five additional test soil studies were used to assess the relationship of the A parameter with material properties. The studies used in the assessment are for a silt, two lean clays, a fat clay and a clayey sand that were used by Sawangsuriya et al. (2009). The soil properties from each study are given in Table 7.2.

Table 7.2 Geotechnical Index Properties of Selected Studies

Sample Name	Soil Type	Fines	CF	LL	PI	G_s	OMC	γ_d
		(%)	(%)	(%)	(%)		(%)	(kN/m^3)
S09silt	Silt, ML	88.1	5.7	28	11	2.69	13.5	17.9
S09lclay1	Lean clay-1, CL-1	91.1	27.3	42	24	2.69	22	15.8
S09lclay2	Lean clay-2, CL-2	59.7	14.5	26	9	2.66	16	17.7
S09fclay	Fat clay, CH	96.4	75.2	85	52	2.75	27.5	14.4
S09csand	Clayey Sand, SC	41	18	28	14	2.7	13.5	18.5

Fines = % passing #200 sieve; CF = % < 0.002 μm; LL = Liquid Limit; PI = Plasticity Index; G_s = Specific Gravity; OMC = Optimum Moisture Content; γ_d = Dry Unit Weight

As previously noted in Section 7.1, Sawangsuriya et al. (2009) used the void ratio function suggested by Hardin (1978) in their efforts. To be able to determine a relationship for the A parameter with material properties from this study and those selected from Sawangsuriya et al. (2009), the analyses in obtaining the A parameter must be consistent. The test data from Sawangsuriya et al., (2009) for the selected five soils were extracted and the data is optimized following the procedures used in this study (see Appendix D for optimization method). The extracted data is presented in Appendix I. Using the extracted data and the given parameters, the void ratio function, $f(e)$, was determined by rearranging the shear modulus equation to solve for $f(e)$. The void ratio, e, was then determined using the form of the void ratio function used by Sawangsuriya et al. (2009). With the void ratios determined, the new void ratio function was calculated using the form presented in Equation (5.5), and optimizations were performed to determine the A parameter, and the saturation exponent parameter κ. The stress exponent, $n = 0.5$, was used. The A parameters determined by Sawangsuriya et al.

(2009) and those determined by this study are presented in Table 7.3, for the selected soils.

Table 7.3 List of the A parameters from Sawangsuriya et al. (2009) and the adjusted A parameters using the void ratio function of this study.

Sample Name	Stress exponent n parameter	A parameter	A parameter adjusted for $f(e)$
S09silt	0.72	1590	13586.5
S09lclay1	0.47	5499	12557.5
S09lclay2	0.4	12503	23014.4
S09fclay	0.64	1412	7199.6
S09csand	0.37	14534	24793.1

Analyses of the A parameters from the five selected studies and the three from this study were performed to determine a suitable relationship with a material property or a combination of material properties. A suitable relationship was determined with the A parameter and the percent fines (amount passing the No. 200 sieve) of the soils and is shown in Figure 7.4. The assumed linear relationship is defined by the correlation of determination of 0.7109.

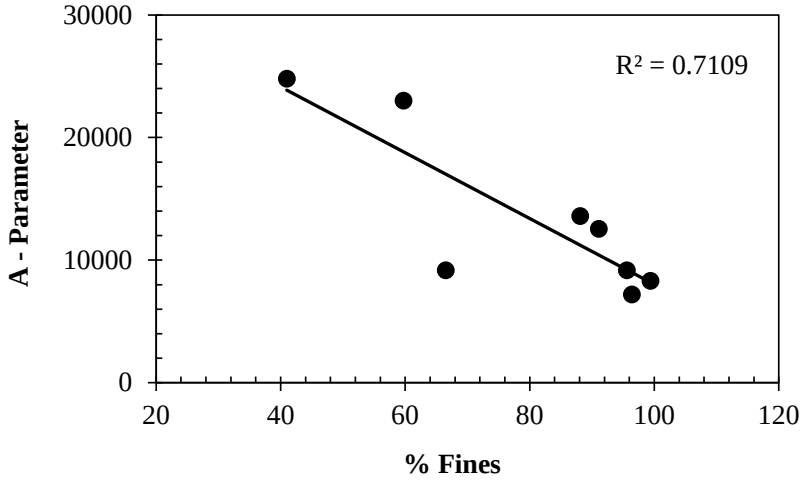

Figure 7.4 A relationship of the A parameter with percent fines.

7.1.3 The effect of normalization on the A parameter

Small strain shear modulus is generally normalized to obtain dimensional consistency, or to allow behaviors to be examined irrespective of previous stress history, or to minimize the effects of soil structure depending on the normalizing parameter. Normalization with the initial shear modulus was performed to determine the effect of normalization on the A parameter of the empirical shear modulus relationship of Equation (7.2). The small strain shear modulus, G obtained during the triaxial shearing tests was normalized with the initial shear modulus G_{ini} at the start of shearing. The resulting equation of normalized shear modulus is as follows:

$$\frac{G}{G_{ini}} = A' F(e) OCR^{k} \left(p + S^{\kappa} s\right)^{n} \tag{7.5}$$

With normalization, the effect of soil structure or changes in soil structure is introduced into the resulting new A' parameter, and therefore, is now assumed to be associated with soil type and macrostructure.

Comparisons between the measured and predicted data were performed by optimizations of the normalized measured shear modulus with the use of Equation (7.5) using the least-squared optimization algorithm. Figure 7.5 shows the agreements between the measured and predicted data for shear modulus data (a) and the normalized shear modulus data (b). In comparison, the normalized measured and predicted data fall closer to the line of unity.

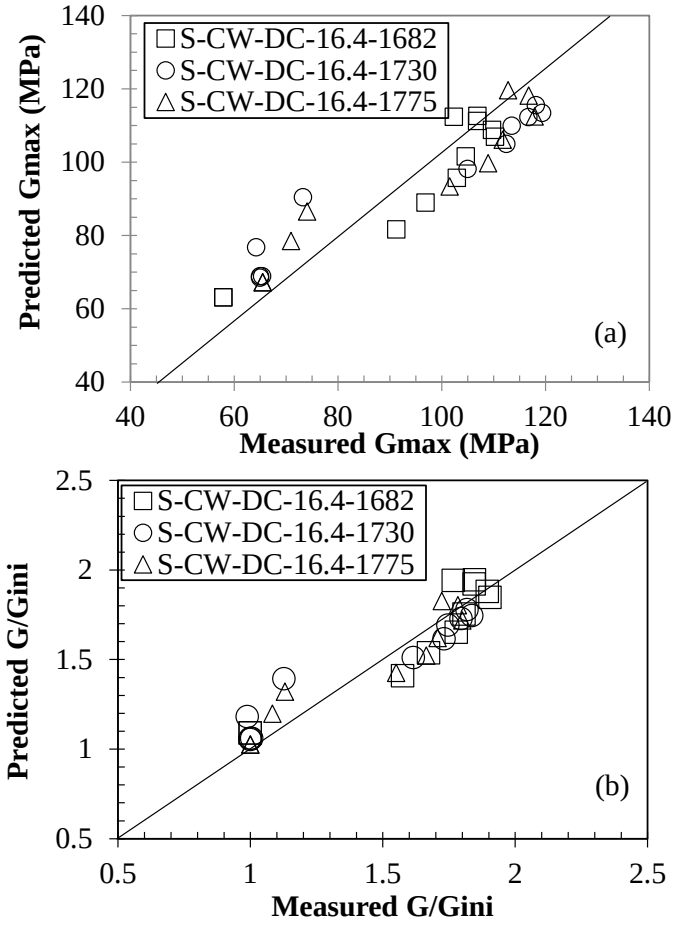

Figure 7.5 Line of unity plot of agreement between predicted and measured anisotropic (a) small-strain shear modulus (b) normalized small-strain shear modulus, for the DCsclay specimens under conditions of constant-water content triaxial shearing stage.

The resulting A' parameters are tabulated in Table 7.4 with their corresponding initial void ratios for all specimens.

Table 7.4 A' parameters determined by optimization procedure of the normalized shear modulus relationship of Equation (7.4)

		Density (kg/m^3)	Initial e	A'
HCclay	CW	1556	0.641	0.1622
		1626	0.597	0.1475
		1679	0.561	0.1347
	CIU	1682	0.607	0.1540
LCesilt	CW	1552	0.687	0.0979
		1570	0.646	0.0974
		1618	0.610	0.0648
	CIU	1618	0.600	0.1353
DCsclay	CW	1682	0.560	0.1583
		1730	0.526	0.1435
		1775	0.481	0.1375
	CIU	1784	0.501	0.1562
FCesilt	CIU	1418	0.959	0.1957

A visual relationship of the A' parameter and their corresponding void ratios are shown in Figure 7.6 for each soil types of HCclay, DCsclay, and LCesilt clay type soils. With the determined A' parameter for the CIU test on the LCesilt soil presented as an anomaly or a statistical outlier, the plots indicate a very good relationship of the A' parameter with void ratio. In general, the A' parameter decreases with decreasing void ratio. The trendlines shown in Figure 7.6 are of the form of a power function $A = ae^b$.

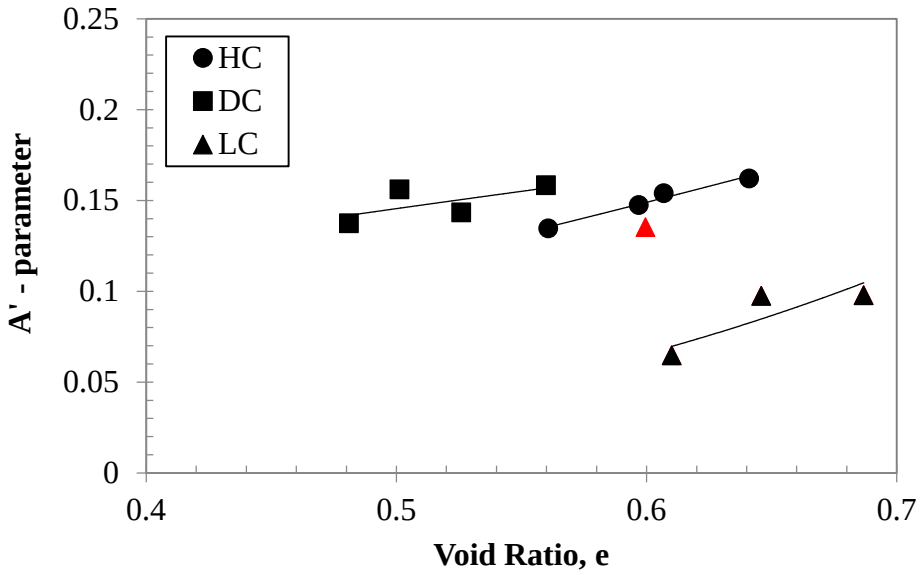

Figure 7.6 Variation of the A' parameter with void ratio for constant-water content (CW) tests and consolidated isotropic undrained (CIU) tests.

Based on previous findings that there exists a relationship between the A parameter and percent fines (see Figure 7.4), and the findings that a reasonable relationship exists for the A' parameter with void ratio (see Figure 7.6), there exists a degree of certainty that the A' parameter can be associated with soil type and macrostructure. The A' parameter data, percent fines and corresponding void ratios were analyzed using the software, CurveExpert to determine a 3-dimensional best fit curves through the data. The data fits a power model function of the form:

$$A' = a(PF)^b(e)^c \tag{7.6}$$

In Equation (7.6), PF is the percent fines, e_{ini} is the initial void ratio, and the parameters a, b, and c are constants for best fit. For this study, the parameters were determined by the best fit power model function using the data from the Kentucky soils.

The resulting best fit equation relating the A' parameter to percent fines and initial void ratio is given as:

$$A' = 0.0002323(PF)^{1.432}(e_{ini})^{0.162} \tag{7.7}$$

With a measure of reliability of a statistical confidence level of 95%, the best fit regression has a standard error of 0.014, a correlation coefficient of 0.922, and a coefficient of determination of 0.850.

7.1.4 The Zeta parameter

Zhou et al. (2012) showed that the ζ parameter can be used to determine the SWCC for the same soil at different initial void ratios. Validation of the ζ parameter was performed using the data from this study as presented in Section 4.2.3. A great advantage of the ζ parameter is its possible use for field determination of matric suction. For example, if a field determination is made that the density or stiffness is less than the desired design value, the ζ parameter can then be used to determine the current state of matric suction, if the design SSSC and its initial void ratio is available. With the known state of the current void ratio and degree of saturation of the compacted soil, the corresponding effective degree of saturation of on the design (reference) SWCC can be determine using the VBA coding, Zhou2012SWCCshiftforsuction, presented in Appendix G. The code then computes the matric suction at the reference SWCC using the determined effective degree of saturation and the Van Genuchten, a, n, and m parameters from the design SWCC.

To use the VBA code in determining matric suction, the ζ parameter can be determined by calibration of an SWCC to that of a reference SSSC with a different initial void ratio. This requires that an additional SWCC test to the design SWCC must be performed in the laboratory. (It is expected that a design SWCC exists and was performed during the discovery phase). SWCC tests on clay soils may take up to two weeks to complete, or even longer on clays with high plasticity. Procedures for a robust solution to determine the ζ parameter are presented herewith.

The ζ parameter defines the effect of changes in void ratio on the degree of saturation. Figure 7.7 shows the line of inflection, which is a line that defines the inflection points on SWCC curves for changes in void ratio. With changes in void ratio, the line of inflection indicates changes in degree of saturation as well as changes in matric suction. Having both the degree of saturation and the matric suction change minimizes the definition of the ζ parameter. With the vertical lines of constant matric suction shown in Figure 7.7, the effect of matric suction on the degree of saturation is minimized. These vertical lines called ζ lines, therefore, define only the enhanced effect of change in void ratio on degree of saturation. A ζ line intersects points on the SWCC that can be represented by the slopes of the SWCC curves. The transition slopes of the SWCC curves are generally controlled by the n parameter, (Fredlund et al., 2012). Therefore, the ζ parameter may be related to the n parameter.

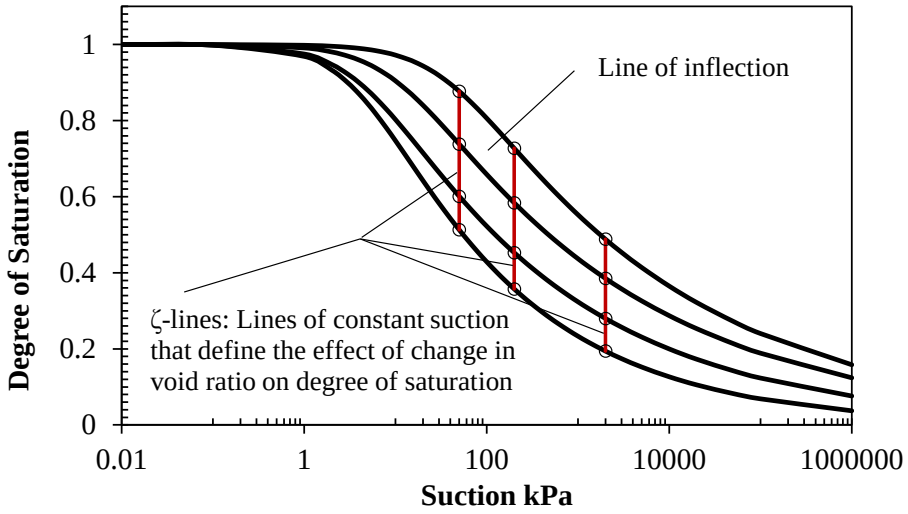

Figure 7.7 Typical clay soil SWCC curves at different initial void ratios, with the defined line of inflection, and general ζ -lines.

Analyses were performed to determine the relationship of the n parameter as a function of the ζ parameter. Nine test soil studies, including the four Kentucky soils, were used to assess the relationship of the n parameter as a function of the ζ parameter. The additional five studies are from various researchers and include a range of soil types. The study references and the soil properties from each study are given in Table 7.5

Table 7.5 Geotechnical index properties of the soils used to assess the n and ζ parameter relationship.

Reference	Sample Name	Clay Fraction (%)	Liquid Limit (%)	Plastic Index (%)	Percent Fines (%)
Daviess County		21	23.3	3.9	95.6
Henderson County		20	28.2	8.5	99.4
Lee County		88	55	23	66.5
Fayette County		74	64.3	29.3	86.8
Romero et al., (2012)	R01clay	50	56	27	---
Tarantino (2009)	T09silt	17.5	32	16	59.4
Vanapalli (1999)	V99ctill	30	35.5	18.7	72
Huang et al., (1998)	H98ssand	10	22.2	5.6	47.5
Salager et al., (2010)	S10csand	10	25	10.5	28

SWCC data from these five studies were extracted from SWCC plots presented by Zhou et al. (2012). The SWCC data extracted includes data for a reference SWCC and a SWCC for calibration of the ζ parameter for each study. The SWCC data were fitted to the Van Genuchten (1980) equation. The VBA coding, Zhou2012zetacalibration, presented in Appendix F was then used to calibrate the reference SWCC to obtain the ζ parameter using both the reference and calibrator SWCC, and the fitted and calculated a, n, and m, Van Genuchten parameter. With different initial void ratios, the calibration was initially performed using the SWCC with the higher void ratio as the reference SWCC, then the calibration performed again using the SWCC with the lower void ratio as the reference SWCC and the SWCC with the higher void ratio as the calibrator. The ζ parameters for each case are presented in Table 7.6, along with the Van Genuchten parameters for the initial reference SWCC, i.e., the SWCC with the higher void ratio.

Table 7.6 Zhou et al., (2012) and van Genuchten (1980) model parameters

	ζ parameter		Reference SSSC		
	$e_i^{ref} > e_i$	$e_i^{ref} < e_i$	a	n	m
Daviess	0	0.18	67.26	1.167	0.143
Henderson	0.13	0.32	10.77	1.183	0.154
Lee	0.08	0.19	158.55	1.108	0.098
Fayette	-0.02	0.15	3000	1.04	0.04
R01clay	0.26	0.46	410	1.342	0.255
T09silt	0.1	0.2	60.6	1.23	0.18
V99ctill	0.08	0.2	64.25	1.157	0.136
H98ssand	0.15	0.32	63.85	1.96	0.49
S10csand	0.25	0.4	1.12	1.2	0.17

e_i^{ref} = Reference Initial Void Ratio; e_i = Initial Void Ratio; a, n, m = Parameters that define the SSSC equation.

Using the ζ parameter for the $e_i^{ref} > e_i$ data in Table 7.6, the effect of the n parameter on the ζ parameter is shown in Figure 7.8, for all nine soil of varying soil types of clays, silts and sands. A linear trendline through the data points in Figure 7.8, with a coefficient of determination of 0.133, indicate a poor relationship of the n parameter as a function of the ζ parameter for varying soil types.

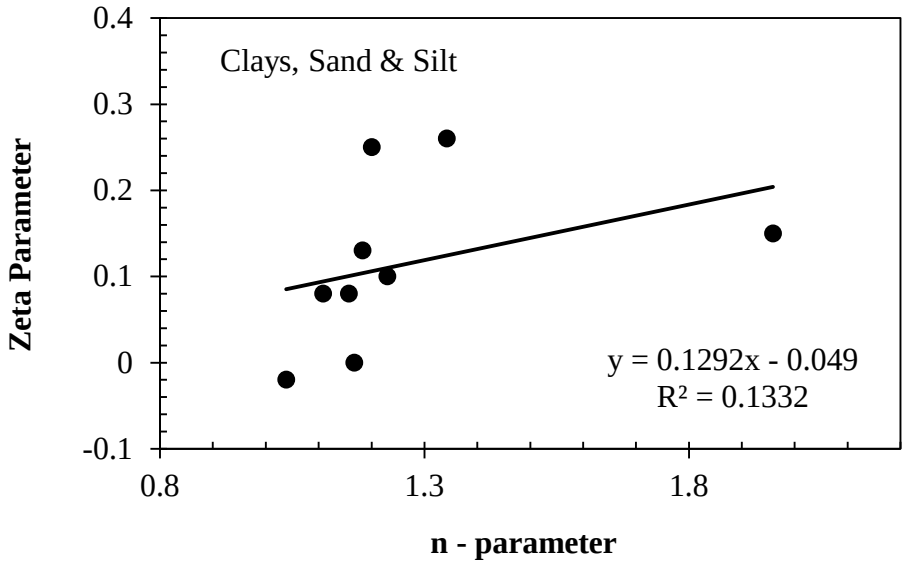

Figure 7.8 ζ parameter with n parameter plot of all soils of varying soil type.

Considering only the clay type soils (clays and silts), a good relationship is noted that can be estimated with a linear trendline as shown in Figure 7.9. The coefficient of determination of the linear trendline is 0.756, which indicates a suitable relationship between the ζ parameter and the Van Genuchten n parameter. This relationship can be defined by a linear representation as follows:

$$\zeta_{e_i^{ref} > e_i} = 0.8407\, n - 0.898 \tag{7.8}$$

The ζ parameters used in Equation (7.8) limit the use of Equation (7.8) to the condition for $e_i^{ref} > e_i$. This limits the use of the ζ parameter for estimating SWCC with initial void ratios lower than the reference.

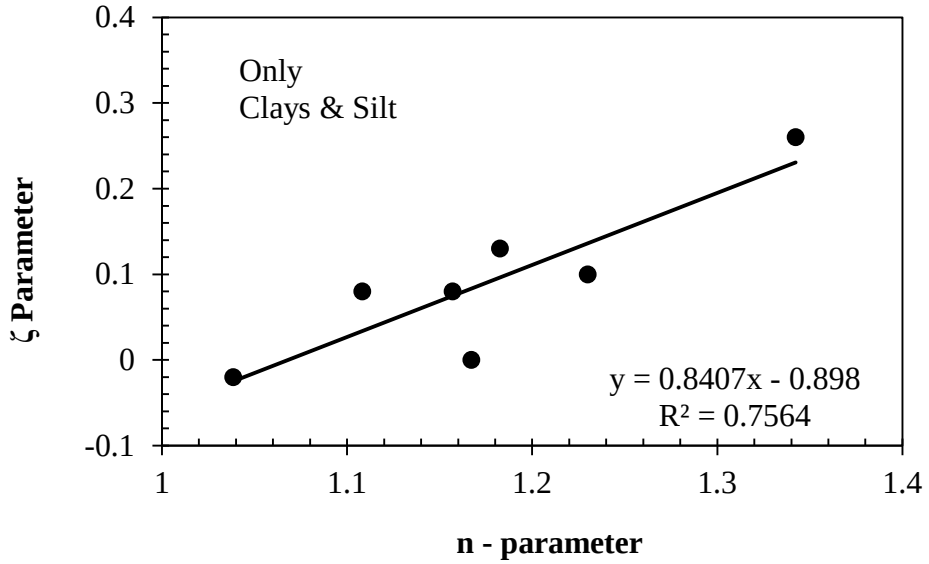

Figure 7.9 ζ parameter with n parameter plot of clay and silt soils.

Figure 7.10 shows the relationship between the ζ parameters for $e_i^{ref} > e_i$, and $e_i^{ref} < e_i$. The ζ parameters appear to increase at a fairly constant rate that can be represented by a linear trend. The coefficient of determination of the data point as a linear fit is 0.8945, which is an indication of a very good approximation. The relationship between the ζ parameters can be represented as a linear fit by the equation:

$$\zeta_{e_i^{ref} > e_i} = 1.075\,\zeta_{e_i^{ref} > e_i} + 0.1458 \tag{7.9}$$

Substituting Equation (7.8) into Equation (7.9) and rearranging;

$$\zeta_{e_i^{ref} < e_i} = 0.782\,n - 1.261 \tag{7.10}$$

Equations (7.8) or (7.10) can be used to robustly estimate the ζ parameter to be used for estimating SWCC with lower or higher initial void ratios respectively.

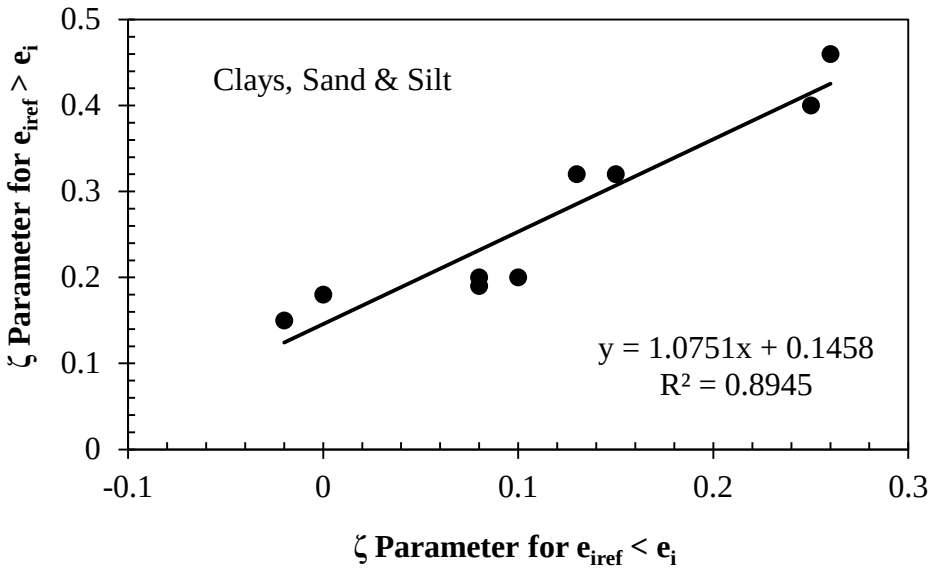

Figure 7.10 A correlation plot of ζ parameters for $e_i^{ref} > e_i$ and $e_i^{ref} < e_i$.

7.2 Constitutive Modelling of Stress – Strain Relationships

Several successful attempts have been made in the past years to model the volume change behavior of unsaturated soils. Insights from some of these models have been used in developing the As-compacted state model presented in this report.

7.2.1 Determination of some of the parameters in the model.

7.2.1.1 The overconsolidation factor

The overconsolidation factor, OCR, used, in the shear modulus equations is defined as the ratio of the preconsolidation stress to the current state of net mean stress exhibited by the soil. Estimation of the shear moduli performed and presented in Section 7.1 of this

dissertation used a constant value of the OCR. This constant value of OCR used, is the initial OCR determined at the start of triaxial shearing. Therefore, the constant value was used for estimation of shear modulus during the triaxial shearing stage regardless of the change in state of stress of the soil.

Since during shearing or loading of soil, the state of stress changes, the OCR is expected to change. The OCR is highest prior to loading for compacted soils, and with loading, the current state of stress increases. Therefore, the OCR increases until the current state of stress is equal to the preconsolidation stress, resulting in an OCR of 1. With continued increase loading, the OCR remains at the value of 1 as the preconsolidation and current state of stress becomes the maximum net mean stress the soil has experienced.

Based on this traditional overconsolidation ratio, OCR and taking into account the effect of the apparent tensile strength, the degree of overconsolidation used in the model is given as follows:

$$R = \frac{p + p_s}{p_o(s) + p_s} \left(0 < R \leq 1\right) \tag{7.11}$$

7.2.1.2 The potential failure stress ratio M_f

The potential capacity in resisting shear failure is represented by the potential failure stress ratio M_f. M_f is related to the peak strength of the overconsolidated unsaturated clay soil. Yao et al. (2013) gives the expression of the potential failure stress ratio as follows:

$$M_f = 6\left[\sqrt{\frac{\chi}{R}\left(1+\frac{\chi}{R}\right)}-\frac{\chi}{R}\right] \tag{7.12}$$

In Equation, (7.12), the parameter χ is given as:

$$\chi = \frac{M^2}{12(3-M)} \tag{7.13}$$

It can be seen that M_f keeps decreasing as R increases. When $R=1$, $M_f = M$, which means a complete loss of overconsolidation.

7.2.1.3 The unified hardening parameter H

This model makes use of the proposed unified hardening parameter H for sands that can also be applied for overconsolidated clays (Yao et al., 2004, 2008, and 2009). It includes the use of the stress ratio parameter η that is defined as:

$$\eta = \frac{q}{p+p_s} \tag{7.14}$$

Incorporating the potential failure stress ratio M_f, stress ratio η, and critical state stress ratio M to describe the mechanical behaviors, such as strain-hardening/softening, shear dilatancy, stress-path-dependent behavior, and suction effect, the unified hardening parameter is given as follows:

$$H = \int dH = \int \frac{M_f^4 - \eta}{M^4 - \eta} d\varepsilon_{vp}^p = \int \frac{1}{\Omega} d\varepsilon_{vp}^p \tag{7.15}$$

In Equation (7.15), the parameter Ω is given as:

$$\Omega = \frac{M_f^4 - \eta}{M^4 - \eta} \tag{7.16}$$

The characteristics of the incremental hardening parameter dH, is always non-negative in the hardening region, therefore:

(1) When $0 < \eta < M$, $d\varepsilon_v^p > 0$, which describes negative dilatancy.

(2) When $\eta = M$, $d\varepsilon_v^p = 0$, this corresponds to the point of the characteristic state.

(3) When $M < \eta < M_f$, $d\varepsilon_v^p < 0$, which means negative dilatancy.

In the softening region, since $dH < 0$, $\eta > M$ and η is slightly higher than M_f, then $d\varepsilon_v^p < 0$, which indicates negative dilatancy.

The overconsolidated parameter R, the potential failure stress ratio M_f, and the unified hardening parameter H all interact with each other, and can reflect the variation in the decay of overconsolidation, the damage caused by shearing, and the volumetric strain increment.

7.2.2 Shear modulus estimation under loading from initial field stiffness measurement.

Modification of the shear modulus relationship used for predictions of unsaturated soil shear modulus in Section 7.1 is presented in this section. Figure 7.11 gives an overview of this section within the overall research program.

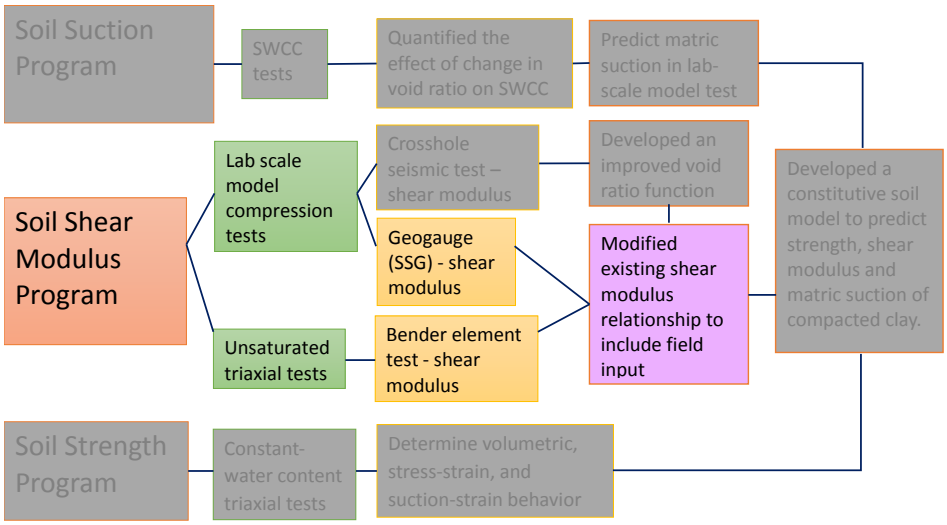

Figure 7.11 A visual of the point of discuss (mechanical behavior of unsaturated triaxial tests) within the overall research program.

Alonso et al. (1990) suggested that as a consequence of the assumed flow rule in the BBM, there is no evolution of plastic shear strains at the start of a triaxial shear test. Wood, (1990), further suggested that for a shear test with increasing axial stress and constant lateral stresses, the initial part of the stress-strain curve that appears linear may thus be used as an elastic response. Therefore, an elastic response would allow for the determination of the elastic shear modulus, G. In general, most shear strength soil models follow these assumptions of initial elastic response.

A closer look at the shear modulus data from the CW triaxial shear tests indicate that the soil shear modulus increases during this apparent linear elastic response phase as shown in Figure 7.12. With increases in shear modulus within this region, elastic shear strains, ε_q^e, will decrease, since the change in elastic shear strain is defined as

$$d\varepsilon_q^e = \frac{1}{3G} dq \tag{7.17}$$

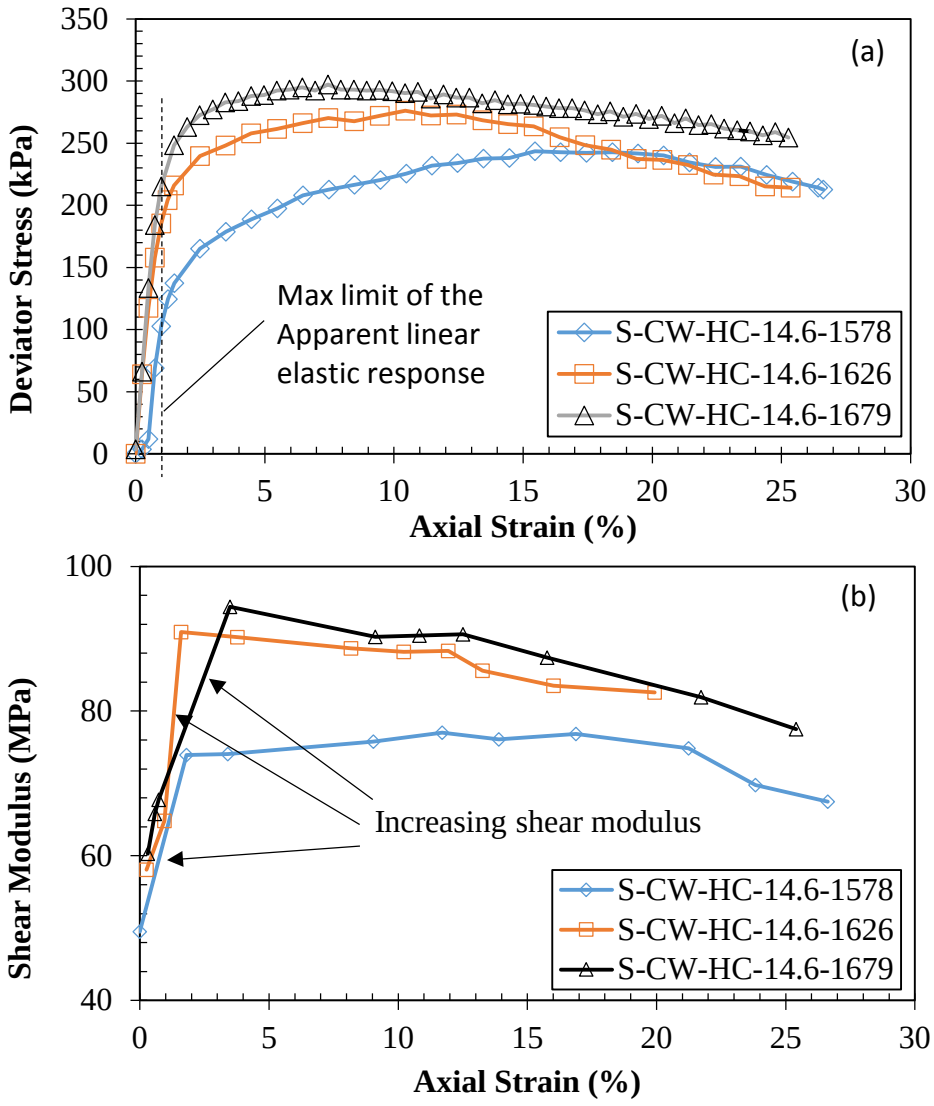

Figure 7.12 Experimental data test results of (a) stress-strain response and (b) shear modulus-strain response, for the HCclay soil specimens.

Therefore, for a purely elastic response within this region, the shear-strain response would be as depicted in Curve A of the schematics presented in Figure 7.13. It is expected that at the onset of an axial stress, anisotropy would cause a change in the macro structure of either a normally consolidated or a lightly overconsolidated soil. Thus, the possibility of plastic shear strain occurring from the onset of shearing in these soils should be considered. Curve B in Figure 7.13 would represents the occurrence of plastic shear strains at onset of shearing.

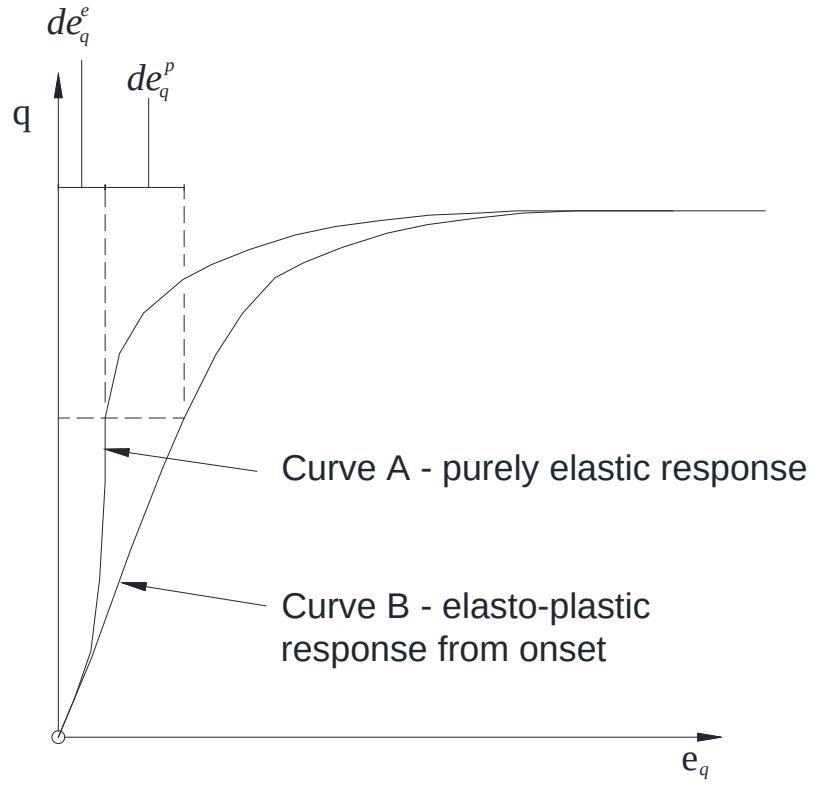

Figure 7.13 Schematic of stress-strain curves for an initial increasing stiffness or shear modulus.

Furthermore, the experimental stress-strain curves for three tests on the overconsolidated LCesilt test samples are shown in Figure 7.14. The curves show points at which the deviatoric stress, q, rapidly decreases with continued shear strain. These points indicate complete failure of the test samples on a shear slip plane, and are considered the onset of critical state condition. All three curves show a peak state, after which the deviatoric stress decreases at an initial slow rate to the point of critical state and then at a rapid rate. Prior to the peak states, the curves show increasing deviatoric stress with shear strain at a decreasing rate until the peak state is reached.

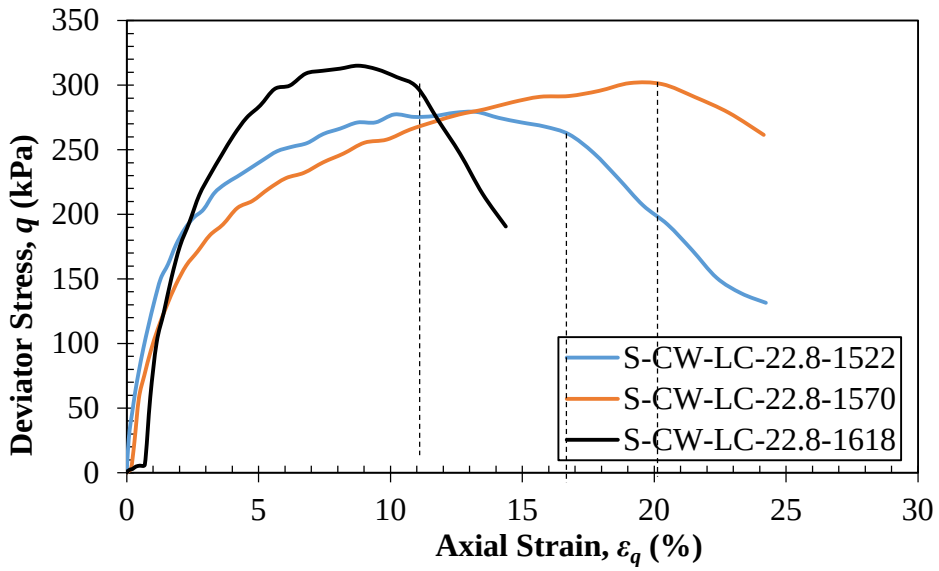

Figure 7.14 Experimental test data results of constant-water content triaxial shearing tests for the LCesilt specimens at different initial densities, showing clear points of complete failure.

Typical shear-strain model representations of heavily overconsolidated soils, generally show that the deviatoric stress increases linearly with axial strain to the peak state as shown by Curve A in the schematics of Figure 7.15. Curve B in this figure represents the typical experimental data for an unsaturated, overconsolidated soil. Due to the decreasing rate of increase of deviatoric stress with strain, the peak state for a typical

experimental curve occurs at a higher strain than that of the typical model assumption. This suggests that plastic shear strains occur in an experimental shear stress test prior to the peak state, which is opposed to the assumption of typical models, that there exist only elastic shear strains within this zone.

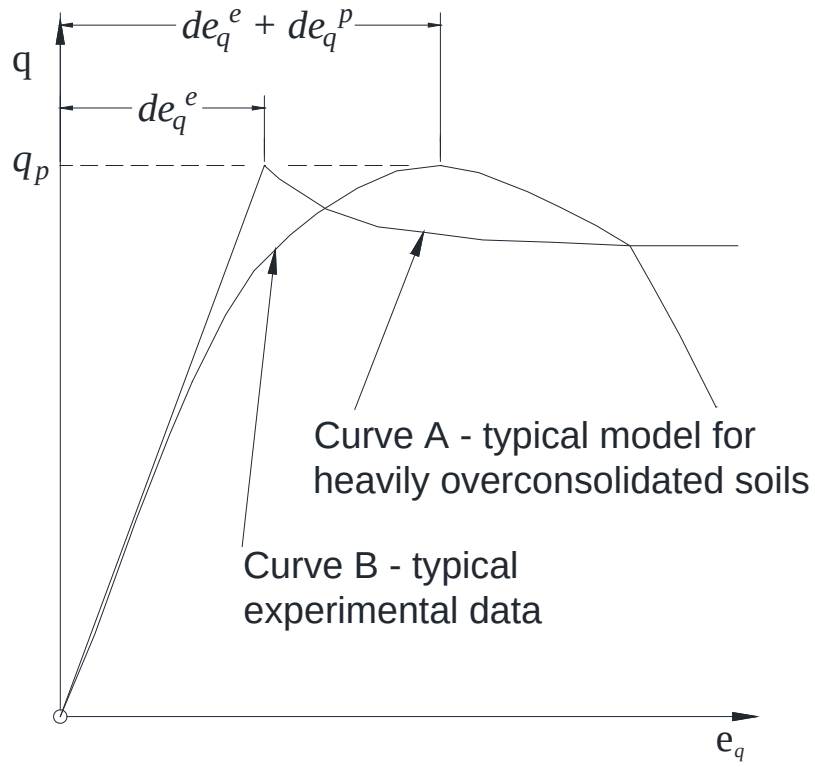

Figure 7.15 Schematics of stress-strain curves showing different strains at the peak state for a typical classic model with an initial elastic strain zone, and a typical experimental data curve.

This model, therefore incorporates the effect of increasing shear modulus within the zone that extends from the start of the test to the peak state, and the inclusion of plastic shear stains within the same zone.

Sawangsuriya et al. (2009) presented a form of the Hardin and Black (1969) small strain shear modulus equation for normally consolidated soil, modified for unsaturated

conditions. A normalized form of the Sawangsuriya et al. (2009) small strain shear modulus relationship was previously discussed in Section 7.1.3 of this dissertation. The normalized form of the Sawangsuriya et al. (2009) equation, with the inclusion of the Hardin and Black (1969) variable for overconsolidation, was given as follows:

$$\frac{G}{G_{ini}} = A' F(e) OCR^{k} \left(p + S^{\kappa} s\right)^{n} \tag{7.5}$$

Prior to the start of shearing the triaxial specimens under CW conditions, for a known initial void ratio, small strain shear modulus, G_{ini}, were determined from the bender element (BE) testing. Also, small strain shear moduli, G_{SSG} were determined from the laboratory scale model testing performed to simulate field conditions, using the soil stiffness Geogauge. The small-strain shear moduli G_{SSG}, selected at the same void ratios, were correlation to the shear moduli, G_{ini} from the triaxial BE testing. Figure 7.16, shows the comparison of both shear moduli data. The experimental trend observed, indicate that the comparison can be described by a simple power function of the form:

$$G_{ini} = \alpha \left(G_{SSG}\right)^{\beta} \tag{7.18}$$

In Equation (7.18), the parameter constant α, controls the magnitude of increase, and the parameter constant β, controls the curvature of the curve. Best fit parameter constants, α and β, of the power function for the shear modulus comparison, with a coefficient of determination of 0.9172 are introduced in the function:

$$G_{ini} = 0.054\left(G_{SSG}\right)^{1.32} \tag{7.19}$$

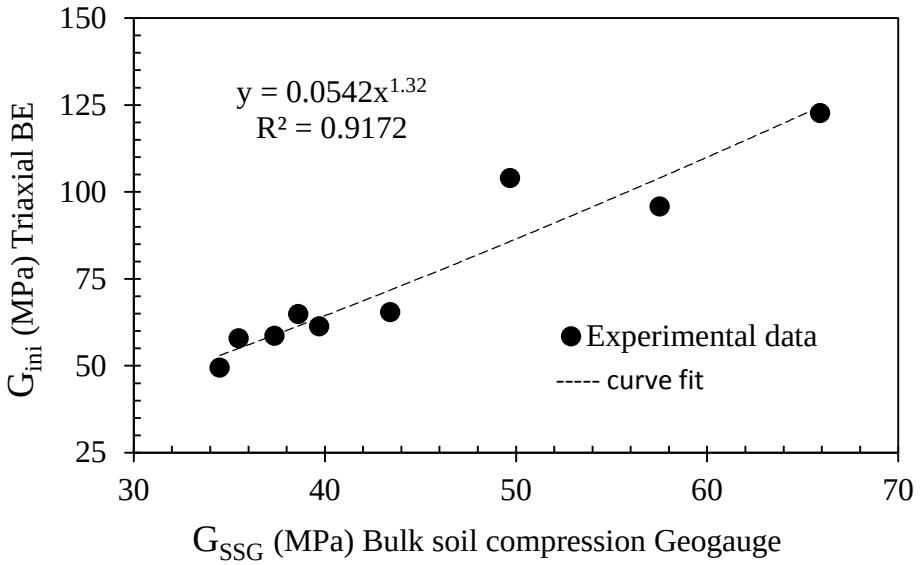

Figure 7.16 Correlation plot of shear modulus data of the bender element tests from the constant-water content triaxial shearing tests to that of the soil stiffness gauge (Geogauge) from bulk soil compression tests.

Substituting Equation (7.19) in Equation (7.5), and rearranging, the small strain shear modulus during shearing can be estimated as follows:

$$G = A'' G_{SSG}\ f(e) OCR^{k} \left(p + S^{\kappa} s\right)^{n} \tag{7.20}$$

In Equation (7.20), $A'' = \alpha A' = 0.0542\, A'$, and A' was robustly determined in Section 8.1.3 of this report by its relationship with percent fines PF, and is of the form, $A' = a\left(PF\right)^{b}\left(e\right)^{c}$.

Equation (7.20), becomes laden with multiple parameters. If a model has many parameters, the best fit of a nonlinear least-squares approximation is difficult to find because of sloppiness, (Transtrum et al., 2011). Sloppiness is a behavioral response of a

model, whereby the model behavior responds very strongly to only a few parameter combinations, and the behavior responds very weakly to all other parameter combinations. The few combinations of parameters that reflect strong responses are known as stiff parameter combinations, and the increased combinations of parameters that reflect weak responses are known as sloppy parameter combinations.

In an attempt to avoid sloppiness, robust determinations of these parameter have been made or presented throughout this report and are summarized in Table 7.7.

Table 7.7 Determined constants or relationships for the modified small-strain shear modulus equation.

Equations	$G = A'' G_{SSG}{}^{\beta} f(e) OCR^{k} \left(p + S^{\kappa} s\right)^{n}$,	
	where $A'' = \alpha A'$ $A' = a(PF)^{b} e_{ini}{}^{c}$	
Parameter constants or relationships		Source
a	0.0002323	Determined in Section 7.1.3 as best fit parameters to a power function
b	1.432	
c	0.162	
α	0.0542	Determined in Section 8.2.4 by best fitting a power curve comparing shear modulus, G_{SSG} by the Geogauge, and G_{ini} by BE in triaxial tests.
β	1.32	
k	$k = -0.00005PI^{2} + 0.0096PI - 0.004$	Presented in Section 8.1, based on best fit curve of data by Hardin and Black (1969)
n	$0.5 - k$	
κ	$\kappa = -0.0008(PI)^{2} + 0.0801(PI) + 1$ $\kappa = -0.0016(PI)^{2} + 0.0975(PI) + 1$	Presented by Oh et al., (2009) from: Vanapalli and Fredlund (2000) Garven and Vanapalli (2006)

7.2.3 Consideration of plastic volumetric strains within the classic elastic zone.

In the previous Section, 7.2.2, increasing shear modulus within the classic elastic zone was discussed which would result in an increasing rate of stress with elastic shear strain (see Curve A in Figure 7.13). The graphical representation of a typical experimental stress-strain data does not show an increasing rate of stress with shear strain

within the classically defined elastic zone (see Figure 7.15). This increasing rate of stress with elastic shear strain appears to be lost. Though stiffness is not lost, this apparent loss in increasing stiffness is attributed to the occurrence of increasing plastic shear strains within this classic elastic zone. If a plastic shear strain does occur within this zone, it begs the question whether plastic volumetric strain may also occur within this zone. Therefore, consideration is given to the possibility of the occurrence of plastic volumetric strain within the classic elastic zone.

The use of Figure 7.17, helps to shape our understanding of the volumetric changes that occur on a specimen during isotropic consolidation under CW conditions. One noticeable feature in the $v - \ln p$ plot in Figure 7.17 with that of other typical $v - \ln p$ plots, is that the $v - \ln p$ plot is not represented by two distinct linear representations for the initial reload and the virgin compression portions of the curve. The other noticeable feature of the plot is that the change in specific volume at the initial section (which represents the reload for non-virgin compression) is at a lower rate than that of the unload-reload section for increased net mean stress. The difference in slopes of the initial reload and the unload-reload sections is attributed to changes in soil suction. Typical $v - \ln p$ curves are shown at constant suction, but the $v - \ln p$ plot show in Figure 7.17 is under CW conditions and therefore exhibits behavior with soil suction changes that is due only to changes in loading (not wetting). Changes in soil suction affect the behavior of the change in specific volume with increasing net mean stress with exception of the latter part of the curve where the soil suction became minimal or zero (because of complete saturation due to continued loading), and it appears to exhibit linear behavior.

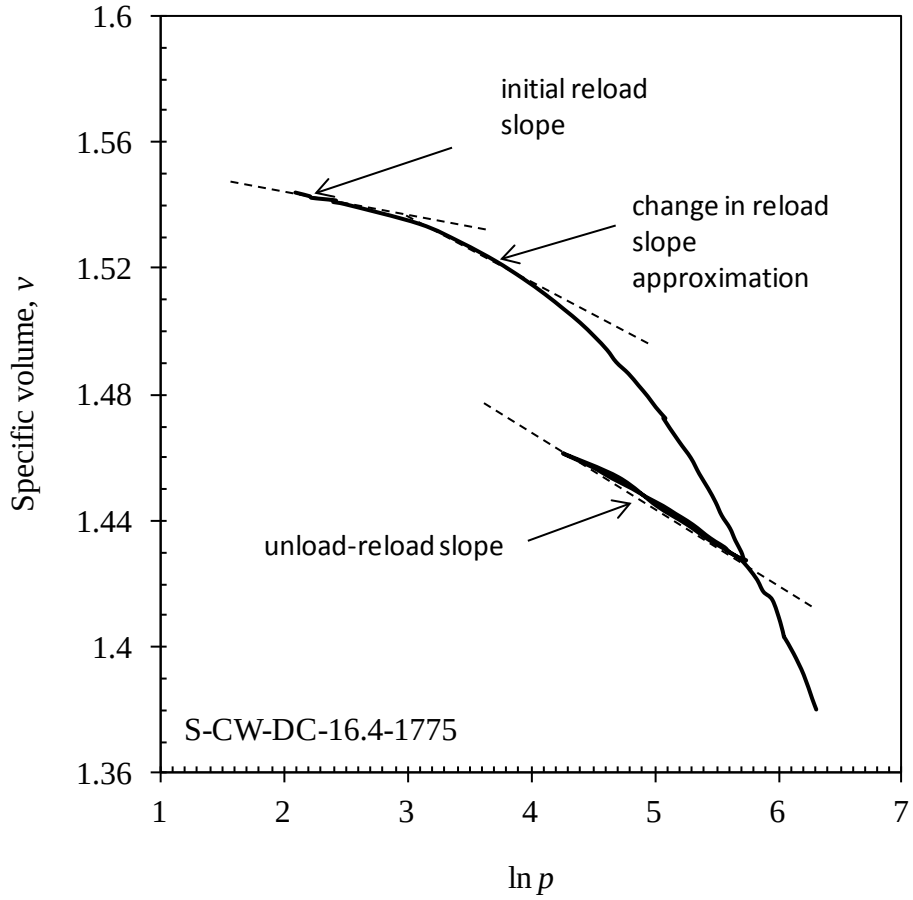

Figure 7.17 Typical compression curve under constant-water content conditions.

Plastic volumetric strains cannot be attributed to the changes in slope of this $v - \ln p$ curve even prior to the preconsolidation stress, as the changes are attributed to soil suction changes. Consistent with this finding are research by others such as Zhou and Sheng (2009), that show changes to slopes of $v - \ln p$ curves under different constant suction tests occurs. In addition, the unload-reload portion of the curve in Figure 7.17, shows that the changes in specific volume remained fairly constant and almost identical, which indicates that all volume change was recovered. Therefore, all volume change within the re-compression state should be attributed to only elastic volumetric strains.

7.2.4 Matric Suction Estimation

Unless a soil is close to or fully saturated, the volume change that occurs under load in the field is assumed to be a due to soil structure change and not of the water phase. Therefore, for an unsaturated soil under isotropic compression, the constant-water content (CW) test simulates soil structure change due to the drained air phase. Since no change in the water content occurs (no wetting or drying), any change in matric suction is only due to changes in the soil structure.

Adsorptive potential will be more sensitive to normally consolidated soils as the pore spaces, hence soil structure changes more significantly as is typical of the $e - \ln p$ curves. Therefore, the point at which the matric suction starts to show significant change represents a change from overconsolidation to a normally consolidated soil.

The volumetric change as represented in the SFG is due to changes in the net mean stress, the matric suction or both. The changes in matric suction as represented in the SFG is due to wetting or drying change, and is strictly defined by the water phase of the soil. The SFG represents the increment of volumetric change as follows:

$$dv = -\lambda_{vp} \frac{dp}{p+s} - \lambda_{vs} \frac{ds}{p+s} \tag{7.21}$$

In the CW test conditions, though the stress state of the water phase (i.e., the pore-water pressure, u_w) may change, the volume of water remains unchanged, because the soil is not subjected to wetting or drying inundation. Therefore, the total volume change is due only to changes in the net mean stress, and can be represented as follows:

$$dv = -\lambda_{vp} \frac{dp}{p+s} \tag{7.22}$$

Based on experimental data for the CW test, changes in soil suction occur during isotropic compressions and also during shearing in the virgin state. The changes in soil suction can therefore be said to occur as a result of the changes in net mean stress. This suggests that the resulting changes in matric suction as a result of changes in the net mean stress would also be a function of the volumetric stiffness parameter λ_{vp}. It is therefore postulated that the volumetric changes due to changes in net mean stress that results in changes in soil suction, can be represented as follows:

$$dv = -\lambda_{vp} \frac{dp}{p+s} = -\lambda_{vp} \frac{ds}{p} \tag{7.23}$$

As such, changes in soil suction can be determined from the relationship:

$$ds = -\frac{1}{\lambda_{vp}} p\, dv \tag{7.24}$$

7.2.5 As Compacted State model calibration

7.2.5.1 Shear Strength Model Parameters

To determine the parameter, p_s, the apparent tensile strength, Alonso et al. (1990) recommends performing drained shear tests at different suction values. Assuming that three different suction values are used, three drained tests at different confining stresses may be required to experimentally determine the tensile yield, p_s at each suction. This

will result in a minimum of nine drained shear test to determine this parameter. Only three tests per soil are available in this research, but they are under conditions of different compaction which resulted in conditions of different matric suction (initial and critical state). Assuming the slope of the critical state line (CSL) is constant for the three specimens for each soil (will be verified later), an optimization procedure can be performed to determine the best fit values of the slope of the critical state line M, for the soil, and p_s for each specimen.

The critical state condition as previously defined within this Chapter, resulted in the critical state net mean and deviatoric stresses as shown in Table 7.8. The slopes of the critical state line can thus be determined using corresponding critical state net mean stress p_{cs}, to predict the critical state deviatoric stress, q_{cs}, by optimizing the values of M, and p_s using the equation of the critical state line as follows:

$$q_{cs} = M\left(p_{cs} - p_s\right) \tag{7.25}$$

The optimized values of M, and p_s, are presented in Table 7.8 with the corresponding critical state net mean and deviatoric stresses.

Table 7.8 Slope of the critical state line with corresponding critical state parameters.

		Critical state values			
Reference	Density	p_{cs}	q_{cs}	p_s	M
	(kg/m^3)	(kPa)	(kPa)	(kPa)	
DCsclay	1682	175.9	314.2	-5.8	1.73
	1730	176.3	321.6	-9.7	
	1775	182.6	334.2	-10.7	
HCclay	1578	148.6	231.2	-12.8	1.43
	1626	148.5	237.3	-17.2	
	1679	162.7	278.2	-31.4	
LCesilt	1522	156.8	261.9	-90.3	1.06
	1570	168.4	300.8	-115.3	
	1618	171.4	298.5	-110.2	

The tensile yield strength p_s and slope of the critical state line M in Table 7.8, were calibrated based on the assumption that the slope of the critical state line is constant for the soil type. To verify this assumption, prediction of the tensile yield strength was performed, and then the tensile yield strength used to determine the slope of the critical state line for each specimen. To predict the tensile yield strengths, one additional parameter was required. This parameter is the maximum soil suction that corresponds to full saturation and is termed the saturation suction, s_{sa}. The saturation suction parameters were determined from the SWCC tests detailed in Chapter 4 of this dissertation, and are presented in Table 7.9. The tensile yield, p_s is determined by the equation:

$$-p_s = \begin{cases} -s & s < s_{sa} \\ -s_{sa} - (s_{sa}+1)\ln\dfrac{s+1}{s_{sa}+1} & s \geq s_{sa} \end{cases} \tag{7.26}$$

Using Equation 7.26, the tensile yield strength at the initial state and critical state condition for each test was determined using the corresponding soil suction at the initial

state, s_{ini}, or the soil suction at the critical state, s_{cr}. The saturation suction, the initial and critical state soil suction and the determined initial and critical state tensile yield stresses are presented in Table 7.9.

Table 7.9 Determined tensile yield strength at initial and critical state with corresponding suction, and the saturation suction.

			Initial state		Critical state	
Reference	Density	s_{sa}	s_{ini}	p_s	s_{cs}	p_s
	(kg/m^3)	(kPa)	(kPa)	(kPa)	(kPa)	(kPa)
DCsclay	1682	0.3	28.31	-4.35	88.8	-5.8
	1730	2.0	30.31	-9.04	87.9	-12.2
	1775	3.0	12.51	-7.87	71.8	-14.6
HCclay	1578	4.6	32.67	-14.65	49.5	-16.9
	1626	5.6	46.13	-18.57	62.6	-20.6
	1679	6.5	39.00	-19.05	56.0	-21.7
LCesilt	1522	19.6	160.11	-62.02	197.6	-66.3
	1570	121.9	72.14	-72.14	152.8	-149.5
	1618	228.2	152.02	-152.02	168.1	-168.1

The predicted tensile yield strengths at critical state were used to determine the slopes of the critical state lines for each specimen by rearranging Equation (7.25). The determined slopes of the CSLs are presented in Table 7.10, with the corresponding critical state values. The results show that for each soil type, M varies slightly with soil suction, s.

Table 7.10 Slope of the critical state line with corresponding critical state parameters.

		Critical state values				
Reference	Density	s_{cs}	p_s	p_{cs}	q_{cs}	M
	(kg/m^3)	(kPa)	(kPa)	(kPa)	(kPa)	
DCsclay	1682	88.8	-5.8	175.9	314.2	1.73
	1730	87.9	-12.2	176.3	321.6	1.71
	1775	71.8	-14.6	182.6	334.2	1.69
HCclay	1578	49.5	-16.9	148.6	231.2	1.40
	1626	62.6	-20.6	148.5	237.3	1.40
	1679	56.0	-21.7	162.7	278.2	1.51
LCesilt	1522	197.6	-66.3	156.8	261.9	1.17
	1570	152.8	-149.5	168.4	300.8	0.95
	1618	168.1	-168.1	171.4	298.5	0.88

The variation of the slope of the CSL with density is small and no definitive relationship of the slope of the CSL, M with density was noted for the Kentucky soils. Figure 7.18 show the variation of M with density. M appears almost constant for the DCsclay soil, but show a slight increase with density for the HCclay soil and a decrease with density for the LCesilt soil. Since the variations of M with density are small for all three soils, and no definitive trend noted, the assumption of a constant value of M for each soil was determined appropriate.

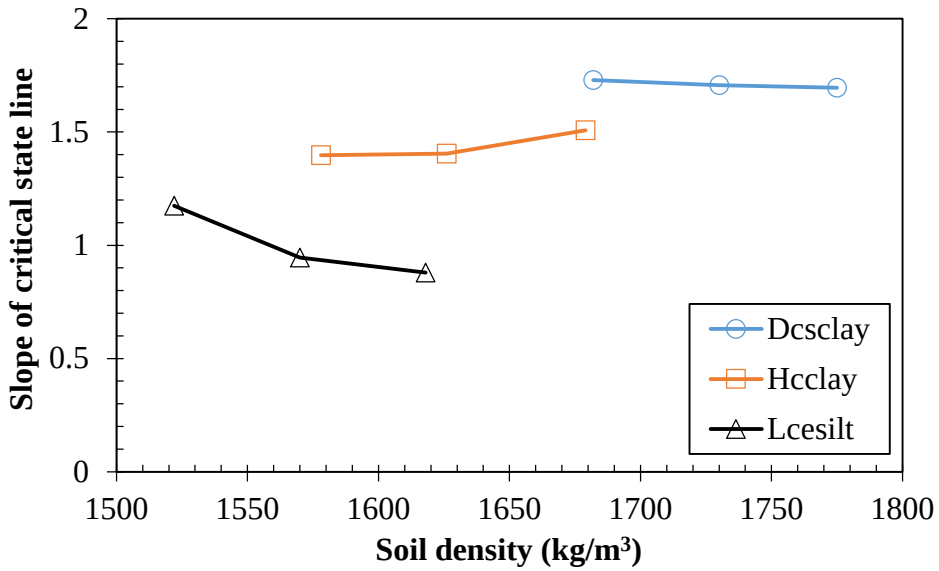

Figure 7.18 Variation of the slope of the critical state line M with soil density.

Similarly, other researchers have reported similar results for the variation of M with matric suction. Though Wheeler and Sivakumar (1995) used this variation to present an unsaturated model based of the BBM, the variation of the slope of the CSL, M, with suction is generally very small. Figure 7.19 shows the variations of the slope of the CSL, M of other researchers including that of Wheeler and Sivakumar (1995). The variations are small and almost constant in some cases, therefore, an assumption of a constant (independent of soil suction) value of the slope of the CSL, M, with suction is also appropriate, and is in fact a basis of the BBM model.

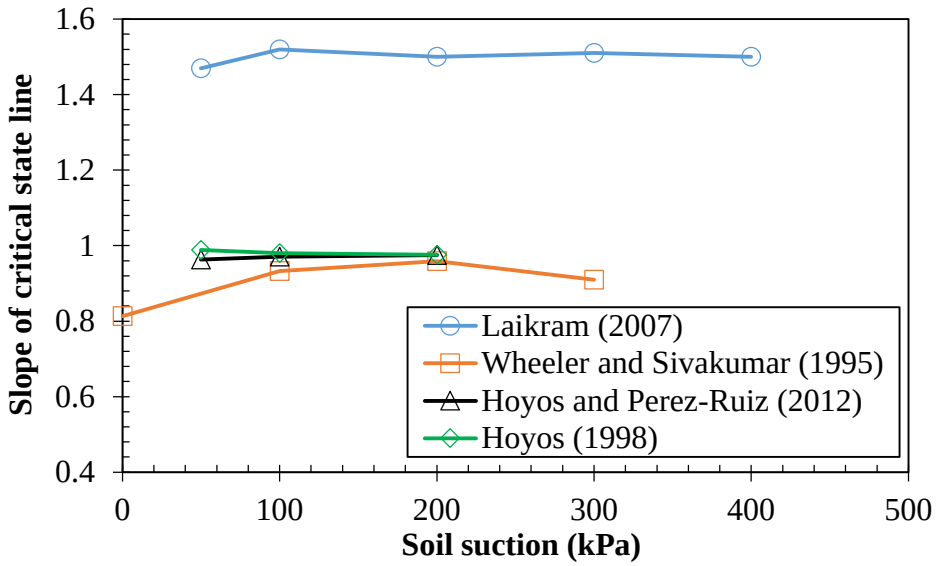

Figure 7.19 Variation of the slope of critical state line, M with soil suction, s (reproduced from Perez-Ruiz, 2009)

Using these concepts for the constant slope of the CSL being independent of soil suction and density, the best fit values determined by the least squares method was determined an appropriate calibration for the slope of the CSL. The calibrated slope of

the CSL and a determined average slope for each soil from the predicted data are presented in Table 7.11.

Table 7.11 Average slope of critical state line for each soil

Reference Soil	Calibrated slope of CSL M	Average predicted slope of CSL M_{avg}
DCsclay	1.73	1.71
HCclay	1.43	1.44
LCesilt	1.06	1.00

In the BBM, and because of the lack of experimental data, a simple linear model, whereby the increase in tensile yield stress p_s due to an increase in matric suction s, is related by the form:

$$-p_s = -ks \tag{7.27}$$

Keeping with the classic form of the BBM, and the use of available experimental data, Hoyos and Perez-Ruiz (2012), presented a potential relationship that considers the linear behavior in the BBM model as follows:

$$-p_s = -ks^m \tag{7.28}$$

In Equation (7.28), m is the parameter controlling the curvature of the curve describing p_s.

Equation (7.28), can become useful, if the SWCC, is not available, whereby the saturation suction, s_{sa} cannot be obtained for use in Equation (8.26). In calibrating the parameters k and m estimations of the initial tensile yield stress, p_s (prior to shearing),

previously presented in Table 7.8, were performed by the least-squares approximation method. The calibrated parameter of k and m, are presented in Table 7.12, with the corresponding slope of the CSL.

Table 7.12 RBBM parameters for the tensile yield stress and slope of critical state line.

Reference	M	k	m
DCsclay	1.710	11.258	-0.150
HCclay	1.436	1.716	0.632
LCesilt	1.000	13.112	0.412

The calibrated parameters in Table 7.12, determine the critical state line (CSL) in accordance with the relationship described by Hoyos and Perez-Ruiz (2012) as:

$$q = M(p + p_s) = M(p + ks^m) \tag{7.29}$$

Calibration of the shear modulus, G is required as an input parameter for the BBM model. The input parameter, G is used as a constant, which is termed the elastic shear modulus, and used to determine the elastic shear strains. The BBM suggests that this parameter can be determined experimentally from the elastic response of the stress-strain curve, whereby, the elastic response is represented by the appearance of an initial linear trend. Experimental results of shear modulus previously presented for this study and determined during the appearance of this initial linear trend in the stress-strain response are shown to increase, and therefore not constant as suggested by the BBM.

To include the variation of shear modulus within the as-compacted model, the relationship of the elastic shear modulus G with Young's modulus, E, as presented in Equation 8.31, is one possible way to predict the small-strain shear modulus.

$$G = \frac{E}{2(1+\nu)} \tag{7.30}$$

In Equation (7.30), ν is the Poisson's ratio, κ is the slope of the recompression line in the $v - \ln p$ plane under constant suction condition; and the Young's modulus E, can be determined as follows:

$$E = \frac{3(1-2\nu)(1+e_0)}{\kappa} p \tag{7.31}$$

Furthermore, a field determination of shear modulus obtained from an as-compacted state, can be used for estimations of shear modulus during shearing. Equation (7.20), which was previously presented gives a form of the relationship of shear modulus presented by Sawangsuriya et al. (2009), and implemented with the inclusion of a field determined shear modulus G_{SSG}, using a shear stiffness gauge.

$$G = A'' G_{SSG}\ f(e) OCR^k \left(p + S^\kappa s\right)^n \tag{7.20}$$

With the use of this form of shear modulus in the model, the model becomes useful to determine the strength of soil, for a known field as-compacted state. Experimental laboratory scale model tests were performed to simulate field conditions and the results and discussion were presented under Chapter 5 of this report. Correlating the void ratios of the bulk soil compression tests to those of the CW triaxial tests at the initial condition, simulated field shear modulus values were obtained as input field shear modulus

parameter for the initial condition in the model. The simulated field shear moduli, used as input parameters for each test sample are presented in Table 7.13.

Table 7.13 Small-strain shear modulus determined from laboratory scale model tests using the soil stiffness gauge (Geogauge), for corresponding initial densities in the triaxial specimens.

Reference	Density	G_{SSG}
	(kg/m^3)	(kPa)
DCsclay	1682	35489.37
	1730	38613.83
	1775	43418.44
HCclay	1578	34505.58
	1626	37368.75
	1679	39711.55
LCesilt	1522	49696.86
	1570	57515.84
	1618	65913.08

7.2.5.2 Isotropic Stress State Compressibility Model Parameters

The general trend for determining the volumetric stiffness parameters is to experimentally determine the slopes of linear representations of the URL and NCL portions of the isotropic compression curve in the $v - \ln p$ plane. As previously discussed in Chapter 6, the slope of the CW isotropic compression curve changes and a linear representation may be inaccurate. The Equation (7.22) relationship previously presented in Section 7.2.4, which is a form of the volumetric change in the SFG model, presents an NCL volumetric stiffness parameter λ_{vp} that can represent the entire monotonic compression curve.

$$dv = -\lambda_{vp} \frac{dp}{p + s} \tag{7.22}$$

The monotonic (without the unload-reload portion) CW isotropic compression curves presented and discussed in Chapter 6 were used to calibrate the NCL volumetric stiffness parameter for each soil. Calibration was performed by using Equation (7.22) to predict the change in specific volume, by optimizing (least-squares approximation) the volumetric stiffness parameter λ_{vp}.

The experimental specific volume data and the specific volume determined from the predicted change in specific volume of the Kentucky soils under CW isotropic compressions conditions are presented in Figures 7.20. The predicted data agrees well with the experimental data and therefore a constant NCL volumetric stiffness parameter can be used to determine the volumetric changes under conditions of CW isotropic compressions. The calibrated NCL volumetric stiffness parameters are presented in Table 7.14.

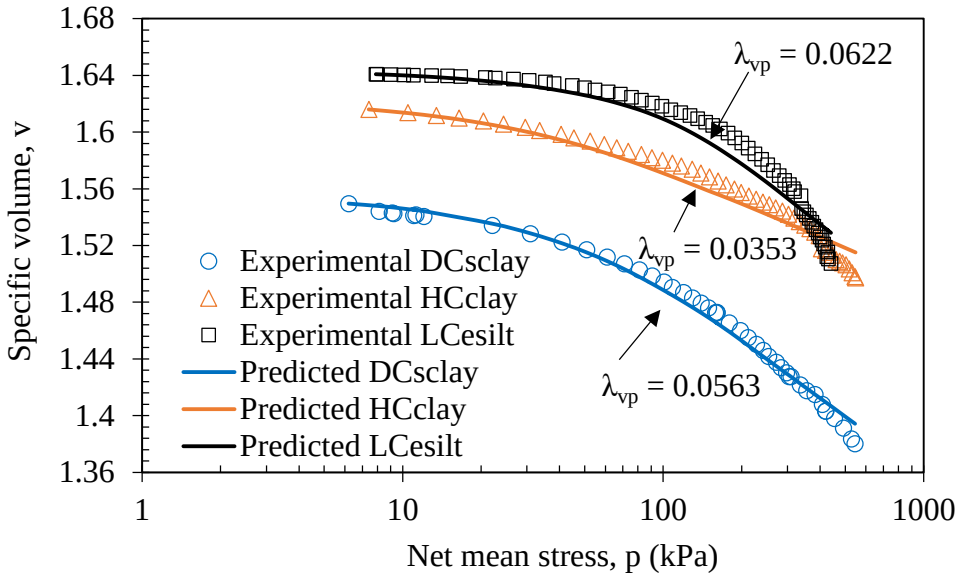

Figure 7.20 Experimental and predicted constant-water content isotropic compression curves for the DCsclay, HCclay, and LCesilt soils under initial compacted conditions of standard Proctor maximum dry density and optimum moisture content.

Table 7.14 Calibrated NCL volumetric stiffness parameter λ_{vp} from isotropic compression curves.

Reference	Density (kg/m^3)	λ_{vp}
DCsclay	1775	0.056
HCclay	1679	0.035
LCesilt	1618	0.062

The URL volumetric stiffness parameter κ_{vp} for each soil was obtained from the volumetric compression curves during triaxial shearing. The volumetric compression curves during the triaxial shearing phase for the DCsclay soil specimens are presented in Figure 7.20, (the compression curves for all specimens and soil types are presented in Appendix H.3. Figure 7.21 shows that there is a defined linear representation of the re-compression portion (or the URL). The slope of the linear representation was graphically determined for the specimens of the three soil types and presented in Table 7.15 as the calibrated URL volumetric stiffness parameter κ_{vp}. Figure 7.21 also shows that the κ_{vp} parameter decreases with density. The κ_{vp} parameter for initial densities of 1682, 1730, and 1775 are respectively 0.018, 0.015, and 0.013 (note that the parameters κ_{vp} and λ_{vp} are negative values, but presented as positive values to be consistent with literature). Though there appears to be an effect of density on the volumetric stiffness parameter, the variation is minimal. For simplicity, the volumetric stiffness parameter κ_{vp} is assumed

to be constant in this model. The average value of the κ_{vp} parameter for each soil type is presented in Table 7.15 and was used as the calibrated parameter in the model.

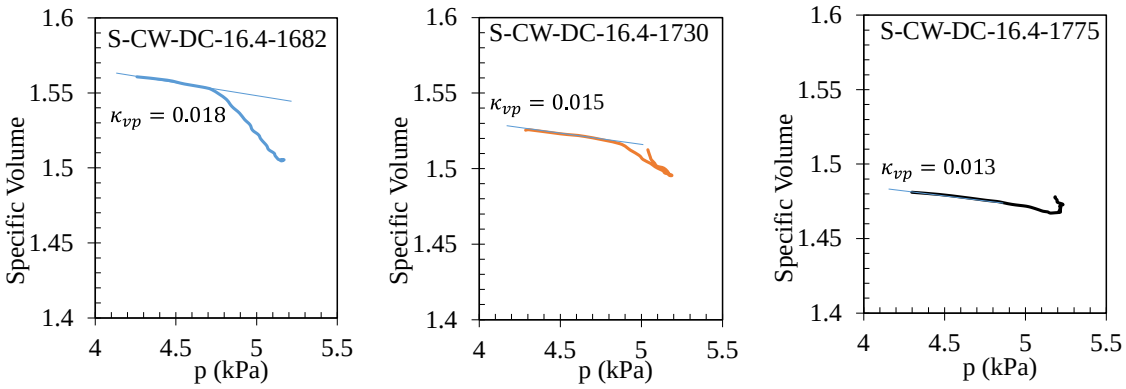

Figure 7.21 Volumetric compression curves during the triaxial shearing phase for the DCsclay soil specimens

Table 7.15 Calibrated NCL volumetric stiffness parameter κ_{vp} from triaxial shearing phase compression curves.

Reference	Density	κ_{vp}	Average κ_{vp}
	(kg/m^3)		
DCsclay	1682	0.018	0.015
	1730	0.015	
	1775	0.013	
HCclay	1578	0.014	0.010
	1626	0.011	
	1679	0.004	
LCesilt	1522	0.009	0.008
	1570	0.008	
	1618	0.007	

The loading-collapse (LC) yield curve in the model is defined by the equation:

$$p_o(s) = p_{yn} = \begin{cases} p_{yn0} - p_s & s < s_{sa} \\ \dfrac{p_{yn0}}{p_{y0}}\left[p_{y0} + s - p_s\right] & s \geq s_{sa} \end{cases} \tag{7.32}$$

Equation (7.32) defines the preconsolidation stress p_{yn}, for increases in matric suction; p_{y0} is the yield stress at zero suction for a normally consolidated soil; and p_{yn0} is the new yield stress at zero suction after the soil is compacted or has experienced a past maximum preconsolidation pressure.

The variables, p_{y0} and p_{yn0} are reference stress variables that are necessary for determining the position of the LC yield curve. Using the graphically determined initial yield stresses, p_y as presented in Table 6.1 in Chapter 6, the major axis of the initial $q-p$ yield curve, also known as the initial preconsolidation stress $p_o(s)$ on the LC yield curve, can be determined by the Equation (7.33) for the $q-p$ yield curve as follows:

$$p_o(s) = \frac{q_y^{\,2}}{M^2(p_y + p_s)} + p_y \tag{7.33}$$

In Equation (7.33), p_y is the net mean stress on the initial yield curve; q_y is the deviatoric stress also on the initial yield curve, where $q_y = 3\left(p_y - p_{ini}\right)$; p_s in this equation is the apparent tensile yield stress on the initial $q-p$ yield curve, p_s, can be determined using the initial soil suction values. The initial soil suction values are the same as the soil suction at the initial yield, $s_{ini} = s_y$, based on the assumption that soil suction in CW tests does not change until the stresses reach or exceed the initial yield curve. The apparent tensile yield stresses, p_s on the initial yield curve were determined using the initial soil suction values and are presented in Table 7.16. Using the

determined tensile yield stresses on the initial yield curve, the initial preconsolidation stresses, $p_o(s)$ were determined using Equation (7.33), and are also presented in Table 7.16, with the corresponding yield stresses.

Table 7.16 Determined initial preconsolidation stresses $p_o(s)$ with corresponding yield stresses.

Reference	Density	p_y	q_y	p_s	$p_o(s)$
	(kg/m^3)	(kPa)	(kPa)	(kPa)	(kPa)
DCsclay	1682	115	121	-4.35	166.09
	1730	126	129	-9.04	197.76
	1775	129	127	-7.87	208.70
HCclay	1578	122	127	-14.65	213.25
	1626	128	135	-18.57	232.78
	1679	129	139	-19.05	222.02
LCesilt	1522	132	134	-62.02	261.36
	1570	122	121	-72.14	262.04
	1618	142	155	-152.02	347.29

The preconsolidation stress $p_o(s)$, can also be determined from the specific volume with net mean stress plots of isotropic compressions under constant suction as suggested by Alonso et al., (1990). For this research, the isotropic compressions or triaxial shear tests were not performed under constant suction but under constant-water content conditions. In addition, for CW tests, the matric suction changed during the isotropic compressions and as suction changes, the slope of the $v - \ln p$ will continue to change, therefore it may make a graphical determination of $p_o(s)$ on the $v - \ln p$ plot for a CW test ineffective. A comparison of both methods of determination of the preconsolidation stress was made and discussed later in this section.

The saturated reference stress parameters, p_{y0} and p_{yn0}, in the LC yield curve Equation (7.32), can now be determined using the initial preconsolidation stress, $p_o(s)$ Calibration of p_{y0} and p_{yn0} was performed for each soil type by estimating the preconsolidation stress, $p_o(s)$, using Equation (7.32), and comparing them to the determined preconsolidation stresses in Table 7.16, by the least-squares approximation method The calibrated values of the parameters p_{y0} and p_{yn0} for each soil type are presented in Table 7.17.

Table 7.17 Calibrated yield stresses p_{y0} and p_{yn0} at zero suction, and corresponding unsaturated initial preconsolidation stresses.

Reference	Density	$p_o(s)$	p_{y0}	p_{yn0}
	(kg/m^3)	(kPa)	(kPa)	(kPa)
DCsclay	1682	166.09	5857644	214.55
	1730	197.76		
	1775	208.70		
HCclay	1578	213.25	61.42	193.23
	1626	232.78		
	1679	222.02		
LCesilt	1522	261.36	8595.67	416.74
	1570	262.04		
	1618	347.29		

The calibrated result of the parameter p_{y0} for the DCsclay appear unreasonable, but can be attributed to the variation of matric suction with density, as there was no defined trend or relationship of the suction variation with density.

In summary, the descriptions of the calibrated parameters are presented in Table 7.18, and the calibrated values of the model parameters for each of the DCsclay, HCclay, and LCesilt, Kentucky soils used to validate the model are summarized in Table 7.19.

Table 7.18 Calibrated model parameter descriptions

Parameter	Parameter Description
λ_{vp}	Compressibility parameter of volumetric stiffness for changes in p and virgin conditions
s_{sa}	Saturation-suction parameter is the maximum soil suction that corresponds to full saturation
p_{y0}	Yield stress at zero suction for a normally consolidated soil;
p_{yn0}	New yield stress at zero suction after the soil is compacted
κ	Compressibility parameter of elastic volumetric stiffness for changes in p
M	Slope of the critical state line (CSL)
G	Shear modulus

Table 7.19 Calibrated model parameters

Soil reference	Density (kg/m^3)	λ_{vp}	p_{y0} (kPa)	p_{yn0} (kPa)	κ	M	s_{sa} (kPa)	G (kPa)
DCsclay	1682	0.056	5857644	214.55	0.015	1.73	0.3	35489.4
	1730						2.0	38613.8
	1775						3.0	43418.4
HCclay	1578	0.035	61.42	193.23	0.010	1.43	4.6	34505.6
	1626						5.6	37368.8
	1679						6.5	39711.6
LCesilt	1522	0.062	8595.67	416.74	0.008	1.06	19.6	49696.9
	1570						121.9	57515.8
	1618						228.2	65913.1

A comparison of data from the calibration process was made in order to consider additional ways to obtain calibrated model parameters from experimental data. The

values of p_{yn0} determined by the calibration process were compared to values obtained experimentally from additional tests.

To determine if the $v - \ln p$ compression curve from the isotropic compression under partially saturated CW conditions can be used to experimentally determine values of the preconsolidation stress, $p_o(s)$ for the model parameter calibration process, values of $p_o(s)$ obtained from the calibration procedures are compared with the preconsolidation stress $p_o(s)$ determined graphically from the $v - \ln p$ plots of isotropic compression under CW conditions. The calibration process uses the experimental yield stresses, p_y, q_y, p_s, and the slope of the CSL, M to determine the initial preconsolidation stress, $p_o(s)$. There is a hesitance in using the plots of $v - \ln p$ curves under CW conditions, as the soil suction is not constant during compression as recommended by Alonso et al., (1990). For this study, the soil suction decreased during isotropic compression under CW conditions, therefore the rate of change of specific volume, for the virgin portion of the plot of $v - \ln p$ will increase as suction decreases, as can be seen in the plots of $v - \ln p$ in Figure 7.20. Though the rate of change in specific volume changes with increasing net mean stress, the slope can be represented by a constant stiffness parameter λ_{vp}, which suggests that linear representations of the slope may be possible.

Using linear projections of the latter part of the virgin portion of the $v - \ln p$ curves, and at the start of the re-compressions portions of the curves, the intersection of the linear projections provides the typical point of the initial preconsolidation stress $p_o(s)$ from

the $v - \ln p$ curves. A comparison of the $p_o(s)$ obtained graphically from the $v - \ln p$ curves and those from the experimental yield stresses are shown in Figure 7.22. The comparison shows that there is a very good agreement between the $p_o(s)$ obtained from the different methods. The comparison plot of initial preconsolidation stress show that all points fall on or close to the line of unity. With the inclusion of a fourth point at $(0,0)$ a coefficient of determination, R^2 value of 0.972 is obtained. This is a very good indication that the graphical method typically employed to determine the preconsolidation stress from a compression curve can still be consider as a method of estimation of the preconsolidation stress, even though the curves do not clearly represent URL and NCL linear trends. This finding is not in agreement with Zhou and Sheng (2009) as they show that the graphically determined preconsolidation stresses are generally higher, therefore care should be used when using the graphical method.

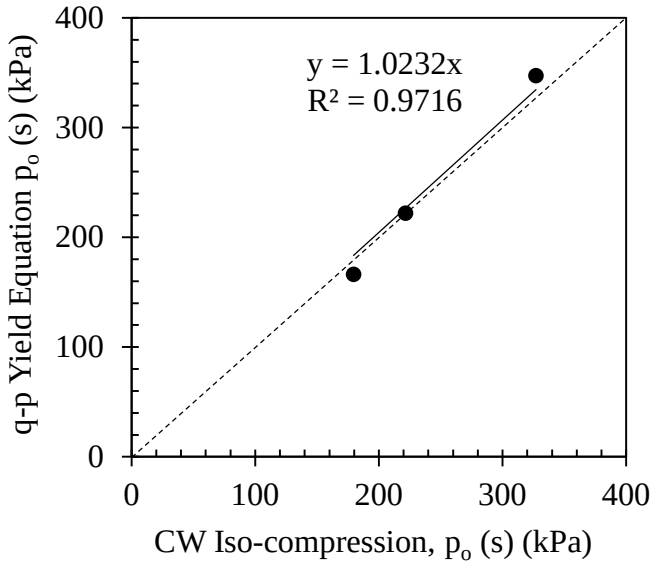

Figure 7.22 Comparison of the preconsolidation stresses by the traditional linear representations of virgin and normal compressions on a $v - \ln p$ curve and from the $q - p$ elliptical yield equation using initial yield

7.2.6 Implementation for the As-Compacted State Soil Model

The experimental programs culminates with the development of the As-Compacted State soil model as depicted Figure 7.23. Previous discussions of Chapter 7 and previous chapters have included behaviors and predictions that are implemented in the model. The discussion of implementation of noted behaviors and trends is presented herein.

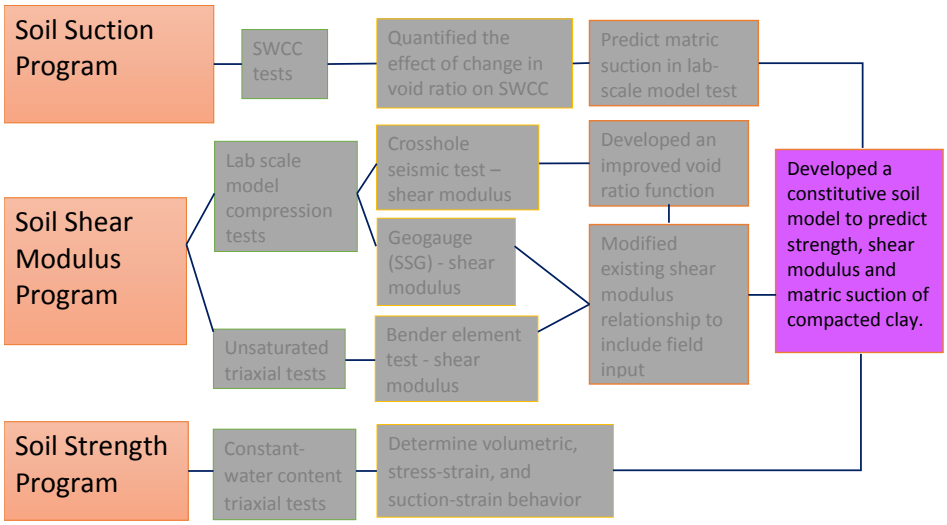

Figure 7.23 A visual of the point of discuss (mechanical behavior of unsaturated triaxial tests) within the overall research program.

The implementation of this model is detailed in the VBA coding presented in Appendix J. It is based on the classic BBM by Alonso et al. (1990) with changes incorporated for improved response of soil behavior for an as-compacted state. As with the BBM, it may be used with care for normally consolidated to lightly overconsolidated, partially saturated soils, such as sand, silts, clayey sands, sandy clays and low plasticity clays. It is not intended to be used for highly expansive clays, or heavily overconsolidated clays. With the use of a field stiffness gauge, a determined field shear modulus is used as input into the model for a response on the shear strength of the field soil.

7.2.6.1 Yield Function

Roscoe and Burland (1968) proposed the yield function in the $p-q$ space that is adopted and expanded into the $p-q-s$ in the BBM model is also used by this model. The yield function takes the form of an elliptical surface defined as follows:

$$f(p,q,s) = q - M^2(p + p_s)\left[p_o(s) - p\right] = 0 \tag{7.34}$$

7.2.6.2 The evolution inside the initial yield curve

Deviating from the BBM, the As-compacted state model assumes that there is an internal yielding (inside the initial yield curve) due to the occurrence of plastic shear strains. The internal yield (IY) curve is represented by an elliptical form similar to the initial $p-q$ yield curve. At the start of shearing, the IY preconsolidation stress is the initial net mean stress, i.e. $q = 0 \rightarrow (p_o)_{IY} = p_{ini}$. As the shearing load evolves, the IY curve expands, causing the IY preconsolidation stress to evolve, and the new IY preconsolidation stress can be determined from the elliptical equation, using the current stresses as follows:

$$(p_0)_{IY} = \frac{q^2}{M^2(p + p_s)} + p \tag{7.35}$$

Following a CW shearing path for a lightly overconsolidated soil, the evolution of the internal yield curve is shown by the hidden lines in Figure 7.24. The IY curve expands until it reaches the initial yield curve, at which point the current stresses are the yielding stresses, p_y and q_y on the initial yield curve.

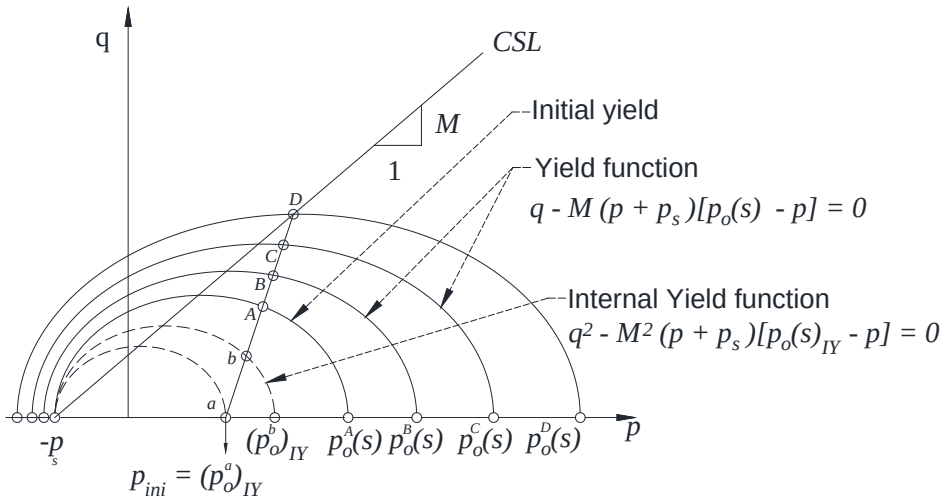

Figure 7.24 Schematic of the evolution of the yield curve from inside the initial yield (internal yield) to after the initial yield, until failure for an overconsolidated soil, under conditions of a constant-water content test.

The plastic shear behavior during unloading and reloading is governed by the flow rule relationship:

$$\frac{d\varepsilon_q^p}{d\varepsilon_{vp}^e} = \frac{2q\alpha}{M^2\left[2p + p_s - (p_o)_{IY}\right]} \tag{7.36}$$

The relationship of Equation (7.36) is similar to that in the BBM for the evolution of plastic strains for the expansion of the initial yield curve, but relates the incremental plastic shear (deviatoric) strain with the incremental elastic volumetric strain as functions of the current stresses and the internal preconsolidation stress $(p_o)_{IY}$.

A small step size is first selected for the increments in plastic shear strain $d\varepsilon_q^p$ and the corresponding increases in the elastic volumetric strain are determined from Equation (7.36). A hardening law is then adopted for the evolution of the internal yield preconsolidation stress $(p_o)_{IY}$ as follows:

$$d(p_o)_{IY} = (p_o)_{IY} \frac{v}{\kappa_{vp}} d\varepsilon_{vp}^e \tag{7.37}$$

With a new internal yield preconsolidation stress $(p_o)_{IY}$, the new net mean stress can be determined from the following equation:

$$p = p_{ini} + \frac{-b + \sqrt{b^2 - 4ac}}{6a} \tag{7.38}$$

The variables a, b, and c, are determined by the relationships: $a = 1 + (1/9)M^2$; $b = (1/3)M^2\left[2p_{ini} - (p_o)_{IY} + p_s\right]$; and $c = M^2(p_{ini} + p_s)\left[p_{ini} - (p_o)_{IY}\right]$.

The incremental step in the net mean stress can thus be determined. Since the air phase is drained in a CW test condition, the resulting stress path follows that of a drained condition, and can be represented incrementally as follow:

$$dq = 3dp \tag{7.39}$$

From the incremental step in deviatoric stress, the new deviatoric stress is determined. The model assumes that both elastic and plastic shear strains occur during unloading and reloading due to changes in the deviatoric stress, q In accordance with the BBM, this model assumes that the elastic shear behavior during unloading and reloading is governed by the relationship:

$$d\varepsilon_q^e = \frac{1}{3G} dq \tag{7.40}$$

7.2.6.3 The evolution past the initial yield curve

Upon the expansion of the internal yield curve reaching the initial yield curve, the internal yield preconsolidation stress $(p_o)_{IY}$ becomes the preconsolidation stress $p_o(s)$. The evolution of elastic volumetric strains is in accordance with those of the SFG model, and is governed by the relationship as follows:

$$d\varepsilon_{vp}^{e} = \frac{\kappa_{vp}}{v}\frac{dp}{p+s} \tag{7.41}$$

The plastic volumetric strains with expansion of the yield curve after the initial yield is similar to that of the BBM, but with the use of the SFG model volumetric stiffness parameters. The plastic volumetric strains are governed by the hardening law relationship as follows:

$$d\varepsilon_{vp}^{p} = \frac{\lambda_{vp} - \kappa_{vp}}{v}\frac{dp_o(s)}{p_o(s)} \tag{7.42}$$

The evolution of the elastic and plastic shear strains with expansion of the yield curve after the initial yield is based on those of the BBM, but includes the hardening parameter dH, which is a basis of the Unified Hardening model and accounts for softening. The elastic and plastic shear strains are governed by the respective relationships:

$$d\varepsilon_{q}^{e} = \frac{1}{3G}dq \tag{7.43}$$

$$d\varepsilon_q^p = \frac{2q\alpha}{M^2\left[2p + p_s - p_o(s)\right]} dH \tag{7.44}$$

In Equation (7.44), the hardening parameter dH is related to the plastic volumetric strain, by the potential failure stress ratio, M_f as follows:

$$dH = \frac{M_f^4 - \eta}{M^4 - \eta} d\varepsilon_{vp}^p = \frac{1}{\Omega} d\varepsilon_{vp}^p \tag{7.45}$$

The variables η is the stress ratio, and M_f is the potential failure stress ratio, and they can be determined based on the following respective relationships:

$$\eta = \frac{q}{p + p_s} \tag{7.46}$$

$$M_f = 6\left[\sqrt{\frac{\chi}{R}\left(1 + \frac{\chi}{R}\right)} - \frac{\chi}{R}\right] \tag{7.47}$$

The parameters χ in Equation (7.47), is given as follows:

$$\chi = \frac{M^2}{12(3 - M)} \tag{7.48}$$

The parameter R is similar to that presented in the Unified Hardening model, but takes on a much simpler form of the classic overconsolidation ratio as follows:

$$R = \frac{p + p_s}{p_o(s) + p_s} \tag{7.49}$$

As with the evolution inside the initial yield, a small step size is first selected for the step increments in plastic shear strain for the evolution past the initial yield. The corresponding plastic volumetric strain can thus be determined using Equations (7.44), and (7.45). The change in the preconsolidation stress $dp_o(s)$ can then be determined by rearranging Equation (7.42).

Increases in the net mean stress are determined from the intersection of the $p-q$ stress path $q = 3(p - p_{ini})$, and the yield surface, Equation (7.34). Substituting and rearranging to solve for the net mean stress, the resulting equation for increases in net mean stress is given by:

$$p = p_{ini} + \frac{-b + \sqrt{b^2 - 4ac}}{6a} \tag{7.50}$$

The variables a, b, and c, are determined from these relationships: $a = 1 + (1/9)M^2$; $b = (1/3)M^2\left[2p_{ini} - p_o(s) + p_s\right]$; $b = (1/3)M^2\left[2p_{ini} - p_o(s) + p_s\right]$. Note that this is similar to the evolution inside the initial yield, but the preconsolidation stress terms in the variables b, and c, are the preconsolidation stress after initial yield, $p_o(s)$, and not $(p_o)_{IY}$, which is the preconsolidation stress inside the initial yield.

Increments of net mean stress, can thus be determined from the step difference in net mean stress, therefore, the increases in deviatoric stress can be determined using the CW stress path condition, both of which are given as follows:

$$dp = p_2 - p_1 \tag{7.51}$$

$$dq = 3dp \tag{7.52}$$

7.2.7 Predictions by the As-Compacted State Soil Model

The experimental model parameters determined for the Kentucky soils used in this study are presented in Table 7.19. Predictions are made and presented in this section for the Daviess County clay soils, tested in a series of constant-water content (CW), shear loading tests conducted on three specimen prepared with compaction efforts to densities of 1682, 1730, and 1775 kg/m3. Predictions for all three Kentucky soils (including the Daviess County clay soils presented here) are also presented in Appendix J.

Figure 7.25 shows the predicted deviatoric stress with axial strain response in comparison with the experimental response for the three Daviess County clay soil specimens, compacted using the same compaction method, but each compacted to a different density. In general, the model prediction can be said to represent the experimental response well. Specifically, the initial strength increase, due to increase in the shear modulus and plastic strains represents the experimental response well. With exception of the experimental specimen S-CW-DC-16.4-1730, which reached a critical state by slip plane failure (see Figure 7.25), the model response to critical state indicates lightly overconsolidated behavior that represents the other two soils well. The model did not represent the slip plane failure. Slip plane failure may be an indication of heavily overconsolidated soils, or maybe the result of shearing under a high net mean stress, none of which are believed to have been an existing condition on this specimen. The slip plane failure is attributed to improper seating of the top cap in a slightly offset position causing

concentrated loading as shown in Figure 7.26. The figure shows the specimen after testing with a slight angle to the top, indicating the top cap was not horizontal. The model's determination of the onset of critical state (i.e., the point on the curves where the rate of change of deviatoric stress with axial strain appears constant), appears to agree with the experimental data for the other two DCsclay soils with densities of 1682 and 1775 1775 kg/m3.

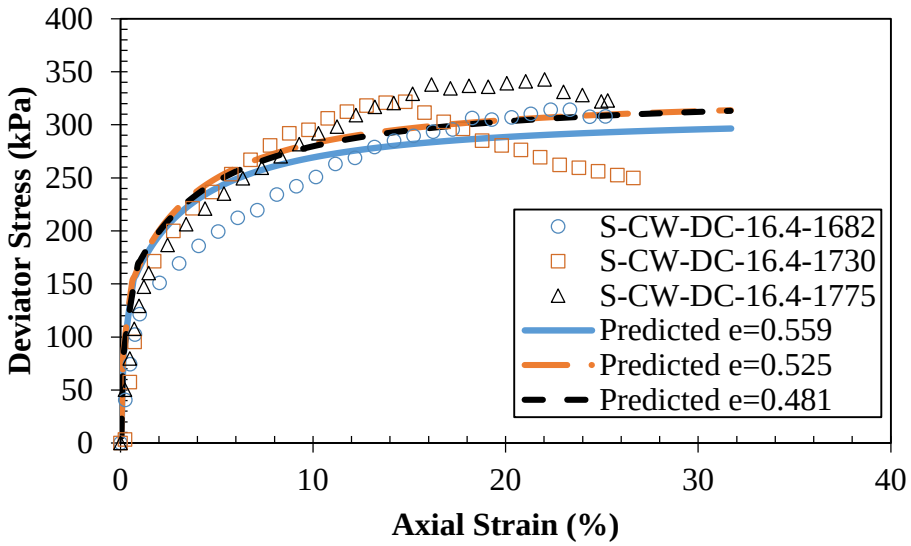

Figure 7.25 Experimental data with predicted stress-strain data based on an internal yield of plastic shear strains, for the DCsclay soil at different densities under conditions of constant water content.

Figure 7.26 Slip plane failure, and offset from horizontal of the top of specimen S-CW-DC-16.4-1730.

Figure 7.27 shows the predicted specific volume with net mean stress response in comparison with the experimental response for the three Daviess County clay soil specimens. The model predictions appear to represent the experimental response well. The initial predicted responses up to the initial yield stress (i.e., the graphical point at which the rate of change of specific volume with net mean stress noticeably changes) represents the experimental behavior well. Though the predicted behavior also represents well the latter or the virgin portion of the experimental curves, slight variations in comparisons are noted in the lowest and highest compacted specimens. The predicted response of specific volume for the virgin portion of the lowest compacted specimen is slightly under predicted, whereas for the highest compacted specimen, it is slightly over predicted. This may be an indication that the effect of compaction on the volumetric stiffness parameter λ_{vp} should be considered for more accurate predictions.

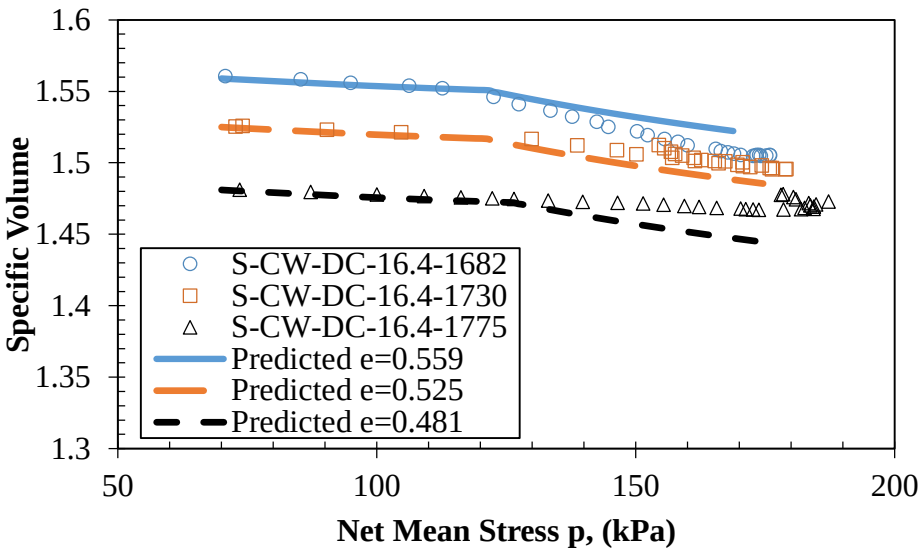

Figure 7.27 Experimental data with predicted data of specific volume with net mean stress, for the DCsclay soil at different densities under conditions of constant water content.

Figure 7.28 shows the predicted matric suction stress with axial strain response in comparison with the experimental response for the three Daviess County clay soil specimens. In general, the model prediction can be said to represent the form of changes of matric suction variation. The defined experimental variation of matric suction with axial strain is twofold. There is an initial stage whereby changes in matric suction are minimal to none, after which the matric suction increases at a high rate and the rate decreases with increase in shear strain to a point of critical state, whereby no further changes in matric suction (or the rate of change in matric suction) is experienced with continued changes in shear strain. The initial stage is represented well by the model predictions for the lower two compacted soils, whereas it under predicts the extents of axial strain for the highest compacted soil. The predicted behavior of matric suction with axial strain for the second stage show over prediction for the lowest compacted sample, though by only as much as about 20 kPa. An improved prediction is noted for the sample

compacted to 1730 kg/m3, but fails to predict the point of critical state failure, which as previously discussed may have been the cause of an experimental error, therefore the prediction behavior may give us insight as to the correct behavior of the specimen. Predicted behavior for the specimen with the highest compacted density shows an increased improvement in comparison to experimental behavior from the latter two specimens. Though improved, the predicted behavior slightly overestimated matric suctions at lower shear strains and underestimated matric suctions at higher shear strains, but appears to predict well the matric suction at critical state, though at a higher strain than that of the experimental data.

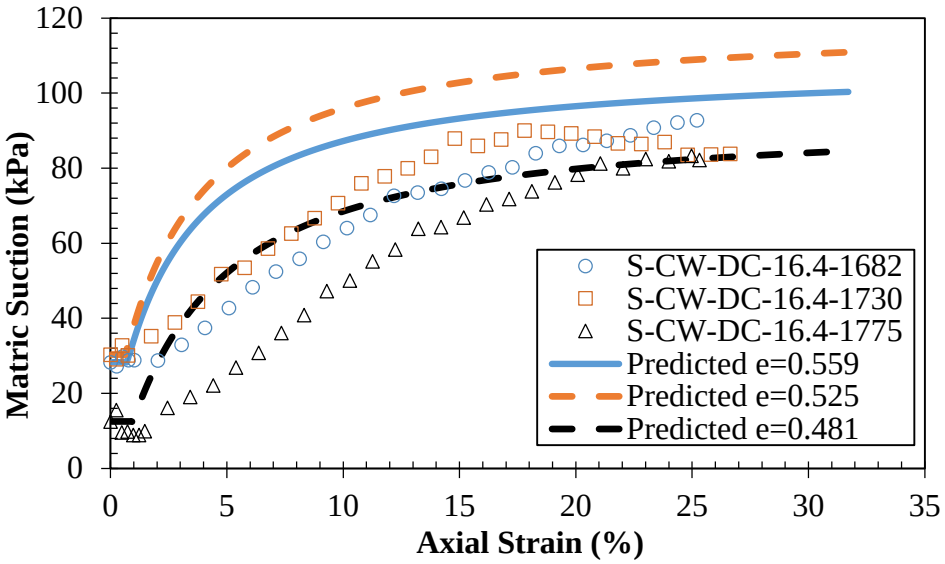

Figure 7.28 Predicted matric suction stress with axial strain response in comparison with the experimental response for the DCsclay soil specimens at different initial densities under conditions of constant-water content.

Though critical state defines a failure state, the shear strains encountered at critical state are typically larger than 15%. Working loads and strains would generally be defined as a percentage of those at critical state. This model becomes very useful as a reference for field performance. Model predictions can be used to determine the points at

which the soil strengths start to cause significant changes in shear strains. Figure 7.29 shows predictions of stress with axial strains for the DCsclay soils with different field measured shear modulus, G_{SSG} by the Soil Stiffness Gauge (Geo-gauge). The commencing of significant yielding can be easily determined from the curves. With a defined working strain and the corresponding design or minimum soil strength, a predicted curve can aid in that determination if field soil stiffness conditions meet designed requirements.

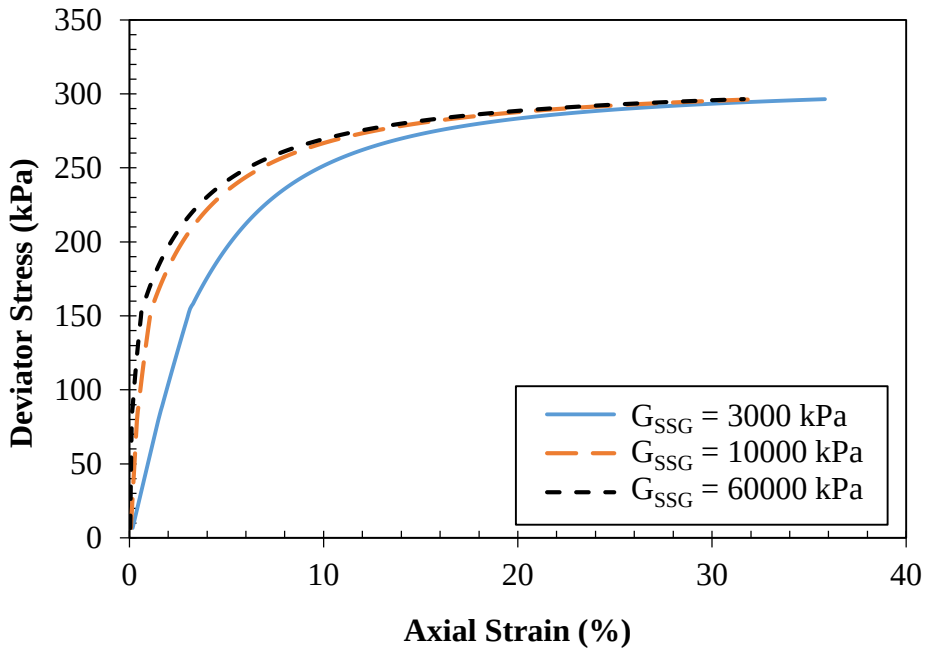

Figure 7.29 Predictions of deviatoric stress with axial strain for varying the field, small strain shear modulus, G_{SSG} .

8 CONCLUSIONS, AND RECOMMENDATION

The main objectives of this research study were to reduce the use of nuclear footprint, by using a non-nuclear, soil stiffness gauge (SSG), and to present a method whereby the parameter (shear modulus) obtained from the use of the SSG, can be used to predict strength of soil.

An experimental program was designed based on the main objectives and it consists of three main parts: A soil suction program; a soil strength program; and a soil shear modulus program. The experimental program for this study was further designed to observe the effect of density on strength, suction, and shear modulus behaviors in unsaturated and saturated soils, and to use the observed properties to develop robust and useful relationships that can be easily used in the civil engineering industry. A summary of the experimental program is presented in Chapter 3 of this dissertation.

8.1 Conclusions

Various conclusions were determined from the experimental test data and test data analyses, and are presented herewith under the section headings of the experimental soil programs.

8.1.1 Soil Suction Program

Based on the mechanical behavior of the soil-water characteristic tests, the water content and the degree of saturation decreased with increase in matric suction. This trend

is consistent with other research studies that show that there is a matric suction dependency on the compaction water content.

The experimental soil-water characteristic curve data indicate that there exists a water content threshold where the matric suctions become equivalent regardless of the initial density (or initial void ratio) for each soil type. Below this critical water content, the rate of decrease in matric suction with water content is also equivalent; therefore there is no effect of change in initial density on the soil-water characteristic property below this critical water content. This deduction of a non–dependent effect of the initial density on soil-water characteristic, is consistent with literature data that indicate that the dependency of soil-water characteristic on water content is little to none. For this reason, the effect of change in initial density on the soil-water characteristic curve of soils is best interpreted using a matric suction and degree of saturation (suction-saturation or $s-S$) plot instead of a suction-moisture plot.

Analyses of the ζ parameter, based on the Zhou et al. (2012) model, indicate that this parameter may not be a material property, but may depend on the state of stress on the sample, the condition of the specimen, or the shape of the SWCC. The magnitude of the ζ parameter changed depending on the selection of the reference and calibration SWCCs. The ζ parameter was consistently lower for a reference SWCC with void ratio greater than that of the calibrating SWCC. The calibration SWCCs initial void ratio direction (higher or lower than that of the reference SWCC), must match the initial void ratio direction of the estimated SWCC from the reference SWCC.

A vertical line of constant matric suction plotted across SWCCs with different initial void ratio is term a ζ line in this study. Since ζ lines are vertical, their effect of matric suction on the degree of saturation is minimized. These vertical lines called ζ lines, therefore, define only the enhanced effect of change in void ratio on degree of saturation. A ζ line intersects points on the SWCC that can be represented by the slopes of the SWCC curves. The transition slopes of the SWCC curves are generally controlled by the n parameter. Therefore, it was determined that the ζ parameter may be related to the n parameter, and two relationships were presented depending on the initial void ratio direction of the estimated SWCC from the reference SWCC.

The Zhou et al. (2012) SWCC shift model portrayed well, the experimental shift due to changes in initial density within reason. The SWCC shifts were consistent with trends of SWCC shifts presented in literature.

Using the principles of the Zhou et al. (2012) model and an SWCC model such as the van Genuchten (1980) model rearranged to solve for matric suction, estimations of matric suction and the corresponding degree of saturation can be determined for changes in void ratio or compaction effort. At different compaction efforts, these estimated points form a suction-saturation path called the soil suction-saturation characteristics (SSSC).

8.1.2 Soil Strength Program

Under conditions of constant-water content (CW) isotropic compression, the unload-reload portions of the compression curves are well defined, but appear to be non-conforming to literature data. In literature, the rate of change of specific volume with net

mean stress (the slope) of the unload-reload portion, is generally of similar magnitude to that at the initial loading portion of the curve. In this study, the rate of change in specific volume loss of the unload-reload portion of the compression curves are generally higher than at the initial loading portions of the curves.

The CW isotropic compression curves cannot be represented by linear projections of the URL and NCL portions. In the $v - \ln p$ plane, the compression curves do not take on the form of linear representations of the URL and NCL either. Therefore, the monotonic isotropic compression curves cannot be represented by the typical two volumetric stiffness parameter, κ and λ for the URL and NCL portions. There is only one volumetric stiffness parameter that represents the monotonic isotropic compression curves well, which is the parameter λ_{vp}.

Under CW isotropic compression conditions, and for all specimens in this study, matric suction decreases with decreasing specific volume, and agrees well with literature data. The change in matric suction is a result of, and only due to the change in the isotropic compression load.

For specimens compacted with very high initial degree of saturation, these specimens may become fully saturated under CW isotropic compression tests. Significant increases in excess pore-water pressure will result under these conditions. Therefore, significant and rapid decreases in matric suction under conditions of CW isotropic compression may result.

Even though the applied rate of the pressure for isotropic compression appeared suitable, and was lower than rates reported in literature for clay type soils, the rate of 7 kPa/hr appears to be high as indicated by the continued decrease in specific volume after the target isotropic compression pressure was reached. This continued decrease in specific volume was not noted in the specimen isotropically compressed to high pressures, but was noted for the shearing specimens that were initially isotropically compressed to a moderate pressure, prior to shearing. It is believed that the matric suction response was not affected, but nonetheless, a reduced rate of compression may be necessary for continuous compressions, or compressions can be done incrementally and the specific volume at the end of each increment used to determine the compression curves.

The specific volume of the HCclay soils during shearing reached a point of critical state whereby all specimens reached the same magnitude of specific volume regardless of initial compaction, and with continued axial strain, no change in specific volume occurred. This was not so for the other clay type soils. Critical state was therefore defined as function of the deviatoric stresses (or the stress-strain curves). Further research is necessary for the use of specific volume in defining critical state.

Matric suction increased during shearing in this study for all specimens. Though this is consistent with literature, matric suction also has been shown to decrease during shearing. Three conclusions were made based on the trends observed in this study (i.e., increasing matric suction with axial strain). The first is that the degree of saturation of the specimens were still below a fully saturated state, and having a pore-air space for the

pore-water pressure to dissipate into, resulted in increasing matric suction. The second is that it appears that isotropic compression loading has a much significant effect on the pore-water pressure, hence, matric-suction, than does loading by shearing. Lastly, the magnitude of isotropic compression (or confining pressure) is critical as to the increase or decrease in matric suction during shearing, i.e., high confining pressure may cause matric suction to decrease whereas, a low confining pressure may cause matric suction to increase as it did in this study.

In this study, the net mean stress with respect to pore-water pressure indicated the CW tests functioned as a drained test condition as did the net mean stress with respect to pore-air pressure.

The point at which the matric suction starts to show significant change represents a change from overconsolidation to a normally consolidated soil. This point of net mean stress is then considered to be the initial yield stress and it lies on the initial yield curve in the $q - p$ plane.

8.1.3 Soil Shear Modulus Program

There appears to be a threshold void ratio, before which, stiffness increased for increasing compaction, and then decreased after the void ratio threshold is exceeded when using a Geogauge. This threshold was not noted when using the seismic crosshole method for the range of void ratio tested

For bulk soil that is at or below (dry of) the optimum moisture content, the shear wave velocity generally increases with decreasing void ratio. When the soil is wet of the

standard Proctor optimum moisture content, the shear wave velocity was essentially constant under initial compaction conditions until a threshold void ratio, after which stiffness increased with decreasing void ratio. These trends agree with data in literature.

The shear modulus of bulk soil was generally lower for samples wet of optimum water content than those at or dry of optimum water content, for a given void ratio.

Though there was no conclusive behavior of the shear modulus ratio with soil types, the normalized shear modulus or modulus ratio, increased as the void ratio decreases for each soil type.

The void ratio function as initially presented by Hardin and Black (1968) becomes an enhance function when a power function trend of shear wave velocity with void ratio is used rather than a linear relationship. A new enhanced relationship of the void ratio function was determined and used in this study.

The initial deflection of the received S-wave from the bender element tests performed during triaxial shearing was due to a near field effect, as it corresponds to the arrival (same travel time) of a P-wave. Therefore the initial deflection of the S-wave should not be used as the time of arrival of the S-wave.

The manual visual technique for the determination of arrival of the S-wave based on the first bump characteristic point is as much an effective method as that of the bender element analysis tool (BEAT) software. The visual technique may in fact be a more efficient method of estimating travel times as the first significant peak point which follows the arrival of an S-wave may not be a point of maximum amplitude, which is a

criteria of the BEAT software. Nonetheless, the cross-correlation method by the BEAT software was determined consistent and suitable for use for the determination of the S-wave travel times.

Though in general, shear wave velocity increases with net mean stress, a definitive relationship on the effect of the intrinsic stress state (density) on shear wave velocity for specimens sheared under the same confining stress could not be determined from the experimental data. This finding is consistent with literature, in that the variation of dry unit weight exerts relatively small effect on the shear modulus.

The critical state parameter M, which represents the slope of the critical state line, varies slightly with density, but due to the minimal variation can be assumed to be a soil type constant, similar to the assumption of the BBM for variations of M with matric suction. For increased accuracy, it is suggested that the variation with density be considered.

8.1.4 A Novel Contribution

Increases in shear modulus occurred for the initial increases in deviatoric stress. This is an indication of increases in shear modulus within the classically defined elastic zone, prior to yielding, which is contrary to the assumptions of a constant shear modulus in constitutive models such as the Barcelona Basic and the Oxford models. Increases in shear modulus within the initial portion of increase in deviatoric stress would cause the rate of change of deviatoric stress with axial strain to increase, but the experimental data showed that the rate of change decreased. This suggested, and therefore was

hypothesized, that plastic shear strains occur within the classic elastic region in an experimental shear stress test prior to the initial yield being reached.

Consideration was given to the possibility of the occurrence of plastic volumetric strain within the classic elastic zone, but observation of the data indicated that all volume change within the re-compression state (the classic elastic zone) should be attributed to only elastic volumetric strains.

The occurrence of plastic shear strains within the initial yield was well modeled within the constitutive As-Compacted state model, which was shown to predict well the stress-strain response using a field determined input of shear modulus, the resulting matric suction from tri-axial loading, and the critical state. Further research and model analyses are necessary for the accurate determination of specific volume for dilating soils. Also further research is necessary for additional validation of the model.

8.2 Recommendations

The apparatus for compaction of specimens used in the triaxial tests was a bi-split mold, which did not work consistently as designed, for high plastic clays. These clays tend to ‘stick’ to the molds and tension cracks are created upon opening. These high plastic clays were pushed or extruded out of the mold to keep them intact as compacted. It is recommended that at a minimum, a tri-split mold be used, but a quad-split mold may work best.

Both pressure chamber and a single cell pressure apparatus were used to determine the soil-water retention property (or SWCC) of the clay type soils. If available, the use of

the single cell apparatus is recommended over that of the pressure chamber. The variations in testing especially that of density is minimized with the use of one sample subjected to the range of applied matric suction.

Due to the continued decreased in specific volume after the target isotropic compression was reached, a reduced rate of isotropic compression (less than 7 kPa/hr) may be necessary for continuous compressions, or compressions can be done incrementally and the specific volume at the end of each increment used to determine the compression curves.

Critical state defined by trends in specific volume was achieved for only one of the clay type soils. Critical state was clearly defined when all three HCclay specimens reached the same magnitude of specific volume, and no further change occurred with increased axial strain. This did not happen for the other clay type soil, therefore, further research is necessary for the use of specific volume in defining critical state.

Further testing is recommended for accurate determination of the cause of the phenomenon of increasing or decreasing matric suction during triaxial shearing. It is generally expected that the matric suction will decrease as the degree of saturation increase, which is in accordance with SWCC trends. But, as data from this study show, matric suction can increase during shearing even as the degree of saturation increases. Though conclusions were made as to the reason, further testing may give much better insight into this phenomenon.

Though conditions of CW show that a triaxial drained test is simulated, it is possible for compacted samples with high initial degree of saturation, to become fully saturated

during testing. If this is to occur, excess pore-water pressure will increase rapidly, thereby, the matric suction will decrease rapidly. Consideration for modeling increasing pore-water pressure under these conditions should be given.

Enhanced parameter calibration may require additional tests. More CW isotropic compression tests may be necessary at different densities to accurately determine the effect of density on the volumetric stiffness parameter λ_{vp}. Additional triaxial CW tests sheared at different confining pressures for each density will result in more accurate experimental calibration of the apparent tensile strength parameter p_s.

APPENDIX A

Historical Background Review That Generally Pertains to Unsaturated Soils

APPENDIX A.1 Soil Suction in Unsaturated Soils

A saturated soil consists of two phases; soil solids and water. Historically, an unsaturated soil was defined as having three phases: soil solids, water and air. Much recently, less than a decade, a fourth phase was suggested as necessary to adequately describe the stress state (Fredlund, 2006). The fourth phase as suggested, is the interface between the existing water and existing air phases, and is termed the contractile skin. Though it seems this phase could be a part of the water phase, Fredlund (2006) suggested that it must be considered as an independent phase. For unsaturated conditions, the pore-air pressure is always greater than the pore-water pressure causing the contractile skin to be concave to air, thereby allowing the contact angle to decrease (ultimately to zero) when the contractile skin makes contact with a wetted soil particle.

The mechanical behavior of an unsaturated soil, would then be influenced by the pore-water and pore-air pressures, and the contractile skin. Therefore, the soil suction is very important in describing the mechanical behavior (water, strength and deformation characteristics) of unsaturated soils (Croney and Coleman, 1948). Aitchison (1965) provided quantitative definitions of soil suction and its components (capillary/matric and osmotic) that are now widely accepted (Krahn and Fredlund, 1972; Wray, 1984; Fredlund and Rahardjo, 1988). An additional adsorptive component of soil suction that relates adsorptive forces with water and a solids was suggested by Yong and Warkentin, (1966). The adsorptive component is a function of the chemistry of the soil water and is affected by surface-reaction minerals. Since the adsorptive component is still not widely accepted or because of its difficulty in its quantification, soil suction, which generally refers to

total suction still remains as having two components (matric and osmotic suctions) when quantifying.

Aitchison (1964) defined total suction, the free energy of soil-water, as the equivalent suction derived from the measurement of the partial pressure of the water vapor in equilibrium with the soil-water relative to the partial pressure of water vapor in equilibrium with free pure water. Total suction relates to its components as follows:

$$\psi = (u_a + u_w) + \pi \tag{A.1}$$

In Equation (A.1), ψ is the total suction, $(u_a - u_w)$ is the matric suction, where u_a and u_w are pore-air and pore-water pressures respectively, and π is the osmotic suction. Since total suction corresponds to the free energy of soil-water, the relationship in Equation (A.1), indicates that matric and osmotic suction are components of free energy.

Osmotic suction

Aitchison (1964) defined osmotic suction, the solute component of free energy as the equivalent suction derived from the measurement of the partial pressure of the water vapor in equilibrium with a solution identical in composition with the soil-water relative to the partial pressure of water vapor in equilibrium with free pure water.

The osmotic suction component relates to the concentration of dissolved salts in the pore water. With changes in salt contents, osmotic suction changes, which results in a change in the mechanical behavior of the soil. When the salt content of a saturated or unsaturated soil is chemically altered deliberately or by contamination, the effect of

osmotic suction change on the mechanical behavior (overall volume and shear strength) of the soil may be significant (Graham et al., 1988; Barbour and Fredlund, 1989; Fredlund et al., 2012). Osmotic suction in the field is simulated in the laboratory, under conditions when distilled water is used when saturating soil specimens, when increasing specimen pore-water volume during testing (such as for swelling test, etc.); and other such tests. The use of distilled water dilutes chemical concentrations in the pore-water, thereby diluting salt content, and in effect, changes osmotic suction. This process is generally unbeknownst to the researcher, or if known, not taken into account, as osmotic suction changes are generally less significant than that of matric suction. Krahn and Fredlund (1972), show that changes in osmotic suction is essentially negligible at higher water contents, with only minimal variation at low water contents. They also show that the trends for both total and matric suction are similar, indicating that the changes in total and matric suction are essentially equivalent, as such:

$$\Delta\psi \approx \Delta\left(u_a + u_w\right) \tag{A.2}$$

Though the discussion of osmotic suction is present in most literature review for geotechnical research involving suction, it is very often neglected, as it was for this study. Osmotic suction is often neglected because osmotic suction changes is of minimal effect on total suction, and matric suction is primarily affected by environmental changes (such as heavy rainfall events), which can cause engineering problems in compacted unsaturated soils (Fredlund, 1989; Fredlund, 1991; Fredlund et al., 2012).

If salt contents are significantly changed, consideration of osmotic suction should be given and can be calculated using thermodynamic principles (Robinson and Stokes, 1968). Metten (1966) presented the Van't Hoff equation for approximating osmotic suction as follows:

$$\pi = RT_K C \tag{A.3}$$

In Equation (A.3), R is the universal gas constant equal to 8.314 J/(mol·K), T_K is the absolute temperature in Kelvins, and C is the sum of the molar concentrations in solution, mol/L. Since osmotic suction is neglected in this study, the term suction, when used throughout this report, would generally refer to matric suction or may refer to total suction, unless specifically noted.

Matric suction

Aitchison, (1964) defined matric suction, the capillary component of free energy as follows: Matric suction is the equivalent suction derived from the measurement of the partial pressure of water vapor in equilibrium with the soil-water relative to the partial pressure of the water vapor in equilibrium with a solution identical in composition with the soil-water.

The matric suction component is commonly associated with the capillary phenomenon developed from the intrinsic surface tension characteristic of water. The capillary component is the dominating component of soil water potential (matric potential), especially in soils composed of minerals with low surface activity. The matric

potential of an unsaturated soil at atmospheric pressure is defined as the product of the matric suction and the unit weight of water (Sivakumar, 1993).

As previously presented in Equation (A.1), the matric suction component $(u_a - u_w)$ is the difference between pore-air u_a and pore-water u_w pressures. For an unsaturated soil, since the pore-air pressure is always greater than the pore-water pressure, the pore-water pressure u_w is negative when subjected to atmospheric pressure (i.e. $u_a = 0$). The negative pressure inducted a compressive stress on soil particles, that results in compression of the soil structure within a soil mass. The negative pore-water pressure is dependent on the surface tension and radius of curvature of the menisci of the contractile skin. The presence of negative pore pressure from capillarity or matric suction, therefore, increases compression and densification in a soil structure, which aligns with the suggested by Alonso et al. (1987), that the shear strength and volume change behavior of unsaturated soil depends on the matric suction rather than the total suction.

Capillary and surface tension

Surface Tension

Matric suction is dependent of surface tension and radius of curvature of the contractile skin menisci, therefore matric suction can be best described by surface tension and capillary phenomenon. Richards (1974) suggested that in highly active clay soils, capillarity and adsorption of water on the surface of clay minerals both contribute to the matric suction. Generally, in sands and silts (typically inert soils), only capillarity contributes to the matric suction.

Surface tension is the stress acting on the contractile skin (i.e., air-water interface), and results from intermolecular forces acting upon the molecules of the contractile skin. The forces acting on a molecule at the surface of a water phase interfacing with air, is different from forces acting on a molecule within the water phase as illustrated in Figure A.1 (a).

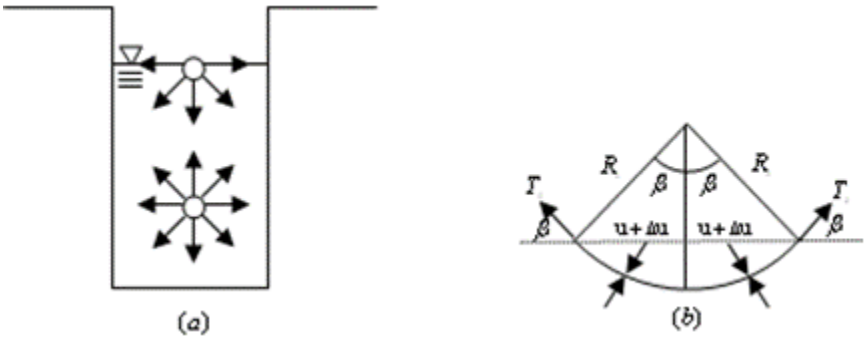

Figure A.1: Surface tension at the air-water interface, (a) Intermolecular forces on contractile skin and water, (b) pressures and surface tension acting on a curved 2-D surface.

The pressure difference across the air-water interface boundary lends to surface tension being the deterministic variable for the interaction. Surface tension of the water phase interfacing with air may be defined as the energy required to either open or close a unit area at a phase interface. In other words, surface tension of water is the maximum energy water can store without breaking a meniscus (Lu and Likos, 2004).

As illustrated in Figure A.1 (a), a balanced system of equal forces in all direction acts upon the water molecule in the interior of the water phase, whereas, an unbalanced system of forces, only in the directions towards the interior of the water phase, act upon the water molecule at the surface (the air-water interface). Consequently, the development of a tensile stress is generated for the contractile skin to be in equilibrium.

This tensile stress acting tangential to the surface is known as surface tension T_s, and is measured as the tensile force per unit length of the contractile skin.

The contractile skin, though in equilibrium due to the development of surface tension, T_s, remains under differential pressure between the phases (air and water) as illustrated in Figure A.1 (b). A pressure differential, Δu, is used to show the difference in air pressure over the water pressure acting on the contractile skin. This pressure difference causes a curvature of the contractile skin, concave to the air phase, and with a radius of curvature R_s. For static equilibrium in the vertical direction:

$$2T_s \sin\beta = 2\Delta u R_s \sin\beta \tag{A.4}$$

Rearranging Equation (A.4), to show the pressure differential as the dependent variable across a two-dimensional surface, the relationship becomes:

$$\Delta u = \frac{2T}{R_s} \tag{A.5}$$

The pores in an unsaturated soil are analogous to capillary tubes with small radii, therefore, R_s represents the pore-throat diameter, or the idealized inter-particle pore-space diameter, and the pressure differential, Δu, acting on the contractile skin represents the difference in the pore-air pressure u_a over the pore-water pressure u_w. For unsaturated conditions, the pressure differential remains positive $u_a > u_w$ (i.e. u_w is negative under atmospheric conditions), otherwise the soil becomes saturated under a negative pressure differential $u_a \leq u_w$ (i.e. u_w becomes positive under atmospheric

conditions). The pressure differential is the matric suction defined in terms of capillarity as:

$$\Delta u = \left(u_a - u_w\right) = \frac{2T}{R_s} \tag{A.6}$$

Equation (A.6) is referred to as Kelvin's capillary model, which shows that for decreasing matric suction, the radius of curvature increases, and extends to infinity when matric suction goes to zero. This model defines the curved contractile skin, or meniscus, of an air-water interface.

Capillary

The capillary phenomenon associated with matric suction is the analogy of the change of the meniscus' radius of curvature with the rise of water in a capillary tube to that of the change in the contractile skin's radius of curvature with the changes in pressure difference across the contractile skin. The capillary phenomenon has direct implications to the water content-matric suction relationship in soils.

Using a similar approach to the surface tension discussion, the imbalance of pressures across the contractile skin may be formulated using the capillary tube concept used in developing the Kelvin capillary model. The physical model of the capillary phenomenon is illustrated in Figure A.2.

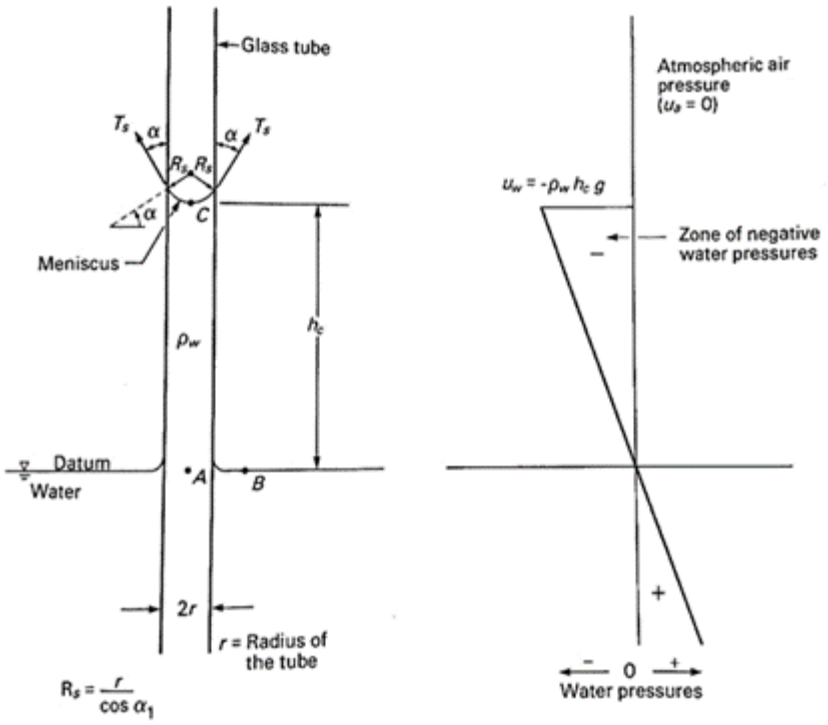

Figure A.2: Physical model and phenomenon related to capillarity (Fredlund and Rahardjo, 1993)

In Figure A.2, a small glass tube is inserted into water under atmospheric conditions. Due to the surface tension in the contractile skin (air-water interface) and the hygroscopic property (tendency of water to wet the surface of the glass tube), a water head in the tube, above the water datum is created. Based on this capillary behavior, the surface tension develops at a contact angle α, from the tube's vertical wall, and with a magnitude that depends on the water adhesion and material properties of the tube (in this case, glass).

The vertical force equilibrium analysis of the water column shown in Figure A.2, indicates that the vertical component of the surface tension is force equivalent to and in opposition to the weight of the water column in the water mass below the contractile skin, and above the water datum. Assigning the height h_c to represent the height of the water column, then the vertical force equilibrium analysis is given as:

$$2\pi T_s \cos\alpha = \pi r^2 h_c \rho_w g \tag{A.7}$$

In Equation (A.7), r is the radius of the capillary tube, T_s is the surface tension of water, α is the contact angle, h_c is the capillary height, ρ_w is the density of water and g is the gravitational acceleration.

Substituting the radius of curvature of the meniscus $R_s = r/\cos\alpha$, into Equation (A.7), and rearranging to give the maximum height of water in the capillary tube, the resulting equation becomes:

$$h_c = \frac{2T_s}{\rho_w g R_s} \tag{A.8}$$

Hydrostatic equilibrium exists between Points A, B, and C in the capillary system. Points A, and B are at atmospheric pressure conditions, therefore the pore-water pressures at Points A, and B are both zero (gage pressures). For a column of water at a capillary rise height equal to h_c, (Point C), hydrostatic equilibrium requires that the hydraulic heads be equal to those at points A and B, therefore, zero. Thus, if the elevation head at point C is h_c, the pressure head must be the negative of the elevation head in order for the hydraulic head to be zero. The water pressure, u_w, at point C can thus be defined as:

$$u_w = -\rho_w g h_c \tag{A.9}$$

The water pressure heads for points below Point A, have positive pressures due to hydrostatic pressure in the water table, and any point above Point A in the water column has negative pressure, and under tension. Since the air pressure at point C is atmospheric $(u_a = 0)$ and water pressure is negative $(u_w = -\rho_w g h_c)$, then the matric suction may be expressed as:

$$(u_a - u_w) = \rho_w g h_c \tag{A.10}$$

Substituting Equation (A.8) into Equation (A.10), results in equivalent form to that of Equation (A.11).

$$(u_a - u_w) = \frac{2T}{R_s} \tag{A.11}$$

Therefore, if the radius of curvature R_s is analogous to the pore radius then smaller pore radii will result in capillary rise and higher matric suctions. The above discussions on surface tension and capillary phenomenon demonstrates that the surface tension of water can support a column of water, in a capillary tube. The surface tension associated with the contractile skin results in a reaction force on the wall of the capillary tube, and the vertical component of this reaction force produces compressive stresses on the wall of the tube. The weight of the water column is transferred to the tube through the contractile skin. If a soil has a capillary zone, the contractile skin results in an increased compression of the soil structure. Thus the presence of matric suction in an unsaturated soil increases the shear strength of the soil (Fredlund and Rahardjo, 1993).

APPENDIX A.2 State of Stress of Unsaturated Soils

Terzaghi, (1936) presented the effective stress as a stress state variable for a saturated soil to describe the mechanical behavior of the soil as a relationship between the effective normal stress σ' the total normal stress σ, and the pore-water pressure u_w, as follows:

$$\sigma' = \sigma - u_w \tag{A.12}$$

Researches have attempted to extend the idea of using one stress state variable into unsaturated soils, (Croney et al., 1958; Bishop, 1959; Aitchison, 1961; Jennings 1961; Richards, 1967; Aitchison, 1965, 1973). The Bishop (1959) effective stress equation, which has been widely used, relates the effective normal stress to the total normal stress σ, pore-air pressure u_a, pore-water pressure u_w, and a parameter χ, that is related to the degree of saturation of the soil, with a value of unity for saturated soils and zero for dry soils as follows:

$$\sigma' = (\sigma - u_w) + \chi(u_a - u_w) \tag{A.13}$$

Coleman (1962) suggested the parameter χ, and its relationship with degree of saturation, is dependent on soil structure. Jennings and Burland, (1962), argued that the χ parameter does not predict well, the unsaturated soil volumetric behaviors below a critical degree of saturation and the possible soil collapse when wetted. Matyas and Radhakrishna (1968) mentioned that the principle of effective stress was inadequate to explain the volumetric behavior of partially saturated soils.

Biot (1941) recognized the need to have stress state variables independent of the physical properties of soil when attempting to describe unsaturated soil. Biot (1941), proposed the use of the effective stress $(\sigma - u_w)$, and pore-water pressures u_w, as two independent stress state variables. Currently, the use of two independent stress state variables are generally used and suggested as adequate to describe the mechanical behavior of unsaturated soils.

Bishop and Blight (1963) and Matyas and Radhakrishna (1968) proposed that the soil behavior can be explained in terms of two independent stress components, $(\sigma - u_a)$ and $(u_a - u_w)$. Fredlund, (1970), and Fredlund and Morgenstern (1977) formulated a theoretical equilibrium analysis for unsaturated soils based on multi-phase continuum mechanics. With the suggestion that under equilibrium conditions, unsaturated soil is a four-phase system, and the assumptions that the soil particles were incompressible and chemically inert, the analysis concluded that any two of three possible variables $(\sigma - u_a)$, $(u_a - u_w)$, and $(\sigma - u_w)$, were justified as independent stress state variables, and therefore could be used to describe the state of normal stress in unsaturated soils.

The most widely used two combination of the stress state variables today are the $(\sigma - u_a)$, and $(u_a - u_w)$ variables because the effect of a change in the total normal stress can be separated from the effect caused by a change in the pore-water pressure. In fact, for field conditions, the pore-air pressure is considered to be atmospheric (i.e., zero gauge pressure), reducing the stress state variables to the total stress σ, and negative pore-water pressures, $-u_w$.

To verify the proposed stress state variables as valid to describing the mechanical properties of unsaturated soils, Fredlund and Morgenstern (1977) performed experimental 'null' tests. In performing the null tests, the components, σ, u_a, and u_w, of the three stress state variables $(\sigma - u_a)$, $(u_a - u_w)$, and $(\sigma - u_w)$, were equally varied, thereby maintaining constant values for each of the stress state variables. The volume changes were monitored. Though the components of the stress state variables were equally varied, the stress state variables remained constants, therefore for the null hypothesis to be true, without changes in the stress state variables, .no volume change or change in degree of saturation should occur. No volume change and little water flow were observed during these null tests. Fredlund and Morgenstern, (1977), concluded that the null tests were true and therefore, the proposed stress state variables are considered valid to describe the mechanical behavior of unsaturated soils.

APPENDIX B

Step-by-step integration procedure of the BBM constitutive relations for an initially lightly overconsolidated soil, responding to a drained (constant–s) conventional triaxial compression (CTC) test

Macari and Arduino (1995) showed that the MCC model does not properly support the response of heavily overconsolidated soils. Therefore, as the MCC is the basis of the BBM, the BBM critical state framework also does not support the response of heavily overconsolidated soil conditions. However, the BBM framework does support the lightly overconsolidated and normally consolidated soil conditions. Hoyos (1998) provides an explicit step-by-step integration procedure of the BBM constitutive relations for an initially lightly overconsolidated soil, responding to a drained (constant–s) conventional triaxial compression (CTC) test. This procedure select equal increments of either deviatoric stress q, or net mean stress , p from the initial yield curve to failure and then calculates the resulting strains based on the stress increments. Since the CSL represents failure, the cumulative increments of stress have to stop just prior to failure on the CSL, otherwise errors are encountered, therefore this procedure allow for modelling only just prior to the onset of critical state. It therefore fails to define or model critical state, whereby no further changes occur in the deviatoric stress q, the net mean stresses, p the net mean stresses, v for continued changes in shear strains, ε_q such that:

$$\frac{dp}{d\varepsilon_q} = \frac{dq}{d\varepsilon_q} = \frac{dv}{d\varepsilon_q} \approx 0 \qquad \text{(B.1)}$$

Though there are many stress paths and test methods of performing a triaxial test, A CTC test would typically be subjected to a constant or controlled strain rate. To simulate or model a strain controlled test, increments of strain are selected, and the resulting deviatoric and net mean stresses calculated. Increments of strains after failure, would prove if the BBM constitutive relations can model within the critical state framework

Explicit step-by-step integration procedure of the BBM are presented for a drained conventional triaxial compression test under constant matric suction, s. The input parameters for this test are: $\lambda(0)$, κ, β, r, p^c, G, M, k, $p_o(0)$, and s. The presented schematics in Figure B.1, of the BBM response, also show the soil to be lightly overconsolidated prior to start of shearing (i.e., the stress states are inside the initial yield curve).

1. Calculate $\lambda(s)$:

$$\lambda(s) = \lambda(0)\left[(1-r)\exp(-\beta s) + r\right] \tag{B.2}$$

2. Calculate the initial preconsolidation stress $p_o^C(s)$:

$$\frac{p_o(s)}{p^c} = \left(\frac{p_o(0)}{p^c}\right)^{\frac{\lambda(0)-\kappa}{\lambda(s)-\kappa}} \tag{B.3}$$

3. Calculate the apparent tensile stress p_s, due to suction:

$$p_s = ks \tag{B.4}$$

4. Calculate the initial yield net mean stress $(p_C)_y$ and deviatoric stress, $(q_C)_y$ i.e., the yield coordinates of Point C by equating at that point, the equations for the initial yield curve, Equation (2.46), and that for a drained, effective stress path from p_{ini} to $(p_C)_y$. If presented geometrically:

$$(p_C)_y = p_{ini} + \frac{-b + \sqrt{b^2 - 4ac}}{6a} \tag{B.5}$$

$$(q_C)_y = 3\left[(p_C)_y - p_{ini}\right] \tag{B.6}$$

where

$a = 1 + (1/9)M^2$

$b = (1/3)M^2\left[2p_{ini} - p_o^C(s) + p_s\right]$

$c = M^2(p_{ini} + p_s)\left[p_{ini} - p_o^C(s)\right]$

5. Calculate the specific volume $(v_C)_y$ at the initial yield point Y on the url-line corresponding to $(p_C)_y$:

$$(v_C)_y = v_{ini} - \kappa \ln\left(\frac{p_C}{p_{ini}}\right) \tag{B.7}$$

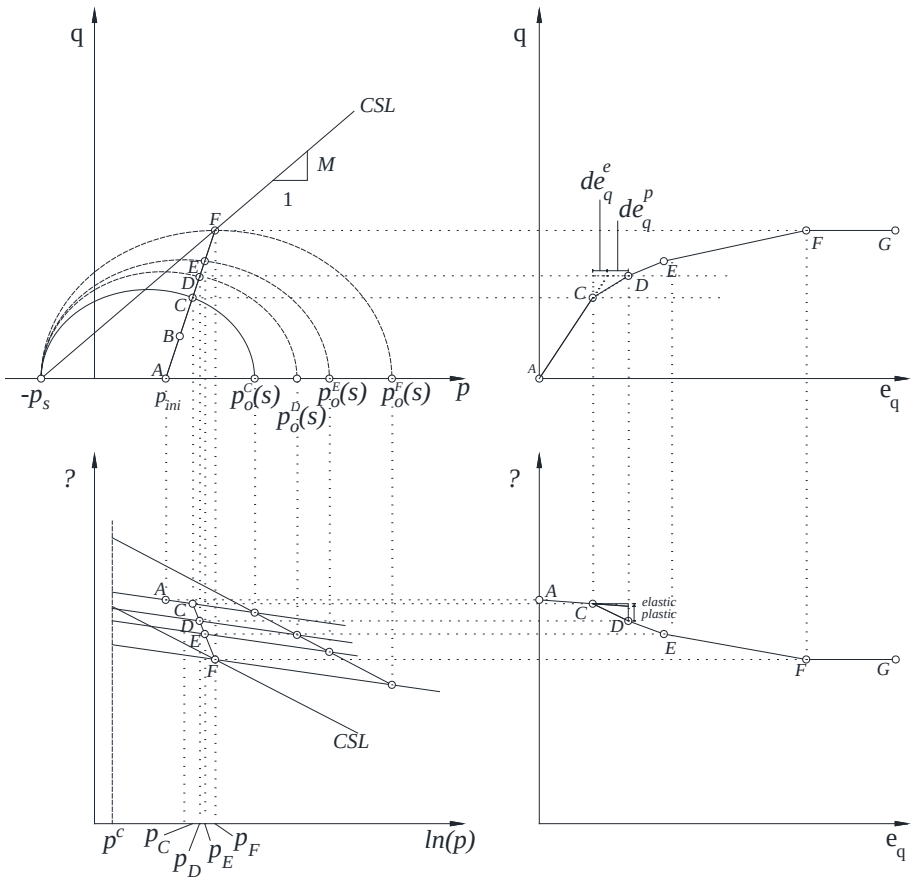

Figure B.1 Schematic of Barcelona model response for a constant suction test (reproduced from Laikram, 2007).

Calculate the failure net mean stress p_F, and deviatoric stress, q_F, i.e., the coordinates of Point F by equating at that point, the equations for the CSL, $q_F = M(p_F - p_s)$ and that for a drained, effective stress path from p_{ini} to p_F.

$$p_F = \frac{Mp_s + 3p_{ini}}{3 - M} \tag{B.8}$$

$$q_F = M(p_F + p_s) = M\left(\frac{Mp_s + 3p_{ini}}{3 - M} + p_s\right) \tag{B.9}$$

6. Within the elastic zone, i.e., $q < q_y$, changes in the deviatoric stress, net mean stress, and specific volume can be calculated based on a selected elastic shear strain increment, $d\varepsilon_q^e$

$$dq = d\varepsilon_q^e (3G) \tag{B.10}$$

$$dp = \frac{1}{3} dq \tag{B.11}$$

$$dv = -k \ln\left(\frac{p + dp}{p} \right) \tag{B.12}$$

7. Within the elasto-plastic zone, first select a plastic shear strain to be subjected on the soil. Then divide the plastic shear strain into equal plastic shear strain increments, $d\varepsilon_q^p$

8. Calculate the plastic volumetric strain increment $d\varepsilon_{vp}^p$, for the stress path segment CD using the non-associative flow rule:

$$\frac{d\varepsilon_q^p}{d\varepsilon_{vp}^p} = \frac{2q\alpha}{M^2 \left[2p + p_s - p_o(s) \right]} \tag{B.13}$$

9. Calculate the hardening parameter, $p_o^D(s)$ for the new yield curve formed when the state stresses reaches Point D:

$$p_o^D(s) = p_o^C(s) + d\varepsilon_{vp}^p \; p_o^C(s) \frac{v}{\lambda(s) - \kappa}$$

10. Calculate the net mean stress p_D and deviatoric stress, q_D i.e., the coordinates of Point D by equating at that point, the equations for the yield curve, Equation (2.46), and that for a drained, effective stress path from from p_{ini} to p_D.

$$p_D = p_{ini} + \frac{-b + \sqrt{b^2 - 4ac}}{6a} \tag{B.14}$$

$$q_D = 3(p_D - p_{ini}) \tag{B.15}$$

Noting that b and c are different than calculated previously for the initial yield:

$a = 1 + (1/9)M^2$,

$b = (1/3)M^2\left[2p_{ini} - p_o^D(s) + p_s\right]$, and

$c = M^2(p_{ini} + p_s)\left[p_{ini} - p_o^D(s)\right]$.

11. Calculate the specific volume v_{ncl}^C on the ncl corresponding to $p_o^C(s)$:

$$v_{ncl}^C = v_{ini} - \kappa \ln\left(\frac{p_o^C(s)}{p_{ini}}\right) \tag{B.16}$$

12. Calculate the specific volume v_{ncl}^D on the ncl corresponding to $p_o^D(s)$:

$$v_{ncl}^D = v_{ncl}^C - \lambda(s) \ln\left(\frac{p_o^D(s)}{p_o^C(s)}\right) \tag{B.17}$$

13. Calculate the specific volume v_D on the ncl corresponding to p_D:

$$v_D = v_{ncl}^D + \kappa \ln\left(\frac{p_o^D(s)}{p_D}\right) \tag{B.18}$$

14. Calculate the elastic volumetric and shear strain increments, $d\varepsilon_{vp}^e$ and $d\varepsilon_q^e$, for the stress path segment CD:

$$d\varepsilon_{vp}^e = \frac{\kappa}{v_C}\left(\frac{dp}{p_C}\right) = \frac{\kappa}{v_C}\left(\frac{p_D - p_C}{p_C}\right) \tag{B.19}$$

$$d\varepsilon_q^e = \frac{1}{3G}dq = \frac{1}{3G}(q_D - q_C) \tag{B.20}$$

15. Calculate the total volumetric and shear strain increments $d\varepsilon_{vp}$, for the stress path segment CD:

$$d\varepsilon_{vp} = d\varepsilon_{vp}^e + d\varepsilon_{vp}^p \tag{B.21}$$

$$d\varepsilon_q = d\varepsilon_q^e + d\varepsilon_q^p \tag{B.22}$$

16. Repeat steps 9 through 17 for Point E, and all subsequent points corresponding to each increment of plastic shear strain.
17. Calculate the cumulative volumetric and shear strains ε_{vp} and ε_q at any point by summing the strain increments up to that point.
18. Graphically plot $q - p$, $v - p$, $q - \varepsilon_q$, and $v - \varepsilon_q$.

As there are many shear stress that can be simulated in a triaxial test, the explicit procedures above can be extended for response to other shear stress paths such as a constant net mean stress, or reductions in net mean stress, or even triaxial extension test response.

APPENDIX C

Experimental Procedures

APPENDIX C.1 Soil Water Characteristic Curve Testing Procedures

Soil-water characteristic curve tests were determined based on guidance from American Standards for Testing Materials (ASTM) Standard Test Method ASTM D6836, for the Determination of the Soil-Water Characteristic Curve (SWCC) for Desorption Using the Hanging Column, Pressure Extractor, Chilled Mirror Hygrometer, or Centrifuge. This research relied on guidance from the pressure extractor method of ASTM D6836 for the desorption path (i.e., drying). Both of the available apparatus for SWCC tests, i.e., the pressure chamber apparatus and the pressure single cell apparatus were used in the determination of the SWCC for matric suctions up to 1,500 kPa. In both test methods, no external pore-water pressures were applied, but were maintained at the atmospheric pressure, whereas the pore-air pressures were elevated above atmospheric pressures and applied, which resulted in the applied matric suctions by the axis translation method.

Both apparatus are similar in that a sealed chamber is used for housing the specimen(s) in the air phase above, but in contact with a fully saturated high air entry porous plate or disk (HAEPD). The water phase below the HAEPD is free of air but open to the atmosphere. Each apparatus was connected to an air compressor used to apply air pressures into the sealed chamber, thereby introducing matric suctions on the specimen(s). The application of matric suction (air pressure) to the specimen(s) allows for increased surface tension (and smaller radius of curvature) of the air-water contractile skin of the specimen(s), which causes the equilibrium of the pore-water pressure to be altered. The specimen will experience volumetric changes due to the outflow of water

from the altered equilibrium. Over time equilibrium is once again reached, and is determined based on monitoring the outflow volume for no further change in volume. The difference between the pressure chamber apparatus and the pressure single cell apparatus is that only one specimen can be placed in the pressure single cell apparatus, whereas a group of specimens can be placed in the pressure chamber and all subjected to the same air pressure applied. With the pressure chamber, after equilibrium has been achieved for each air pressure applied, one or more of the specimen(s) are used to determine saturation based on their gravimetric water content, thereby providing one point on the SWCC for desorption. For the experimental SWCC using the pressure chamber, several (about ten to twelve) identical specimens were needed to be tested at different matric suctions and all used to determine the SWCC by desorption. Only one specimen was used in the pressure single cell apparatus for the determination of the SWCC by desorption. With the pressure single cell apparatus, the saturation at an applied matric suction was determined from the monitored change in volumetric water content, as this change was due to only one specimen. Application of increased matric suction was then continued in the pressure single cell apparatus on the same specimen after each corresponding change in volumetric water content determination was made.

SWCC Pressure Chamber Apparatus

The pressure chamber apparatus used in this research was manufactured by Soil moisture Equipment Corporation with headquarters in Santa Barbara, California. It is a pressure plate extractor with a recommend pressure capacity of 15 bar (1,500 kPa). The

pressure chamber can be accessed via a top lid, that when sealed by screw clamps and an O-ring, provides the resistance to the maximum recommended pressure. The pressure chamber is also designed for use with one or two pressure plates, and contains removable sealed, non-collapsible plastic outflow tubes that can be used to connect the pressure plates to atmospheric pressures outside of the chamber. The chamber also includes an access for the application of air pressure. Figure C.1 shows a photo of the system of apparatus necessary for the SWCC tests, which includes the pressure chamber, the pressure control manifold, the air compressor, and a pressure plate.

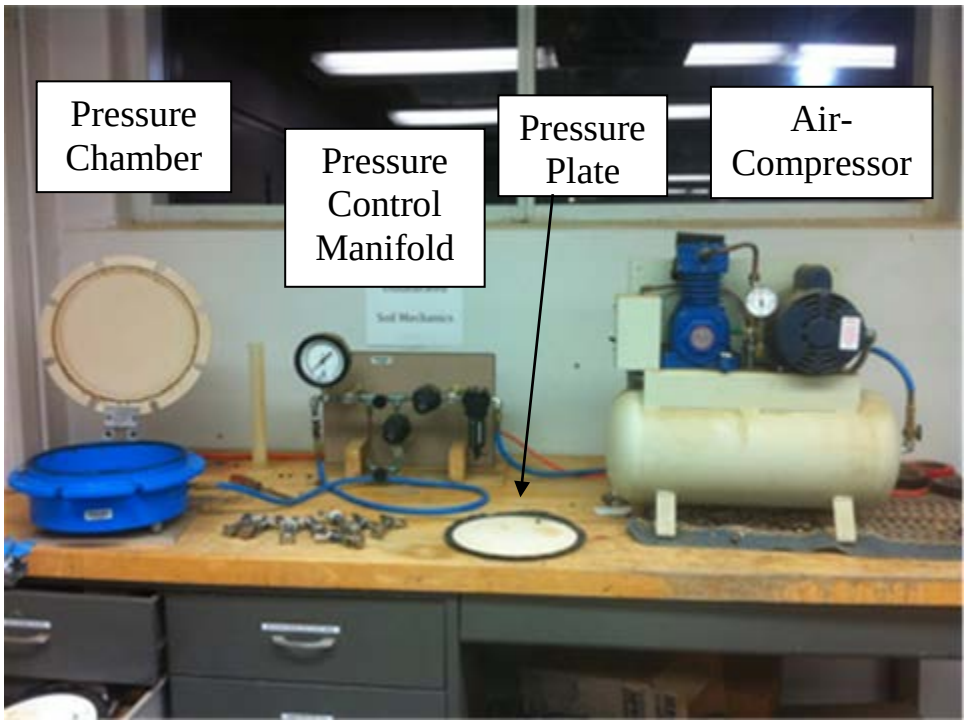

Figure C.1 System of apparatus for the SWCC test by the pressure chamber.

Air Pressure System for the Pressure Chamber

The air pressure was supplied by the Soilmoisture Equipment Corporation air compressor, Model #0500F, designed for use with the pressure chamber. The air compressor is rated for a maximum air pressures of 20 bar (300 psi), but has an on-compressor regulator to set lower maximum pressure supply. An on-compressor dial gauge reads the pressure build up in the compressor. Connected to the air compressor and in-line to the pressure chamber is the pressure control manifold. The control manifold provides dual regulators for additional pressure regulation and finer regulator for enhanced control of lower pressures. The control manifold is installed with an analog pressure gauge that is used to determine the regulated pressure transferred to the pressure chamber. Figure C.1 shows a photo of both the air compressor and the pressure control manifold in-line with the pressure chamber.

Pressure Plates

The pressure plates used with the pressure chamber apparatus are high air-entry porous ceramic disks (HAEPD), which are also generally called pressure plates, and are manufactured by Soilmoisture Equipment Corporation. Figure C.2 shows a pressure plate with a black rubber ring around it, and a connector that accesses the bottom (water phase) side of the disk. The rubber ring allows for the ease of saturating the pressure plate prior to testing. The HAEPD used in the SSSC testing program are designed to withstand pressures up to and including their high air-entry values of 0.5, 3, 5, and 15 bar. For accuracy and consistency of results, a one-third rule was employed for use with

the HAEPD, i.e., the minimum pressure used for any HAEPD cannot be less than 1/3 of its air-entry value.

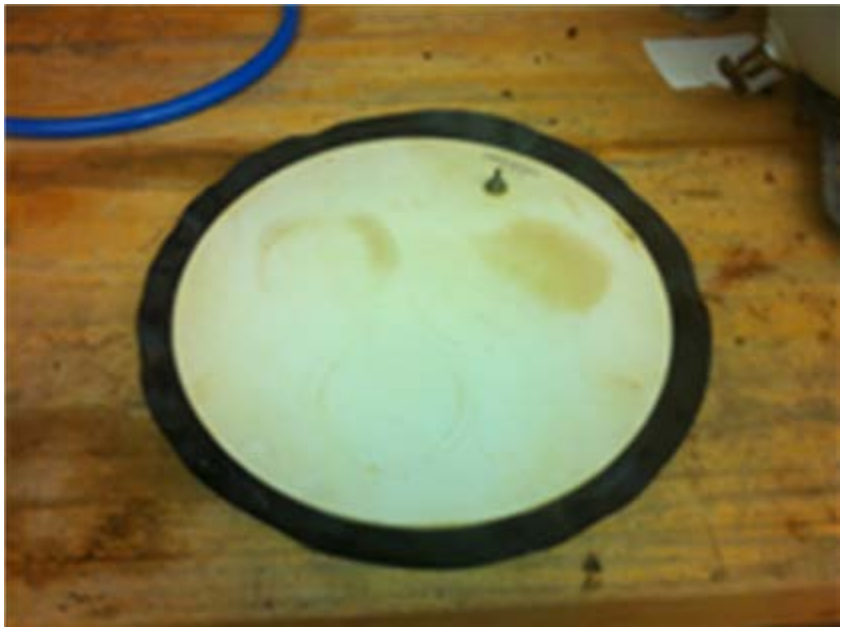

Figure C.2 Typical pressure plate used in the SWCC pressure chamber, (a high air-entry porous ceramic disk with rubber ring).

SWCC Single Cell Pressure Apparatus

The single cell pressure apparatus used in this research was the Model SWC-150 Soil-water characteristic cell, manufactured by the GCTS Testing Systems Company, with headquarters in Tempe Arizona. The cell is made of stainless steel with an attached load piston to apply normal stresses and/or measure specimen volume change. The apparatus allows you to control matric suctions from near zero values up to 1500 kPa (15 bars), and is also capable of applying one-dimensional loading, Ko, to a specimen with a diameter up to 75 mm. Dual pressure gauges on the apparatus allows for the over load protection by manual selection of applied pressures of a low range up to 200 kPa, and a high range up 1,500 kPa. Several HAEPD up to 1,500 kPa, manufactured for this cell are

interchangeable, but for this research an HAEPD with a recommend maximum pressure capacity of 15 bar (1,500 kPa) was used for the entire range of applied matric suction. Though capable of applying one-dimensional loading, all specimens were only subjected to the applied air pressures and no external directional loading was applied (i.e., zero net mean stress). The pressure cell can be accessed via a top lid, that when sealed by screw clamps and an O-ring, provides the resistance to the maximum recommended pressure. The base of the pressure cell is designed with groves to allow water into or out of the cell below the HAEPD. The grooves extend into two external connectors that connect the cell to the water columns on the board that are open to the atmosphere. The cell also includes an access for the application of air pressure. Figure C.3 shows a photo of the system of apparatus necessary for the SWCC tests, which includes the pressure cell, the pressure board, the pressure control manifold, and the air compressor.

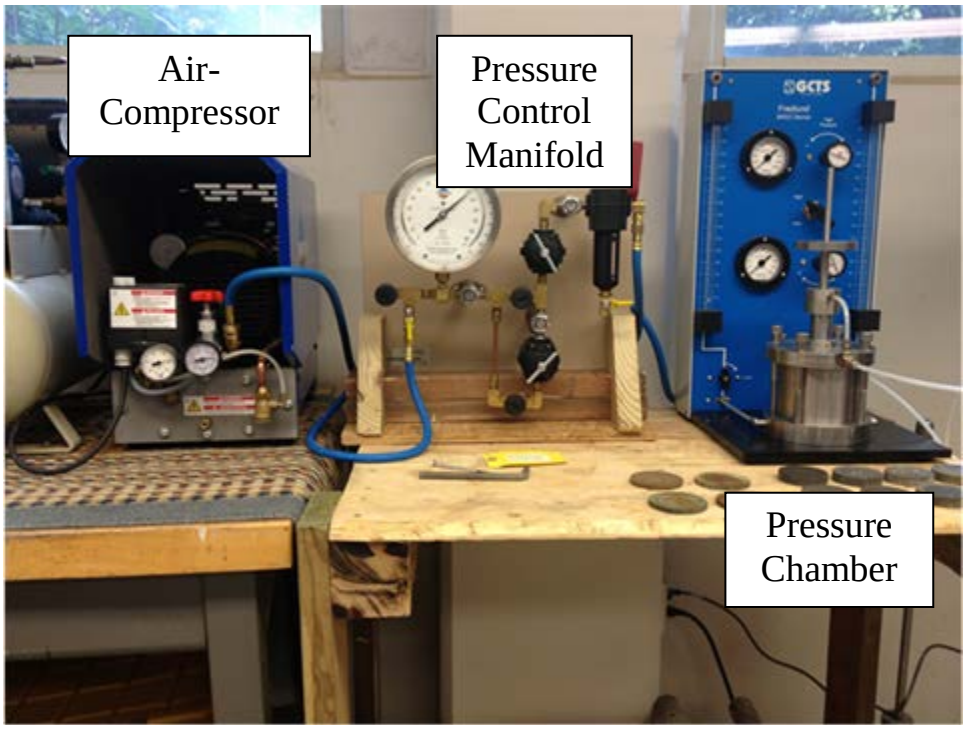

Figure C.3 System of apparatus for the soil-water retention test using the single cell pressure device.

Air Pressure System for the Single Cell Pressure Apparatus

The pressure system for the SWC-150 single cell apparatus is very similar to that of the pressure system for the pressure chamber apparatus. The air pressure is supplied by an air compressor connected in-line to a pressure control manifold, which is connected in-line to the SWC-150. The air compressor is manufactured by the Soilmoisture Equipment Corporation air compressor, Model #0500F, designed for use with the pressure chamber. The air compressor is rated for a maximum air pressures of 20 bar (~300 psi), but has an on-compressor regulator to set lower maximum pressure supply. An on-compressor dial gauge reads the pressure build up in the compressor. The pressure control manifold provides dual regulators for additional pressure regulation with a finer regulator for enhanced control of lower pressures. The control manifold is

installed with an analog pressure gauge that is used to determine the regulated pressure transferred to the pressure chamber. Figure C.3 shows a photo of both the air compressor and the pressure control manifold in-line with the pressure cell.

Ceramic Pressure Stone

The ceramic pressure stones/disks available for use with the pressure chamber apparatus are ceramic high air-entry-value porous disks, which can be obtained from the manufacturer of the SWCC pressure chamber, Soilmoisture Equipment Corporation. Several ceramic HAEPD rated at 100, 300, 500, and 1500 kPa are available, and can be easily interchanged. In this study, the 1,500 kPa HAEPD was used to determine the range of SSSC. Figure C.4 shows the 100, 300, 1,500 and 500 kPa HAEPD in a clockwise motion from the top left HAEPD, with the 100 kPa HAEPD without the stainless steel ring. The HAEPD is mounted on a stainless steel ring for ease of installing into and removal from the single cell apparatus. The stainless steel ring has a beveled edge, which should be installed bevel side down into the bottom of the cell. The one-third rule (i.e., the minimum pressure used for any HAEPD cannot be less than 1/3 of its air-entry value) employed for the pressure plates used with the pressure chamber was not employed for use with the SWC-150 single cell apparatus. This apparatus was designed to allow the use of a single soil specimen to obtain the entire SWCC with any number of data points.

Figure C.4 High air-entry porous ceramic disks for the single cell pressure device shown with and without the stainless steel rings.

Specimen Retaining Rings

The retaining rings, shown Figure C.5 and used for the specimens were machine cut from a nominal 2 inches (50.8 mm), Schedule 40 PVC plastic pipe at a height of 25.4 mm (1 inch) with a tolerance of less than 0.25mm. The internal diameter of a 2-inch nominal Schedule 40 PVC pipe is 52.5 mm (2.067 inches). These pipes are generally manufactured with a tolerance of +/- 0.25 mm (0.01 inches) for the outside diameter, but with a higher variance of the internal diameter. The diameter of selected samples of the machine cut specimen rings were each measured three times and averaged to obtain a mean diameter. The average mean diameter of the selected sample rings were 51.31 mm (2.020 inches), which is very close to the nominal size of 50.8 mm (2 inches), therefore for ease of calculation, the nominal diameter size was used for all specimen rings. The

weight of the PVC specimen rings varied from about 25.5 to 26.5 grams. The purpose of the retaining rings was to prevent lateral expansion of the soil during the saturation phase. The rings were cut from a 50.8 mm (2 inches) nominal size pipe to allow for the convenience and ease of transferring samples fabricated with the use of a 50.8 mm diameter static compaction split mold.

Figure C.5 Retaining rings for soil-water retention tests machined cut from a Schedule 40, PVC pipe.

Static Compactor, Mold, and Pistons

The static compactor used for specimen fabrication is the Model S-242 Static Compactor and Extruder, which is in essence a hydraulic jack manufactured by Durham Geo-Enterprises, headquartered in Stone Mountain, Georgia. A photo of the Static Compactor and Extruder is shown in Figure C.6. The Static Compactor and Extruder is designed to compact 73 mm (2.8 inches) diameter specimen, which is larger than the 50.8 mm split mold, selected for soil-water retention sample fabrication. The split molds and

pistons that were used for the fabrication of soil-water retention sample fabrication were specially manufactured for the fabrication of unsaturated triaxial specimens using the Static Compactor. The dimensions and details of the machined pistons and the split mold are included in this dissertation under the Section Appendix C.4.

Figure C.6 Static Compactor and Extruder

Specimen Fabrication for SWCC Tests

The samples used in the SWCC development for each of the four clays examined herein were statically compacted in one lift, to a height of 37.7 mm (1.485 inches) using the Static Compactor, and the machined split mold and pistons, shown in Figure C.7. The height of the split mold in combination with the height of the top and bottom pistons, allow for the molded soil height of 37.7mm (1.485 inches), and the diameter of the split mold allowed for the specimen diameter to be 50.8 mm (2 inches). Details of the split mold and top and bottom pistons are included in Appendix C.

Figure C.7: SWCC specimen molding system consisting of split mold, and the static compactor.

A batch of sample was prepared by mixing dry soil or soil at a known moisture content with water to bring the soil to the standard Proctor optimum moisture content for each respective soil. Figure C.8 shows a batch of oven dried soil and water to be added to bring the batch soil to the desired moisture content. The batch mix was then sealed and stored for at least one day to allow for moisture equilibrium. The batch mix was used to remold each sample to a percentage of the standard Proctor maximum dry density and at the standard Proctor optimum moisture content for each respective soil. The molded densities were of 80, 90, 100, and 110 percentage of the standard Proctor maximum dry density for each of the four clay type soils. To achieve the targeted dry density, the total density was first determined based on the targeted moisture content, then, the exact soil

total weight necessary to fit the volume of the 37.7 mm (1.485 inches) high by 50.8 mm (2 inches) diameter mold space was used

Figure C.8 Soil sample preparation of a batch of oven-dried soil to be mixed with the weighed water to bring the batch sample to the desired moisture content.

Upon completion of the molding of each SWCC sample, the compacted soil was removed by either opening of the split mold or extruded from the split mold (usually depends on its density structure). In extruding the remolded soil samples, the Static Compactor and Extruder was used. A remolded sample with a looser density structure is shown in Figure C.9. Following removal from the mold, the sample was placed into a 25.4 mm (1 inch) high PVC plastic specimen retaining ring, and a soil trimming wire saw was used to trim the sample to the 25 mm (1 inch) height of the retaining ring. The soil trimmings were used to check and verify the moisture content of the specimen in accordance with ASTM D2216, Standard Test Method for Laboratory Determination of Water (Moisture Content of Soil and Rock by Mass. Using the known volume of the retaining ring, the weight of the ring and the weight of the ring and trimmed specimen

were used to determine the density of the specimen. This determined density was verified against the targeted density for quality control purposes.

Figure C.9 (a) Shelby tube section containing molded SWCC sample mounted on extrusion piston (b) extruded SWCC specimen.

For the soil-water retention property program using the pressure chamber, the soil batch preparations allowed for two specimens at each targeted density for a total of eight specimens of a given soil per batch. Figure C.10 shows a sample of four prepared specimens within the retaining rings, ready for saturation. Saturation and testing of the entire group of specimens were each performed simultaneously. Only one specimen at a time was fabricated, saturated and tested using the SWC-150 single cell pressure apparatus. The advantage of testing groups of specimens in the pressure chamber is that equilibrium was reached for the group of samples, for each consecutive increasing matric suction interval in less time than testing each sample from saturation to a desired matric

suction stress state. Another advantage of testing groups of specimens of a particular soil with different densities simultaneously is that the possible errors of testing between the different densities are minimized which aided in the programs objective to determine the effect of density on the soil-water retention property. The advantage of testing single specimen in the single pressure cell apparatus is that one specimen can be used to determine the entire SWCC, thereby increasing the accuracy of testing by decreasing the sources of possible errors.

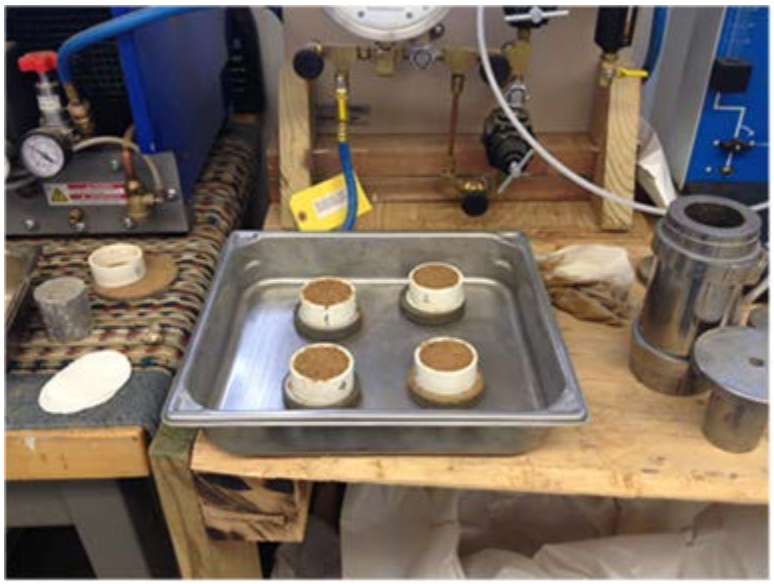

Figure C.10 group of four SWCC samples inserted into PVC retaining rings and prepped for saturation.

Specimen Saturation for SWCC Tests

In accordance with ASTM D6836 standards, the SWCC specimens were saturated within the retaining rings to prevent distortion, sloughing or lateral expansion of the soil. Varying from the ASTM D6836, the specimen were not completely inundated, but saturated with deaired and demineralized water in a bath to depths of about 2 mm below the top of the soil specimen for at least 24 hours, as shown in Figure C.11. This allows

for the soils to be saturated from the bottom up avoiding entrapping air within the specimen. Porous stones were used and placed at the top and bottom of each specimen. Filter papers were placed between the porous stones and soil specimen to prevent loss of soil sample. . To prevent swelling, weights were placed on the top porous stones on the specimens that were heavy enough to counteract the swelling potential of the samples that would develop from the saturation process as, shown in Figure C.12. The weights were typically placed on the samples before the de-aired water was added for saturation. Just prior to SWCC testing, and after at least 24 hours under saturating conditions, each sample was weighed and the weight compared with the calculated theoretical saturated unit weight for quality assurance. After saturation, the specimen had to be handled with care during the transferring of the specimens for weighing, and placement on the HAEPD in the pressure chamber/cell for testing. The cohesive nature of the soils allowed for ease of transfer of the specimens without losing soil structure, but extreme care was necessary for some of the soil specimens compacted to 80 percent of the standard Proctor maximum dry density

Figure C.11 De-aired water poured around SWCC samples sandwiched between porous stones and filter paper, to a depth below the top of the specimens.

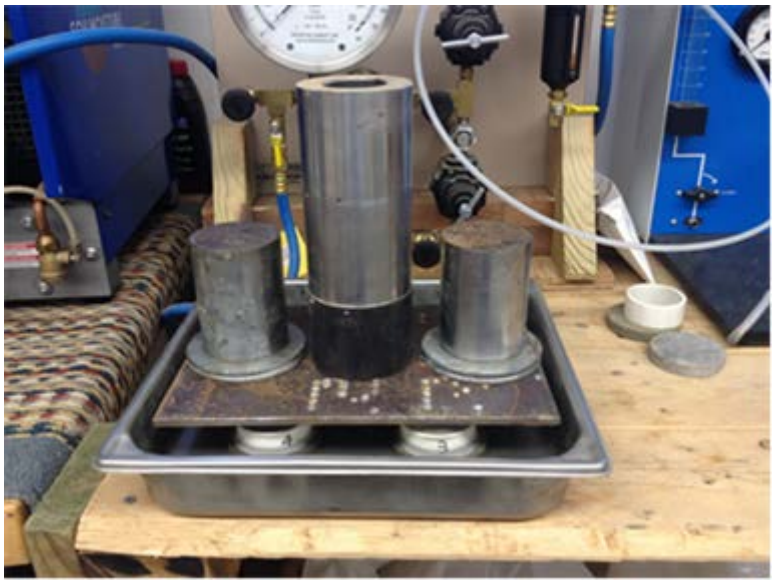

Figure C.12 Weights placed atop porous stones on top of the SWCC specimens for the duration of saturation to stop potential swelling of the specimens.

Saturation of Pressure Plates for Pressure Chamber Apparatus

Saturation of the ceramic high air-entry pressure plates by gravity water flow through them was considered inadequate for saturation. Saturation was performed by

total submersion of the surface of the pressure plates in de-aired water within the pressure chamber, under an applied pressure. Figure C.13 shows a pressure plate in the pressure chamber with excess water over its surface, ready to be pressurized. An air pressure of approximately 0.5 bar below the air entry value of the disk was applied to the pressure chamber, causing the water to flow through the pressure plate. The entire volume of water that was placed on top of the ceramic plate proceeded to expel from the effluent tube and into a catch basin. Bubbles in the effluent water were noted, as this indicated the presence of air within the pores of the pressure plate. As air bubbles diminished from the effluent water, it was assumed that the pressure plate was reaching saturation. Typically, 500 to 600 mL of de-aired water was forced to flow through the ceramic plates before complete saturation was reached.

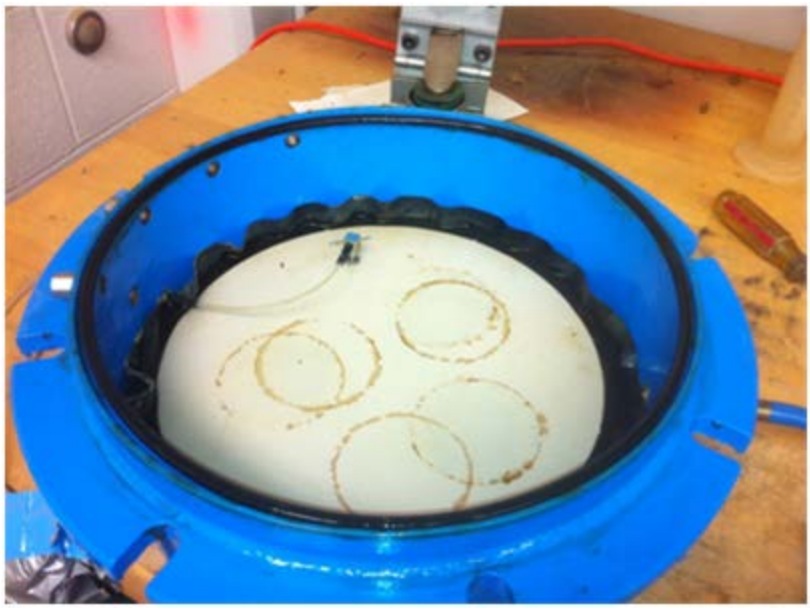

Figure C.13 SWCC pressure chamber with high air entry ceramic plate

Saturation of Pressure Stone for Single Cell Apparatus

The initial process of saturation of a dry ceramic stones is to place it under water overnight, as shown in Figure C.14. This process though necessary for dry stones, is not sufficient for complete saturation of the ceramic stones. Complete saturation was achieved by submerging the ceramic stone disk in de-aired water in the pressure cell apparatus, and applying a pressure up to the maximum pressure to be used during testing. Ensuring that that water phase below the ceramic stone disk in the pressure cell is completely free of air, allows for any diffused air through the disk during pressure saturation to be easily expelled with the effluent water, through the water column on the pressure panel to a connected catch basin. Diminishing air bubbles can be easily seen rising through the water column on the pressure panel. The pressure was maintained for a minimum of 24 hours if saturation of the HAEPD commenced immediately after the last test, or maintained for a minimum of 48 hours if otherwise

At end of saturation, any excess water above the ceramic stone disk is removed, and then the ceramic disk itself is removed. A sponge or similar item is used to remove the excess water on the ceramic stone to achieve a saturated surface dry (SSD) condition, after which, the ceramic disk is weighed. The weights of the ceramic disk after saturation and at the end of testing are compared to ensure the ceramic disk stayed saturated throughout the testing process.

Figure C.14 Initial saturation process of the high air-entry porous ceramic disk elevated with spacers, but completely submerged in de-aired water.

Procedures for SWCC Development Using the Pressure Chamber Apparatus

For the development of soil suction-saturation characteristic curves for each clay soil type, at the four different dry densities, about ten identical specimens were fabricated at each density. Each specimen was saturated as described previously under the heading "Specimen Saturation for SWCC Test" of this Appendix. As many as eight specimens were placed on each saturated ceramic pressure plate within the pressure chamber.

Upon carefully placing the compacted specimens on the pressure plate, the specimens were ensured of good contact between the specimen and the plate by twisting the specimens approximately 45 degrees. Figure C.15 shows samples placed in contact with the ceramic plate.

Figure C.15 SWCC pressure chamber with soil samples placed on the ceramic plate.

Each group of saturated specimens placed in the pressure chamber was subjected to a matric suction stress state equal to that of the applied air pressure. The application of the pressure immediately began the process of volumetric change in the specimens by allowing water to flow out of the specimen, through the pressure plate and to an effluent until the specimens reached matric suction equilibrium stress state. Equilibrium was assumed to be achieved when effluent water ceased to flow. Normally, equilibrium was reached after approximately 36 hours. However, for high matric suctions determined using the 15 bar pressure plate, at least two days was allowed for equilibrium development of the applied 800 kPa matric suction, and at least four days was allowed for equilibrium development of the applied 1,400 or 1,500 kPa matric suction.

After equilibrium was reached for each group of specimens, the chamber was opened and one sample of each density and soil type was removed for the determination of gravimetric water content corresponding to the particular applied matric suction. The remainder of the sample group was subjected to a higher matric suction value, and the

process was repeated until the applied pressure was close to the pressure limit of the plates and chamber was reached. The maximum matric suction applied for this study was 1,400 kPa

The gravimetric results were used in the determination of the degree of saturation of the specimens. The collective results of the matric suction and the corresponding degree of saturation for a given soil and density generated a soil suction-saturation characteristics. The SWCC data was then plotted for all four densities of each soil to produce four SWCC curves, each corresponding to a compaction state.

Procedures for SWCC Development Using the SWC-150 Single Cell Apparatus

The procedure for the SWCC development using the SWC-150 single cell apparatus is similar to that using the pressure chamber. Only one sample is used to determine the entire SWCC range of a soil at a given density. For each soil, only four specimens, compacted to different densities were fabricated. Saturation and placement on the 15 bar HAEPD for testing was performed as previously discussed for the pressure chamber specimens. Each specimen was then subjected to incremental matric suction stress states equal to that of the applied air pressures.

Equilibration was considered attained after each increment of matric suction when the change in volume readings was about one division (about 0.079 mL) or less over a 24-hour period with the 15-bar ceramic stone. In general, equilibrium was reached in about 36 hours for the lower applied pressures, and about three days for the higher pressures of 1,400 kPa. After equilibrium was reached for each increment, and the volumetric change noted, the next matric suction increment was then applied. This

process was repeated until the final application and equilibrium of matric suction. The specimen was then removed from the cell for the determination of gravimetric water content corresponding to the final applied matric suction, and the actual weight of soil solids of the specimen.

The weight of soil solids was used in the determination of the gravimetric water content at each applied matric suction, based on the weight of water lost at each stage. The gravimetric water content, dry density, and specific gravity of the soil were then used to determine the degree of saturation of the specimens. The collective results of the matric suction and the corresponding degree of saturation for a given soil and density generated a soil suction-saturation characteristics. The SWCC data was then plotted for all four densities of each soil to produce four SWCC curves, each corresponding to a compaction state.

APPENDIX C.2 Soil Strength Testing Procedures

Two types of triaxial testing was performed for this research program, namely saturated and unsaturated triaxial testing. More specifically, the unsaturated triaxial testing consisted of the constant water content test method. Different equipment, including the cells, were used for each type of triaxial test. Both triaxial cells for saturated and constant-water content tests were equipped with piezoelectric transducers to measure shear wave velocities during testing. More details of the apparatus and testing procedures for each type of triaxial testing are presented in the following sections of this chapter.

Saturated Triaxial Testing

Apparatus for Saturated Triaxial Testing

The triaxial testing system of apparatus used in this study consisted of the Load Trac II triaxial load frame machine, and two triaxial Flow Trac II volume pressure controllers manufactured by Geocomp Corporation, headquartered in Acton, Massachusetts, and a triaxial cell, manufactured by Trautwein Soil Testing Equipment, headquartered in Houston, Texas. The Load Trac II includes a built in displacement transducer. The load was measured via the load cell transducer that was mounted below the crossbar of the load frame, and in contact with the triaxial cell. The Flow Trac II pressure controllers have a maximum pressure capacity of 1,400 kPa (200 psi) and volume capacities of 250 ml and 750 ml. The 250 ml capacity controller was used to control pore pressures within the specimen and the 750 ml was used to control the cell pressure. The 101.6 mm (4 inches) diameter triaxial cell is designed for use with 71 mm (2.8 inches) diameter

specimens, with an axial loading rod that extends through the top end cap. The triaxial cell's base and top platens were fitted with Bender elements that transmit and receive shear waves through the specimen. A photo of the saturated triaxial testing system is shown in Figure C.16

For full automation, test control and data acquisition, the triaxial system was networked with a computer that ran the Geocomp Triaxial software

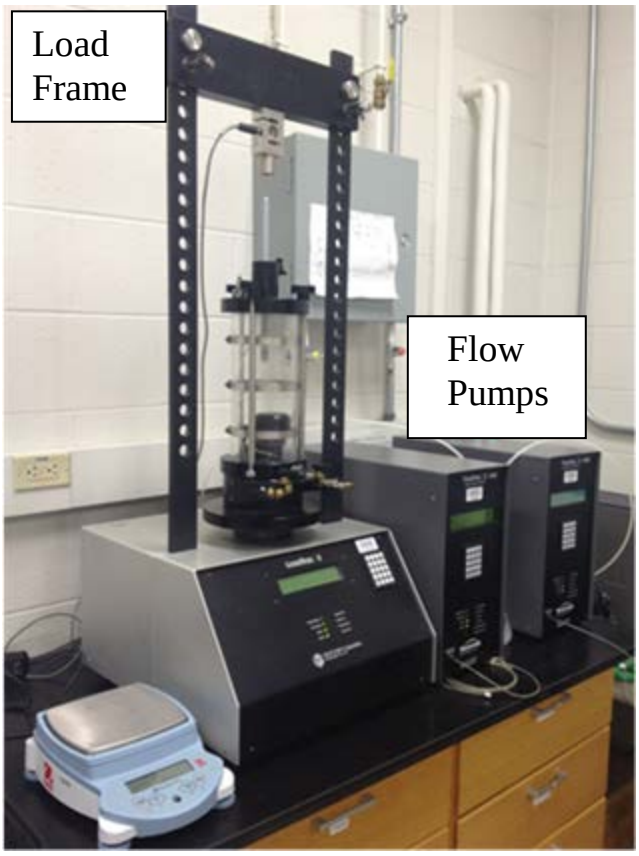

Figure C.16 Triaxial load frame and flow pumps used in the saturated CIU tests.

Specimen Fabrication for Saturated Triaxial Testing

ASTM D4767, Standard Test Method for Consolidated Undrained Triaxial Compression Test for Cohesive Soils was used as guidance for saturated triaxial testing; therefore the procedures presented herewith are in general accordance with this standard, with some modifications. A split mold as shown in Figure C.17, was designed and machine fabricated to be used for fabricating consolidated isotropic undrained (CIU) triaxial specimens. Details for the split mold for fabrication soil specimens for the consolidated isotropic undrained triaxial tests are included in Appendix C.4.

Figure C.17 CIU specimen molding system consisting of split mold, top and bottom pistons, spacer rings, extruder piston, and the static compactor.

Similar to the fabrication of the soil-water retention test specimen, a batch soil mix was made for each of the four Kentucky clay type soil tested, at their standard Proctor optimum moisture content. After storing the batch mix for at least one day for moisture equilibrium, triaxial specimens were fabricated using the Durham Geo-Enterprises Model S-242 Static Compactor and Extruder. In fabricating the specimens, spacer rings were used in conjunction with the static compactor, the pistons, and the split mold to develop a preset volume at which samples for each lift were compressed. The system of spacer rings, mold, pistons and the static compactor are shown in Figure C.17. Five compacted lifts, each of approximately 25.4 to 31.0 mm (1.0 to 1.22 inches) in height and 73.0 mm (2.875 inches) in diameter constituted the fabricated specimen. Vanapalli (1996), presented similar procedures for preparing compacted specimens. The predetermined soil weight, based on the preset lift volume, to achieve the desired specimen density for each lift was obtained from the batch mix. The initial lift was statically compacted without any spacer ring to the predetermined height of 25.4 mm (1.0 inch). Each subsequent lift was placed with the use an added spacer ring of height, 31.0 mm (1.22 inches), to create the desired volume for the current lift as shown in Figure C.18. Prior to the placement of a subsequent lift, the latter compacted soil layer was scarified to prevent planar weaknesses between compacted layers. Each subsequent lift was also placed and compacted on alternating ends of the specimen. The fifth and final lift was placed using a fourth spacer ring (Figure C.18).

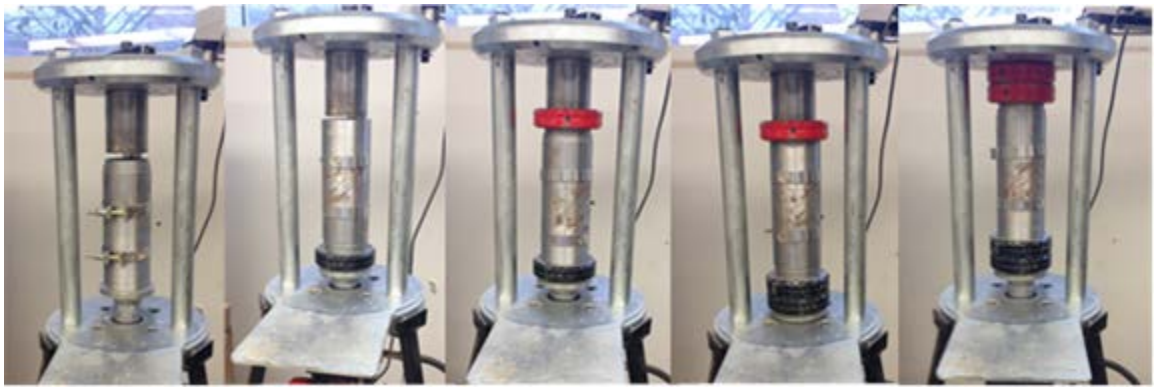

Figure C.18 Series of sequential layered/lift compaction process for triaxial specimens.

At the completion of fabricating the specimen, a small soil sample from the batch mix was taken for moisture determination. The pistons were removed and the split mold opened in order to remove the specimen. For the high plastic soils, it was found that sometimes, the soil capillary suction forces exerting on the surface of the bi-split (two sections) compaction mold were high enough to cause the sample itself to split upon removal from the split mold. Therefore, the high plastic soils specimens were extruded using the static compactor/extruder. Sivakumar (1993) and Sharma (1998), used a bi-split mold similar to this study, but other researchers, such as Salem, (2006), and Chen, (2007), used tri-split and quad-split molds respectively to avoid this problem. To extrude the specimen, the split mold was braced at the top rim of the static compactor/extruder, and the extrusion piston advanced to push the specimen out. The A photo image of a typical saturated triaxial specimen is shown in Figure C.19.

Figure C.19 Typical CIU triaxial soil specimen.

The removed specimen was weighed and dimensioned using the average of three heights and three diameter measurements. The total height of the triaxial sample was preselected to be at least twice that of the specimen diameter, therefore, the lengths to width ratios of all the saturated triaxial specimens were at least 2:1. After fabrication, weighing and dimensioning, the compacted specimen was then protected from moisture loss by skin wrapping in a plastic wrap, placing in an industrial plastic bag and sealed. Skin wrapping constitutes placing of the plastic wrap in contact with all surfaces of the samples, which aided in preventing moisture loss. The protected specimen was then stored for a minimum of two days to allow dissipation of excess pore pressures developed during compaction. Though storing of the specimen for excess pore pressure dissipation is not required by ASTM D4767, this procedure was performed to be consistent with the testing procedures of the unsaturated triaxial specimens.

Mounting of Specimen for Saturated Triaxial Testing

In accordance with ASTM D4767, a wet mounting procedure of the specimens into the triaxial cell was performed. Since the base and top platens had protruding Bender elements, the filter paper placed between the sample and the platens had the center cut-out to accommodate the protrusions as shown in Figure C.20. The triaxial apparatus tubing were filled with de-aired water and the filter paper wetted before placement on the base platen.

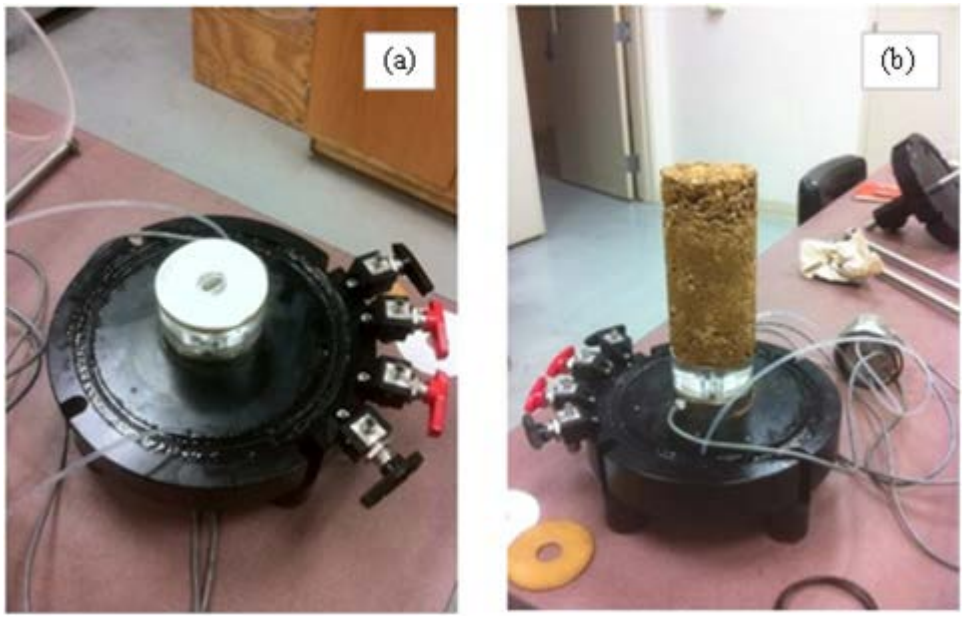

Figure C.20 (a) bottom platen of cell with Bender element and cut-out filter paper; (b) remolded clay sample placed on base pedestal.

The compacted specimen was removed from its protective wrap, re-weighed and re-dimensioned, then placed on the wetted filter paper on the base platen. The specimen was pressed firmly unto the protruding Bender element for positive contact between the element and soil. For a specimen that may require high forces for proper seating on the protruding element, a small slit cut was first made to allow ease of seating such that the

forces necessary for seating does not destroy or affect the specimen. A saturated vertical filter was then placed on the perimeter of the clay specimen as shown in Figure C.21, to aid in saturation and uniform moisture transfer during saturation,

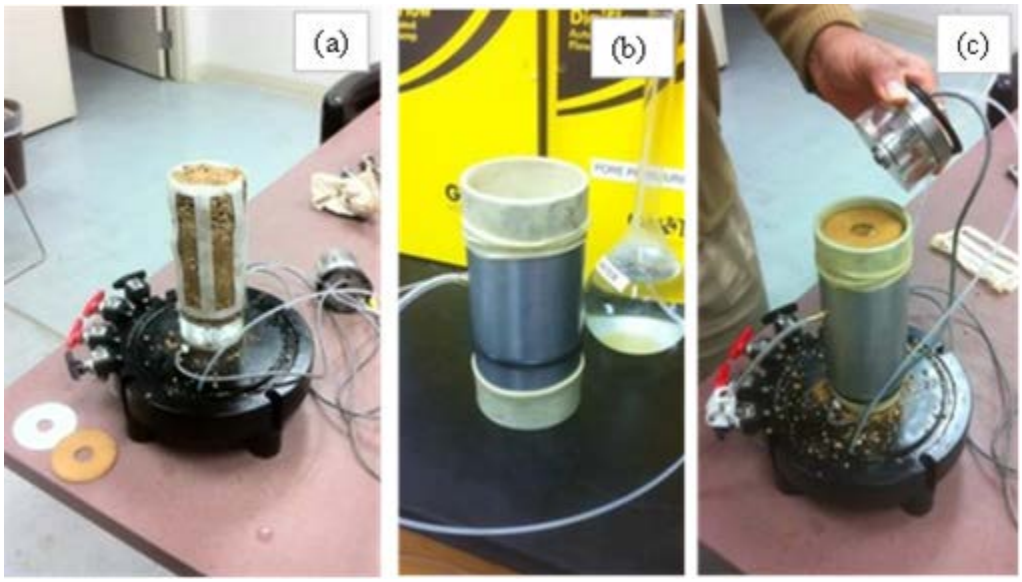

Figure C.21 (a) vertical filter paper placed around remolded clay samples; (b) membrane stretcher with vacuum suction of latex membrane for placement around the sample; (c) placement of top cap platen containing an embedded Bender element.

A latex membrane, stretched on a vacuum mold with applied vacuum to keep the membrane stretched and open, was placed over the specimen. With the vacuum mold removed, a saturated filter paper was placed on the top of the specimen, followed by a porous stone and the top platen. The membrane sealed the sample by use of rubber O-rings holding the membrane against the top and bottom platens. The top platen also included a protruding Bender element and was placed in such a way to minimize detrimental effects on the soil specimen, but with positive contact, and aligned with Bender element on the base platen as shown in Figure C.21(a). The acrylic cell and top cap was then placed over the sample, secured and the loading rod extended down carefully to be in contact with the top platen as shown in Figure C.21(b).

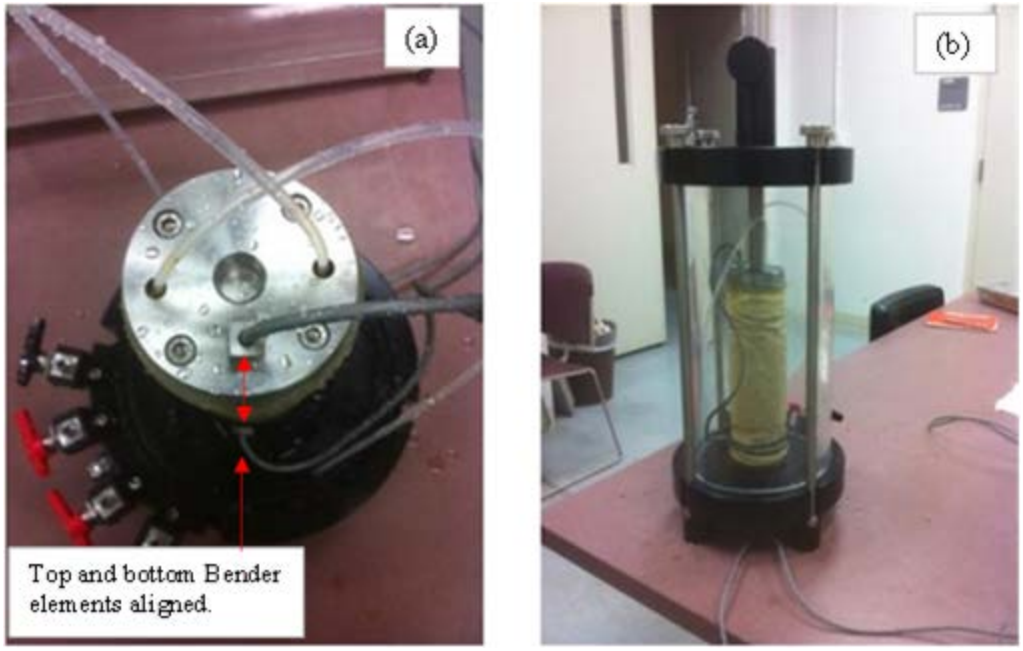

Figure C.21 (a) alignment of the bender elements for proper function, (b) final configuration of bender element test cell.

Saturation of Specimen for Saturated Triaxial Testing

Saturation of the triaxial specimen for CIU tests was performed using de-aired water in two phases. A flooding phase and a back-saturation phase. With the specimen connected to the Flow Trac II sample pressure controllers and the triaxial cell connected to the Flow Trac II cell pressure controller, a sample pressure of 6.89 kPa (1 psi) was used to flood or push water through the specimen from the bottom, allowing entrapped air to escape through the top of the specimen that remained open to the atmosphere. A slightly higher pressure of 13.78 kPa (2 psi) was used to apply a cell pressure, to keep a positive effective pressure on the specimen, and to ensure the membrane does not de-couple from the specimen. The flooding process was performed manually independent of the Triaxial software. It is recommended that the software be used to monitor for changes in deformation or pressure from possible collapse or swelling of the sample. Flooding of

the specimen allowed water to traverse the sample upwards resulting in a wetting front that is noted as flooding continued. Monitoring of the volumetric changes during the wetting front and performing Bender element testing during the wetting front allowed for analysis of shear modulus with wetting. Flooding was continued until at least 750 ml of water had been collected from the effluent line connected to the top of the specimen.

After flooding, the effluent line valve connector was closed and the sample no longer open to the atmosphere. Automation of testing was now performed by the Triaxial software commencing with back saturation by increasing the cell and sample pressures of 723.9 kPa (105 psi) and 68.5 kPa (100 psi) respectively for an effective pressure of 34.5 kPa (5 psi). The pressure increases were performed at a rate of 3.54 kPa/min (0.5 psi/min). The pressures were then held until saturation achieved based on a Skempton pore-pressure parameter $B \geq 0.95$. The B parameter was determined by closing the sample drainage valve and recording the saturation back pressure and the sample pore pressure. Then, an increase in cell pressure of 5 kPa above the saturation back pressure was applied and the sample pore pressure monitored. The result of the ratio of change in the sample pore pressure to the change in cell pressure constitutes the B parameter.

Consolidation of Specimen for Saturated Triaxial Testing

Upon completion of saturation, the specimen was subsequently consolidated. Since the specimen was now considered to be fully saturated without any air-phase, consolidation was performed under a drained water-phase condition. The specimen was isotropically loaded by increasing the applied effective stress, which was achieved by only increasing the cell pressure and keeping the sample pressure constant at its back

saturation pressure to achieve an effective consolidation pressure of 68.95 kPa (10 psi). The rate of increase of the cell pressure was 3.54 kPa/min (0.5 psi/min). The water expelled from the specimen during consolidation was measured and used as the indication of sample volume change. Bender element tests were performed during consolidation with procedures as discussed in the succeeding Section 3.7 of this Chapter.

The selected rate of loading during the isotropic consolidation phase was 3.54 kPa/min (0.5 psi/min), and the selected axial strain rate of loading during the shearing phase was 3 %/hr (0.05%/min). Typical strain rates in literature for consolidated undrained tests generally range from 0.05 to 1 %/min (Maleki and Bayat, 2012).

Procedure for Shearing of Saturated Triaxial Testing

Shearing was also performed after the monitored volume change during consolidation induced the specimen was in a secondary consolidation phase (i.e., the rate of change of volume change with time is minimal with only residual changes in volume). A strain-controlled rate of 3 %/hr (0.05%/min) for vertical axial loading was used. This strain rate was at the minimum rate of 0.05 to 1 %/min, generally used for saturated undrained tests (Maleki and Bayat, 2012). Shearing of the specimen was performed under an undrained condition, thereby, no volume change was allowed to occur.

Unsaturated Triaxial Testing

Apparatus for Unsaturated Triaxial Testing

The unsaturated triaxial testing system of apparatus used in this study consisted of load frame machine, three standard pressure volume controllers, a double walled triaxial cell, a pneumatic pressure controller, a data serial acquisition pad, and the bender element system, all manufactured and sold by GDS Instruments, with headquarters in Hook, Hampshire, United Kingdom.

The GDS load frame model GDSLF50, is rated for a maximum loading capacity of 50 kN (67,443 kips), and can operate in either speed or displacement control mode. The load frame is shown in Figure C.22. The standard pressure volume controllers model STDDPC are shown in Figure C.23. The STDDPC are rated for maximum pressures of 3 MPa (435 psi), and have a volume capacity of 200 mL (12.2 cubic inches) capable of resolution of volume measurements of 0.001 mL (6.1×10^{-5} cubic inches). They can be used for both water pressure source and water volume change gauge, as such, each of the three STDDPC were used to control the cell pressure in the outer cell, the cell pressure and volume changes in the inner cell, and the pore-pressure within the specimen.

The inner and outer cell are the two compartments of the 150 mm double walled triaxial cell, with the inner cell wall composed of Perspex, and the outer cell wall of glass, and reinforcing outer rings. The double walled cell was used to control the radial stretch/creep of the cell wall that typically occur with use of a single walled cell, by allowing no pressure difference across the inner cell wall. This allowed for more accurate volume change measurements of the inner cell water volume, which can

therefore, be attributed to sample volume change. The 150 mm double walled triaxial cell is designed for use with 50 mm (2 inches) diameter specimens. A high air-entry porous disk (HAEPD) is bonded into the base pedestal to separate the pore-air and pore-water, and thereby maintain differential pressures, and a bender element is also bonded in the center of the HAEPD and base pedestal as shown in Figure C.24. The top cap is equipped with a bender element, and pore-air pressures are applied through the top cap. The triaxial cell is equipped with an internal, submersible load cell, rated with a maximum load capacity of 8 kN (1,800 lbs). A great advantage of the internal submersible load cell is that the pressure does not affect the load readings, therefore no corrections for ram upthrust and friction of the ram is necessary. A schematic of the double wall triaxial cell is shown in Figure C.25.

Figure C.22 GDS 50 kN capacity load frame and double walled unsaturated triaxial cell configured for testing.

Figure C.23 Standard pressure volume controller v2, STDDPC.

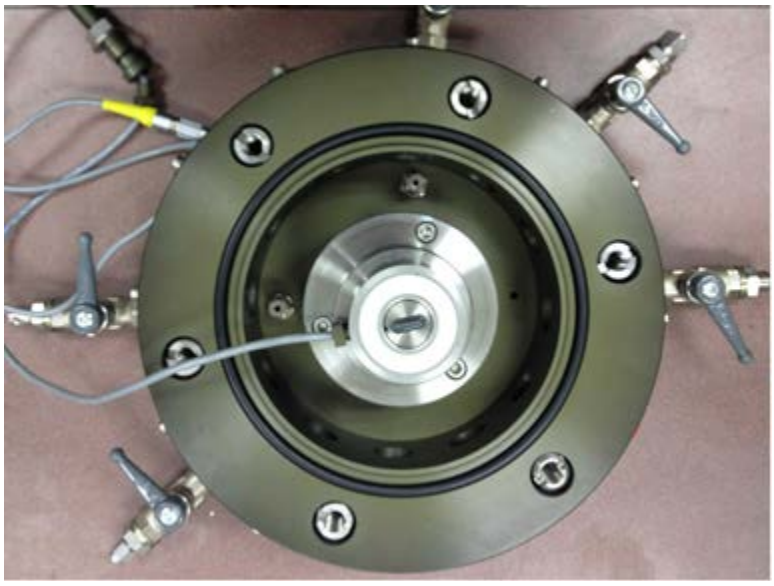

Figure C.24 Base pedestal of double walled unsaturated triaxial cell showing HAEPD and bender element centered on base pedestal.

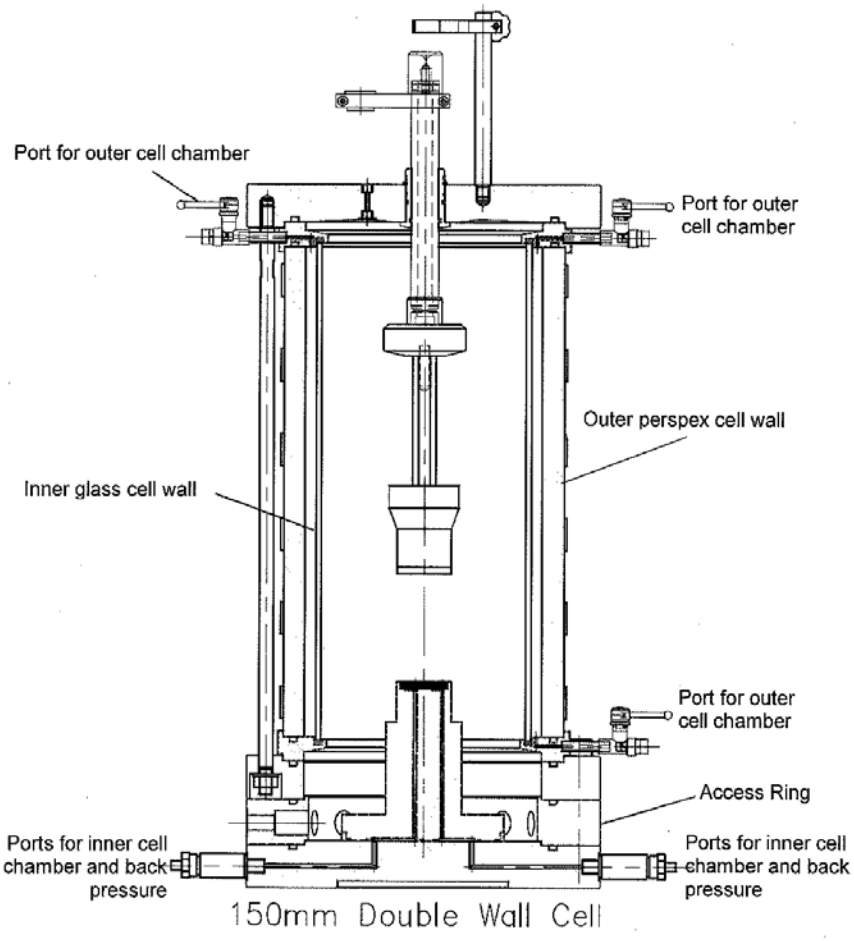

Figure C.25 Schematic of the 150mm double wall unsaturated triaxial cell.

The GDS pneumatic pressure controller (GDSPPC) was used to automate the control of the pore-air pressure applied to the specimen. The GDSPPC is the bottom control box shown in Figure C.26. An external house air pressure source was input into the GDSPPC and it provides a regulated output air-pressure. Control of air pressures are done by the attached PC and software. The GDSPPC is capable of controlling 2 channels of air pressure output, though for this study, only 1 channel was used.

The data acquisition device is an 8 channel serial pad, and was used to acquire the data from the load cell, displacement transducer, pressure transducer for ambient pressure monitoring, and the air pressure controller. The data acquisition device is the top control box shown in Figure C.26. For full automation, test control and data acquisition, the triaxial system was networked with a computer that ran the GDSLAB Triaxial software

Figure C.26 Control boxes for unsaturated triaxial testing: (bottom) GDS pneumatic pressure controller, GDSPPC; (middle) bender element master control box; and (top) data acquisition 8 channel serial pad.

The bender elements embedded in the top and bottom cap of the triaxial cell were connected to the bender element master control box which is the middle box shown in Figure C.26. The bender element master control box is directly connected to a PC that ran the bender element control software, GDSBES. The GDSBES is independent of the triaxial testing software GDSLAB, but both were installed and ran on the same PC, and both can be run simultaneously.

Specimen Fabrication for Unsaturated Triaxial Testing

The fabrication of unsaturated triaxial test specimen is very similar to that for fabricating saturated triaxial test specimen as previously discussed under the heading "Specimen Fabrication for Saturated Triaxial Testing, in the Saturated Triaxial Testing Section of Appendix C.2, and therefore briefly discussed herein. The significant changes to the fabrication procedures are that of the size of the mold and pistons used to fabricate the specimen, the number of layers or lifts and their thicknesses, hence the total size of the specimen.

The split mold as shown in Figure C.27, with the top and bottom pistons were designed and machine fabricated to be used for fabricating unsaturated triaxial specimens. The split mold was fabricated with dimensions of 50.8 mm (2 inches) internal diameter, and 177.8 mm (7 inches) in height. The detailed designs for the split mold and pistons for the fabrication of unsaturated triaxial soil specimens are included in Appendix C.4.

Figure C.27 Unsaturated triaxial specimen 2 inch internal diameter split mold, spacer rings, extruder piston, and the static compactor.

As with fabrication of specimen for saturated triaxial tests, a batch mix at the standard Proctor optimum moisture content was prepared, then stored for at least one day for moisture equilibrium. The static compactor shown in Figure C.27 was used to compact each of four layers of soil with the use of spacer rings. The first layer of soil was compacted without a spacer ring, with an approximate layer thickness of about 36.1 mm (1.42 inches), and the latter three layers, compacted at alternating ends of the specimen (see Figure 3.35), were approximately 28.7 mm (1.13 inches) thick. This constituted a total specimen average height of 122.2 mm (4.81 inches) and 50.8 mm (2

inches) average diameter, resulting in a length to diameter ratio of about 2.4. All layer for each specimen were compacted to the same density based on the predetermined volume of each layer by using the soil mass necessary to achieve the desired density. Three specimens, compacted to different densities, were made for each of three of the Kentucky clay type soils

A moisture content test was made using the loose batch mix. As with the saturated samples, the high plastic soil (i.e., the elastic silt soil from Lee County, LCesilt) was extruded (pushed out) using the extruding capability of the static compactor, instead of opening the split mold for removal. The specimen was weighed and dimensioned, skin wrapped for protection of moisture loss, sealed and stored for a minimum of 48 hours, allowing any developed pore-pressure to dissipate. After 48 hours, the specimen was mounted in the GDS unsaturated triaxial cell in a process very similar to that for the saturated triaxial specimens as previously discussed in Section 3.6.1.3. A remolded unsaturated triaxial specimen that is being mounted in the GDS triaxial cell is shown in Figure C.28.

Figure C.28 A typical unsaturated triaxial specimen being mounted on the GDS triaxial cell for testing.

Saturation of High-Air Entry Porous Disk

The high-air-entry porous disk (HAEPD) is a ceramic disk epoxy sealed into the base pedestal, and it acts as a semipermeable membrane that separates the air and water phases. A 15 bar (1500 kPa) HAEPD was used for this research program. Based on typical values of properties for a 15 bar HAEPD manufactured by Soilmoisture Equipment Corporation, the approximate pore diameter is 1.6×10^{-4} mm and the coefficient of permeability is 2.59×10^{-9} cm/s.

Saturation of the HAEPD is accomplished in three stages and in the following order: Purging; Bottom-up approach; and Top-down approach.

Stage 1 - Purging

Purging ensures all pipework and tubing are purged of air. The connector tubes are purged of air and then connected to the pore-water pressure valve on the base pedestal. A water pressure of 25 kPa (pressure not to exceed 50 kPa) was then applied and the water allowed to flow-through to the non-pressurized connector through the cavity beneath the HAEPD. The non-pressurized connector tube was dipped below the surface of a beaker of water. This procedure was considered complete when no further bubbles were expelled, and none visible in the tubes.

Stage 2 - Bottom-up

The Bottom-up approach involved an application of 30 kPa water pressure to the underside of the HAEPD. The pressure was maintained for a minimum of 24 hours allowing water to pool on the top of the surface of the HAEPD as shown in Figure C.29. The Bottom-up approach removes air from the HAEPD.

Figure C.29 Water pooling on surface of HAEPD during bottom-up phase of the HAEPD saturation process.

Stage 3 - Top-down

The Top-down approach involved pressurizing the HAEPD with water in the normal direction (a reverse approach to the Bottom-up stage). The cell (inner and outer) is filled with water and pressurized to 500 kPa, and the pore-pressure connectors open to the atmosphere (dipped below the surface of a beaker of de-aired water or open to the pore water pressure pump (allows for measurement of outflow if necessary). The pressure was maintained for a minimum of 24 hours if saturation of the HAEPD commenced immediately after the last test, or maintained for a minimum of 48 hours if otherwise. Top-down approach ensures that no air remains in the system.

Procedure for Constant-Water Content Testing

In the constant water content triaxial test, the water content of the sample is not allowed to change by not allowing the pore water pressure to drain (an undrained condition), whereas, the pore air pressure is allowed to drain during testing. There are three major phases of testing which include an *equalization* stage, an *isotropic compression* stage and a *shearing* stage. All stages are performed in the constant water content test mode with the use of the 15 bar HAEPD.

In conjunction with the reasons for using constant-water content (CW) test method presented in the Introduction chapter of this report, presented herein are some reasons for using CW test method for all stages of the triaxial testing:

- Clay and clay type soils, and especially higher plastic soils tend to retain water even under loading.
- The assumption of this study is that volume change under load in field is due to a soil structure change and not of a change in the water phase, (which is essentially true for an as-compacted state), therefore under isotropic compression, CW simulates soil structure change due to the drained air phase.
- Ma et al., (2013) stated that "Unsaturated shear strength parameters are generally obtained from the consolidated drained (CD) or consolidated undrained (CU) triaxial tests, which are not typical stress paths for soils in engineering practice." Even with the anticipated rapid compressions during, and after construction, the excess pore-air pressure is anticipated to dissipate very quickly, possibly, almost instantaneously, (Ma et al., 2012), but the excess pore-water pressure is expected

to slowly dissipate over time. Therefore, the lasting effects of the excess pore-water pressure is a very important aspect in geotechnical engineering problems, such that it could be the cause of slope failure, and long term settlements (Thu et al., 2006).

Equalization stage

This stage allows for the determination of the initial matric suction acting on the specimen after fabrication, and it is a near estimate of the matric suction on the specimen in the as-compacted state. After fabrication and storing of the specimen, the net stress $(\sigma_c - u_a)$ on the specimen was considered to be zero, as both confining and pore-air pressures were atmospheric. This is an assumption that any residual stress from the compaction procedure has dissipated completely prior to testing. Maintaining a near zero net stress, the confining and pore-air pressures are increased simultaneously (axis translation technique) to a predetermined confining pressure at an applied rate of 7 kPa/hr. Since the pore-water pressure in the specimen, cavitation in the water phase below the HAEPD may occur, therefore, the pore-air pressure is increased to bring the pore-water pressure to a value greater than the cavitation limit of less than -1 atm. This process is known as the axis-translation technique, believed to be first used by Hilf (1956).

A small positive net stress is maintained as an aid in keeping the membrane on the sample. The small net stress set at the start of the equalization phase for this research program ranged from 3 to 8 kPa. At the onset of increasing both confining and pore-air pressures, the specimen tend to expel water but since the pore-water pressure is

undrained, no water is allowed to be expelled, therefore the pore-water pressure increases. Equilibrium was inferred when the pore-water pressure readings is stabilized. The initial matric suction of the specimen is determined from the difference between the pore-air and the stabilized pore-water pressures.

During the prolonged time for the equalization stage, air can diffuse through the HAEPD, into the water filled cavity beneath and into the tubing connected to the pumps measuring the pore-water pressure. This can result in erroneous readings if left unchecked, therefore, periodic flushing of diffused air was performed. To flush diffused air, the current pore-air pressure reading was noted. The testing was paused which allowed manual access to the pressure pump regulators. The pore-water pressure pump was set to apply a pressure of 400 kPa to the system to the cavity beneath the HAEPD. The other end of the cavity was connected to a tube with the free end inserted below the water line of a flask (the open end). The other end of the cavity, with the tube and water flask was first opened and then the pore-water pressure port opened to allow the water pressure to flush the deaired water through the cavity, thereby expelling any diffused air in the system. After flushing the pressure port was first closed, then the open end was then closed. The order of opening and closing ports is necessary to avoid pressurizing the water cavity system beneath the HAEPD. The pore-pressure pump is then reset to the current pore-pressure noted just before pausing the test, then the pore-water pressure port opened and testing continued. The volume of diffused air was considered to be small and therefore, not determined for this research program.

Bender Element testing was performed at the end of the equalization stage in accordance with the procedure outlined in Appendix C.3.

Isotropic compression stage

After the equilibrium stage, isotropic compression was performed on all specimens to be triaxially sheared and also on all specimens fabricated solely for subjection to high isotropic compressions (non-sheared specimens). The pore-air pressure was maintained at the maximum value to which the specimen was subjected during the equalization stage.

For each test specimen to be sheared, isotropic compression was first performed in order to bring all specimens to an equivalent baseline reference prior to shearing. A target isotropic compression pressure of 70 kPa was applied to the specimen. This pressure is the minimum pressure in the range of pressures applied during fabrication of the specimen to achieve desired unit weights. Using this pressure for a baseline reference for the specimens to be sheared, the effect of compaction on, or the over-consolidation characteristics of the specimen were not compromised.

For each test specimen subjected only to isotropic compression and not sheared, the specimens were initially, isotropically loading to a net mean stress in the range of 300 to 400 kPa (43.5 to 58 psi), and isotropic unloading to a net mean stress in the range of 70 to 100 kPa (10.2 to 14.5 psi), and finally reloaded isotropically to a maximum net mean stress in the range of 440 to 550 kPa (63.8 to 79.8 psi).

For all specimens, the pore-water pressure was monitored and measured by the pore-water standard pressure volume controller connected to the base pedestal below the

HAEPD. The target isotropic compression pressure was applied at a rate of 7 kPa/hr, which is below the applied rate used and reported by Macari and Hoyos (2001), and Salem (2006), as appropriate without destroying the matric suction within the specimen. The compressions stage was inferred to reach equilibrium when the pore-water pressure readings stabilized. The matric suction at end of the isotropic compression of the specimen is determined from the difference between the pore-air and the stabilized pore-water pressures.

Bender Element testing was performed at the end of the equalization stage in accordance with the procedure outlined in Section 3.7 in this report.

Shearing stage

The shearing stage as with the other two previous stages is performed in the constant water content test mode allowing shearing under a drained condition for the pore-air phase and an undrained condition for the pore-water phase. The pore-air pressure maintained on the specimen during the isotropic compression stage was maintained during the shearing phase. The pore-water pressure was monitored and measured by the pore-water standard pressure volume controller connected to the base pedestal below the HAEPD. The volume change of the specimen was monitored flow of water within the inner cell and measured by the inner cell standard pressure volume controller connected to the base of the inner cell.

Strength testing of unsaturated soils is generally strain-controlled at a constant rate of axial strain, (Fredlund et al., 2012). The strain rate for constant water content tests

should be chosen to ensure the dissipation of the drained pore-air phase and the equalization of the undrained pore-water phase.

Efforts were made to determine the strain rates empirically, but the calculated range of the time to failure was about 220 to 644 days. The resulting strain rates ranged from 0.0057 to 0.0019 %/hr for 30% strain at failure. The calculated times to failure were determined to be unreasonable for constant water content tests.

The constant strain rate of 0.5 %/hr (0.0083 %/min) was selected and used in shearing at constant water content, based on the study by Ong (1999) which showed that strain rates ranging from 0.009 to 0.081 %/min resulted in consistent matric suction readings in constant water content tests. The pilot study by Ong (1999) also showed that at the strain rate of 0.009 %/min, the pore-water pressures within the sample had dissipated well due statistically equivalent pore-water pressures at the ends of the specimen. The selected strain rate of 0.5 %/hr is equivalent to a time to failure of 2.5 days for a total strain of 30%.

APPENDIX C.3 Soil Shear Modulus Testing Procedures

Laboratory Scale Model Testing

Bulk Soil Apparatus

To simulate field testing conditions, a program was developed to include the use of bulk soil, whereby larger field type instrumentations can be used for soil property determination. A large containment was constructed for placement of bulk soils to be tested when incrementally compacted. Figure C.30 shows a schematic rendering of the constructed bulk box, built of wood that are mainly of a minimum nominal size thickness of two inches, and the base is of a nominal thickness of one inch. The interior of the bulk apparatus was coated with an impervious liner to ensure the absorptive nature of wood does not affect the soil condition in the apparatus. The as-build apparatus has interior length, width and height dimensions of length 38.60 cm by width 38.35 cm and by height 34.48 cm (15.2 by 15.1 by 13.67 inches).

Bracing was applied to the containment bulk apparatus to limit the lateral deflection that may be occur to reasonable lateral deflections that may occur in the field during compaction and also to distribute the loading equally along the height of the face of the containment. The bracing included the use of two sets of steel bars and rods with steel bars on opposite faces of the bulk containment apparatus and braced together with the steel rods. The bracing were placed at one-third heights of the bulk containment with each face having one steel bar and one steel rod. Steel plates that extend across both wood seams/joints at one-third heights, were placed between the bracings and the faces of

the bulk containment to redistribute and transfer lateral loads throughout the faces of the bulk containment. The bracing configuration is shown in the photo of Figure C.31.

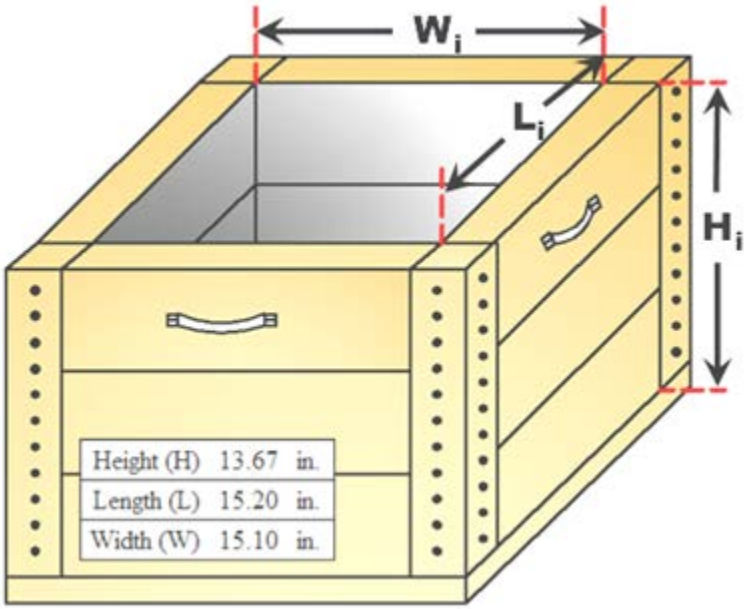

Figure C.30 Schematic of bulk soil compression containment apparatus with interior dimensions.

Figure C.31 Bracing of the bulk soil compression containment.

Earth Pressure Cells

The Earth Pressure Cells used in this research were of Model 4800 manufactured by Geokon, Inc., with headquarters in Lebanon, New Hampshire. Three Earth Pressure Cells were used to measure the transfer of loading during compaction of the bulk soil specimens, and placed at the bottom (for vertical loading transfer measurements) and on two adjacent sides (for lateral loading transfer measurements). Figure C.32 shows the Earth Pressure Cells and their configuration within the bulk containment apparatus. The Earth Pressure Cell on the bottom had a loading capacity of 1 MPa, and the two on the sides had loading capacities of 350 kPa. The Earth Pressure Cells were all of height 6 mm by diameter 230 mm (~ 1/4 inch by 9 inches).

Figure C.32 Earth pressure cell configuration in the bulk soil compression containment apparatus (an overhead view).

Hydraulic Load Frame

The load frame used to statically compact the bulk soil in the bulk containment apparatus was a Satec series load frame manufactured by Baldwin Southwark division of Southwark-Emery Corporation, who were headquartered in Philadelphia, Pennsylvania. The Satec load frame has a maximum capacity of 1334.47 kN (300,000 lbf). The load frame is shown in Figure C.33.

Figure C.33 The Satec load frame used for the bulk soil compression test.

Specimen Preparation for Laboratory Scale Model Testing

The soils used in the bulk soil compression testing program were the four Kentucky clay type soils also used in the SSSC development. For the four clays herein, each was prepared at four different moisture contents, with at least one prepared to a targeted moisture content below, at, and above the standard Proctor optimum moisture content.

A large soil / concrete open mixer was employed to bring each soil sample to a moisture of 1/2 percent higher than its targeted desired moisture content. Continued handling of the sample causes some moisture content to be lost, and in general, the sample was at or very close to the targeted moisture content by the start of testing. The bulk mixer uses a mixing blade that spins in the opposite direction of the mixing barrel, and also has a scraper to ensure complete and proper mixing of the sample. For the initial test on a soil, the soil was first air-dried and the residual moisture content determined. In the process of mixing, the amount of water added was determined based on the air-dried weight of the soil sample. The water was added slowly and in increments until all the water was added to achieve the desired moisture content. For consequent testing at increased moisture content, the soil moisture content determined at the end of testing was used as the initial moisture content to determine the necessary amount of water needed to achieve the increased moisture content.

The mix sample at the desire moisture content was then placed in 5 gallon plastic containers, sealed, then stored in a cool air-conditioned room for at least 24 hours prior to use for testing to allow for moisture equilibrium throughout the entire bulk soil sample.

Enough soil was mixed for each bulk sample to ensure at least three 5-gallon buckets of soil are available for testing.

Stiffness and Shear Modulus Testing - GeoGauge

The field GeoGauge is generally used to measure soil stiffness in field testing and supports the ASTM D6758, Standard Test Method for Measuring Stiffness and Apparent Modulus of Soil and Soil-Aggregate In-Place by Electro-Mechanical Method. The GeoGauge is manufactured by Humboldt Manufacturing Company, headquartered in Elgin, Illinois, USA. The Humboldt Model H-4140 GeoGauge used in the bulk soil testing program, is capable of measuring soil layer stiffness within the range of 3 to 70 MN/m (17 to 400klbf/in), and the soil Young's Modulus within the range of 26 to 610 MPa (4 to 90 ksi). Figure C.34 shows a photo image of the Humboldt GeoGauge.

Figure C.34 A photo image of the Humboldt Model H-4140 GeoGauge.

After each incremental compaction of the bulk soil by static loading uniaxially within the bulk soil containment, the load was removed, and the soil allowed to rebound. The GeoGauge was then placed on the surface of the bulk soil, simulating field testing conditions and in accordance with ASTM D6758 as shown in Figure C.35. Using an applied vibrating force at 25 different frequencies that causes small deflections less than 0.00127 mm in soil, the GeoGauge determines the resulting stiffness (ratio of force to displacement) of the soil. At least two Geogauge tests were performed for each incremental compaction, by rotating the Geogauge 90 degrees for the second or sequential tests. The stiffness results were averaged for each incremental compaction effort. Knowing the soil stiffness K, the outside radius of the Geogauge ring foot R, and also knowing or assuming the soil's Poisson's ratio ν, the Young's modulus E and hence the Shear modulus G of the bulk was determined at each compaction increment as follows:

$$E = K\frac{(1-\nu^2)}{1.77R} \tag{C.1}$$

$$G = E\frac{(1-\nu)}{2(1+\nu^2)} \tag{C.2}$$

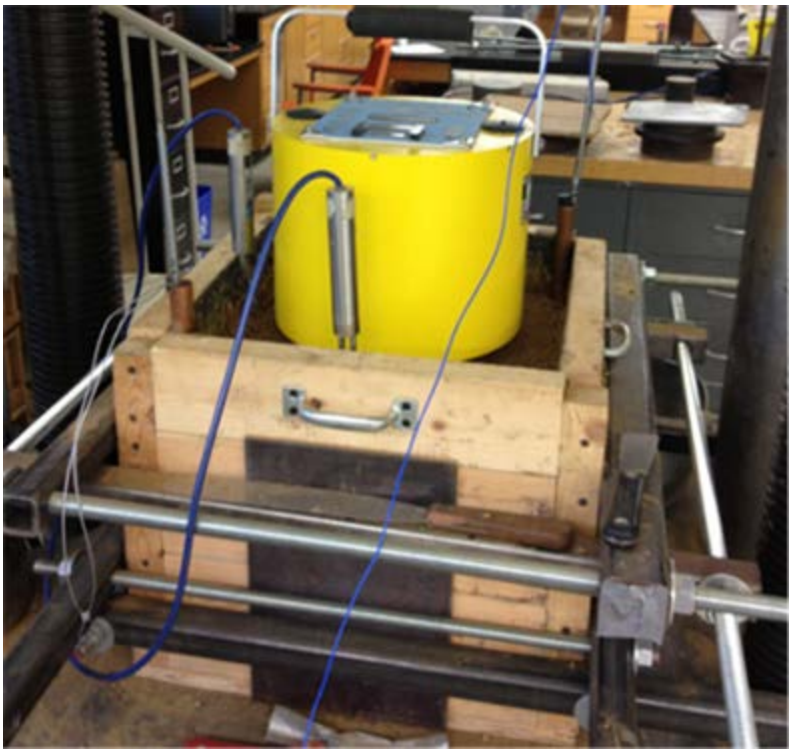

Figure C.35 Obtaining a stiffness measurement with the Humboldt Geogauge.

Stiffness and Shear Modulus Testing - Picoscope

The oscilloscope, named Picoscope for its manufacturer, that was used in this study was designed and manufactured by Pico Technology, headquartered in Eaton Socon, St. Neots, Cambridgeshire, United Kingdom. Oscilloscopes are generally used to observe change of an electrical signal over time, and therefore, have been used in the geotechnical industry and in conjunction with accelerometers to determine vibration wave propagation velocities in soil. The Picoscope model 3200 used is shown in Figure C.36 with the connector ports labelled. This model has bandwidths ranging from 60 to 250 MHz, and real time sampling rates of up to 1 GS/s. The Picoscope interfaces with a PC software via USB. The oscilloscope was used with an electrical hammer (the exciter), shown in Figure C.37, that was used to generate the signal waves by hitting the top of a metal rod

with a wedging system at bottom as shown in Figure C.38. The electrical hammer was circuited through the Picoscope to an accelerometer (the receiver) mounted vertically on a metal rod (receiver rod), as seen in Figure C.39.

Figure C.36 Photo of the PicoScope oscillator, Model 3200.

Figure C.37 Electrical Hammer (the exciter) used to generate wave signals

Figure C.38 Metal rod with wedging system for proper contact at require depth

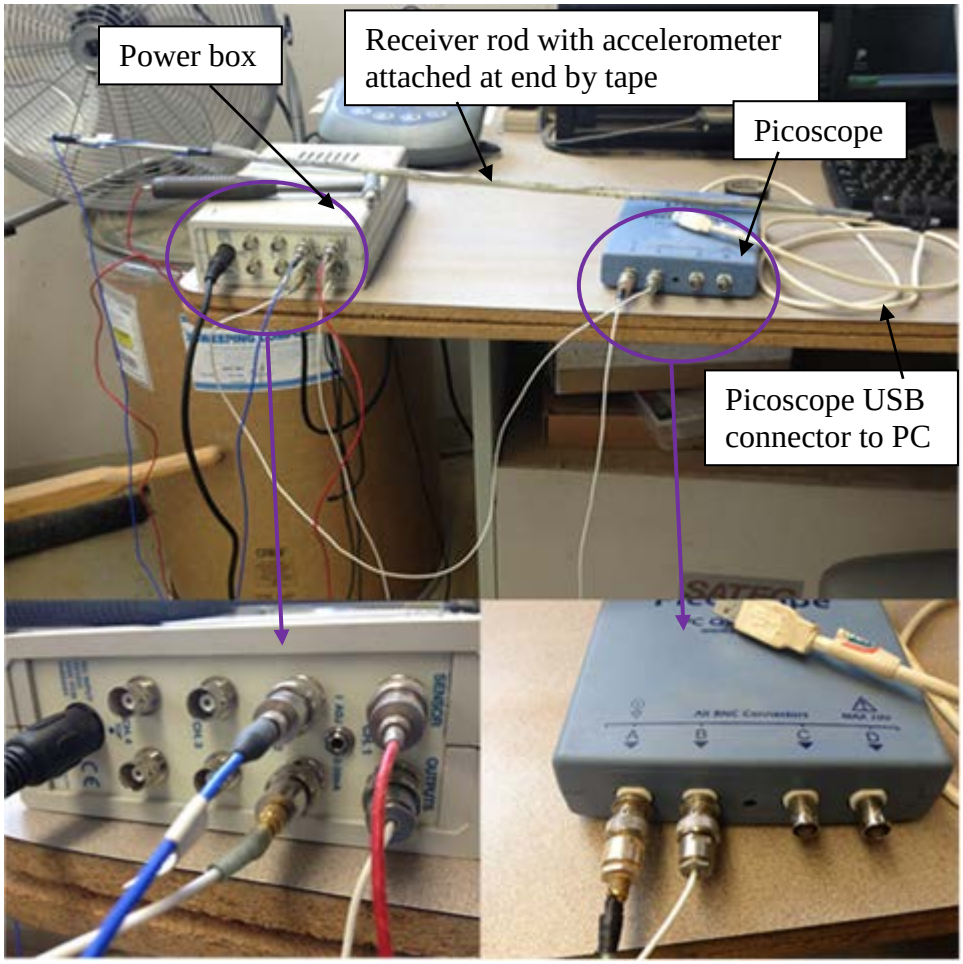

Figure C.39 Connection circuit of Picoscope to the receiver rod with accelerometer, and the electrical hammer

The oscilloscope, hammer and accelerator were used to perform simulations of field cross-hole seismic testing as discussed herein. The accelerometer was attached to the receiver rod by tape, in a vertical position in order for the predominant received wave to

be a shear wave. To determine shear wave velocities using the oscilloscope device, the rod used for transmitting the wave was first wedged in the copper tube at the midpoint depth of the bulk sample. With the receiver rod in the other tube positioned such that the attached accelerometer is also at mid-depth of the bulk sample, the electrical exciter hammer is used to strike the top of the transmitting rod ensuring that the sensor tip strikes the top of the rod perpendicularly. The transmitted wave is logged by the oscilloscope and the received shear wave based on the directional position of the accelerator is also recorded when received.

Figure C.39 shows the USB connector that connects the Picoscope to a PC that has the Picoscope 6 software, which aids in collection, storing and analyzing of the transmitted waves. To aid in data collection, the software allows manual input sampling, and amplitude settings. The software allows the visual display of the source wave and received wave on the same chart axes. The software also allows for exporting of the logged data to other software, for example, to Microsoft Excel software, where further analyses and interpretation of the data can be performed. A minimum of five shear wave tests were performed and the averaged shear wave amplitude at each period used to determine the time of arrival of the received wave. Averaging of the shear wave amplitudes was performed in Microsoft Excel. Averaging of the shear wave amplitude was possible because the sampling time and frequency were the same for each of the five tests. The time of arrival extends from the start of the source wave (the time at which the exciter hammer made contact with the rod) to the first trough characteristic point of the received shear wave data. The shear wave velocity was then determined as the ratio of

the source to receiver distance (the shortest straight line distance between the two copper tubes), and the time of arrival, with units in meters per second:

$$V_s = \frac{Wave\ travel\ length}{Travel\ time} = \frac{L}{t} \tag{C.3}$$

Procedure for the Laboratory Scale Model Testing

The objective of the bulk soil compression testing was to incrementally compact each soil at each of the four moisture contents, from a loose state to a state past the standard Proctor maximum dry density of the soil. At each incremental compacted state, a series of tests to determine shear modulus is performed, and therefore, the effect on density or void ratio on shear modulus can be determined.

Prior to each test, the dimensions of the bulk containment apparatus was measured to ensure no changes to the apparatus has occurred. The Earth Pressure Cells were placed on the bottom and two adjacent sides of the apparatus, then the Type M copper tubes were placed at diagonal ends. For each test, approximately three 5-gallon buckets of prepared soil was used. Each bucket was weighed before and after to determine the total weight of soil placed into the testing apparatus. After each bucket of soil was placed, the soil was carefully levelled, and a small strip of wax paper was placed in one corner and the depth to the soil layer measured. The depths of the wax papers were measured after the final incremental comp active effort and upon careful removal of the soil from the bulk containment apparatus. The measurements of depths of the wax paper aided in the

determination of any density gradient that may occur from the uni-axial form of static compaction loading.

After all the soil was placed in the apparatus, a spray-sealed wooden plate was placed on top of the soil which acted as the interface for compaction load transfer to the soil. Spacers were then placed over the board to extend the top of the soil to be in contact with the bottom of the loading head. The spacers and board exerted an initial load on the bulk sample. This initial free weight static load was determined and the resulting deformation was also determined. The initial free weight static load was added to the compaction load exerted by the loading frame for determination of the total comp active loading effort. The initial deformation was used to determine the initial starting density of the bulk sample. Prior to loading (under free weight loading), a shear wave velocity determination was made using the oscilloscope device in accordance with the procedure discussed in the preceding Section "Stiffness and Shear Modulus Testing – Picoscope", of this Appendix

Static strain loading was commenced to desired incremental depths of about 38, 64, 90, 115, and 140 mm (1.5, 2.5, 3.5, 4.5, and 5.5 inches respectively) to achieve different densities. A strain rate of 5.08 mm/min (0.2 in/min) was used to apply the static strain loading. At the completion of each incremental loading, and with the load still applied, a shear wave velocity determination was made using the oscilloscope device. The compaction load, loading spacers and the wooden soil-load interface plate were removed, and the bulk soil allowed to rebound. Rebound of the bulk soil was considered adequate

and complete when the rate of change in the residual pressure was less than 41.37 Pa/min (0.006 psi/min) as indicated by the pressure cells.

After rebounding of each incremental static comp active loading was complete, shear wave velocity and stiffness determinations were again made by two methods; with the oscilloscope device measuring shear wave velocity and the GeoGauge measuring stiffness. The process of shear wave determination using the oscilloscope, after rebound of the bulk soil, simulated a seismic crosshole field testing of soil, and was made in accordance with the procedures discussed in the preceding Section “Stiffness and Shear Modulus Testing – Picoscope”, of this Appendix.

The stiffness determination using the GeoGauge was made according to the procedure discussed in the preceding Section “Stiffness and Shear Modulus Testing – GeoGauge”, of this Appendix.

The entire process was then repeated to the next incremented depth for a different density, until at least five densities stages were achieved. The last achieved density was generally obtained at depths just short of the targeted 140 mm total deformation. During the comp active static loading, and as the density increases, the loading on the pressure cell must be carefully monitored to ensure that the maximum capacities of the cells are not exceeded.

After the final density is achieved and all testing for shear wave velocities are complete, a Shelby tube was pushed through the compacted bulk soil sample to a predetermined depth just short of the pressure cell installed at the bottom of the bulk containment apparatus. The load frame was used to push the Shelby tube to the desired

depth and extrusion of the tube was done with use of the load frame or by hand. Figure C.40 shows a photo of the Shelby tube placed above the bulk sample prior to being pushed. The extruded sample was trimmed with a wire saw to ensure perpendicular ends. The trimmed sample was weighed and three determinations each of the diameter and height averaged and recorded for use of determining the wet density. The moisture content of the sample was also determined and used to determine its dry density.

Figure C.40 Shelby tube sampling of the bulk soil.

Bender Element Testing

Apparatus for Bender Element Tests

The Bender element system of apparatus used consisted of two Bender elements in each cell for saturated and unsaturated triaxial testing, a Master control box and the GDSBES control and acquisition software, manufactured by GDS Instruments, headquartered in Hook, Hampshire, United Kingdom. The Bender elements are bonded

in titanium with a protrusion of about 2.25 mm (0.089 inch) and inserted into the center of the base pedestal and top caps of the triaxial cell system. Figure C.41 shows the bender elements in the top cap and bottom pedestal attached to the saturated triaxial cell base. For the unsaturated triaxial cell, the Bender element inserted in the base pedestal, is centered on the installed HAEPD as shown in Figure C.42.

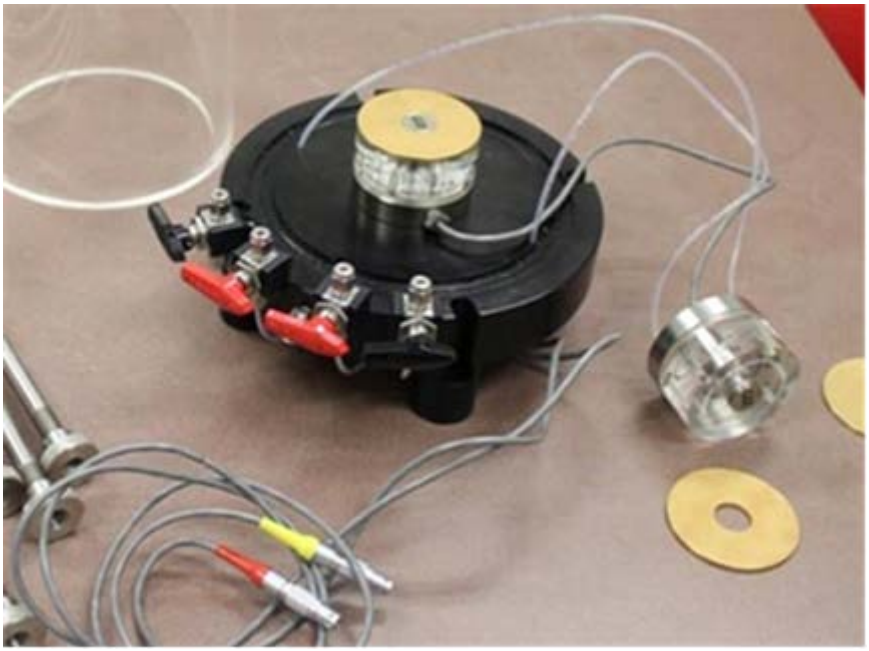

Figure C.41 Bender element inserts in the top cap and bottom pedestal of a saturated triaxial cell.

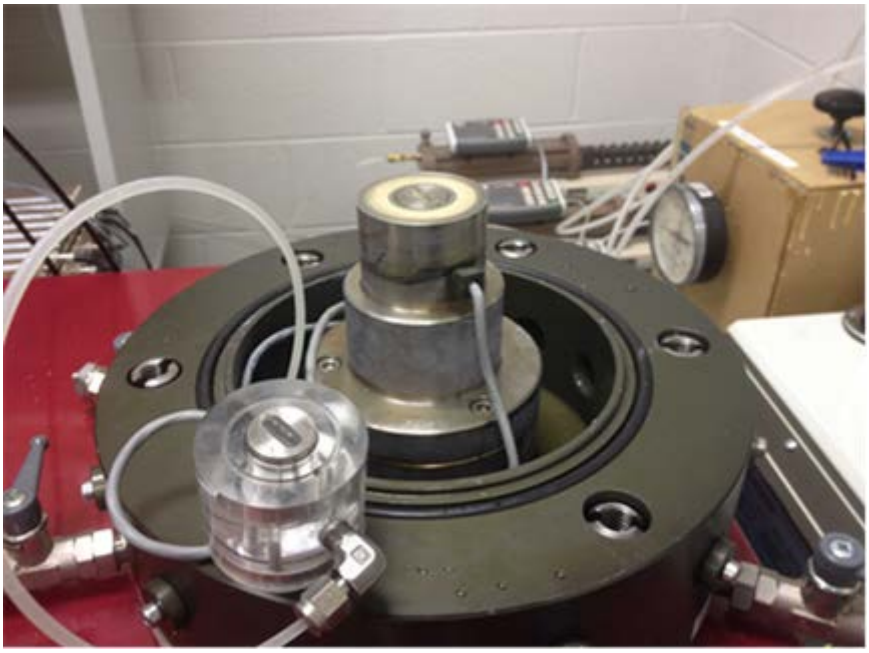

Figure C.42 Bender element inserts in the top cap and base pedestal of an unsaturated triaxial cell.

The Bender elements connects directly into the Master control box used, which is used for signal conditioning and to generate and record the propagated body (P- and S-) wave. The Master control box allows for 16 bit data resolution of the source and receiver signal with sampling rates per channel of up to a maximum frequency of 200 kHz and a maximum voltage acquisition speeds up to 2,000,000 samples/second. The Master control box is connected to a computer that runs the GDSBES control software, which allows for the selection of different source signal types and their control using input parameters for amplitude, period and repeat time. The software also allows for automatic or manual stacking of data to enhance the recorded signal. A schematic diagram of the Bender elements system used for this study is shown in Figure C.43.

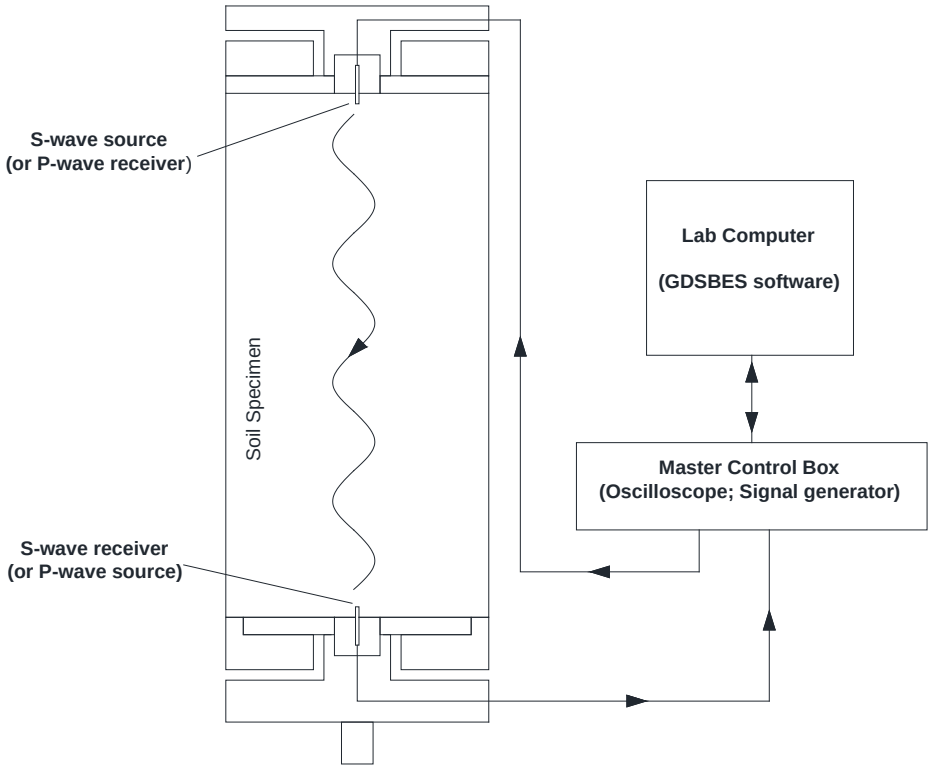

Figure C.43 Schematic of the bender element system.

Bender Element Tests

Bender element tests were performed on all specimens when undergoing triaxial testing. Specifically, Bender element tests were performed on the three CW triaxial specimens that were only subjected to isotropic compressions (non-shear specimens); to the CIU specimens during a wetting front phase, and the isotropic consolidation and shearing phases; and to the CW triaxial specimens during the isotropic compressions and shearing phases. The results of the BE tests during the CIU wetting front phase are not included in this dissertation.

Alignment of the piezoelectric Bender element source and receiver were ensured during mounting the triaxial specimens as suggested by Cherry (1962), Ladd and Dutko

(1985), Bates (1989), Gohl and Finn (1991), and Brignoli et al. (1996). Alignment of the source above the receiver and in the same vertical plane, the dominated transmitted waves will be the shear waves, Cherry (1962).

Excitation Voltage

The Bender element voltage was controlled with GDS Bender Element System software. In order to avoid depolarization, the thickness of the transducer limits the excitation voltage (Leong et al., 2005). An amplitude voltage of 10 V was selected to be supplied to the transmitter. Dyvik and Madshus (1985), Viggiani and Atkinson (1995 a & b), and Callisto and Rampello et al. (2002) used an excitation voltage of 10 V, identical to that used in this research program. High excitation voltage increases the signal to noise ratio, hence, a large received signal form with better defined arrivals (Leong et al., 2005). This made the received signal form easier to interpret.

Waveform

The Bender element waveform signal shapes were controlled with GDS Bender Element System software. A square wave form was used for transmitting the P-waves and a sinusoidal wave form was used for transmitting the S-waves. Square wave forms to excite bender elements were used by Theron et al. (2003), Leong et al. (2005), and Sawangsuriya et al. (2009). Sawangsuriya (2009) noted that the square signal provided a clear response independent of the soil modulus. Leong et al. (2005) noted that the received signal was not of the same form as transmitted, and there was more distortion close to the point of arrival.

Since the S-wave was of more prominence in this research, the sinusoidal signal was used for transmitting S-waves, as its received signal is the same as transmitted and its interpretation is clearer and easier. Dyvik and Madshus (1985), Viggiani and Atkinson (1995 a), and Callisto and Rampello et al. (2002) used the sinusoidal signal similar to that used in this research.

Excitation Frequency

The frequency of the driving signal is automatically adjusted during testing, in order to get optimal amplitude and shape of the received signal.

Travel Time

In literature, the two categories to interpret travel time are time and frequency domains (Fonseca et al., 2009). Time domain include methods such as the Characteristic points (first deflection, first bump/trough, zero crossing, first peak); Cross-correlation; and Second arrival. The time-domain characteristic points are shown in Figure C.44. Frequency domain include a cross-power spectrum calculation of signals (Yamashita et al., 2009). The determination of the arrival time is controversial (Lee and Santamarina, 2005). Salem (2006) reviewed several literature and concluded that the studies are contradicting regarding the preferred approach for travel time determination. This research considered three techniques for determination of travel time. A manual visual technique was used to select the first bump characteristic point. The first bump was selected because, 1) it reduces the errors of the near field effect, and 2) it is the point at which the polarization of the wave signal goes from negative to positive, matching that at the start of the source wave. The other two techniques are automated techniques for first

bump and cross-correlation determination, by use of the Bender Element Analysis Tool (BEAT) software.

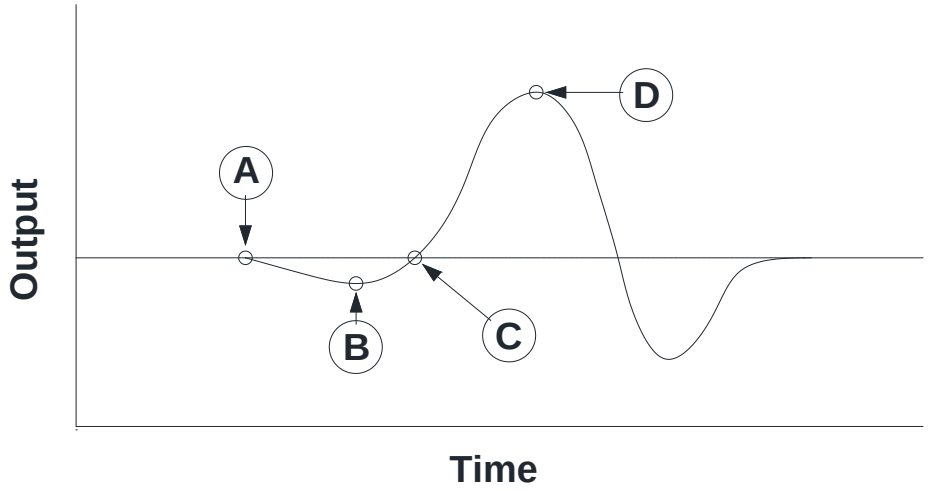

Figure C.44 Idealized received shear wave signal showing the characteristic points (A) first deflection; (B) first trough; (C) zero-crossing; and (D) first peak (reproduced from Lee and Santamarina, 2005)

Testing Procedures

For the CW and CIU tests subjected to shearing, BE tests were made at the end of equilibrium or saturation, end of compression or consolidation, and periodically during shearing with an increased number of tests at the start of shearing to about 2 % axial strain. The increase in tests at the start gave insight into shear modulus behavior prior to initial yielding of the specimen. For the CW specimens only subjected to isotropic compression, BE tests were made periodically, and in general, at increases in net mean stress less than 100 kPa.

The software was used to generate a signal for S-waves. A stack of 10 generated signals were used for each test, with a waveform period of 0.1 ms, a sampling frequency of 100,000 samples/sec, and a sampling time of 2 msec. The BEAT software was used to

determine the travel time t, using the cross-correlation method. The travel distance was determined based on the tip-to-tip distance L between the Bender elements as suggested by Dyvik and Madshus (1985) and consistently applied in BE research testing in literature. The shear wave velocity V_s, was then determined as follows:

$$V_s = \frac{L}{t} \qquad \text{C.4}$$

The shear wave velocity, V_s, and the total mass density, ρ, of the soil were then used in the subsequent relationship to determine the shear modulus G, at small strains as follows:

$$G = \rho V_s^2 \qquad \text{C.5}$$

APPENDIX C.4 Compaction Split Mold Details

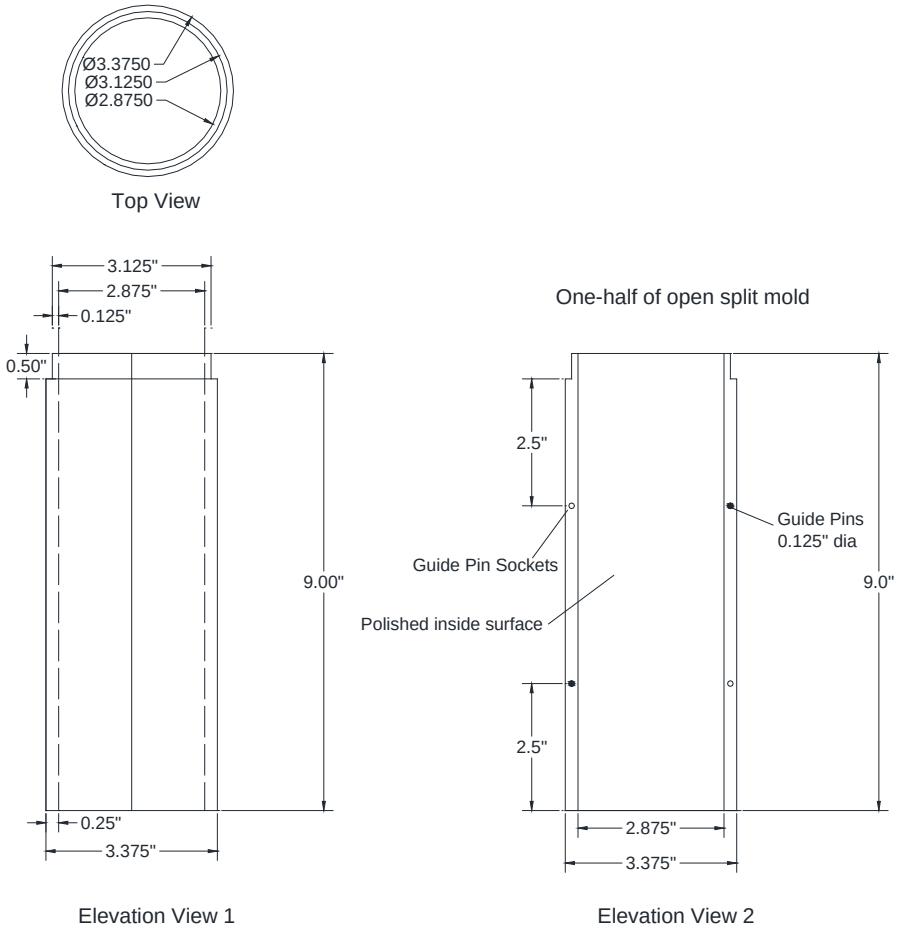

Figure C.45 Details of the compaction split mold for fabricating the saturated consolidated isotropic undrained triaxial test specimens.

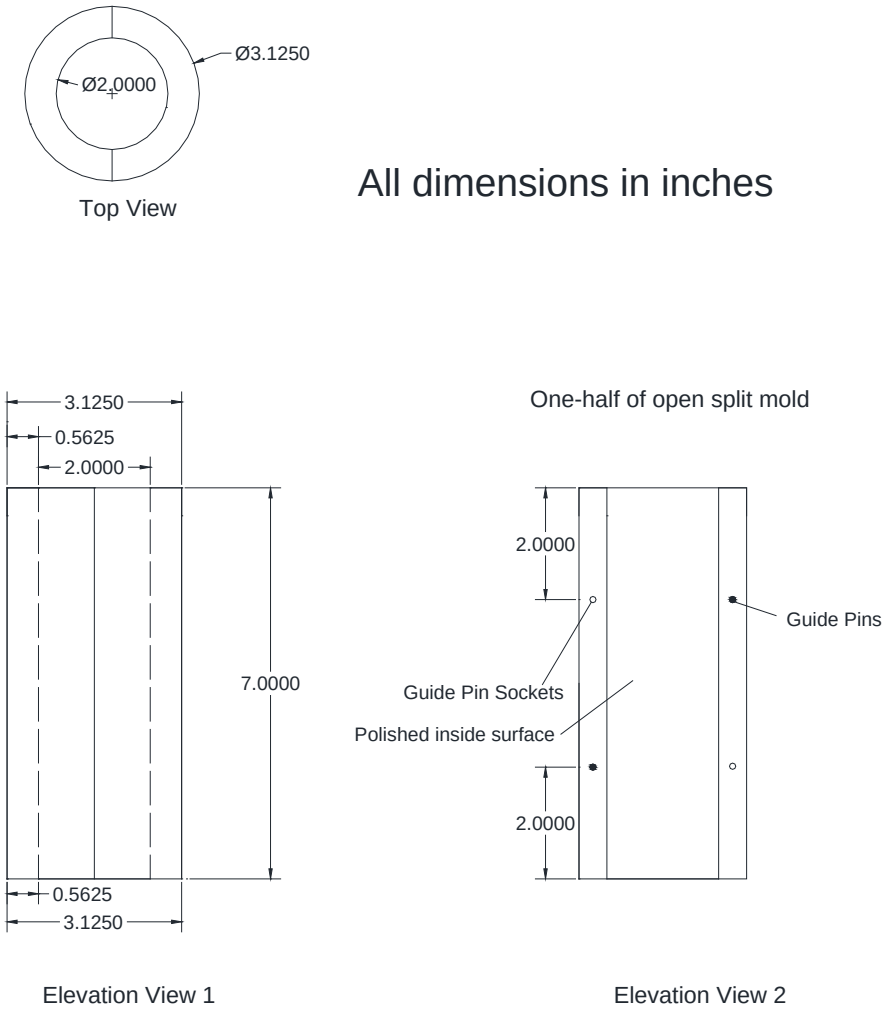

Figure C.46 Details of the compaction split mold for fabricating the unsaturated triaxial and soil-water retention test specimens.

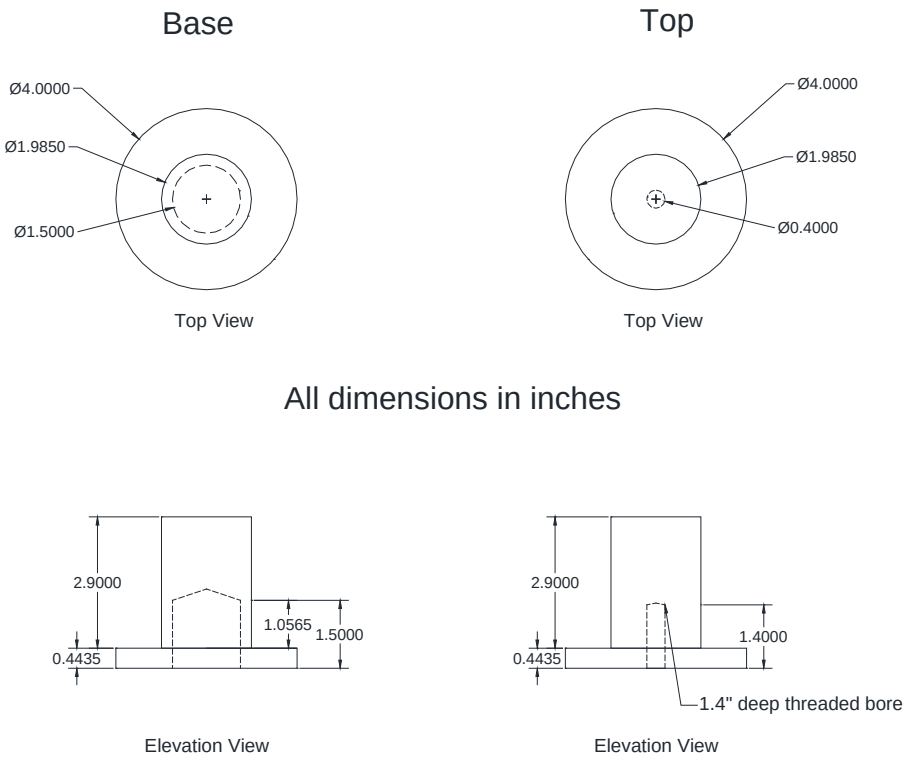

Figure C.47 Details of the top and bottom pistons of the compaction split mold for fabricating the unsaturated triaxial and soil-water retention test specimens.

APPENDIX D

Optimization Process for Model Parameters by a Non-Linear Regression Using the Microsoft Excel Solver Function.

Equation Parameter Optimization Technique

The fitting parameters in the Fredlund and Xing (1994) equation were optimized to fit measured data using Microsoft Excel Solver.

How to install Microsoft Excel Solver

Step 1 - File/Options/Add-Ins/Go/Check Solver Add-In/OK

NOTE: Be sure "Excel Add-ins" is selected in the drop down menu under "Manage:" as shown below.

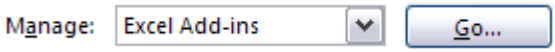

NOTE: Add-ins checkbox should appear as shown below.

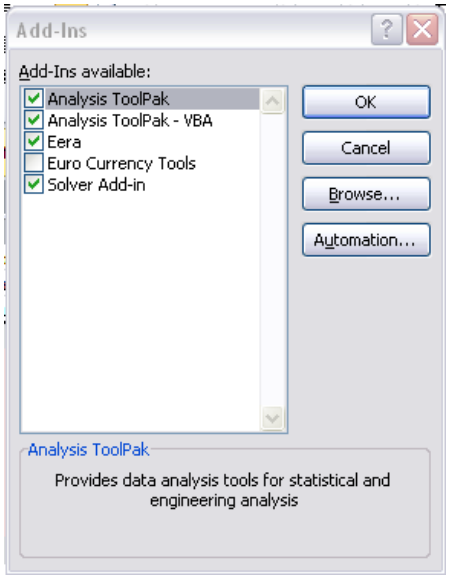

Step 2 - Access Microsoft Excel Solver by selecting the "Data" tab, and then the "Solver" icon at the far right of the graphical interface menu, as shown below.

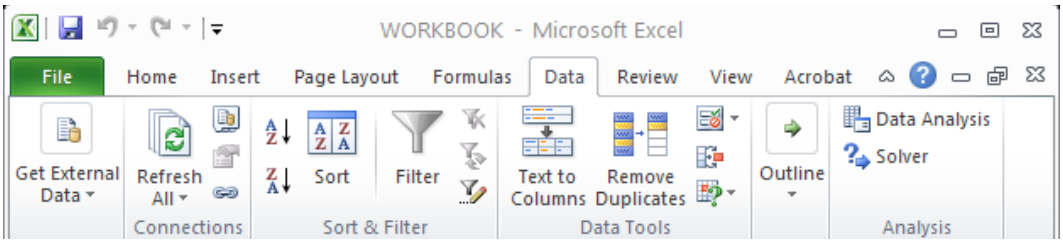

Optimization Procedure

The figures given in this section serve as an example of the methodology used to optimize the Fredlund and Xing (1994) equation parameters. Follow the steps given below.

Step 1 – Set up your parameter optimization spreadsheet as shown in Figure D.1

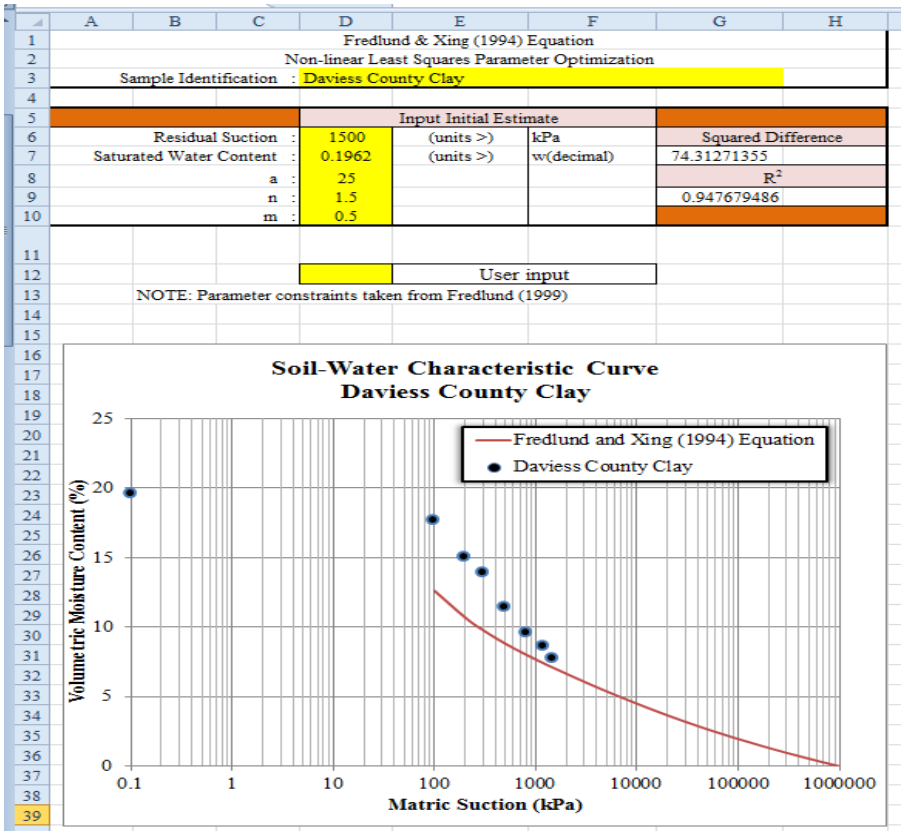

Figure D.1. General Layout of Fredlund and Xing (1994) Optimizer in Microsoft Excel with initial parameter estimates.

- The initial input variables are: **Residual Suction**, **a**, **n**, and **m**. Initial estimates of these variables, as suggested by Fredlund (1999), are given in Table D.1

Table D.1: Initial Parameter Estimates.

Parameter	Coarse Grain Soils	Fine Grain Soils
Residual Suction:	100	1500
a:	2	25
n:	5	1.5
m:	1	0.5

- The **Saturated Water Content** is the measured water content at 100% saturation, input as a decimal.
- The **Squared Difference** given in cell G7 is the summation of the squared difference between the measured and predicted values of moisture content for a given matric suction. See Step 2 for instructions on formatting cell G7

Step 2 – Create the data arrays of measured and predicted data. Figure D.2 shows the arrays of measured and predicted data.

- Bolded data are measured data from laboratory experiments (Note, you may have as many or as few measured points as are available).
- The predicted data are values predicted by utilizing the fitting parameters given in cells **D6**, **D8**, **D9**, and **D10 (Residual Suction**, **a**, **n**, and **m**, respectively).
- The **Corr Factor** in the figure is an independent calculation of the Fredlund and Xing (1994) $C(\psi)$ factor.

$$\theta = C(\psi)\frac{\theta_s}{\left\{\ln\left[\exp(1)+\left(\frac{\psi}{a}\right)^n\right]\right\}^m}$$

$$C(\psi)=1-\frac{\ln\left(1+\frac{\psi}{\psi_r}\right)}{\ln\left(1+\frac{1{,}000{,}000}{\psi_r}\right)}$$

			Test Results		Fitted Results	
			User Input		Predicted Data	
	Units:	Suction	Water content	Water content	Corr. Factor
		kPa	(%)	(%)	C
		0.1	**19.62**	19.62	0.99998975
		1			
		5			
		10			
		50			
		100	**17.75**	12.61290284	0.990076781
		200	**15.057**	10.7024474	0.98075535
		300	**13.975**	9.794688241	0.971966871
		500	**11.44**	8.816819729	0.955767004
		800	**9.6**	8.028047439	0.934277694
		1200	**8.669**	7.400962336	0.909623965
		1500	**7.795**	7.069891429	0.893424099
		3000		6.083876004	0.831081193
		5000		5.390171921	0.774541109
		10000		4.494890789	0.686816114
		20000		3.659428707	0.59060975
		30000		3.1999571	0.531884811
		40000		2.886934981	0.489493233
		50000		2.651366219	0.456298986
		60000		2.463455431	0.429014066
		70000		2.307698925	0.405849065
		80000		2.175032653	0.38572148
		90000		2.059713512	0.367926322
		100000		1.95788095	0.351978722
		200000		1.317450064	0.246543171
		300000		0.964825951	0.184582269
		400000		0.72361883	0.140540632
		500000		0.541351767	0.106345784
		600000		0.395416606	0.078389323
		700000		0.274049087	0.054742436
		800000		0.17036468	0.034252215
		900000		0.079995257	0.016174281
		1000000		0	0

Measured values

Values input *after* optimization

Figure D.2. Initial data array of measured versus predicted data for optimizing fitting parameters (Note: **Bold** and highlighted data from laboratory measurements).

Format for Cell G7: (see Figure D.2)

- Cell G7 is coded as =SUM((E46:E57-F46:F57)^2). *Note: No values are initially given for E47:E50*.
- Instead of clicking "ok" (or hitting "Enter") after cell G7 is coded, execute keystrokes **Ctrl+Shift+Enter**, which utilizes matrix operations in Microsoft Excel.

Format for Cell G9: (see Figure D.2)

- Cell G9 is coded as:
  =1-(SUM((E46:E78-F46:F78)^2)/SUM((E46:E78-AVERAGE(E46:E78))^2)).

  Note: No values are initially given for F47:F50 and G47:G50.

- Instead of clicking "ok" (or hitting "Enter") after cell G9 is coded, execute keystrokes **Ctrl+Shift+Enter**, which utilizes matrix operations in Microsoft Excel.

Step 3 – Access the ***Solver*** and input the **Parameter Constraints** for the fitting parameters in the Fredlund and Xing (1994) equation. Figure D.3 shows the Solver Parameter input screen.

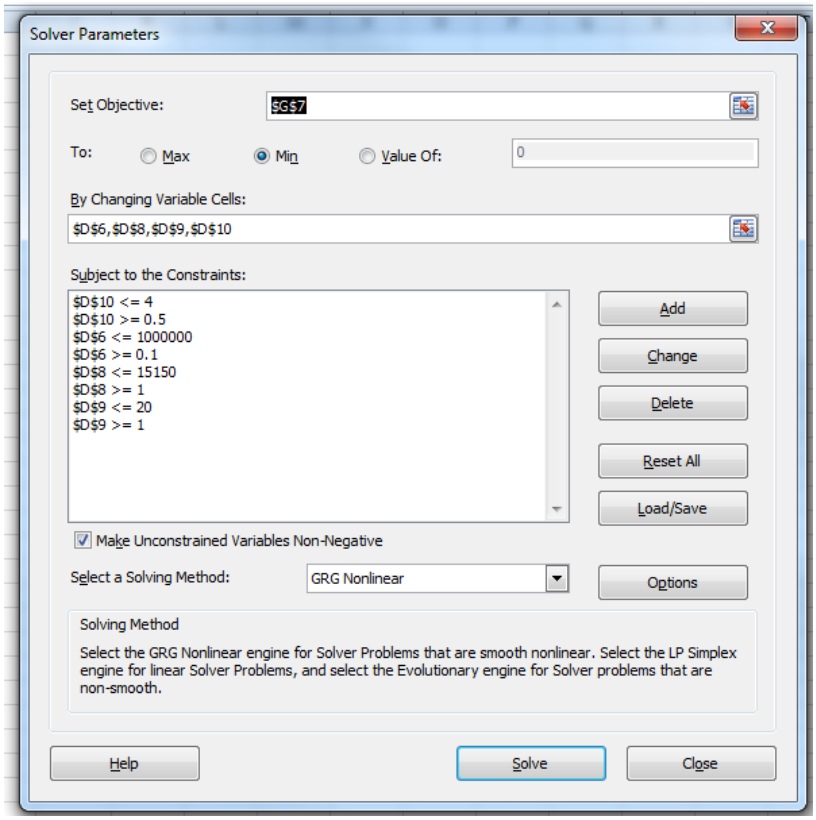

Figure D.3. Microsoft Solver Setup for Optimizing Fredlund and Xing (1994) Equation Parameters.

- Step 3A – Set the location of the **Objective** value. The **Objective** value is the squared difference given in cell G7.
- Step 3B – Set the optimization criterion to Min.
- Step 3C – Determine the variables that will be optimized (By Changing Variable Cells). Here, the cells that will be changed are **D6**, **D8**, **D9**, and **D10**. These cell correspond to the **Residual Suction**, **a**, **n**, and **m**, respectively.
- Step 3D – Add the **Parameter Constraints** for the optimization. Recommended lower and upper boundary constraints for both coarse grain and fine grain soils are listed in Table D.2.

Table D.220: Parameter Constraints.

Parameter	Lower Boundary	Upper Boundary
Residual Suction:	0.1	1000000
a:	1	15150
n:	1	20
m:	0.5	4

Step 4 – Optimize the fitting parameters by clicking the Solve button.

- Microsoft Excel Solver will optimize the fitting parameters (**Residual Suction**, **a**, **n**, and **m**) subjected to the Parameter Constraints (Table D.2) by minimizing the squared difference between measured and fitted moisture content values at corresponding matric suctions. The least squared difference is achieved by setting the Objective value to be the cell containing the squared differences (i.e. cell G7). The sum of the squared differences in cell G7 iterates to a minimum value by changing cells D6, D8, D9, and D10

Step 5 – Plot the results (see Figure D.4).

- Input intermediate suction values such that the SWCC will be continuous from suction of 0.1 kPa to 1,000,000 kPa (i.e. drag the prediction equations to predict **Water Content** and **Corr Factor** values for cells F47:F50 and G47:G50).
- Plot the results using the optimized fitting parameters.

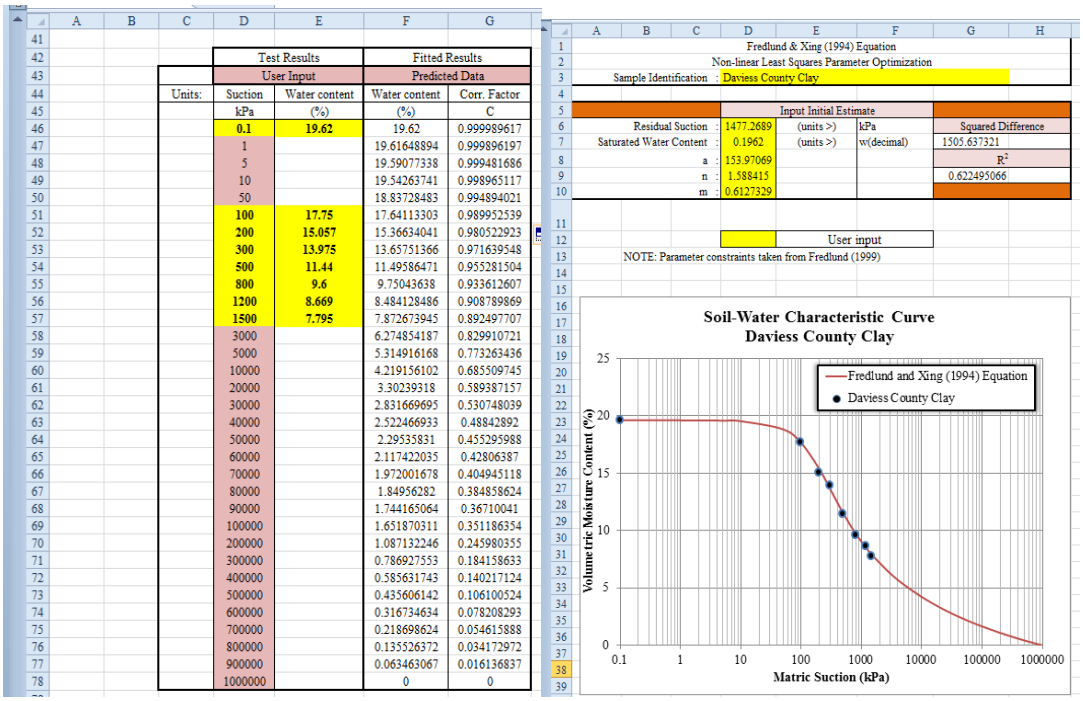

	Test Results		Fitted Results	
	User Input		Predicted Data	
Units:	Suction	Water content	Water content	Corr. Factor
	kPa	(%)	(%)	C
	0.1	**19.62**	19.62	0.999989617
	1		19.61648894	0.999896197
	5		19.59077338	0.999481686
	10		19.54263741	0.998965117
	50		18.83728483	0.994894021
	100	**17.75**	17.64113303	0.989952539
	200	**15.057**	15.36634041	0.980522923
	300	**13.975**	13.65751366	0.971639548
	500	**11.44**	11.49586471	0.955281504
	800	**9.6**	9.75043638	0.933612607
	1200	**8.669**	8.484128486	0.908789869
	1500	**7.795**	7.872673945	0.892497707
	3000		6.274854187	0.829910721
	5000		5.314916168	0.773263436
	10000		4.219156102	0.685509745
	20000		3.30239318	0.589387157
	30000		2.831669695	0.530748039
	40000		2.522466933	0.48842892
	50000		2.29535831	0.455295988
	60000		2.117422035	0.42806387
	70000		1.972001678	0.404945118
	80000		1.84956282	0.384858624
	90000		1.744165064	0.36710041
	100000		1.651870311	0.351186354
	200000		1.087132246	0.245980355
	300000		0.786927553	0.184158633
	400000		0.585631743	0.140217124
	500000		0.435606142	0.106100524
	600000		0.316734634	0.078208293
	700000		0.218698624	0.054615888
	800000		0.135526372	0.034172972
	900000		0.063463067	0.016136837
	1000000		0	0

Fredlund & Xing (1994) Equation
Non-linear Least Squares Parameter Optimization
Sample Identification : Daviess County Clay

		Input Initial Estimate		
Residual Suction	:	1477.2689	(units >) kPa	Squared Difference
Saturated Water Content	:	0.1962	(units >) w(decimal)	1505.637321
a	:	153.97069		R^2
n	:	1.588415		0.622495066
m	:	0.6127329		

User input

NOTE: Parameter constraints taken from Fredlund (1999)

Figure D.4: Fredlund and Xing (1994) Optimizer in Microsoft Excel: (left side) intermediate input data added to create a continuous curve; (right side) measured versus predicted values with optimized parameters.

APPENDIX E

SWCC Test Data and Estimations

Soil water retention property tests were performed for the four Kentucky soils used in this study. The soil samples were subjected to a range of matric suction from zero to 1500 kPa, which was the maximum HAEPD available. Two apparatus were used for testing: an SWCC pressure chamber apparatus and a single cell apparatus. The tests were performed in accordance with procedures, which are presented in Appendix C.1, of this dissertation. The plots of the experimental test data for all four soils are presented in this Appendix, as Figures E.1 and E.2. Figure E.1, presents the experimental data for the DCsclay and the FCesilt soils, and Figure E.2 presents the experimental data for the HCclay and the LCesilt soils. In the figures, the plots labeled (a) show the data with respect to water content and the plots labeled (b) show the data with respect to the degree of saturation.

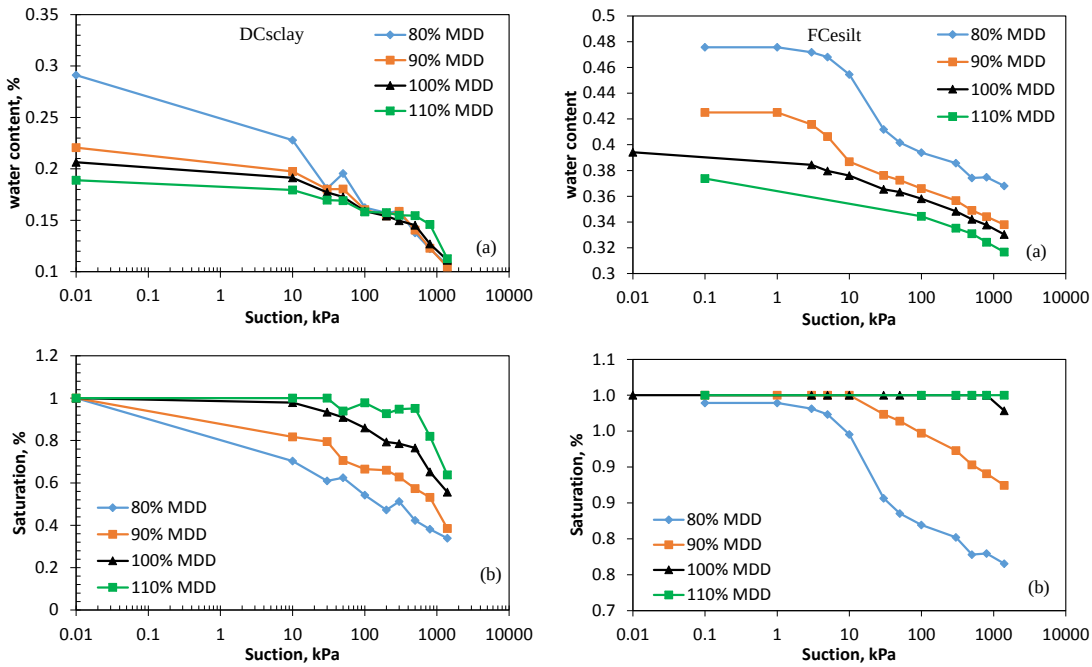

Figure E.1 Experimental soil-water retention test data for the DCsclay (left) and FCesilt (right) soils at different compacted states (a) with respect to water content; (b) with respect to degree of saturation.

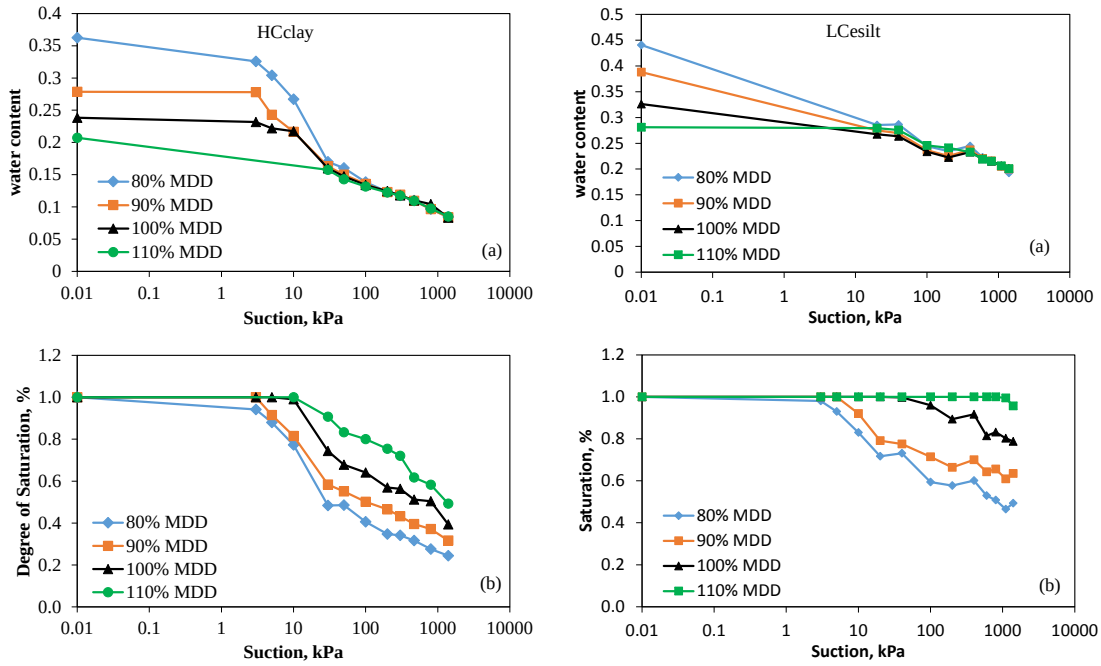

Figure E.2 Experimental soil-water retention test data for the HCclay (left) and LCesilt (right) soils at different compacted states (a) with respect to water content; (b) with respect to degree of saturation.

The experimental soil water retention property test data were fitted to the SWCC model presented by van Genuchten (1980), with the assumptions of a zero residual degree of saturation, $S_r = 0$ and that at zero suction ($\psi = 0$),the degree of saturation is one, (i.e. $S(0) = 1$). The van Genuchten (1980) model is simplified based on the assumptions used, and it relates the degree of saturation as a function of matric suction $S(\psi)$ to the matric suction ψ, and three fitting parameters a, n, and m, and is given as follows:

$$S(\psi) = \left[1 + \left(\frac{\psi}{a}\right)^{n}\right]^{-m} \qquad \text{(E.1)}$$

Furthermore, as suggested by van Genuchten (1980), the Mualem (1976) relationship between the two parameters n, and m, was used, in order to reduce the number of the independent fitting parameters of the model from three to two. The Mualem (1976) relationship between the two parameters n, and m, is given as:

$$m = 1 - \frac{1}{n} \tag{E.2}$$

The fitted parameters for each SWCC were presented in Table 4.1 in Chapter 4 of this report. The fitted or predicted results for each of the SWCC at different initial void ratios for each of the four soils are presented as Figures E.3 through E.6 in this appendix.

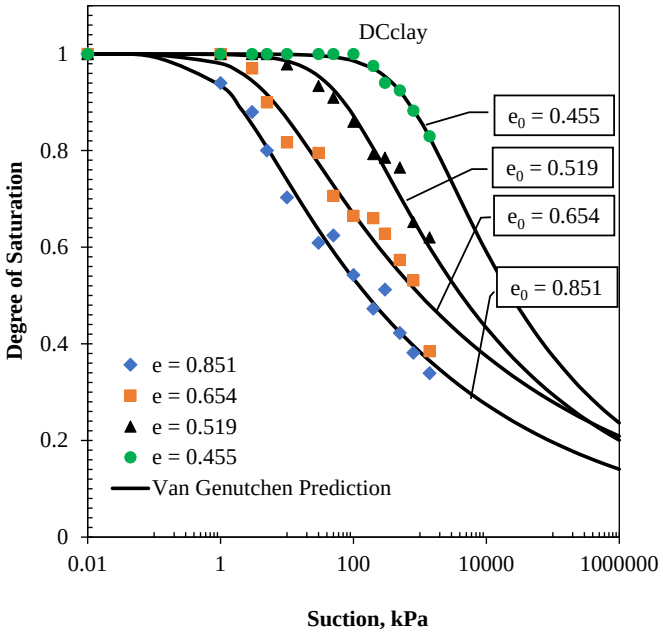

Figure E.3 Soil-water retention properties at different initial void ratio for Kentucky HCclay soil with optimized van Genuchten (1980) – Mualem (1976) model predictions

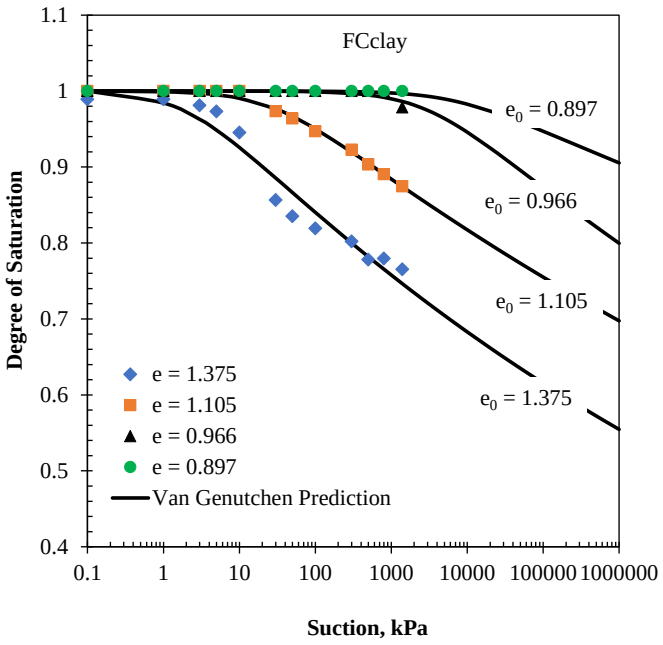

Figure E.4 Soil-water retention properties at different initial void ratio for Kentucky HCclay soil with optimized van Genuchten (1980) – Mualem (1976) model predictions

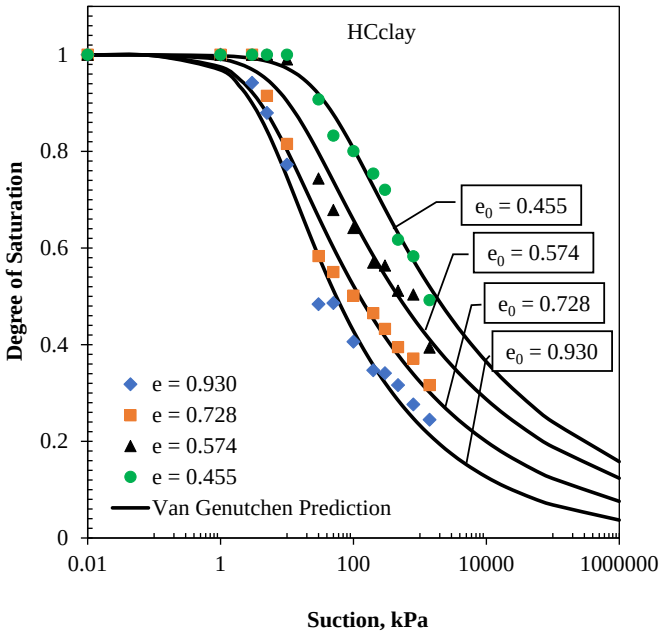

Figure E.5 Soil-water retention properties at different initial void ratio for Kentucky HCclay soil with optimized van Genuchten (1980) – Mualem (1976) model predictions

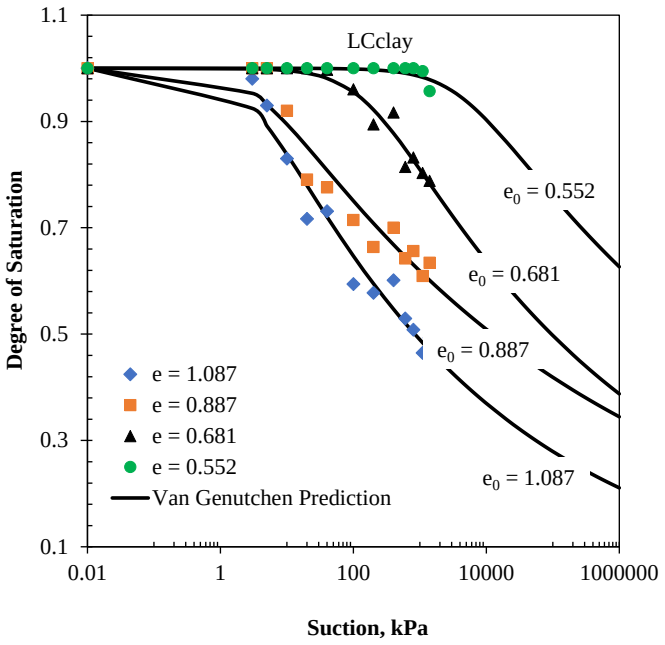

Figure E.6 Soil-water retention properties at different initial void ratio for Kentucky HCclay soil with optimized van Genuchten (1980) – Mualem (1976) model predictions.

APPENDIX F

Estimation of SWCC shifts due to Density Changes – Parameter Calibration and Model Validation (Based on the Zhou et al., 2012 model)

In this Appendix:

1. The ζ parameter calibration procedure.
2. The prediction of SSSC based on changes in initial void ratio.
3. The VBA codes are presented for the calibration procedure (Zhou2012zetacalibration); and the SWCC predictions based on a change in initial void ratio (Zhou2012SWCCshift).

APPENDIX F.1 The ζ Parameter Calibration Procedure

Based on Zhou et al., (2012), a VBA code, Zhou2012zetacalibration, was developed to perform the calibration of a reference SWCC to another SWCC with a different initial void ratio to obtain the ζ parameter. The ζ parameter is used to determine the effect of initial void ratio on degree of saturation. It is used to estimate SWCC for the same soil at different initial void ratios.

To determine the ζ parameter, two laboratory SWCC test data at different initial void ratios must be available. One of the SWCC data is selected as the reference and the other the calibration SWCC. Both SWCC data must be fitted to the Van Genuchten (1980) equation, or other such equations, to determine the a, n, and m Van Genuchten parameter. These SWCC data, the determined parameter values, the residual degree of saturation and void ratio for the selected reference and calibration SWCC are then input values for the VBA code. The VBA code is based on the Zhou et al. (2012) equation, and for a given ζ parameter and matric suction, it uses iteration to determine the effective degree of saturation away from the reference SWCC, by minimizing a residual value, R, such that;

$$R = v - z \cong 0 \tag{F.1}$$

where

$$v = \ln \frac{e_{iref}}{e_i} \tag{F.2}$$

$$z = \frac{\left(S_e - S_e^{ref}\right)}{6}\left(f_w + 4f_x + f_y\right) \tag{F.3}$$

and

$$f_w = \frac{1}{\left[S_e^{ref}\left(1 - S_e^{ref}\right)^{\zeta}\right]} \tag{F.4}$$

$$f_x = \frac{1}{\left[\left(\frac{S_e^{ref} + S_e}{2}\right)\left(1 - \left(\frac{S_e^{ref} + S_e}{2}\right)\right)^{\zeta}\right]} \tag{F.5}$$

$$f_y = \frac{1}{S_e\left(1 - S_e\right)^{\zeta}} \tag{F.6}$$

Iteration continues for a given range of matric suction from $0 < \psi < 1{,}000{,}000$ kPa, and the effective degree of saturation determined at each matric suction, in essence providing a SWCC for a given single value ζ parameter. Iteration then continues for a range of ζ parameters from $-1 \le \zeta < 1$, in increments of 0.01, which provides a SWCCC for each ζ parameter.

A calibration SWCC is then computed with the same range and increments of matric suction for comparison using the calibration SWCC data and previously determined a, n, and m Van Genuchten parameter. The squared difference of the degree of saturation at each corresponding matric suction between each SWCC and the calibration SWCC is determined and the sum of the squared differences taken. The VBA code then evaluates

the sum of the squared difference of SWCC at each ζ to that of the calibration SWCC. These sum of the squared differences for each SWCC and its corresponding ζ parameter are then plotted or evaluated to determine the ζ parameter with the lowest sum of the squared difference.

A typical plot which represents the data from the Daviess County soil is shown in Figure F.1. The direction of calibration is very important as show by the second curve in the figure. When the two SWCC data are switched, i.e., the reference SWCC data becomes the calibration SWCC and the calibration SWCC data becomes the reference SWCC data, a different ζ parameter is obtained, and is typical of all soils evaluated.

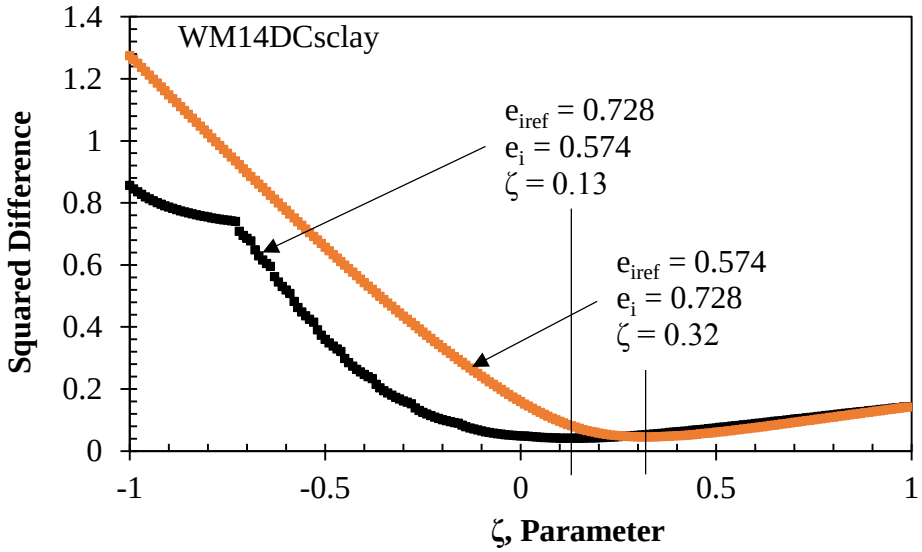

Figure F.1 ζ parameter calibration plot of least squared difference between experimental and predicted SWCC.

The calibrated ζ parameter and the Van Genuchten a, n, and m parameters for the reference SWCC for each soil of the four Kentucky soils are listed in Table F.1

Table F.1 ζ Parameters and corresponding van Genuchten parameters for the Kentucky soils.

	Parameters for $e_i^{ref} > e_i$			
Reference Parameters	WM14DCsclay	WM14FCesilt	WM14HCclay	WM14LCesilt
ζ	0.00	-0.02	0.13	0.08
a	4.32	28.63	4.61	3.47
n	1.13	1.03	1.21	1.08
m	0.11	0.03	0.17	0.08
	Parameters for $e_i^{ref} < e_i$			
ζ	0.18	0.15	0.32	0.19
a	67.26	3000.00	10.77	158.55
n	1.17	1.04	1.18	1.11
m	0.14	0.04	0.15	0.10

APPENDIX F.2 Prediction of SWCC based on Changes in Initial Void Ratio

Predictions of SWCC based on changes in void ratio were performed with use of a VBA code, Zhou2012SWCCshift, developed for the experimental validation of the Zhou et al., (2012) model to the soils used in this research. The model uses a ζ parameter which defines the effect of void ratio on the degree of saturation. The ζ parameter is obtained by calibration of a reference SWCC to another known SWCC of different initial void ratio, as presented in the previous section of this Appendix, or can be obtained robustly with use of an empirical relationship as presented in Chapter 8 of this report. The model requires that one SWCC be available and be used as a reference SWCC

To use the VBA code, the selected reference a, n, and m SWCC parameters, such as those obtained from the Van Genuchten (1980) equation for fitting SWCC data must be known; as well as the residual degree of saturation, the ζ parameter; the initial void ratio of the reference SWCC; and the initial void ratio of new SWCC to be estimated. The process of computing a predicted SWCC is very similar to the calibration process previously discussed in Appendix F.1, but with only one SWCC to be predicted.

The VBA code is based on the Zhou et al. (2012) equation, and for the input ζ parameter and a matric suction, it uses iteration to determine the effective degree of saturation away from the reference SWCC, by minimizing a residual value, R defined by Equations (F.1) through (F.6) in this Appendix. Iteration continues for a given range of incremental matric suction of $0 < \psi < 1{,}000{,}000$ kPa, with the effective degree of

saturation determined at each matric suction, providing a SWCC for the single input ζ parameter.

Validations of the experimental SWCC data from this study were performed using the VBA code Zhou2012SWCCshift. The validations of SWCC shifts were made using the experimental data with the largest void ratio as the reference SSSC and predicting the SWCC for the remaining three experimental SWCC data at lower void ratios for each soil. Plots of the experimental and predicted data SWCC data are shown Figure F.2, with the data for Daviess, Fayette, Henderson, and Lee County soils shown in Figure B.2(a), B.2(b), B.2(c), and B.2(d) respectively.

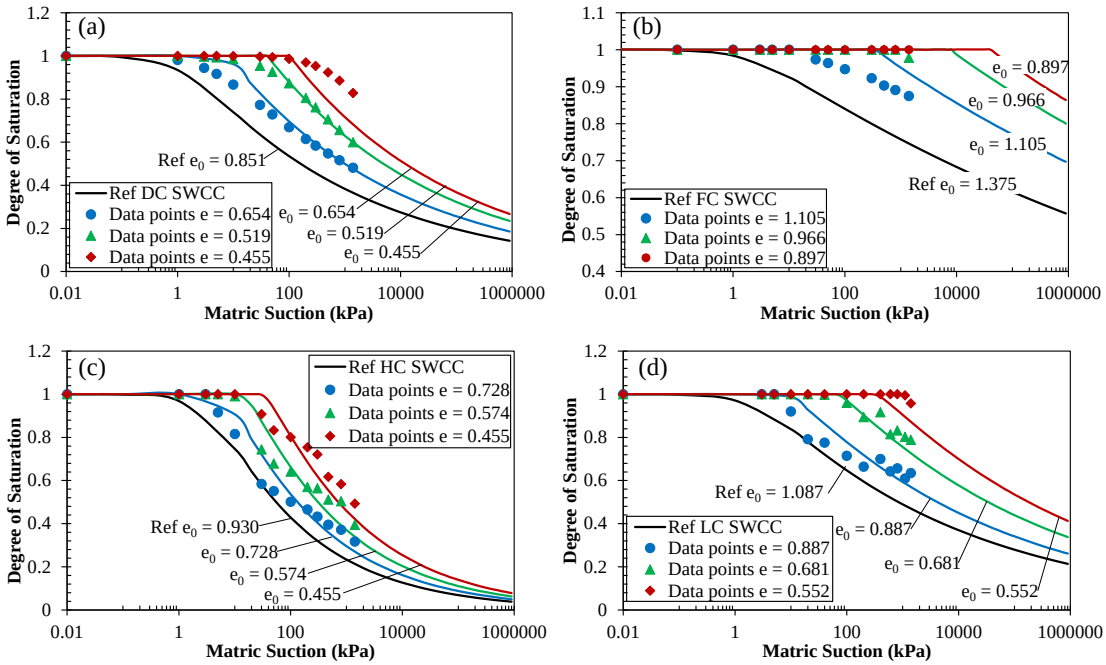

Figure F.2 Selected reference SWCC, and the measured and predicted SWCC for different initial densities based on a form of the van Genuchten (1980) and the Zhou et al., (2012) model; for the (a) DCsclay soil, $a = 1.36$, $n = 1.15$, and $m = 0.13$, $\zeta = 0.00$ (b) FCesilt soil, $a = 2.16$, $n = 1.05$, and $m = 0.04$, $\zeta = -0.02$ (c) HCclay soil, $a = 4.61$, $n = 1.21$, and $m = 0.17$, $\zeta = 0.13$(d) LCesilt soil, $a = 2.85$, $n = 1.12$, and $m = 0.11$, $\zeta = 0.08$.

APPENDIX F.3 VBA Codes – ζ Parameter Calibration; SWCC Estimations

The VBA codes for calibrating the ζ parameter, Zhou2012zetacalibration; and for determining SWCC shift, Zhou2012SWCCshift; are presented here. Each VBA code references a Microsoft Excel worksheet and cells within the worksheet for input and output data. The format of the Microsoft Excel worksheets are presented after each code.

VBA code for calibrating the ζ parameter (Zhou2012zetacalibration)

```
Sub Zhou2012zetacalibration()


' The model parameters

Dim eiref, Seref, ei, Se As Double
Dim Sr, Srref, Srres As Double
Dim psi0, psi, a, n, m As Double
Dim v, fw, fx, fy, z, R As Double
Dim zeta As Double
Dim Rowcount, Columncount As Integer
Dim Count As Integer
Dim array_Srref() As Variant
Dim array_Sr() As Variant
Dim array_Sr_calibrate() As Variant
Dim array_D2() As Variant
Dim D2 As Double
Dim sum_D2 As Double

a = Worksheets("Zhou2012 Calibrate").Range("E10").Value
n = Worksheets("Zhou2012 Calibrate").Range("E11").Value
m = Worksheets("Zhou2012 Calibrate").Range("E12").Value
psi0 = 0.01

Srres = Worksheets("Zhou2012 Calibrate").Range("E8").Value
eiref = Worksheets("Zhou2012 Calibrate").Range("E14").Value
ei = Worksheets("Zhou2012 Calibrate").Range("I14").Value

Columncount = 1

zeta = -1#
i = 9
j = 9
```

```
Do While zeta < 1
   Rowcount = 130

sum_D2 = 0


   psi = psi0
   Do Until psi = 1000000

      Seref = (1 / (1 + (psi / a) ^ n)) ^ m
      Srref = Srres + Seref * (1 - Srres)

         If Seref = 1 Then
            Se = 1
         Else
            If Seref = 0 Then
               Se = 0
            Else
               Se = Seref
                  If ei < eiref Then
                     Do Until Se >= 1
                        fw = 1 / (Seref * (1 - Seref) ^ zeta)
                        fx = 1 / (((Seref + Se) / 2) * (1 - ((Seref + Se) / 2)) ^ zeta)
                        fy = 1 / (Se * (1 - Se) ^ zeta)
                        z = ((Se - Seref) / 6) * (fw + 4 * fx + fy)
                        v = Log(eiref / ei)
                        R = v - z
                           If R < 0 Then
                              Exit Do
                           End If
                        Se = Se + 0.0001
                     Loop
                  Else
                     Do Until Se <= 0
                        fw = 1 / (Seref * (1 - Seref) ^ zeta)
                        fx = 1 / (((Seref + Se) / 2) * (1 - ((Seref + Se) / 2)) ^ zeta)
                        fy = 1 / (Se * (1 - Se) ^ zeta)
                        z = ((Se - Seref) / 6) * (fw + 4 * fx + fy)
                        v = Log(eiref / ei)
                        R = v - z
                           If R > 0 Then
                              Exit Do
                           End If
                        Se = Se - 0.0001
                     Loop
                  End If
            End If
         End If
```

```
    Sr = Srres + Se * (1 - Srres)

    Worksheets("Zhou2012 Calibrate").Cells(129, Columncount).Value = "psi"
    Worksheets("Zhou2012 Calibrate").Cells(129, Columncount + 1).Value = "Seref"
    Worksheets("Zhou2012 Calibrate").Cells(129, Columncount + 2).Value = "Se"
    Worksheets("Zhou2012 Calibrate").Cells(129, Columncount + 3).Value = "Srref"
    Worksheets("Zhou2012 Calibrate").Cells(129, Columncount + 4).Value = "Sr"
    Worksheets("Zhou2012 Calibrate").Cells(129, Columncount + 5).Value = "R"
    Worksheets("Zhou2012 Calibrate").Cells(129, Columncount + 6).Value = "zeta"
    Worksheets("Zhou2012 Calibrate").Cells(Rowcount, Columncount).Value = psi
    Worksheets("Zhou2012 Calibrate").Cells(Rowcount, Columncount + 1).Value = Seref
    Worksheets("Zhou2012 Calibrate").Cells(Rowcount, Columncount + 2).Value = Se
    Worksheets("Zhou2012 Calibrate").Cells(Rowcount, Columncount + 3).Value = Srref
    Worksheets("Zhou2012 Calibrate").Cells(Rowcount, Columncount + 4).Value = Sr
    Worksheets("Zhou2012 Calibrate").Cells(Rowcount, Columncount + 5).Value = R
    Worksheets("Zhou2012 Calibrate").Cells(Rowcount, Columncount + 6).Value = zeta

    Count = Rowcount - 129
    ReDim array_Sr(1 To Count, 1)
    array_Sr(Count, 1) = Sr

    ReDim array_Sr_calibrate(1 To Count, 1)
array_Sr_calibrate(Count, 1) = Worksheets("Zhou2012 Calibrate").Cells(Rowcount - 108, 15)

    ReDim array_D2(1 To Count, 1)
    array_D2(Count, 1) = (array_Sr(Count, 1) - array_Sr_calibrate(Count, 1)) ^ 2

    sum_D2 = sum_D2 + array_D2(Count, 1)

    Rowcount = Rowcount + 1

    If psi < 10 Then
       psi = psi * 10
    Else
       If psi < 100 Then
          psi = psi + 10
       Else
          If psi < 1000 Then
             psi = psi + 100
          Else
             If psi < 10000 Then
                psi = psi + 1000
             Else
                If psi < 100000 Then
                   psi = psi + 10000
                Else
                   If psi < 1000000 Then
                      psi = psi + 100000
                   End If
                End If
```

```
                End If
            End If
        End If
    End If
Loop

If zeta < 0 Then
    Worksheets("Zhou2012 Calibrate").Cells(i, 17) = zeta
    Worksheets("Zhou2012 Calibrate").Cells(i, 18) = sum_D2
    i = i + 1
Else
    Worksheets("Zhou2012 Calibrate").Cells(j, 20) = zeta
    Worksheets("Zhou2012 Calibrate").Cells(j, 21) = sum_D2
    j = j + 1
End If


Columncount = Columncount + 8

zeta = zeta + 0.01


Loop

End Sub
```

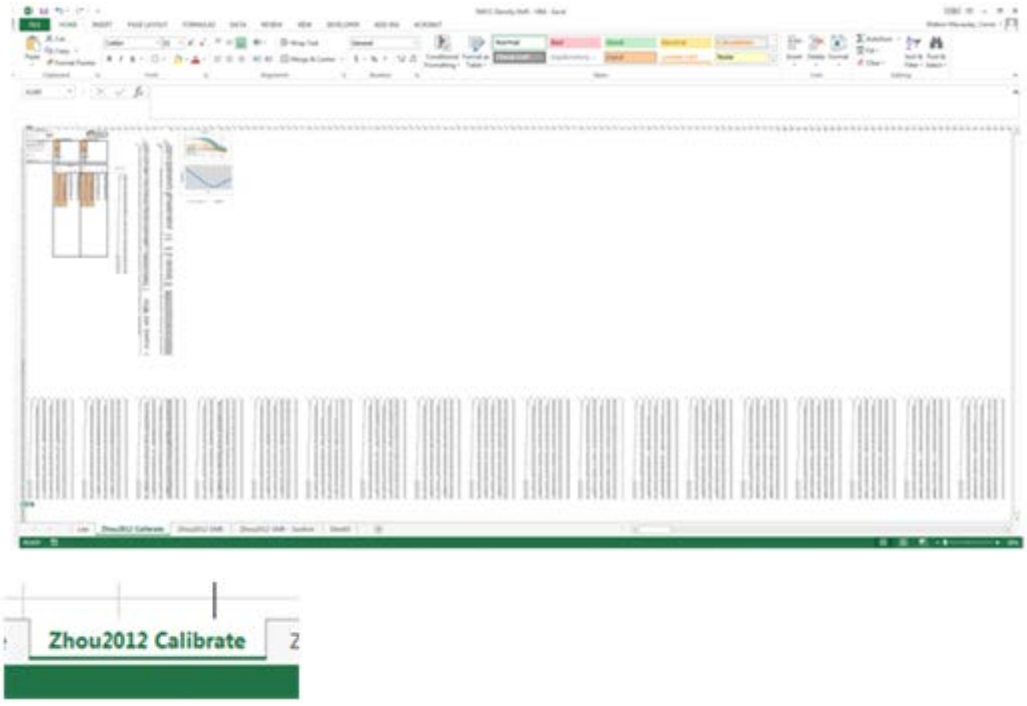

Figure F.3 An overview of the Worksheet that accompany the VBA code for calibrating the ζ parameter.

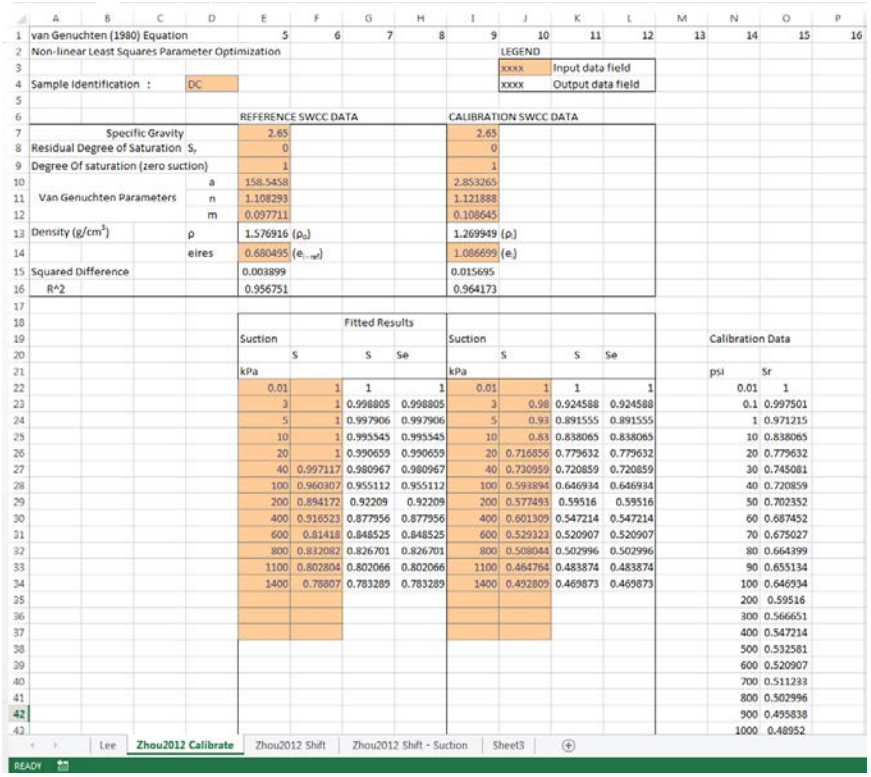

van Genuchten (1980) Equation

Non-linear Least Squares Parameter Optimization

LEGEND

xxxx	Input data field
xxxx	Output data field

Sample Identification : DC

		REFERENCE SWCC DATA	CALIBRATION SWCC DATA
Specific Gravity		2.65	2.65
Residual Degree of Saturation	S_r	0	0
Degree Of saturation (zero suction)		1	1
Van Genuchten Parameters	a	158.5458	2.853265
	n	1.108293	1.121888
	m	0.097711	0.108645
Density (g/cm^3)	ρ	1.576916 (ρ_d)	1.269949 (ρ_d)
	eires	0.680495 ($e_{...ref}$)	1.086699 (e_i)
Squared Difference		0.003899	0.015695
R^2		0.956751	0.964173

Fitted Results

Suction	S	S	Se	Suction	S	S	Se	Calibration Data	
kPa				kPa				psi	Sr
0.01	1	1	1	0.01	1	1	1	0.01	1
3	1	0.998805	0.998805	3	0.98	0.924588	0.924588	0.1	0.997501
5	1	0.997906	0.997906	5	0.93	0.891555	0.891555	1	0.971215
10	1	0.995545	0.995545	10	0.83	0.838065	0.838065	10	0.838065
20	1	0.990659	0.990659	20	0.716856	0.779632	0.779632	20	0.779632
40	0.997117	0.980967	0.980967	40	0.730959	0.720859	0.720859	30	0.745081
100	0.960307	0.955112	0.955112	100	0.593894	0.646934	0.646934	40	0.720859
200	0.894172	0.92209	0.92209	200	0.577493	0.59516	0.59516	50	0.702352
400	0.916523	0.877956	0.877956	400	0.601309	0.547214	0.547214	60	0.687452
600	0.81418	0.848525	0.848525	600	0.529323	0.520907	0.520907	70	0.675027
800	0.832082	0.826701	0.826701	800	0.508044	0.502996	0.502996	80	0.664399
1100	0.802804	0.802066	0.802066	1100	0.464764	0.483874	0.483874	90	0.655134
1400	0.78807	0.783289	0.783289	1400	0.492809	0.469873	0.469873	100	0.646934
								200	0.59516
								300	0.566651
								400	0.547214
								500	0.532581
								600	0.520907
								700	0.511233
								800	0.502996
								900	0.495838
								1000	0.48952

Lee | Zhou2012 Calibrate | Zhou2012 Shift | Zhou2012 Shift - Suction | Sheet3

READY

Figure F.4 Detailed view of the input data section of the Workbook.

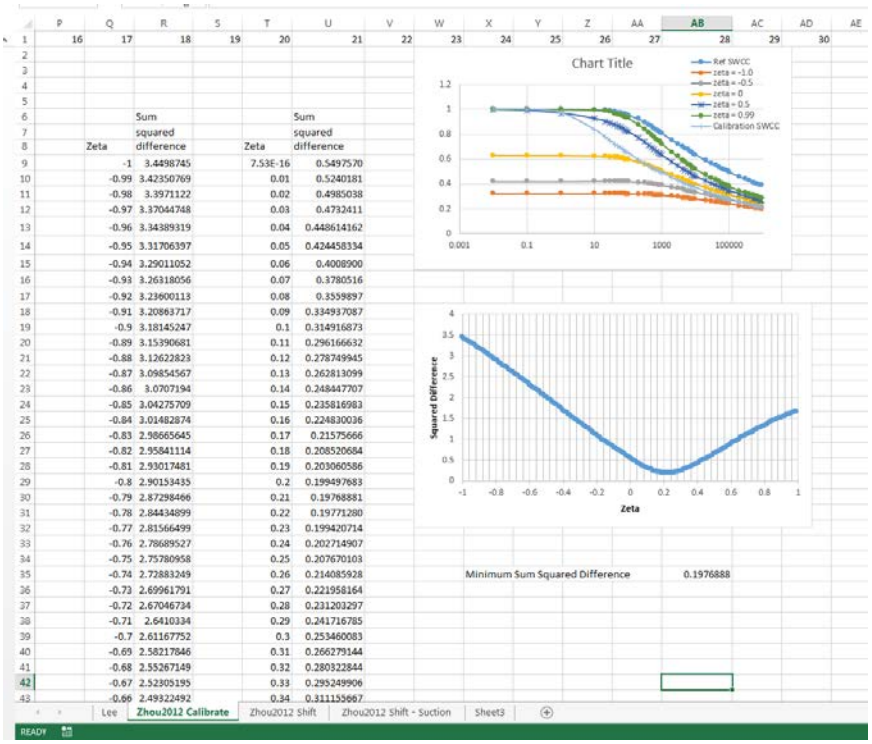

Zeta	Sum squared difference	Zeta	Sum squared difference
-1	3.4498745	7.53E-16	0.5497570
-0.99	3.42350769	0.01	0.5240181
-0.98	3.3971122	0.02	0.4985038
-0.97	3.37044748	0.03	0.4732411
-0.96	3.34389319	0.04	0.448614162
-0.95	3.31706397	0.05	0.424458334
-0.94	3.29011052	0.06	0.4008900
-0.93	3.26318056	0.07	0.3780516
-0.92	3.23600113	0.08	0.3559897
-0.91	3.20863717	0.09	0.334937087
-0.9	3.18145247	0.1	0.314916873
-0.89	3.15390681	0.11	0.296166632
-0.88	3.12622823	0.12	0.278749945
-0.87	3.09854567	0.13	0.262813099
-0.86	3.0707194	0.14	0.248447707
-0.85	3.04275709	0.15	0.235816983
-0.84	3.01482874	0.16	0.224830036
-0.83	2.98665645	0.17	0.21575666
-0.82	2.95841114	0.18	0.208520684
-0.81	2.93017481	0.19	0.203060586
-0.8	2.90153435	0.2	0.199497683
-0.79	2.87298466	0.21	0.19768881
-0.78	2.84434899	0.22	0.19771280
-0.77	2.81566499	0.23	0.199420714
-0.76	2.78689527	0.24	0.202714907
-0.75	2.75780958	0.25	0.207670103
-0.74	2.72883249	0.26	0.214085928
-0.73	2.69961791	0.27	0.221958164
-0.72	2.67046734	0.28	0.231203297
-0.71	2.6410334	0.29	0.241716785
-0.7	2.61167752	0.3	0.253460083
-0.69	2.58217846	0.31	0.266279144
-0.68	2.55267149	0.32	0.280322844
-0.67	2.52305195	0.33	0.295249906
-0.66	2.49322492	0.34	0.311155667

Chart Title

Ref SWCC
zeta = -1.0
zeta = -0.5
zeta = 0
zeta = 0.5
zeta = 0.99
Calibration SWCC

Squared Difference

Zeta

Minimum Sum Squared Difference 0.1976888

Lee | Zhou2012 Calibrate | Zhou2012 Shift | Zhou2012 Shift - Suction | Sheet3

READY

Figure F.5 Detailed view of a section of the results and plots in the Workbook

VBA code for determining SSSC shift (Zhou2012SWCCshift)

```
Sub Zhou2012SWCCshift()

' The model parameters
Dim eiref, Seref, ei, Se As Double
Dim Sr, Srref, Srres As Double
Dim psi0, psi, a, n, m As Double
Dim v, fw, fx, fy, z, R As Double
Dim zeta As Double
Dim Rowcount, Columncount As Integer
Dim array_Srref()
Dim array_Sr()

Srres = Worksheets("Zhou2012 Shift").Range("E6").Value
a = Worksheets("Zhou2012 Shift").Range("E9").Value
n = Worksheets("Zhou2012 Shift").Range("E10").Value
m = Worksheets("Zhou2012 Shift").Range("E11").Value
psi0 = 0.0001

zeta = Worksheets("Zhou2012 Shift").Range("E13").Value
eiref = Worksheets("Zhou2012 Shift").Range("E14").Value
ei = Worksheets("Zhou2012 Shift").Range("E15").Value

Columncount = 1


   Rowcount = 21


   psi = psi0
   Do Until psi = 1000000

      Seref = (1 / (1 + (psi / a) ^ n)) ^ m
      Srref = Srres + Seref * (1 - Srres)

         If Seref = 1 Then
            Se = 1
         Else
            If Seref = 0 Then
               Se = 0
            Else
               Se = Seref
                  If ei < eiref Then
                     Do Until Se >= 1
                        fw = 1 / (Seref * (1 - Seref) ^ zeta)
                        fx = 1 / (((Seref + Se) / 2) * (1 - ((Seref + Se) / 2)) ^ zeta)
                        fy = 1 / (Se * (1 - Se) ^ zeta)
                        z = ((Se - Seref) / 6) * (fw + 4 * fx + fy)
                        v = Log(eiref / ei)
```

```
            R = v - z
               If R < 0 Then
                  Exit Do
               End If
            Se = Se + 0.001
         Loop
      Else
         Do Until Se <= 0
            fw = 1 / (Seref * (1 - Seref) ^ zeta)
            fx = 1 / (((Seref + Se) / 2) * (1 - ((Seref + Se) / 2)) ^ zeta)
            fy = 1 / (Se * (1 - Se) ^ zeta)
            z = ((Se - Seref) / 6) * (fw + 4 * fx + fy)
            v = Log(eiref / ei)
            R = v - z
               If R > 0 Then
                  Exit Do
               End If
            Se = Se - 0.001
         Loop
      End If
   End If
End If

Sr = Srres + Se * (1 - Srres)
Worksheets("Zhou2012 Shift").Cells(Rowcount, Columncount).Value = psi
Worksheets("Zhou2012 Shift").Cells(Rowcount, Columncount + 1).Value = Seref
Worksheets("Zhou2012 Shift").Cells(Rowcount, Columncount + 2).Value = Srref
Worksheets("Zhou2012 Shift").Cells(Rowcount, Columncount + 3).Value = Se
Worksheets("Zhou2012 Shift").Cells(Rowcount, Columncount + 4).Value = Sr
Worksheets("Zhou2012 Shift").Cells(Rowcount, Columncount + 5).Value = R
Worksheets("Zhou2012 Shift").Cells(Rowcount, Columncount + 6).Value = zeta




Rowcount = Rowcount + 1

If psi < 10 Then
   psi = psi * 10
Else
   If psi < 100 Then
      psi = psi + 10
   Else
      If psi < 1000 Then
         psi = psi + 100
      Else
         If psi < 10000 Then
            psi = psi + 1000
         Else
```

```
                    If psi < 100000 Then
                        psi = psi + 10000
                    Else
                        If psi < 1000000 Then
                            psi = psi + 100000
                        End If
                    End If
                End If
            End If
        End If
    End If
Loop


End Sub
```

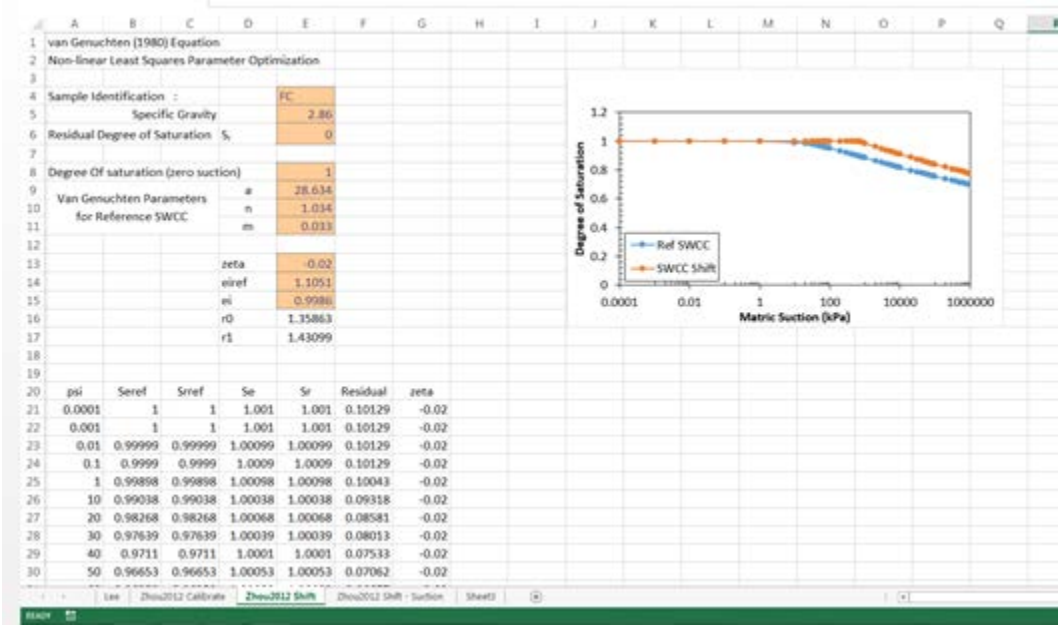

Figure F.6 Detail of the input data section of the Workbook that accompany the VBA code for shifting SWCC.

APPENDIX G

SSSC paths in bulk compression tests for Kentucky soils at or close to optimum moisture content.

In this Appendix:

1. The estimation of matric suction based on changes in initial void ratio.
2. The VBA codes are presented for the calibration procedure (Zhou2012zetacalibration); the SSSC predictions based on a change in initial void ratio (Zhou2012SWCCshift) and the predictions of matric suction for known changes in void ratio and degree of saturation (Zhou2012SWCCshiftforsuction).

APPENDIX G.1 The Estimation of Matric Suction based on Changes in Initial Void Ratio

Matric suction can be estimated using the Zhou et al., (2012) model. Based on the need for iterations, a VBA code was developed to perform the necessary iterations and calculations for estimating matric suction when the degree of saturation and a reference SSSC are known.

In order to use the VBA code, the reference a, n, and m SWCC parameters, such as those obtained from the Van Genuchten (1980) equation for fitting SWCC data must be known; as well as the residual degree of saturation, the ζ parameter; the initial void ratio of the reference SWCC. In addition, the current degree of saturation and corresponding void ratio must be known and used as input values. The VBA code can determine the matric suctions for 5 known degree of saturation and their corresponding void ratios in a single run.

For each known degree of saturation and corresponding void ratio, the VBA code first determines the effective degree of saturation, then iterates to determine the effective degree of saturation on the reference SWCC by minimizing a residual value, R defined by Equations F.1 through F.6 in this Appendix. The code then uses the reference effective degree of saturation to determine the matric suction using the Van Genuchten (1980) equation, rearranged to solve for matric suction.

Figure G.1 show the estimated matric suction as the SSSC path during incremental compaction in the laboratory scale model test, for the four Kentucky soils.

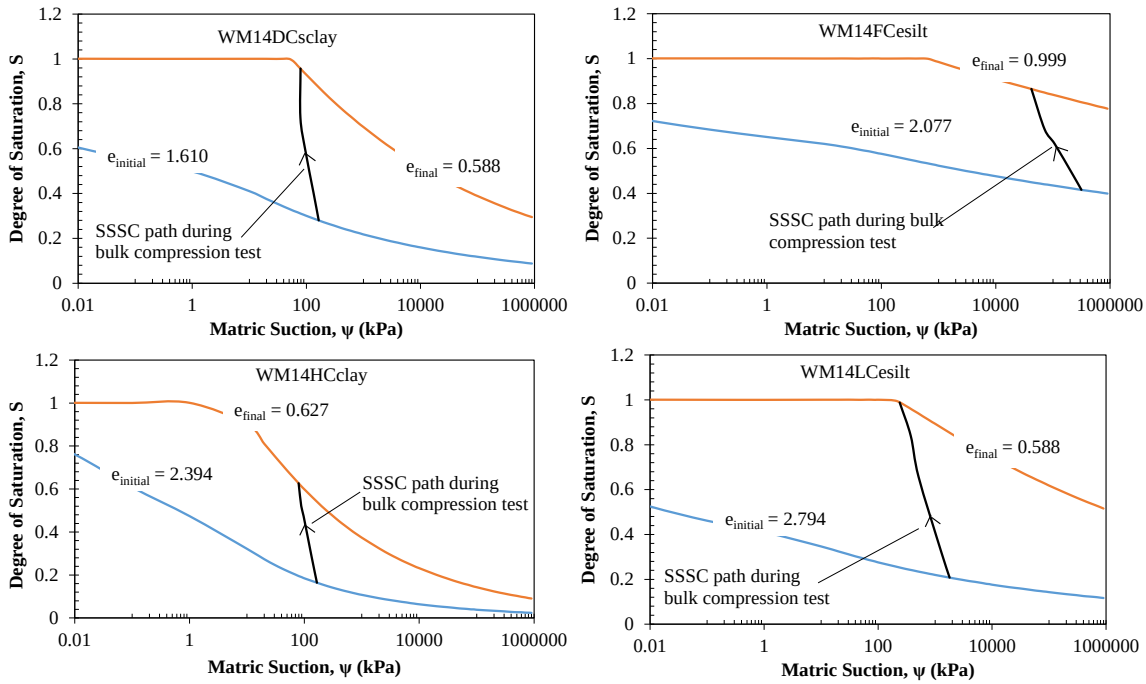

Figure G.1 SSSC paths determined from estimated matric suctions using the ZhouSWCCshiftforsuction VBA Code.

In Table G.1, the estimated matric suction are tabulated with the corresponding parameters used in the estimation.

Table G.1 Estimated matric suctions and reference SWCC data for corresponding measured test data, and the reference void ratio and ζ parameters used for estimating the matric suction for the DCsclay soil.

DCsclay						
Measured Experimental Data				Estimated data		
Moisture Content (%)	Void Ratio	Degree of Saturation	zeta parameter	Reference Void Ratio	Reference Degree of Saturation	Matric Suction
w	e	S_r	ζ	e_{iref}	S_{rref}	ψ (kPa)
11.4%	1.440	0.215	0.18	0.654	0.449	2388.0
	1.099	0.282	0.18	0.654	0.455	2158.0
	0.802	0.386	0.18	0.654	0.465	1805.3
	0.666	0.466	0.18	0.654	0.474	1573.6
	0.581	0.534	0	0.654	0.474	1569.4
13.2%	1.415	0.254	0.18	0.654	0.516	801.9
	1.049	0.342	0.18	0.654	0.525	694.4
	0.867	0.414	0.18	0.654	0.532	625.6
	0.625	0.575	0	0.654	0.549	491.4
	0.545	0.659	0	0.654	0.548	496.0
16.6%	1.610	0.280	0.18	0.654	0.629	164.5
	1.127	0.401	0.18	0.654	0.646	134.1
	0.763	0.592	0.18	0.654	0.673	96.0
	0.612	0.738	0	0.654	0.690	78.6
	0.472	0.957	0	0.654	0.689	79.0
19.2%	1.726	0.303	0.18	0.654	0.712	60.7
	1.174	0.445	0.18	0.654	0.733	47.4
	0.786	0.664	0.18	0.654	0.769	31.4
	0.615	0.849	0	0.654	0.797	22.7
	0.514	1.017	0	0.654	0.798	22.6

Estimated matric suctions and reference SWCC data for corresponding measured test data, and the reference void ratio and ζ parameters used for estimating the matric suction for the FCesilt soil.

FCesilt						
Measured Experimental Data				Estimated data		
Moisture Content (%)	Void Ratio	Degree of Saturation	zeta parameter	Reference Void Ratio	Reference Degree of Saturation	Matric Suction
w	e	S_r	ζ	e_{iref}	S_{rref}	ψ (kPa)
24.5%	1.721	0.407	0.15	1.105	0.607	1000000
	1.549	0.452	0.15	1.105	0.612	1000000
	1.269	0.552	0.15	1.105	0.624	1000000
	1.175	0.597	0.15	1.105	0.630	1000000
	1.088	0.644	-0.02	1.105	0.633	1000000
27.8%	1.859	0.428	0.15	1.105	0.679	1000000
	1.601	0.497	0.15	1.105	0.688	1000000
	1.255	0.633	0.15	1.105	0.706	691885
	1.131	0.703	0.15	1.105	0.717	449952
	0.997	0.798	-0.02	1.105	0.717	451692
30.2%	2.077	0.416	0.15	1.105	0.726	314676
	1.786	0.484	0.15	1.105	0.735	222112
	1.393	0.620	0.15	1.105	0.753	107373
	1.261	0.685	0.15	1.105	0.764	71683.1
	0.999	0.865	-0.02	1.105	0.778	42038.4
34.0%	2.022	0.481	0.15	1.105	0.807	14556.4
	1.828	0.532	0.15	1.105	0.814	11276.4
	1.433	0.678	0.15	1.105	0.837	4929.2
	1.316	0.739	0.15	1.105	0.849	3317.2
	1.106	0.879	0.15	1.105	0.880	1139.5

Estimated matric suctions and reference SWCC data for corresponding measured test data, and the reference void ratio and ζ parameters used for estimating the matric suction for the HCclay soil.

HCclay						
Measured Experimental Data				Estimated data		
Moisture Content (%)	Void Ratio	Degree of Saturation	zeta parameter	Reference Void Ratio	Reference Degree of Saturation	Matric Suction
w	e	S_r	ζ	e_{iref}	S_{rref}	ψ (kPa)
	2.086	0.147	0.32	0.728	0.382	452.7
	1.458	0.210	0.32	0.728	0.391	403.3
11.4%	1.189	0.258	0.32	0.728	0.398	371.7
	0.850	0.361	0.32	0.728	0.412	315.6
	0.701	0.438	0.13	0.728	0.422	281.6
	2.393	0.164	0.32	0.728	0.471	165.3
	1.371	0.287	0.32	0.728	0.493	133.2
14.6%	0.829	0.474	0.32	0.728	0.526	96.9
	0.754	0.521	0.32	0.728	0.536	88.1
	0.627	0.627	0.13	0.728	0.548	79.4
	2.016	0.213	0.32	0.728	0.516	105.8
	1.206	0.357	0.32	0.728	0.542	83.7
16.0%	0.724	0.595	0.13	0.728	0.591	54.5
	0.654	0.658	0.13	0.728	0.598	51.3
	0.577	0.746	0.13	0.728	0.609	46.6
	1.899	0.279	0.32	0.728	0.618	43.4
	1.168	0.454	0.32	0.728	0.655	32.3
19.7%	0.696	0.762	0.13	0.728	0.733	17.5
	0.647	0.820	0.13	0.728	0.743	16.2
	0.579	0.915	0.13	0.728	0.764	13.7

Estimated matric suctions and reference SWCC data for corresponding measured test data, and the reference void ratio and ζ parameters used for estimating the matric suction for the LCesilt soil.

LCesilt						
Measured Experimental Data				Estimated data		
Moisture Content (%)	Void Ratio	Degree of Saturation	zeta parameter	Reference Void Ratio	Reference Degree of Saturation	Matric Suction
w	e	S_r	ζ	e_{iref}	S_{rref}	ψ (kPa)
20.9%	2.551	0.217	0.19	0.887	0.568	2739.4
	1.799	0.308	0.19	0.887	0.581	2106.1
	1.214	0.456	0.19	0.887	0.599	1454.4
	0.770	0.720	0.08	0.887	0.632	781.2
	0.582	0.952	0.08	0.887	0.660	468.4
21.9%	2.794	0.208	0.19	0.887	0.589	1797.1
	1.817	0.319	0.19	0.887	0.605	1292.9
	0.884	0.657	0.08	0.887	0.655	513.2
	0.692	0.839	0.08	0.887	0.672	374.5
	0.587	0.988	0.08	0.887	0.698	239.4
24.2%	3.310	0.194	0.19	0.887	0.634	752.0
	2.172	0.295	0.19	0.887	0.653	525.2
	1.037	0.619	0.19	0.887	0.704	217.5
	0.795	0.807	0.08	0.887	0.732	136.2
	0.628	1.022	0.08	0.887	1.000	1.0
26.7%	3.848	0.184	0.19	0.887	0.679	332.8
	2.624	0.270	0.19	0.887	0.702	224.5
	1.219	0.581	0.19	0.887	0.753	96.9
	0.928	0.763	0.19	0.887	0.790	53.7
	0.697	1.015	0.08	0.887	1.000	1.0

APPENDIX G.2 VBA Codes – Matric Suction Estimation

The VBA code for estimating matric suction, Zhou2012SWCCshiftforsuction is presented here. The VBA code references a Microsoft Excel worksheet and cells within the worksheet for input and output data. The format of the Microsoft Excel worksheets are presented after each code.

VBA code for estimating matric suction, (Zhou2012SWCCshiftforsuction)

```
Sub Zhou2012SWCCshiftforsuction()

' The model parameters
Dim eiref, Seref, ei, Se As Double
Dim Sr, Srref, Srres As Double
Dim psires, psi, a, n, m As Double
Dim v, fw, fx, fy, z, R As Double
Dim zeta As Double
Dim Rowcount, Columncount As Integer
Dim array_Srref()
Dim array_Sr()
Dim ei0() As Double
Dim Sr0() As Double
Dim k As Long

Srres = Worksheets("Zhou2012 Shift - Suction").Range("E6").Value
psires = Worksheets("Zhou2012 Shift - Suction").Range("E7").Value
a = Worksheets("Zhou2012 Shift - Suction").Range("E9").Value
n = Worksheets("Zhou2012 Shift - Suction").Range("E10").Value
m = Worksheets("Zhou2012 Shift - Suction").Range("E11").Value

zeta = Worksheets("Zhou2012 Shift - Suction").Range("E13").Value
eiref = Worksheets("Zhou2012 Shift - Suction").Range("E14").Value

ReDim ei0(1 To 5) As Double
ReDim Sr0(1 To 5) As Double
ei0(1) = Worksheets("Zhou2012 Shift - Suction").Range("A21").Value
ei0(2) = Worksheets("Zhou2012 Shift - Suction").Range("A22").Value
ei0(3) = Worksheets("Zhou2012 Shift - Suction").Range("A23").Value
ei0(4) = Worksheets("Zhou2012 Shift - Suction").Range("A24").Value
ei0(5) = Worksheets("Zhou2012 Shift - Suction").Range("A25").Value
Sr0(1) = Worksheets("Zhou2012 Shift - Suction").Range("B21").Value
Sr0(2) = Worksheets("Zhou2012 Shift - Suction").Range("B22").Value
Sr0(3) = Worksheets("Zhou2012 Shift - Suction").Range("B23").Value
Sr0(4) = Worksheets("Zhou2012 Shift - Suction").Range("B24").Value
```

```
Sr0(5) = Worksheets("Zhou2012 Shift - Suction").Range("B25").Value

Columncount = 3
Rowcount = 21

k = 1
Do While k <= 5

   ei = ei0(k)
   Sr = Sr0(k)
   Se = (Sr - Srres) / (1 - Srres)

   If Se <= 0 Then
   Se = 0
   End If

         If Se = 1 Then
            Seref = 1
         Else
            If Se = 0 Then
               Seref = 0
            Else
               Seref = Se
                  If ei < eiref Then
                     Do Until Seref <= 0
                        fw = 1 / (Seref * (1 - Seref) ^ zeta)
                        fx = 1 / (((Seref + Se) / 2) * (1 - ((Seref + Se) / 2)) ^ zeta)
                        fy = 1 / (Se * (1 - Se) ^ zeta)
                        z = ((Se - Seref) / 6) * (fw + 4 * fx + fy)
                        v = Log(eiref / ei)
                        R = v - z
                           If R < 0 Then
                              Exit Do
                           End If
                        Seref = Seref - 0.001
                     Loop
                  Else
                     Do Until Seref >= 1
                        fw = 1 / (Seref * (1 - Seref) ^ zeta)
                        fx = 1 / (((Seref + Se) / 2) * (1 - ((Seref + Se) / 2)) ^ zeta)
                        fy = 1 / (Se * (1 - Se) ^ zeta)
                        z = ((Se - Seref) / 6) * (fw + 4 * fx + fy)
                        v = Log(eiref / ei)
                        R = v - z
                           If R > 0 Then
                              Exit Do
                           End If
                        Seref = Seref + 0.001
                     Loop
                  End If
```

```
            End If
        End If

        If Seref <= 0 Then
            psi = psires
        Else
            If Seref >= 1 Then
                Seref = 1
                psi = 0.001
            Else
                psi = a * (((1 / Seref) ^ (1 / m)) - 1) ^ (1 / n)
            End If
        End If

        If psi > psires Then
        psi = psires
        End If

        Srref = Srres + Seref * (1 - Srres)
      Worksheets("Zhou2012 Shift - Suction").Cells(Rowcount, Columncount).Value = Se
      Worksheets("Zhou2012 Shift - Suction").Cells(Rowcount, Columncount + 1).Value = Seref
      Worksheets("Zhou2012 Shift - Suction").Cells(Rowcount, Columncount + 2).Value = Srref
      Worksheets("Zhou2012 Shift - Suction").Cells(Rowcount, Columncount + 3).Value = psi
      Worksheets("Zhou2012 Shift - Suction").Cells(Rowcount, Columncount + 4).Value = R
      Worksheets("Zhou2012 Shift - Suction").Cells(Rowcount, Columncount + 5).Value = zeta

    k = k + 1
    Rowcount = Rowcount + 1
Loop


End Sub
```

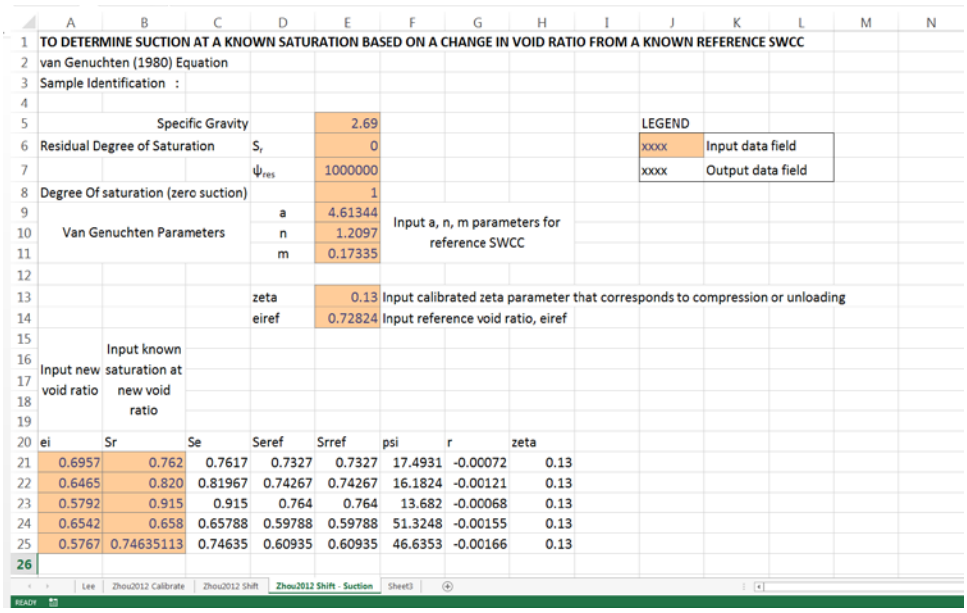

TO DETERMINE SUCTION AT A KNOWN SATURATION BASED ON A CHANGE IN VOID RATIO FROM A KNOWN REFERENCE SWCC

van Genuchten (1980) Equation

Sample Identification :

Specific Gravity		2.69	
Residual Degree of Saturation	S_r	0	
	ψ_{res}	1000000	
Degree Of saturation (zero suction)		1	
Van Genuchten Parameters	a	4.61344	Input a, n, m parameters for reference SWCC
	n	1.2097	
	m	0.17335	
	zeta	0.13	Input calibrated zeta parameter that corresponds to compression or unloading
	eiref	0.72824	Input reference void ratio, eiref

LEGEND

xxxx	Input data field
xxxx	Output data field

Input new void ratio	Input known saturation at new void ratio	Se	Seref	Srref	psi	r	zeta
ei	Sr						
0.6957	0.762	0.7617	0.7327	0.7327	17.4931	-0.00072	0.13
0.6465	0.820	0.81967	0.74267	0.74267	16.1824	-0.00121	0.13
0.5792	0.915	0.915	0.764	0.764	13.682	-0.00068	0.13
0.6542	0.658	0.65788	0.59788	0.59788	51.3248	-0.00155	0.13
0.5767	0.74635113	0.74635	0.60935	0.60935	46.6353	-0.00166	0.13

Lee | Zhou2012 Calibrate | Zhou2012 Shift | Zhou2012 Shift - Suction | Sheet3

READY

Figure G.1 An overview of the Worksheet that accompany the VBA code for calibrating the ζ parameter.

APPENDIX H

Experimental Test Data from the Laboratory Scale Model Tests and Triaxial Tests

Appendix H comprises of a graphical presentation of the experimental data and tabulated lists of all test specimens showing the tests and test conditions the specimens were subjected to and the summarized experimental results obtained. The Appendix is arranged in the following order:

1. Results of measurements of stiffness and shear modulus in the bulk compression tests.
2. Results of measurements of the saturated CIU triaxial tests.
3. Results of measurements of the unsaturated CW triaxial tests.

APPENDIX H.1 Results of Measurements of Stiffness and Shear Modulus in the Bulk Compression Tests

The simulated field bulk soil compression test was developed to investigate the effect of compaction state on the mechanical and dynamic properties of compacted soils. The dynamic property of shear modulus was of interest in this testing and was determine in two ways: by a seismic cross-hole method, and with use of a field stiffness gauge. The results are presented as Figures H.1 through H.4 with the experimental data presented in Tables H.1 through H.4.

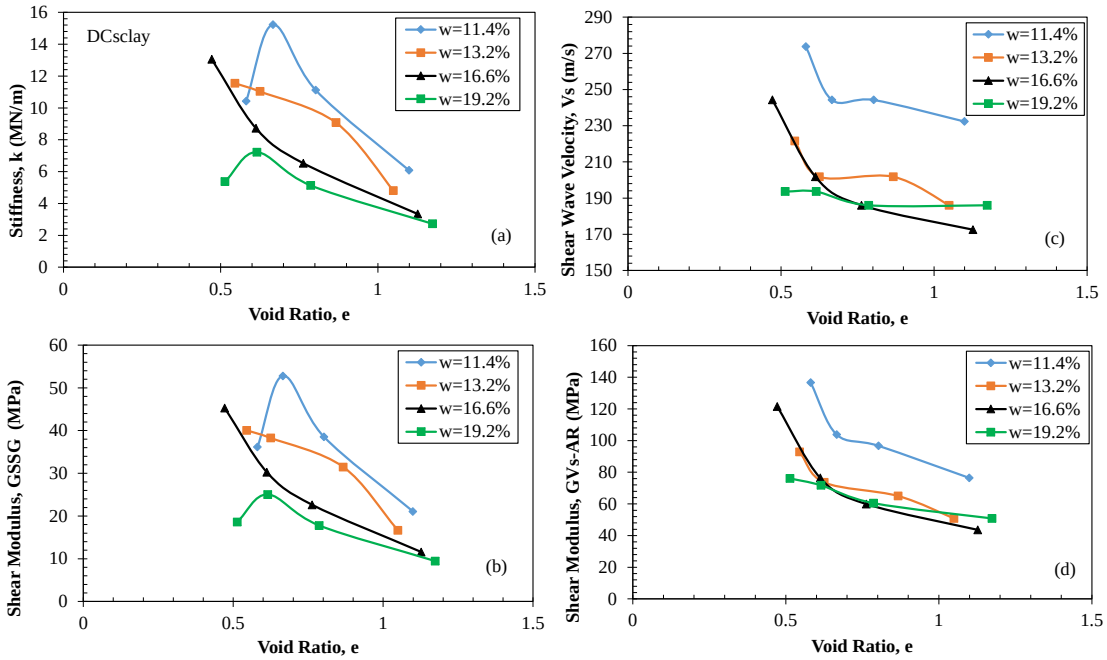

Figure H.1 Experimental data for dynamic tests of (a) Stiffness and (c) Shear wave velocity and calculated data for (a) Shear modulus from the stiffness data and (d) Shear modulus from the shear wave velocity data, all plotted with void ratio for the DCsclay soil at different constant moisture contents during the bulk soil compression tests.

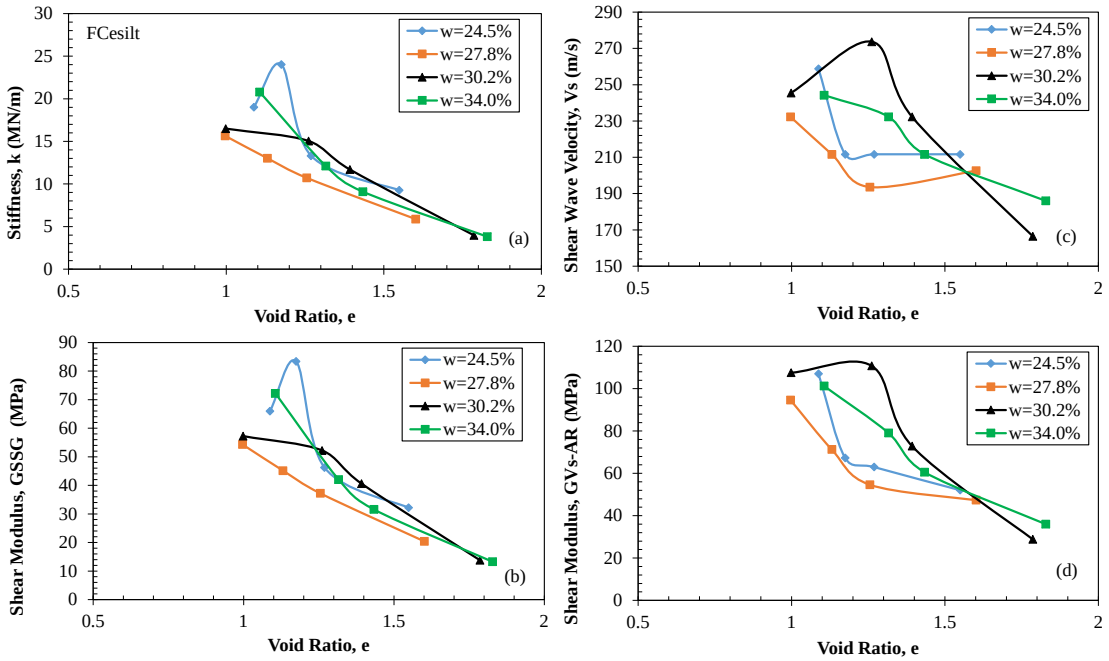

Figure H.2 Experimental data for dynamic tests of (a) Stiffness and (c) Shear wave velocity and calculated data for (a) Shear modulus from the stiffness data and (d) Shear modulus from the shear wave velocity data, all plotted with void ratio for the FCesilt soil at different constant moisture contents during the bulk soil compression tests.

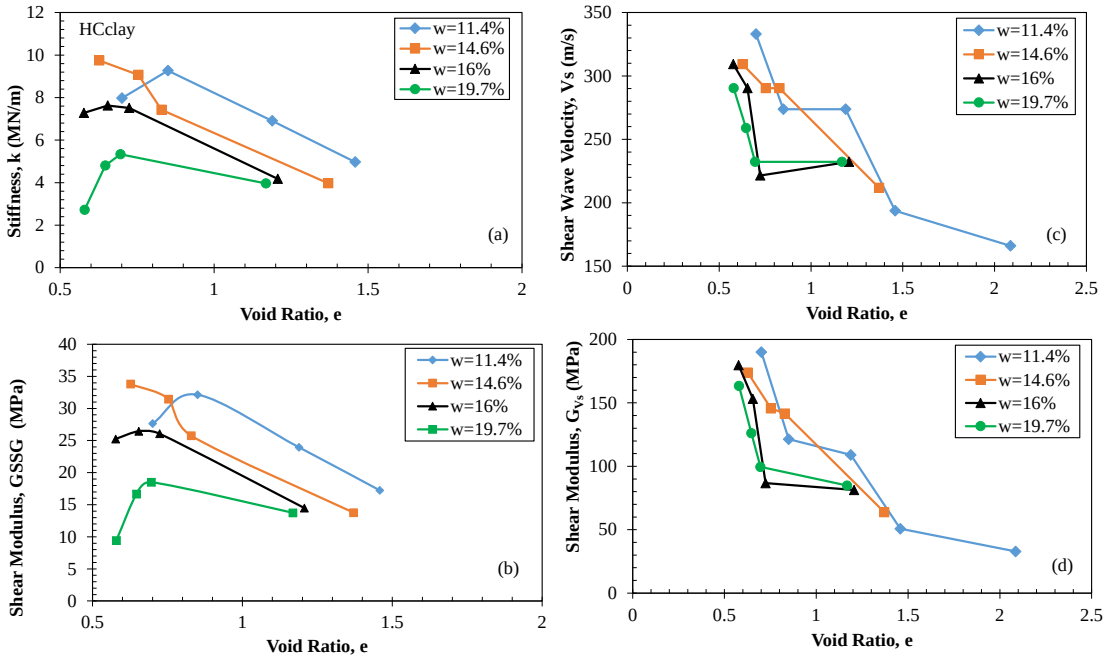

Figure H.3 Experimental data for dynamic tests of (a) Stiffness and (c) Shear wave velocity and calculated data for (a) Shear modulus from the stiffness data and (d) Shear modulus from the shear wave velocity data, all plotted with void ratio for the HCclay soil at different constant moisture contents during the bulk soil compression tests.

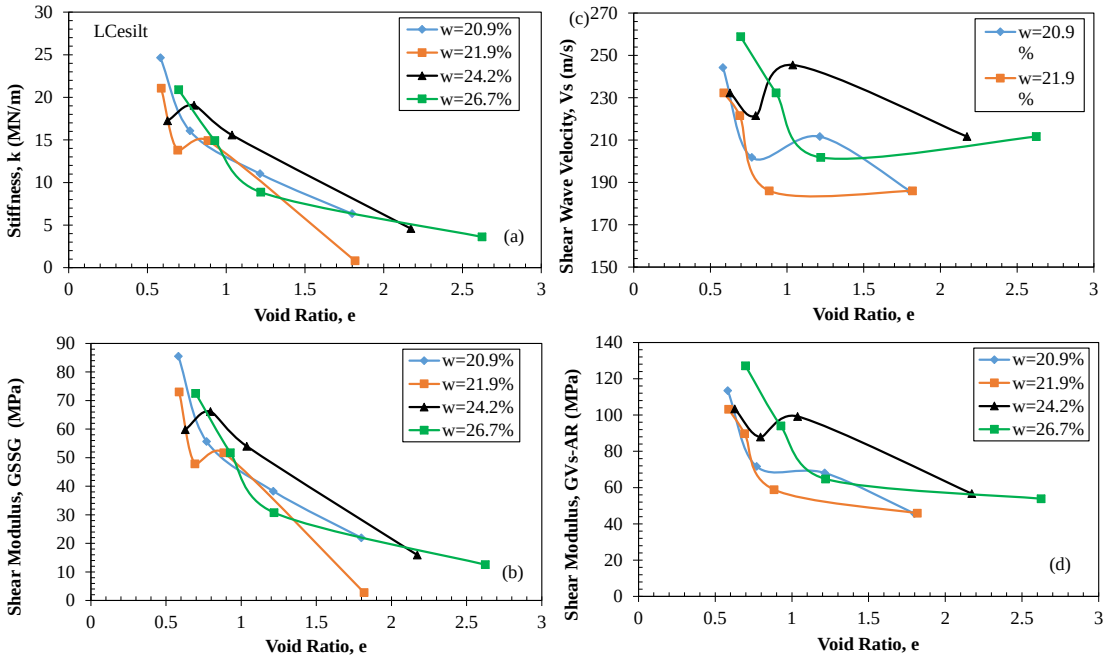

Figure H.4 Experimental data for dynamic tests of (a) Stiffness and (c) Shear wave velocity and calculated data for (a) Shear modulus from the stiffness data and (d) Shear modulus from the shear wave velocity data, all plotted with void ratio for the LCesilt soil at different constant moisture contents during the bulk soil compression tests.

The experimental and analyzed data for all four Kentucky soils are also presented in Tables H.1 through H.4. The parameter variables in the Tables represents the following: w is the gravimetric moisture content; e is the void ratio; θ is the volumetric water content; S is the degree of Saturation, V_s is the shear wave velocity, E is the Young's modulus, and G is the shear modulus.

Table H.1 Experimental and analyzed dynamic data from the crosshole seismic and the soil stiffness gauge tests performed during the bulk soil compression tests for the DCsclay at different constant moisture contents.

DCsclay									
				Crosshole seismic			SSG		
w	e	θ	S	V_s	G	E	k	E	G
(%)		(%)		(m/s)	(MPa)	(MPa)	(MN/m)	(MPa)	(MPa)
	1.440	14.15	0.215						
	1.099	16.45	0.282	232.32	76.429	198.716	6.081	54.845	21.094
11.4	0.802	19.17	0.386	244.23	96.710	251.445	11.117	100.275	38.567
	0.666	20.73	0.466	244.23	103.795	269.867	15.222	137.301	52.808
	0.581	21.85	0.534	273.71	136.686	355.382	10.423	94.011	36.158
	1.415	16.83	0.254						
	1.049	19.83	0.342	186.04	50.856	132.224	4.811	43.392	16.689
13.2	0.867	21.77	0.414	201.80	64.994	168.985	9.078	81.880	31.492
	0.625	25.01	0.575	201.80	73.625	191.424	11.032	99.508	38.272
	0.545	26.31	0.659	221.51	92.862	241.441	11.548	104.160	40.062
	1.610	20.17	0.280						
	1.127	24.75	0.401	172.55	43.628	113.432	3.341	30.139	11.592
16.6	0.763	29.86	0.592	186.04	59.906	155.756	6.527	58.873	22.643
	0.612	32.66	0.738	201.80	76.398	198.635	8.724	78.689	30.265
	0.472	35.77	0.957	244.23	121.564	316.066	13.050	117.706	45.271
	1.726	22.84	0.303						
	1.174	28.64	0.445	186.04	50.839	132.182	2.728	24.603	9.463
19.2	0.786	34.85	0.664	186.04	60.490	157.275	5.133	46.299	17.807
	0.615	38.55	0.849	193.60	71.743	186.531	7.219	65.112	25.043
	0.514	41.13	1.017	193.60	76.087	197.827	5.372	48.455	18.637

Table H.2 Experimental and analyzed dynamic data from the crosshole seismic and the soil stiffness gauge tests performed during the bulk soil compression tests for the FCesilt at different constant moisture contents.

FCesilt									
				Crosshole seismic			SSG		
w	e	θ	S	V_s	G	E	k	E	G
(%)		(%)		(m/s)	(MPa)	(MPa)	(MN/m)	(MPa)	(MPa)
	1.721	32.06	0.407						
	1.549	34.22	0.452	211.67	52.058	130.146	9.269	83.602	32.154
24.5	1.269	38.44	0.552	211.67	62.958	157.394	13.317	120.115	46.198
	1.175	40.12	0.597	211.67	67.278	168.196	24.026	216.709	83.349
	1.088	41.78	0.644	258.83	107.048	267.621	19.015	171.508	65.965
	1.859	35.55	0.428						
	1.601	39.06	0.497	202.66	47.330	118.324	5.875	52.988	20.380
27.8	1.255	45.06	0.633	193.60	54.608	136.521	10.720	96.689	37.188
	1.131	47.68	0.703	211.67	71.257	178.143	13.014	117.382	45.147
	0.997	50.89	0.798	232.32	94.655	236.637	15.650	141.155	54.290
	2.077	36.55	0.416						
	1.786	40.36	0.484	166.52	28.834	72.085	3.975	35.850	13.788
30.2	1.393	47.00	0.620	232.32	72.884	182.209	11.692	105.456	40.560
	1.261	49.73	0.685	273.71	110.733	276.832	15.044	135.690	52.188
	0.999	56.27	0.865	245.49	107.514	268.785	16.497	148.801	57.231
	2.022	43.11	0.481	244.6071					
	1.828	46.08	0.532	186.04	36.030	90.074	3.821	34.467	13.257
34.0	1.433	53.55	0.678	211.67	60.553	151.381	9.098	82.061	31.562
	1.316	56.26	0.739	232.32	79.023	197.557	12.112	109.247	42.018
	1.106	61.87	0.879	244.23	101.250	253.125	20.805	187.651	72.174

Table H.3 Experimental and analyzed dynamic data from the crosshole seismic and the soil stiffness gauge tests performed during the bulk soil compression tests for the HCclay at different constant moisture contents.

HCclay									
				Crosshole seismic			SSG		
w	e	θ	S	V_s	G	E	k	E	G
(%)		(%)		(m/s)	(MPa)	(MPa)	(MN/m)	(MPa)	(MPa)
	2.086	11.07	0.147	165.9408	32.81099	85.30858			
	1.458	13.90	0.210	193.60	50.799	132.078	4.969	44.822	17.239
11.4	1.189	15.61	0.258	273.71	108.965	283.309	6.904	62.269	23.950
	0.850	18.47	0.361	273.71	121.361	315.539	9.266	83.578	32.145
	0.701	20.09	0.438	333.04	190.095	494.248	7.976	71.944	27.671
	2.393	13.26	0.164						
	1.371	18.99	0.287	211.67	63.867	166.055	3.972	35.826	13.779
14.6	0.829	24.61	0.474	290.40	141.663	368.324	7.426	66.984	25.763
	0.754	25.67	0.521	290.40	145.693	378.803	9.071	81.817	31.468
	0.627	27.67	0.627	309.25	173.886	452.104	9.744	87.890	33.804
	2.016	16.55	0.213						
	1.206	22.63	0.357	232.32	81.320	211.433	4.177	37.674	14.490
16.0	0.724	28.97	0.595	221.51	86.763	225.583	7.513	67.766	26.064
	0.654	30.18	0.658	290.40	153.340	398.683	7.623	68.761	26.447
	0.577	31.67	0.746	309.25	179.757	467.367	7.278	65.649	25.250
	1.899	21.88	0.279						
	1.168	29.26	0.454	232.32	84.860	220.635	3.961	35.731	13.743
19.7	0.696	37.41	0.762	232.32	99.603	258.969	5.334	48.115	18.506
	0.647	38.53	0.820	258.83	126.146	327.979	4.806	43.345	16.671
	0.579	40.17	0.915	290.40	163.433	424.927	2.716	24.500	9.423

Table H.4 Experimental and analyzed dynamic data from the crosshole seismic and the soil stiffness gauge tests performed during the bulk soil compression tests for the LCesilt at different constant moisture contents.

LCesilt									
				Crosshole seismic			SSG		
w	e	θ	S	V_s	G	E	k	E	G
(%)		(%)		(m/s)	(MPa)	(MPa)	(MN/m)	(MPa)	(MPa)
	2.551	18.86	0.217						
	1.799	23.92	0.308	186.04	45.678	118.764	6.337	57.159	21.984
20.9	1.214	30.25	0.456	211.67	68.092	177.039	11.033	99.516	38.276
	0.770	37.84	0.720	201.80	71.665	186.328	16.060	144.859	55.715
	0.582	42.33	0.952	244.23	113.426	294.907	24.651	222.348	85.518
	2.794	18.65	0.208						
	1.817	25.11	0.319	186.04	45.876	119.278	0.805	7.258	2.792
21.9	0.884	37.55	0.657	186.04	58.861	153.040	14.913	134.513	51.736
	0.692	41.82	0.839	221.51	89.772	233.406	13.797	124.443	47.863
	0.587	44.56	0.988	232.32	103.210	268.346	21.054	189.902	73.039
	3.310	18.48	0.194						
	2.172	25.11	0.295	211.67	56.658	147.311	4.588	41.386	15.918
24.2	1.037	39.11	0.619	245.49	99.243	258.031	15.570	140.437	54.014
	0.795	44.37	0.807	221.51	87.857	228.427	19.072	172.021	66.162
	0.628	48.94	1.022	232.32	103.364	268.746	17.240	155.498	59.807
	3.848	18.49	0.184						
	2.624	24.74	0.270	211.67	53.898	140.134	3.618	32.635	12.552
26.7	1.219	40.40	0.581	201.80	64.778	168.422	8.867	79.976	30.760
	0.928	46.50	0.763	232.32	94.001	244.402	14.915	134.529	51.742
	0.697	52.81	1.015	258.83	127.143	330.572	20.897	188.489	72.496

APPENDIX H.2 Results of Measurements from the Saturated, CIU Triaxial Tests

The saturated CIU triaxial tests were performed on the four Kentucky clay type soils to investigate the effect of compaction state on the mechanical and dynamic properties of compacted soils at points of zero suction. The results are presented graphically as Figures H.5 and H.6 for the consolidation and shearing phase respectively. A tabulated report of the triaxial data is also presented subsequent to the graphical presentation, as Table H.5.

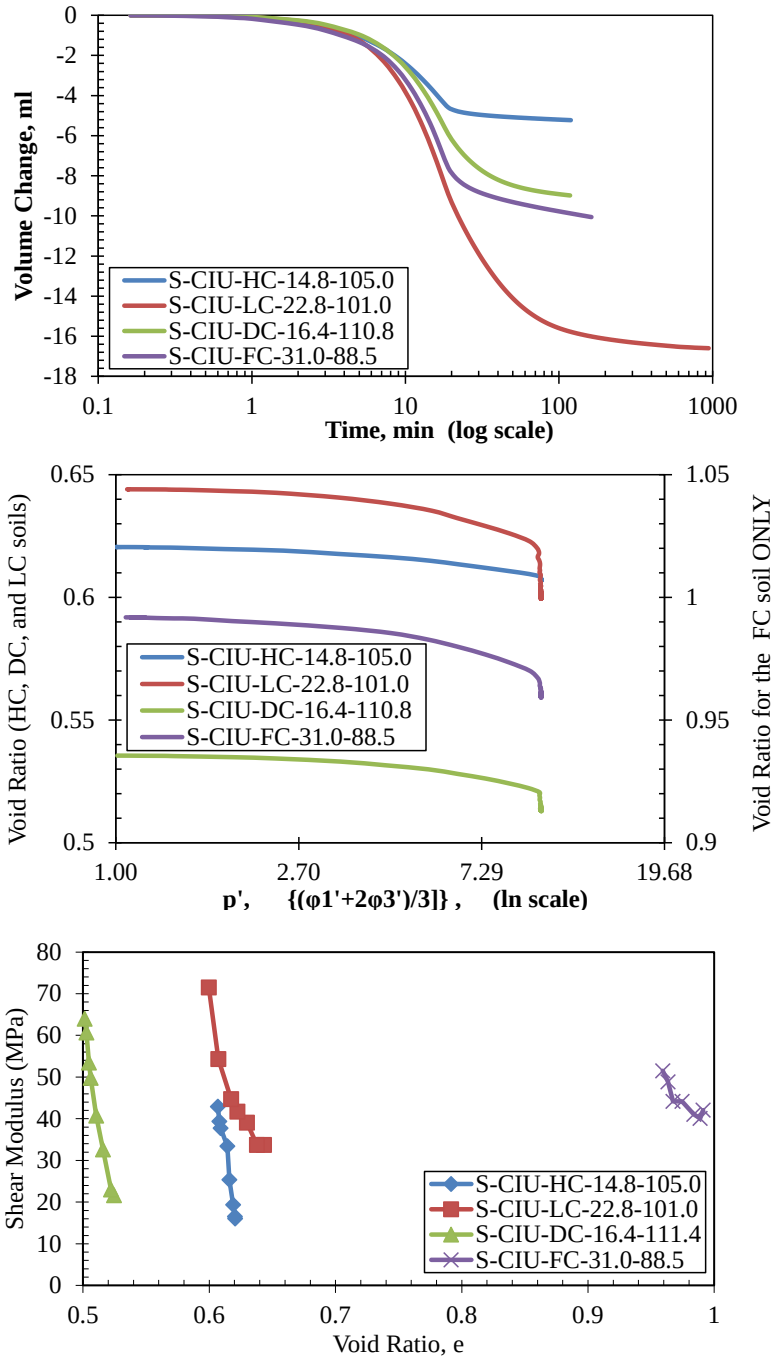

Figure H.5 Experimental results of the consolidation phase of the saturated triaxial CIU tests.

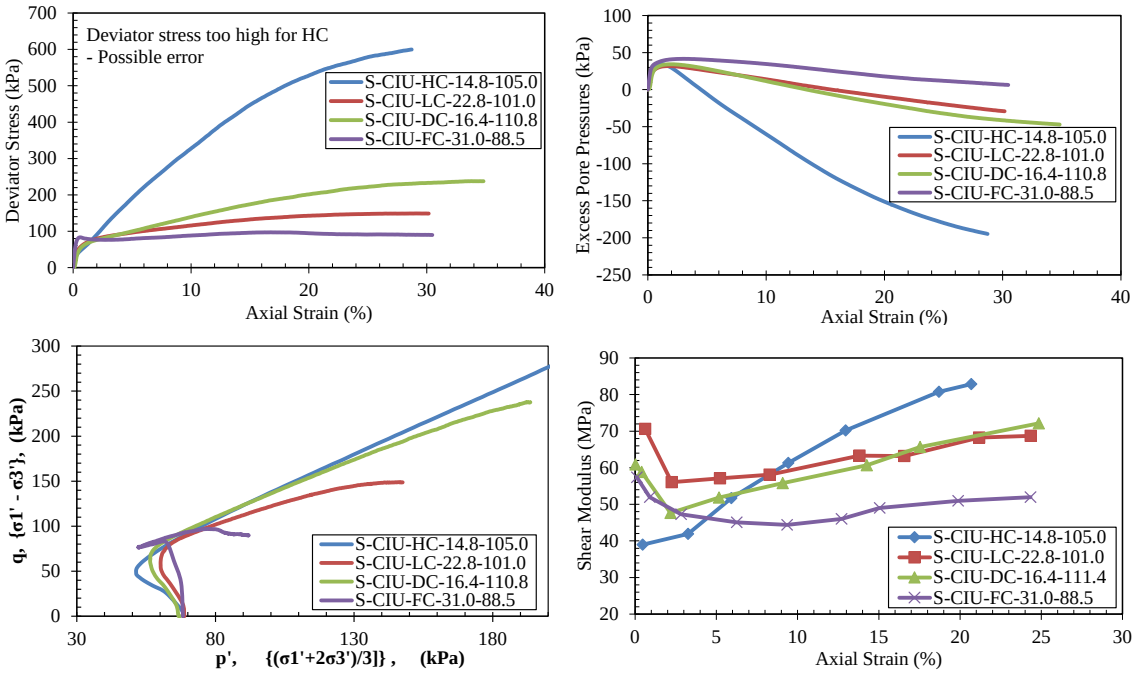

Figure H.6 Experimental results of the shearing phase of the saturated triaxial CIU tests.

Table H.5 CIU triaxial test report for the four KY clay type soils at MDD.

Sample #		HC	LC	DC	FC
	Weight of Dry Sample (g)	1028.4	989.8	1078.2	879.1
	Initial Height of Sample (in)	5.854	5.792	5.688	5.750
	Initial Sample Diameter (in)	2.868	2.869	2.884	2.876
	Soil Specific Gravity	2.69	2.65	2.72	2.86
	Initial Volume (in3)	37.818	37.444	37.157	37.354
	Initial Dry Unit Weight (pcf)	103.60	100.70	110.55	89.66
	Initial Void Ratio	0.620	0.642	0.535	0.991
	Cell Pressure (psi)	101	101	101	101
Back Saturation Stage	Back Pressure (psi)	100	100	100	100
	Pore Pressure (psi)	99.99	99.9	99.99	99.9
	B-Value	0.97	0.97	0.98	0.978
	Effective Pressure (psi)	1	1	1	1
	Cell Pressure (psi)	109.99	109.99	110	109.99
	Back Pressure (psi)	100	100	100	100
	Pore Pressure (psi)	99.99	99.9		99.94
	Effective Pressure (psi)	9.99	9.99	10	9.99
Consolidation Stage	Volume Change (ml)	5.227	16.597	8.980	10.058
	Volume After Consolidation (in3)	37.499	36.431	36.609	36.740
	Height After Consolidation (in)	5.838	5.740	5.660	5.719
	Area After Consolidation (in2)	6.424	6.347	6.468	6.425
	Dry Unit Wt. After Consolidation (pcf)	104.48	103.50	112.20	91.15
	Void Ratio After Consolidation	0.607	0.598	0.513	0.958
	Strain Rate (% per hour)	3.0	3.0	3.0	3.0
Shearing Stage Peak Failure Condition	Strain (%)	3.3	3.41	6.3	0.61
	Undrained Shear Strength, t (psi)	3.12	6.44	7.99	6.03
	Effective Vertical Stress (psi)	27.73	18.61	22.27	16.91
	Effective Horizontal Stress (psi)	7.82	5.72	6.28	4.85
	Peak Friction Angle (degrees)	34.1	32.0	34.1	33.7
	Strain (%)	28.7	30.2	33.7	25.0
	Undrained Shear Strength (psi)	43.49	10.78	17.24	6.6
Shearing Stage Critical State Failure Condition	Effective Vertical Stress (psi)	125.14	35.78	50.87	21.39
	Effective Horizontal Stress (psi)	38.15	14.21	16.4	8.2
	Critical Friction Angle (degrees)	32.2	25.6	30.8	26.5
	Net mean stress at failure, p'f	67.15	21.40	27.89	12.60
	Deviatoric stress at failure, qf	86.98	21.57	34.47	13.19
	Slope of critical state line, M	1.30	1.01	1.24	1.05
	Net mean stress at yield, py=pini	9.90	9.90	9.76	9.90
	Preconsolidation pressure, p'c=po(0)	12	40	31	60
	Deviatoric stress at yield, qy	5.91	17.40	17.79	23.31

APPENDIX H.3 Results of Measurements from the Unsaturated, CW Triaxial Tests

The experimental data for the CW triaxial tests are presented in this section of this Appendix. CW triaxial tests were performed using three Kentucky clay type soils (DCsclay, HCclay, and LCesilt). Graphical presentations of the mechanical experimental data are presented in consecutive order of equilibrium, compression, and shear tests phases for each soil. The dynamic experimental data (shear modulus)

The typical trends and responses of the experimental test data for the triaxial specimens Kentucky clay type soils, subjected to equalization, isotropic, shearing stages, and bender element test during the shearing phases are presented in this Chapter

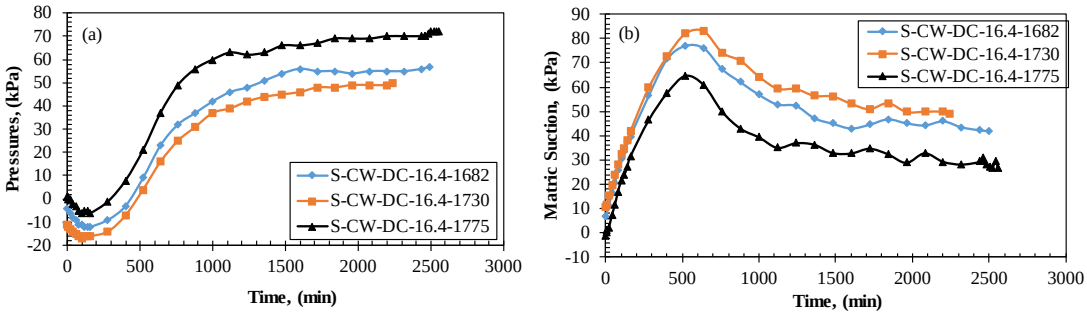

Figure H.7 Equilibrium phase CW triaxial tests experimental data for the DCsclay at different initial densities

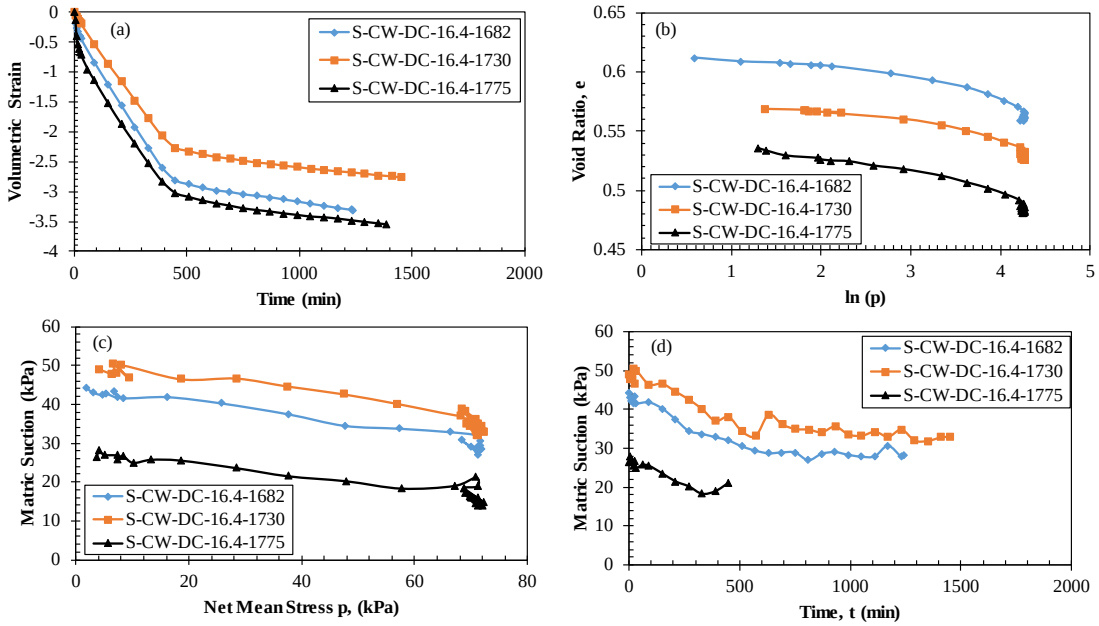

Figure H.8 Compression phase CW triaxial tests experimental data for the DCsclay at different initial densities

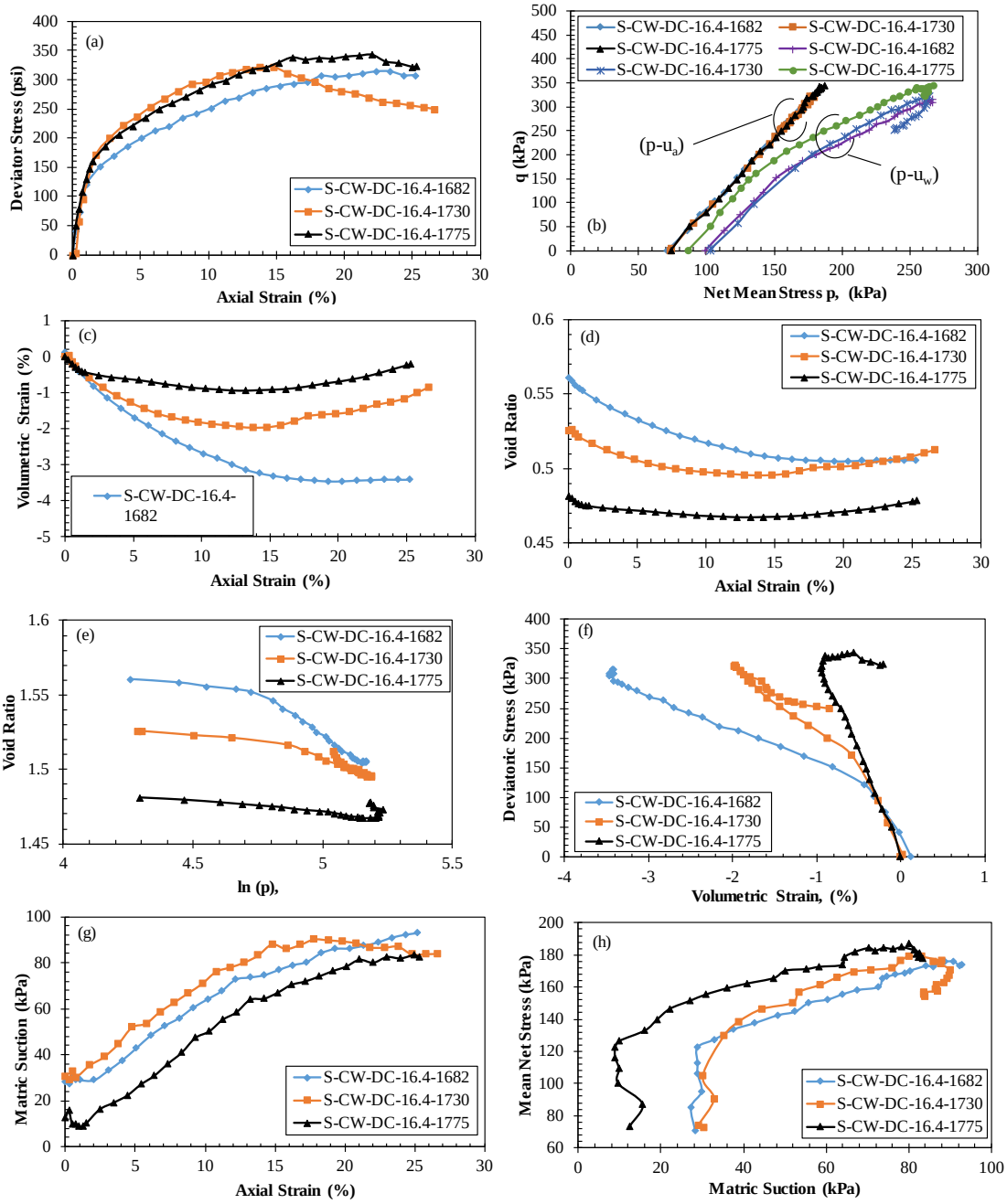

Figure H.9 Shear phase CW triaxial tests experimental data for the DCsclay at different initial densities

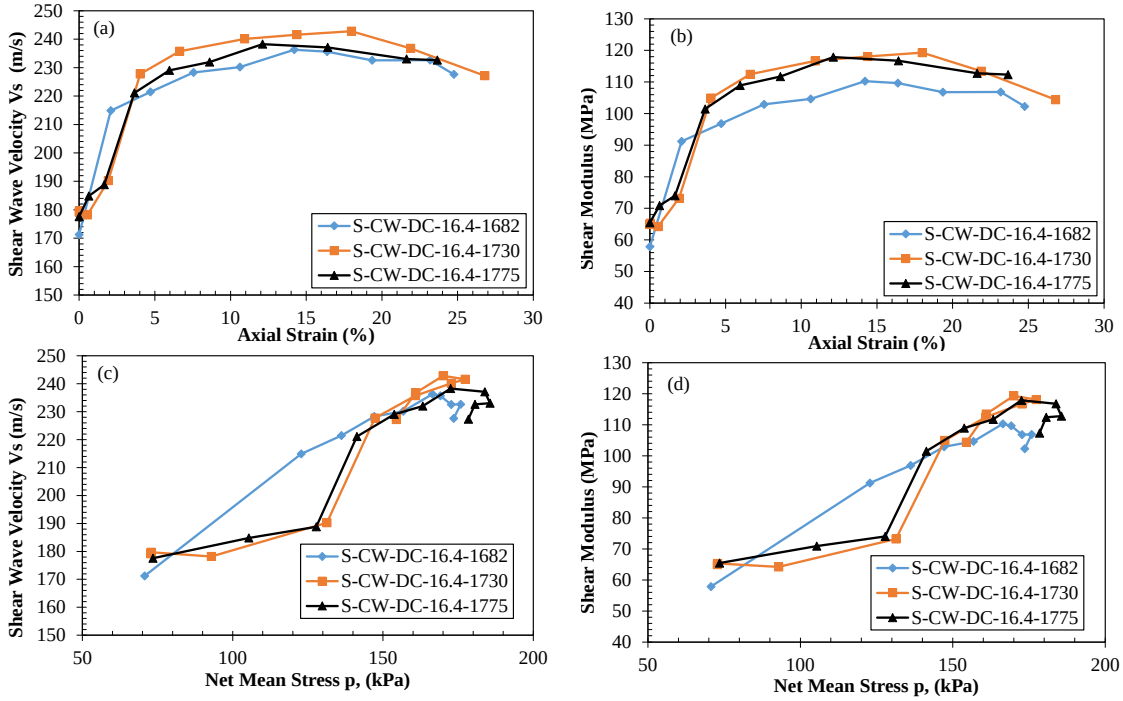

Figure H.10 Dynamic experimental and analyzed data during the shear phase CW triaxial tests for the DCsclay at different initial densities.

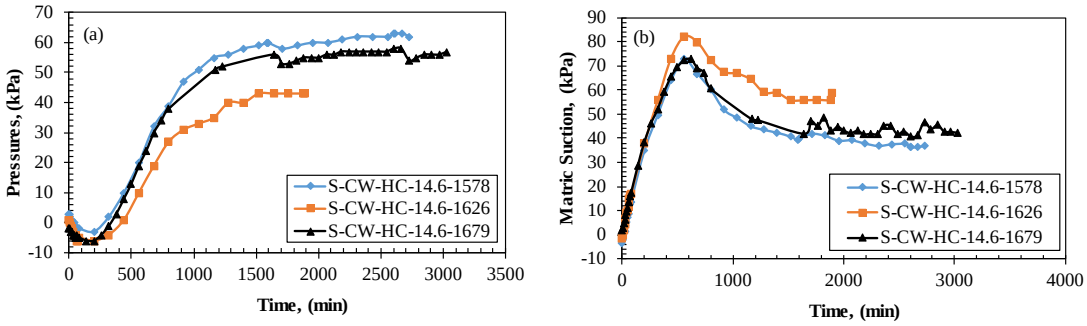

Figure H.11 Equilibrium phase CW triaxial tests experimental data for the HCclay at different initial densities

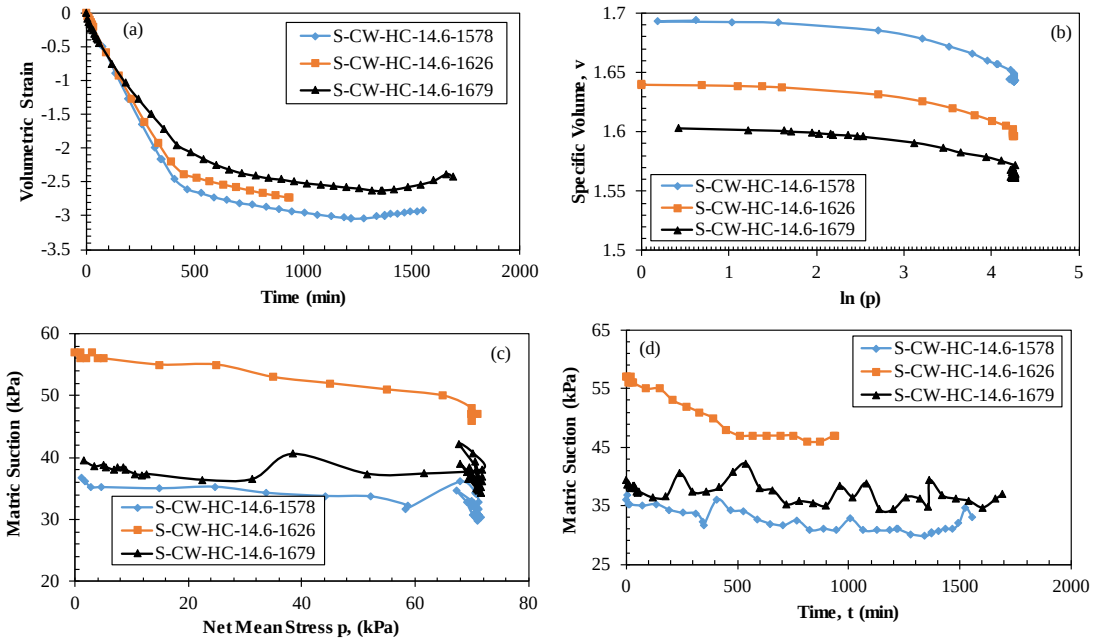

Figure H.12 Compression phase CW triaxial tests experimental data for the HCclay at different initial densities

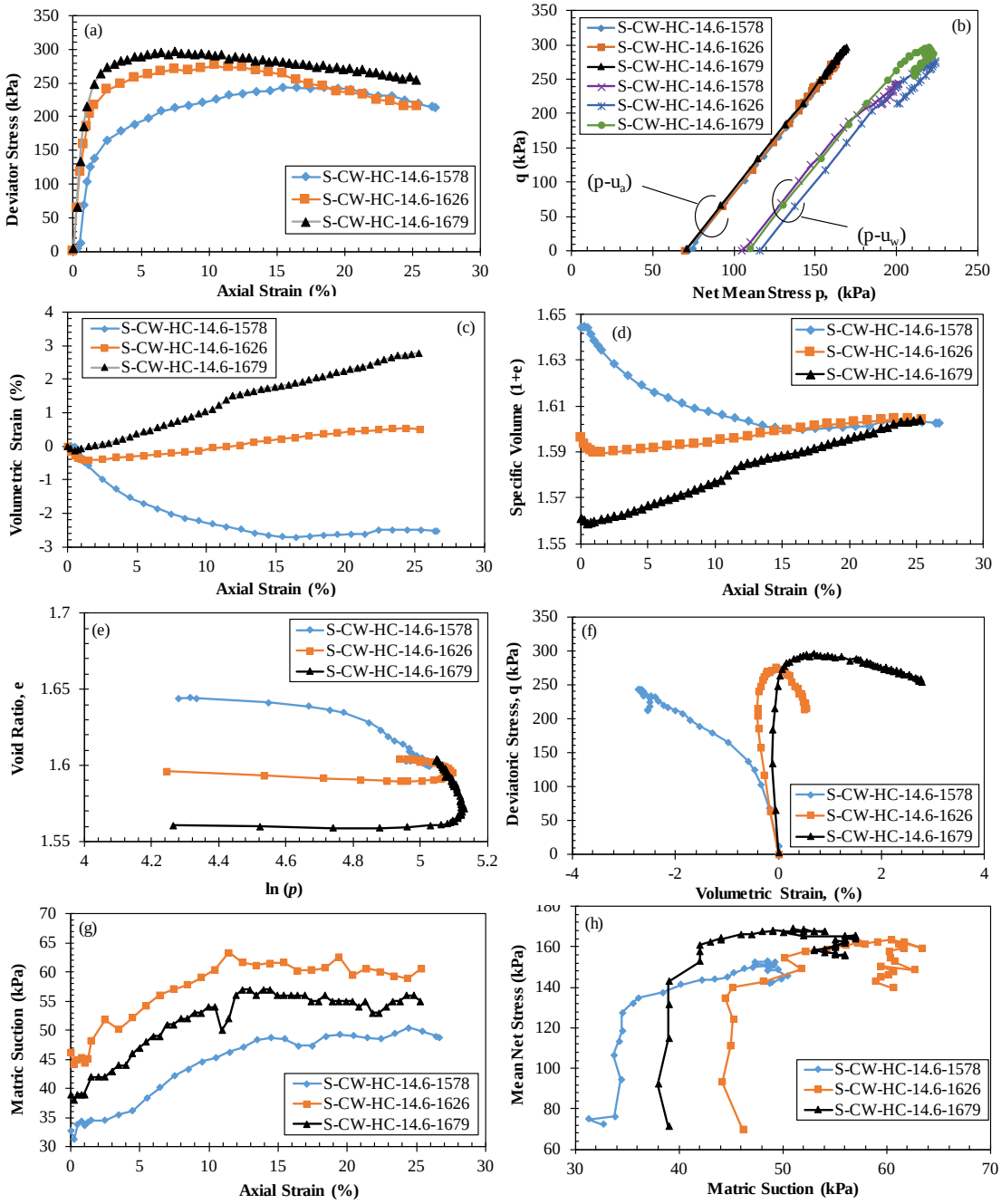

Figure H.13 Shear phase CW triaxial tests experimental data for the HCclay at different initial densities

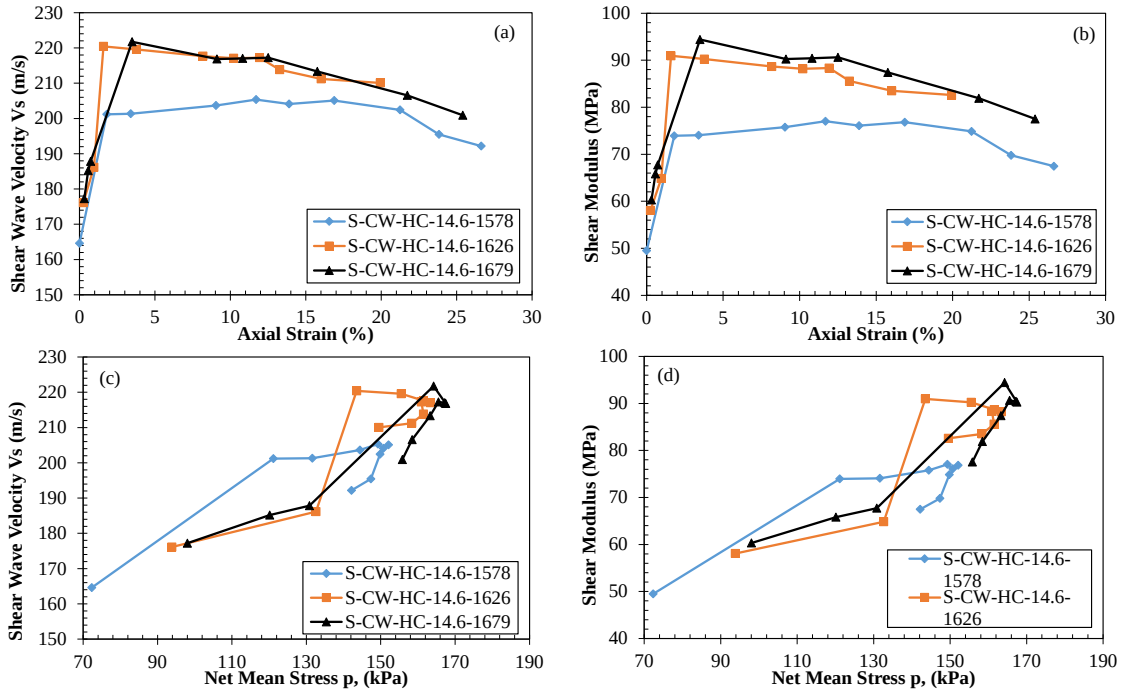

Figure H.14 Dynamic experimental and analyzed data during the shear phase CW triaxial tests for the DCsclay at different initial densities.

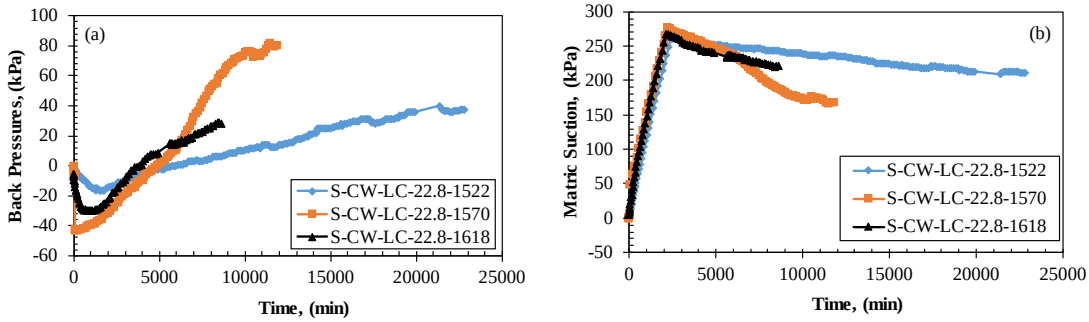

Figure H.15 Equilibrium phase CW triaxial tests experimental data for the LCesilt at different initial densities

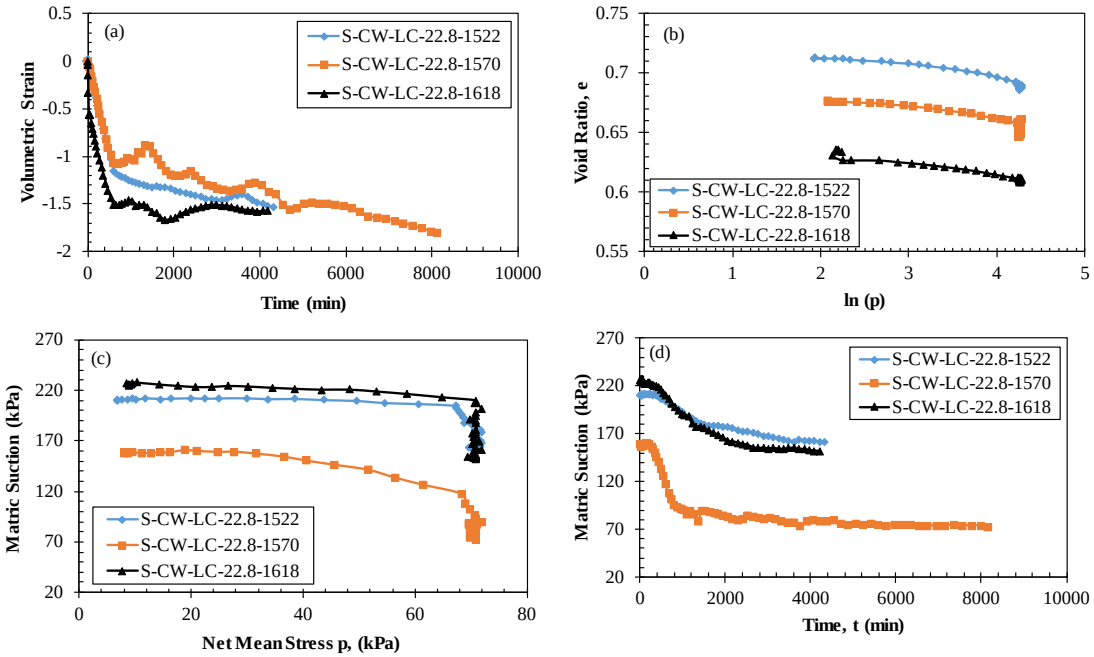

Figure H.16 Compression phase CW triaxial tests experimental data for the LCesilt at different initial densities

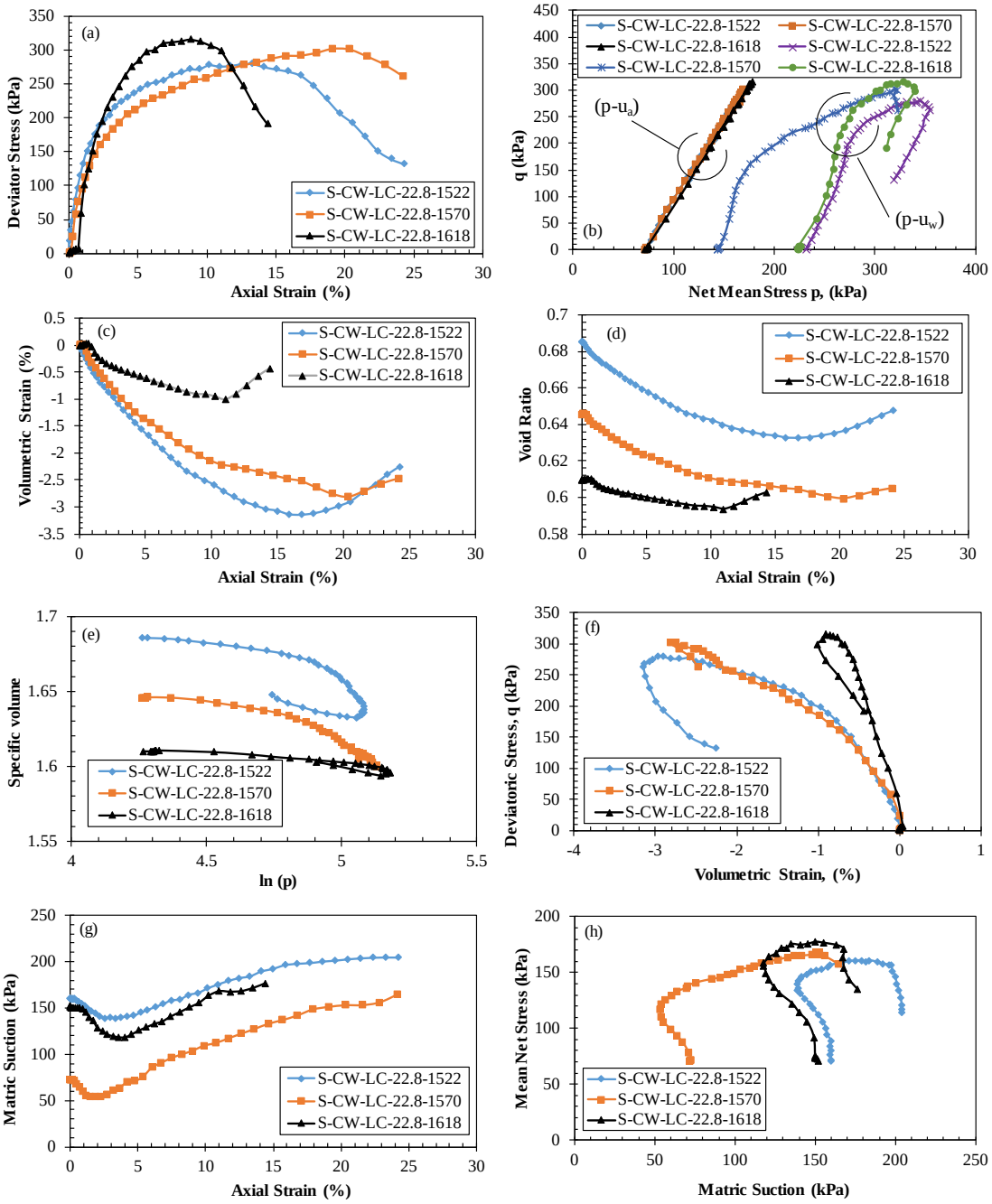

Figure H.17 Shear phase CW triaxial tests experimental data for the LCesilt at different initial densities

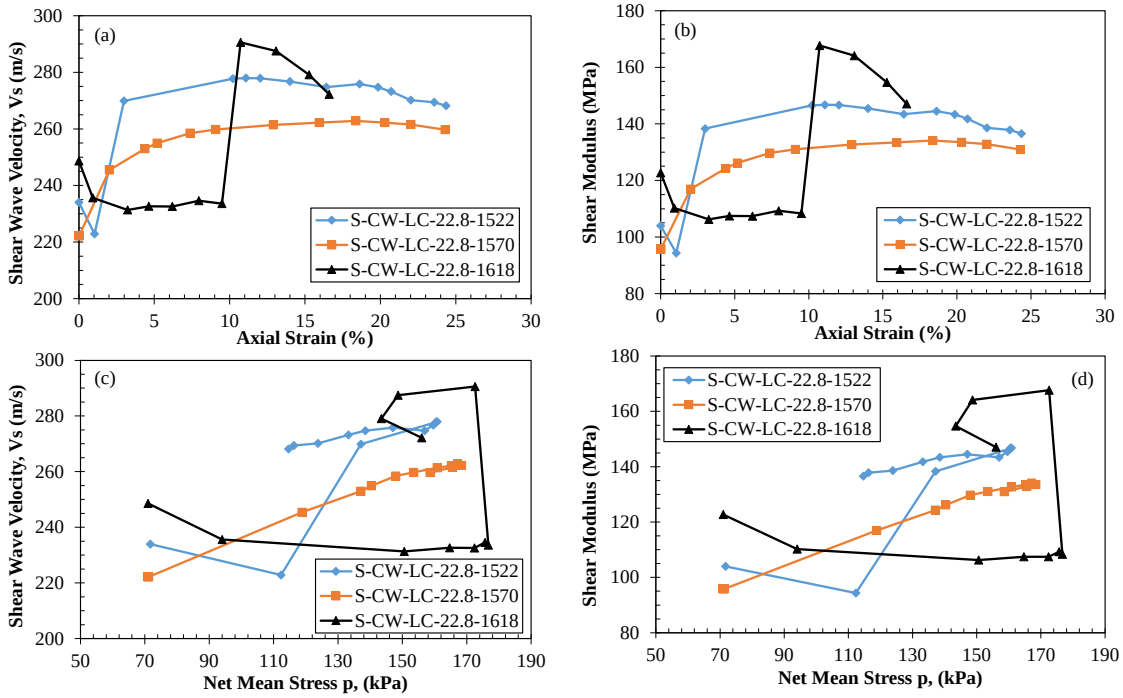

Figure H.18 Dynamic experimental and analyzed data during the shear phase CW triaxial tests for the DCsclay at different initial densities.

Table H.6 CW triaxial test report for the DCsclay soil at different initial densities.

Sample #	S-CW-DC-16.4-1682	S-CW-DC-16.4-1730	S-CW-DC-16.4-1775
Initial Sample Height (mm)	120.9	121.0	121.7
Initial Sample Diameter (mm)	50.8	50.9	50.8
Initial Wet Weight of Sample, g	484.0	497.8	511.3
Initial Moisture, %	17.1	16.7	17.2
Specific Gravity	2.7	2.7	2.7
Initial Volume of Sample, cm3	245.1	246.0	246.3
Initial Total Density, kg/m3	1975.0	2023.4	2076.0
Initial Dry Weight, g	413.5	426.6	436.2
Initial Dry Density, kg/m3	1687.3	1733.9	1771.3
Initial Void Ratio e0	0.6	0.6	0.536
Initial Saturation, %	75.8	79.9	87.4
Initial Volume of Solids, cm3	152.0	156.8	160.4
Compression Stage			
Compression Rate (kPa / hr)	7.0	7.0	7.0
Axial Strain, %	0.157	0.091	-0.124
Volume Change, ml	-8.110	6.798	-8.735
Compressed Volume of Sample, cm3	236.974	239.237	237.542
Compressed Total Density, kg/m3	2042.5	2080.9	2152.3
Compressed Dry Density, kg/m3	1745.0	1783.1	1836.5
Compressed Void Ratio, e0	0.559	0.525	0.481
Height After Consolidation, mm	121.11	121.07	121.55
Area After Consolidation, mm2	1956.7	1976.0	1954.3
p_0	70.69	72.69	73.49
$\psi 0$	28.31	30.31	12.51
k	2.50	2.40	5.87
Shear Stage Critical State Failure Condition			
Strain Rate (% per hour)	0.50	0.50	0.50
Axial Strain (%)	22.34	14.79	17.13
$(\sigma_3 - u_a)_f$, Net Confining Pressure (kPa)	71.20	69.07	71.20
$(\sigma_1 - u_a)_f$, Net Major Principal Stress (kPa)	385.39	390.65	405.39
p_f	175.93	176.26	182.60
q_f	314.19	321.58	334.19
Void Ratio at failure, e_f	0.51	0.50	0.47
Matric Suction at failure, $(u_a - u_w)_f$ (kPa)	88.80	87.93	71.80
Degree of Saturation Suction, s_{sa}	0.30	2.00	3.00
p_{0f}	-5.81	-9.57	-12.53
Slope of Critical State Line (CSL), M	1.73	1.73	1.71
Intercept of CSL, (μ_s) kPa	10.04	16.56	21.45
Critical State Friction Angle (degrees)	43.5	44.4	44.5

Table H.7 CW triaxial test report for the HCclay soil at different initial densities.

Sample #	S-CW-HC-14.6-1578	S-CW-HC-14.6-1626	S-CW-HC-14.6-1679
Initial Height of Sample (in)	121.1	121.3	121.9
Initial Sample Diameter (in)	50.7	50.9	50.9
Initial Wet Weight of Sample, g	446.6	461.1	476.0
Initial Moisture, %	15.0	14.2	14.4
Specific Gravity	2.69	2.69	2.69
Initial Volume of Sample, cm3	244.5	246.4	247.9
Initial Total Density, kg/m3	1826.9	1871.7	1919.8
Initial Dry Weight, g	388.3	403.9	416.1
Initial Dry Density, kg/m3	1588.3	1639.4	1678.2
Initial Void Ratio e0	0.694	0.641	0.603
Initial Saturation, %	58.3	59.5	64.2
Initial Volume of Solids, cm3	144.4	150.1	154.7
Compression Stage			
Compression Rate (kPa / hr)	7.0	7.0	7.0
Axial Strain, %	-0.025	0.239	-0.041
Volume Change, ml	7.134	-6.740	-6.537
Compressed Volume of Sample, cm3	237.345	239.619	241.406
Compressed Total Density, kg/m3	1881.818	1924.350	1971.824
Compressed Dry Density, kg/m3	1636.079	1685.513	1723.623
Compressed Void Ratio, e0	0.644	0.596	0.561
Height After Consolidation, mm	121.020	121.600	121.800
Area After Consolidation, mm2	1961.208	1970.548	1981.985
p_0	72.33	69.87	71.20
$\psi 0$	32.67	46.13	39.00
k	2.21	1.51	1.83
Shear Stage			
Strain Rate (% per hour)	0.500	0.500	0.500
Critical State Failure Condition			
Axial Strain (%)	23.43	19.39	16.39
$(\sigma_3 - u_a)_f$, Net Confining Pressure (kPa)	71.52	69.36	70.00
$(\sigma_1 - u_a)_f$, Net Major Principal Stress (kPa)	302.75	306.68	348.18
p_f	148.60	148.47	162.73
q_f	231.23	237.32	278.18
Void Ratio at failure, e_f	0.603	0.602	0.590
Matric Suction at failure, $(u_a - u_w)_f$ (kPa)	49.48	62.64	56.00
Degree of Saturation Suction, s_{sa}	4.6	5.6	6.5
p_{0f}	-16.913	-20.557	-21.711
Slope of Critical State Line (CSL), M	1.397	1.404	1.508
Intercept of CSL, (μ_s) kPa	23.63	28.86	32.75
Critical State Friction Angle (degrees)	38.2	39.1	41.7

Table H.8 CW triaxial test report for the LCesilt soil at different initial densities.

Sample #	S-CW-LC-22.8-1522	S-CW-LC-22.8-1570	S-CW-LC-22.8-1618
Initial Height of Sample (in)	119.3	119.8	120.6
Initial Sample Diameter (in)	50.9	51.0	51.1
Initial Wet Weight of Sample, g	460.1	474.3	490.5
Initial Moisture, %	22.7	22.8	22.6
Specific Gravity	2.65	2.65	2.65
Initial Volume of Sample, cm3	242.2	244.3	247.0
Initial Total Density, kg/m3	1899.6	1941.6	1985.6
Initial Dry Weight, g	374.9	386.3	400.2
Initial Dry Density, kg/m3	1547.9	1581.1	1620.1
Initial Void Ratio e0	0.712	0.676	0.636
Initial Saturation, %	84.6	89.4	94.0
Initial Volume of Solids, cm3	141.5	145.8	151.0
Compression Stage			
Compression Rate (kPa / hr)	7.0	7.0	7.0
Axial Strain, %	0.327	0.108	-0.373
Volume Change, ml	-3.7	-4.4	-3.9
Compressed Volume of Sample, cm3	238.5	239.9	243.2
Compressed Total Density, kg/m3	1929.3	1977.2	2017.3
Compressed Dry Density, kg/m3	1572.1	1610.1	1645.9
Compressed Void Ratio, e0	0.686	0.646	0.610
Height After Consolidation, mm	119.7	119.9	120.2
Area After Consolidation, mm2	1993.1	2000.0	2023.9
p_0	70.89	70.86	70.98
$\psi 0$	160.11	72.14	152.02
k	0.44	0.98	0.47
Shear Stage			
Strain Rate (% per hour)	0.500	0.500	0.500
Critical State Failure Condition			
Axial Strain (%)	16.77	20.30	11.00
$(\sigma_3 - u_a)_f$, Net Confining Pressure (kPa)	69.5	68.2	71.9
$(\sigma_1 - u_a)_f$, Net Major Principal Stress (kPa)	331.4	369.0	370.4
p_f	156.8	168.4	171.4
q_f	261.9	300.8	298.5
Void Ratio at failure, e_f	0.633	0.600	0.594
Matric Suction at failure, $(u_a - u_w)_f$ (kPa)	197.6	152.8	168.1
Degree of Saturation Suction, s_{sa}	19.6	121.9	228.2
p_{0f}	-66.3	-149.5	-168.1
Slope of Critical State Line (CSL), M	1.174	0.946	0.879
Intercept of CSL, (μ_s) kPa	77.87	141.45	147.77
Critical State Friction Angle (degrees)	40.8	43.5	42.4

APPENDIX I

Soil Data from Sawangsuriya et al. (2009)

In Section 7.1.2 in this report, analyses were performed to determine the relationship of the A parameter with functions of material properties. The A parameter was originally presented by Hardin and Black (1968), and used by Sawangsuriya et al., (2009). The Sawangsuriya model was introduced with the inclusion of the OCR parameter as follows:

$$G_{\max} = A\, f(e) OCR^{k} \left(p + S^{\kappa} s\right)^{n} \tag{H.1}$$

The A parameter is generally discussed as a soil material parameter. In Section 8.1.2, five additional test soil studies were used to assess the relationship of the A parameter with material properties. The studies used in the assessment are for a silt, two lean clays, a fat clay and a clayey sand that were used by Sawangsuriya et al., (2009). The extracted data from Sawangsuriya et al., (2009), for the five soils are presented in this Appendix, and shown in the Tables H.9 and H.10.

Table H.9 Data from Sawangsuriya et al. 2009 Fig 5 (std-opt), Fig.7, Table 2

Reference	Soil Type	A	n	θ_s	κ	OCR	p (kPa)
S09silt	Silt, ML	1590	0.72	0.338	1	1	35
S09lclay1	Lean clay-1, CL-1	5499	0.47	0.375	1	1	35
S09lclay2	Lean clay-2, CL-2	12503	0.4	0.325	1	1	35
S09fclay	Fat clay, CH	1412	0.64	0.535	1	1	35
S09csand	Clayey Sand, SC	14534	0.37	0.269	1	1	35

Table H.10 Extracted data from Sawangsuriya et al., (2009).

Sample	Suction (kPa)	G0 (kPa)	θ	S	f(e)	e	f(e)
S09silt (Silt, ML)	0	59669	0.342	1.011	2.901	0.253	1.061
	7.6	59669	0.314	0.928	2.540	0.366	0.902
	21.5	61326	0.310	0.918	2.161	0.482	0.785
	35.2	62983	0.279	0.824	1.983	0.540	0.738
	55.7	64641	0.237	0.702	1.831	0.593	0.700
	104.8	79558	0.208	0.616	1.823	0.596	0.698
	172.8	96133	0.184	0.544	1.827	0.594	0.699
	278.1	125967	0.166	0.491	1.951	0.551	0.729
	485.8	157459	0.145	0.429	1.895	0.570	0.715
	626.5	175691	0.135	0.400	1.886	0.574	0.713
	975.7	246961	0.126	0.372	2.088	0.506	0.765
S09lclay1 (Lean clay-1, CL-1)	0	56757	0.395	1.053	1.941	0.554	0.727
	6.9	56757	0.381	1.015	1.782	0.611	0.688
	21.5	60000	0.374	0.997	1.639	0.666	0.653
	34.6	68108	0.365	0.974	1.696	0.643	0.667
	56.2	79459	0.357	0.953	1.757	0.620	0.681
	104.8	95676	0.340	0.906	1.766	0.617	0.684
	172.8	111892	0.328	0.875	1.745	0.625	0.678
	278.1	136216	0.313	0.835	1.792	0.607	0.690
	419.1	158919	0.300	0.801	1.792	0.607	0.690
	626.5	180000	0.291	0.777	1.729	0.631	0.675
S09lclay2 (Lean clay-2, CL-2)	0	145020	0.351	1.079	2.798	0.286	1.007
	6.9	145020	0.325	1.000	2.604	0.346	0.925
	20.8	159363	0.313	0.964	2.565	0.358	0.910
	48.4	168924	0.300	0.925	2.344	0.425	0.837
	104.8	178486	0.288	0.885	2.052	0.517	0.755
	172.8	207171	0.283	0.871	2.051	0.518	0.755
	278.1	234263	0.279	0.859	1.985	0.540	0.738
	419.1	317131	0.267	0.822	2.357	0.421	0.842
	621.4	360159	0.257	0.792	2.348	0.424	0.839

Continued in the following Table on next page.

Continued from previous Table

Table H.10 Extracted data (continued) from Sawangsuriya et al., (2009).

Sample	Suction (kPa)	G0 (kPa)	θ	S	f(e)	e	f(e)
S09fclay (Fat clay, CH)	0	30400	0.525	0.981	2.212	0.466	0.799
	6.9	30400	0.520	0.973	1.978	0.542	0.736
	20.8	30400					
	48.4	30400					
	104.8	36800	0.503	0.939	1.137	0.910	0.534
	172.8	52800	0.484	0.905	1.295	0.821	0.572
	243.9	62400	0.473	0.884	1.289	0.825	0.570
	347.0	72000	0.456	0.853	1.244	0.848	0.560
	553.9	108800	0.444	0.830	1.453	0.745	0.609
S09csand (Clayey Sand, SC) Opt	0	151282	0.282	1.048	2.793	0.288	1.005
	13.8	151282	0.249	0.926	2.490	0.381	0.884
	34.3	164103	0.239	0.889	2.403	0.407	0.856
	103.6	208974	0.229	0.850	2.423	0.401	0.862
	242.2	267949	0.211	0.784	2.485	0.382	0.883

APPENDIX J

As-Compacted State Model Predictions and VBA code

Based on the findings in this study, a stress-strain model was developed for predicting the strength of compacted clays using a field input variable of shear modulus obtained from a soil stiffness gauge (the Geogauge). The model is called the As-Compacted State Model and the implementation of this model was discussed in Section 7.2.6 of this report. The model predicted data in comparison with the experimental data are presented in the figures in this Appendix. The predicted mechanical behaviors are presented for each the three Kentucky clay type soils (DCsclay, HCclay, and LCesilt) tested under CW conditions. The VBA coding of the model is also presented in this Appendix.

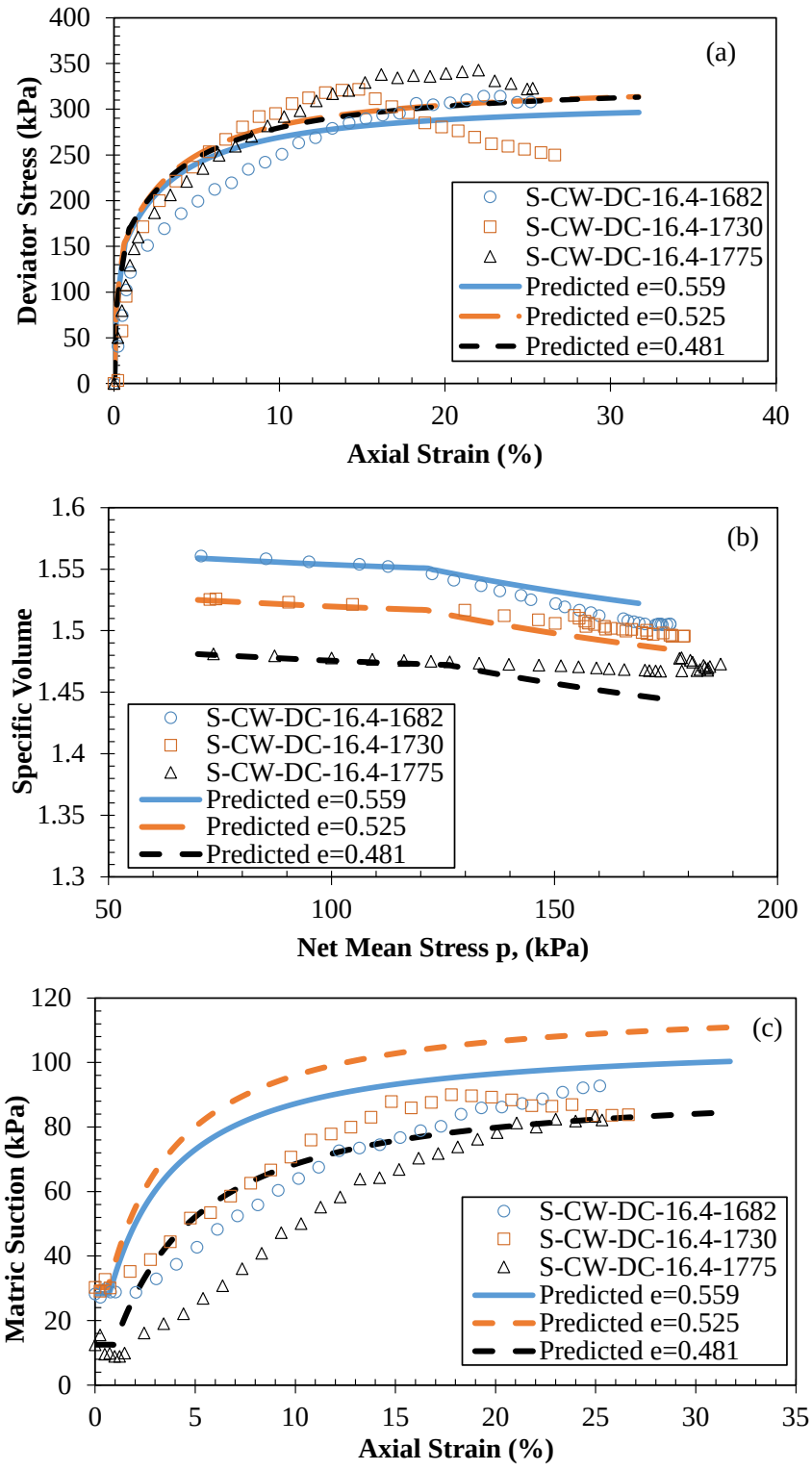

Figure J.1 The As-Compacted Model predicted mechanical behavior for the DCsclay soil at different initial densities of (a) stress-strain behavior, (b) volumetric compression behavior (c) suction-strain behavior.

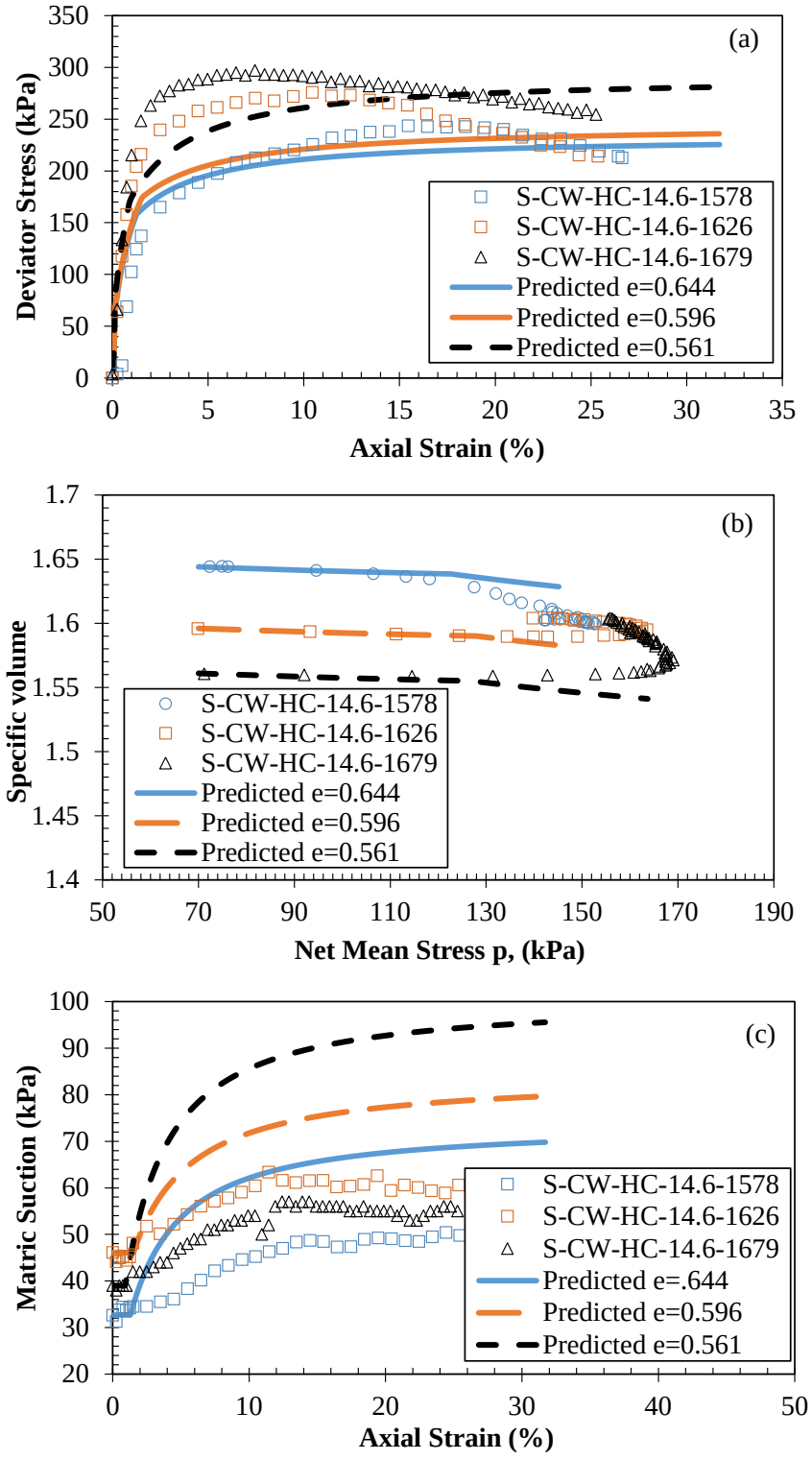

Figure J.2 The As-Compacted Model predicted mechanical behavior for the HCclay soil at different initial densities of (a) stress-strain behavior, (b) volumetric compression behavior (c) suction-strain behavior.

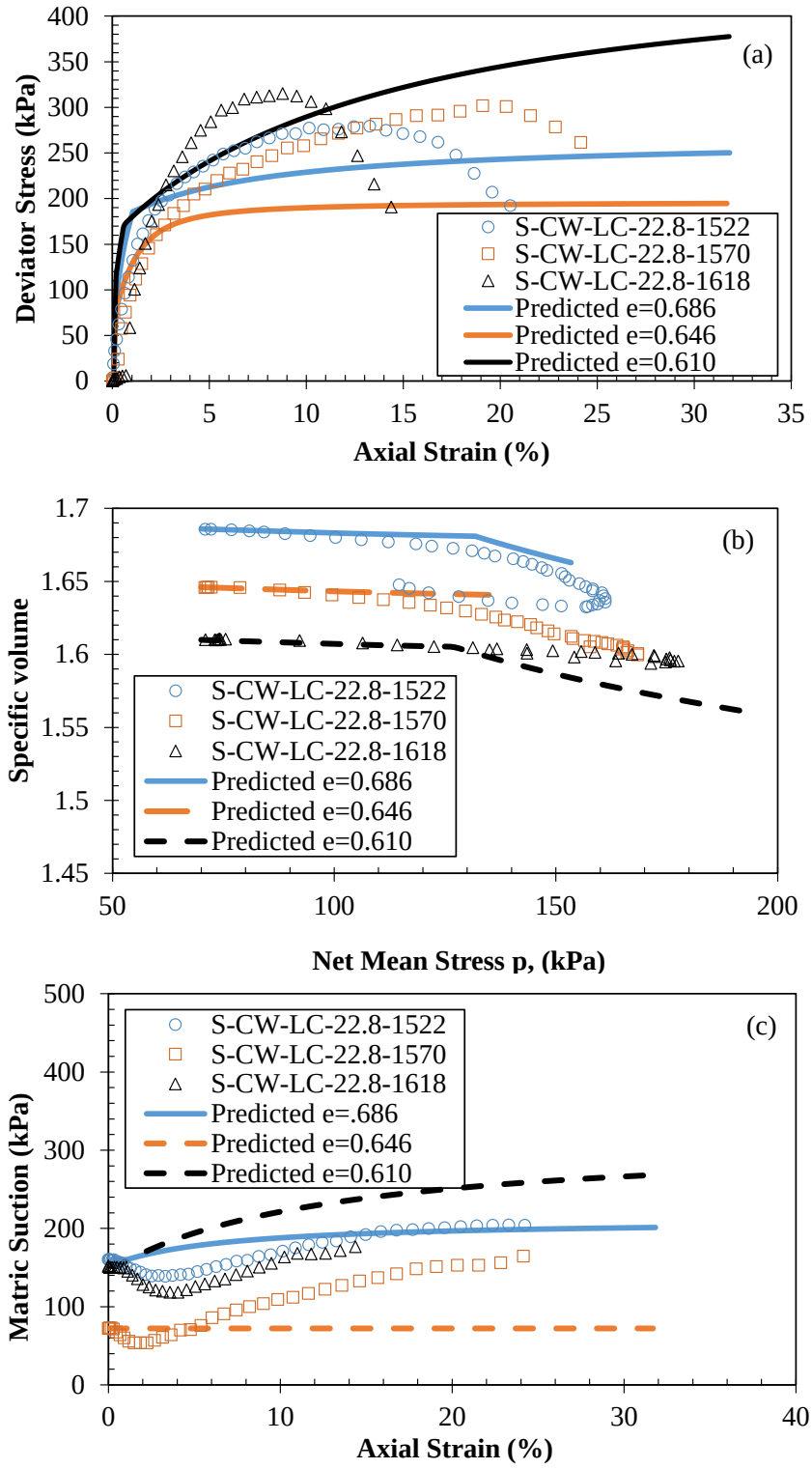

Figure J.3 The As-Compacted Model predicted mechanical behavior for the LCesilt soil at different initial densities of (a) stress-strain behavior, (b) volumetric compression behavior (c) suction-strain behavior.

VBA code for the As-Compacted State Model

```
Sub IYSFGhardeningSFGVolandSuction()

'THE AS-COMPACTED STATE MODEL
'This model is based on the BBM, and includes
'functions in the SFG model (Sheng et al., 2008)
'functions in the UH Model (Yao et al., 2014)
'a function for plastic shear strains inside the initial yield zone
'and an input for a field shear modulus

Dim kappa_vp, lamda_vp, Mc, Gssg As Double  'The model parameters
Dim Gs, PI, PF As Double                    'The material parameter
Dim p_ini, q_ini, s_ini, e_ini, w As Double 'The initial state parameters
Dim p_00, p0s_0, s_sa As Double             'The saturated state stresses

'Specific Volume
Dim v_ini, vy_esp As Double
Dim v0_ncl, v, v_old As Double

'Strains
Dim eqe, eqp, eq, evpe, evpp, evp, evse, evsp, evs, ev, e1 As Double
Dim Deqe, Deqp, Deq, Devpe, Devpp, Devp, Devse, Devsp, Devs, dilatancy As Double

'Stresses
Dim q, p, p_0s, s, q_old, p_old, p0s_old As Double
Dim dq, dp, dp_0s, ds, ds_0  As Double
Dim p_s, p_y, q_y, p_f, q_f As Double
Dim p_cs, q_cs, p0s_cs, eta_cs, st_cs As Double
Dim p0s_ini, p0s_f As Double
Dim eta As Double

'Elasticity Modulus equation parameters
Dim G, e, fe, kay, sat, kap, n As Double

'Non-associated flow rule parameter
Dim alpha As Double

ActiveWorkbook.Worksheets("WORKBOOK NAME GOES HERE").Activate
Application.ScreenUpdating = False

kappa_vp = ActiveSheet.Cells(4, 7).Value
lamda_vp = ActiveSheet.Cells(5, 7).Value
p_00 = ActiveSheet.Cells(6, 7).Value
p0s_0 = ActiveSheet.Cells(7, 7).Value
s_sa = ActiveSheet.Cells(8, 7).Value
Mc = ActiveSheet.Cells(9, 7).Value
Gssg = ActiveSheet.Cells(10, 7).Value

p_ini = ActiveSheet.Cells(11, 7).Value
```

```
q_ini = ActiveSheet.Cells(12, 7).Value
s_ini = ActiveSheet.Cells(13, 7).Value
w = ActiveSheet.Cells(14, 7).Value  'initial moisture content
e_ini = ActiveSheet.Cells(15, 7).Value

Gs = ActiveSheet.Cells(16, 7).Value 'Specific Gravity
PI = ActiveSheet.Cells(17, 7).Value 'Plasticity Index
PF = ActiveSheet.Cells(18, 7).Value  'Percent Fines


alpha = (Mc * (Mc - 9) * (Mc - 3)) / (9 * (6 - Mc) * (1 - (kappa_vp / lamda_vp)))

'Geometry
    s = s_ini
    If s < s_sa Then
       p_s = s_ini
       p0s_ini = p0s_0 - s
   Else
       p_s = s_sa + (s_sa + 1) * Log((s_ini + 1) / (s_sa + 1))
       p0s_ini = (p0s_0 / p_00) * (p_00 + s - p_s) - s
   End If

   p_y = (18 * p_ini + Mc ^ 2 * (p0s_ini - p_s) + Mc * Sqr(Mc ^ 2 * (p_s + p0s_ini) ^ 2 + 36 *
(p_s * p0s_ini - p_s * p_ini + p0s_ini * p_ini - p_ini ^ 2))) / (2 * (Mc ^ 2 + 9))
   q_y = 3 * (p_y - p_ini)
   p_f = (Mc * p_s + 3 * p_ini) / (3 - Mc)
   q_f = Mc * (p_f + p_s)
   p0s_f = p_f + q_f ^ 2 / (Mc ^ 2 * (p_f + p_s))
   v_ini = 1 + e_ini
   vy_esp = v_ini - kappa_vp * Log(p_y / p_ini)              'The Log function in excel VBA returns
the natural log (ln) of a number.
   v0_ncl = v_ini - kappa_vp * Log(p0s_ini / p_ini)

   ActiveSheet.Cells(4, 15).Value = p_y
   ActiveSheet.Cells(5, 15).Value = q_y
   ActiveSheet.Cells(6, 15).Value = p_f
   ActiveSheet.Cells(7, 15).Value = q_f
   ActiveSheet.Cells(8, 15).Value = p0s_ini
   ActiveSheet.Cells(9, 15).Value = p0s_f
   ActiveSheet.Cells(10, 15).Value = vy_esp
   ActiveSheet.Cells(11, 15).Value = v0_ncl
   ActiveSheet.Cells(12, 15).Value = p_s

'Initial values
   Deqp = 0
   Deqe = 0
   dp = 0
   dq = 0
   p = p_ini
   q = 0
```

```
    eta = 0
    p_0s = p0s_ini
    p_0s_cy = p_ini
    s = s_ini
    v = v_ini
    Devpp = 0
    Devp = 0
    evp = 0
    evs = 0
    ev = 0
    eqp = 0
    Deq = 0
    eq = 0
    e1 = 0
    OCR_ini = (p + p_s) / (p0s_ini + p_s)

    ActiveSheet.Cells(21, 2).Value = Deqp
    ActiveSheet.Cells(21, 3).Value = Deqe
    ActiveSheet.Cells(21, 4).Value = dp
    ActiveSheet.Cells(21, 5).Value = dq
    ActiveSheet.Cells(21, 6).Value = p
    ActiveSheet.Cells(21, 7).Value = q
    ActiveSheet.Cells(21, 8).Value = p_0s_cy
    ActiveSheet.Cells(21, 9).Value = p_0s
    ActiveSheet.Cells(21, 10).Value = s
    ActiveSheet.Cells(21, 11).Value = v0_ncl
    ActiveSheet.Cells(21, 12).Value = v
    ActiveSheet.Cells(21, 13).Value = Devpe
    ActiveSheet.Cells(21, 14).Value = Devpp
    ActiveSheet.Cells(21, 15).Value = Devp
    ActiveSheet.Cells(21, 16).Value = evp
    ActiveSheet.Cells(21, 17).Value = evs
    ActiveSheet.Cells(21, 18).Value = ev
    ActiveSheet.Cells(21, 19).Value = eqp
    ActiveSheet.Cells(21, 20).Value = Deq
    ActiveSheet.Cells(21, 21).Value = eq
    ActiveSheet.Cells(21, 22).Value = e1
    ActiveSheet.Cells(21, 26).Value = OCR_ini

'Start the loop
        Dim step, j As Long
        step = 630

For j = 1 To step

        eta = q / (p + p_s)
        OCR = (p + p_s) / (p_0s + p_s)
        chi = Mc ^ 2 / (12 * (3 - Mc))
        Mf = 6 * (Sqr((chi / OCR) * (1 + (chi / OCR))) - (chi / OCR))
        omega = (Mc ^ 4 - eta ^ 4) / (Mf ^ 4 - eta ^ 4)
```

```
        A = 0.0542 * (0.000232325 * PF ^ 1.432 * e_ini ^ 0.162)
        e = v - 1
        fe = 1 / (e ^ 0.207 * (1 + e))
        kap = -0.0008 * PI ^ 2 + 0.0801 * PI + 1
        n = 0.00005 * PI ^ 2 - 0.0096 * PI + 0.5044
        kay = 0.5 - n
        sat = w * Gs / e
        G = A * (Gssg ^ 1.32) * fe * (1 / OCR) ^ kay * (p + sat ^ kap * s) ^ n

    'Internal Yield

    If q < q_y Then

        Deqp = 0.0005

            If q = 0 Then
                dilatancy = Mc      'This is because dilatancy is 0 when q=0
            Else
                dilatancy = (Mc ^ 2 * (2 * p + p_s - p_0s_cy)) / (2 * q * alpha)
            End If

        Devpe = dilatancy * Deqp * omega
        dp_0s_cy = Devpe * p_0s_cy * (v / kappa_vp)          'Hardening rule - p_0s increases under
plastic conditions
        p_0s_cy_old = p_0s_cy
        p_0s_cy = p_0s_cy_old + dp_0s_cy
        p_old = p
        p = (18 * p_ini + Mc ^ 2 * (p_0s_cy - p_s) + Mc * Sqr(Mc ^ 2 * (p_s + p_0s_cy) ^ 2 + 36 *
(p_s * p_0s_cy - p_s * p_ini + p_0s_cy * p_ini - p_ini ^ 2))) / (2 * (Mc ^ 2 + 9))
        dp = p - p_old
        dq = 3 * dp
        q = q + dq

        'volume
        v0_ncl = v_ini - kappa_vp * Log(p0s_ini / p_ini)
        v = v - kappa_vp * Log(p / p_old)
        Devpp = 0
        Devp = Devpe + Devpp

        'suction
        ds = 0
        s = s_ini + ds

        'Strains
        evp = evp + Devp
        evs = 0
        ev = evp + evs
        Deqe = dq / (3 * G)
        Deq = Deqe + Deqp
```

```
        eq = eq + Deq
        eq_percent = eq * 100
        e1 = (3 * eq + ev) / 3
    End If

 If q >= q_y Then

        Deqp = 0.0005

            If q = 0 Then
                dilatancy = Mc      'This is because dilatancy is 0 when q=0
            Else
                dilatancy = (Mc ^ 2 * (2 * p + p_s - p_0s)) / (2 * q * alpha)
            End If

     Devpp = dilatancy * Deqp * omega
        dp_0s = Devpp * p_0s * (v / (lamda_vp - kappa_vp))       'Hardening rule - p_0s increases
under plastic conditions
        p0s_old = p_0s
        p_0s = p_0s + dp_0s
        p_old = p
        p = (18 * p_ini + Mc ^ 2 * (p_0s - p_s) + Mc * Sqr(Mc ^ 2 * (p_s + p_0s) ^ 2 + 36 * (p_s *
p_0s - p_s * p_ini + p_0s * p_ini - p_ini ^ 2))) / (2 * (Mc ^ 2 + 9))
        dp = p - p_old
        dq = 3 * dp
        q = q + dq

        'volume
        v0_ncl = v0_ncl - lamda_vp * Log(p_0s / p0s_old)

        Devp = Devpe + Devpp
        dv = -Devp * v
        v_old = v
        v = v_old + dv
        de = v - v_old

        'suction
        ds = -(p) * de / lamda_vp
        s = s + ds
            If s < s_sa Then
                p_s = s
            Else
                p_s = s_sa + (s_sa + 1) * Log((s + 1) / (s_sa + 1))
            End If

        'Strains
        Devpe = (kappa_vp / v_old) * (dp / (p_old + s))
        Devp = Devpe + Devpp
        evp = evp + Devp
        evs = 0
```

```
    ev = evp + evs
    Deqe = dq / (3 * G)
    Deq = Deqp + Deqe
    eq = eq + Deq
    eq_percent = eq * 100
    eqp = eqp + Deqp
    e1 = (3 * eq + ev) / 3

End If


'Critical state condition: dp=0
If dp < 0.007 And dp > 0.001 Then
    p_cs = p
    q_cs = q
    eta_cs = q / p
    p0s_cs = p_0s
    st_cs = eq
        ActiveSheet.Cells(13, 15).Value = p_cs
        ActiveSheet.Cells(14, 15).Value = q_cs
        ActiveSheet.Cells(15, 15).Value = eta_cs
        ActiveSheet.Cells(17, 15).Value = p0s_cs
        ActiveSheet.Cells(18, 15).Value = st_cs
End If

ActiveSheet.Cells(j + 21, 1).Value = j
ActiveSheet.Cells(j + 21, 2).Value = Deqp
ActiveSheet.Cells(j + 21, 3).Value = Deqe
ActiveSheet.Cells(j + 21, 4).Value = dp
ActiveSheet.Cells(j + 21, 5).Value = dq
ActiveSheet.Cells(j + 21, 6).Value = p
ActiveSheet.Cells(j + 21, 7).Value = q
ActiveSheet.Cells(j + 21, 8).Value = p_0s_cy
ActiveSheet.Cells(j + 21, 9).Value = p_0s
ActiveSheet.Cells(j + 21, 10).Value = s
ActiveSheet.Cells(j + 21, 11).Value = v0_ncl
ActiveSheet.Cells(j + 21, 12).Value = v
ActiveSheet.Cells(j + 21, 13).Value = Devpe
ActiveSheet.Cells(j + 21, 14).Value = Devpp
ActiveSheet.Cells(j + 21, 15).Value = Devp
ActiveSheet.Cells(j + 21, 16).Value = evp
ActiveSheet.Cells(j + 21, 17).Value = evs
ActiveSheet.Cells(j + 21, 18).Value = ev
ActiveSheet.Cells(j + 21, 19).Value = eqp
ActiveSheet.Cells(j + 21, 20).Value = Deq
ActiveSheet.Cells(j + 21, 21).Value = eq
ActiveSheet.Cells(j + 21, 22).Value = e1
ActiveSheet.Cells(j + 21, 23).Value = eq_percent
ActiveSheet.Cells(j + 21, 24).Value = Mf
ActiveSheet.Cells(j + 21, 25).Value = eta
```

```
    ActiveSheet.Cells(j + 21, 26).Value = OCR
    ActiveSheet.Cells(j + 21, 27).Value = omega
    ActiveSheet.Cells(j + 21, 28).Value = dilatancy
    ActiveSheet.Cells(j + 21, 29).Value = G
    ActiveSheet.Cells(j + 21, 30).Value = p_s


    Next j

Application.ScreenUpdating = True


End Sub
```

Within the VBA code, there is an input for the Microsoft Excel Workbook name. The name is input into the Code line as follows: ActiveWorkbook.Worksheets("*WORKBOOK NAME GOES HERE*").Activate. The figures in this section show how the Microsoft Excel Workbook is setup to work with the VBA code. Figure J.4 gives an overview, Figure J.5 presents the legend or input and output value sections, Figure J.6 presents a more detailed view of the data input section, and Figure J.7 presents the output value column headings.

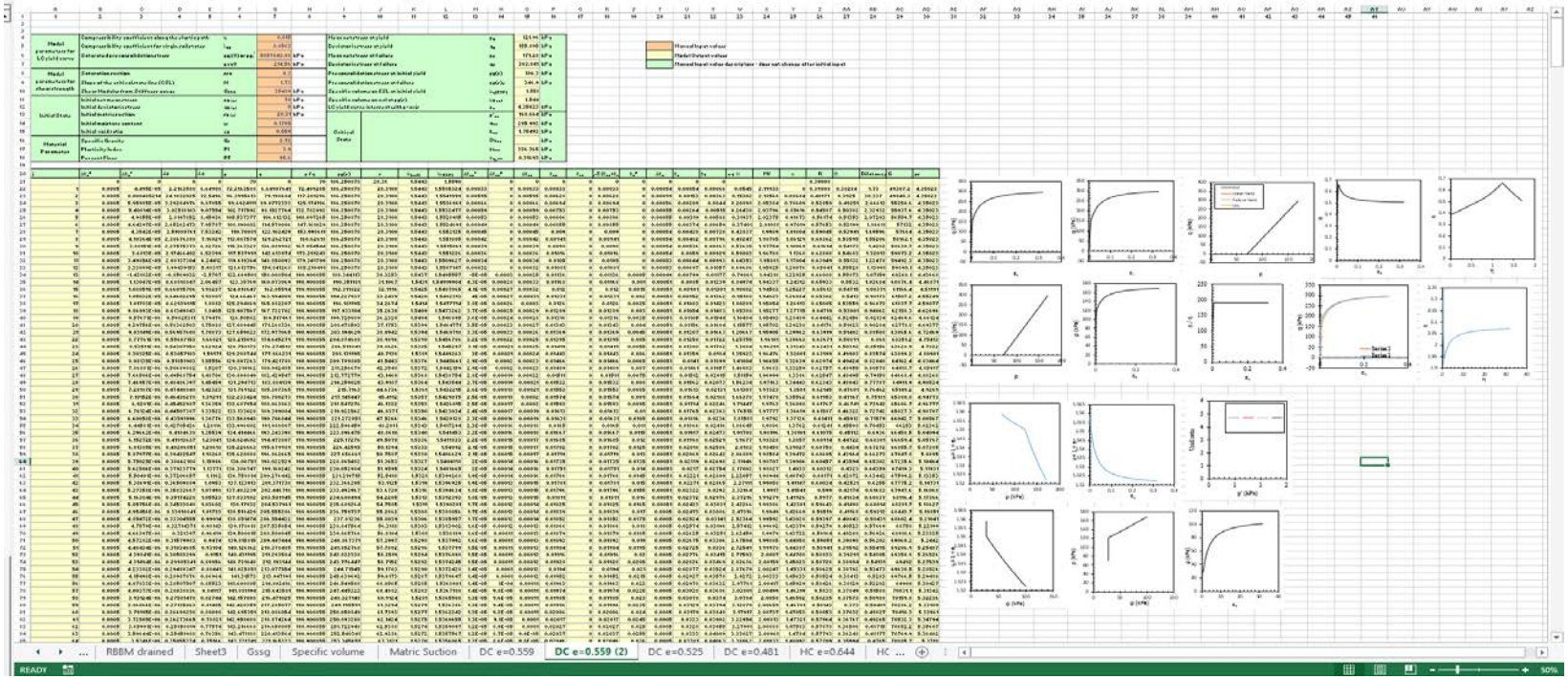

Figure J.4 An overview of the Excel Worksheet with input and output data for the As-Compacted State Model.

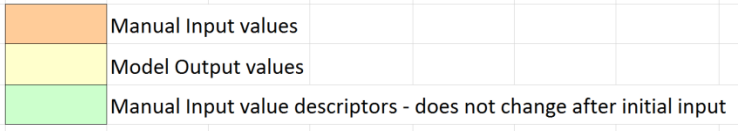

Figure J.5 The color coded legend of the input and output values and their descriptors for the Excel Worksheet of the As-Compacted State Model.

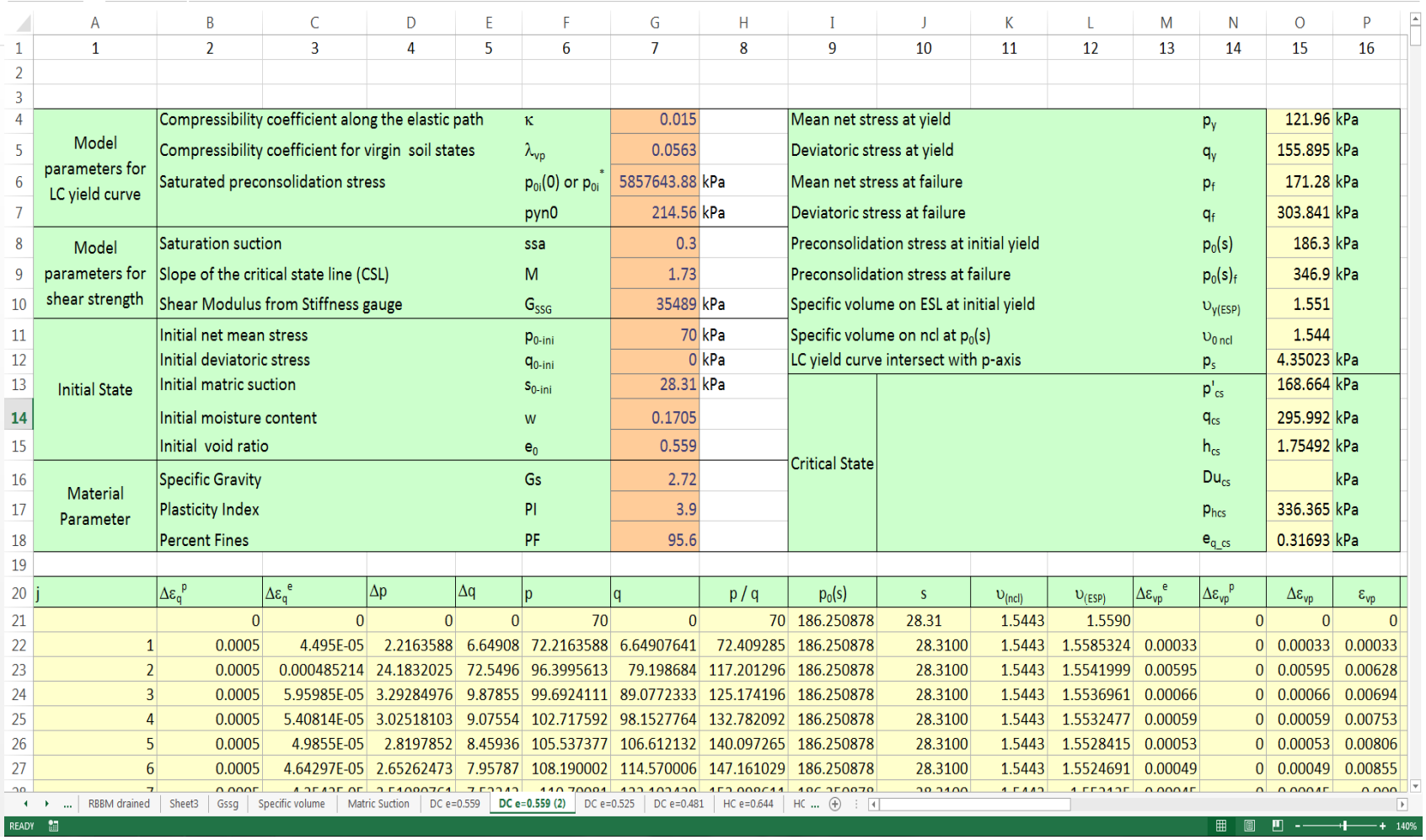

1	1	2	3	4	5	6	7	8	9	10	11	12	13	14	15	16
2																
3																
4	Model parameters for LC yield curve	Compressibility coefficient along the elastic path				κ	0.015		Mean net stress at yield					p_y	121.96	kPa
5		Compressibility coefficient for virgin soil states				λ_{vp}	0.0563		Deviatoric stress at yield					q_y	155.895	kPa
6		Saturated preconsolidation stress				$p_{0i}(0)$ or p_{0i}^*	5857643.88	kPa	Mean net stress at failure					p_f	171.28	kPa
7						pyn0	214.56	kPa	Deviatoric stress at failure					q_f	303.841	kPa
8	Model parameters for shear strength	Saturation suction				ssa	0.3		Preconsolidation stress at initial yield					$p_0(s)$	186.3	kPa
9		Slope of the critical state line (CSL)				M	1.73		Preconsolidation stress at failure					$p_0(s)_f$	346.9	kPa
10		Shear Modulus from Stiffness gauge				G_{SSG}	35489	kPa	Specific volume on ESL at initial yield					$\upsilon_{y(ESP)}$	1.551	
11	Initial State	Initial net mean stress				$p_{0\text{-ini}}$	70	kPa	Specific volume on ncl at $p_0(s)$					$\upsilon_{0\ ncl}$	1.544	
12		Initial deviatoric stress				$q_{0\text{-ini}}$	0	kPa	LC yield curve intersect with p-axis					p_s	4.35023	kPa
13		Initial matric suction				$s_{0\text{-ini}}$	28.31	kPa	Critical State					p'_{cs}	168.664	kPa
14		Initial moisture content				w	0.1705							q_{cs}	295.992	kPa
15		Initial void ratio				e_0	0.559							h_{cs}	1.75492	kPa
16	Material Parameter	Specific Gravity				Gs	2.72							Du_{cs}		kPa
17		Plasticity Index				PI	3.9							p_{hcs}	336.365	kPa
18		Percent Fines				PF	95.6							e_{q_cs}	0.31693	kPa
19																

20	j	$\Delta\varepsilon_q^p$	$\Delta\varepsilon_q^e$	Δp	Δq	p	q	p / q	$p_0(s)$	s	$\upsilon_{(ncl)}$	$\upsilon_{(ESP)}$	$\Delta\varepsilon_{vp}^e$	$\Delta\varepsilon_{vp}^p$	$\Delta\varepsilon_{vp}$	ε_{vp}
21		0	0	0	0	70	0	70	186.250878	28.31	1.5443	1.5590		0	0	0
22	1	0.0005	4.495E-05	2.2163588	6.64908	72.2163588	6.64907641	72.409285	186.250878	28.3100	1.5443	1.5585324	0.00033	0	0.00033	0.00033
23	2	0.0005	0.000485214	24.1832025	72.5496	96.3995613	79.198684	117.201296	186.250878	28.3100	1.5443	1.5541999	0.00595	0	0.00595	0.00628
24	3	0.0005	5.95985E-05	3.29284976	9.87855	99.6924111	89.0772333	125.174196	186.250878	28.3100	1.5443	1.5536961	0.00066	0	0.00066	0.00694
25	4	0.0005	5.40814E-05	3.02518103	9.07554	102.717592	98.1527764	132.782092	186.250878	28.3100	1.5443	1.5532477	0.00059	0	0.00059	0.00753
26	5	0.0005	4.9855E-05	2.8197852	8.45936	105.537377	106.612132	140.097265	186.250878	28.3100	1.5443	1.5528415	0.00053	0	0.00053	0.00806
27	6	0.0005	4.64297E-05	2.65262473	7.95787	108.190002	114.570006	147.161029	186.250878	28.3100	1.5443	1.5524691	0.00049	0	0.00049	0.00855

Figure J.6 A detailed view of the input data field of the input, initial state and material parameters for the As-Compacted State Model.

	A	B	C	D	E	F	G	H	I	J
20	j	$\Delta\varepsilon_q^{\ p}$	$\Delta\varepsilon_q^{\ e}$	Δp	Δq	p	q	p / q	$p_0(s)$	s

	K	L	M	N	O	P	Q	R	S	T
20	$\upsilon_{(ncl)}$	$\upsilon_{(ESP)}$	$\Delta\varepsilon_{vp}^{\ e}$	$\Delta\varepsilon_{vp}^{\ p}$	$\Delta\varepsilon_{vp}$	ε_{vp}	ε_{vs}	$\varepsilon_v=\Sigma(\varepsilon_{vp}+\varepsilon_{vs}$	$\varepsilon_q^{\ p}$	$\Delta\varepsilon_q$

	U	V	W	X	Y	Z	AA	AB	AC	AD
20	ε_q	ε_1	eq %	Mf	η	R	Ω	Dilatancy	G	ps

Figure J.7 A detailed view of row # 20 of the descriptors for the output data columns A through AD for the As-Compacted State Model.

REFERENCES

Abbiss, C. P. (1981). “Shear wave measurements of the elasticity of the ground,” Géotechnique, Vol. 31, No. 1, pp. 91-104.

Agarwal, T.K., and Ishibashi, 1. (1991). "Multi-directional wave velocity by piezoelectric crystals," ASCE Geotechnical Special Publication, No. 29, pp. 102-117.

Agus, S.S., and Schanz, T. (2006). "Drying, wetting, and suction characteristic curves of a bentonite-sand mixture," ASCE Geotechnical Special Publication, No. 147, Vol. 2, pp. 1405-1414.

Ahuja, L. R., and Swartzendruber, D., (1972). “An improved form of soil-water diffusivity function,” Soil Science Society of American Journal. Vol. 36, No. 1, pp. 9-14.

Aitchison, G.D. (1961). “Relationship of moisture and effective stress functions in unsaturated soils,” Pore Pressure and Suction in Soils, conference organized by the British National Society of the International Society of Soil Mechanics and Foundation Engineering, at the Institution of Civil Engineers, London, England: Butterworths, pp. 47-52.

Aitchison, G. D. (1965). “Discussion in,” Proceedings of the 6th International Conference on Soil Mechanics and Foundation Engineering, Montreal, QC, Vol. 3, pp. 318-321

Alonso E. E., Gens A. and Gehling W. Y. Y. (1994). “Elastoplastic model for unsaturated expansive soils,” *Proceedings of the 3rd European Conference on Numerical Methods in Geotechnical Engineering*, Manchester, pp. 11–18.

Alonso E. E., Gens A. and Josa A. (1990). “A constitutive model for partially saturated soils,” Géotechnique, Vol. 40, No. 3, pp. 405–430.

Alonso E. E., Vaunat J. and Gens A. (1999). “Modelling the mechanical behaviour of expansive clays,” Engineering Geology, Vol. 54, No. 1, pp. 173–183.

Alvarado, G., and Coop, M. R. (2012). “On the performance of bender elements in triaxial tests,” Géotechnique, Vol. 62, No. 1, pp. 1-17. [http://dx.doi.org/10.1680/geot.7.00086]

Assouline, S. (2006). “Modeling the relationship between soil bulk density and the water retention curve,” Vadose Zone Journal, Vol. 5, No. 2, pp. 554–562

Atkinson, (1993). “A note on modelling small strain stiffness in cam clay,” Predictive Soil Mechanics, Proceedings Of The Wroth Memorial Symposium, 27-29 July 1992, St Catherine's College, Oxford, pp. 111-120

Bao, C. G., Gong, B., and Zhan, L. (1998), “Properties of Unsaturated Soils and Slope Stability of Expansive Soil,” Keynote Lecture, Proceedings of the International Conference on Unsaturated Soils, Beijing.

Barbour, S. L. (1998). “Nineteenth Canadian Geotechnical Colloquium: The soil-water characteristic curve: a historical perspective,” Canadian Geotechnical Journal, Vol. 35, No. 5, pp. 873-894.

Bernier, F., Volckaert, G., Alonso, E., and Villar, M. (1997). “Suction-controlled experiments on Boom clay,” Engineering Geology, Vol. 47, No.4, pp. 325-338.

Biglari, M., d’Onofrio, A., Mancuso, C., Jafari, M.K., Shafiee, A., and Ashayeri, I. (2012). “Small-strain Stiffness of Zenoz kaolin in unsaturated conditions,” Canadian Geotechnical Journal, Vol. 49. No. 3, pp 311–322. doi:10.1139/t11-105.

Bishop, A. W. (1959). “The principle of effective stress,” Teknisk Ukeblad, Vol. 106, No. 39, pp. 859-863.

Bishop, A W., Alpan, I., Blight, G.E., and Donald, I.B. (1960). "Factors controlling the strength of partly saturated cohesive soils," Research Conference on Shear Strength of Cohesive Soils, Boulder, Colorado, pp. 503-53l.

Bishop, A.W., and Blight, G. E. (1963). “Some aspects of effective stress in saturated and unsaturated soils,” Géotechnique, Vol. 13, No. 3, pp. 177-197.

Bishop, AW., and Donald, I.B. (1961). “Experimental study of partly saturated soil in the triaxial apparatus,” Proceedings of the 5th International Conference on Soil Mechanics and Foundation Engineering, Paris, Vol. 1, pp. 13-2l.

Blewett, J., Blewett, I.J., and Woodward, P.K. (1999). “Measurement of shear-wave velocity using phase-sensitive detection techniques,” Canadian Geotechnical Journal, Vol. 36, No. 5, pp. 934–939.

Blewett, J., Blewett, I.J., and Woodward, P.K. (2000). “Phase and amplitude responses associated with the measurements of shear wave velocity in sand by bender element,” Canadian Geotechnical Journal, Vol. 37, pp. 1348-1357.

Brignoli, E.G.M., Gotti, M., and Stokoe, K.H. (1996). “Measurement of shear waves in laboratory specimens by means of piezoelectric transducers,” Geotechnical Testing Journal, Vol. 19, No.4, pp. 384-397.

Brooks, R.H., and Corey, A.T. (1964). “Hydraulic properties of porous media,” Hydrology Paper No.3, Civil Engineering Department, Colorado State University, Fort Collins, Colorado.

Brutsaert, W. (1967). “Some methods of calculating unsaturated permeability,” Transactions of the American Society of Agricultural Engineers, Vol. 10, pp. 400–404.

Cabarkapa, Z., Cuccovillo, T., and Gunn, M. (1999). “Some aspects of the pre-failure behavior of unsaturated soil,” Proceedings of the 2nd International Conference on Pre-failure Behavior of Geomaterials, Turin, Vol. 1, pp. 159-165.

Callisto, L., and Rampello, S. (2002). “Shear strength and small-strain stiffness of a natural clay under general stress conditions,” Géotechnique, Vol. 52, No. 8, pp. 547-560.

Campbell, G. S. (1974). "A simple method for determining unsaturated conductivity from moisture retention data," Soil Science Journal, Vol. 117, No. 6, pp. 311-314

Chavez, C., Romero, E., and Alonso, E.E. (2005). 'Volume change measurement of partially saturated rockfill in triaxial tests,' Advanced Experimental Unsaturated Soil Mechanics - Trento, Italy, 27-29 June, pp. 93-98.

Chen, D.H., Wu, W., He, R., Bilyeu, J., Arrelano, M. (1999). "Evaluation of In Situ Resilient Modulus Testing Techniques," ASCE Geotechnical Special Publication: No. 86, pp. 1-11.

Childs, E. C. (1969). "An Introduction to the Physical Basis of Soil Water Phenomena," Wiley-Interscience, London, UK.

Clayton, C. R. I. (2011). "Stiffness at small strain: research and practice," Géotechnique, Vol. 61, No. 1, pp. 5–37 [doi: 10.1680/geot.2011.61.1.5]

Coleman, lD. (1962). "Stress/strain relations for partly saturated soils," Géotechnique, Vol. 12, No.4, pp. 348-350.

Croney, D., and Coleman, J. D. (1948). "Soil Thermodynamics Applied to the Movement of Moisture in Road Foundations," Proceedings of the 7th International Congress for Applied Mechanics, London, Vol. 3, pp. 163-177.

Croney, D., and Coleman, J. D. (1954). "Soil structure in relation to soil suction (pF)," Journal of Soil Science, Vol. 5, No., 1, pp. 75-84.

Cui Y. J. and Delage P. (1996). "Yielding and plastic behaviour of an unsaturated compacted silt." Géotechnique, 46(2), 291 – 311.

D'Onforio, A., and Penna, A (2003). "Influence of compaction variables on the small strain behaviour of a clayey silt," Deformation Characteristics of Geomaterials: Proceedings of the 3rd International Symposium on Deformation Characteristics of Geomaterials, Lyon, France, pp. 337-344.

Delage, P. (2002). "Experimental unsaturated soil mechanics," Proceedings, 3rd International Conference on Unsaturated Soils, Recife, Brazil (2002)

Dyvik, R., and Madshus, C. (1985). "Laboratory measurements of Gmax using bender elements," Advances in the Art of Testing Soils Under Cyclic Conditions, ASCE, pp. 186-196.

Dyvik, R., and Olsen, T.S. (1989). "Gmax measured in oedometer and DSS tests using bender elements," Proceedings of the 12th International Conference on Soil Mechanics and

Edil, T. B. and Motan, S. E. (1979), "Soil-Water Potential and Resilient Behavior of Subgrade Soils," Transportation Research Record, No. 705, Washington, D.C., pp. 54-63.

Edil, T. B., Motan, S. E., and Toha, F. X. (1981). "Mechanical behaviour of unsaturated soils," Laboratory shear strength of soils, ASTM, STP 740.

Edil, T. B. and Sawangsuriya, A. (2005), "Earthwork Quality Control Using Soil Stiffness," Proceedings of the 16th International Conference on Soil Mechanics and Geotechnical Engineering, Osaka, Japan, pp. 1689-1692.

Endelman, F. J.,. Box, G. E. P., Boyle, J. R., Hughes, R. R., Keeney, D. R., Northrup, M. L., and Saffigna, P. G., (1974). "The mathematical modeling of soil-water-nitrogen phenomena," EDFB-IBP-74-8. Oak Ridge National Laboratory, Oak Ridge, Tennessee.

Fam, M., and Santamarina, C. (1995). "Study of geoprocesses with complementary mechanical and electromagnetic wave measurements in an oedometer," Geotechnical Testing Journal, Vol. 18, No.3, pp. 307-314.

Fredlund, D. G., and Morgenstern, N. R. (1977). "Stress state variables for unsaturated soils," Journal of the Geotechnical Engineering Division, ASCE, Vol. 103, No. 5, pp. 447-466.

Fredlund, D. G., and Rahardjo H. (1993). "Soil mechanics for unsaturated soils," John Wiley & Sons, New York, 560 p.

Fredlund, D. G. and Xing, A. (1994). "Equations for the soil water characteristic curve," Canadian Geotechnical journal, Vol. 31, No. 3, pp. 521–532.

Fredlund, D. G., Rahardjo H, and Fredlund, M. D., (2012). "Unsaturated soil mechanics in engineering practice," John Wiley & Sons, Inc., Hoboken, New Jersey

Gajo, A., Fedel, A., and Mongiovi, L. (1997). "Experimental analysis of the effects of fluid-solid coupling on the velocity of elastic waves in saturated porous media," Géotechnique, Vol. 47, No.5, pp. 993-1008.

Gardner, W. R. 1958. "Some steady state solutions o f the unsaturated moisture flow equation with application to evaporation from a water-table," Soil Science Journal., Vol. 85, No. 4, pp. 228-232.

Geiser, F., Laloui, L. and Vulliet, L. (2000). "On the volume measurement in unsaturated triaxial test," Proceedings of the Conference of Unsaturated Soils for Asia, Singapore, pp.669-674.

Gens A. and Alonso E. E (1992). "A framework for the behaviour of unsaturated expansive clays," Canadian Geotechnical Journal, Vol. 29, pp. 1013–1032.

Gonzalez, N. A., and Colmenares, J. E. (2006). "Influence of matric suction on the volume change behaviour of a compacted clayey soil," Geotechnical Special Publication, No. 147, Vol. 1, pp. 825-836.

Hardin, B. O., (1965). "Dynamic versus static shear modulus for dry sand," Materials Research and Standards, American Society of Testing Materials, Vol. 5, No. 5, pp. 232-235

Hardin, B.O. (1978). "The nature of stress-strain behavior of soils," Proceedings of the ASCE Geotechnical Engineering Division Specialty Conference on Earthquake Engineering and Soil Dynamics, Pasadena, CA, pp. 3-90.

Hardin, B. O., and Black, W. L. (1968). “Vibration modulus of normally consolidated clay,” Journal of Soil Mechanics and Foundations Division, ASCE, Vol. 94, No. SM2, pp. 353-369.

Hardin, B. O., and Blandford, G. E., 1989, Elasticity of particulate materials. Journal of Geotechnical Engineering, Vol. 115, No. 6, pp. 788-805.

Hardin, B. O., and Drnevich, V. P. (1972a). “Shear modulus and damping in soils: Measurement and parameter effects,” Journal of Soil Mechanics and Foundations Division., ASCE, Vol. 98, No. 6, pp. 603-624.

Hardin, B. O., and Drnevich, V. P. (1972b). “Shear modulus and damping in soils: Design equations and curves,” Journal of Soil Mechanics and Foundations Division., ASCE, Vol. 98, No. 7, pp. 667-692.

Hardin, B. O. and Richart, F. E. Jr. (1963). “Elastic wave velocities in Granular soils,” Journal of Soil Mechanics and Foundations Divisions, Proceedings of the American Society of Civil Engineers, Vol. 89, SM1, Feb., pp. 33-65.

Haverkamp, R., Vauclin, M., Touma, J, Wierenga, P. J., and Vachaud, G., (1977). “A comparison of numerical simulation models for one-dimensional infiltration,” Soil Science Society of American Journal. Vol. 41, pp. 285-294.

Head, K.H. (1992). “Manual of soil laboratory testing,” ELE International Limited, Pentech Press, London.

Hight, D. W., Higgins, K. G. (1995). “An approach to the prediction of ground movements in engineering practice: background and application,” Keynote lecture, Proceedings, First International Conference on Pre-failure Deformation Characteristics of Geomaterials, Sapporo, Japan, Vol. 2, pp. 909-945.

Hilf, J. W. (1956). “An investigation of pore-water pressure in compacted cohesive soils,” Ph.D. Dissertation, Technical Memorandum No. 654, U.S. Department of the Interior, Bureau of Reclamation, Design and Construction Division, Denver, Colorado.

Hoyos, L.R., (1998). “Experimental and computational modeling of unsaturated soil behavior under true triaxial stress states,” PhD dissertation, Georgia Institute of Technology, Atlanta, Georgia, 358 p.

Hoyos, L. R., and Pérez-Ruiz, D. D. (2012). “A refined approach to Barcelona Basic Model using the apparent tensile strength concept,” Unsaturated Soils: Research and Applications: Volume 2 By Claudio Mancuso, Cristina Jommi, Francesca D’Onza

Humboldt Manufacturing Company (2007). GeoGauge User Guide. User Guide, Norridge: Humboldt Manufacturing Company.

Inci, G., Yesiller, N., and Kagawa, T. (2003). “Experimental investigation of dynamic response of compacted clayey soils,” Geotechnical Testing Journal, Vol. 26, No. 2, pp. 125-141.

Jamiolkowski, M., Lancellotta, R. and Lo Presti, D. C. F. (1994). “Remarks on the stiffness at small strains of six Italian clays,” Proceedings: Pre-failure Deformation of Geomaterials, Balkema, Vol 2, pp. 817-836.

Jardine, R. J. (1995). “One perspective of the pre-failure deformation characteristics of some geomaterials,” Keynote lecture, Proceedings, First International Conference on Pre-failure Deformation Characteristics of Geomaterials, Sapporo, Japan, Vol. 2, pp. 855-885

Jennings, J. E., and Burland, J. B. (1962). “Limitations to the use of effective stresses in partly saturated soils,” Géotechnique, Vol. 12, No.2, pp. 125-144.

Jommi, C. (2000). “Remarks on the constitutive modelling of unsaturated soils,” In Proceeding of Experimental Evident and Theoretical Approaches in Unsaturated soils, Taratino & Mancuso, Balkema, Rotterdam, ISBN 90 5809 186 4, pp. 139-153.

Josa, A., Alonso, E.E., Lloret, A., and Gens, A. (1987). “Stress-strain behaviour of partially saturated soils,” Proceedings of the 9th European Conference on Soil Mechanics and Foundation Engineering, Dublin, pp. 561-564.

Jovicic, V., and Coop, M.R. (1997). “Stiffness of coarse-grained soils at small strains,” Géotechnique, Vol. 47, No.3, pp. 545-561.

Jovicic, M., Coop, R., and Simic, M. (1996), “Objective criteria for determining Gmax from bender element tests,” Géotechnique, Vol. 46, No. 2, pp. 357-362.

Jung, M.J (2005). “Shear wave velocity measurements of normally consolidated Kaolinite using bender elements,” M.Sc. Thesis, The University of Texas at Austin.

Kawaguchi, T, Mitachi, T, and Shibuya, S. (2001). “Evaluation of shear wave travel time in laboratory bender element test,” Proceedings of the 15th International Conference on Soil Mechanics and Geomechanics Engineering, pp. 155-158

Kawaguchi, T, Tanaka, H. (2008). “Formulation of Gmax from reconstituted clayey soils and its application to Gmax measured in the field,” Soils and Foundations, Vol. 48, No. 6, pp. 821-831

Khalili, N. and Khabbaz, M. H. (1998), “A Unique Relationship for X for the Determination of the Shear Strength of Unsaturated Soils,” Géotechnique, Vol. 48, No.5, pp. 681-687.

Khosravi, A., and McCartney, J. S. (2009). “Impact of stress state on the dynamic shear moduli of unsaturated, compacted soils.” 4th Asia-Pacific Conference on Unsaturated Soils.

Kohgo Y., Nakano M. and Miyazaki T. (1993a). “Theoretical aspects of constitutive modelling for unsaturated soils.” Soils and Foundations, Vol. 33, No. 4, pp. 49–63.

Krahn, J., and Fredlund, D. G. (1972). “On total matric and osmotic suction, Journal of Soil Science Journal, Vol. 114, No. 5, pp. 339-348.

Kramer, S. L. (1996), “Geotechnical earthquake engineering,” Prentice Hall, First Edition.

Kurtay, T. and Reece, A. R. (1970). “Plasticity theory and critical state soil mechanics,” Journal of Terramechanics, Vol. 7, Nos. 3 and 4, pp. 23–56.

Lade, P. V. and Nelson, R. B. (1987). “Modelling the elastic behaviour of granular materials.” International Journal for Numerical and Analytical Methods in Geomechanics, Vol. 11, No. 5, pp. 521–542.

Laikram, A. (2007). “Modeling unsaturated soil response under suction-controlled multi-axial stress states,” [Report] : PhD Dissertation, University of Texas at Arlington.

Laliberte, G. E. (1969). “A mathematical function for describing capillary pressure-desaturation data,” Bulletin of the International Association Hydrological Sciences, Vol. 14, No. 2, pp. 131-149.

Lauer, C., and Engel, J (2004). “A triaxial device for unsaturated sand – new developments,” Unsaturated Soils: Proceedings of the International Conference ‘From Experimental Evidence Towards Numerical Modeling of Unsaturated Soils’, Weimar, Germany, 18-19 September, 2003, Vol. 1, pp. 301-314.

Lauer, C., and Engel, J (2005). “Investigations on the unsaturated stress-strain behavior and on the SWCC of Hostun Sand in a double-walled triaxial cell,” Advanced Experimental Unsaturated Soil Mechanics - Trento, Italy, 27-29 June, pp. 185-19l.

Lee, J. S., and Santamarina, J. C. (2005). “Bender Elements: Performance and Signal Interpretation,” Journal of Geotechnical and Geoenvironmental Engineering, ASCE, Vol. 131, No.9, pp. 1063-1070.

Lenke, L.R., McKeen, R.G., Grush, M.P. (2001). “Evaluation of a Mechanical Stiffness Gauge for Compaction Control of Granular Media.” Albuquerque, NM.

Leong, E. C., and Rahardjo, H. (1997). “Review of soil-water characteristic curve equations,” Journal of Geotechnical and Geoenvironmental Engineering, ASCE, Vol. 123, No. 12, pp. 1106-1117.

Leong, E.C., Cahyadi, 1, and Rahardjo, H. (2006). “Stiffness of a compacted residual soil,” Geotechnical Special Publication, No. 147, Vol. 1, pp. ll69-ll80.

Leong, E.C., Yeo, S.H., and Rahardjo, H. (2005). “Measuring shear wave velocity using bender elements,” Geotechnical Testing Journal, Vol. 28, No.5, pp. 488-498.

Lloret A., Gens A., Battle F. and Alonso E. E. (1987). “Flow and deformation analysis of partially saturated soils.” Proceeding 9th International Conference on Soil Mechanics and Foundation Engineering, Dublin, Vol. 2, pp 565–568.

Lohani, T.N., Imai, G., and Shibuya, S. (1999). “Determination of shear wave velocity in bender element test,” Proceedings of the 2nd International Conference on Earthquake Geotechnical Engineering, Rotterdam, Vol. 1, pp. 101-106.

Ma, S., Huang, M., Hu, P., and Yang, C., (2013). “Soil-water characteristics and shear strength in constant water content triaxial tests on Yunnan red clay.” Journal of South Central University, Vol. 20, No. 5, pp. 1412-1419.

Maâtouk, A., Leroueil, S., and Rochelle, P. L. A, (1995). “Yielding and critical state of a collapsible unsaturated silty soil,” Géotechnique, Vol. 45, No. 3, pp. 465-477.

Macari, E.J., Hoyos, L.R.., Arduino, P., (2003). “Constitutive Modeling of Unsaturated Soil Behavior under Axisymmetric Stress States using a Stress/Suction-Controlled Cubical Test Cell,” International Journal of Plasticity, Vol. 19, pp. 1481-1515.

Macari, E. J., and Arduino, P. (1995). “Overview of state-of-the-practice modeling of overconsolidated soils,” Transportation Research Record - Engineering Properties and Practice in Overconsolidated Clays, No. 1479, pp. 51-60.

Mair, R.J. (1993). Developments in geotechnical engineering research: application to tunnels and deep excavations. Proceedings of the Institution of Civil Engineers, London, Vol. 93, pp. 27–41.

Maleki, M., and Bayat, M. (2012). “Experimental evaluation of mechanical behavior of unsaturated silty sand under constant water content condition,” Engineering Geology, Vol. 141–142, pp. 45–56. doi:10.1016/j.enggeo.2012.04.014

Mancuso, C., Simonelli, A. L., and Vinale, F. (1989), “Numerical analysis of in situ S-wave measurements,” Proceedings, Twelfth International Conference on Soil Mechanics and Foundation Engineering, Rio de Janeiro, Vol. 3, pp 277-280.

Mancuso, C., Vassallo, R., and d’Onofrio, A. (2002). “Small strain behavior of a silty sand in controlled-suction resonant column-torsional shear tests,” Canadian Geotechnical Journal, Vol. 39, No. 1, pp. 22–31.

Manke, P.G., and Gallaway, B.M. (1966). “Pulse velocities in flexible pavement construction materials,” Highway Research Record, No. 131, pp. 128-153.

Marinho, E.A.M., Chandler, R.J, and Crilly, M.S. (1995). “Stiffness measurements on an unsaturated high plasticity clay using bender elements,” Proceedings of the 1st International Conference on Unsaturated Soils, Paris, Vol. 1, pp. 535-539.

Matsuoka, H., Sun, D.A., Kogane, A., Fukuzawa, N., and Ichihara, W. (2002). “Stress-strain behavior of unsaturated soil in true triaxial tests,” Canadian Geotechnical Journal, Vol. 39. Pp. 608-619.

Matyas, E.L., and Radhakrishna, H.S. (1968). “Volume change characteristics of partially saturated soils,” Géotechnique, Vol. 18, pp. 432-448.

McKee, C.R., and Bumb, A.C. (1984). “The importance of unsaturated flow parameters in designing a monitoring system for hazardous wastes and environmental emergencies,” Proceedings, Hazardous Materials Control Research Institute National Conference, Houston, TX, March 1984. pp. 50-58.

McKee, C.R., and Bumb, A.C. (1987). “Flow-testing coalbed methane production wells in the presence of water and gas,” *In* SPE Formation Evaluation, December, pp. 599-608.

Mendoza, C.E., Colmenares, J.E. & Merchán. (2005). “Stiffness of an unsaturated compacted clayey soil at very small strains,” In Tarantino, Romero & Cui (eds), Advanced Experimental Unsaturated Soil Mechanics: pp. 199–204. Rotterdam: Balkema.

Mohsin, A.K.M., and Airey, D.W. (2003). “Automating Gmax measurement in triaxial tests," Deformation Characteristics of Geomaterials,” Proceedings of the 3rd International Symposium on Deformation Characteristics of Geomaterials, Lyon, France, 22-24 September, pp. 73-80.

Motan, S. E. and Edil, T. B. (1982). “Repetitive-Load Behavior of Unsaturated Soils,” Transportation Research Record, No. 872, Washington, D.C., pp. 41-48.

Mou, C.H., and Chu, T.Y. (1981). “Soil suction approach for swelling potential evaluation.” Transportation Research Record No. 790, pp. 54-60.

Mualem (1976). “A new model for predicting the hydraulic conductivity of unsaturated porous media,” Water Resources, Res. 12, pp. 513-522.

Muller, R. K. (1978). “Mathematical and physical models,” Experimental Mechanics, Vol. 18, No. 7, pp. 241–245.

Mun, B., Aubeny, C.P., and Lytton, R.L. (2006). “Calculation of pseudo strain and dissipated pseudo strain energy in unsaturated soil,” Geotechnical Special Publication, No. 147, Vol. 2, pp. 1956-1967.

Ng, C. W. W., and Menzies, B. (2007). “Advanced unsaturated soil mechanics and engineering,” New York: Taylor and Francis.

Ng, C.W.W., Xu, J., and Yung, S.Y. (2009). “Effects of wetting–drying and stress ratio on anisotropic stiffness of an unsaturated soil at very small strains,” Canadian Geotechnical Journal, Vol. 46, No. 9, pp. 1062–1076. doi:10.1139/T09-043.

Ng, C.W.W., and Yung, S.Y. (2008). “Determination of the anisotropic shear stiffness of an unsaturated decomposed soil,” Géotechnique, Vol., 58, No. 1, pp. 23–35. doi:10.1680/geot.2008.58.1.23.

Ng, C.W.W., Zhan, L.T., and Cui, Y.l (2002). “A new simple system for measuring volume changes in unsaturated soils,” Canadian Geotechnical Journal, Vol. 39, No.3, pp. 757-764.

Öberg, A. L. (1997). “Matrix suction in silt and sand slopes.” PhD thesis. Chalmers University of Technology, Sweden.

Öberg, A and Sallfors, G. (1997), “Determination of Shear Strength Parameters of Unsaturated Silts and Sands Based on the Water Retention Curve,” Geotechnical Testing Journal, Vol. 20, No.1, pp. 40-48.

Oh, W.T. & Vanapalli, S.K. (2009). “A simple method for predicting the shear modulus of unsaturated sandy soils,” Proceedings of the 4th Asia-Pacific Conference on Unsaturated soils.

Oloo, S. Y., and Fredlund, D. G. (1998). “The application of unsaturated soil mechanics theory to the design of pavements.” Proceedings of the 5th Int. Conference on the Bearing Capacity of Roads and Airfields, Trondheim, Norway, 1419–1428.

Olson, R.E., and Langfelder, L.J. (1965). “Pore water pressures in unsaturated soils,” Journal of Soil Mechanics and Foundations Division, ASCE, Vol. 91, No. SM4, pp. 127-150.

Ooi, P.S.K., and Pu, J (2002). “Evaluating compaction of tropical soils using soil stiffness,” Bearing capacity of roads, railways and airfields: Proceedings of the 6th International Conference on the Bearing Capacity of Roads and Airfields, Lisbon, Portugal, pp. 1143-1149.

Ooi, P.S.K., and Pu, J (2003). “Use of stiffness for evaluating compactness of cohesive pavement geomaterials,” Transportation Research, No. 1849, Paper No. 03-4052, pp. ll-19.

Padilla, 1M., Houston, W.N., Lawrence, C.A, Fredlund, D.G., Houston, S.L., and Perez, N.P. (2006). “An automated triaxial testing device for unsaturated soils,” ASCE Geotechnical Special Publication, No. 147, Vol. 2, pp. 1775-1786.

Pennington, D.S., Nash, D.F.T., and Lings, M.L. (2001). “Horizontally mounted bender elements for measuring anisotropic shear moduli in triaxial clay specimens,” Geotechnical Testing Journal, Vol. 24, No.2, pp. 133-144.

Pereira, J. H. F., and Fredlund, D. G. (2000). “Volume change behaviour of a residual soil of gneiss compacted at metastable-structure conditions,” Journal of Geotechnical and Geoenvironmental Engineering, ASCE, Vol. 126, pp. 907-916.

Pham, H. Q., and Fredlund, D. G. (2005). “A volume-mass constitutive model for unsaturated soils,” Proceedings of the Fifty-Eighth Canadian Geotechnical Conference, Saskatoon, SK, Vol. 2, pp. 173-181.

Puppala, A1, Kadarn, R., Madhyannapu, R.S., and Hoyos, L.R. (2006). “Small-strain shear moduli of chemically stabilized sulfate-bearing cohesive soils,” Journal of Geotechnical and Geoenvironmental Engineering, Vol. 132, No.3, pp. 322-336.

Qian, X., Gray, D.H., and Woods, R.D. (1991). “Resonant column tests on partially saturated sands,” Geotechnical Testing Journal, Vol. 14, No.3, pp. 266-275.

Rampello, S., Viggiani, G.M.B., and Amorosi, A (1997). “Small- strain stiffness of reconstituted clay compressed along constant triaxial effective stress ratio paths,” Géotechnique, Vol. 47, No.3, pp. 475-489.

Rampino, C., Mancuso, C., and Vinale, F. (1999). “Laboratory testing on an unsaturated soil: equipment, procedure, and first experimental results,” Canadian Geotechnical Journal, Vol. 36, No.1, pp. 1-12.

Rampino, C., Mancuso, C., and Vinale, F. (2000). "Experimental behaviour and modeling of an unsaturated compacted soil," Canadian Geotechnical Journal, Vol. 37, No.4, pp. 748-763.

Rees, S., Le Compte, A., Snelling, K. (2013). "A new tool for the automated travel time analyses of bender element tests," Proceedings 18th International Conference on Soil Mechanics and Geotechnical Engineering, Paris 2013, Vol. 4, pp. 2843-2846.

Roesler, S. K. (1979). "Anisotropic Shear Modulus due to Stress Anisotropy," Journal of the Geotechnical Engineering Division, ASCE, Vol. 105, No. GT7, pp. 871-880.

Romero, E. (1999). "Characterisation and thermo-mechanical behaviour of unsaturated Boom clay," An experimental study, PhD thesis, UPC, Barcelona, Spain.

Romero, E., Facio, J. A, Lloret, A, Gens, A, and Alonso, E. E. (1997). "A new suction and temperature controlled triaxial apparatus," Proceedings of the 14th International Conference on Soil Mechanics and Foundation Engineering, Hamburg, Vol. 1, pp. 185-188.

Romero, E., Vecchia, G. D., and Jommi, C. (2011). "An insight into the water retention properties of compacted clayey soils," Géotechnique Vol. 61 No. 4, pp. 313-328.

Roscoe, K. H., Schofield, A. N. and Wroth, C. P. (1958). "On the yielding of soils." Géotechnique, Vol. 8, pp. 22–53.

Roscoe K. H. & Burland J. B. (1968). "On the generalised stress-strain behaviour of 'wet' clay," Engineering Plasticity, Cambridge University Press, pp. 535-609.

Roscoe K. H. & Schofield A. N. (1963). "Mechanical behaviour of an idealised 'wet' clay". Proceeding 2nd European Conference on Soil Mechanics and Foundation Engineering, Wiesbaden, Vol. 1, pp. 47–54.

Salem, M. A. (2006). "Stiffness of unsaturated compacted clay at small strains," [Report]: PhD Dissertation, University of Texas at Austin.

Sanchez-Salinero, I., Roesset, J.M., and Stokoe, K. H. II. (1986). "Analytical studies of body wave propagation and attenuation," Geotechnical Engineering Report GR86-15, The University of Texas at Austin.

Santamarina, J. C., and Fam, M.A (1997). "Discussion: Interpretation of bender element tests," Géotechnique, Vol. 47, No.4, pp. 873-877.

Sawangsuriya, A., 2006, "Stiffness-suction-moisture relationship for compacted soils," [Report]. PhD Dissertation, University of Wisconsin – Madison.

Sawangsuriya, A., Edil, T. B., and Bosscher, P. J., 2009, "Modulus-Suction-Water Relationship for Compacted Soils in Postcompaction State," J. Geotech. Geoenviron. Eng., Vol. 135, No. 10, pp. 1390–1403.

Sawangsuriya, A, Edil, T. B., Bosscher, P. J, and Wang, X. (2006). "Small-strain stiffness behavior of unsaturated compacted subgrade," Geotechnical Special Publication, No. 147, Vol. 1, pp. ll21-ll32.

Schofield,· A. N., (1935). “The pF of the water in soil. Transactions, 3rd International Congress of Soil Sience, Vol. 2, pp 37-48,

Schwarz, V., Becker, A, and Vrettos, C. (2006). “An initial study on the viscous behaviour of a partially saturated kaolinite clay based on triaxial tests,” Geotechnical Special Publication, No. 147, Vol. 2, pp. 18ll-1820.

Shackel, B. (1973). “Changes in soil suction in a sand-clay subjected to repeated triaxial loading,” Highway Research Record, No. 429, pp. 29-39.

Sheng, D., Fredlund, D. G., and Gens, A. (2008). A new modelling approach for unsaturated soils using independent stress variables. Canadian Geotechnical Journal, Vol. 45, No. 4, pp. 511-534.

Shibuya, S., Hwang, S.C., and Mitachi, T. (1997). “Elastic shear modulus of soft clays from shear wave velocity measurement," Géotechnique, Vol. 47, No.3, pp. 593-60l.

Shirley, D.J. & Hampton, L.D. (1978). “Shear-wave measurements in laboratory sediments”, Journal of Acoustical Society of America., Vol. 63, No. 2, pp. 607-613.

Shuai, F. and Fredlun, D. G. (1998). “Model for the simulation of swelling-pressure measurements on expansive soils.” Canadian Geotechnical Journal, Vol. 35, No. 1, pp. 96–114.

Sivakumar, V. (1993). “A critical state framework for unsaturated soil,” PhD Dissertation / Sheffield University, No. DX187788.

Sivakumar, V., and Wheeler, S.J (2000). “Influence of compaction on the mechanical behaviour of an unsaturated compacted clay. Part 1: wetting and isotropic compression,” Géotechnique, Vol. 50, No.4, pp. 359-368.

Strassburger, E. (1982). “Use of piezoelectric transducers for stiffness and density measurements of soils,” M.Sc. Thesis, The University of Texas at Austin.

Stephenson, R.W. (1978). “Ultrasonic testing for determining dynamic soil moduli,” Dynamic Geotechnical Testing, ASTM STP 654, ASTM International, West Conshohocken, PA, pp. 179-195.

Sudhakar, M.R., and Revanasiddappa, K. (2000). “Role of matric suction in collapse of compacted clay soil,” Journal of Geotechnical and Geoenviromental Engineering, Vol. 126, No. 1, pp. 85-90.

Sudhakar, M.R., and Revanasiddappa, K. (2003). “Role of soil structure and matric suction in collapse of a compacted clay soil,” Geotechnical Testing Journal, Vol. 26, No. 1, pp. 102-110.

Sun, D.A., Matsuoka, H., Yao, Y.P., and Ichihara, W. (2000). “Three-dimensional elastoplastic model for unsaturated soils,” In Proceedings of the 1st Asian Conference on Unsaturated Soils (UNSAT-ASIA 2000), Singapore, 18-19 May 2000. Edited by H. Rahardjo, D.G. Toll, and E.C. Leong. Balkema, Rotterdam, ISBN 90 5809 1392, pp. 153-158.

Sun, D., Yao, Y. P. and Matsuoka, H. (2006). “Modification of critical state models by Mohr-Coulomb criterion.” Mechanics Research Communications, 33, 217 – 232.

Takkabutr, P. (2006). “Experimental Investigations on small-strain stiffness properties of partially saturated soils via resonant column and bender element testing,” PhD Dissertation, University of Texas at Arlington.

Tang, G.X., and Graham, J. (2002). “A possible elasto-plastic framework for unsaturated soils with high plasticity,” Canadian Geotechnical Journal, Vol. 39, pp. 894-907.

Terzaghi, K. (1936). “The shear resistance of saturated soils,” Proceedings of the 1 st International Conference on Soil Mechanics and Foundation Engineering, Cambridge, Vol. 1, pp. 54-56.

Theron, M., Clayton, C.R.I., and Best, A.I. (2003). “Interpretation of side-mounted bender element results using phase shift and group velocity,” Deformation Characteristics of Geomaterials: Proceedings of the 3rd International Symposium on Deformation Characteristics of Geomaterials, Lyon, France, pp. 127-132.

Thomann, T. G., and Hryciw, R.D. (1990). “Laboratory measurement of small strain shear modulus under Ko conditions,” Geotechnical Testing Journal, Vol. 13, No.2, pp. 97-105.

Thu, T M., Rahardjo, H., and Leong, E. C. (2006). “Shear strength and pore-water pressure characteristics during constant water content triaxial tests,” Journal of Geotechnical and Geoenvironmental Engineering, Vol. 132, No. 3, pp. 411-419.

Toll, D. G. (1990). “A Framework for Unsaturated Soil Behavior,” Géotechnique, Vol. 40, No. 1, pp. 31-44.

Toll, D.G. (1995). “A conceptual model for the drying and wetting of soil,” In Proceeding of the first international conference on unsaturated soil, France. Alonso and Delage (eds), 1995 ISBN 90 5410 5836, pp.805-810.

Toyota, H., Sakai, N., and Nishimura, T (2001). “Effects of stress history due to unsaturation and drainage condition on shear properties of unsaturated cohesive soil,” Soils and Foundations, Vol. 41, No.1, pp. 13-24.

Tsai, C., and Petry, TM. (1995). “Suction study on compacted clay using three measurement methods,” Transportation Research Record, No. 1481, pp. 28-34.

Valle, C. (2006). “Measurements of V p and V s in dry, unsaturated, and saturated sand specimens with piezoelectric transducers,” Ph.D. Dissertation, The University of Texas at Austin, Texas, USA.

van Genuchten, M.T. (1980). “A closed-form equation for predicting the hydraulic conductivity of unsaturated soils,” Soil Science Society of America Journal, Vol. 44, pp. 892-898.

van Genuchten, M. T., Leij, F. J., and Yates, S. R. (1991). “RETC code for quantifying hydraulic functions of soils.” EPA Rep. 600/2-91/065, U.S. Salinity Lab., Agr. Res. Service, U.S. Department of Agriculture, Riverside, Calif.

Vanapalli, S. K. and Fredlund, D. G. (2000), “Comparison of Different Procedures to Predict Unsaturated Soil Shear Strength,” Proceedings of Sessions of Geo-Denver 2000, Advances in Unsaturated Geotechnics, ASCE, Geotechnical Special Publication, No. 99, Denver, CO, pp. 195-209.

Vanapalli, S. K., Fredlund, D. G., Pufahl, D. E., and Clifton, A. W. (1996), “Model for the Prediction of Shear Strength with Respect to Soil Suction,” Canadian Geotechnical Journal, Vol. 33, No. 3, pp. 379-392.

Vanapalli, S.K., Fredlund, D.G., Pufahl, D.E. (1999). “The influence of soil structure and stress history on the soil-water characteristics of a compacted till.” Géotechnique, Vol. 49, No. 2, pp. 143–159.

Vassallo, R., Mancuso, C., and Vinale, F., (2007). “Modelling the influence of stress-strain history on the initial shear stiffness of an unsaturated compacted silt,” Canadian Geotechnical Journal, Vol. 44, pp. 463-472.

Vaunat, J., Cante, J.C., Ledesma, A., Gens, A., (2000). “A stress point algorithm for an elastoplastic model in unsaturated soils,” International Journal of Plasticity Vol. 16, No. 2, pp. 121–141.

Viggiaini, G., and Atkinson, J. H. (1995a). “Interpretation of bender element tests,” Géotechnique, Vol. 45, No.1, pp. 149-154.

Viggiaini, G., and Atkinson, J. H. (1995b). “Stiffness of fine-grained soil at very small strains,” Géotechnique, Vol. 45, No.2, pp. 249-265.

Vucetic, M. and Dobry, R. (1991), “Effect of soil plasticity on cyclic response”. Journal of Geotechnical Engineering, ASCE, vol. 117, no. GT1, pp. 89-107.

Wan, A. W. L., Gray, M. N., and Graham, J. (1995). “On the relations of suction, moisture content, and soil structure in compacted clays,” Proceedings of the 1st International Conference on Unsaturated Soils, Vol. 1, pp. 215-222.

Wheeler, S.J. (1986). “The stress-strain behaviour of soils containing gas bubbles. PhD thesis, University of Oxford,” Woods, R. D. (1978). “Measurement of dynamic soil properties,” Proceedings of the ASCE geotechnical engineering division specialty conference on earthquake engineering and soil dynamics, Pasadena" Vol. 1, pp. 91-178.

Wheeler S. J. and Karube D. (1996). “Constitutive modelling: state of the art report.” Unsaturated Soils, Balkema, Rotterdam, pp. 1179–1200.

Wheeler, S. J., and Sivakumar, V. (1995). “An elasto-plastic critical state framework for unsaturated soil,” Géotechnique, Vol. 45, pp. 35-53.

Wood, D. M. (1990). “Soil Behaviour and Critical State Soil Mechanics,” Cambridge University Press, New York.

Wu, S., Gray, D.H., and Richart, F.E. (1984). “Capillary effects on dynamic modulus of sands and silts,” Journal of Geotechnical Engineering, Vol. 1l0, No.9, pp. 1188-1203.

Yamashita, S., Fujiwara, T., Kawaguchi, T., Mikami, T., Nakata, Y., and Shibuya, S. (2007). “International Parallel Test on the Measurement of Gmax Using Bender Elements Organized by TC-29,” ISSMGE TC-29 Report, pp.1–76.

Yamashita S., Kawaguchi T., Nakata Y., Mikami T., Fujiwara T. and Shibuya S. (2009). “Interpretation of international parallel test on the measurement of Gmax using bender elements,” Soils and Foundations Vol. 49, No. 4, pp. 631-650.

Yao, Y.P., Hou, W., and Zhou, A.N. (2009). “UH model: three-dimensional unified hardening model for overconsolidated clays,” Géotechnique, Vol. 59, No. 5, pp. 451-469.

Yao, Y. P., Niu, L., and Cui, W. J. (2014). “UH model for overconsolidated unsaturated soils,” Canadian Geotechnical Journal, Vol. 51, No. 7, pp. 810–821. dx.doi.org/10.1139/cgj-2013-0183

Yong, R. N. (1980). “Some aspects of soil suction, shear strength and soil stability,” Geotechnical Engineering, Vol. ll, No.1, pp. 55-76.

Zhou, A. N., Sheng, D., and Carter, J. P. (2012). “Modelling the effect of initial density on soil-water characteristic curves,” Géotechnique Vol. 62, No. 8, pp. 669-680.

VITA

CORRIE WALTON-MACAULAY, P.E.

EDUCATION

DOCTOR OF PHILOSOPHY, Civil Engineering May 2015
University of Kentucky
Lexington, KY
Dissertation: Prediction of Strength and Shear Modulus of Compacted Clays within an Unsaturated Critical State Framework.

MASTER OF SCIENCE, Civil Engineering May 1997
University of Arkansas
Fayetteville, AR
Thesis: Potential effects of Superpave implementation on the Arkansas aggregate industry

BACHELOR OF SCIENCE, Civil Engineering May 1995
University of Arkansas
Fayetteville, AR

REGISTRATIONS

Registered Professional Engineer: Kentucky, 24035
Registered Professional Engineer: Arkansas, 10662

ACADEMIC EXPERIENCE

RESEARCH ASSISTANT 2009 to 2015
University of Kentucky, Department of Civil Engineering

Performed advanced unsaturated triaxial testing, laboratory scaled model testing, and dynamic wave propagation tests. Developed a predictive soil stress-strain and suction-strain constitutive model, based on the experimental test data.

Performed advanced saturated triaxial testing in support of research to investigate a Geogauge for quality control of compacted subgrade, and also in support of research to develop constitutive mechanical relationships for compacted unsaturated soils.

Performed laboratory scaled model testing in support of research to develop calibration techniques for predictive geotechnical relationships for a coaxial impedance soil sensor, and also in support of research to determine unsaturated soil parameters from field stiffness measurements.
Managed the advanced geotechnical engineering research laboratory. Supervised and coordinated the updating of all soil testing equipment. Installed, setup, and calibrated new testing equipment and verified their performance as intended.

Researched the current detect and track technologies suitable to detect, deter and defeat any potential waterside threat or attacks on dams.

Performed a brief literature review of geothermal shaft and pile foundations

Assisted with mineralogy composition testing for sample characterization.

FACULTY INTERN 2009 to 2015
Assisted in and taught sections of the following undergraduate and graduate-level courses.
University of Kentucky, Department of Civil Engineering
CE 471 – Soil Mechanics Lab
CE 579 – Geotechnical Engineering
CE 671 – Advance Soil Mechanics
CE 699 – Introduction to Finite Elements

Developed course lecture in unsaturated soils for CE 671 – Advance Soil Mechanics

RESEARCH ASSISTANT 1990 to 1991
University of Arkansas, Department of Civil Engineering

Conducted various material research experiments. Performed material related research on asphalt, aggregates, and hot mix asphalt to establish potential effects of Superpave implementation on the Arkansas aggregate industry.

REFEREED JOURNAL ARTICLES

Walton-Macaulay, C., Bryson, L.S., Hippley, B.T., and Hardin, B.O. (2014). "Uniqueness of Constitutive Shear Modulus Surface for Unsaturated Soils," *International Journal of Geomechcanics*, ASCE, in print.

REFEREED CONFERENCE ARTICLES

Walton-Macaulay, C.[1], Bryson, L.S., and Guenther, K.J., (2014). "Experimental Study on the Stiffness Degradation of Railroad Ballast Subjected to Clay Fouling," *2014 Joint Rail Conference*, Colorado Springs, CO, 2-4 April 2014.

Kirkendoll, J.[1] and Bryson, L.S. (2011), "Optical Sensor Technology for Dam Security Using LIDAR," *Dam Safety 2011*, The Association of State Dam Safety Officials, Washington, DC, 25-29 September, 2011.

Bryson, L.S., and Walton-Macaulay, C.[1] (2011). "The Effects of Fouling on the Deformation and Stiffness Behavior of Railroad Ballast," 5th *International Symposium on Deformation Characteristics of Geomaterials*, 31 August -3 September, 2011, Seoul, Korea.

REVIEWED TECHNICAL REPORTS

Curd, J., Kirkendoll, J., Dennison, D., Walton-Macaulay, C., Bryson, L.S., Kalinski, M.E., and Lusk, B. (2012), "Waterside Attacks on Dams Detect and Track Technologies," *Technical Report*, submitted to the National Institute for Hometown Security, Somerset, KY, June 2012, For Official Use Only (FOUO).

RESEARCH REPORTS

Walton-Macaulay, C., (2011), "Waterside Attacks on Dams – Detect and Track Technologies," *Progress Report*, Bryson, L.S, Subcontract #04-09-UK, National Institute for Hometown Security, Somerset, KY.

Walton-Macaulay, C., (2010), "Shaft and Pile Foundation Systems Used for Geothermal Applications – A Literature Review," Bryson, L. S., Doctoral Fellowship program SREB, Univeristy of Kentucky, April.

CONFERENCE PUBLICATION REVIEWED

- Reviewer for the Railway Engineering Conference - 2013

Invited Presentations

Technical Presentations

- Prediction of Strength and Small-Strain Stiffness of Compacted Clay," *Dissertation Proposal Progress Presentation*, University of Kentucky, Lexington, KY, June, 2011.
- Prediction of Strength and Small-Strain Stiffness of Compacted Clay," *Dissertation Proposal Presentation*, University of Kentucky, Lexington, KY, June, 2011.
- "Unsaturated Soils" - Institute on Teaching and Mentoring, Atlanta, Georgia, October 21, 2011.
- "Assessment and Mitigation of Water-Side Attacks on Dams," *Project Introduction Presentation*, Waterside Security R&D Advisory Task Group Meeting, Lexington, KY, October 2010.

Non-Technical Presentations

- Minority Representation in Academia - Southern Regional Education Board, Tampa, FL, October 2012.
- "Voices from the Field," The National GEM Consortium, University of Kentucky, Lexington, KY, March 24, 2012.

SPECIAL SERVICES PERFORMED FOR UNIVERSITY

University of Kentucky

- Civil Engineering Department Chair Search Committee Partner (committee member) for the CE Department, University of Kentucky (Spring 2013 – Fall 2014)

FELLOWSHIP

SREB – Southern Regional Education Board 2010 to 2015
Doctoral fellowship
Sponsor: University of Kentucky
Award Amount: Full Tuition, and $20,000 stipend per year

University of Kentucky 2009

Graduate Student Research Assistant Award
Award Amount: Tuition, and $10,000 stipend

PROFESSIONAL AFFILIATIONS

- American Society of Civil Engineers
- Geo Institute
- National Society of Professional Engineers
- Kentucky Society of Professional Engineers, KY Bluegrass Chapter
- National Society of Black Engineers, Professional
- Chi Epsilon National and Honor Society

INDUSTRY EXPERIENCE

CONSULTING ENGINEER 2008 to 2013
CWME, PLLC
Lexington, KY

PROJECT MANAGER / ENGINEER 2006 to 2008
FRA Engineering Inc.
Danville, KY

SENIOR GEOTECHNICALENGINEER 2004 to 2006
Central Associated Engineers, Inc.
Lexington, KY

GEOTECHNICAL / MATERIALS ENGINEER 1999 to 2004
Grubbs, Huskyn, Barton and Wyatt Inc.
Lexington, KY

STAFF ENGINEER 1997 to 1999
Grubbs, Huskyn, Barton and Wyatt Inc.
Lexington, KY

HIGHWAY ENGINEERING INTERN Summer 1995, 1994, 1993
Arkansas State Highway and Transportation Department
Construction Division
Little Rock, AR
